DEVELOPMENT OF A NEW RING SHEAR APPARATUS FOR INVESTIGATING THE CRITICAL STATE OF SANDS

BY

ABOUZAR SADREKARIMI

B.S., University of Tehran, 2002
M.S., University of Tehran, 2004

DISSERTATION

Submitted in partial fulfillment of the requirements
for the degree of Doctor of Philosophy in Civil Engineering
in the Graduate College of the
University of Illinois at Urbana-Champaign, 2009

Urbana, Illinois

Doctoral Committee:

Assistant Professor Scott Olson, Chair
Professor Gholamreza Mesri
Professor Timothy Stark
Associate Professor Youssef Hashash
Professor Erol Tutumluer

ABSTRACT

The present study investigates the shearing behavior of sands pertinent to liquefaction and critical state soil mechanics using an improved ring shear apparatus designed and constructed at the University of Illinois. Undrained/constant volume and drained triaxial compression and ring shear tests (sheared to about 30 m of shear displacement) were performed on two clean sands and one silty sand. Shear displacements localized when the peak friction angle was mobilized and subsequent shear displacements occur only within the shear band which was (10 -14)×D_{50} thick.

Considerable particle damage and crushing was observed within the shear band, particularly for dilative specimens, which led to volumetric contraction in the shear band. The critical state line (corresponding to the critical state after particle damage and crushing was complete) was much steeper and plotted below conventional critical state lines in e – log σ' space measured using triaxial tests. Both dense and loose sands reached this final state. Accordingly, two definitions of critical state of sands with and without particle damage are proposed.

The critical state friction angle from the ring shear tests was independent of the initial sand fabric and decreased only slightly with stress level, becoming essentially constant at stresses larger than 100 - 200 kPa. Particle crushing induced in the ring shear tests increased the critical state friction angle by a few degrees by producing a wider grain size distribution and more angular particles. However, because some of the triaxial specimens likely did not reach a critical state, the mobilized friction angle from triaxial tests was influenced by the initial fabric of the sand.

A constant critical shear strength was achieved at very large shear displacements (>750 cm) in the ring shear tests, and before this the shear resistance of sands was dependant on the amount of shear displacement and particle crushing. Yield strength ratios of contractive specimens ranged from 0.15 to 0.31, while the critical strength ratios of both contractive and dilative specimens decreased from a range of 0.04 – 0.21 (for the original sand) to 0.01 – 0.07 (for the crushed sand).

To the owner of the science which I have studied and researched:

To GOD

ACKNOWLEDGMENTS

I am very grateful to my advisor Professor Scott Olson throughout my doctoral program. I highly appreciate his guidance, support, and encouragement. His commitment to me and my research was far exceeding my expectations of an advisor/graduate student relationship. I am fortunate to have worked with him.

I also would like to express my sincere appreciation to the members of my doctoral defense committee members: Professors Gholamreza Mesri, Timothy Stark, Youssef Hashash, and Erol Tutumluer for their constructive criticism and input. In particular Professor Gholamreza Mesri who I benefited from his great wisdom, vision, and experience throughout my entire study and research.

Thanks to Mr. Tim Prunkard (head of the machine shop at the Civil and Environmental Engineering Department, University of Illinois) for his critical review of various designs for the new ring shear device, Dr. Grzegorzas Banas for guidance on the instrumentation, and Mr. Darold Marrow for his assistance in constructing the device.

I extend my thanks to all former and current geotechnical engineering graduate students for their friendship and thoughtful discussions which contributed greatly to my education, especially Dr. Nejan Huvaj and Kashif Muhammad for their continuous support, company, and encouragement during the thousands of hours spent in my office, library, or cafes preparing this dissertation.

I owe the most to my parents Professor Jamshid Sadrekarimi (who introduced me to the challenging and rewarding profession of geotechnical engineering) and my mother Vajiheh Sadeghi-Farshi for their love, support, and understanding in the course of my Ph.D. studies. I could never thank them enough for all of the sacrifices they have made for me so that I may achieve every one of my goals. Thanks to my sisters Dr. Shabnam Sadrekarimi and Shaghayegh Sadrekarimi for their continuous support. I would especially like to thank my wife for her support and patience during the demanding period of my life.

TABLE OF CONTENTS

LIST OF FIGURES

LIST OF TABLES

CHAPTER 1: INTRODUCTION

1.1 STATEMENT OF PROBLEM

Liquefaction is an important issue for geotechnical engineers and predicting soil resistance during and after liquefaction (both static and cyclic) is key to determining deformations of and potential damage to structures. During liquefaction, shear stresses (induced by cyclic or static loadings) generate positive excess pore water pressures in contractive saturated sandy soils. In response, the effective stress and the shear resistance decrease. Continued shearing then causes the shear resistance to drop to a minimum critical value, the critical shear strength [s_u(critical)]. This shear strength is significant in evaluating the safety of some earth structures, particularly those subject to earthquakes. Numerous liquefaction flow failures such as Fort Peck Dam slide, Calaveras Dam slide, Lake Merced Bank slides, and Lower San Fernando Dam slide (Olson 2001) in sandy soils clearly indicate the importance of this parameter. The critical state of soil is a state of indefinite plastic shearing at constant stress and constant volume (Schofield and Wroth 1968) and is an important concept in geotechnical engineering applications and serves as the basis for failure, failure criteria, and liquefaction susceptibility for many constitutive models. Therefore, reliable determination of the critical state of a soil and the overall validity of the critical state theory are very important in many geotechnical engineering applications.

s_u(critical) is estimated as the liquefied shear strength [s_u(liq)] analyzed from field flow failure cases (e.g. Stark and Mesri 1992; Olson 2001). An alternative approach for defining s_u(critical) is by laboratory experiments on reconstituted specimens. However, measuring this strength in the laboratory is challenging since it is difficult to fulfill all of the requirements to measure s_u(critical) with existing devices, e.g., large shear strain/displacement, uniformity of stress and strain at large shear strain/displacement, undrained or constant volume shearing, direction of shearing relative to depositional planes, constant cross sectional area, etc. A reliable laboratory technique to measure s_u(critical) would be beneficial to complement estimates of s_u(liq) back-calculated from field case histories – the current state-of-practice. The triaxial test which is commonly used to defined s_u(critical) doesn't fulfill most of the requirements for measuring this

strength and s_u(critical) determined from the triaxial tests is in general larger than the s_u(liq) back-calculated from field flow failures and as a result of triaxial tests some researchers have questioned the critical state soil mechanics for sands. However, the ring shear (RS) test is able to shear a soil to very large shear displacements and does not have most of the limitations of the triaxial test. A larger shear displacement would allow a state of complete particle rearrangement and particle crushing (critical state) to be reached in RS tests and to model soil behavior in very large displacement flow slides. In contrast the limited displacement capacity of the triaxial device may not achieve complete particle rearrangement and particle crushing, thus limiting its application for studying large displacement landslides.

Most laboratory shear tests on sands have been performed on very loose moist tamped specimens of rather incompressible siliceous sands (e.g., Bjerrum et al. 1961; Castro 1969; Sladen et al. 1985; Kramer and Seed 1988; Konrad 1990a; Ishihara 1993; Pitman et al. 1994; Chu and Leong 2002) whereas field sand deposits are rarely as loose as moist tamped specimens and often include non-siliceous minerals (e.g., carbonates, mica and clay minerals). Moreover, in many geotechnical field situations such as landslides, failure of soils beneath long foundations (e.g. strip or wall), and failure of retaining structures are close to plane strain situations (Tatsuoka et al. 2003; Liu 2006; Wanatowski and Chu 2007; Chu and Wanatowski 2009), whereas most laboratory experiments on granular materials are performed with triaxial compression (TxC) tests. Strength and deformation characteristics of granular materials loaded in plane strain may differ considerably from those observed in triaxial tests and the use of strength parameters defined from TxC tests may results in conservative designs (Lee 1970; Ko and Davidson 1973).

Strain localization into a shear band of a finite thickness has been observed in many field failures of geotechnical systems, such as landslides, shallow foundations, and earth retaining structures (e.g., Hsu and Liao 1998; Watanabe et al. 2003; Cheuk et al. 2008). Understanding the mechanism of shear band formation and its characteristics has been of increased interest over the past two decades (Vardoulakis and Graf 1985; Peters et al. 1988; Vardoulakis 1996; Finno et al. 1997; Viggiani et al. 2001; Torabi et al. 2007). However, this issue has not been clearly studied at very large shear displacements that are associated with most of the cases where shear localization readily happens.

Crushing of sand particles is a common phenomenon in many geotechnical engineering applications and practices. For example, failures involving steep slopes often lead to crushing and spreading of the failed material upon impacting the toe of the slopes. Granular materials in sand drains and stone columns also may experience crushing as they are subjected to static and dynamic loads (Chik 2004). Particle crushing and damage changes the initial engineering properties by which the structure was designed for, such as the hydraulic conductivity, shear strength and elastic modulus (e.g., Vesic and Barksdale 1963; Bishop 1966; Lee and Seed 1967; Terzaghi et al. 1996; Feda 2002). However there have been limited studies on how particle crushing affects the engineering properties of the soil after they are crushed and thus the potential effects on the construction design of an engineering project.

According to the critical state theory, a unique relation exists between void ratio and effective stress for every sand after shearing to large displacement (Roscoe et al. 1958; Schofield 1980). This concept has been widely debated among researchers (e.g., Vaid et al. 1990; Been et al. 1991; Castro et al. 1992; Negussey and Islam 1994) who have mostly focused on the behavior of loose sands. Some researchers have found that critical state also happens within the shear band of dense sands, but the globally measured effective stress and void ratio are not sufficient to quantify the localized behavior within these shear bands (e.g., Mooney et al. 1998; Rechenmacher and Finno 2004). Moreover, whether or not a critical state is reached in the small shear strain testing devices (e.g. triaxial, direct shear, or simple shear) particularly when particles crush, would make the judgments regarding such critical state concepts questionable. Furthermore, yield and critical state friction angles are the most important soil parameters in stability analysis and are used in most soil constitutive models. The effects of particle shape, initial soil fabric, consolidation stress, intermediate principal stress, interparticle friction, and particle crushing on these friction angles have been debated by many researchers who mainly did triaxial tests (e.g., Lee and Seed 1967; Skinner 1969; Been et a. 1991; Chan and Page 1997; Liu and Matsuoka 2003) and the limited displacements of the triaxial device may have had contributed to some of the disagreements among these research. The critical state friction angle could be very different if particles crush and this has not

been previously studied because of the very large shear displacement required to reach a critical state when particle crushing happens.

Finally, the dependency of yield and liquefied shear strengths on the consolidation stress and the ranges of yield and liquefied strength ratios have also been discussed among researchers (e.g., Hanzawa 1980; Sladen et al. 1985; Stark and Mesri 1992; Ishihara 1993; Sasitharan et al. 1993; Baziar and Dobry 1995; Vaid and Sivathayalan 1996; Olson and Stark 2003a, b). Triaxial and direct simple shear (DSS) tests have been used to address this issue (Olson 2001) but the laboratory results have been in general larger than those back-analyzed from field liquefaction case histories which displaced larger than the few centimeters of displacements in the triaxial and DSS tests and were at a plane strain condition.

1.2 RESEARCH OBJECTIVES

The objective of this research is to investigate the behavior of sands particularly at shear displacements larger than those attained in relatively small shear displacement triaxial and simple shear tests. This would allow studying the effects of shear banding, particle crushing, and shear displacement on the shear strength of sand and the critical state concepts.

1.3 SCOPE AND OUTLINE OF CURRENT STUDY

The current research includes four major parts to pursue the research objectives. These are:

1.3.1 Developing a new ring shear device for testing of sands

1.3.2 Selecting a few sands with different characteristics

1.3.3 Triaxial compression (TxC) and ring shear (RS) experiments on sands

1.3.4 Interpreting critical state, and yield and liquefied strengths using the experimental results

The remainder of this thesis is organized as follows. Chapter 2 presents a brief review of liquefaction behavior of sands. In Chapter 3, common laboratory shear tests are

described and the design and construction of a new RS apparatus for large shear displacement testing is presented. Chapter 4, describes the sands tested and the details of the experiments. Chapter 5 presents and compares some typical results from TxC and RS tests. In Chapter 6, shear localization in RS tests, and characteristics and importance of shear bands are studied. Chapter 7 describes the role of particle damage and crushing on the shear behavior observed in RS tests. In Chapter 8, the critical states and critical state lines of the test sands are studied using TxC and RS test results and the factors that influence the critical state line (CSL) are thoroughly discussed. Also, the implications of using CSLs from TxC or RS tests are explained. In Chapter 9, the effective stress friction angle mobilized in sands is examined using both RS tests at virtually unlimited displacements and parallel TxC tests at limited displacement, and some of the factors which influence the effective friction angle are discussed. In Chapter 10, the yield and critical shear strengths obtained from TxC and RS tests are studied. The factors affecting the yield and critical strength ratios are further assessed and the strength ratios are compared with previous laboratory experiments and field observations. Chapter 11 presents the conclusions derived from this study, and Chapter 12 describes avenues for future research.

CHAPTER 2: PREVIOUS RESEARCH AND BACKGROUND

2.1 LARGE STRAIN (LIQUEFACTION) BEHAVIOR OF SANDS

2.1.1 Liquefaction

Casagrande (1976) defines liquefaction as the response of loose, saturated sand when subjected to strain or shock that causes substantial strength loss and, in extreme cases, flow slides. Casagrande goes on to describe cyclic liquefaction as the response of a dilative sample to cyclic loading when the peak pore pressure reaches the total confining pressure momentarily in each shearing cycle. Seed (1979) defines liquefaction as a condition where a soil undergoes continued deformation at a constant low residual stress due to high pore water pressure and the consequent drop of effective confining pressure to a very low value; further he states that the pore water pressure is built up by static or cyclic stresses. Castro et al. (1982) define liquefaction as a phenomenon in which a mass of soil subjected to undrained monotonic, cyclic or shock loading loses considerable shear strength and flows like a liquid until the driving shear stress becomes as small as the shear resistance of the soil mass. Robertson (1994) uses the term "flow liquefaction" to differentiate this from cyclic liquefaction. He proposed that depending on whether a sand is strain-hardening or strain-softening, it may experience "flow liquefaction" or "cyclic liquefaction". Strain-softening material can experience either "flow liquefaction" or "cyclic liquefaction"; however, strain-hardening material can only experience "cyclic liquefaction". Terzaghi et al. (1996) define liquefaction as the tendency of contractive sands to generate large positive pore water pressures and reduce the undrained shear strength to the critical shear strength when sheared under undrained conditions. Poulos (1997) defines liquefaction as the undrained shear failure of loose sand or soft clay that happens when the in-situ driving shear stresses on the soil mass prior to failure exceed the undrained shear strength of the mass at large displacement. The manifestation of this behavior is the liquefaction flow failure of a slope, or an embankment which can move at high speeds for distances of hundreds of meters, and has been observed in both natural and man-made soils. The triggering of liquefaction can be caused by monotonic or dynamic loading. Monotonic loadings which could trigger liquefaction include: underwater soil deposition, surface runoff, heavy rainfall or snow melt, and etc. Dynamic

loads which may cause liquefaction are earthquakes, tidal changes, traffic vibration, geophysical explorations, and blasting. When the loading on the soil is applied so quickly that no volume change occurs, the loading is referred to as undrained. During this period, the interaction between soil particles and pore water in contractive sands tends to reduce the contact force among soil particles. The diminishing contact force among particles contributes to the overall loss of stability, or strength of the entire soil matrix. After liquefaction has been initiated and soil matrix transforms into a fluid-like material, all the bonding history has been destroyed and rearranged (Hryciw et al. 1990; Kramer 1996). Example of liquefaction flow failures caused by static loading include Calaveras Dam (Hazen 1918) and Fort Peck Dam (Casagrande 1965) and examples of flow failures induced by seismic loading include Lower San Fernando Dam (Castro et al. 1989; Seed et al. 1989) and Sheffield Dam (Seed et al. 1969). Casagrande (1936) used the term "flow structure" to describe the conditions that existed in the liquefied soil. Casagrande (1976) postulated that when flow structure develops, soil particles constantly rotate around the surrounding particles in order to maintain a minimum frictional resistance. This agitation forms a chain reaction of particle movement and spreads the flow structure within the shearing liquefied soil. After the movement is terminated, the liquefied soil structure has been totally rearranged and then densified due to dissipation of excessive pore water pressure. As indicated by Castro and Poulos (1977), the development of soil liquefaction is affected by the initial conditions, including void ratio, confining pressure, and shear stress. Evaluating the potential for liquefaction and flow slide requires evaluating the shear strength of liquefied soil. This issue has been one of the most challenging topics in geotechnical engineering because the liquefied shear strength is difficult to measure accurately.

2.1.2 Sliding Surface Liquefaction

Localized liquefaction in saturated sandy soil along the shear zone due to grain crushing (Figure 2.1) during shearing after failure (Sassa 2000) is termed "sliding surface liquefaction". Grain crushing leads to tendency for contraction, generates high pore water pressures, and lowers the pore water pressure dissipation rate. This phenomenon is responsible for the rapid long run out motion of some landslides. In contrast, mass

liquefaction is caused by destabilizing the structure of a loose saturated soil mass, causing rapid generation of pore water pressure and a flow slide (Hutchinson 1986; Spence and Guymer 1997) where grain crushing is not necessary. Sliding surface liquefaction can occur in soils of nearly any density if crushing happens along the sliding surface, generating excess pore water pressure. Even in initially drained conditions, excess pore water pressure can accumulate in the shear band and trigger sliding surface liquefaction (Okada et al. 2000b). Grain crushing continues until the effective normal stress decreases to a certain value below which grain crushing does not occur. Since the shearing takes place only along the sliding surface it can be termed landslide with basal flow and can transport the sliding mass without much disturbance. For example the 1995 Kobe earthquake triggered a rapid sliding surface landslide in Nikawa that transported a standing forest on it (Sassa 2000). However, if the landslide mass is wet and soft, then it would be prone to be disturbed by sliding and may transform to a debris flow or debris avalanche (Sassa 2000).

One of the most famous landslides in the world, the 1903 Franc landslide in Canada (Cruden and Krahn 1978) where the moving mass traveled over the terrace deposits up to 1800 m was also a landslide with basal flow or a debris avalanche with basal flow (Sassa 1984). Sassa (2000) describes more instances of sliding surface liquefaction landslides, suggesting that further liquefaction happened likely by grain crushing and therefore they are not liquefaction induced landslides but landslide induced liquefactions.

2.1.3 Shear Localization and Bifurcation

It is well known that shear banding occurs during testing of dense specimens. Several researchers have studied how shear banding affects critical state. The Cambridge University group (Cole 1967; Coumoulos 1968; Stroud 1971) studied the behavior of shear bands through simple shear testing on Leighton Buzzard sand. Coumoulos (1968) incorporated a technique involving the use of gamma rays to quantify void ratio evolution within shear bands that formed during tests. The results indicated that the local area where the shear band formed dilated to a much greater degree than the surrounding material throughout shearing. The material outside the shear band continued to dilate even after the material within the band had achieved a constant void ratio. In contrast,

research by Roscoe (1970) and Rechenmacher (2000) indicated that once the shear band had formed, all subsequent deformation was concentrated within the shear band. Experiments by Stroud (1971) further illustrated the difference between the behaviors in the shear band versus that of the surrounding material. Stroud incorporated 1 mm diameter lead shots spaced approximately 4 mm, into samples of Leighton Buzzard sand. X-Rays were used to track movements of the steel balls and measure void ratio evolution, while global void ratio was calculated from boundary displacements. The measurements indicated that the sand within the shear band dilated to a much greater degree than what was indicated from global measurements. Thus, the experiments of the Cambridge Group confirmed that the specimen behavior inside and outside of the shear band was different and that this difference persisted through the evolution to critical state.

Harris (1994) showed that material behavior within a shear band was highly erratic. Mooney (1996) further found that averaging techniques, such as linear regression of groups of many displacement points, were needed to obtain appropriate, reliable quantification of shear band strains. Harris (1994) also found that shear banding occurred both in undrained and drained plane strain tests on loose to very loose sands. However, Finno et al. (1996) found that the effect of shear bands on the critical state derived from loose specimens was minimal since density variations between the shear band and the surrounding material were insignificant in loose specimens. Desrues et al. (1996), using X-ray tomography, confirmed that previously assumed uniform deformation patterns occurring in sands during triaxial compression (TxC) tests were actually symmetric patterns of strain localization. These illustrate that shear banding occurs in loose and dense specimens, during both drained and undrained loading, and both triaxial and plane strain conditions.

2.2 DEFINITIONS AND TERMINOLOGIES

2.2.1 Critical State and Steady State

Following the work of Casagrande (1940), Roscoe et al. (1958), and Schofield and Wroth (1968), the critical state is the state at which the soil continues to deform at constant stress and constant void ratio under drained conditions. Schofield and Wroth (1968) envisioned that soil at the critical state would flow as a frictional fluid; however,

they stopped short of discussing structure, rate of shearing, and neglected the possibilities of crushing or orientation of particles partly. Crushing however was recognized by Bolton (1986) as the cause of loss of dilatancy with increasing stress, and as the mechanism generating Schofield's critical state. Grain crushing in sands during both isotropic compression and triaxial shearing was found by Coop (1990), McDowell et al. (1996), and Lade et al. (1996). However, the final states in which soils sheared continuously without change in shear and mean stresses and void ratio were very difficult to obtain even using a ring shear (RS) apparatus (Coop et al. 2004).

Cognitive of the limitations in the definition of critical state (structure, rate and particle crushing), Castro (1969) and Poulos (1981) extended the critical state concept to undrained shearing of contractive sands. They used the term "steady state" (in analogy to the steady state flow of fluids which happens under no acceleration) and included the term "deformation" to emphasize that the steady state exists only after the structure of the soil is completely remolded into a flow structure by deformation that differs from the at-rest. According to Poulos (1981), the "steady state of deformation" for any mass of particles is a state in which the mass continuously deforms at constant volume, constant normal effective stress, constant shear stress, and constant velocity. The steady state of deformation is achieved only after all particle reorientation and rearrangement have reached a statistically steady state condition and after all particle breakage, if any, is complete, so that the shear stress needed to continue deformation and the velocity of deformation remains constant.

These differences between critical state and steady state are in definition only, and the particular flow structure and applicable strain rate have not been defined (Been et al. 1991). There is no documented evidence of a flow structure, (or for that matter, lack of structure) at steady state and it seems that only the inertia of the static mass should be overcome to regain a steady state. Therefore, a clear distinction of the steady state from the critical state is not possible and this has led to some disagreement regarding whether critical state and steady state are the same (Been and Jefferies 1985; Been et al. 1991). In general, the steady state has traditionally been measured using undrained tests on contractive sand specimens, whereas the critical state is generally inferred from drained tests on dilative sands (Been et al. 1991).

Following the precedent set by many previous researchers (Sladen et al. 1985; Poorooshasb 1989; Been et al. 1991; Verdugo and Ishihara 1996; Riemer and Seed 1997; Li and Wang 1998; Jang and Frost 2000), a single term, the critical state, is used here to describe critical state, steady state, residual state (Finn 1971; Iverson et al. 1998) and ultimate state (Konrad and Pouliot 1997; Infante-Sedano 1998; Iverson et al. 1998) of sands.

2.2.2 Critical State Line

The critical void ratio reached at critical state is a function of stress and the stress dependency of the critical void ratio can be represented by a single curve in void ratio versus effective stress space. This curve is termed the critical state line (CSL) (Roscoe et al. 1958; Schofield 1980). Critical state line has been traditionally (Roscoe et al. 1958; Roscoe and Burland 1968; Schofield and Wroth 1968) represented by a linear-log relationship as below:

$$e_{cs} = \Gamma_{cs} - \lambda_{cs} \log \sigma'_{cs} \qquad 2.1$$

Where e_{cs} and σ'_{cs} are the void ratio and effective stress at critical state and Γ_{cs} and λ_{cs} are the intercept (at σ'_{cs} = 1 kPa) and slope of the CSL, respectively. All states above the CSL are volumetrically contractive and all states below the CSL are dilative.

2.2.3 Uncertainty in the Critical State Line

According to critical state theory, a unique critical void ratio exists for a given sand, dependent only on confining stress. This means that CSL, which defines the relationship between critical void ratio and effective confining stress is independent of initial state. Several researchers have investigated this uniqueness and have questioned the existence of single CSL (e.g. Vesic and Clough 1968; Murphy 1970; Konrad 1990a, b; Vaid et al. 1990; Konrad 1993; Lade and Yamamuro 1996; Riemer and Seed 1997; Mooney et al. 1998; Finno and Rechenmacher 2003; Cheng et al. 2005). In particular the effects of consolidation stress level (Konrad, 1990a; Riemer and Seed 1992; Konrad and Pouliot, 1997; Yamamuro and Lade 1998; Vaid and Sivathayalan 1999), shearing stress path

(Vaid et al. 1990; Negussey and Islam 1994; Vaid and Thomas 1995), particle crushing (Konrad and Pouliot, 1997), sample preparation method (Kuerbis and Vaid 1989; Vaid et al. 1990), strain rate (Hird and Hassona 1990; Been et al. 1991), and drainage conditions (Casagrande 1975; Alarcon-Guzman et al. 1988) on the CSL have been debated.

Castro et al. (1992) performed drained and undrained triaxial tests on loose samples and found that the location of the CSL was unaffected by sample preparation, initial state, and drainage conditions. Negussey and Islam (1994) performed TxC and TxE shear tests on loose sands to assess the effects of bedding orientation on the uniqueness of CSL, and found that the CSL was unique only for a particular mode of shearing (compression or extension). Vaid et al. (1990) found that the location of CSL derived from extension loading was dictated by the depositional void ratio. Based on these findings, the critical state appears to be dependent on mode of shearing. Been et al. (1991) tested Erksak sand in triaxial compression and found that the critical state was independent of sand fabric and shear strain rate. Similarly the triaxial tests of Verdugo (1992) on Toyoura sand indicated that the CSL was independent of initial soil fabric and initial state (density and pressure) of the soil (Ishihara 1993; Verdugo and Ishihara 1996).

The majority of data that has addressed the uniqueness of critical state, including those of the research described above, has been based on the response of loose sands only (e.g., Been et al. 1991). This has been in part because of the importance of critical state in evaluating liquefaction potential, to which loose, contractive sands are most susceptible. More importantly, measurements become problematic while trying to reach the critical state within dense, dilative sands in the triaxial apparatus. Specifically, prior to critical state, deformations localize into shear bands of concentrated strain. In triaxial tests global measurements are generally used to quantify specimen deformation. These methods are adequate to quantify specimen response during uniform global shear deformation. But in the presence of nonuniform deformations, such as shear bands, global measurements do not reflect true specimen response. Thus, dense specimens are either not used in establishing the location of CSL, or methods to avoid shear banding in the evolution to critical state are used (e.g., Chu and Lo 1993).

2.2.4 Phase Transformation and Quasi-Critical State

Phase transformation state (PTS) is the point of minimum effective mean stress at which the sand response changes from contractive to dilative (Ishihara et al. 1975). In addition to the effective mean stress, the shear stress may drop to a minimum value and the soil may temporarily shear with nearly constant effective stress, and constant shear strength; this state is commonly termed a quasi-critical state (Alarcon-Guzman et al. 1988). This kind of behavior is also called "limited liquefaction" or "flow with limited deformation". The range of strain over which the soil is in the quasi-critical state (QCS) condition is variable and phase transformation point can exist for conditions in which QCS does not develop and phase transformation occurs without a post-peak reduction in shear resistance. Some researchers have treated liquefaction and limited liquefaction within the same framework (Sladen et al. 1985; Mohamad and Dobry 1986; Vaid et al. 1990). Plane strain experimental results show that the QCS produces a distinct soil state, which strictly speaking, doesn't coincide with the PTS (Finno et al. 1997). In other words, the local minimums in deviator stress and mean effective stress do not occur at the same axial strain, with the QCS preceding PTS. Despite the fact that the PTS and QCS are very close to each other in the stress path plots, the QCS may occur at axial strains 40% lower than that required for reaching PTS, though in absolute terms, this strain difference rarely exceeds 1.5%. Unlike the PTS, a QCS is not mobilized in tests that start from soil states that are well below the CSL (Murthy et al. 2007). This indicates that the change in effective stress with respect to axial strain was not constant at the point of minimum shear since the excess pore pressure was still changing. And therefore the point of phase transformation cannot lie on the CSL and there is no fundamental reason to use the point of quasi-critical state (or the phase transformation point) as a critical state point.

2.2.5 State Parameter

Several parameters have been proposed to express the liquefaction susceptibility of a sand deposit (Jefferies and Been 1987; Yamamuro and Lade 1998; Klotz and Coop 2001). Among them, the most widely used is the difference between the consolidation void ratio (e_c) and the critical state void ratio (e_{cs}) corresponding to the consolidation stress, σ'_c (Roscoe and Poorooshasb 1963; Wroth and Bassett 1965; Been and Jefferies 1985;

Ishihara et al. 1991), which is commonly referred to as the (critical) state parameter (ψ_{cs}) and indicates soil behavior as a combined function of density and effective stress. For negative values of ψ_{cs} no liquefaction is observed; for positive values of ψ_{cs} the severity of liquefaction, in terms of strength loss, increases with increasing ψ_{cs}. Thus, by means of the state parameter, the behavior of a soil can be correlated with the distance of its consolidation state from the CSL (Sladen et al. 1985; Jefferies and Been 1987). Several advanced constitutive models make use of ψ_{cs} by defining a number of their components, such as the dilatancy, the plastic modulus and the peak strength, as functions of ψ_{cs} (e.g. Jefferies 1993; Manzari and Dafalias 1997; Gajo and Muir Wood 1999). State parameter approaches have been increasingly used in the analysis of geotechnical structures and the interpretation of site investigation data in sands (e.g. Been and Jefferies 1993; Konrad 1998; Klotz and Coop 2001). Here, ψ_{cs} is used to evaluate the strength ratios and a general state parameter (ψ_s) is introduced as the difference between the void ratio on the compression line (e_c) and the void ratio on a particular state line in the e-log σ' space at the same σ'_c. This includes both ψ_{cs} and ψ_{yield} (difference between e_c and the void ratio at σ'_c on the line connecting e and log σ' pairs at yield).

2.3 FACTORS AFFECTING LIQUEFACTION BEHAVIOR

2.3.1 Initial Effective Stress

The initial state of a sand (initial void ratio and effective stress) affects its susceptibility to liquefaction. As shown schematically in Figure 2.2 when the initial state of the sand plots to the right of the critical void ratio line, the soil exhibits a tendency to contract under drained conditions. This strain-softening behavior can produce static liquefaction when static loading is applied. When the initial effective stress falls to the left of the line, the tendency to dilation in strain-hardening behavior prevents static liquefaction.

2.3.2 Initial Void Ratio

Under undrained conditions, the global void ratio of a soil remains constant throughout the process of deformation. Figure 2.3 schematically illustrates that tests with different initial effective stresses but at constant void ratio arrive at the same point on the

critical void ratio line. By projecting the same behaviors on the stress-path space with the same initial void ratio, various initial effective stresses and various stress paths mobilize the same critical shear strength.

2.3.3 Particle Size Distribution and Fines Content

While a small percentage of silt "rattling around" within the void structure will have little or no effect on the liquefied shear strength, it can significantly alter the density of the sand. In addition, because of the much wider variety of possible fabrics in silty sands, it is very difficult to accurately replicate the fabric of in-situ silty sands with reconstituted laboratory specimens (Riemer and Seed 1997) and therefore great care must be taken in drawing conclusions from comparing tests with varying fines contents.

The influence of fines content on sand behavior has been interpreted in several ways. Some studies have used the density of the entire silty sand for their comparisons and have concluded that the presence of fines decreases liquefaction potential (Tokimatsu and Yoshimi 1983; Seed et al. 1983; Robertson and Campanella 1985; Kuerbis et al. 1988; Pitman et al. 1994). For example, Pitman et al. (1994) tested Ottawa sand (C109) with non-plastic crushed quartz fines and kaolinite. They performed undrained TxC tests at an initial confining pressure of 350 kPa, and they varied the fines content from 0 to 40% and concluded that the effect of non-plastic fines was to create a slightly more dilative response resulting in a sand that is less likely to liquefy. They computed relative densities based on the maximum and minimum void ratios of the entire silty sand. Hence in their comparisons the relative density increases very quickly as the finer fraction is increased. This rapid increase tends to explain the reasons for their subsequent conclusions, namely that the presence of fines slightly decreases the liquefaction potential of the sand due to increased dilatancy. Similarly, it has been reported by Seed et al. (1985) that if silty sand has the same standard penetration value $(N_1)_{60}$ as the clean sand, the addition of fines increases its liquefaction resistance (Seed et al. 1985).

Based on the idea that it is the coarser sand skeleton which actually carries the shearing load, some studies have interpreted the effect of fines using the density of the sand matrix alone and have concluded that fines increase liquefaction potential (Salden et al. 1985; Troncoso and Verdugo 1985; Finn et al. 1994; Lade and Yamamuro 1997;

Ovando-Shelly and Perez 1997; Yamamuro and Lade 1998). They argue that this effect is due to the particle arrangement between larger and smaller grains that develops within a specimen. With a greater percentage of fines, a lower sand matrix density is achieved and the specimen has a higher compressibility, making it more susceptible to liquefaction. For example, Yamamuro and Lade (1997) studied the effect of nonplastic fines on static liquefaction behavior of four different clean sands (Nevada 50/80, Nevada 50/200, Ottawa 50/200, and Ottawa F-95) by undrained triaxial compression tests. The basis of comparison for different gradations of sands with varying fines content was to obtain the loosest possible density by utilizing the dry funnel deposition method. They found that increasing the fines content greatly increased the liquefaction potential and the clean sand always indicated the highest resistance to liquefaction.

And finally some researchers have found that there is an optimal silt content at which the sand's resistance to liquefaction reaches its minimum value. Silt content greater or less than this optimal value will lead to an increase of the sand's resistance to liquefaction (Law and Ling 1992; Koester 1994; Zlatovic and Ishihara 1995; Thevanayagam and Mohan 1998; Garga and Infante-Sedano 2002). For example, Garga and Infante-Sedano (2002) performed a series of RS tests on Unimin 2010 sand at various fines contents and showed that at a particular void ratio increasing the fines content reduces the critical shear strength up to a fines content of 30% and further increase in fines content increases the critical shear strength. This threshold amount of fines content is similar to the limit proposed by Zlatovic and Ishihara (1995). Up to this threshold limit of 30%, the fines simply float in the voids while the strength is provided by the skeleton formed by the parent sand; above this threshold fines content, fines begin to contribute to the interparticle structure and strength. It has also be observed that increasing the fines content up to a threshold fines content (e.g. 30%) lowers the position of CSL in the e – log σ' space and beyond this fines content the location of CSL rises to larger void ratios (Pitman et al. 1994; Yang et al. 2006). Overall it is not the global void ratio controlling the critical shear strength of silty soils but rather the skeleton void ratio of the sand structure (Rahman and Gnanendran 2008).

2.3.4 Plasticity of Fines

Ishihara (1993) suggested that the influence of fines on post-liquefaction strength is likely described by the plasticity index of the fines. He concluded that: "plastic fines increase the cyclic strength of the fine-grained sand, but the nonplastic fines reduce the strength of the fine-grained sand". However, Prakash et al. (1998) believe that an increase of the plasticity of fines does not necessarily mean increased resistance to liquefaction. They argue that there is a critical value of plasticity index (PI) below which the increase of plasticity index lowers the cyclic stress ratio for liquefaction and beyond this critical value, the increase of plasticity index increases the value of the cyclic stress ratio for initial liquefaction.

The effects of fabric, aging, and cementation are also quantitatively unknown. It appears that cementation and aging may slow down the pore pressure generation and clearly the importance of fabric in fine grained soils, such as silts, needs to be recognized when evaluating the pore pressure generation (Prakash et al. 1998). Poulos (1997) suggested that the fines content, or more broadly, the particle size distribution cannot be separated from the soil composition as a distinctly quantifiable parameter.

2.3.5 Particle Crushing and Damage

Experimental observations made by Drescher and de Josselin de Jong (1972) and Mandl et al. (1977), as well as DEM simulations (e.g., Djordjevic and Morrison 2006) have shown that local contact stresses among sand particles can be much larger than the average stress applied to the surface of a sand bed, and particle crushing occurs primarily as a result of large stress concentrations developed along particle asperities. In a shearing granular mass, large internal shear stresses (τ) apply a torque to individual particles (Davies et al. 1999). As particles attempt to rotate in a confined environment, contact torques are resisted by overburden stresses, and stresses at grain contacts increase. When the contact stresses exceed the particle strength, crushing is initiated and stress concentrations at particle contacts quickly decrease due to the increase in the size of the contact area. Since overburden stress prevents particle rotation, more particle crushing occurs as overburden stress increases. However, because particle crushing during shearing is largely a consequence of the shear-induced torque, the effective overburden

stress required to initiate crushing in the absence of shearing is several times greater than that required to initiate shear-induced crushing (Luzzani and Coop 2002). The shearing motion continuously alters the position of individual particles such that they eventually fracture under the combined action of local contact forces (Mandl et al. 1977). Iverson et al. (1996) modeled the criterion for particle crushing as below:

$$\sigma'_{nl}\, sec(\omega+\beta) d_N \geq \pi T d_m / 2 \qquad \text{(for} \quad 0 < \beta + \omega < 90^{\circ}) \qquad 2.2$$

where β is the angle between the macroscopic shear plane and intergranular slip plane; σ'_{nl} is the local effective stress supported by a particle normal to the macroscopic shear plane; ω is the friction angle defined parallel to β; and d_N is the diameter of the largest neighboring grain. The term $4T/\pi d_m^2$ is the grain strength defined in a Brazilian tensile strength test (ISO 1996), where T is the failure load required to split a grain and d_m is the mean diameter of the grain that undergoes fracture. According to Equation 2.2, the tendency for a granular deposit to fail by crushing increases by increasing with both σ_{nl} and β. That is, a larger effective normal stress (σ'_n) inhibits sliding by increasing frictional resistance between grains and reducing local dilation and consequently reduces the β that is required to cause relative movements among grains (Biegel et al. 1989). When the above inequality is not satisfied, the grain structure fails by frictional sliding and grain rolling. As discussed above, multiple factors influence grain crushing and Table 2.1 summarizes many of the inherent soil mass properties, particle properties, and external parameters that affect particle damage and crushing.

2.3.6 Effect of Mode of Shear

Some investigators (e.g., Vaid et al. 1990; Riemer and Seed 1997; Yoshimine et al. 1998) suggest that the critical shear strength, and thus the position of CSL, depends on the mode of shear. Figure 2.4 presents hollow cylinder torsional shear results from Yoshimine et al. (1998) that indicate significantly different stress-strain behavior for several tests on Toyoura sand ranging from conditions approaching axial compression (α = 15°) to conditions approaching axial extension (α = 75°). Riemer and Seed (1997) presented similar results in terms of CSLs for Monterey #9 sand (Figure 2.5).

In contrast, other investigators (e.g., Been et al. 1991; Poulos 1988) suggest that the critical shear strength, and thus the position of the CSL is independent of the mode of shear. Poulos (1988) suggested that at large strains, often beyond the range that can be measured in conventional laboratory equipment, a unique critical shear strength is achieved for a given void ratio, regardless of the mode of shear. Been et al. (1991) also point out that many investigators appear to incorrectly assume that the quasi-critical state corresponds to the true critical state, and therefore find that the critical state depends on the mode of shear.

Figure 2.6 and Figure 2.7 present CSLs for Erksak 300/0.7 and Toyoura sands (Been et al. 1991), respectively. These results, which include TxC and TxE results, indicate that CSL is unique and independent of mode of shear. However, the peak (or yield) and quasi-critical shear strengths likely are dependent on soil fabric anisotropy because these strengths are mobilized at small to intermediate strains where the initial soil structure affects stress – strain behavior.

2.3.7 Sample Preparation Methods (fabric)

To simulate liquefied soil behavior, samples used for laboratory testing are usually reconstituted from materials collected from the field. The most common sample preparation procedures are water pluviation, dry pluviation (or air pluviation), and moist tamping. In this research the specimens are only prepared by dry pluviation and moist tamping, which are described here.

2.3.7.1 Dry pluviation

The dry pluviation method best models the natural deposition in aeolian environments. In this method dry sand is used to fill the sample space confined by a specimen mold. Sand particles are dropped through a funnel with a controlled drop height to form the specimen. Sand is placed by moving the funnel in radial and circumferential directions until the specimen mold is completely filled and excess sand is removed from the top of the specimen using a straightedge to produce a flat surface (Kramer et al. 2002).

Dry pluviation (Miura and Toki 1982; Gilbert 1984; Jang 1997) allows specimens to be prepared over a broad range of densities to a high level of global repeatability through

careful control of the intensity and fall height of the sand particles during reconstitution and is well suited to use for uniformly graded sands (Frost et al. 2000; Towhata 2008). In this method density can be controlled by adjusting the height of pluviation or tapping the sides of the specimen mold (Gilbert and Marcuson 1988; Vaid and Negussey 1988; Mooney et al. 1998).

2.3.7.2 Moist tamping

A moist-tamped sample is prepared by mixing dry sand with water (about 5% water content for clean sands) (Ishihara 1993). Moist soil is then placed into several layers in the mold. The moisture creates a capillary effect among particles that forms an extremely loose fabric. The density can be controlled by tamping the top of each layer. With proper densification of the sample, this procedure can produce specimens that cover wide ranges of the initial void ratios (Ladd 1978; Verdugo and Ishihara 1996). Many liquefaction studies have been performed using the moist-tamping method of specimen preparation (Bjerrum et al. 1961; Castro 1969; Sladen et al. 1985; Kramer and Seed 1988; Konrad 1990a; Ishihara 1993; Pitman et al. 1994). Moist tamping is used because it is much easier to achieve the low densities required to make clean sands liquefy, with sample relative densities as low as -20% (Ishihara 1993). The moist-tamping method artificially creates void spaces in the deposited soil structure by developing "apparent cohesion" among the sand particles, generated from water surface tension among grains, so upon shearing there can be a volumetric collapse in the soil. Whether this method really simulates a soil created from a natural depositional process is debatable. It could be argued that clean sands with such low densities ($D_r \cong$ -20%) are unlikely to exist in nature. However, some studies (Mulilis et al. 1978; Ishihara 1993) have shown that at similar densities and stresses moist-tamped specimens can be more resistant to liquefaction than the the dry and water pluviation specimens. This is most likely caused by the tamping process, which may overconsolidate portions of the specimen by compacting the grains together at fairly large stresses. This may help explain why specimens created in this manner rarely undergo complete liquefaction during monotonic testing, unless unrealistically low densities are utilized. Saada (1988) suggested that moist tamping prevents the development of an anisotropic fabric and produces a material that responds

more isotropically to hydrostatic stress increments. And besides the contradictory opinions regarding the uniformity of moist tamped specimens (Chen and van Zyl 1988; Frost and Park 2003), a better specimen uniformity can be achieved by increasing the compaction effort towards the top of the specimen in the manner suggested by Ladd (1974) and Mulilis et al. (1977).

Studies (Mulilis et al., 1975; Tatsuoka et al., 1982) have shown that samples with identical densities can have very different strengths if their initial fabrics are different. Many investigators (e.g., Dennis 1988; Vaid et al. 1999) suggest that the critical shear strength, and thus the position of CSL, depends on sample preparation and thus soil structure or fabric. For example, Figure 2.8 and Figure 2.9 from Vaid et al. (1998) and Dennis (1988) show significantly different stress-strain and CSLs responses from TxC tests on respectively Syncrude sand and Ottawa Banding sand, prepared by different methods.

In contrast, other investigators (e.g., Poulos et al. 1988; Been et al. 1991; Ishihara 1993; Verdugo et al. 1995) suggest that the critical shear strength, and thus the position of the CSL is independent of the sample preparation and thus soil structure or fabric. Poulos et al. (1988) suggested that at large strains, often beyond the range that can be measured in conventional laboratory equipment, a unique critical strength is achieved for a given void ratio, regardless of the sample preparation method. Figure 2.10, Figure 2.11, and Figure 2.12 present CSLs for Erksak 300/0.7 sand (Been et al. 1991), Syncrude tailings sand (Poulos et al. 1988), and Toyoura sand (Ishihara 1993), respectively. These results indicate that CSL is unique and independent of initial soil structure. However, the peak (or yield) shear strengths likely are dependent on soil fabric because these conditions occur at small to intermediate strains where the initial soil structure affects stress – strain behavior.

2.3.8 Shearing Rate

Hungr and Morgenstern (1994) conducted ring shear and flume tests with a number of cohesionless and polystyrene beads. From these tests, conducted at shearing rates up to 98 cm/s, they concluded that the rate of shearing does not affect the frictional characteristics of the particulate medium. They also demonstrated, in flume experiments,

that granular material retains the same frictional properties under very high rates of shearing. The RS test allowed them to explore this phenomenon at larger normal stresses.

2.3.9 Particle Shape

Wang and Sassa (1998) found that grain shape was one of the main factors affecting the displacement of a moving soils mass (for example a landslide) under a certain stress level. This is because angular grain sands usually have higher critical shear strengths than sands with rounded grains. Angular particles develop greater macro-interlocking and develop larger shear strengths and friction angles. Smoother, more rounded, and finer particles, as well as more uniform gradation tend to result in greater collapse potential (Castro 1969; Alarcon-Guzman et al. 1988). The CSL is at larger void ratios and steeper for angular sands and therefore it is more difficult to liquefy sands with angular particles than sands with rounded grains (Poulos et al. 1985).

2.4 YIELD AND LIQUEFIED SHEAR STRENGTHS

Figure 2.13 shows the behavior of saturated, contractive sand during an undrained TxC shear test. The peak shear strength mobilized at point B is the yield shear strength, s_u(yield), and represents the triggering condition for static liquefaction and flow failures (Vaid and Chern 1983; Vasquez-Herrera et al. 1988; Konrad 1993; Terzaghi et al. 1996; Olson and Stark 2003a). Liquefaction is triggered when the stress state in the soil reaches or attempts to exceed the yield strength under undrained conditions (Olson 2006; Hanzawa 1980). Yielding that triggers liquefaction of sand can be produced by a single monotonic or a cyclic loading under undrained conditions (Terzaghi et al. 1996).

The constant shear stress available at point C where the sand has completely liquefied at a constant volume is the critical shear strength, s_u(critical) (Terzaghi et al. 1996). In the field, void redistribution, water layer formation, soil mixing, and hydroplaning may occur, violating the constant volume condition. Therefore, Olson and Stark (2002) termed the post-liquefaction shear strength mobilized in the field the liquefied shear strength, s_u(liq). s_u(liq) is required for the post-earthquake stability analysis of flow-type failures which happen near the end of seismic loading and appropriate selection of s_u(liq) is an important component in the assessment of post-seismic deformations. The s_u(liq) based approach of

analyzing liquefaction susceptibility is widely used in practice and procedures have been suggested to determine s_u(liq) to be used in flow failure stability analyses (Poulos et al. 1985; Seed 1987; Alarcon-Guzman et al. 1988; Seed and Harder 1990; Vaid et al. 1990; Stark and Mesri 1992; Ishihara 1993; Olson and Stark 2002). The yield and liquefied strength ratios are defined respectively as the yield and liquefied strengths normalized by the consolidation stress σ'_c (which is equal to the initial vertical stress, σ'_{v0} in normally consolidated, unaged, and uncemented sandy soils). Using strength ratios (s_u/σ'_c) would allow us to account for the variation of the shear strength throughout the soil depth. At larger depths, the increase in consolidation (prefailure) vertical stress would increase the shear strength of the soil. This can be used in assessing the shear strength of a particular liquefied zone and also liquefaction remediation techniques (e.g. stabilization berm, or soil densification) can be design by using the liquefied strength ratios (Olson and Stark 2002). A more fundamental study of s_u and s_u/σ'_c is provided in Chapter 10.

2.5 SUMMARY

1. In order to correctly study soil behavior, the void ratio in the shear band should be considered, especially in dense sands where the difference between the local void ratio within the shear band and the rest of the sample becomes large.
2. A contractive, saturated, cohesionless soil subjected to undrained monotonic loading will mobilize yield and liquefied shear strengths. Critical shear strength is the liquefied shear strength at critical state.
3. Terms "critical state", "steady state", "ultimate state" and "residual" all refer to the same behavior and the term "critical state" is used throughout this thesis.
4. The undrained behavior of a saturated, cohesionless soil is a function of its initial void ratio, effective confining pressure, and state parameter (Been and Jefferies 1985) can be used to indicate contractive or dilative behavior during shear to a particular displacement level.
5. The effects of consolidation stress, stress path, particle crushing, sample preparation method (fabric), shearing history, mode of shearing, and drainage conditions on critical state are still debated.

6. Particle size distribution, and mineralogy of a sand affect its behavior and liquefaction susceptibility.
7. Particle crushing plays a major role in the behavior of sands and may still occur even if the applied global stress is less than the breaking strength of the sand particles.
8. Moist tamping produces very loose sand structures that may not develop in the field and may lead to wrong conclusions regarding liquefaction potential. And inferring all soil behavior from the behavior of clean sands using the moist-tamping method may not be appropriate.

2.6 TABLES

Table 2.1: Inherent soil mass properties affecting particle damage and crushing

Soil mass properties	
Grain size distribution	In a well-graded soil, more particles surround individual grains reducing the average contact stress and decreasing particle damage (Lee and Farhoomand 1967; Lade et al 1996).
Initial void ratio	Decreasing void ratio (at a given confining stress) decreases particle damage because smaller void ratios generally yield a higher number of particle contacts (coordination number) and thus a better distribution of stresses (i.e., confinement) produced by neighboring particles (Hagerty et al 1993; Lade et al 1996; McDowell and Bolton, 1998; Tsoungui et al 1999; Nakata et al 2001)
Grain properties	
Hardness	Increasing hardness decreases particle damage (Marsal 1967; Lade et al 1996; McDowell and Bolton 1998; Feda 2002)
Shape	Increasing angularity increases particle damage as a result of greater stress concentrations at asperities (Lee and Farhoomand 1967; Hagerty et al 1993; Lade et al 1996).
Size	Increased particle size generally increases crushing as a result of the increased probability of inherent flaws and defects occurring in the particles (Billam 1972) and the decrease of Brazilian tensile strength (Lee, 1992; Lade et al. 1996; Nakata et al. 1999). However, in a well graded sand, the coordination number for large particles surrounded by large numbers of finer particles is very high while the opposite is true for the finest particles. In this case, the tensile splitting stress for the large particles is relatively small while that of the small particles with a low coordination number is much larger. Thus the probability of splitting of the finer particles would be higher (McDowell et al. 1996; McDowell and Bolton 1998; Muir Wood and Maeda 2008)
External parameters	
Effective confining stress	Increasing effective confining stress increases particle damage (Lade et al. 1996).
Shear displacement	Increasing shear displacement increases particle damage (Agung et al. 2004; Coop et al. 2004; Lobo-Guerrero and Vallejo 2005).
Time	Some particle damage continues with time, resulting in creep (Lade et al 1996; Leung et al 1996; Takei et al 2001; McDowell and Khan 2003)
Mode of loading (or stress path)	More particle damage occurs during shearing than during isotropic compression (e.g., Hall and Gordon 1963; Bishop 1966)
Temperature	Temperature can affect the crushing susceptibility of some mineral constituents (Nakata et al 2003; Chester et al 2004)

2.7 FIGURES

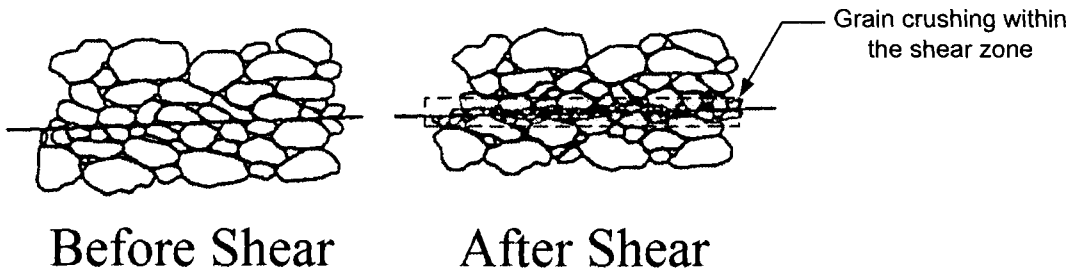

Figure 2.1: Mechanism of sliding surface liquefaction (after Sassa 1996)

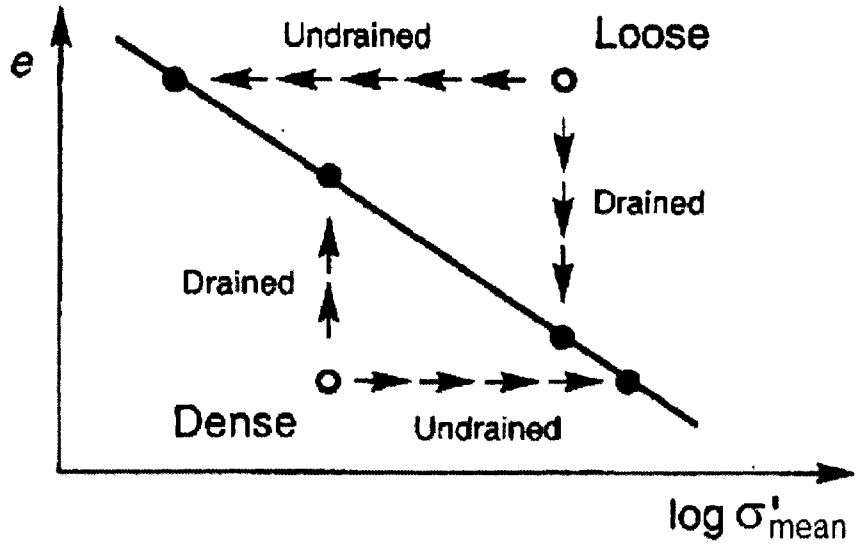

Figure 2.2: Behavior of loose and dense sands under drained and undrained conditions (from Kramer 1996)

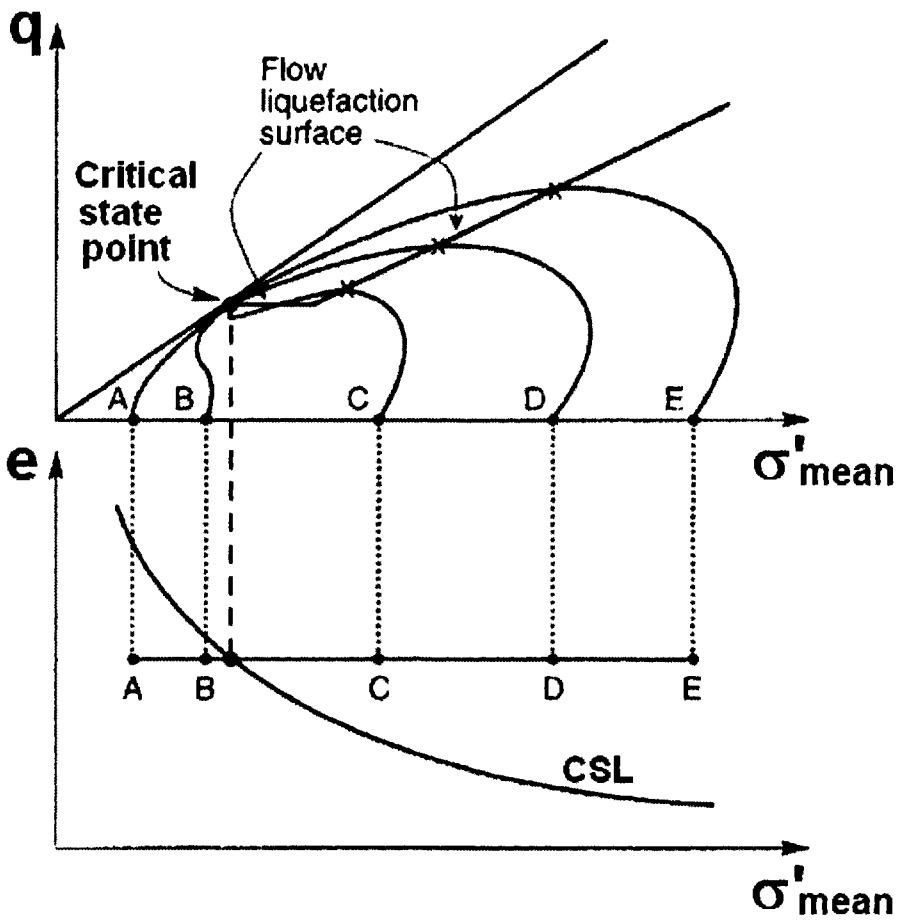

Figure 2.3: Liquefaction induced by monotonic loading (after Kramer 1996)

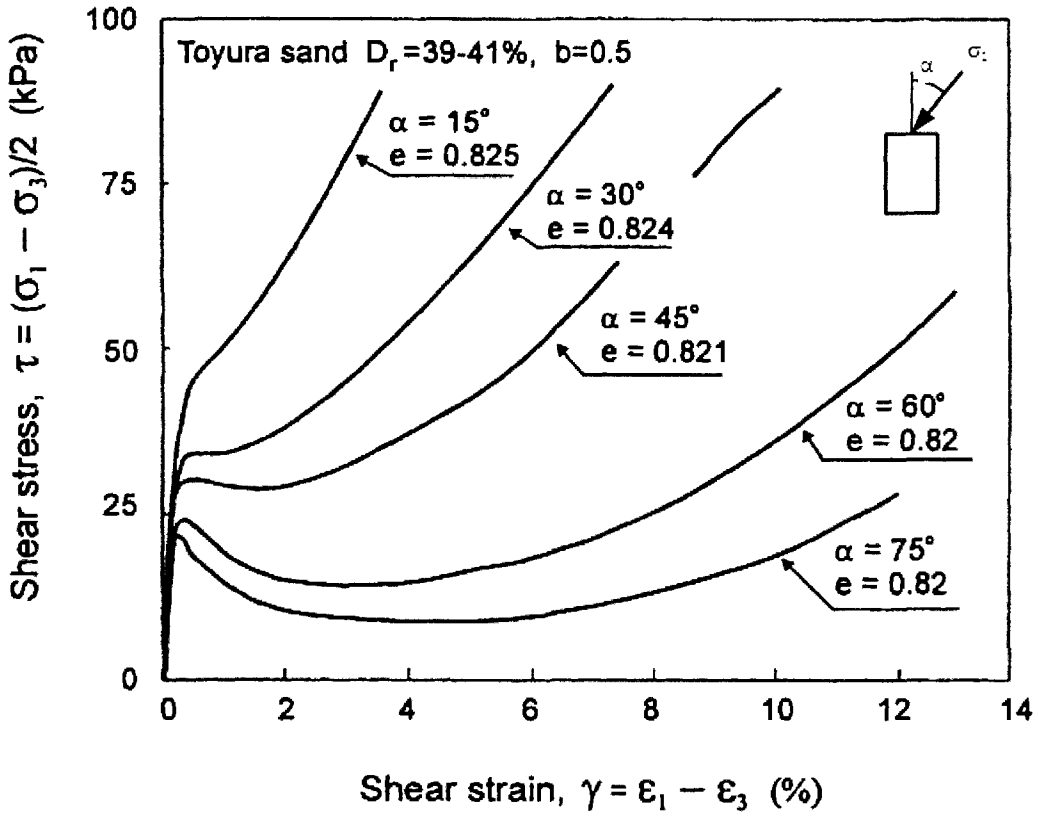

Figure 2.4: Hollow cylinder torsional shear tests on Toyoura sand showing effect of mode of shear (from Yoshimine et al. 1998)

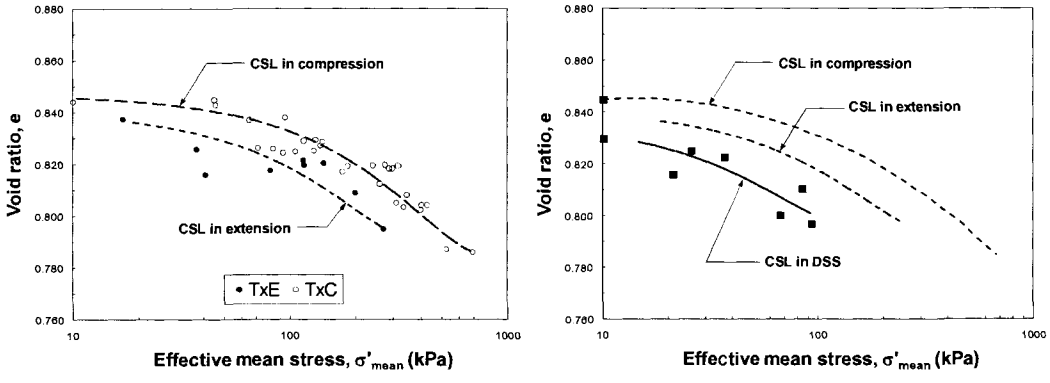

Figure 2.5: Effect of mode of shear on CSL of Monterey #9 sand (from Riemer and Seed 1997)

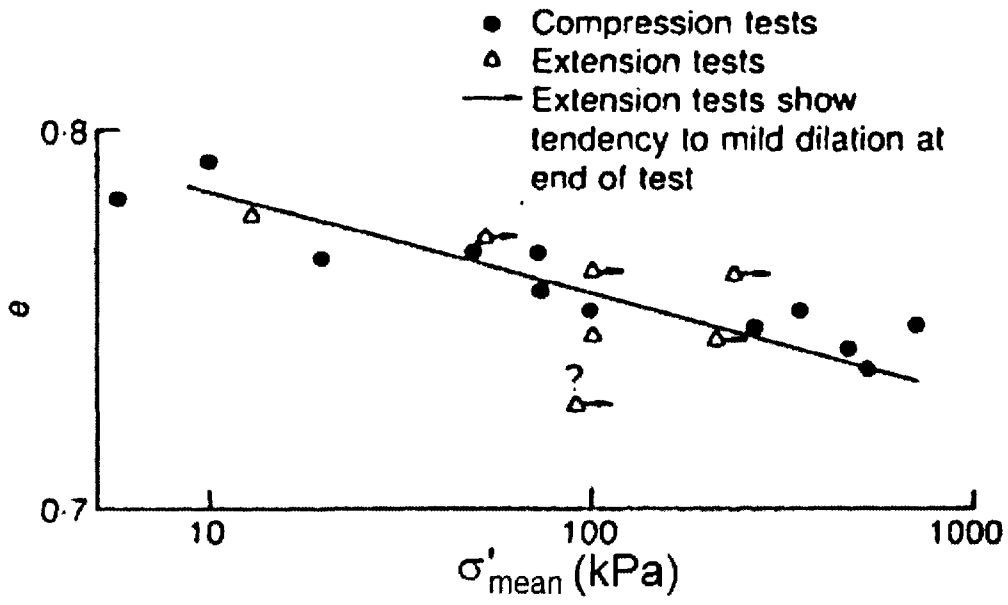

Figure 2.6: Effect of mode of shear on CSL of Erksak sand (from Been et al. 1991). e is void ratio and σ'_{mean} is mean effective stress.

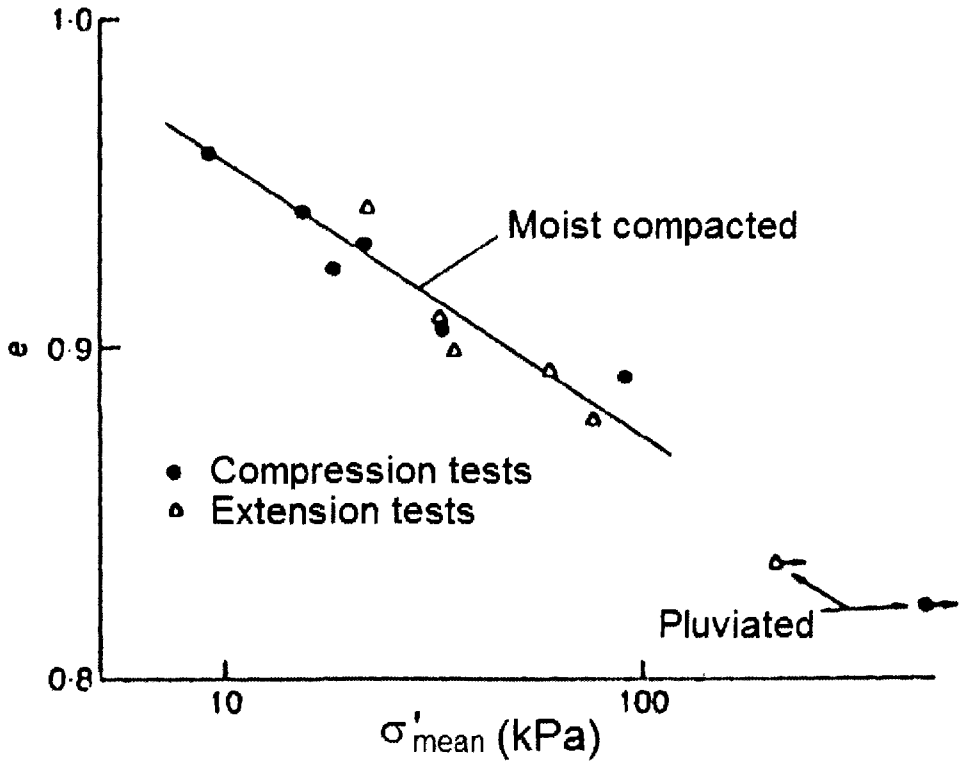

Figure 2.7: Effect of mode of shear on CSL of Toyoura sand (from Been et al. 1991). e is void ratio and σ'_{mean} is mean effective stress.

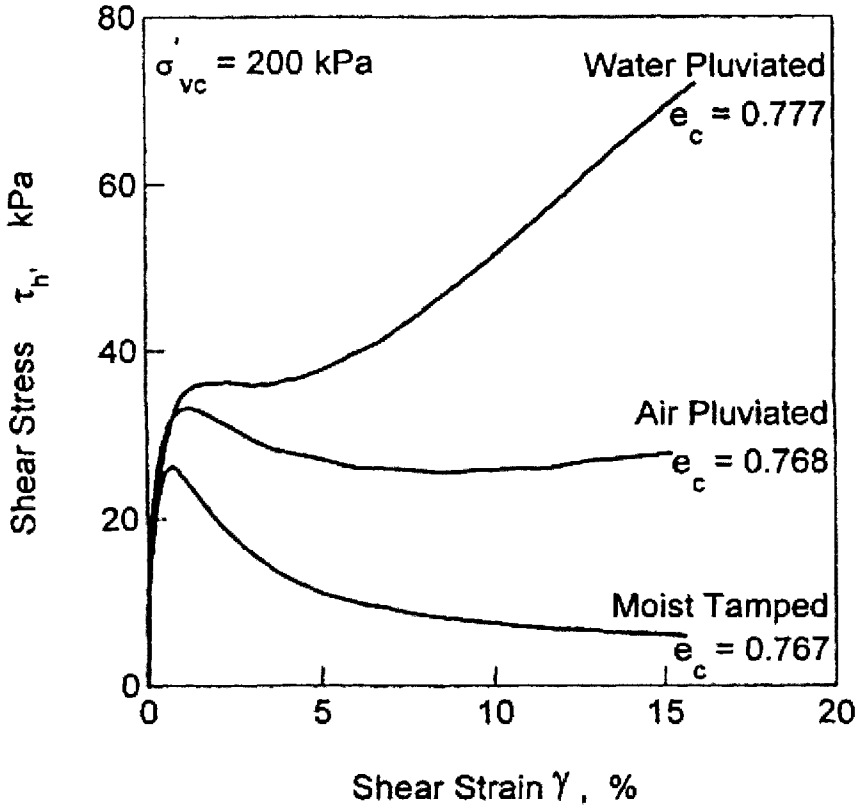

Figure 2.8: Effect of specimen preparation on undrained stress-strain behavior (from Vaid et al. 1999)

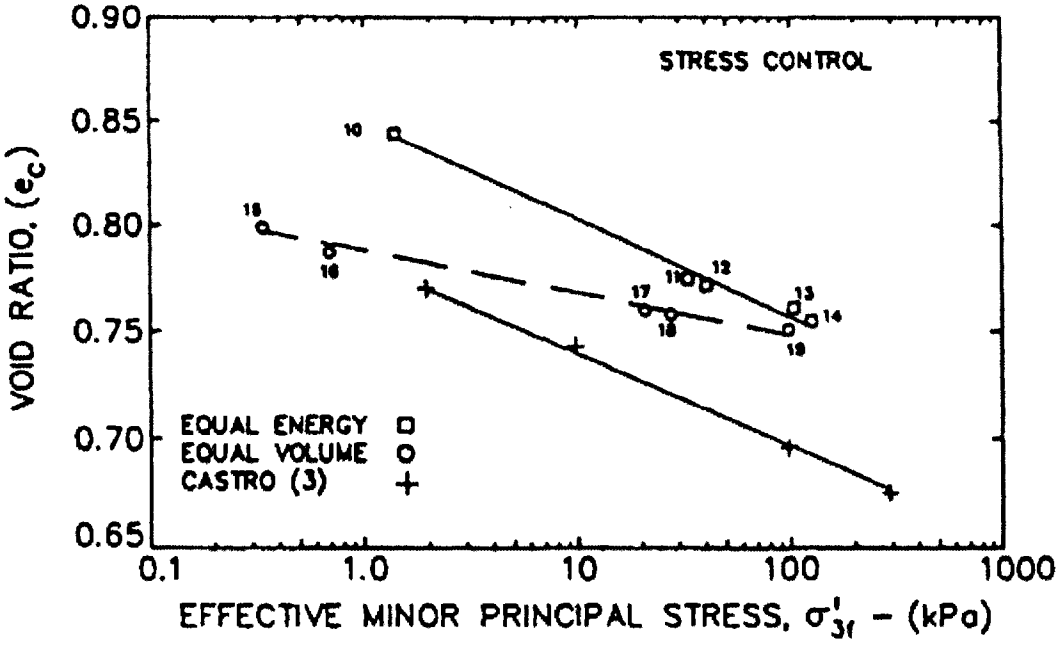

Figure 2.9: Effect of specimen preparation on CSL of Banding sand compared with CSL obtained from Castro (1969) (from Dennis 1988)

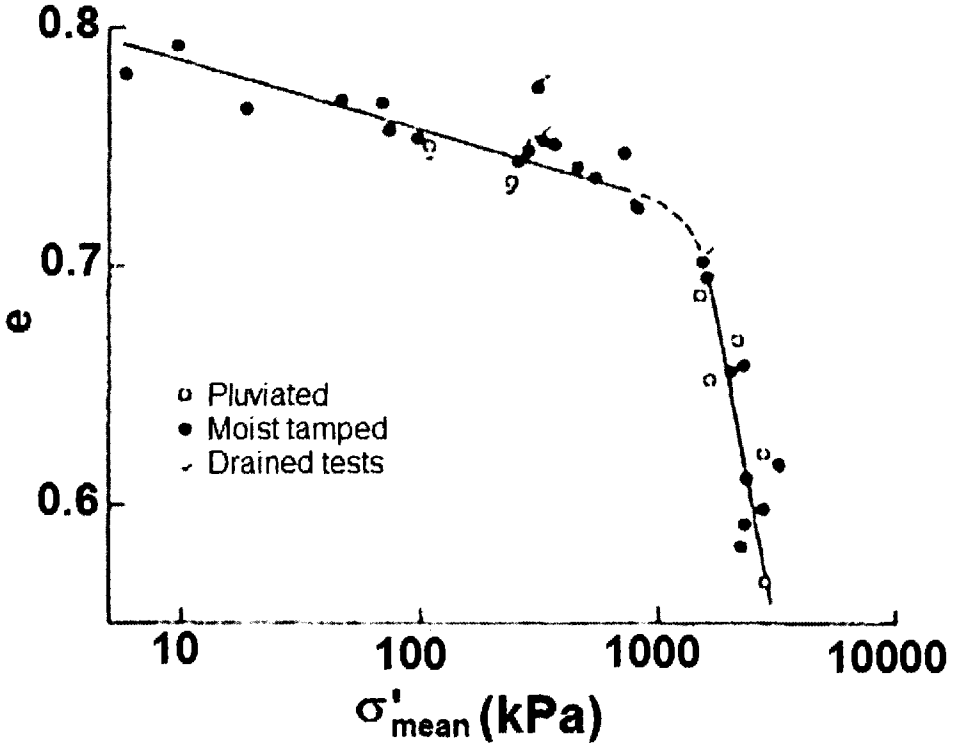

Figure 2.10: Effect of specimen preparation on CSL of Erksak sand (from Been et al. 1991)

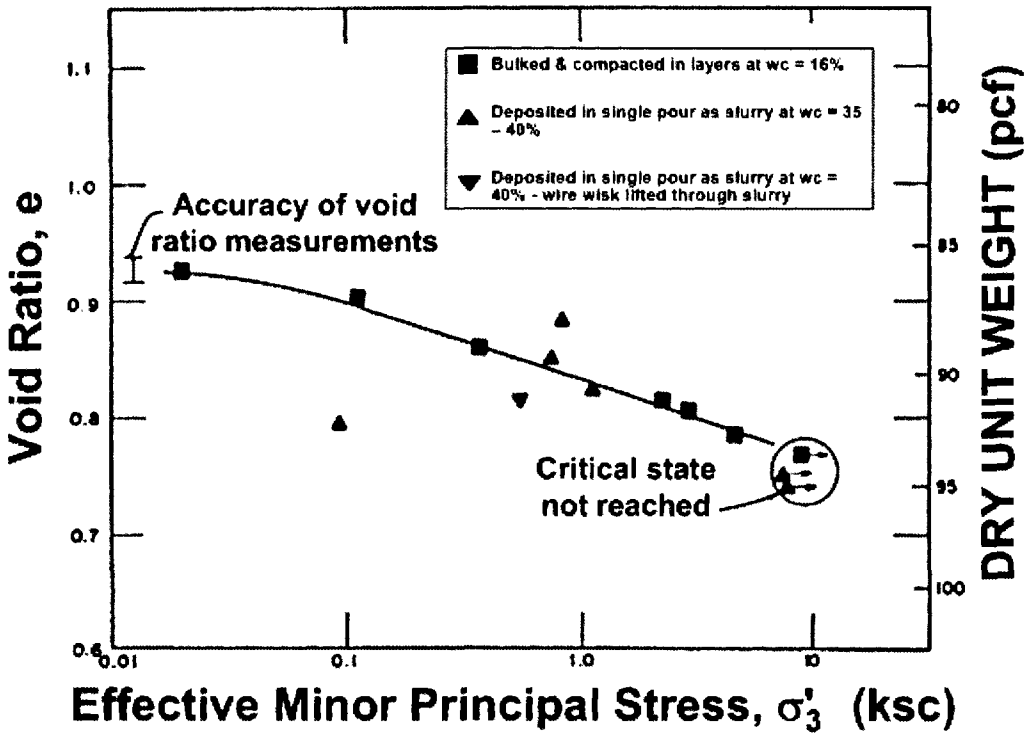

Figure 2.11: Effect of sample preparation on CSL of Syncrude tailings sand (from Poulos et al. 1988)

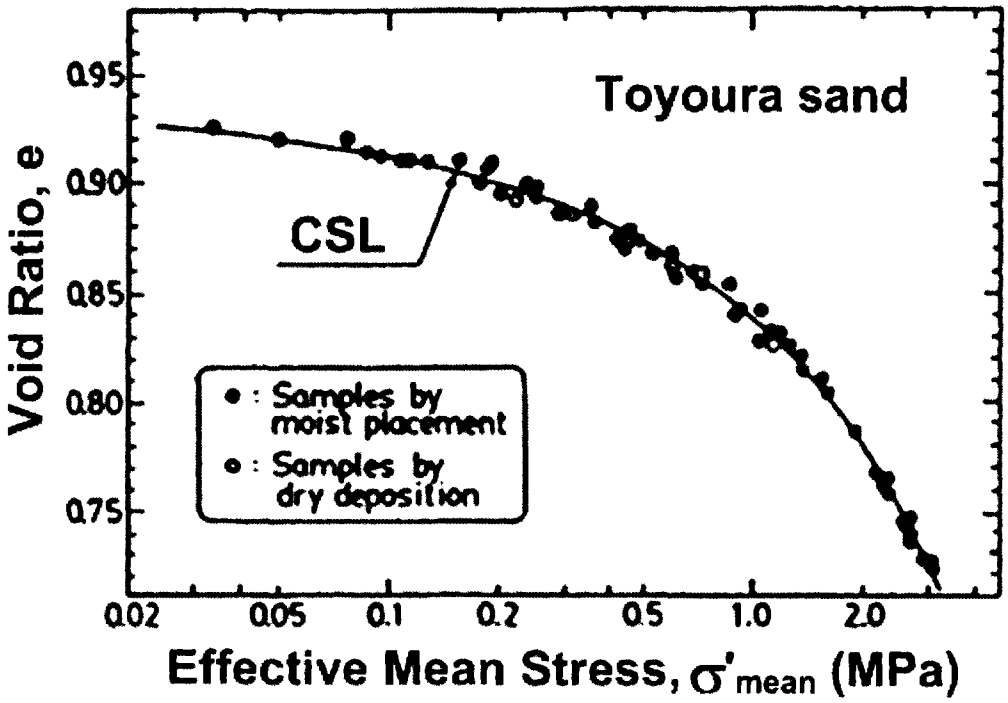

Figure 2.12: Effect of sample preparation on CSL of Toyoura sand (from Ishihara 1993)

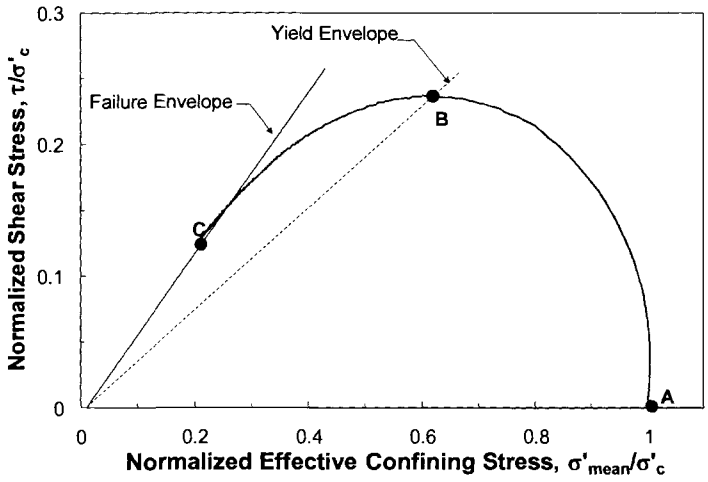

(a)

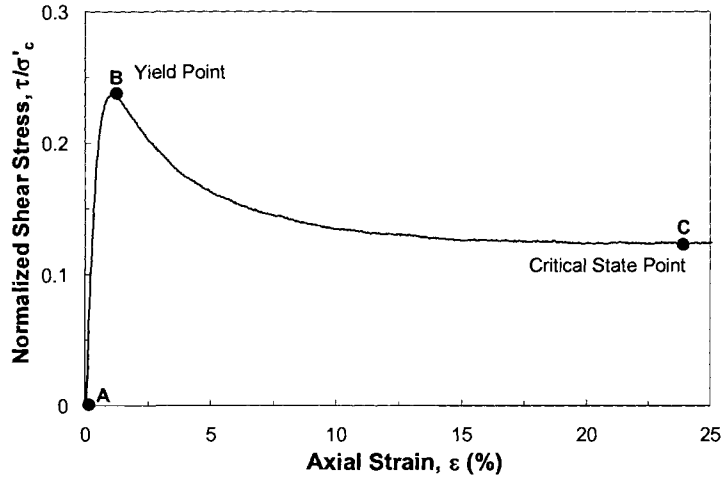

(b)

Figure 2.13: Undrained (a) stress path and (b) stress – strain history of Illinois River sand specimen (σ'_c = 773 kPa; Dr_c = 27%) in TxC normalized with respect to the mean consolidation stress (σ'_{mean}).

CHAPTER 3: LARGE SHEAR DISPLACEMENT TESTING OF SOILS

3.1 INTRODUCTION

The shearing behavior of sands at large displacements can be an important design consideration, particularly in cases where liquefaction can occur. In these cases, many investigators and practitioners have attempted to measure the undrained, large displacement strength (i.e., the critical shear strength) in the laboratory to supplement empirical correlations based on in situ measurements and field case histories. Of course, it is difficult or even impossible in the laboratory to properly account for the potential effects of drainage, void redistribution, hydroplaning, etc., that can occur in the field; but element-level testing provides a constitutive framework from which to interpret field case histories, and as such have proven quite valuable.

In this chapter, some of the laboratory testing devices that are commonly used to measure the large displacement shearing response of sandy soils are briefly described, and their relative merits and limitations are also discussed. Then a new ring shear (RS) device developed at the University of Illinois is introduced which measures both the constant volume and drained, large displacement shearing behavior of sands and overcomes many of the limitations associated with other devices.

3.2 DEVICES COMMONLY USED FOR SHEAR TESTING OF SANDS

Researchers have been performing laboratory monotonic-loading tests on sands since about the 1930s, and since the 1960s our understanding of sand behavior during cyclic loading has greatly improved. However, the limitations of some testing devices used in these studies have contributed to the considerable disagreement over key behavioral aspects, such as the existence and uniqueness of a critical state line (CSL) (e.g., Jefferies and Been 2006).

To provide reliable results, devices used to measure the shearing behavior of sands must meet certain principle requirements. These include:

(1) The ability to consolidate a sample to desired confining stresses (under drained conditions) and then shear the specimen under either drained or undrained/constant volume conditions.
(2) The ability to rotate principal stress directions.
(3) The ability to accurately measure applied stresses.

Measuring the large-displacement shearing behavior of sands imposes further requirements. Most importantly, any laboratory apparatus used to measure the large displacement shearing resistance should be able to:

(1) Operate consistently at large shear displacement.
(2) Apply uniform stresses and strains in the test specimen so that stresses and strains measured at the specimen boundaries represent the actual stresses and strains within the specimen.
(3) Utilize a sample large enough to develop a well-defined shear band.
(4) Shear the sample in a direction parallel to depositional planes (often subhorizontal in many geologic settings) in order to replicate the conditions exhibited by many long run-out landslides, liquefaction flow failures, and some liquefaction-induced lateral spreads.

Several devices have been used to measure the small- and large-displacement shearing behavior of sands; however, the most commonly used are the direct simple shear (DSS), triaxial compression (TxC), and RS devices. The following paragraphs highlight the merits and limitations of these devices.

3.2.1 Direct Simple Shear (DSS)

Drained, undrained (e.g., Franke et al. 1979; Silver et al. 1980; Tatsuoka and Silver 1981), and constant volume (e.g., Finn and Vaid 1977) DSS tests are commonly used to investigate the shearing behavior of sands at small strains, but less frequently for evaluating large-strain behavior. The merits of DSS include:

(1) The ability to test either undisturbed or reconstituted specimens.
(2) Well-established sample preparation and testing methods.
(3) The ability to shear under stress- or strain-controlled conditions.
(4) Readily controlled drainage.

(5) The ability to rotate principal stress directions during shear.

(6) The ability to apply shear stresses on depositional planes.

(7) The cross sectional area of shear remains constant.

(8) Small boundary friction.

(9) Shear-induced lateral deformations are distributed fairly uniformly over the specimen height and cross section.

(10) A better resemblance to in-situ ground deformations (Hosono and Yoshimine 2004).

However, the magnitude of shear displacement that can be imposed on a specimen is limited by the device itself and further limited due to the possibility of "pinching" at the specimen corners where acute angles form (Kramer et al. 2002). Furthermore, the lack of complementary shear stresses on the sides of the specimen requires that the moment produced by the horizontal shear stresses be balanced by nonuniform normal and shear stress distributions. As shearing progresses, the nonuniformities of normal and shear stress distributions increase. Hence (as is well-known), the post-peak shear resistance is reliable only to a limited displacement (Saada and Townsend 1981).

3.2.2 Triaxial Shear (TxC/TxE)

Triaxial is the most commonly used device to measure the shear strength of soils because of its many merits, including:

(1) The ability to test both undisturbed and reconstituted specimens.

(2) Well-established sample preparation and testing methods.

(3) The ability to shear under stress- or strain-controlled conditions.

(4) Readily controlled drainage.

(5) The ability to apply a stress state that closely approximates the actual axisymmetric stress state under foundations or earth structures.

However, there are several issues that limit this test's suitability for measuring the shearing response of some soils (Bishop et al. 1971; Sassa 1992). The main drawback of the triaxial device is the limited available shear displacement. This limitation can lead to incomplete particle reorientation and/or breakage, making it difficult (if not impossible) to measure the large displacement shear resistance of medium dense and dense sands

(Chandler 1985; Luzzani and Coop 2002; Coop et al. 2004). In addition, sample bulging at larger strains (and the resulting increase in specimen cross-section and change in cross-sectional shape) leads to potential errors in measuring shear resistance because of the uncertainty in the actual specimen shape, just as the conditions are of greatest interest for evaluating large-displacement behavior of sands (Kramer et al. 1999). Sample shape irregularities induce nonuniform stress distributions, making it difficult to evaluate any local void ratio changes in sand specimens, as well as the shear surface area and location. These uncertainties can lead to errors in computing the stress on the shear surface (Hvorslev and Kaufman 1952; Shoaei and Sassa 1994). The triaxial test also does not allow the continuous rotation of principal stress directions that occurs during actual flow failures (Kramer et al. 2002), and the maximum shear stresses occur on planes inclined to typical subhorizontal depositional planes. Lastly, the restraint exerted by the rubber membrane induces indeterminate forces which are most important when the displacements are large and soil strength is small (Hvorslev and Kaufman 1952) for example in modeling many liquefaction problems.

3.2.3 Ring Shear (RS)

In a RS test, an annular specimen is confined between outer and inner rings and is sheared at its bottom (or top, or midheight) surface depending on the configuration and fixity of the rings as illustrated in Figure 3.1. Both the split-ring and solid-ring devices are widely used in the U.S. and internationally, and both have advantages for specific types of testing. A fixed plate on the top surface measures the soil specimen's resistance to shearing. The RS test provides many advantages for measuring the large displacement shear resistance of sands, including:

(1) Ability to shear a sample uninterrupted to virtually unlimited displacements.

(2) Ability to apply known shear stresses on a horizontal (depositional) shearing plane.

(3) Ability to rotate (although uncontrolled) principal stress directions.

(4) Ability to consolidate a specimen prior to shear.

(5) Ability to accurately track volume changes because changes occur only in one dimension.

(6) The cross-sectional area of the shear plane remains unchanged during shearing.

(7) The geometry of the test specimen remains unchanged during shearing. (In contrast, the specimen in a triaxial test changes from a rectangular to nearly an ovoid.)

(8) Similar to DSS, the simple shearing mode in the RS test is more similar to the in-situ ground deformation (Hosono and Yoshimine 2004).

Of course, like any other testing method, there are a number of limitations associated with this test, including potentially nonuniform stress and strain distributions, potential soil extrusion, difficult undrained testing procedures, and wall friction.

3.3 LIMITATIONS OF THE RING SHEAR TEST

3.3.1 Nonuniform Stress and Strain Distributions

In a RS test, shear strain increases with radius; therefore failure occurs progressively. This effect can be reduced by decreasing the annulus width; but this, in turn, increases the significance of wall friction (Scarlett and Todd 1969), particularly when testing sands. Alternatively, strain rate and progressive failure effects can be minimized by reducing the ratio of the outside to inside ring diameters (e.g., using a larger diameter and narrower sample). However, reducing this ratio by increasing the outer diameter is limited practically by the size of the apparatus and its torque and normal loading system. Because of this limitation, the RS device is best suited to measure shear strengths at large displacement since at this condition any progressive failure phenomenon is irrelevant (Hvorslev 1939; Sembenelli and Ramirez 1969; La Gatta 1970; Bishop et al. 1971). Despite this, the RS is commonly used to determine the fully softened shear resistance in remolded clayey soils (e.g., Stark and Contreras 1996) because the induced error is small for optimal ring dimensions (Hvorslev 1939).

3.3.2 Soil Extrusion

Soil may extrude between the upper (or lower) loading platen and the confining rings or through the gap between the upper and lower rings (for split-ring devices). This is a chronic problem in RS tests (Bishop et al. 1971; Tika et al. 1996; Iverson et al. 1998) and may cause more scatter in RS test results on sands than any other soil testing device

(Vargas-Monge 1997). It also has been a limiting factor in continuing some tests to very large displacements (Iverson et al. 1996). Soil extrusion affects the shear resistance measured by the upper loading platen. During consolidation and shear, any soil that extrudes into the seam between the confining rings and loading platen increases the shearing resistance due to side friction (Stark and Vettel 1992). In addition, soil extrusion precludes the accurate measurement of vertical sample deformation during shear.

Excessive extrusion also affects the normal stress distribution across the annular specimen. If soil extrudes during shearing, the normal stress will become nonuniform (even at large displacements), becoming lower than average where extrusion occurs and larger elsewhere. Soil will then be extruded from the zone where the normal stress is larger than average. Thus, a large displacement condition is achieved with a normal stress distribution that is constant but not uniform. Lastly, since the normal stress is lower at the boundaries of a specimen than at its center for any given average normal stress (as a result of wall friction locally reducing the effective normal stress), the measured moment (i.e., torque) will be smaller than if the normal stress was uniform. This condition would cause the measured shear strength at large displacement to be smaller than the true value (La Gatta 1970).

3.3.3 Undrained and Constant Volume Testing

Generally the ring shaped geometry of the RS device and shearing to large displacements make undrained testing very difficult. Nevertheless, Sassa et al. (2003) recently developed a split-ring RS device where the upper and lower confining rings are pressed against a rubber gasket to maintain undrained conditions and shear-induced pore water pressures are measured using transducers installed through the outer fixed confining ring. While successful and powerful, this device is complex and approximately 10 times more expensive to manufacture than the new device that is described subsequently (Dr. Fawu Wang, Disaster Prevention Research Institute, email communication, 2008).

Alternately, Taylor (1952) developed a constant volume direct shear device to measure peak undrained shear strengths of clays. In a constant volume test, the decrease in applied vertical stress during shearing is assumed to be equal to the increase in shear-

induced pore water pressure that would occur in an undrained test with constant total stress. Bjerrum and Landva (1966) and Dyvik et al. (1987) verified this assumption for DSS tests, and Berre (1982) and Sasitharan et al. (1994) verified it for triaxial tests. Similarly, it is anticipated that constant volume RS tests on dry specimens are equivalent to undrained tests performed on fully saturated specimens.

3.3.4 Wall Friction

During consolidation and shear, wall friction develops between the specimen and the confining rings, reducing the applied normal stress and increasing the apparent shear resistance of the specimen (Hvorslev and Kaufman 1952). La Gatta (1970) showed that the magnitude of vertical stress relief depends strongly on the amount of relative displacement between the soil and confining rings. In constant volume tests on sands, wall friction initially increases (as the friction is mobilized), then decreases or increases, respectively, based on changes in effective normal stress related to the specimen's tendency to contract or dilate during shear. The significance of both consolidation- and shear-induced wall friction can be reduced using a wider annulus; however, this would increase strain non-uniformity and the effects of progressive failure.

3.4 DESIGN AND CONSTRUCTION OF A NEW RING SHEAR DEVICE

The numerous benefits of the RS device led to design and construction of a new RS device at the University of Illinois at Urbana-Champaign (Figure 3.2) that is intended to overcome many of the limitations discussed above and evaluate the stress-displacement-strength behavior of sands, particularly at large displacements. Specifically the new device:

(1) Reduces stress and strain non-uniformities by optimizing the inner and outer confining ring diameters.

(2) Reduces sand extrusion by using solid inner and outer confining rings and sealing the seams by quad-rings.

(3) Tests specimens under constant volume conditions to avoid the complex issues of undrained testing in the RS.

(4) Measures wall friction using separate torque and load cells.

3.4.1 Design

The new RS apparatus is designed to perform tests up to a normal stress of 700 kPa. Different parts of the machine, including the steel plates, torque transmitting shafts, supporting shafts, rotating base gear, and several other pieces (see Figure 3.2) were designed by simple mechanical analyses, and some finite element analyses were performed to check the most critical parts carrying the largest loads. For example, a finite element analysis of the central shaft (C in Figure 3.2) was performed using the finite element software ABAQUS to see if it would yield at its contact with the pin connecting it to upper plate. As indicated in Figure 3.3, the stress concentrates at the bottom surface of the pin up to a value of 654 MPa (94.68 ksi). Therefore a shaft made of hardened steel alloy with a yield strength of 690 MPa (100 ksi) was selected. By calculating the stresses required to compress and shear the sand, the dimensions of the other parts of the machine were determined.

3.4.2 Instrumentation

Instruments and sensors are vital parts of this device, particularly when a test is run for a long time and measurements are taken frequently. The electrical instruments (transducers) for the new RS apparatus are:

3.4.2.1 Torque cells (T1 and T2)

Torque cells are used to measure the resisting torques of the sand and sand-wall interface friction. Both torque cells were manufactured by Lebow Inc. and have capacities of 2256 N.m (T1) and 1129 N.m (T2). It was ensured that both cells had very large torsional stiffness so they would not twist excessively as the sand specimen was being sheared. Any coupled twisting of the sand and torque cells would lead to some error in the measured torques, shear stresses and strains. Two signal conditioners were used to amplify the output voltage of these torque cells so the output could be measured by the data-logger. In the new apparatus, the lower shearing disc (LP in Figure 3.2) rotates while the upper shearing disc (UP in Figure 3.2) is stationary and is used to

measure the total shear resistance via torque cell T1. Both of the inner and outer confining rings are also stationary and are fixed to torque cell T2 and load cell N2.

3.4.2.2 Load cells (N1 and N2)

These are 22220 N (N1) and 4444 N (N2) capacity load cells that measure the normal load on the specimen and the downward pulling force developed by side friction between the sand and confining rings. Both of these load cells were internally amplified and did not need separate amplifiers. In addition, these load cells were equipped with protection plates, so overloading would not damage them.

3.4.2.3 Displacement transducer

A Linear Variable Differential Transformer (LVDT) with a stroke of ±25 mm was used to measure the vertical movement of the upper loading plate and thus the change in the height of the specimen. Specimen height is used to compute void ratio.

3.4.2.4 Power supply

The electrical power of the transducers was supplied by two very precise electrical adaptors. These power supplies provide a constant voltage to the transducers.

3.4.2.5 Data logger

A high speed data logger (National Instruments DAQPad-6015) was selected to obtain measurements. The data logger has 16 analog input channels and a maximum data logging frequency of 2×10^5 samples/second. However, a rate of 1 sample/second was sufficient and used in the tests for the current research. The data logger and power supplies are shown in Figure 3.4.

3.4.3 Other Major Components

Besides the sensors and instrumentation, the other major components of the new RS device are shown in Figure 3.5 and are:

3.4.3.1 Central shaft (C in Figure 3.2)

This is one of the most important parts of the machine. It is a 5.08 cm (2 inch) diameter and 70.6 cm (27.8 inch) long shaft made of hardened steel alloy. It not only transmits the normal stress to the soil but also conveys the resisting torque of the soil to the torque cell T1.

3.4.3.2 Central linear bearing (LB in Figure 3.2)

Nonuniform compression and soil extrusion potentially can cause the upper loading platen or the confining rings to tilt. Additionally, if the forces on the upper loading platen and the central shaft transmitting the resisting torque have a small resultant force (i.e., they do not constitute a pure moment), then these elements may drift. A resultant force can be caused by nonuniform shear resistance over the entire specimen cross-section as well as excessive deflection of the normal loading lever. And any tilting or eccentricity of the central shaft would lead to wrong measurements, progressive wearing of the other parts of the machine, and serious damage to the torque cell. A central linear bearing (Figure 3.6) was used to align the central shaft to a vertical position and its double bearings do not allow any deviation and misalignment of the shaft even at the largest operational loads of the machine. Auxiliary linear bearings were also installed to align the confining rings.

3.4.3.3 Confining rings (OR and IR in Figure 3.2)

The confining rings form the specimen container and carry the lateral stresses during both compression and shearing. These rings are very precisely machined and their walls facing the specimen chamber are highly polished and smoothened to reduce wall friction as much as possible. To minimize scratching, these pieces were machined from hardened steel alloy.

3.4.3.4 Upper and lower loading discs (UP and LP in Figure 3.2)

The lower disc (LP) shears the soil at its bottom surface, and the fixed upper disc (UP) measures sand shear resistance. Both discs are serrated with radial and circumferential

grooves (with a projection depth of 1.5 mm) to effectively transfer shear stress and prevent slip at its contact with the sand. This was visually confirmed by performing RS tests using a Plexiglas (ploy-methyl methaacrylate) outer confining ring. Figure 3.7 shows the upper disc and its grooves.

3.4.3.5 Rotating base (RB in Figure 3.2)

The sand specimen, the loading disks and confining rings, all sit on the rotating base disk. This disk is custom-made with its outer circumference machined as a gear. Torque developed by the motor is transfer to this rotating base and then to the lower loading plate (LP) and thus to the specimen. The rotating base is also connected to the steel table via a large normal load capacity rotary bearing.

In order to minimize any soil extrusion during shearing, the seams between the annular loading platens (UP and LP) and the confining rings were sealed using quad-rings installed in grooves machined on the sides of the loading platens and inner confining ring (IR) (Figure 3.8). Note that quad-rings are O-rings with an x-shaped cross section so they can seal at two contact surfaces. This not only prevents fine sands from escaping during shear, but trial tests also showed that they could hold water pressure up to 500 kPa. To minimize friction developed along the quad-rings during shearing, they were coated with a thin film of high vacuum silicon grease prior to installation.

Any remaining system friction (torque of 19.4 N.m and load of 578 N) was measured in a calibration test with an empty soil container and subtracted from the total normal and shear forces measured during tests.

3.4.3.6 Lever arm and weights (LA, W in Figure 3.2)

The normal load is applied by a lever arm and dead weights. The lever arm applies a normal load ten times larger than the dead weights placed on its tip.

3.4.3.7 Four threaded shafts

There are four threaded shafts of hardened steel with a diameter of 2 inches. These shafts are the backbone of the RS apparatus. All parts of the machine are installed on

these shafts and through these shafts the total weight of the apparatus is transferred to the steel table and then to the laboratory floor.

3.4.3.8 Electric motor

A Kollmorgen AKM54K servo motor was selected to shear the soil (Figure 3.9a). This motor can apply a continuous torque of 12.6 N.m (112 lb.in) at a continuous speed of 1800 rpm. The motor is operated by an amplifier drive (Figure 3.9b) that provides the electrical supply, and controls the motion of the motor. This combination of motor and drive can perform both strain-controlled testing (using a constant speed of rotation) as well as stress-controlled tests (using a constant torque). With proper modification (e.g. adding a heat sink resistor to absorb inertial energy) the drive can be programmed to perform cyclic tests. In addition, the motor has a 24VDC brake which can be utilized to apply a specific shear stress in the drained mode and then switch to the constant volume shearing mode while the brake retains the initial shear stress. For this study, the constant velocity mode was used for all tests. In addition to the capabilities of the motor-drive system, the motor includes a very precise encoder that accurately measures rotation of the rotor, allowing direct computation of the exact shear displacement.

The torque produced by this strong electromotor alone however, was not sufficient to shear the sand, therefore a gear reducer with a ratio of 70:1 was used. Figure 3.10 shows the gear reducer. This gear reducer increases the motor torque to 882 N.m (7840 lb.in), but reduces the operating rotational speed to 26 rpm.

3.4.4 Operating Software

Readings from all instruments were recorded with a personal computer. A code was developed using Labview software from National Instruments to read the output from the data-logger and store them in an output file. In addition, a convenient graphical interface was provided by the motor-drive manufacturer to control the drive and motor system. Figure 3.11 shows screenshots of these softwares during operation.

3.4.5 Specifications and Testing Method of the New Ring Shear Apparatus

The specimen container of the new RS device has inner and outer diameters of approximately 20.3 cm and 26.9 cm, respectively, and a height of 2.6 cm, complying with ASTM D6467-99 requirements for RS testing. The ratio of the outer to inner ring diameter is 1.33. This diameter ratio results in an error of less than 2% at the peak shear stress due to strain nonuniformity (this will be discussed in a more detail in the next section). The wide sample section (3.3 cm) also reduces wall friction effects; however, the large sample size requires a large normal load (17.1 kN) to achieve the target normal stress of 700 kPa (the limit of the device). Normal load is applied by a lever arm (LV, with a loading ratio of 10:1), transmitted to the sample by the central shaft (C), and measured by the lower load cell (N1). During compression and shearing, any normal load relieved by wall friction is measured by the upper load cell (N2). This value is deducted from the N1 load cell readings to calculate the effective normal stress at the bottom of the specimen (where shearing primarily occurs).

After applying the desired normal load and consolidating the specimen, the sample can be sheared under either drained or constant volume conditions. A constant volume condition is maintained by tightening the locking nuts (L1 and L2) below the lower load cell, thereby preventing the upper loading platen (UP) from moving vertically. Shear load is applied by the computer-controlled servo-motor attached to the gear reducer (70:1 ratio). The torque produced by the motor-gear reducer system (882 N.m) is further increased by the geared rotating base (RB in Figure 3.2) and a maximum torque of 2290 N·m corresponding to a maximum shear stress of 788 kPa is applied to the specimen.

The upper torque transducer (T2) measures any shear-induced wall friction between the confining rings (IR and OR) and the specimen which reduces the shear resistance mobilized at the shear plane in the specimen (near the specimen bottom in this device). This value is later added to the lower torque transducer (T1) readings, which measures the torque mobilized at the top of the specimen.

In summary, the major improvements of the new solid-ring apparatus for testing sands to large displacements include the following:

(1) The new device uses fixed, solid inner and outer confining rings instead of the split confining rings (Imperial College/Norwegian Geotechnical Institute type)

commonly used by other researchers (e.g., Hvorslev 1939; Iverson et al. 1996; Tika et al. 1996; Sassa et al. 2003). The fixed, solid ring design eliminates the loss of lateral confinement at the confining ring gap, reduces variations in shear resistance across the cross section of the specimen, and virtually eliminates soil extrusion.

(2) The new device independently measures wall friction (both normal and shear) mobilized during consolidation and shearing using load and torque cells (N2 and T2) coupled mechanically to the confining rings. This wall friction can considerably influence the testing of sands (as discussed later) and are not measured by other solid-ring devices (e.g., Healy 1963; Carr and Walker 1967; Bromhead 1979; Savage and Sayed 1984).

(3) The cost of the new device is roughly 1/10 of the split-ring device developed by Sassa et al. (2004) and is comparable to commercially available RS devices that are subject to the limitations described above when testing sands.

3.5 STATE OF STRESS IN THE RING SHEAR DEVICE

Figure 3.12 presents a free-body diagram of the state of stress in the RS device. By applying the conditions of moment and force equilibrium, respectively, torque $T_{\theta,sb}$ and normal force $F_{z,sb}$ mobilized at the shear band (sb) are obtained as follows:

$$T_{\theta,sb} = T_{\theta,U} - \left(T_{\theta,sU} + T'_{\theta,sU}\right) \qquad \textbf{3.1}$$

$$F_{z,sb} = F_{z,U} - F_{z,U2} \qquad \textbf{3.2}$$

where $T_{\theta,sb}$ = shear torque at the shear band; $T_{\theta,U}$ = total resisting torque (measured by torque cell T1); ($T_{\theta,sU}$ + $T'_{\theta,sU}$) = shear torque mobilized on inner and outer confining rings (measured by torque cell T2); $F_{z,sb}$ = normal force on the shear band; $F_{z,U}$ = total normal force applied to the specimen (measured by load cell N1); $F_{z,U2}$ = shear forces mobilized on tangential planes on the inner and outer confining rings (measured by load

cell N2). Therefore, the instruments capture the normal and shear forces at the shear band.

Assuming uniform distributions of mean shear (τ_{sb}) and normal stresses ($\sigma'_{n,sb}$) at the shear band, these values as well as the mobilized friction angle can be calculated as (La Gatta 1970; Bishop et al. 1971):

$$T_{\theta,sb} = 2\pi \int_{R_i}^{R_o} \tau_{sb} r^2 dr \qquad \textbf{3.3}$$

$$\tau_{sb} = \frac{3T_{\theta,sb}}{2\pi\left(R_o^3 - R_i^3\right)} \qquad \textbf{3.4}$$

$$\sigma'_{n,sb} = \frac{F_{z,sb}}{\pi\left(R_o^2 - R_i^2\right)} \qquad \textbf{3.5}$$

$$\tan\phi' = \frac{\tau_{sb}}{\sigma'_{n,sb}} = \frac{3T_{\theta,sb}\left(R_o + R_i\right)}{2F_{z,sb}\left(R_o^2 + R_o R_i + R_i^2\right)} \qquad \textbf{3.6}$$

where R_o and R_i = the outer and inner radii of the RS specimen chamber, respectively, and r = radius.

The error induced by using Equation 3.4 is calculated using the analytical method described by Hvorslev (1939). Assuming that: (1) in the zone of failure all planes perpendicular to the axis of rotation remain planar; (2) the unit shearing strain varies directly with distance r from the axis of rotation; (3) the vertical loads and horizontal stress are uniformly distributed and remain constant during shear; and (4) the friction between the specimen and the confining rings only causes a uniform concentration of the shearing strains, and the shearing strain γ for a given twist θ can be expressed by:

$$\gamma = \frac{\theta}{h} r \qquad \textbf{3.7}$$

where h is the height of the specimen. The unknown stress-strain function can be assumed to be $\tau = f(\gamma)$. Assuming that $f(\gamma)$ is continuous throughout the strain interval under consideration ($d\gamma$), moment T is obtained as (Hvorslev 1939):

$$T = 2\pi \int_{R_i}^{R_o} \tau_{sb} r^2 dr = \frac{2\pi h^3}{\theta^3} \int_{\gamma_i}^{\gamma_o} f(\gamma)\gamma^2 d\gamma \qquad \textbf{3.8}$$

Since $\gamma_o = \frac{\theta}{h} R_o$ and $\gamma_i = \frac{\theta}{h} R_i$, the above integral becomes a function of θ, or T = $F(\theta)$. Assuming that this function and its first derivative are continuous, differentiation with respect to θ gives:

$$\frac{dT}{d\theta} = -\frac{3}{\theta} \cdot \frac{2\pi h^3}{\theta^3} \int_{\gamma_i}^{\gamma_o} f(\gamma)\gamma^2 d\gamma + \frac{2\pi h^3}{\theta^3} \left(\frac{\theta}{h} R_o\right)^2 \frac{R_o}{h} f\left(\frac{\theta}{h} R_o\right) - \frac{2\pi h^3}{\theta^3} \left(\frac{\theta}{h} R_i\right)^2 f\left(\frac{\theta}{h} R_i\right) \qquad \textbf{3.9}$$

Since $\tau_i = f\left(\frac{\theta}{h} R_i\right)$ and $\tau_o = f\left(\frac{\theta}{h} R_o\right)$, the above equation can be reduced to:

$$\tau_o - \tau_i \left(\frac{R_i}{R_o}\right)^3 = \frac{3}{2\pi R_o^3} \left(T + \frac{\theta}{3} \frac{dT}{d\theta}\right) \qquad \textbf{3.10}$$

The left side of this equation has the same form as the Duguet-Ludwig-Prandtl equation, but there are two unknowns on the right side. In order to solve Equation 3.10, Hvorslev (1939) used the moment-twist curve (obtained from a RS test) in Figure 3.14, where:

$$F_i(\theta) = T + \frac{\theta}{3} \frac{dT}{d\theta} \qquad \textbf{3.11}$$

With n = R_i/R_o and using Equations 3.10 and 3.11, the shear stresses at outer and inner rings can be computed as:

$$\tau_o = \frac{3}{2\pi R_o^3} F_i(\theta) + n^3 \tau_i \qquad \textbf{3.12}$$

For equal amounts of shear displacements at the inner and outer radii, the amount of θ at the inner radius of the specimen would be *n* times the twist (θ) at the outer radius, therefore τ_i would be similar to Equation 3.12 but at nθ:

$$\tau_i = \frac{3}{2\pi R_o^3} F_i(n\theta) + n^3 \tau(n\theta) \qquad \textbf{3.13}$$

$$\tau(n\theta) = \frac{3}{2\pi R_o^3} F_i(n^2\theta) + n^3 \tau(n^2\theta) \qquad \textbf{3.14}$$

Subsequent functions of $\tau(n^2\theta)$, $\tau(n^3\theta)$, and etc. can be defined and τ_o can be obtained by summing these series as below:

$$\tau_o = \frac{3}{2\pi R_o^3}\left(F_i(\theta) + n^3 F_i(n\theta) + n^6 F_i(n^2\theta) + n^9 F_i(n^3\theta) + \cdots\right) \qquad \textbf{3.15}$$

And:

$$F_o(\theta) = F_i(\theta) + n^3 F_o(n\theta) + n^6 F_o(n^2\theta) + n^9 F_o(n^3\theta) + \cdots \qquad \textbf{3.16}$$

Therefore the actual magnitudes of the shear stresses mobilized at the outer and inner walls of the RS specimen are $\tau_o = \frac{3}{2\pi R_o^3} F_o(\theta)$ and $\tau_i = \frac{3}{2\pi R_i^3} F_i(n\theta)$.

Using torque-rotation (i.e. moment-twist) data from a typical RS test (, Figure 3.15 compares the average shear resistance computed using Equation 3.4 with the boundary shear stresses computed using Equations 3.14 and 3.15. As indicated in this figure, at large shear displacements (> 10 cm) the average and actual shear stresses are equal, indicating that the sand is at or near to a critical state where the shear resistance is a function of the void ratio alone and does not depend on the magnitude of strain. The worst agreement occurs at small shear displacements (< 0.1 cm), but even at these displacements the maximum difference between the average and actual shear stresses is

less than 2%. This indicates that the new RS device can be used to measure both the critical strength and the peak strength with reasonable accuracy.

Further verification of the results and operation of the new RS apparatus is described in Chapter 4.

3.6 SUMMARY AND CONCLUSIONS

Several laboratory devices have been used to measure the large displacement behavior of sands, most common of which are the DSS, TxC shear, and RS devices. The primary requirement is that the device should be able to shear a soil to large displacements without significant stress or strain non-uniformities in an undrained (or constant volume) and drained conditions. Based on this requirement and its other merits, the RS test appears to be best suited (of the devices reviewed) to define the large displacement behavior of sands. The other merits of the RS test include: (1) the ability to reach virtually unlimited shear displacements without creating substantial non-uniformities in stress and strain distributions at small to moderate shear displacement levels; (2) the ability to shear a soil on its depositional planes; (3) the ability to rotate principal stress directions in a manner similar to that expected under field conditions; and (4) a constant specimen cross-sectional area and geometry during shearing. However, like all laboratory devices, the RS test has some limitations, such as potential stress and strain non-uniformities associated with specimen dimensions, potential soil extrusion during shearing, difficulties in performing undrained testing, and friction that develops along the walls of the specimen confining rings.

Aware of these limitations, a new RS device was designed and constructed at the University of Illinois that minimizes the impacts of the aforementioned limitations. Specifically, the device can perform either constant volume or drained tests, and confining ring dimensions are selected to reduce stress and strain non-uniformities to a negligible amount at smaller shear displacements, noting that these non-uniformities become irrelevant at larger shear displacements. Auxiliary load and torque cells measure any wall friction that develops along the confining rings, allowing to compute the normal effective stress and shear resistance at the shear plane. In addition, the device utilizes

quad rings along the confining rings to prevent soil extrusion and a specialized computer controlled servo-motor can perform RS tests under strain- or stress-controlled loading.

3.7 FIGURES

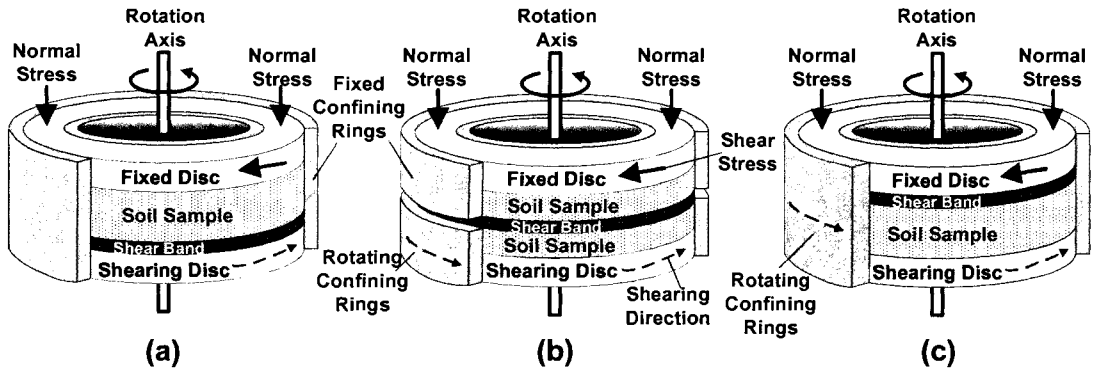

Figure 3.1: Schematic of RS test shearing mechanism in: (a) solid-ring device with shear band at the bottom of the specimen (current design); (b) split-ring device with shear band at mid-height (Imperial College/Norwegian Geotechnical Institute design); (c) solid-ring device with shear band at the top of the specimen (Bromhead design). The solid and dashed arrows indicate directions of measured and applied shear stresses, respectively.

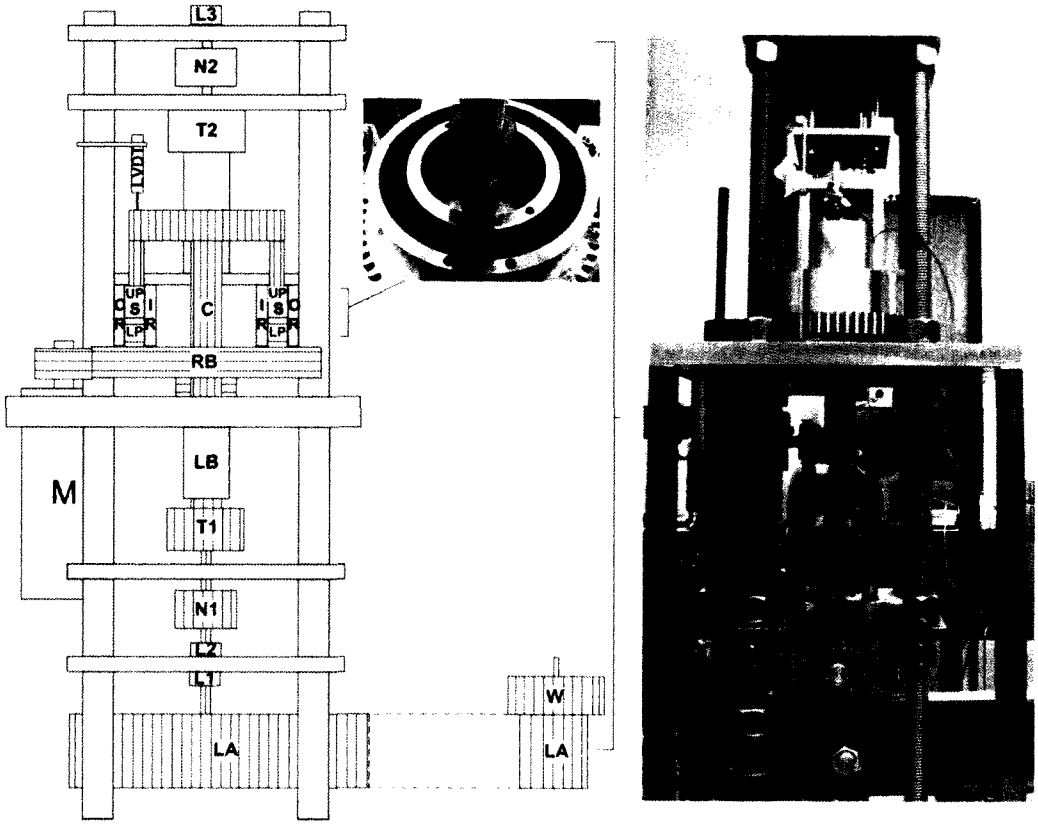

Figure 3.2: Photographs and schematic of the new RS device constructed at the University of Illinois.

Rotating parts are hatched horizontally; vertically moving parts are hatched vertically; fixed parts are colored gray. Labels (from the top of the device): L3 = nut used to lift the confining rings; N2 = upper load cell; T2 = upper torque cell; LVDT = linear variable differential transformer; UP = upper loading ring platen; IR = inner confining ring; S = soil specimen; OR = outer confining ring; LP = lower ring platen; RB = rotating base; C = central shaft; LB = central linear bearing; M = motor; T1 = lower torque cell; N1 = lower load cell; L1, L2 = locking nuts; LV = lever arm. Note N2 and T2 are mechanically coupled to the confining rings.

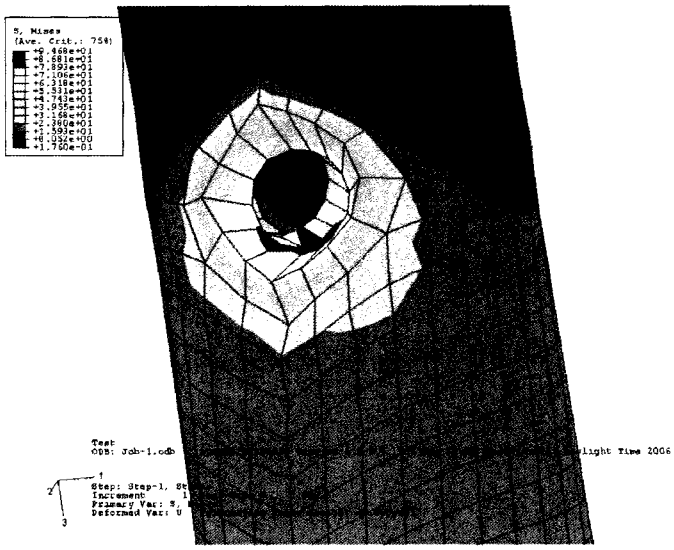

Figure 3.3: Finite element analysis of the central shaft

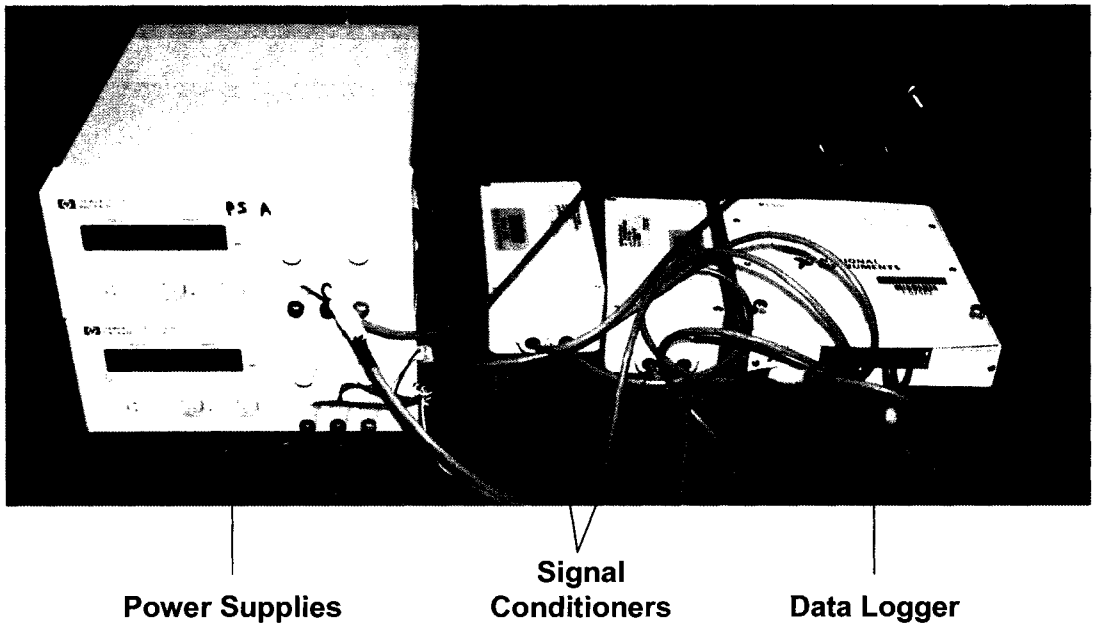

Figure 3.4: Photos of the power supplies, signal conditioners, and data logger

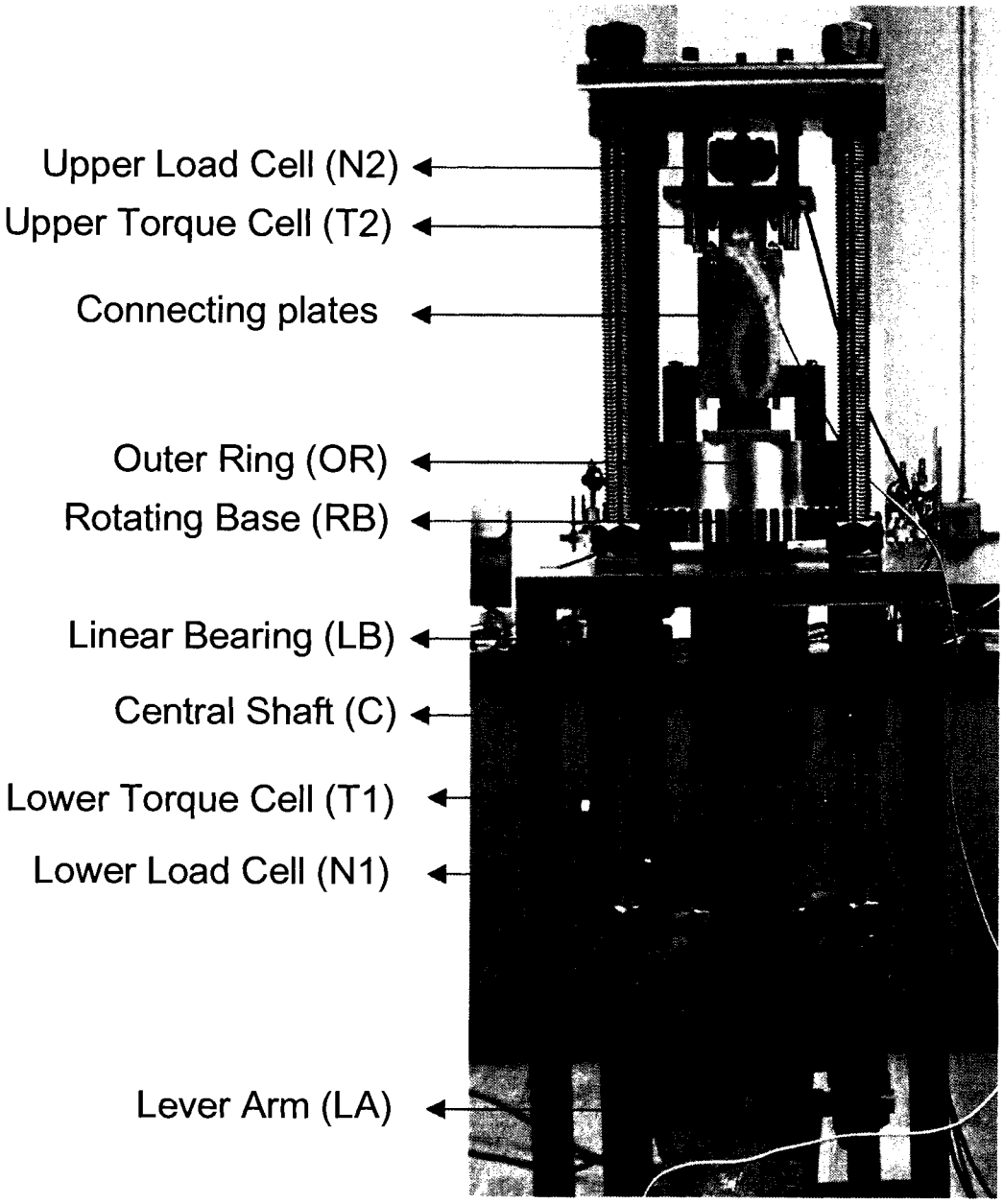

Figure 3.5: Major parts of the new RS device

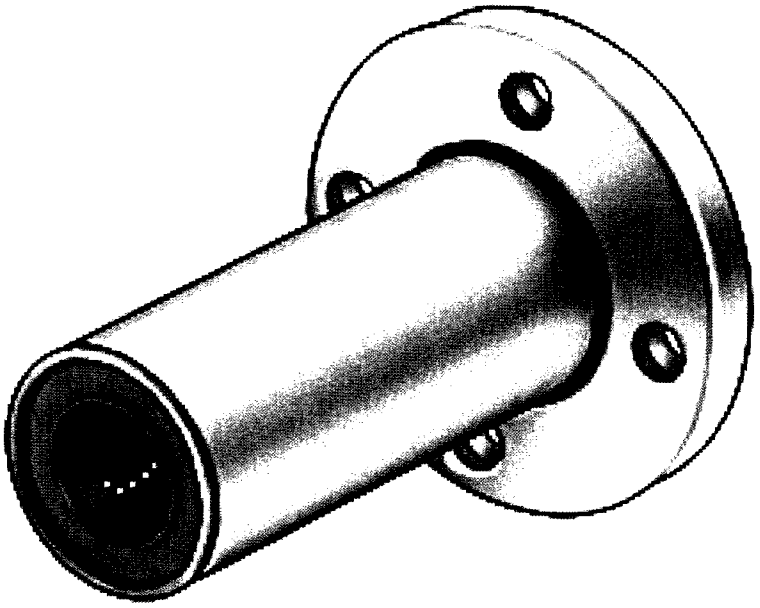

Figure 3.6: Central linear bearing (LB) (from website of McMaster-Carr supply company: www.mcmaster.com)

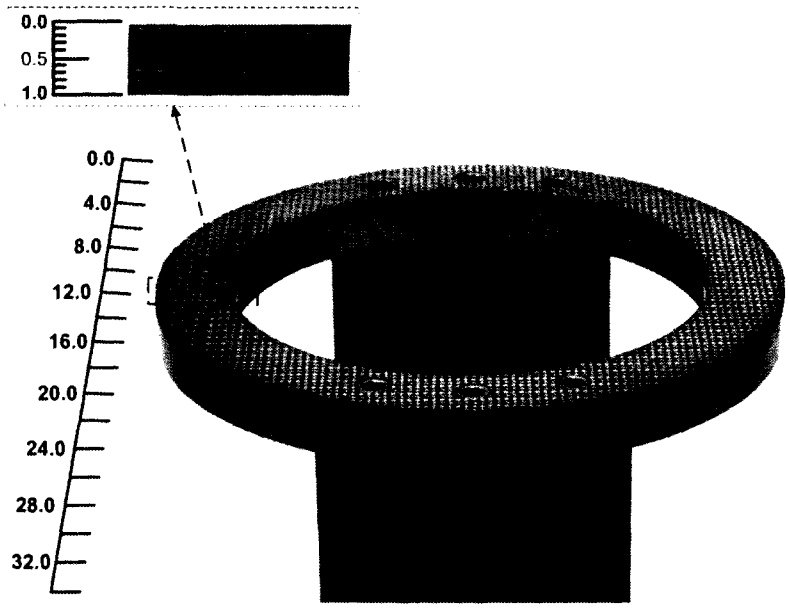

Figure 3.7: Upper loading disc and its serrated surface

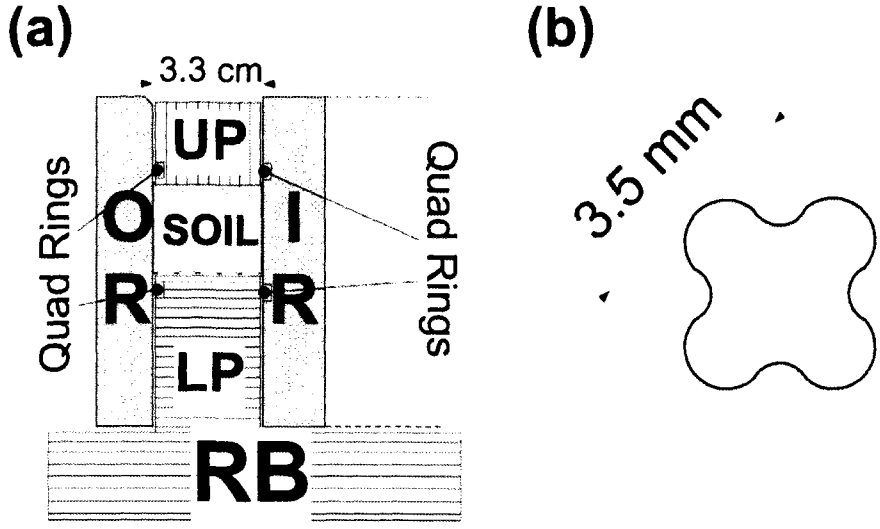

Figure 3.8: Cross-sections of: (a) specimen container; and (b) quad-ring. See Figure 3.2 for abbreviations

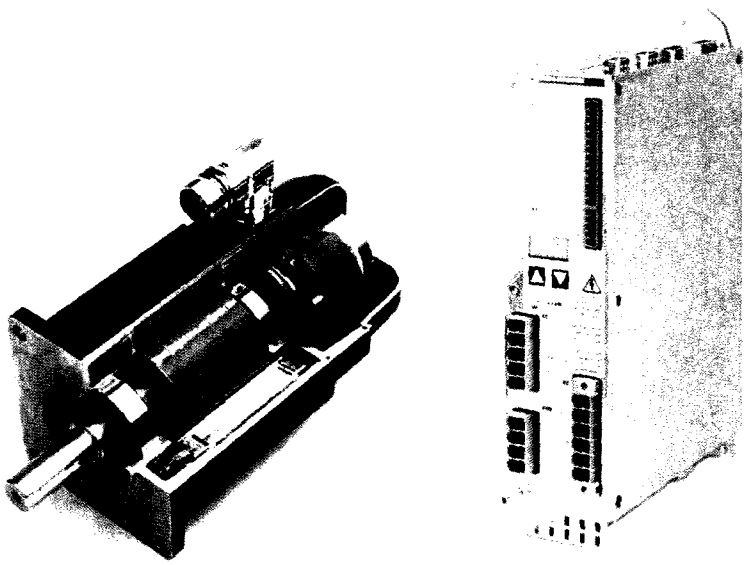

(a) (b)

Figure 3.9: (a) AKM54K servo motor, (b) Servostar S61000 drive (from www.danahermotion.com)

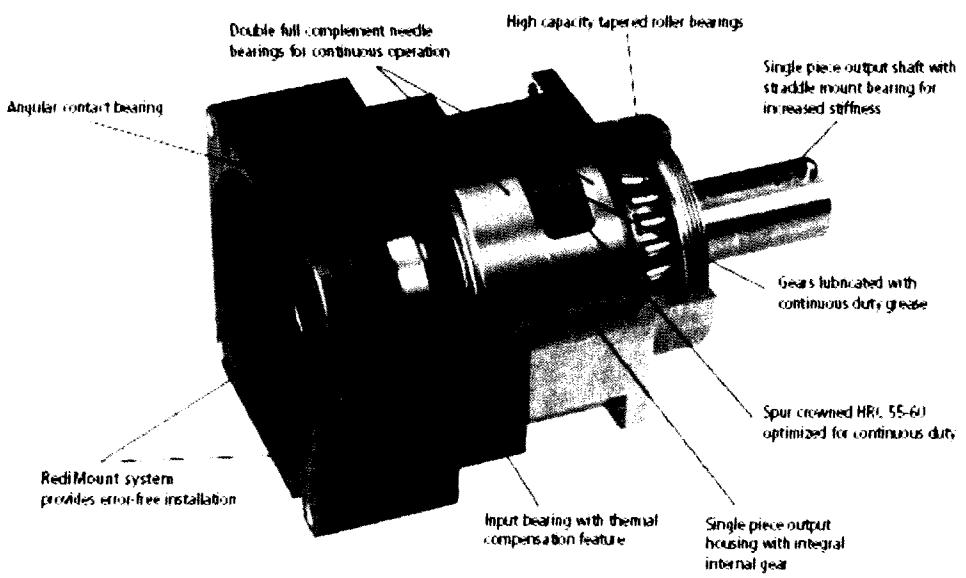

Figure 3.10: Gear reducer (Evertrue model #: ET018-070 from www.danahermotion.com)

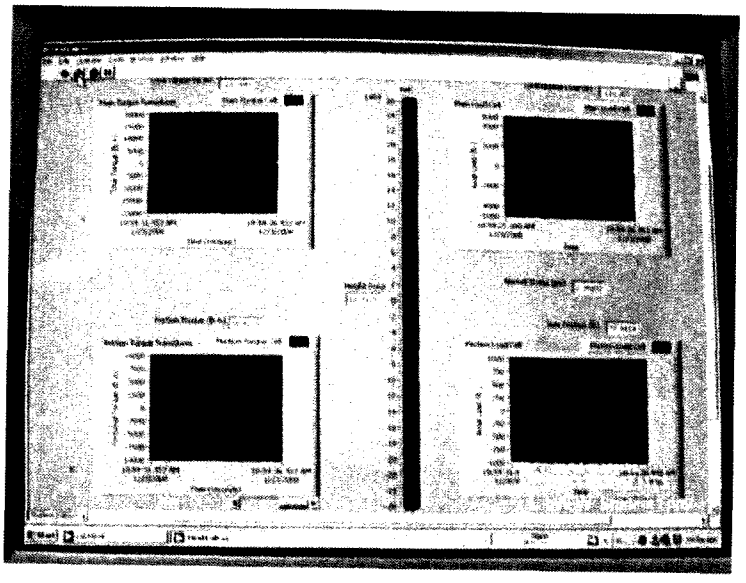

(a)

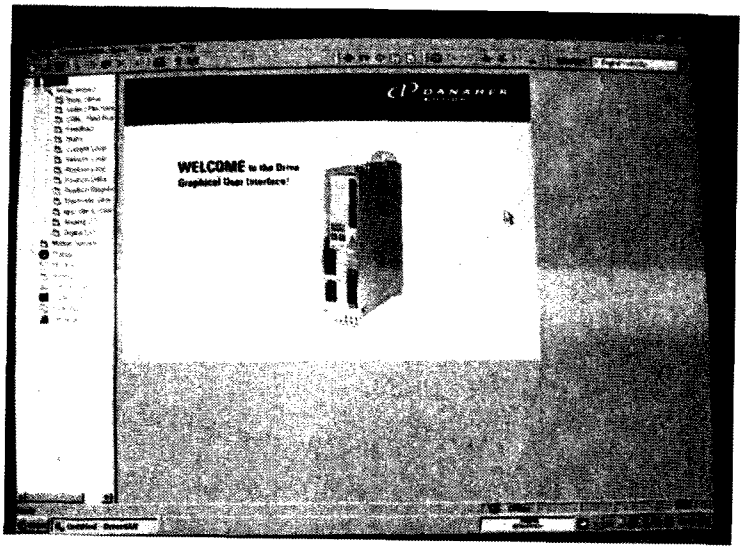

(b)

Figure 3.11: Screenshots of Labview and Motor Driver software

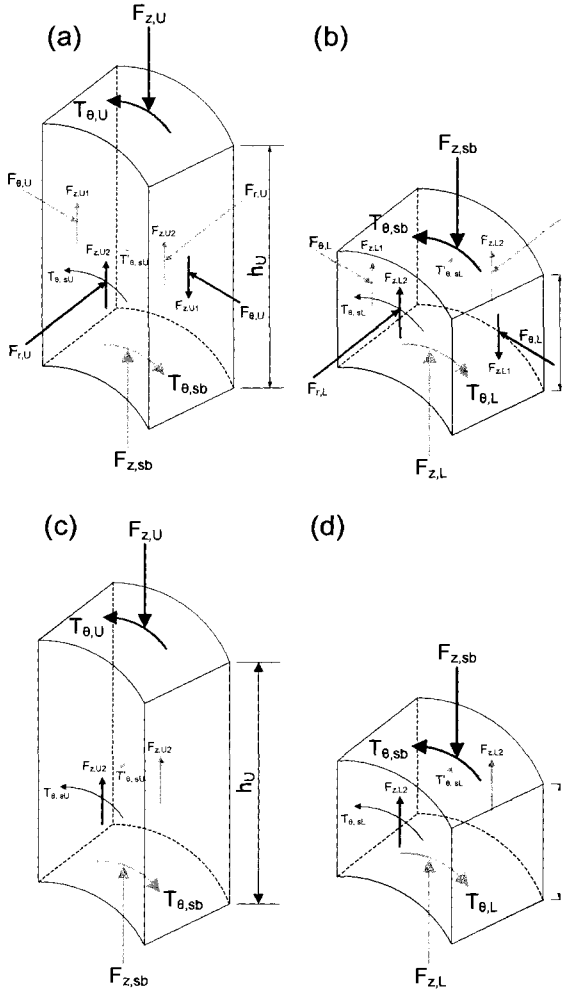

Labels (based on polar coordinate system): $F_{z,U}$ = total normal force applied to sample (measured by load cell N1); $T_{\theta,U}$ = total resisting torque (measured by torque cell T1); $F_{\theta,U}$ = normal force on radial plane through specimen above shear band; $F_{z,U1}$ = shear force on radial plane through specimen above shear band; $F_{r,U}$ = normal (radial) force on tangential plane above shear band; $F_{z,U2}$ = shear force on tangential plane above shear band; $T_{\theta,sU}$ = shear torque on inner confining ring; $T'_{\theta,sU}$ = shear torque on outer confining ring; $T_{\theta,sb}$ = resisting torque at top of shear band, $F_{z,sb}$ = normal force at top of shear band; h_U = height of specimen above shear band; $F_{\theta,L}$ = normal force on radial plane through specimen in shear band; $F_{z,L1}$ = shear force on radial plane through specimen in shear band; $F_{r,L}$ = normal (radial) force on tangential plane in shear band; $F_{z,L2}$ = shear force on tangential plane in shear band; $T_{\theta,sL}$ = shear torque on inner confining ring; $T'_{\theta,sL}$ = shear torque on outer confining ring; $F_{z,L}$ = total normal force at bottom of specimen; $T_{\theta,L}$ = total driving torque at bottom of specimen; h_{sb} = shear band thickness).

Figure 3.12: State of stress in the RS specimen: (a) Above the shear band; (b) in the shear band (sb) at the base of the specimen; (c) unbalanced forces (only) above the shear band; (d) unbalanced forces (only) in the shear band at the base of the specimen.

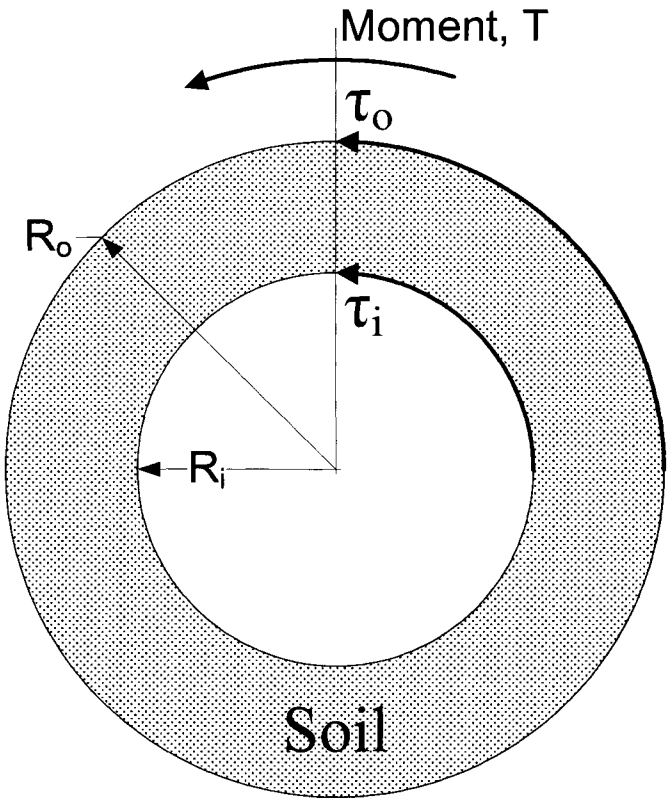

Figure 3.13: Soil specimen in RS test

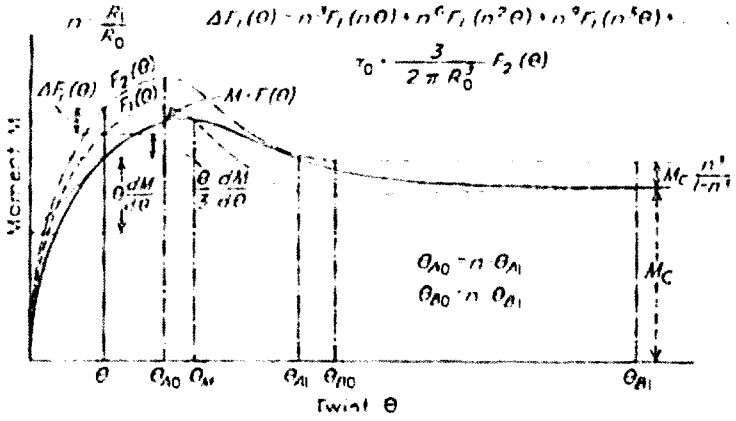

Figure 3.14: Moment – twist curve (from Hvorslev 1939)

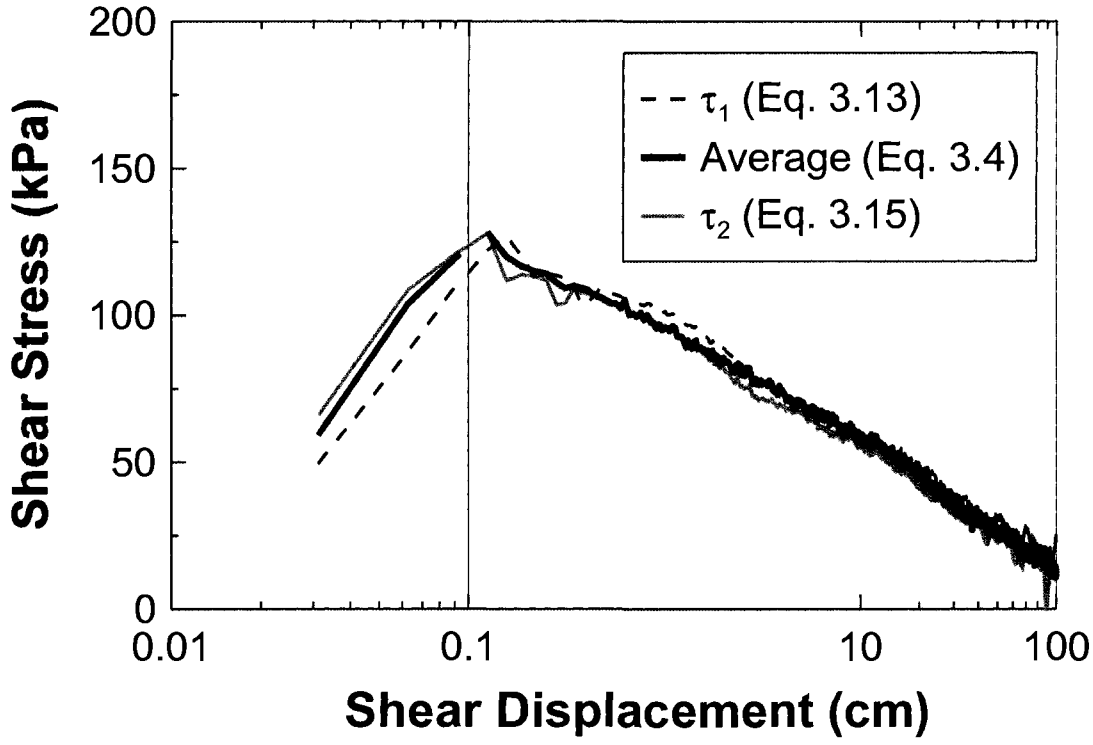

Figure 3.15: Average and actual boundary shear stresses in the new RS device

CHAPTER 4: EXPERIMENTAL PROGRAM

4.1 INTRODUCTION

This chapter describes the sands used in the experimental program, as well as the details and methodologies of the experiments. These include index tests (grain size distributions, maximum and minimum void ratios, specific gravity of grains, mineralogical compositions), oedometer tests, triaxial compression (TxC) shear tests, ring shear (RS) tests, X-ray diffraction test, and Scanning Electron Microscope (SEM) observations. In addition, typical results obtained using the new RS device, are presented to illustrate its capabilities, and compared to parallel TxC test results.

4.2 TESTED SANDS

Three sands were selected for this study: Ottawa 20/40 sand (OT), an Illinois River sand (IR), and a Mississippi River sand (MR). The OT sand is a commercially-available, medium-grained, uniform, pure quartz sand with rounded particles from Ottawa, Illinois. The IR sand is a medium-grained, uniform alluvial sediment from the Illinois River, with a fines content of less than 1% by weight. Silty sands are the most common type of soils involved in liquefaction (Yamamuro and Lade 1998). Despite this, most liquefaction research is performed on clean sands (like OT and IR sands) with the assumption that the behavior of silty sands is similar to that of clean sands. However, some researchers (e.g. Lade and Yamamuro 1997; Zlatovic and Ishihara 1997) have indicated that sands deposited with significant amount of silts are more liquefiable than clean sands. Therefore, MR sand (sampled near Cape Girardeau, Missouri) which is a very fine-grained silty sand with an average fines content of about 38% was selected to compare with clean IR and OT sands. The physical index properties of these sands are described in the following.

4.3 INDEX TESTS

4.3.1 Particle Shape

Scanning Electron Microscope (SEM) was used to define the shape of the particles. Representative samples of each sand were gold coated and SEM images were taken. Figure 4.1, Figure 4.2, and Figure 4.3 show the SEM images of OT, IR and MR sands, respectively. According to these figures OT sand has round particles, IR sand has round to subround grains, and MR sand is composed of subround to subangular particles.

4.3.2 Mineralogy

OT sand is a pure quartz sand from Ottawa Illinois, and IR sand is composed of quartz with traces of muscovite, chlorite, and hematite (Mueller 2000). The mineral content of MR sand, as indicated in the following paragraphs, was defined by acid dissolution and X-ray diffraction methods.

4.3.2.1 Acid dissolution

In this method 20g of the sand was soaked in HCl acid. Extreme care was taken when using this acid since even its vapor is detrimental to human respiratory system. After an hour the mixture was washed and dried and the lost weight indicated the amount of carbonates in the sand. MR sand showed strong reaction (sizzling) with HCl and 1g of it was dissolved in acid, indicating 5% carbonates.

4.3.2.2 X-ray diffraction

X-ray diffraction is the most widely used method for identification of fine-grained soil minerals and the study of their crystal structure. X-rays have wavelengths of 0.01 to 100 Å and since wavelengths of about 1 Å are of the same order as the spacing of atomic planes in crystalline materials, X-rays are useful for analysis of crystal structures. When X-rays strike a crystal, they penetrate to a depth of several million layers before being absorbed. At each atomic plane a minute portion of the beam is absorbed by individual atoms that then oscillate as dipoles and radiate waves in all directions. Radiated waves in certain directions will be in phase and can be interpreted in simplistic fashion as a wave resulting from a reflection of the incident beam. In-phase radiations emerge as a coherent

beam that can be detected on film or by a radiation counting device (Mitchell 1993). The orientation of parallel atomic planes, relative to the direction of the incident beam, at which radiations are in phase depends on the wave length of the X-rays and the spacing between the atomic planes. According to Bragg's law, the wavelength (λ), distance between atomic planes (d), and the X-ray reflection angle (θ) are related as:

$$n\lambda = 2d\sin\theta \qquad 4.1$$

Equation 4.1 is the basis for identification of crystals. Since no two minerals have the same spacing of interatomic planes in three dimensions, the angles at which diffractions occur can be used for identification. In this equation, n can be any whole number. The reflection corresponding to n = 1 is termed the first-order reflection. A complete X-ray diffraction pattern consists of a series of reflections of different intensities at different values of 2θ. Each reflection must be assigned to some component of the sample. Figure 4.4 shows the X-ray diffraction results of MR sand. The dominant wavelengths are 3.34 Å and 3.19 Å which according to Mitchell (1976) correspond to quartz (SiO_2) and albite [$Na(Si_3Al)O_8$], respectively. The relative quantities of these minerals were determined from the area of the reaction peaks. The resulting mineral composition is therefore, 70% albite and 21% quartz.

4.3.3 Specific Gravity

The standard procedure of ASTM D854-00 was used to determine the specific gravity (G_S) of these sands. The average values are shown in Table 4.1.

4.3.4 Maximum (e_{max}) and Minimum (e_{min}) Void Ratios

Due to the relatively large fines content (38%) of MR sand, the ASTM standard for defining the extreme densities was not applicable. Hence the method described by Yamamuro and Lade (1997) was used for all of the test sands to ensure consistency among the results. In this method the minimum void ratio was obtained by placing approximately 50g of soil into a graduated cylinder and tapping twice on the four opposing sides of the cylinder with a rubber-coated tool. This procedure was repeated

until 800g of sand was deposited in the graduated cylinder and the volume of the soil was then read to compute e_{min}. The maximum void ratio was then obtained by covering the end of the cylinder by a latex sheet and turning it upside down and back again very slowly (about 45-60 seconds) for the movement. The new volume of the soil was read to obtain e_{max}. This method was repeated three times for each sand and Table 4.1 shows the average e_{max} and e_{min} for each sand.

4.3.5 Particle Size Distribution

The particle size distributions of OT and IR sands were defined by sieving. But for MR sand, sedimentation analyses were also performed. Figure 4.5 presents the average grain size distributions of these sands.

4.4 SAMPLE PREPARATION METHOD

Air pluviation and moist tamping methods were used to prepare the specimens. Air pluviation is a commonly used and reliable method to achieve the most uniform densities (Mulilis et al. 1977; Jefferies and Been 2006). In this method, dry sand is poured into a funnel with its tip resting on the bottom of the specimen mold. The funnel is gently raised to deposit the particles with nearly zero drop height. This technique produces the loosest possible structure using air pluviation (Lade et al. 1998) and reduces segregation between the fine and coarse grains. Specimen uniformity was verified by preparing a number of specimens in four lifts and measuring the weight and height of sand deposited in each lift. It was observed that the void ratio of an individual lift deviated by a maximum of only 5.3% from the average void ratio of the entire specimen using this sample preparation method. The moist tamping method was used to prepare looser specimens, except for MR sand in TxC tests. This was because moist tamped TxC specimens of MR sand deformed significantly during flushing and saturation. In this method, dry sand was moistened and thoroughly mixed with 5% water, and then poured and gently tamped in 20 layers into the specimen container. Under-compaction as proposed by Ladd (1978) was used to achieve a relatively uniform density throughout the specimen. In this method the tamping energy is progressively increased from the bottom layer to the top layer assuming that some

portion of the tamping energy is transferred from the upper layer to all of the lower layers.

4.5 OEDOMETER TESTS

Oedometer tests were conducted to measure the compression behavior of the sands. These tests were done on dry sands pluviated in the oedometer mold. The mold has an internal diameter of 6.256 cm (2.463 inches) and a height of 1.877 cm (0.739 inches). Before the tests, machine deflection was determined by compressing a very stiff steel specimen instead of sand and the soil specimen results were corrected for machine deflection. Figure 4.6 shows the normal compression behavior of the tested sands. OT sand is the most incompressible sand; IR sand is more compressible than OT sand and MR sand is the most compressible sand among these sands.

4.6 TRIAXIAL COMPRESSION TESTS

Undrained and drained TxC tests were performed with an automatic stress path triaxial apparatus (TruePath from GEOTAC) shown in Figure 4.7. The TxC specimen has a diameter of 5.08 cm (2 inches) and a height of 10.16 cm (4 inches). Two electromechanical pumps are used to drive water into the specimen and the cell fluid (silicon oil in these tests) into the triaxial cell. The volume and fluid pressure in these pumps are measured with resolutions of 1 mm^3 and 0.1 kPa, respectively and are recorded by the data-logger to the computer. The load frame shears the specimen by applying an axial force while measuring the amount and rate of deformation. In addition to the pressure transducer of the water pump, there is another transducer which measures the pore water pressure within the soil specimen, separately. And although the axial load is measured by an external load cell, an internal load cell connected to the tip of the axial loading shaft measures the axial force on the specimen, hence preventing the complexities of the effects of the weight and friction of the axial shaft on measurements.

4.6.1 TxC Specimen Preparation

A split mold was used to form the triaxial specimens and keep the rubber membrane (diameter of 50.8 mm and thickness of 0.3 mm). After placing the sand in the triaxial split mold (by either moist tamping or dry deposition), the top of the specimen was leveled using a straight-edge and a filter paper and porous steel disc were placed on top of the specimen. Then the top cap was set in place and the membrane was rolled over the top cap. The membrane was sealed to the top cap using three rubber O-rings. To minimize end restraint and thus strain localization during shear, the end platens were lubricated using a thin layer of silicon grease. According to Rowe and Barden (1964), Bishop and Green (1965), and Ueng et al. (1988), the effect of end restraint on the shear strength decreases with increasing void ratio and confining pressure, and it was assumed that the use of lubricated platens combined with very loose specimens would effectively eliminate end restraint. A vacuum of approximately 20 kPa was applied to maintain the specimen shape while removing the split mold. After removing the mold, the specimen dimensions were measured with a caliper and the remaining sand not used during specimen preparation was oven dried and weighed. Thus the initial void ratio of the sample was calculated by knowing the dry weight and initial dimensions of the specimen. Then the confining cell was assembled and filled with silicon oil and the vacuum was gradually released by slowly applying a confining pressure of approximately 20 kPa. Potential uncertainties involved in computing the void ratio will be discussed later in this chapter.

4.6.2 Saturation

Carbon dioxide gas was circulated through the sample for 30 minutes (Mulilis et al. 1975), and then the sample was flushed with a volume of de-aired water of roughly three times the volume of the voids. To prevent pore pressure build-up and minimize disturbance to the initial soil structure, flushing was performed at a very slow rate of 3 ml/min. Then the backpressure saturation procedure recommended by Bishop and Henkel (1962) and Black and Lee (1973) was used to dissolve any remaining air and saturate the specimen until a pore pressure parameter (B), of at least 0.97 was obtained at a backpressure of about 300 kPa. Care was taken to ensure that the effective stress on the

specimen never exceeded approximately 20 kPa while preparing each specimen. The triaxial device's data acquisition system recorded any volume changes and indicated that the void ratio decreased by an average of 2.5% after flushing, but then increased by an average of 1.6% after backpressure. These changes were taken into account when calculating the void ratios. Figure 4.8 shows the prepared triaxial specimen before consolidation.

4.6.3 Consolidation

Following preparation, each specimen was consolidated to the target effective confining pressure at a rate of 13.8 kPa/min which allowed sufficient time for the pore water pressure to dissipate. During this stage the volume of water driven out of the sample was measured and consolidation void ratio was calculated. Figures C.1 through C.3 (Appendix C) show typical compression behaviors of the sands.

4.6.4 Shearing

After consolidation, the drainage lines were closed or left opened for undrained or drained shearing, respectively. The samples were sheared at a constant strain rate of 1.25%/min (displacement rate of 0.127 cm/min) up to an axial strain of 25%. This rate was slow enough to allow at least 95% pore pressure equalization during drained and undrained shear (requiring a minimum c_v = 102 m^2/day) in the TxC tests. During undrained shearing, it was found that pore pressure would build up in the sample after primary consolidation was complete and the drainage valve was closed to begin shearing. It is thought that the pore pressure build up was due to "arrested secondary compression" (Mesri 1987) or "undrained creep" (Head 1986). However, the amount of this excess pore water pressure was very minor due to the small amount of time which took for the piston to travel into the seating groove in the top cap before making contact with the sample. Table 4.1 summarizes the preparation methods and consolidation conditions for each TxC test.

4.6.5 Corrections to Triaxial Test Data

Area correction and membrane resistance corrections were applied to all TxC tests conducted on the sands of this study. A standard area correction was used, assuming that the sample deforms as a right circular cylinder. These are described here.

4.6.5.1 Area correction

The cross sectional area of the specimen during consolidation and shearing phases was corrected assuming that the specimen deforms as a right circular cylinder. This correction is used in the standard test method (ASTM D4767) for TxC tests and is recommended by La Rochelle et al. (1988) for bulging type failure. All of the TxC specimens exhibited a bulging type failure. The area correction is given as:

$$A_c = \frac{A_0(1-\varepsilon_{vol})}{1-\varepsilon_a} \qquad \textbf{4.2}$$

where A_c = corrected area of specimen; A_0 = the initial area of specimen; ε_{vol} = volumetric strain of sample; and ε_a = axial strain of sample.

4.6.5.2 Membrane resistance correction

During the consolidation phase, cell pressure applies axial and radial stresses to the sample and membrane. Most of the pressure is taken up by the sample, but a small part of the axial and radial loads is taken up by the membrane. During shearing, an additional axial load is applied to the specimen and membrane, and again the membrane takes up part of the applied axial load. To calculate the loads in the membrane, the membrane is treated as a thin walled cylinder so that the tangential stress can be considered constant throughout the thickness of the membrane. Here the corrections made for the membrane resistance are described.

The ASTM standard D4767 provides a membrane resistance correction and recommends correcting for the resistance of the membrane if the error in deviator stress due to strength of the membrane is greater than 5%. The ASTM correction was used in the TxC test results as below:

$$\Delta(\sigma_1 - \sigma_3) = \frac{4E_m t_m}{D_c}\left(\varepsilon_a + \frac{\varepsilon_{vol}}{3}\right) \qquad 4.3$$

In this equation, $\Delta(\sigma_1 - \sigma_3)$ = correction to be subtracted from the mean principal stress difference, D_c = diameter of specimen after consolidation, E_m = Young's modulus of the membrane material (= 1.3 MPa for the membrane used in this study), t_m = membrane thickness (= 0.305 mm), ε_a = axial strain, and ε_v = volumetric strain. This error could be significant in tests on very loose moist tamped specimens where the liquefied shear strength is very small. The extra radial stress due to membrane stiffness was also taken into account. Considering the membrane as a thin elastic cylinder undergoing the same deformations as the specimen, the extra radial stress caused by the deforming membrane is (Fukushima and Tatsuoka 1984):

$$\Delta\sigma_{rm} = -\frac{2E_m t_m \varepsilon_{\theta m}}{d} \qquad 4.4$$

where d = sample diameter (which varies during shearing), and $\varepsilon_{\theta m}$ = membrane orthoradial strain (assumed equivalent to sample radial strain). Most references (ASTM D4767; La Rochelle et al. 1988; Head 1986) recommend the same procedure to measure the Young's modulus (E_m), of the membrane based on an extension test proposed by Henkel and Gilbert (1952). The test involves stretching a 2.54 cm (1 inch) wide loop of the membrane with weights and measuring the axial deformation. This test was performed on the membranes used for the TxC tests. The stress in the membrane was calculated based on the original dimensions of the membrane and a membrane modulus of about 1.3 MPa was obtained.

4.6.5.3 Membrane penetration effects

As the cell pressure is increased in a triaxial test, the lateral pressure on the membrane will not be balanced by the pore water pressure and consequently, the membrane will be deformed and the volume of the specimen will be reduced. This volume reduction is

called membrane penetration. The lateral penetration of the membrane into a triaxial sample affects either the volumetric strains in drained tests or the pore pressures in undrained tests (Baldi and Nova 1984). This phenomenon has been studied by several researchers (e.g. Newland and Allely 1957, 1959; Raju and Sadasivan 1974; Martin et al. 1978; Raju and Venkataramana 1980; Molenkamp and Luger 1981) assuming that the membrane has no flexural rigidity, its thickness doesn't change due to penetration, and the penetration is equal to the volume between the original position and the deformed membrane, Baldi and Nova (1984) found that the volume change due to membrane penetration is equal to:

$$V_m = \frac{1}{2}\frac{\sigma'_{mean} D_{50}}{E_m t_m}\frac{D_{50}}{d}\frac{V_0}{\sin^2\left[\left(\frac{\sigma'_{mean} D_{50}}{E_m t_m}\right)^{1/3}\right]} \qquad \textbf{4.5}$$

where, σ'_{mean} = effective mean stress, D_{50} = median particle size, and V_0 = volume of the specimen before shearing. The membrane penetration effect can be quantified using a normalized membrane penetration parameter e_m as:

$$e_m = \frac{V_m}{A_s \Delta \log \sigma_{mean}} \qquad \textbf{4.6}$$

where A_s is sample area covered by the membrane, and σ_{mean} is total mean pressure acting on the membrane. The parameter e_m is primarily a function of D_{50} (Sladen et al. 1985). Accordingly, the effect of membrane penetration strongly depends on D_{50} and σ'_{mean} in a particular TxC test. In addition, the effect of membrane penetration not only depends on the flexibility of the membrane but also on the volumetric stiffness of the soil sample, which further depends on the state of stress and changes during the test. The effect of membrane penetration was considered by correcting the void ratios during shear according to Equation 4.6. The average void ratio change was 0.007 for IR and OT sands and 0.0005 for MR sand specimens. The very small effect of membrane penetration on void ratio resulted from the very fine gradation of the test sands, thus no attempt was

made to compensate for membrane penetration effects (e.g. by injecting water into undrained TxC specimens) (Been et al. 1991; Riemer 1992; Huang et al. 1999).

4.6.6 Data Reduction

The critical state convention was used to present the TxC stress paths (Wood 1984). The variables of this convention are as below:

$$q = (\sigma'_1 - \sigma'_3) \qquad \textbf{4.7}$$

$$\sigma'_{mean} = \frac{(\sigma'_1 + \sigma'_2 + \sigma'_3)}{3} \qquad \textbf{4.8}$$

in which σ'_1, σ'_2, and σ'_3 are the major, intermediate, and minor principle effective stresses, respectively. The projection of the CSL in $q - \sigma'_{mean}$ space is called the M line.

4.7 RING SHEAR TESTS

Constant volume and drained RS tests were performed using the newly developed solid confining ring type RS apparatus designed and built at the University of Illinois. Detailed specifications and photos of this machine are provided in Chapter 3. Since no pore water pressure measurement system was implemented, none of the RS tests were saturated and all were performed on dry air pluviated or moist tamped specimens. At small displacements, the mode of shearing in the new RS device is similar to a plane strain simple shear test which better represents conditions in the ground in many cases, for example under strip foundations, in earth dams, slopes, retaining structures, and levees than a TxC test (Alshibli and Sture 2000; Hosono and Yoshimine 2004; Alshibli and Akbas 2007).

4.7.1 Ring Shear Specimen Preparation

Since all tests were dry and not saturated, no saturation (flushing and back-pressuring) was required; hence the specimen preparation procedure in the RS tests was shorter than

the TxC tests. In the RS tests, after depositing the sand into the ring shaped chamber of the apparatus, the top surface of the specimen was leveled using a straight-edge, the upper disk platen was carefully lowered on the specimen, the LVDT was installed and initialized, the remaining sand was weighed and then the initial height of the specimen was measured to calculate initial void ratio with an accuracy of ±0.005.

Afterwards, the central shaft (C in Figure 3.2) was connected to the upper platen (UP in Figure 3.2) and then this platen was released (by loosening the locking nuts L1 and L2 in Figure 3.2) to rest on the top of the specimen (seating load). Following this stage, the friction measuring system (the coupled torque and load cells, T2 and N2 in Figure 3.2) was attached to the confining rings and by lifting this system by about 1 mm, the rings were basically suspended, thus not in contact with the rotating base (RB in Figure 3.2). From this point on, the effective stress on top of the shear band was calculated from the measurements of load cells N1 and N2 and using Equation 3.5.

4.7.2 Consolidation

The RS specimen was consolidated by placing the dead loads at the tip of the level arm. As described in Chapter 3, a ten times larger load is applied on the top surface of the specimen. About one hour was allowed for all densification to be completed. Figures C.1 through C.3 show the compression behavior of the sands in the ring shear tests.

4.7.3 Shearing

Before shearing, a constant volume condition was imposed by tightening nuts L1 and L2 to the plate between them. This plate restrains the movement of the upper platen (UP) and maintains a constant volume during shearing. In drained tests, nuts L1 and L2 were left loose so that the upper platen could freely move up (dilative soil) or down (contractive soil). Shearing was then started by rotating the bottom disk (RB in Figure 3.2) at a rate of 18.6 cm/min. This rapid shearing rate was selected so that a test to very large shear displacement (i.e., more than 10 m) could be completed in a day, and was considered acceptable since numerous investigators (e.g., Novosad 1964; Scarlett and Todd 1969; Savage 1982; Hungr and Morgenstern 1984; Lemos 1986; Sassa 2000) have

shown that the rate of shearing has a negligible effect on the shearing behavior of sands tested in RS devices.

Table 4.3 provides the preparation methods and consolidation conditions for each of the RS tests. Data reduction and interpretation of the RS measurements are provided in Chapter 3.

4.8 UNCERTAINTIES IN VOID RATIO MEASUREMENTS

A number of authors have discussed the difficulties of accurately defining the critical state conditions of a soil due to the uncertainties in global void ratio determination, in both in-situ and laboratory test specimens (e.g., Poulos et al. 1985; Castro et al. 1985; Sladen and Handford 1987; Kramer 1989; Vaid and Sivathayalan 1996; Garga and Zhang 1997). Errors in global void ratio can result from uncertainties in specimen dimensions, specimen mass, and specific gravity. Void ratio by definition is:

$$e = \frac{V}{V_S} - 1 \qquad \textbf{4.9}$$

where V and V_S are the total volume and volume of the soil solids of the specimen, respectively. For a cylindrical triaxial specimen of height, h, diameter, d, and specific gravity of solids G_S, void ratio can be written as:

$$e = \frac{\pi d^2 h G_S}{4 M_S} - 1 \qquad \textbf{4.10}$$

where M_S is the mass of soil solids. By differentiating Equation 4.10 with respect to each of its parameters, the deviation of the void ratio from its true value is:

$$de = (1+e)\left(\frac{2\pi \partial d}{d} + \frac{\partial h}{h} + \frac{\partial G_S}{G_S} - \frac{\partial M_S}{M_S}\right) \qquad \textbf{4.11}$$

where e is the actual void ratio. In a series of tests on a given sand one can assume, ∂G_S = 0.0 and by replacing the partial differentials with finite differences of each parameter in Equation 4.11, the maximum error in void ratio becomes:

$$\Delta e = (1+e)\left(\frac{2\pi\Delta d}{d} + \frac{\Delta h}{h} - \frac{\Delta M_S}{M_S}\right) \qquad \textbf{4.12}$$

Equation 4.12 implies that for a given specimen size, the uncertainty in void ratio, Δe, depends on the void ratio of the sand as well as uncertainties in diameter (Δd), height (Δh), and mass (ΔM_S) of the specimen. Equation 4.12 indicates that at a given void ratio, Δe increases with decrease in specimen diameter and for a given specimen diameter, Δe increases with increase in void ratio, i.e., the uncertainty in void ratio measurements is greater in loose sands, which are most prone to liquefaction. Also, uncertainties in measuring specimen diameter contributes the largest uncertainty to void ratio while the resolution of weighing the specimen mass contributes the least.

In the TxC tests of this study, the specimen diameter was measured using a caliper with a resolution of 0.025 mm. A reference dial indicator with a resolution of 0.01 mm was used to measure the specimen height. Solids mass was measured using a digital scale with a resolution of 0.1 grams. Accordingly, for TxC test for example, MTIRDR54 with the e = 0.672, d = 50.800 mm, h = 96.16 mm, and M_S = 294.5 grams, the uncertainty in void ratio is ±0.0049, that is consistent with the range reported by Garga and Zhang (1997) and an order of magnitude smaller than the largest possible error of 0.05 in conventional triaxial testing techniques reported by Papageorgiou (2001).

In the ring shear tests, for a ring shaped specimen of outer and inner diameters of D_o and D_i and a height of h the void ratio can be calculated as below:

$$e = \frac{\frac{\pi}{4}\left(D_o^2 - D_i^2\right)h}{\frac{M_S}{G_S}} - 1 \qquad \textbf{4.13}$$

Similar to Equation 4.11, by differentiating Equation 4.13 with the assumptions that the specimen circumferential dimensions are fixed ($\partial D = 0.0$) and in a series of tests on a given sand $\partial G_S = 0.0$:

$$de = (1+e)\left(\frac{dh}{h} - \frac{dM_S}{M_S}\right) \qquad \textbf{4.14}$$

and in finite difference terms Equation 4.14 becomes:

$$\Delta e = (1+e)\left(\frac{\Delta h}{h} - \frac{\Delta M_S}{M_S}\right) \qquad \textbf{4.15}$$

Equation 4.15 shows that the resolution of void ratio measurements in the ring shear test is chiefly a function of the accuracy of specimen height and specimen mass. For example, for RS test MTIRCV18 the uncertainty in void ratio measurement is 0.0071 using values of h = 23.87 mm, M_S = 910.4 grams, Δh = 0.1 mm, and ΔM_S = 0.1 grams. Again this uncertainty is within acceptable limits (Garga and Zhang 1997; Papageorgiou 2001).

4.9 TYPICAL RING SHEAR TEST RESULTS AND INTERPRETATION

To evaluate the performance of the new RS device, parallel sets of constant volume and drained RS and TxC tests were performed on MR sand, and the results were compared. All RS tests were performed on dry specimens, while TxC tests were performed on water saturated specimens. As discussed earlier in Chapter 3, other researchers have verified that constant volume tests performed on dry specimens yield results identical to parallel undrained tests performed on saturated specimens. In addition, many researchers (e.g., Terzaghi et al. 1996; Infante-Sedano 1998) have shown that the presence of water does not affect the shearing behavior of sands.

4.9.1 Constant Volume Ring Shear Test Results

Figure 4.9 presents the LVDT measurements obtained during a typical constant volume RS test on an air pluviated specimen of MR sand. As seen in Figure 4.9, the LVDT captures minor changes in the position of the upper platen (UP). Finite element calculations indicate that the observed change in LVDT measurements (less than 0.2 mm) are the result of elastic rebound of the central shaft, lower load and torque cells, threaded rod, and the lower supporting steel plate (i.e., system compliance) as the normal effective stress decreases during shearing. This system compliance results in almost negligible changes in global void ratio (a maximum deviation of about 2%, and almost zero deviation at displacements larger than 1 cm) as a result of the large specimen volume, providing an essentially constant volume shearing condition. Furthermore, post-test observations indicated that no soil extruded past the quad rings, i.e., no loss of volume occurred during the test.

Figure 4.10 presents the corresponding load measurements made by load cells N1 and N2, as well as the values of effective normal stress measured at the top of the specimen ($\sigma'_{n,top}$) and at the shear band ($\sigma'_{n,\,sb}$) computed using Equations 3.2 and 3.5. Because the shear band generally develops near the bottom of the specimen of sand in a RS device with fixed confining rings, it is critical to differentiate $\sigma'_{n,sb}$ from $\sigma'_{n,top}$. The value of $\sigma'_{n,sb}$ is computed from the normal load applied to the top of the sample ($F_{z,U}$, which is typically measured in RS tests and provides $\sigma'_{n,top}$) minus the vertically-oriented wall friction mobilized between the specimen and the inner and outer confining rings ($F_{z,U2}$, which is not typically measured in RS tests).

Figure 4.11 presents the corresponding torque measurements made by torque cells T1 and T2. At the start of shear the side friction was approximately 40 to 50% of the shear resistance measured at the top of the sample, while at large displacement the side friction became less than 5% of the total shear resistance.

Figure 4.12(a) presents the stress paths from the RS test corresponding to multiple combinations of shear and normal stresses: (1) shear and normal stresses mobilized at the shear band (τ_{sb} and $\sigma'_{n,sb}$) which are measured using the unique combination of normal and torque load cells in the new RS device; (2) shear and normal stresses mobilized at the top of the specimen (τ_{top} and $\sigma'_{n,top}$) which would be measured using a conventional solid-

ring RS device; (3) τ_{sb} and $\sigma'_{n,top}$; and (4) τ_{top} and $\sigma'_{n,sb}$. For comparison, Figure 4.12(b) shows the stress path of a parallel TxC test performed on an air pluviated specimen of MR sand.

Using Equation 3.6, Figure 4.12(a) also presents the mobilized friction angle for each stress path at the end of the RS test, and Figure 4.12(b) includes the friction angle mobilized at the end of the parallel TxC test, computed as:

$$\phi' = \sin^{-1}\left[\frac{3\left(q/\sigma'_{mean}\right)}{6+\left(q/\sigma'_{mean}\right)}\right] \qquad \textbf{4.16}$$

Figure 4.13 compares the shear and effective normal/mean stresses measured during the parallel constant volume RS and TxC tests on MR sand. Here, the TxC specimen dilates slightly at an axial compression of 1.3 cm. In contrast, the RS specimen contracts throughout shearing and reaches a critical state after a shear displacement of about 100 cm – a much larger displacement than can be reached with other shear testing devices.

4.9.2 Drained Test Results

Figure 4.14 presents the LVDT measurements obtained during a typical drained RS test on a MR sand specimen. Here the LVDT measures the significant changes in the position of the upper platen (UP) which correspond to a void ratio decrease of about 15%. Note that over 10 m of displacement was required for the void ratio to approach an approximate critical state in this particular test. Again, post-test observations indicated that no soil extruded past the quad rings, i.e., no loss of volume occurred during the test. For comparison, the void ratio change observed in a parallel TxC test is also included. In this case, the void ratio reaches a temporary minimum and then begins to increase until the test reaches its practical displacement limit.

Figure 4.15 presents the loads measured by load cells N1 and N2, as well as the computed values of effective normal stresses at the top of the specimen ($\sigma'_{n,top}$) and at the shear band ($\sigma'_{n,sb}$). These measurements indicate that side friction ($F_{z,U2}$) was approximately 14% of the normal load ($F_{z,U}$), nearly identical to the ratio measured in the

constant volume test. As anticipated, $\sigma'_{n,sb}$ should remain essentially constant throughout the drained test, however, the decrease/increase in $\sigma'_{n,sb}$ during drained shearing (Figure 4.15) was due to the unavoidable rotation of the lever arm as the specimen contracted/dilated during shear.

Figure 4.16 provides the corresponding torque measurements made by torque cells T1 and T2 as well as the values of shear stress at the top of the specimen (τ_{top}) and at the shear band (τ_{sb}) for the drained RS test. The measured total torque ($T_{\theta,L}$), frictional torques ($T_{\theta,sU}$ and $T'_{\theta,sU}$), and shear stress at the shear band (τ_{sb}) increase until reaching a peak, then decrease to a temporary minimum plateau, and then increase to a slightly higher plateau after approximately 2 m of displacement. It is possible that the higher plateau may be the result of particle damage that occurs at large displacements (this was confirmed by comparing the grain size distributions of the sand collected from the shear band before and after shearing), resulting in a slightly more well-graded soil that has a slightly higher constant volume friction angle. Similar to the initial portion of the constant volume test, the side friction was approximately 40% of the shear stress measured at the top of the specimen.

Figure 4.17(a) presents the stress paths from the RS test corresponding to multiple combinations of shear and normal stresses from the drained RS test: (1) shear and normal stresses mobilized at the shear band (τ_{sb}; $\sigma'_{n,sb}$) which are measured using the unique combination of normal and torque load cells in the new RS device; (2) shear and normal stresses mobilized at the top of the specimen (τ_{top}; $\sigma'_{n,top}$) which would be measured using a conventional solid-ring RS device; (3) τ_{sb} and $\sigma'_{n,top}$; and (4) τ_{top} and $\sigma'_{n,sb}$. For comparison, Figure 4.17(b) shows the results of a parallel TxC test performed on a specimen of MR sand, as well as the TxC effective stress friction angle mobilized at the end of test.

The constant volume and drained large-displacement effective stress friction angles computed using the stresses on the shear plane (τ_{sb}; $\sigma'_{n,sb}$) are approximately equal to 37°, while the corresponding friction angles measured in TxC are about 32°. The difference of about 5° is consistent with published data on the relationship between plane strain and TxC friction angles (Rowe 1969; Terzaghi et al. 1996), as these RS tests subject the soil to a condition similar to plane strain. This agreement confirms that the stresses mobilized

on the shear plane must be measured when testing sands in a solid-ring RS device (where shearing occurs at the base of the specimen), and could not be properly measured in a conventional solid-ring RS device that does not separately measure wall friction. Not considering these forces (that are not typically measured in solid-ring devices) when testing sands can result in large displacement strengths that are too small. Furthermore, the results presented here suggest that the displacement limits of the triaxial device may preclude measuring the critical shear strength even for loose, contractive specimens. In contrast, the new RS device appears to reach a critical state in both constant volume and drained conditions.

Well-defined shear bands developed in both the drained and constant volume RS tests, as observed in some tests performed with a Plexiglas outer confining ring. The shear band measured 1.3 mm thick, or 14 x D_{50} of the MR sand, which is consistent with findings of Alshibli and Sture (1999) (among others) who observed that shear bands formed during plane strain tests were approximately 13 - 14 x D_{50} for fine-grained sands. Further discussion regarding shear band formation in the RS device is presented in Chapter 6.

4.10 SUMMARY

Two clean sands and a silty sand were selected for testing in this research program. The clean sands have rounded to subrounded particle shapes, however the silty sand has subangular particle shapes. Table 4.1 and Figure 4.5 show the physical index properties and average particle size distributions of the selected sands. Undrained and drained TxC tests were performed on moist tamped or air pluviated specimens of these sands. Care was taken in sample preparations, and all volume changes were measured during saturation and consolidation of the specimens. The data were also corrected for the enlarged cross sectional area of the triaxial specimen during shear and for the extra axial and radial resistances applied by the membrane.

Constant volume and drained RS test procedures are also described. A constant volume was maintained by fixing the position of the upper loading platen by two locking nuts. These nuts were left loose for drained shearing. Furthermore, uncertainties in void ratios due to the measurements of mass and dimensions of the specimens are very small

and well within acceptable ranges. Comparative RS and TxC shear tests on a silty, fine-grained sand demonstrate the capabilities of the new RS device and illustrate that the large displacement friction angles obtained from constant volume and drained RS tests are essentially identical and are consistent with the effective stress friction angles measured in drained and undrained TxC tests (based on correlations between plane strain and TxC effective stress friction angles).

Lastly, the comparative RS and TxC tests appear to indicate that the triaxial test does not shear specimens of silty MR sand to sufficient displacement to reach critical shear strengths. In contrast, the new RS is capable of shearing specimens to unlimited shear displacements and appears to reach critical shear strengths for this silty sand at shear displacements from about 1 to 10 m.

4.11 TABLES

Table 4.1: Average index properties of the tested sands

Sand	G_s	e_{max}	e_{min}	Average fines content (%)
OT sand	2.63	0.679	0.391	0
IR sand	2.63	0.757	0.464	<1
MR sand	2.65	1.038	0.563	38

Table 4.2: Specifications of the TxC shear tests

Test No.[1]	σ'_c (kPa)	e_c	Dr_c (%)[2]	Test No.	σ'_c (kPa)	e_c	Dr_c (%)
MTIRUN29	199	0.844	-30	MTOTUN92	635	0.771	-32
MTIRUN17	117	0.835	-27	MTOTUN82	566	0.766	-30
MTIRUN52	359	0.707	17	MTOTUN63	435	0.722	-15
MTIRUN54	373	0.732	9	MTOTDR55	380	0.655	8
MTIRUN83	569	0.659	33	MTOTDR21	143	0.628	18
MTIRUN112	773	0.677	27	MTOTDR88	610	0.675	1
MTIRUN109	752	0.627	44	MTOTDR39	266	0.659	7
MTIRUN12	85	0.818	-21	MTOTDR71	487	0.656	8
MTIRUN55	381	0.674	28	APOTUN54	369	0.643	13
MTIRUN43	298	0.756	0	APMRUN32	221	0.714	68
MTIRUN54	373	0.712	15	APMRUN62	425	0.636	85
MTIRUN26	177	0.744	4	APMRUN92	636	0.594	93
MTIRDR74	511	0.670	30	APMRUN47	326	0.640	84
MTIRDR37	252	0.693	22	APMRUN39	272	0.645	83
MTIRDR54	372	0.672	29	APMRUN58	397	0.658	80
MTIRDR20	137	0.677	27	APMRUN23	161	0.719	67
APIRUN82	566	0.627	44	APMRDR29	200	0.693	73
APIRUN43	295	0.658	34	APMRDR29	200	0.712	69
MTOTUN83	571	0.724	-16	APMRDR16	109	0.753	60
MTOTUN52	361	0.787	-38	APMRDR81	560	0.658	80
MTOTUN103	711	0.700	-7	APMRDR64	443	0.695	72
MTOTUN102	704	0.770	-32	APMRDR41	281	0.663	79
MTOTUN42	290	0.796	-41	APMRDR54	373	0.726	66

[1] MT and AP in test number indicate moist tamping or air pluviation method of preparations, respectively. UN and DR indicate undrained or drained conditions, respectively. And OT, IR and MR indicate OT, IR and MR sands, respectively.

[2] Relative density after consolidation.

Table 4.3: Specifications of the RS tests

Test No.[1]	σ'_{nc} (kPa)	e_c	Dr_c (%)[2]	Test No.	σ'_{nc} (kPa)	e_c	Dr_c (%)
APOTCV52	357	0.598	28	APIRCV82	590	0.612	49
MTOTCV54(1)	389	0.658	7	APIRCV81	553	0.653	35
MTOTCV21	149	0.697	-6	APIRCV17	137	0.717	14
MTOTCV87	624	0.693	-5	APIRCV94	646	0.676	28
MTOTCV63	448	0.669	3	APIRCV78	541	0.672	29
MTOTCV54(2)	376	0.701	-8	APIRCV41	309	0.634	42
APOTCV83	541	0.544	47	APIRCV45	323	0.617	48
APOTCV85	620	0.573	38	APIRCV39	272	0.657	34
APOTCV28	217	0.605	26	APIRDR52	360	0.588	58
APOTCV54	392	0.591	31	APIRDR42	301	0.592	56
MTOTDR40	279	0.670	3	APIRDR5	48	0.583	59
APOTDR40(1)	279	0.611	24	APIRDR38	277	0.601	53
MTOTDR4	28	0.584	33	APIRDR72	490	0.639	40
MTOTDR38(1)	287	0.689	-3	APIRDR85	550	0.593	56
MTOTDR38(2)	289	0.685	-2	APIRDR76	540	0.610	50
APOTDR5	29	0.613	23	APMRCV57	378	0.756	59
APOTCV17	120	0.663	6	APMRCV43	298	0.709	69
APOTDR40(2)	278	0.676	1	APMRCV87	602	0.706	70
APOTDR78	562	0.541	48	APMRCV89	624	0.768	57
MTOTCV52	383	0.645	12	APMRCV103	728	0.677	76
MTIRCV46	318	0.782	-8	APMRCV97	708	0.619	88
MTIRCV53	351	0.748	3	APMRCV22	151	0.728	65
MTIRCV58	403	0.629	44	APMRDR39	271	0.740	63
MTIRCV75	628	0.643	39	APMRDR4	29	0.773	56
MTIRCV52	360	0.681	26	APMRDR40	276	0.719	67
MTIRCV56	396	0.707	17	APMRDR77	523	0.693	73
MTIRCV18	124	0.744	4	APMRCV48	355	0.625	87
MTIRDR41	278	0.673	29	MTMRCV48	334	0.752	60
MTIRDR75	516	0.673	29	MTMRDR40	266	0.794	51
MTIRDR54	364	0.728	10				

[1] MT and AP in test number indicate moist tamping or air pluviation method of preparations, respectively. CV and DR indicate constant volume or drained conditions, respectively. And OT, IR and MR indicate OT, IR and MR sands, respectively.

[2] Relative density after consolidation.

4.12 FIGURES

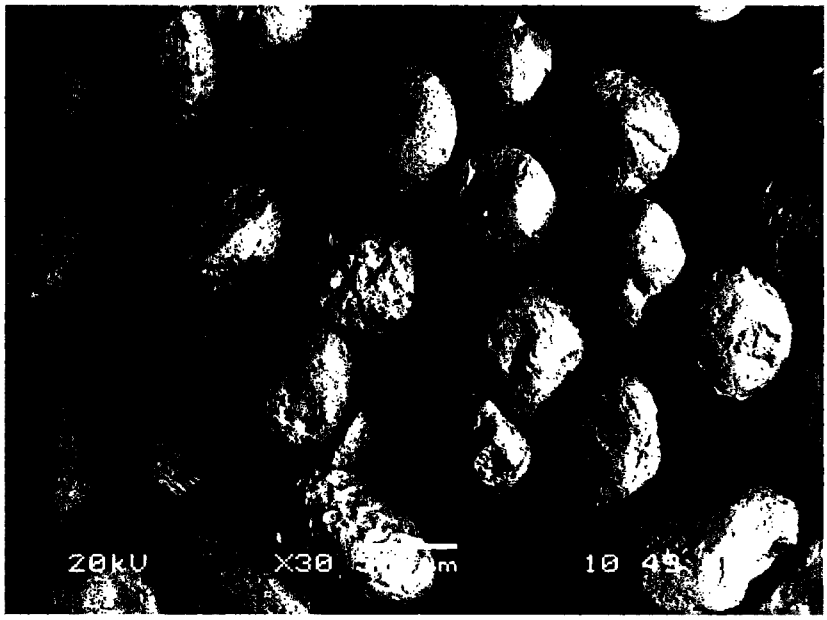

Figure 4.1: SEM image of OT sand at 30x magnification

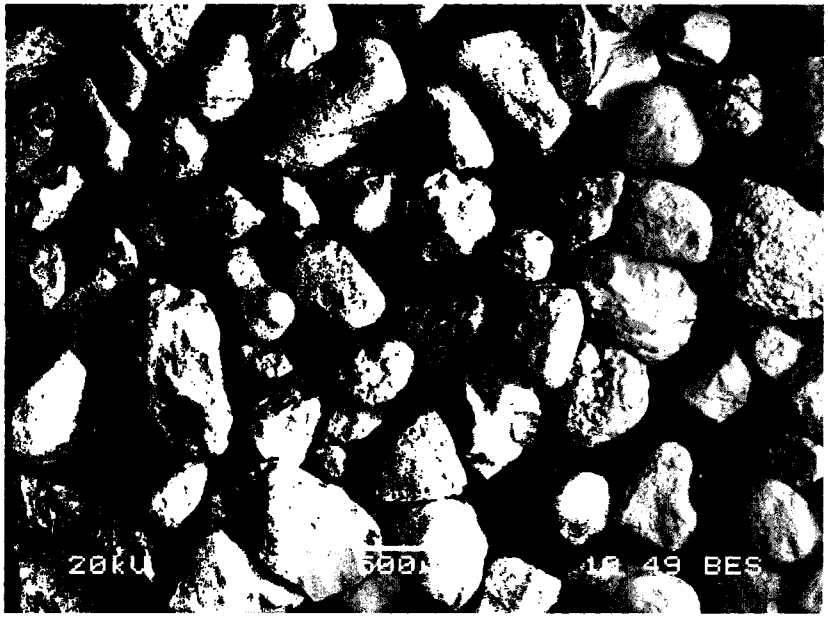

Figure 4.2: SEM image of IR sand at 30x magnification

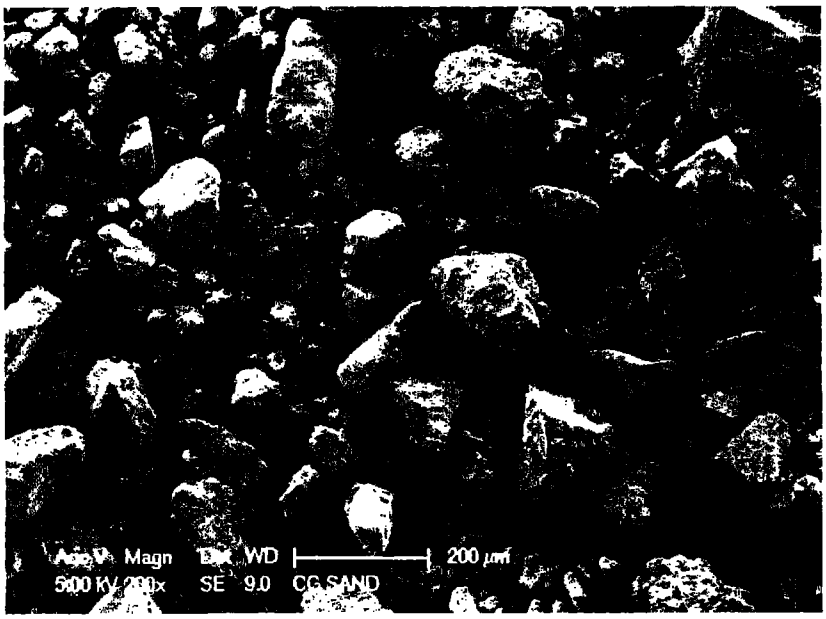

Figure 4.3: SEM image of MR sand at 100x magnification

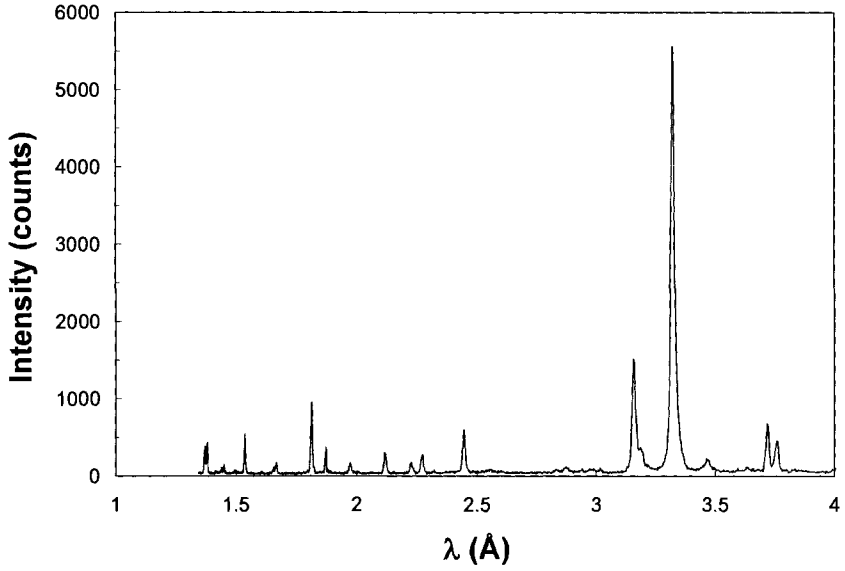

Figure 4.4: X-ray intensity vs. wavelength from X-ray diffraction test on MR sand

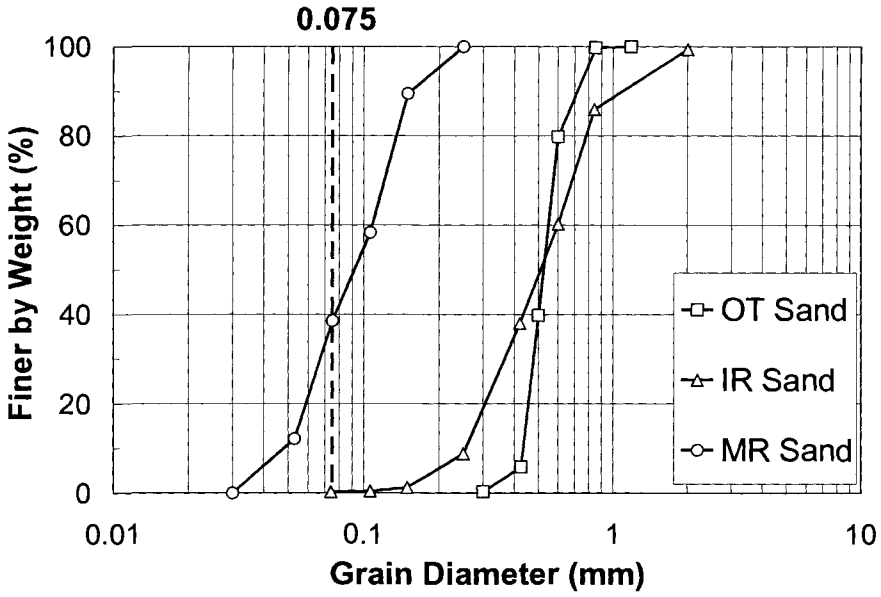

Figure 4.5: Avergae particle size distributions of the test sands

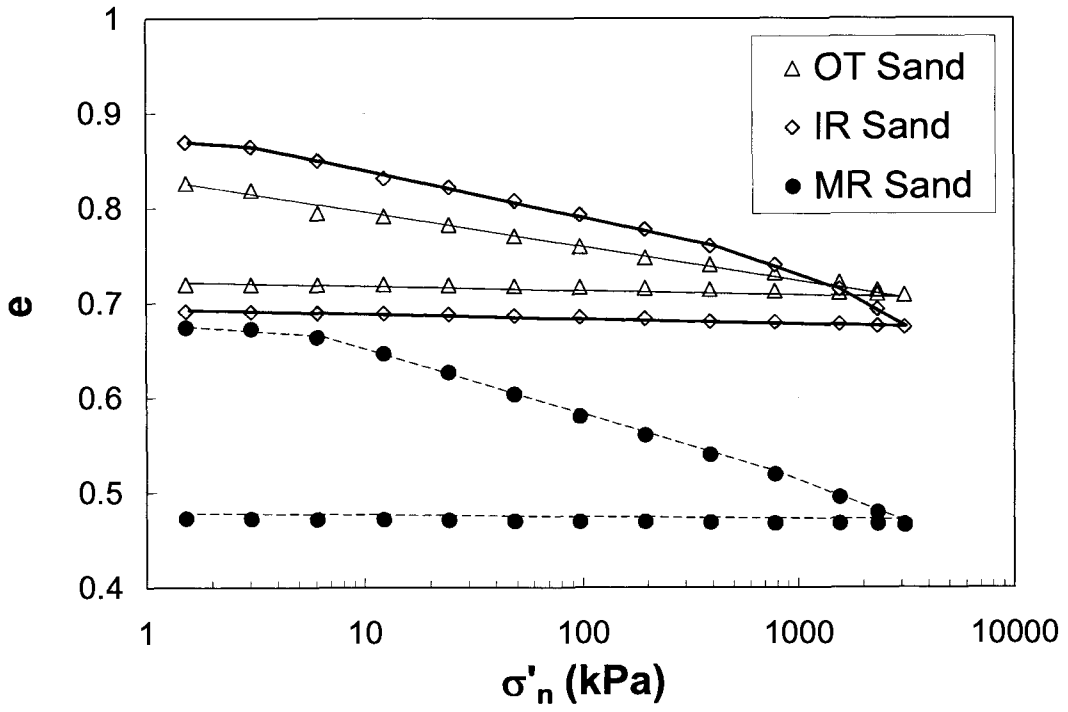

Figure 4.6: Normal compression behavior of the sands prepared by air pluviation

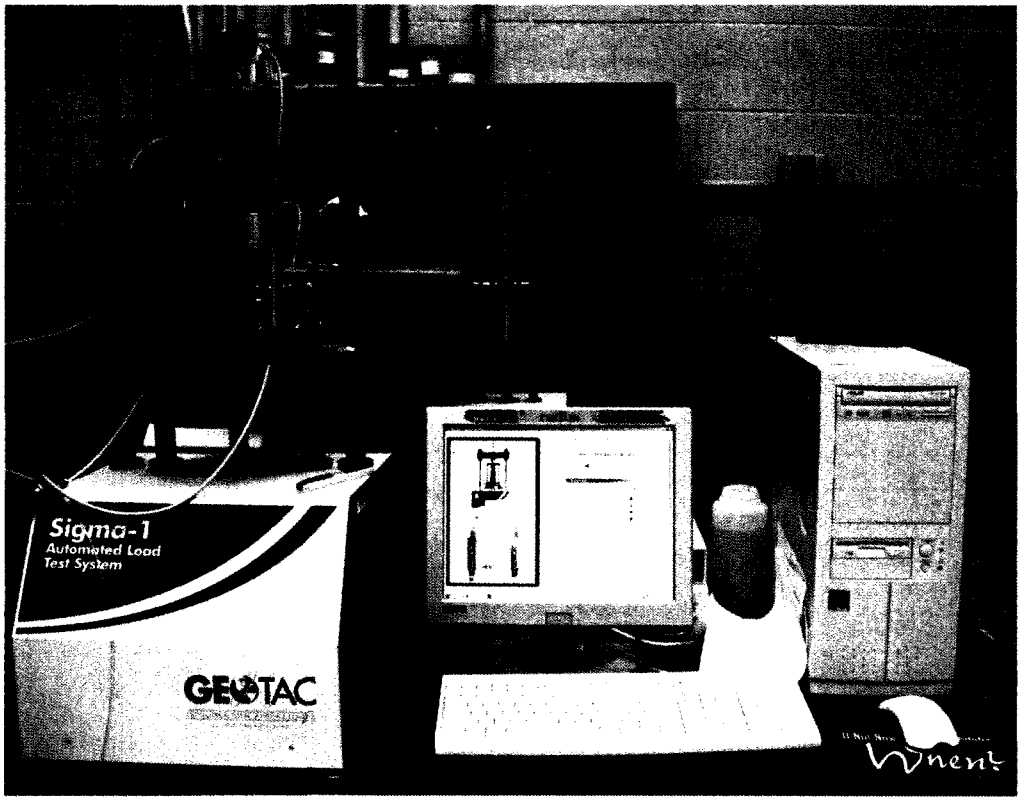

Figure 4.7: Automated TxC apparatus

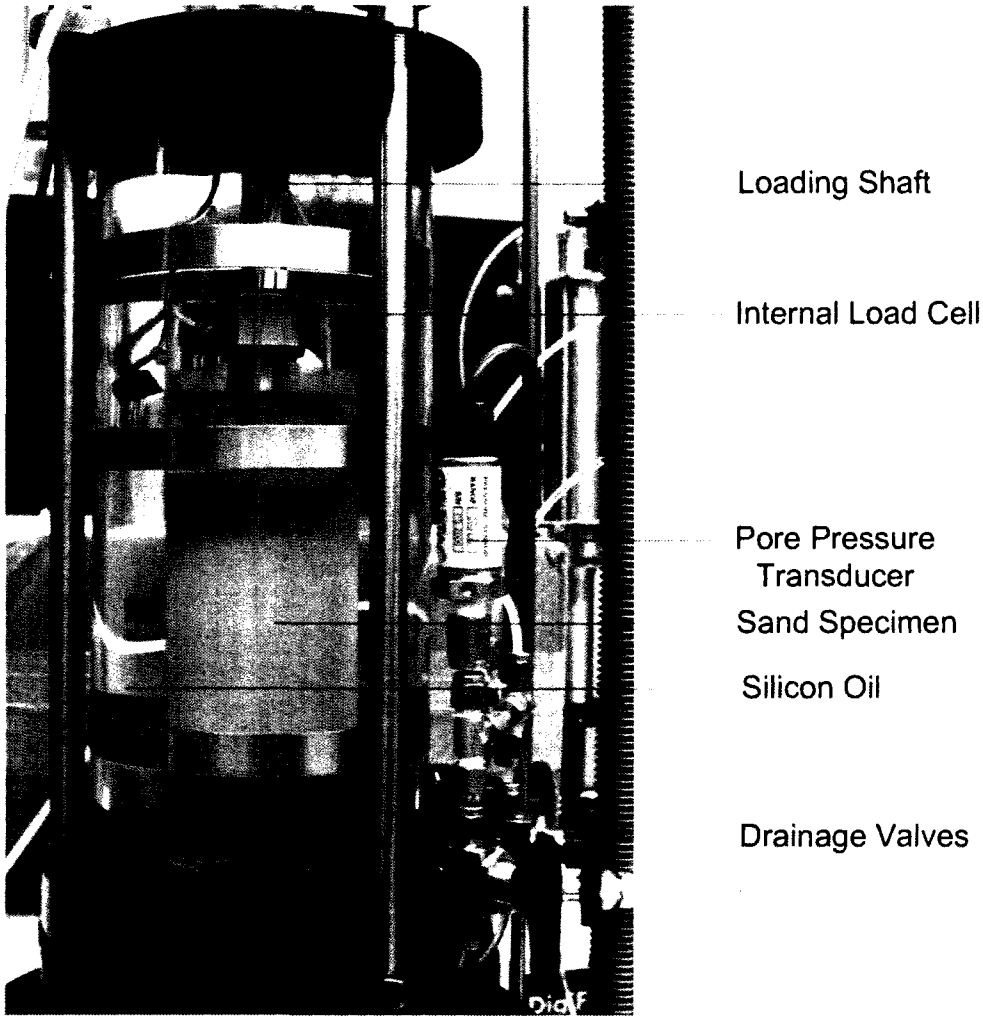

Figure 4.8: Triaxial specimen after backpressure saturation and before consolidation

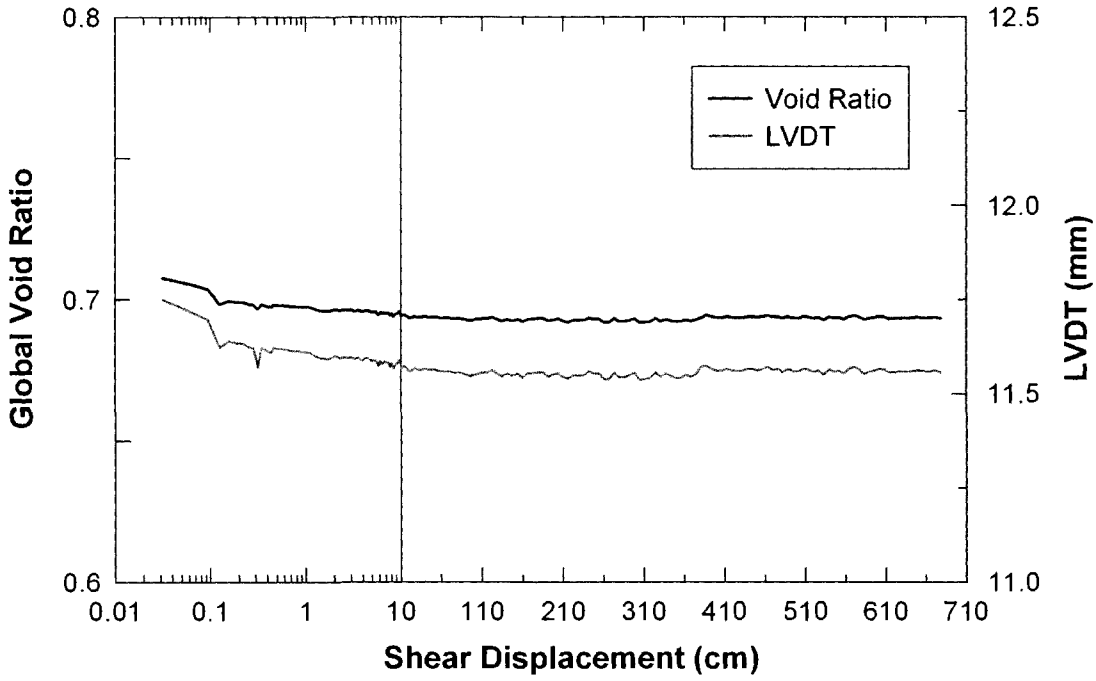

Figure 4.9: Global void ratio computed from LVDT measurements during a constant volume RS test on MR sand.

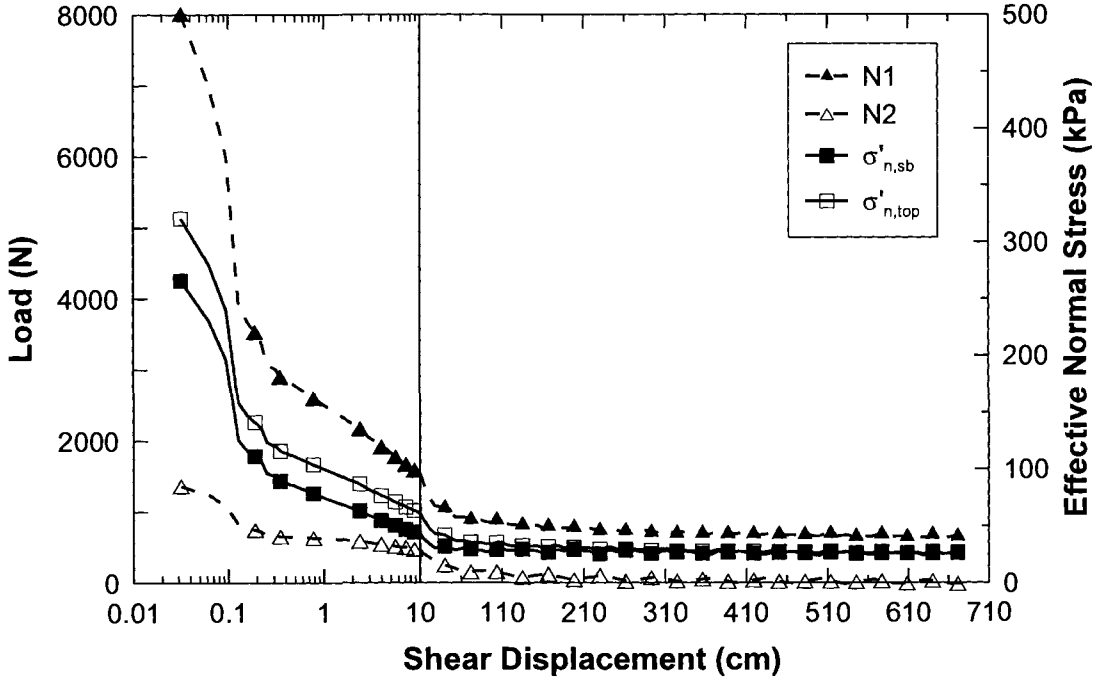

Figure 4.10: Normal load measurements and associated normal stress at top of specimen ($\sigma'_{n,top}$) and on the shear plane ($\sigma'_{n,sb}$) computed from load measurements obtained during a constant volume RS test on MR sand (only a limited number of data are shown for clarity).

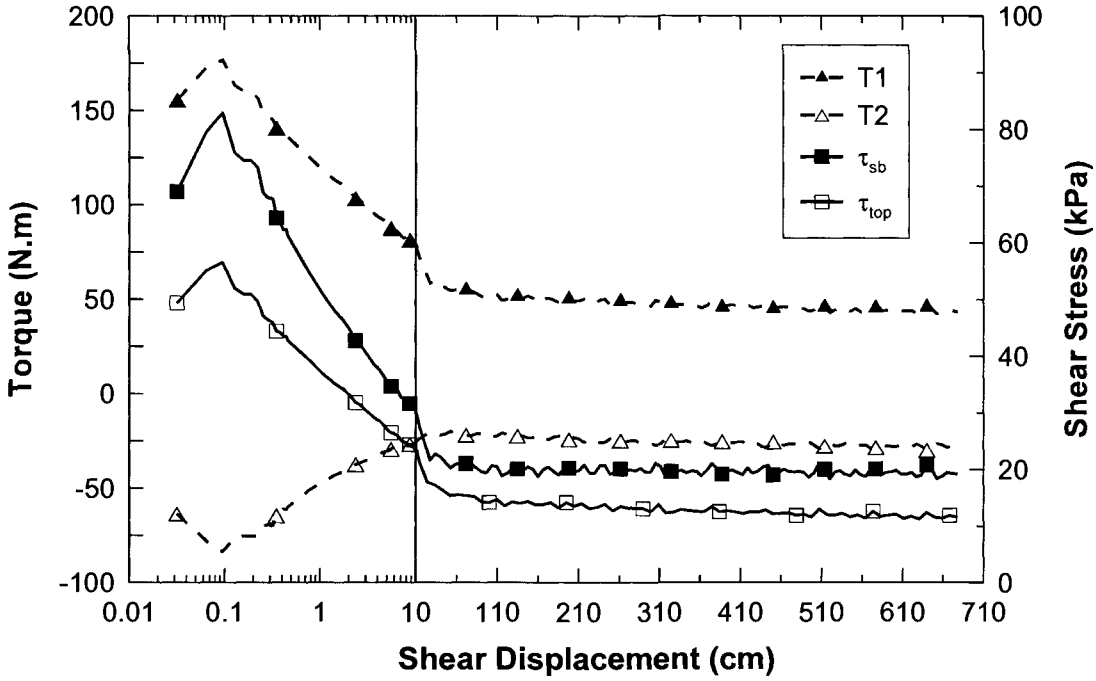

Figure 4.11: Torque measurements and associated shear stress at top of specimen (τ_{top}) and on the shear plane(τ_{sb}) computed from torque measurements obtained during a constant volume RS test on MR sand (only a limited number of data are shown for clarity).

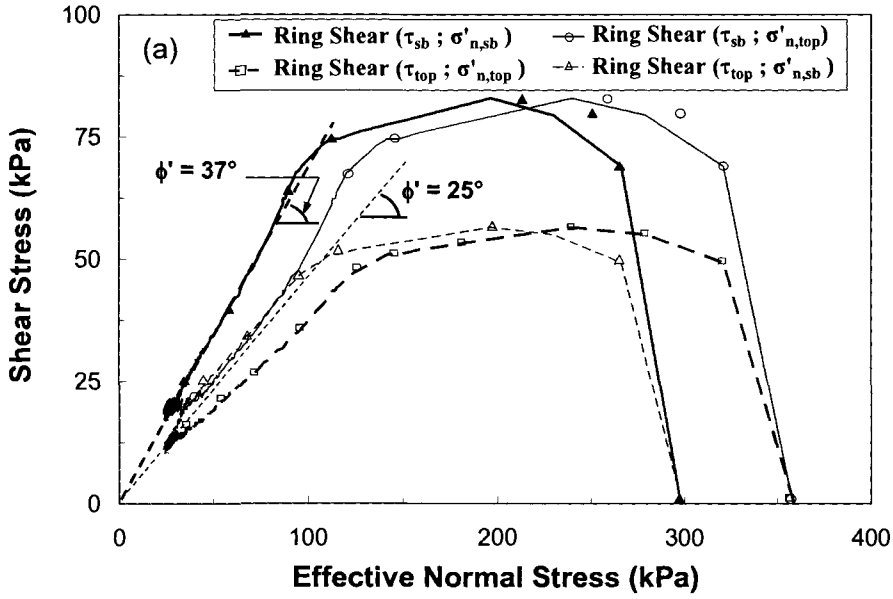

(a)

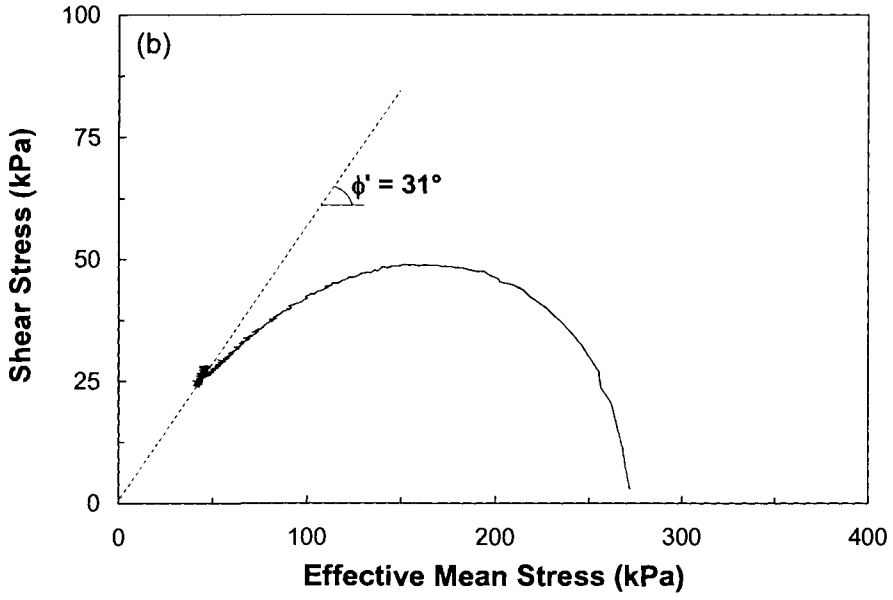

(b)

Figure 4.12: Stress paths from sample (a) constant volume RS and (b) undrained TxC shear tests on MR sand (only a limited number of data are shown for clarity).

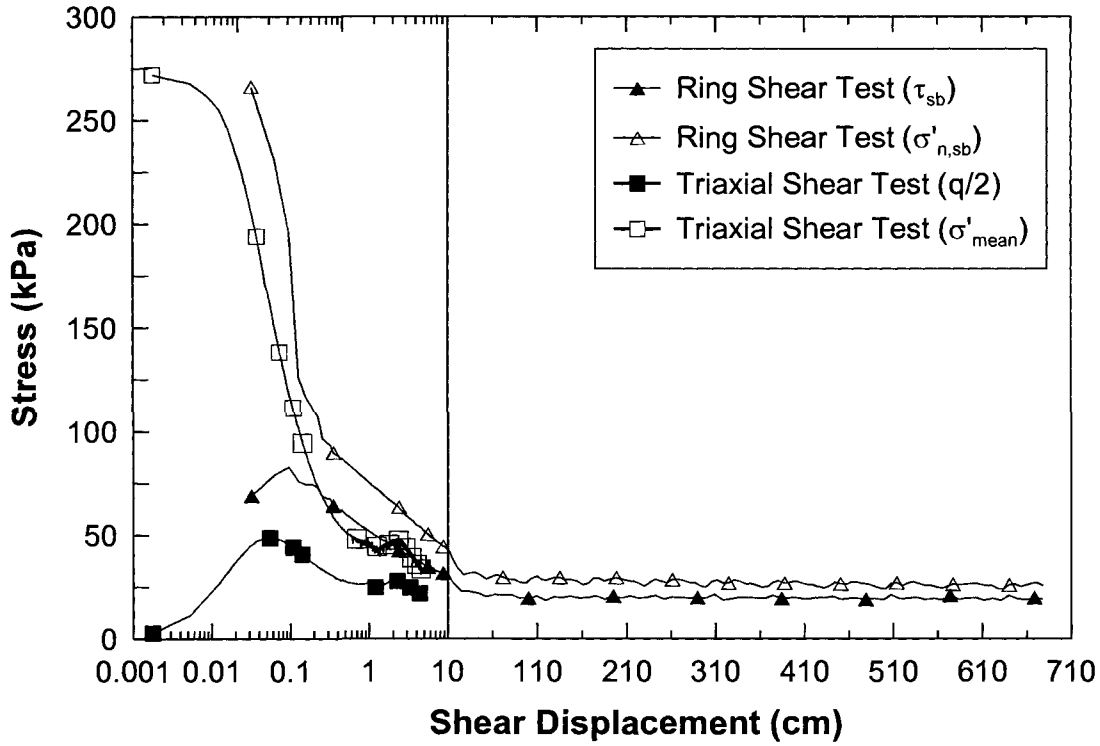

Figure 4.13: Comparison of effective normal stress on the shear plane ($\sigma'_{n,sb}$) measured during a constant volume RS test, effective mean stress [$\sigma'_{mean} = (\sigma'_1 + 2\sigma'_3)/3$] measured during sample undrained TxC test, and shear stresses [τ_{sb} and $q/2 = (\sigma'_1 - \sigma'_3)/2$] on MR sand (only a limited number of data are shown for clarity).

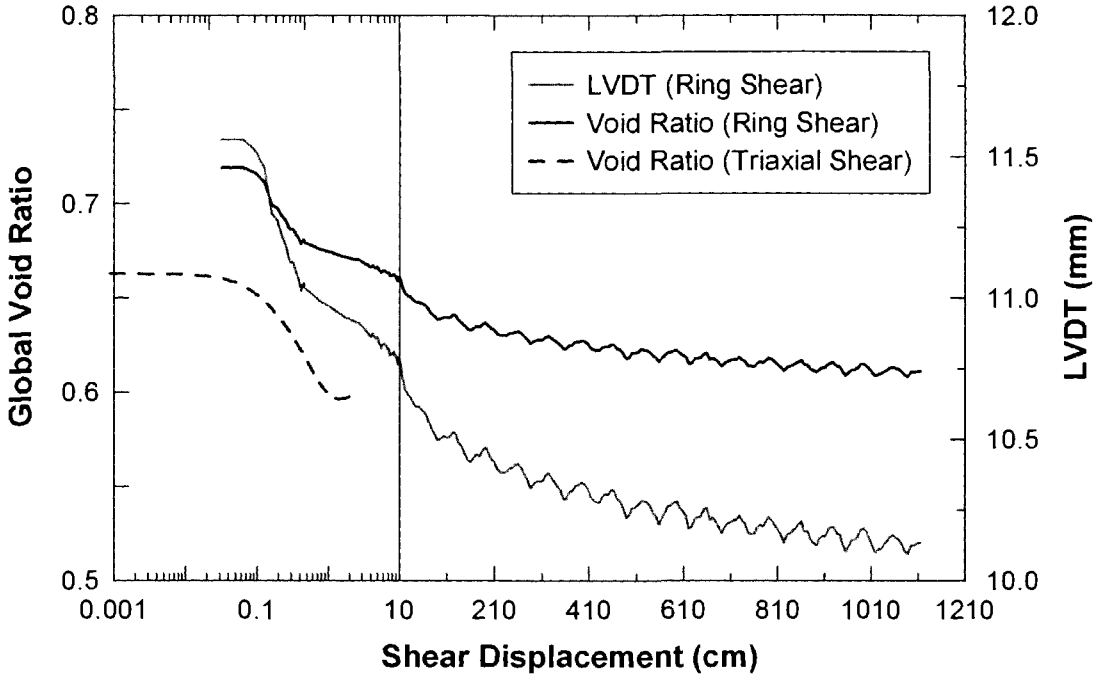

Figure 4.14: LVDT measurement and computed global void ratio obtained during sample drained RS test as well as void ratio change observed in a parallel drained TxC shear test on MR sand. Note that over 10 m (!) of displacement is required to approach an approximate critical state (for this particular specimen under these specific initial conditions) in the RS test.

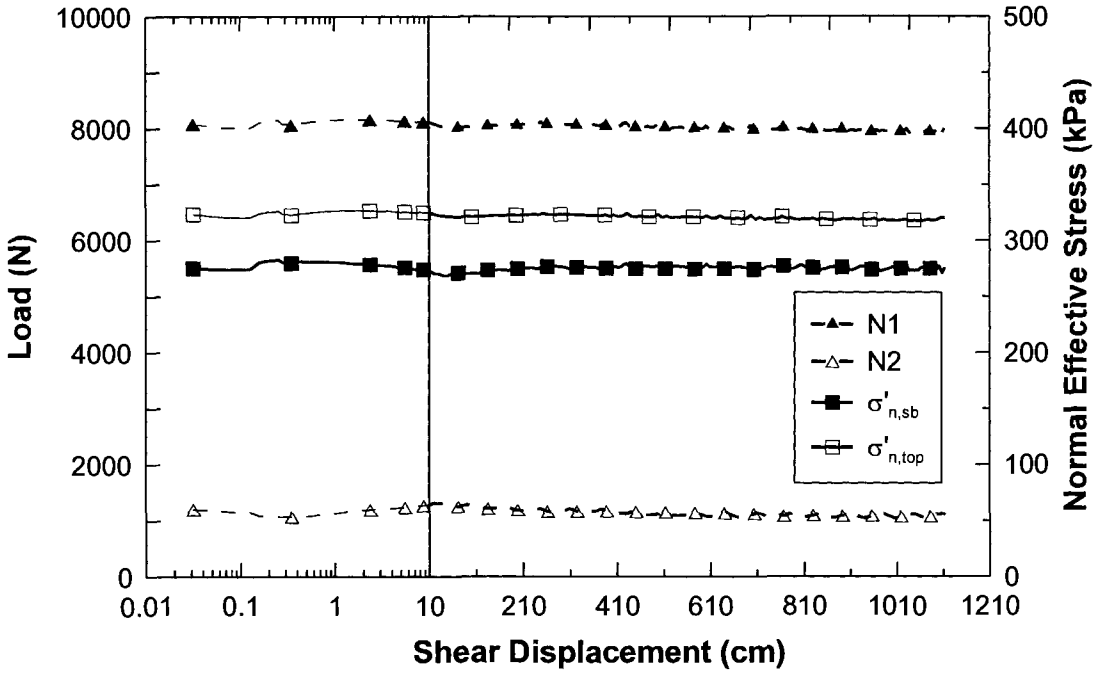

Figure 4.15: Load measurements and normal stresses at top of specimen ($\sigma'_{n,top}$) and on the shear plane ($\sigma'_{n,sb}$) computed from load measurements obtained during sample drained RS test on MR sand (only a limited number of data are shown for clarity).

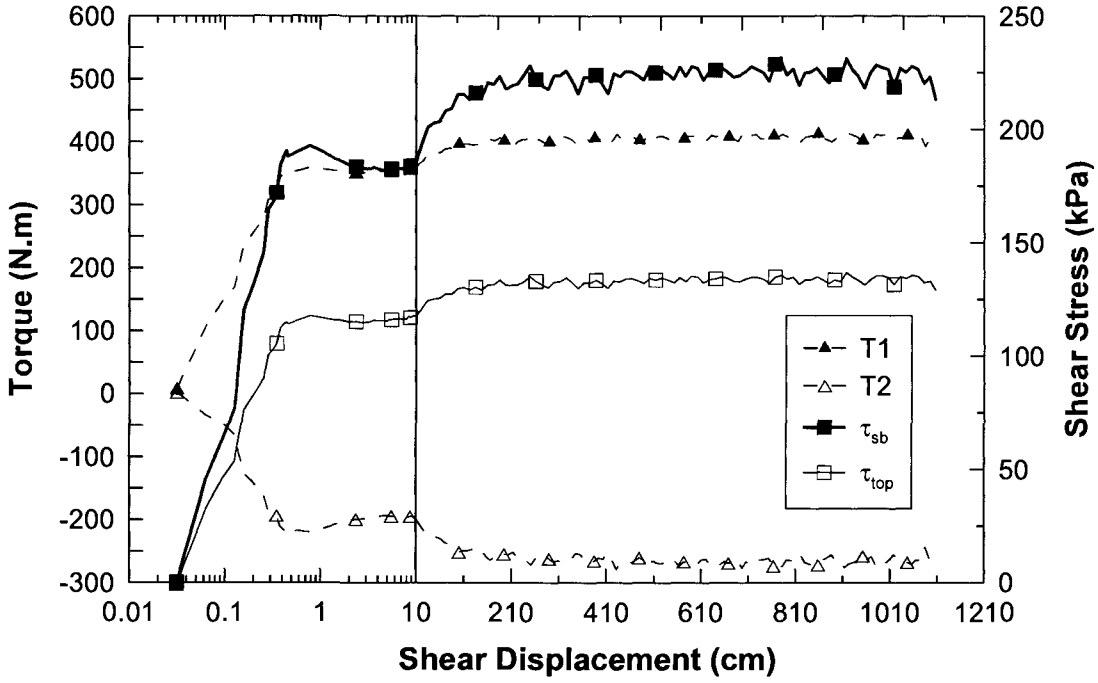

Figure 4.16: Torque measurements and shear stresses at top of specimen (τ_{top}) and on the shear plane (τ_{sb}) computed from torque measurements obtained during sample drained RS test on MR sand (only a limited number of data are shown for clarity).

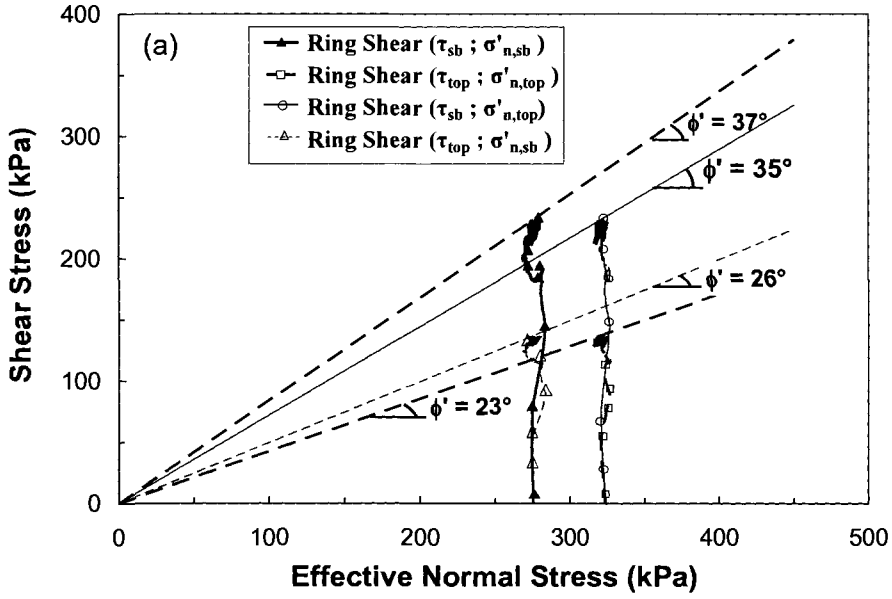

(a)

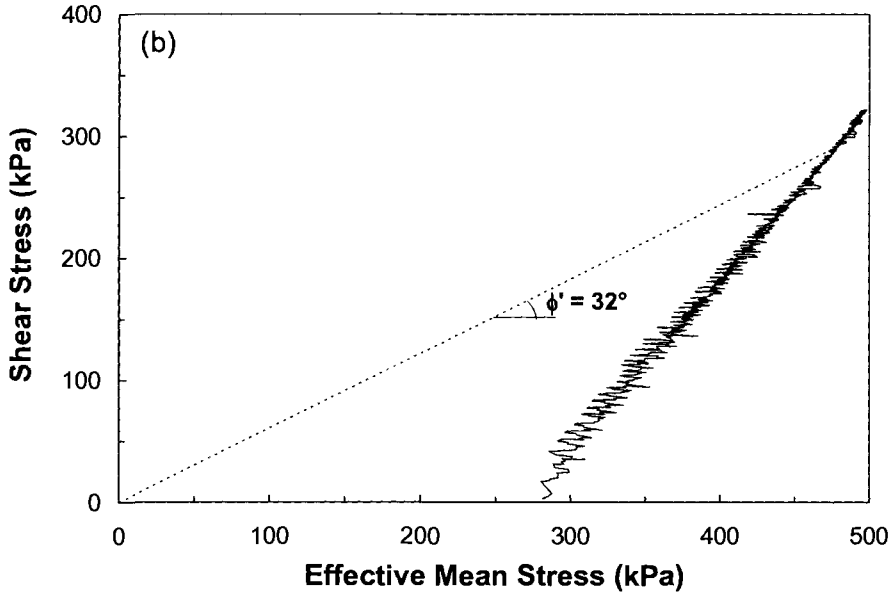

(b)

Figure 4.17: Stress paths from sample (a) drained RS and (b) drained TxC shear tests on MR sand (only a limited number of data are shown for clarity).

CHAPTER 5: TRIAXIAL AND RING SHEAR TEST RESULTS

5.1 INTRODUCTION

This chapter compares the ring shear (RS) and triaxial compression shear (TxC) test results in terms of stress paths and stress-displacement plots in order to evaluate the benefits and limitations of both tests for understanding the large displacement behavior of sands.

The failure patterns of the TxC and RS tests were very different. The mode of shearing of the RS tests resembles a plane strain shearing condition, while the RS tests are also able to reach virtually unlimited shear displacement compared to typical plane strain tests. Therefore the observations made in plane strain tests would also apply to the RS tests conducted in this study.

5.2 COMPARING THE STRESS PATH AND STRESS – DISPLACEMENT PLOTS

Stress path and stress-displacement plots of all TxC and RS tests are presented in Appendices A and B, respectively. Figure 5.1 through Figure 5.16 show typical results for RS and TxC shear tests. In the stress paths, the conventional critical state nomenclature (Equations 4.7 and 4.8) of q (black lines) versus σ'_{mean} (grey lines) is used for the TxC shear tests but the shear stress, τ (black lines) versus effective normal stress, σ'_n (grey lines) on the shear plane, are used for the RS tests. The consolidation stress (mean stress in TxC and normal stress in RS) and relative density for each tests are provided in the legends. To facilitate comparison, displacements (shear in RS and axial in TxC) rather than strains are used to illustrate the test results. Note that in order to clearly show the initial variation of the stresses measured in the large displacement RS tests a log scale is used to show the first 10 cm of shear displacement of the RS test results.

As illustrated in the figures, only the very loose moist tamped specimens of OT and IR sands (in Figs. 5.1, 5.2, 5.4, 5.9, 5.10, 5.12, and 5.14) contracted throughout the RS and TxC shear tests. A more-or-less constant stress state was reached in both modes of shear; however, a constant state was maintained for much larger displacements (> 2000 cm) in

the RS tests. As expected, moist tamping must therefore impart to the sand a fabric that promotes contractive behavior. Casagrande (1976) pointed out that moist dumped sands were particularly prone to liquefaction because of their metastable honeycomb structure. As indicated in the legends of these figures, moist tamped specimens can be prepared in the laboratory at void ratios much looser than the loosest possible void ratios by the air pluviation method (the latter of which resembles the maximum void ratio from the ASTM D4254 standard method). Evidence of similar collapsible behavior has been also reported by several other researchers (e.g., Marcuson and Gilbert 1972; Chang et al. 1981; Sladen et al. 1985).

Similar to the water-deposited Fraser River sand specimens tested in TxC by Vaid and Thomas (1995), air pluviated specimens of OT and IR sands all strain hardened during shearing because of their initially denser fabric. Air pluviated OT sand specimen sheared in undrained TxC (Figure 5.5) did not achieve a critical state. In contrast, some undrained TxC tests on air pluviated IR sand specimens (Figure 5.3) reached a plateau at an axial displacement of about 2 cm. This value could be potentially interpreted as a critical state; however because this plateau was achieved at the maximum reasonable displacement capacity of the triaxial test, it was not clear if this plateau could be maintained, making it impossible to confidently assess the critical state. Similarly, the denser air pluviated specimens tested in RS (in Figure 5.11 and Figure 5.13) initially strain hardened. But in contrast to the TxC tests, these specimens exhibited a second phase transformation from dilative to contractive behavior. As discussed in Chapter 7, this was possibly caused by the destruction of the soil structure due to grain crushing. Such a point was not reached in the TxC tests, due to its limited displacement capacity. The shear resistance then leveled off at larger displacements in the RS tests, and reached a constant state (from 1000 cm to more than 1500 cm).

Furthermore, the occurrence of failure in the dry constant volume RS tests where no pore water pressure was present, shows that pore pressure generation is the consequence of failure and not a cause. This indicates that the failure and collapse of a dry sand is the result of progressive destabilization of the grain structure and particle crushing. Similar observations were also made by Eckersley (1990) in instrumented flow slide model tests on coal materials and by other investigators (Sasitharan et al. 1993; Skopek et al. 1994).

In contrast to the air pluviated specimens of clean OT and IR sands, a contractive particle structure was formed in the MR sand specimens by dry air pluviation, in which the larger load bearing sand grains were held apart by the smaller silt grains. Upon shearing the particle structure destabilized, with the silt grains migrating into the void spaces, and leading to large contractive volumetric strains (Yamamuro and Lade 1998). The drained stress paths from TxC and RS tests differ as a result of the different modes of shear.

The friction angles mobilized at the end of the tests are also noted in the stress path plots. Generally, the RS specimens exhibited larger friction angles than TxC specimens as a result of particle damage and crushing, which produces rougher and more angular particles. Furthermore, the influence of intermediate principal stress (σ'_2) differs for RS and TxC tests. The friction angles will be discussed in detail in Chapter 9.

The stress-displacement plots indicate the very large displacements achieved in the RS tests. Excluding TxC test APOTUN54 (Figure 5.5), which dilated severely and reached the load cell capacity at an axial displacement of 1.25 cm, all of the TxC shear tests were sheared to an axial displacement of 2.5 cm (corresponding to a shear displacement of about 2.8 cm on the theoretical failure plane of $45+\phi'/2$ measured from the minor principal plane for an average effective friction angle = 30°) after which the specimen bulged severely and the results became unreliable. The RS tests were sheared to displacements exceeding 10 meters until a state of constant shear and effective normal stresses was reached. The high frequency small fluctuations in the RS response (especially at very large shear displacements) were likely due to particle interactions (Skinner 1969) which were manifested as periodic softening (due to particle crushing) and hardening (due to particle rearrangement and rolling over each other) and stress heterogeneity (Drescher and de Josselin de Jong 1972; Mandl et al. 1977). Similar fluctuations were also observed by Feda (2002) in direct shear tests on a crushable silica sand.

5.3 COMPARING THE VOID RATIO-DISPLACEMENT PLOTS

Figure 5.17, presents global void ratios versus displacement for the drained ring shear and TxC shear tests presented earlier. Local void ratios within the shear bands differed

from the global void ratios, as discussed in Chapter 6, but global void ratios are shown here. Similar to the stress-displacement plots, the TxC shear test results are plotted versus axial displacement and the RS test results are plotted versus shear displacement (where the initial shear displacements are plotted on a log-scale).

Both TxC and RS tests on MR sand reached a constant volume state by the end of each test. However, the void ratios in the TxC tests on OT and IR sands were still dilating and contracting, respectively, while the RS tests on these sands reached a constant volume at over 5 meters of shear displacements. As is explained in Chapter 7, particle crushing resulted in much larger shear displacements being required to reach a critical void ratio state. These required shear displacements clearly exceed the displacement capacity of other laboratory shear tests such as TxC, direct shear, and simple shear tests.

5.4 SHORTCOMINGS OF THE TRIAXIAL TEST AT LARGE SHEAR DISPLACEMENTS

As illustrated in Figure 5.1 through Figure 5.16, only moist tamped IR and OT sand specimens were loose enough to contract in the TxC tests. The air pluviated IR and OT sand specimens both dilated and obtaining the behavior of these specimens at larger displacements was not possible in the TxC tests. Even the drained tests on the moist tamped IR and OT sands as well as the tests on MR sand did not reach unequivocal critical states within the displacement limits of the TxC test.

Also, most of the TxC tests were terminated at an axial displacement of 2.5 cm (corresponding to an axial strain of 25%), excluding those that reached the load cell capacity at smaller displacements. At larger displacements, the triaxial specimen bulged significantly, producing a complicated state of stress and strain and precluding further meaningful shearing of the specimen as an element of soil.

5.5 SUMMARY AND CONCLUSIONS

Most laboratory experiments on granular materials are performed with TxC tests for evaluating constitutive soil behavior and for stability analysis, whereas most geotechnical field behaviors such as landslides, soil behavior under strip footings, behavior of earth dams, stability analysis of slopes and levees, and failure of retaining structures are close

to plane strain situations. Strength and deformation characteristics of granular materials loaded in plane strain may be considerably different from those observed in TxC tests and the use of strength parameters defined from TxC tests may results in conservative designs (Lee 1970; Ko and Davidson 1973). The RS device used in this research, resembles a plane strain simple shear mode at small shear displacement and plane strain direct shear at large displacement.

The results presented in this chapter suggest that the TxC test may not produce critical state, even in very loose samples, because the test is terminated at limited displacements before particle reorientation and crushing are complete. In contrast, the RS device can impose very large shear displacements, which may be required to reach a critical state where particle reorientation and crushing are complete. As a result, the RS device may be very useful in analyzing some liquefaction flow failures and other rapid, large runout landslides that develop shear bands.

Furthermore, as discussed by Vaid et al. (1999) the specimen reconstitution method, which controls the soil fabric, should closely simulate the mode of deposition of the soil being modeled if these results are to have meaningful applications to the in-situ soils. The moist tamped fabric results in a highly contractive response, and may not mimic in-situ soil behavior. However, it may be reasonable to mimic loose dumped moist sands. Thus, the particular specimen preparation method should be selected to mimic the actual in-situ sand deposition as nearly as possible.

5.6 FIGURES

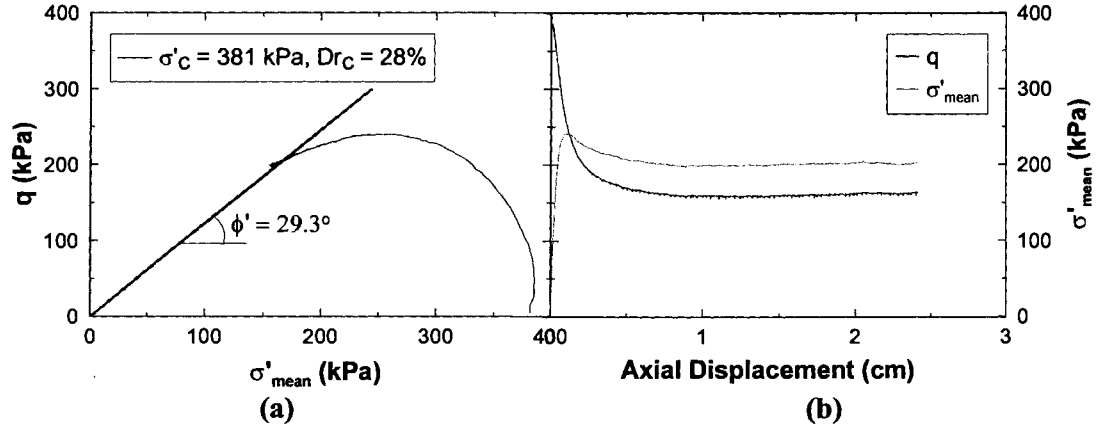

Figure 5.1: Undrained TxC test on moist tamped specimen of IR sand (MTIRUN55): (a) stress path, (b) stress – axial displacement plot.

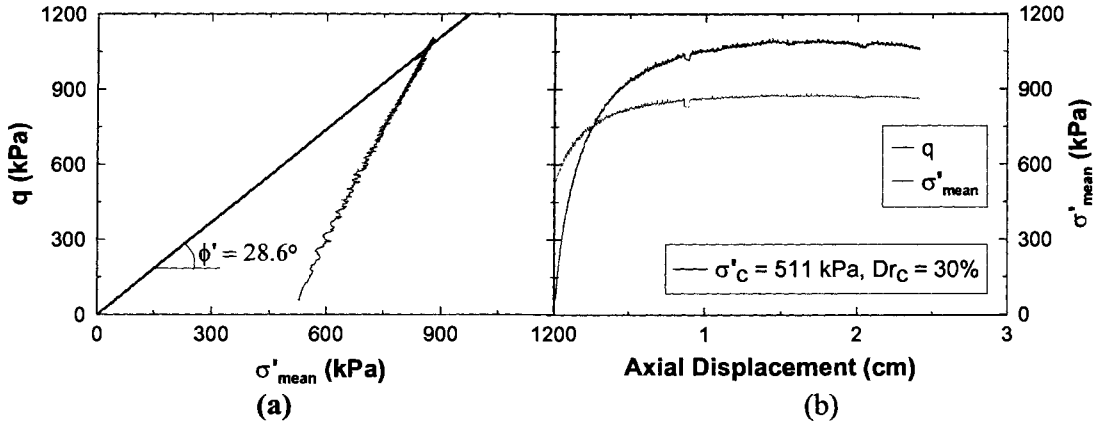

Figure 5.2: Drained TxC test on moist tamped specimen of IR sand (MTIRDR74): (a) stress path, (b) stress – axial displacement plot.

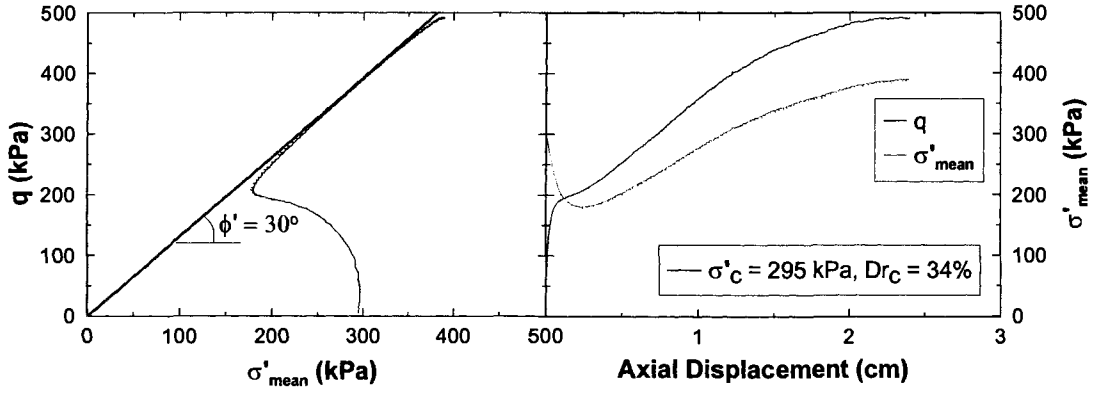

(a) (b)

Figure 5.3: Undrained TxC test on air pluviated specimen of IR sand (APIRUN43): (a) stress path, (b) stress – axial displacement plot.

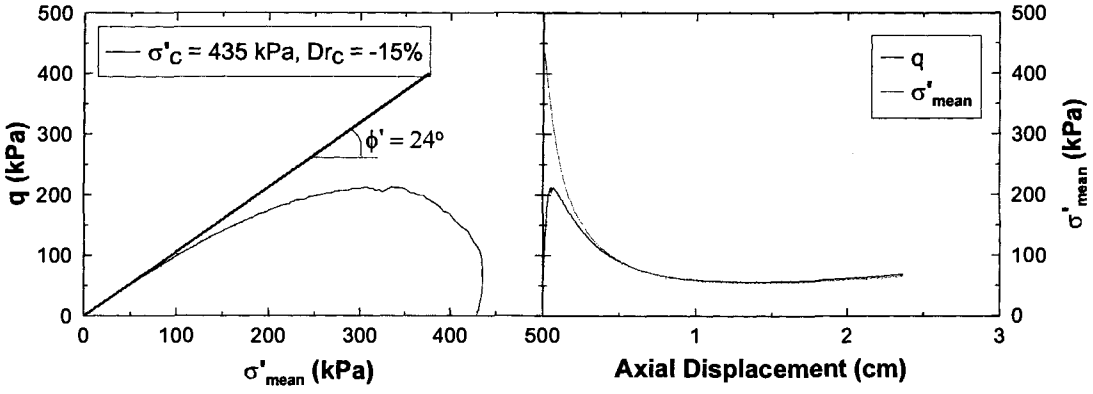

(a) (b)

Figure 5.4: Undrained TxC test on moist tamped specimen of OT sand (MTOTUN63): (a) stress path, (b) stress – axial displacement plot.

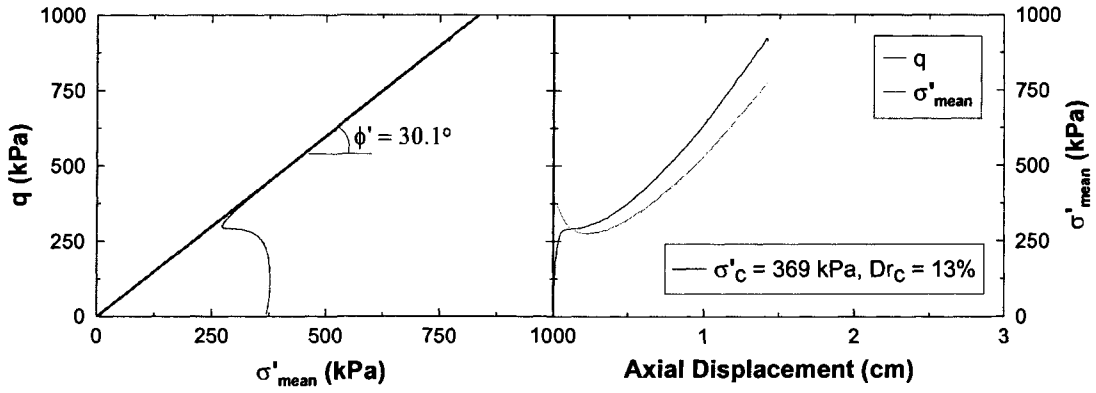

(a) (b)

Figure 5.5: Undrained TxC test on air pluviated specimen of OT sand (APOTUN54): (a) stress path, (b) stress – axial displacement plot.

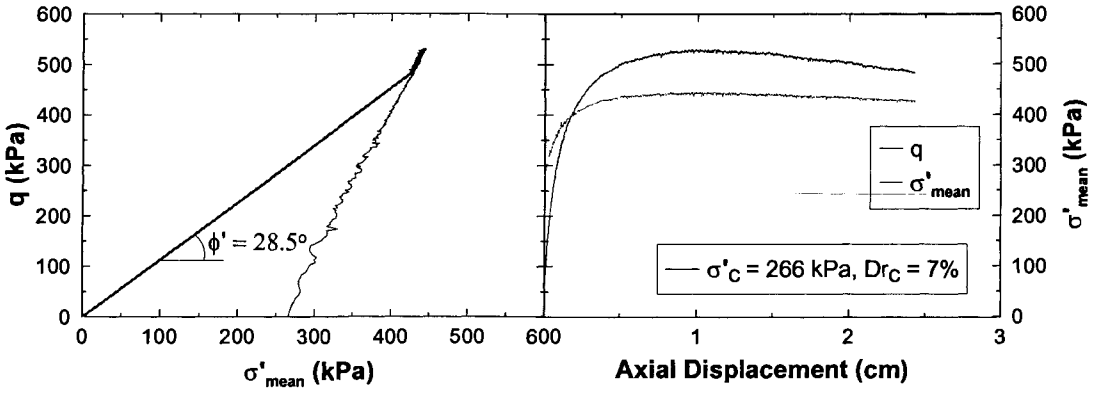

(a) (b)

Figure 5.6: Drained TxC test on moist tamped specimen of OT sand (MTOTDR39): (a) stress path, (b) stress – axial displacement plot.

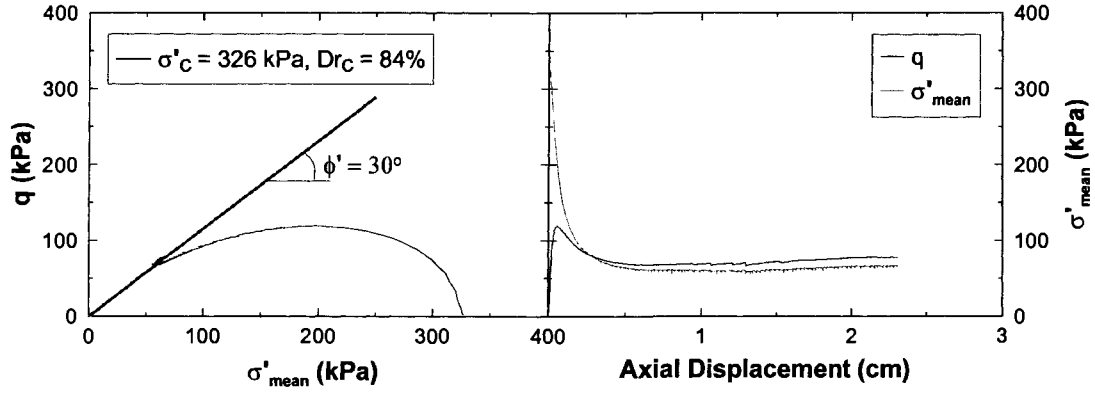

(a) (b)

Figure 5.7: Undrained TxC test on air pluviated specimen of MR sand (APMRUN47): (a) stress path, (b) stress – axial displacement plot.

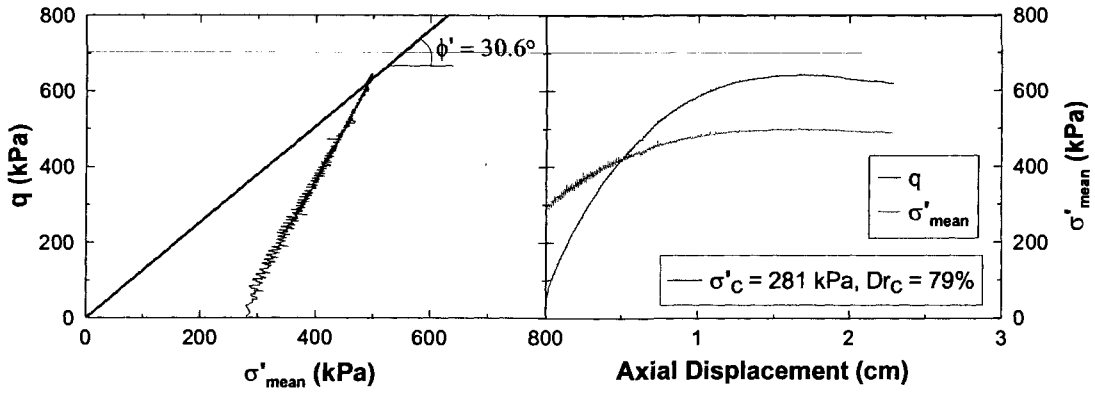

(a) (b)

Figure 5.8: Drained TxC test on air pluviated specimen of MR sand (APMRDR41): (a) stress path, (b) stress – axial displacement plot.

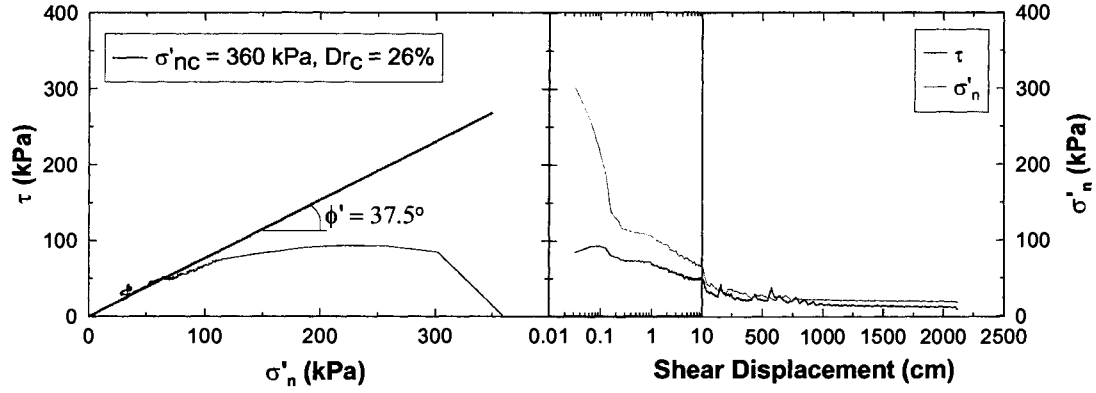

(a) (b)

Figure 5.9: Constant volume RS test on moist tamped specimen of IR sand (MTIRCV52): (a) stress path, (b) stress – shear displacement plot.

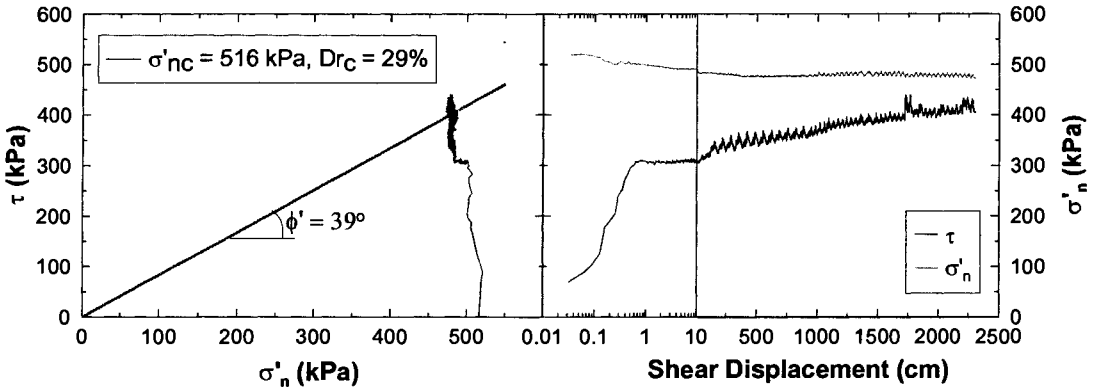

(a) (b)

Figure 5.10: Drained RS test on moist tamped specimen of IR sand (MTIRDR75): (a) stress path, (b) stress – shear displacement plot.

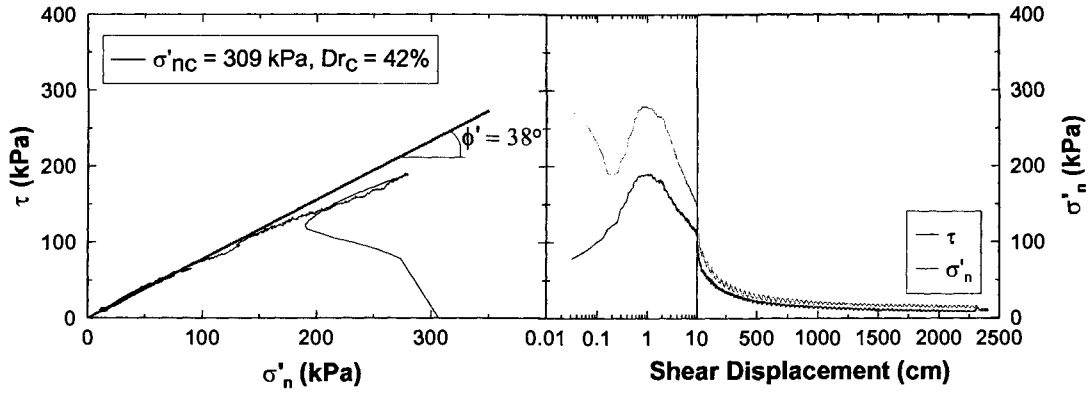

(a) (b)

Figure 5.11: Constant volume RS test on air pluviated specimen of IR sand (APIRCV42): (a) stress path, (b) stress – shear displacement plot.

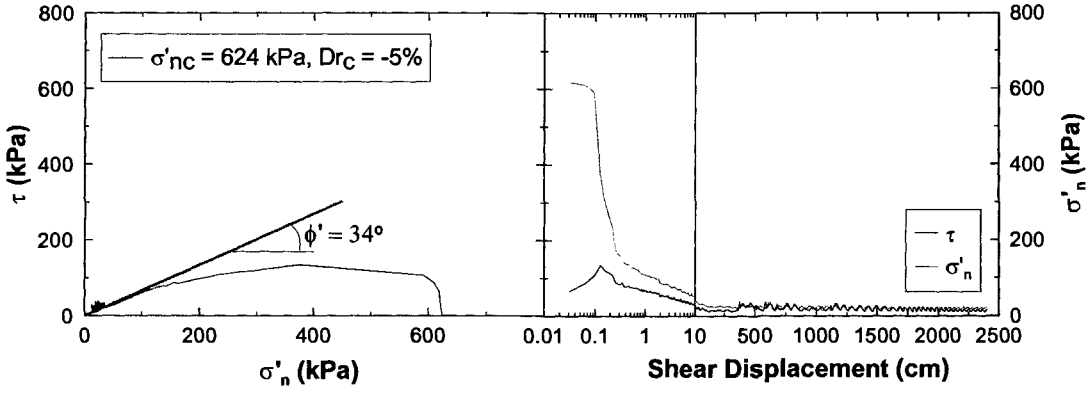

(a) (b)

Figure 5.12: Constant volume RS test on moist tamped specimen of OT sand (MTOTCV87): (a) stress path, (b) stress – shear displacement plot.

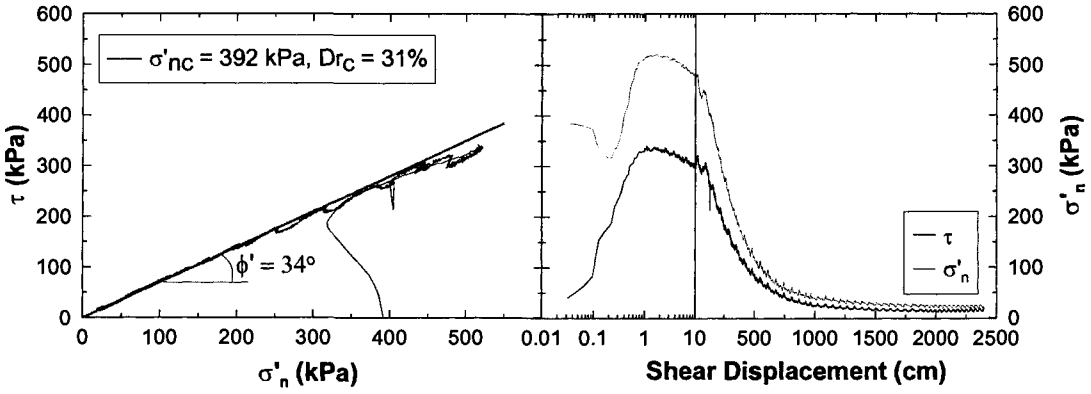

(a) (b)

Figure 5.13: Constant volume RS test on air pluviated specimen of OT sand (APOTCV53): (a) stress path, (b) stress – shear displacement plot.

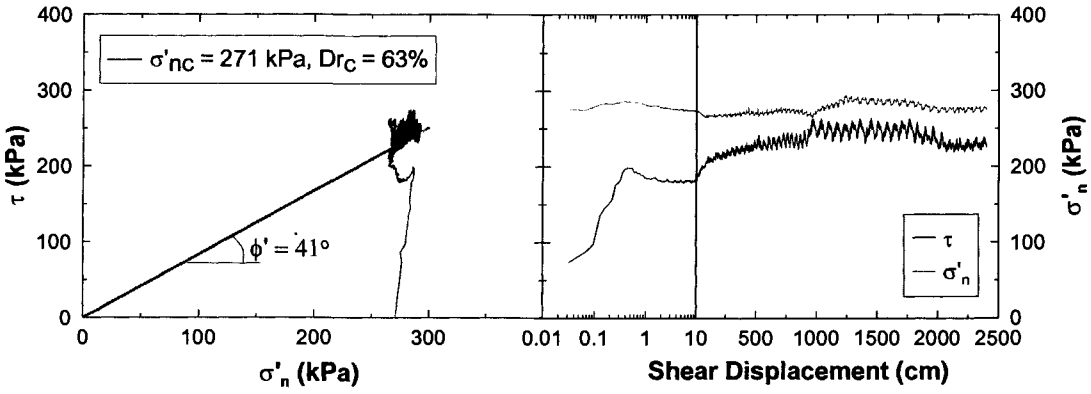

(a) (b)

Figure 5.14: Drained RS test on moist tamped specimen of OT sand (MTOTDR40): (a) stress path, (b) stress – shear displacement plot.

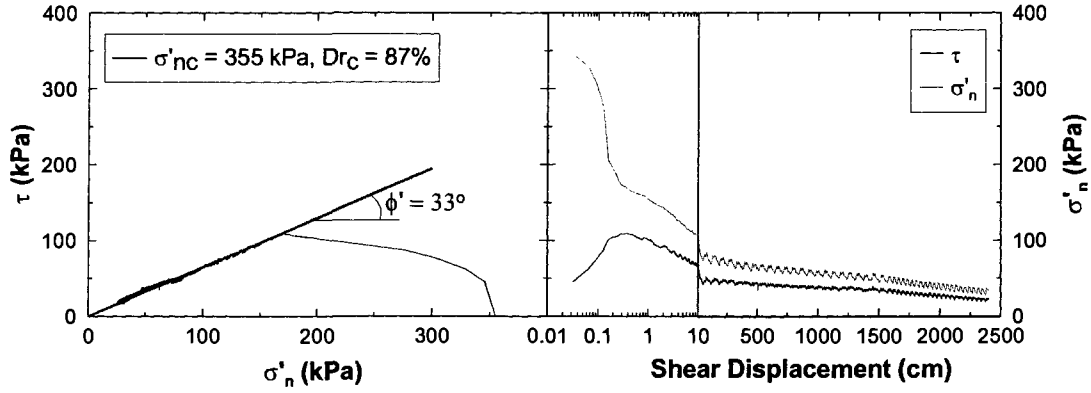

(a) (b)

Figure 5.15: Constant Volume RS test on air pluviated specimen of MR sand (APMRCV48): (a) stress path, (b) stress – shear displacement plot.

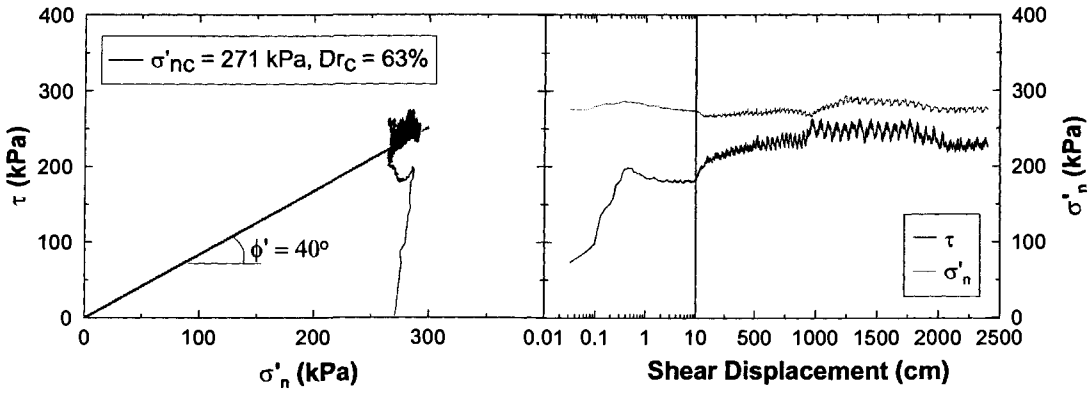

(a) (b)

Figure 5.16: Drained RS test on air pluviated specimen of MR sand (APMRDR39): (a) stress path, (b) stress – shear displacement plot.

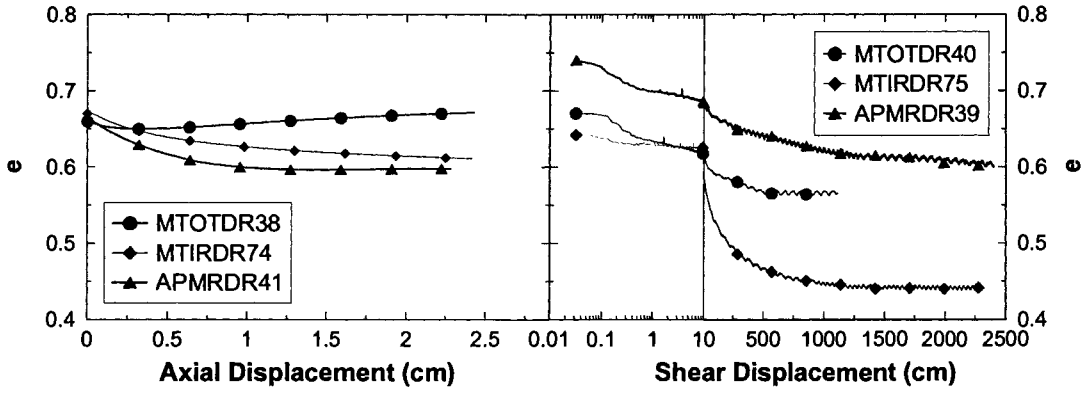

(a) (b)

Figure 5.17: Void ratio - displacement plots in drained (a) TxC (b) RS tests

CHAPTER 6: SHEAR BAND FORMATION IN RING SHEAR TESTS

6.1 INTRODUCTION

Discrete zones of localized deformation formed by intense shearing in unconsolidated sediments and highly porous rocks are commonly referred to as shear bands (e.g., Torabi et al. 2007). Localization of shear deformations and shear band formation can be an important factor in the failure of many geotechnical structures like earth dams, slopes, and foundations (e.g., Desrues et al. 1985). Furthermore, natural sand deposits seldom (if ever) exhibit uniform density laterally or vertically, and as a result, localization is likely to occur in sands when they are sheared (Lade 1982) under either drained or undrained conditions.

Investigators have studied shear banding since the late 1950's, and this research continues today with experimental (e.g., Torabi et al. 2007) and theoretical studies (e.g., Vardoulakis 1996). For example, Desrues et al. (1985) analyzed the local density of shear bands formed in drained plane strain compression tests using gamma-ray absorption and observed that volume change became essentially localized in the shear bands. Soil in the shear band exhibited large dilatancy while other parts of the specimen exhibited almost no volume change. Vardoulakis and Graf (1985) studied localization phenomenon in dilative granular materials and found that bifurcation and localization occurred before the peak shear resistance was mobilized, and that bifurcation propagated from a fixed point in a single direction. They also observed that the essential factor in strain localization was the decreasing local shear resistance within the shear band caused by the rapid evolution of the local void ratio. Peters et al. (1988) studied shear band formation theoretically and via drained triaxial compression (TxC), triaxial extension (TxE), and plane strain compression tests and found that shear band formation was influenced significantly by the mode of shear, with drained plane strain tests exhibiting the most prominent shear banding. Finno et al. (1997) studied shear banding in undrained plane strain compression tests on loose saturated sands and found that the onset of strain localization slightly preceded the mobilization of the effective friction angle of the soil. Viggiani et al. (2001) conducted drained plane strain compression tests on saturated sands and found that shear

band thickness was directly related to the grain size distribution of the sand, but its orientation was independent of median particle size. Both the orientation and thickness of the shear band were found to be independent of the initial relative density of the specimen.

In this chapter, the formation of shear bands in the ring shear device is examined. For the tests described here, the ring shear (RS) device was fitted with a thick Plexiglas outer confining ring to observe the shearing process and visualize shear band formation, similar to plane strain tests performed with transparent outer walls (e.g., Finno et al. 1997). However, because the RS device can shear specimens to virtually unlimited displacements, the shear band behavior could be observed up to very large displacements using the new device. Based on these observations, the relevance of shear banding to particle crushing, field behavior of geotechnical structures, critical state concepts, and the constitutive behavior of sands is discussed.

6.2 SHEAR BAND FORMATION IN LABORATORY TESTS

6.2.1 Plane Strain Compression

The constitutive behavior of soils and shear localization most commonly have been studied under plane strain conditions (e.g., Desrues et al. 1985; Tatsuoka et al. 1990; Peters et al. 1988; Han and Drescher 1993; Finno et al. 1997). Rice (1976) theoretically illustrated that elasto-plastic materials exhibited a greater tendency for localization in plane strain than under axisymmetric conditions. Numerous studies (e.g., Peters et al. 1988; Alshibli et al. 2003) have supported this conclusion and have shown that the plane strain mode of shearing is very susceptible to early bifurcation, and failure of a plane strain specimen always occurs along a well-defined shear band.

6.2.2 Triaxial Compression

In contrast to plane strain testing, failure of contractive sand specimens in axisymmetrical, TxC tests is commonly characterized by specimen bulging (as discussed previously in Chapter 5), thus some researchers have suggested that localization of deformation into shear bands was essentially impossible to achieve in triaxial tests (e.g., Lade 1982; Alshibli et al. 2003). TxC tests performed in this research confirmed this

conclusion. In contrast, Desrues et al. (1985) tested cubical samples in a true triaxial device with rigid platens and observed localization of deformations in the specimens. Furthermore, Desrues et al. (1996) performed undrained TxC tests on sands and used computed tomography to study local void ratio changes during shearing. They concluded that sample bulging was actually an external manifestation of a complex internal failure pattern involving multiple shear bands that do not clearly manifest at the specimen surface. These studies generally illustrate that shear bands (while they may form) are not visible in TxC without using advanced techniques (e.g., X-ray imaging, CT scan, etc.). As a result, the impact of shear banding in evaluating soil behavior and the performance of geotechnical structures often may be underestimated in TxC tests.

6.2.3 Ring Shear

The RS apparatus was originally designed to study the residual strength of fine-grained soils (Hvorslev 1939; Bishop et al. 1971). However, Mandl et al. (1977) used the RS device to study shear band formation in granular soil. Lang et al. (1991) developed a transparent outer ring for low-stress, high-speed RS tests in order to observe the movement of dry high-strength glass beads during drained shearing. They found that the shear band thickness decreased under increasing normal stresses and that its thickness increased slightly during rapid shearing. However, their tests used only glass beads tested under drained conditions. Wang and Sassa (2002) studied shear band formation at very large shear displacements under undrained conditions. They inserted a column of different sand within the RS specimen to evaluate shear band thickness, but were unable to physically observe shear band formation during shearing because of the metal outer rings. Similarly, Wafid et al. (2004) performed parallel undrained RS tests to different shear displacement magnitudes to investigate shear band formation from the initiation of failure to the critical state, but also were unable to physically observe the shear band.

Using a RS apparatus with transparent confining rings, Fukuoka et al. (2006) captured digital images of specimens above and below the shear band during shear to evaluate the grain velocity profile and shear band formation. However, they made no direct observations of the shear band because of the limitations of their ring shear apparatus. They found that shear band thickness was essentially identical during drained and

undrained tests. More recently, Torabi et al. (2007) studied shear band formation in sands using a RS apparatus designed and constructed at Norwegian Geotechnical Institute (NGI). However, the device's metal outer ring precluded them from directly observing the shear band; therefore, they collected thin section samples after completing the test. By studying the thin sections they observed two types of shear bands: (1) shear bands with diffuse boundaries formed at low stresses; and (2) shear bands with sharp boundaries formed at higher stresses. They concluded that burial depth and applied shear displacement were two significant factors influencing shear band formation and grain crushing.

In order to observe shear band formation, the steel outer ring (OR) shown in Figure 3.2 was replaced by a Plexiglas ring as shown in Figure 6.1. Cardboard spacers were inserted in the specimen chamber to subsequently create columns of colored sand to clearly show the deformation profile. Digital video and photographs were taken during the shearing process. For tests performed at large normal stresses (greater than 300 kPa), the Plexiglas ring needed to be reinforced with ring-shaped clamps at the top and bottom. However, the visualization tests described here were performed at moderate normal stresses (less than 300 kPa) so that reinforcement was not needed. These moderate stresses are similar to the initial stresses that existed in some larger liquefaction flow slides, e.g., Calaveras Dam, Fort Peck Dam, Sheffield Dam, and Lower San Fernando Dam (Olson and Stark 2002).

6.3 INITIATION OF BIFURCATION AND SHEAR BAND DEVELOPMENT

Figure 6.2 through Figure 6.7 present typical specimen photographs, stress paths, and stress-displacement plots at various stages of shearing for the OT, IR, and MR sands, respectively. In the early stages of shearing prior to forming shear bands, shear strains developed uniformly over the entire specimen height for each sand. The air pluviated specimens of OT and IR sands initially contracted slightly, but then exhibited a phase transformation to dilative behavior. Initial phase transformations for the OT and IR sands occurred at displacements of about 1.0 mm and 1.6 mm, respectively, corresponding to shear strains of about 4 to 6% (considering the full specimen height because bifurcation had not yet occurred). In contrast, air pluviated specimens of MR sand contracted

throughout shearing and exhibited a peak shear resistance at a displacement of about 0.9 mm (approximately 4% shear strain), prior to forming a shear band. Again, no localization was observed at the peak shear resistance for the contractive specimens or at the initial phase transformation for the dilative specimens.

Bifurcation started in all of the tests at a displacement of roughly 5.3 mm, corresponding to a shear strain of about 20% (considering the full specimen height). It is possible that localization may have initiated earlier than this within the specimen before it was manifest along the outer confining ring, but it is anticipated that any difference between the actual and apparent displacement at the initiation of shear banding likely would be small. Furthermore, it appears that bifurcation occurred just as the maximum effective friction angle was fully mobilized, although again it is possible that bifurcation may have occurred within the specimen interior prior to fully mobilizing its effective friction angle. This could also explain why Han and Vardoulakis (1991) did not observed shear bands forming in loose specimens tested in plane strain compression. They stopped their tests at 5% global axial strain, but based on the findings of this study larger strains (i.e., 20% or greater) are required to develop shear bands.

As a shear band developed in each specimen, all of the subsequent deformations localized within the shear band while the portion of each specimen above the shear band remained essentially stationary. Thus the strain and strain rate normal to the shear band orientation became practically zero at the inception of shear banding. In other words, the shear band corresponds to a zero extension line. This observation can be used as a basis for numerous analytical predictions in geotechnical engineering (e.g., Poorooshasb et al. 1967; Roscoe 1970; Lade 2003). Subsequent shear displacements occurred only within the shear band and the global behavior measured for the specimen was a reflection of the soil response in the shear band, similar to observations reported by others (e.g., Yoshida, 1994; Viggiani et al. 2001).

6.4 SHEAR BEHAVIOR AFTER BIFURCATION

For the dilative OT and IR specimens (Figure 6.3 and Figure 6.5), localization initiated while the specimen was strain-hardening and before reaching a peak shear resistance, supporting the theoretical findings from some constitutive models (e.g.,

Rudnicki and Rice 1975; Tatsuoka et al. 1990). After continued shearing within the shear band (see Figure 6.3 and Figure 6.5), the OT and IR specimens reached peak shear resistances at displacements of 14.8 mm and 11.9 mm, respectively. After reaching this peak, both sands exhibited a second phase transformation from net dilation to net contraction and strain softening. The term "net" here is used because after the first phase transformation in the OT and IR sands, the specimen is responding to competing shearing mechanisms (under constant volume shearing): (1) dilation of the original grain structure within the shear band leading to increased shear resistance; and (2) particle damage and crushing leading to increased compressibility, local contraction, and decreased shear resistance. From the first to the second phase transformations, grain dilation dominates and the shear resistance increases. The second phase transformation marks the point at which a sufficient volume of sand within the shear band has been damaged to result in net contraction. Contraction continues as more grains are damaged and grain dilation decreases. Both OT and IR specimens exhibited net contraction until reaching a critical state, and the tests were terminated at shear displacement of 2 meters. Okada et al. (2004) observed similar undrained stress-displacement behavior in dense sands sheared in a split ring-type RS device. The role of grain damage and crushing on the shear behavior of sands will be discussed in more detail in chapter 7.

In contrast to the OT and IR sands, MR sand specimens exhibited net contraction throughout constant volume shearing to large displacements as illustrated in Figure 6.7. Note that although dilation may have occurred locally within the shear band, it was not sufficient to generate net dilation. As illustrated in Figure 4.5, MR sand is a silty sand with about 40% non-plastic fines. The air pluviated fabric of this silty sand (when deposited with zero drop height) was contractive, and minor particle damage that occurred in the shear band during constant volume shearing added to its net contractive behavior.

6.5 SHEAR BAND THICKNESS

Theoretical and experimental studies have shown that frictional materials exhibit shear bands with specific and reasonably constant thicknesses that can be related to grain properties (e.g., Alshibli and Sture 2000). Many researchers have expressed this thickness

in terms of median particle diameter (D_{50}) of the sand. In general, shear band thickness varies from about 10 to 25 times D_{50} (Finno et al. 1997). For example, in drained simple shear tests Roscoe (1970) observed shear band thicknesses of 10 x D_{50} by means of X-ray images in sands and scanning electron microscope (SEM) photographs in clays. Vardoulakis and Graf (1985) have suggested that shear band thickness is about 16 x D_{50}. Vardoulakis and Aifantis (1991) modified a plasticity-based constitutive model by incorporated second-order gradients into the flow rule and yield condition and found that shear band thickness was about 20 x D_{50}. Yoshida (1994) reported a shear band thickness of (7-20) × D_{50}, depending on the mean effective stress and particle shape. Discounting rotational resistance among particles, DEM simulations performed by Bardet and Proubet (1991) and Iwashita and Oda (1998) yielded a shear band thickness of (15-18) × D_{50}; however, when Oda et al. (1997) and Iwashita and Oda (1998) accounted for rotational resistance, the shear band thickness became about 10 x D_{50}. Alshibli and Sture (1999) also suggested that the ratio of shear band thickness to D_{50} varies, but they related this ratio to overall sand gradation, with coarse-, medium-, and fine-grained sands exhibiting ratios of 10-11, 11-12, and 13-14, respectively, based on the results of drained plane strain compression tests.

Figure 6.2d, Figure 6.4d, and Figure 6.6c illustrate the shear band thickness at the end of constant volume RS tests on air pluviated specimens of OT, IR, and MR sands, respectively, with the OT, IR, and MR sands exhibiting shear band thicknesses of 5.0 mm, 5.4 mm and 1.3 mm, respectively. Combined with the median particle diameters of OT, IR, and MR sands (0.50 mm, 0.54 mm, and 0.09 mm, respectively) from Figure 4.5 yields shear band thicknesses of 10 x D_{50}, 10 x D_{50}, and 14 x D_{50}, agreeing with the observations of Alshibli and Sture (1999). Furthermore, despite differences in particle size distribution between the OT and IR sands (i.e., IR sand is more widely-graded), the ratios of shear band thickness to D_{50} for these two sands are the same.

6.6 PARTICLE CRUSHING WITHIN THE SHEAR BAND

Considerable grain damage and particle crushing was observed in the shear band of RS specimens when sheared to very large shear displacements, especially for the dilative OT and IR sands at moderate consolidation normal stresses. To illustrate the significance

of grain crushing, Figure 6.8 presents grain size distributions of an IR sand specimen measured before and after RS testing. Figure 6.8a includes the grain size distribution of the sand collected solely from the shear band, where grain damage and crushing occurred. No crushing was observed in the specimen above the shear band. This damage also was visually apparent by comparing the color of the soil from the shear band with the soil before shearing, as shown in Figure 6.8b. The role of grain crushing and particle damage will be discussed in detail in Chapter 7.

6.7 EFFECT OF SHEAR BANDING ON CRITICAL STATE

Casagrande (1936) performed a series of drained TxC tests on dry, loose and dense sand specimens, and found that loose specimens deformed in an apparently homogenous manner throughout shearing, while dense specimens developed shear bands just after the peak shear stress was reached. He concluded that the critical void ratio of dense sands could not be determined from globally measured responses in triaxial tests. As a result, Poulos (1981) (among others) recommended that only contractive specimens be used to evaluate the critical state.

As shear bands have been found subsequently to occur in both contractive and dilative sands, critical state concepts (i.e., constant volume, shear stress, and effective confining stress) strictly apply only within shear bands. However, Desrues et al. (1996) concluded that globally-measured void ratios in contractive specimens do not differ significantly from local void ratios within the shear bands, supporting the approach proposed by Poulos (1981). In contrast, globally measured void ratios in dilative specimens do not reflect the true responses of the soil actually participating in the deformation process (e.g., Finno and Rechenmacher 2003), making it difficult to define the critical state from dilative specimens.

Roscoe (1970) first attempted to quantify local void ratio evolution within shear bands formed in sands during drained simple shear tests. Stroud (1971) performed drained simple shear tests on Leighton Buzzard sand and used X-rays to track the movement of steel balls placed on a 4 mm grid within the specimens and compute local strains. More recently, global measures (Han and Drescher 1993), stereophotogrammetry (e.g., Desrues et al. 1985; Yoshida et al. 1994; Mooney et al. 1996), and X-ray tomography (Desrues et

al. 1996) have been used to quantify void ratio changes in shear bands formed in dense sands. Desrues et al. (1985) conducted drained plane strain compression tests on dense sands and using stereophotogrammetric techniques they tracked the displacements of a grid painted onto the membrane. Their results showed erratic volumetric strains both within and outside the shear band, and they concluded that the technique was too difficult to apply regularly. Mooney et al. (1996) conducted drained plane strain compression tests on specimens of masonry sand and used stereophotogrammetric techniques to quantify displacements of individual sand grains. Based on their work, Mooney et al. (1996) suggested that loose and dense masonry sand did not form a unique CSL. Finno and Rechenmacher (2003) also found that critical state reached within the shear band of drained plane strain compression tests was non-unique, depending on the initial state and consolidation history of the sand specimen. Interestingly, they found that although separate, loose and dense specimens produced parallel CSLs and that these CSLs were parallel to the normal compression line measured for the sand.

In the RS tests performed in this study, the global void ratio variations are computed based on vertical LVDT measurements (see Figure 3.2). As discussed in Chapter 4, minor variations in global void ratio during constant volume tests result from system compliance of the RS device. However, local void ratio changes may occur while the global void ratio remains (approximately) constant. Local void ratio changes (volumetric compression) in the shear band resulting from grain crushing and particle rearrangement are manifested externally as changes in total height of the ring shear specimen and in constant volume tests would lead to the rebound of the soil above the shear band due to unloading of the soil structure (as effective normal stress decreases). The void ratio of the soil in the shear band (e_{sb}) can be crudely estimated as follows:

$$e_{sb} = \frac{V_{V,sb}}{V_{S,sb}} = \frac{(V_{sb} - V_{S,sb}) - \Delta V_{global} - \Delta V_{above}}{V_{S,sb}} \qquad \textbf{6.1}$$

where $V_{V,sb}$ = volume of voids in the shear band; $V_{S,sb}$ = volume of soil solids in the shear band; V_{sb} = total volume of the shear band; ΔV_{global} = global volume change of the specimen estimated from specimen height changes (resulting from system compliance

during constant volume tests); and ΔV_{above} = volume change of soil above the shear band, which can be estimated as:

$$\Delta V_{above} = C_s \cdot log\left(\frac{\sigma'_{n,i}}{\sigma'_{n,bs}}\right) V_{s,above} \qquad 6.2$$

where C_s = swelling index (= Δe / $\Delta \log \sigma'_n$); $\sigma'_{n,i}$ = current effective normal stress; and $\sigma'_{n,bs}$ = effective normal stress when shear band forms. Swelling indices of 0.0028, 0.0039, and 0.0053 for OT, IR and MR sands, respectively, were measured in unloading cycles of one-dimensional compression tests.

Figure 6.9 presents approximate shear band void ratios for sample RS tests estimated using Equations 6.1 and 6.2. The specimen global void ratios are also plotted in this figure, illustrating the very small changes in global void ratio resulting from system compliance. Despite the fact that Equations 6.1 and 6.2 only crudely estimate the shear band void ratio (and may overestimate the actual void ratio changes), the marked difference between the volumetric behavior of the shear band and that measured globally highlights the need to consider the volumetric evolution within the shear band to better quantify the critical state, even in contractive specimens. This finding differs from that reported by Desrues et al. (1996) primarily because of the particle damage that develops within the shear band (even in contractive specimens) at large shear displacements. Desrues et al. (1996) based their conclusions on the sand behavior at relatively smaller strains (less than 30%). At larger shear strains (greater than about 30%), the local void ratio starts to deviate considerably from the global void ratio in their tests. Similarly, the RS specimens exhibited nearly identical global and local void ratios at small to moderate shear strains prior to and slightly after bifurcation (less than about 20-25%). However, at larger shear displacements after bifurcation (i.e., at shear strains >> 25%), the local void ratio began to deviate from the global void ratio.

Lastly, given that the shear band thickness is small [(10-14) × D_{50} for the sands tested here], the shear strains within the shear band become extremely large as the soil reaches the critical state. Hence, any modeling of critical state within a shear band requires a large strain formulation.

6.8 IMPLICATIONS OF SHEAR BAND FORMATION

Shear bands form in almost all field deformations of geotechnical structures, such as around offshore pipelines (Cheuk et al. 2008), around anchors used to resist uplift (Hsu and Liao 1998), in shaking table model tests of retaining walls (Watanabe et al. 2003), and in landslides (Sassa 2000). Iverson et al. (2004) suggested that soil behavior within the shear band of landslides is the most important factor in landslide mobility, in part because "sliding surface liquefaction" (Sassa 1996) can occur within the shear band. The primary mechanism of sliding surface liquefaction is grain crushing along the sliding surface, which leads to net contraction in the shear band, concurrent excess pore water pressure generation, and a consequent reduction in shear resistance. For example, Sassa (2000) illustrated that the Nikawa landslide (triggered by the 1995 Hyogoken-Nanbu earthquake) exhibited a distinct shear band in a cohesionless soil. However, the main difference in shear band development between field failures and laboratory samples is that multiple shear surfaces may develop in the field, which can lead to a thicker, more diffuse shear zone, while laboratory specimens typically exhibit a single, discrete shear band. This difference in thickness would lead to differences in shear displacements and strain rates within the shear zone.

For contractive specimens, shear band formation occurred very soon after the peak shear resistance was exceeded (i.e., after liquefaction was triggered) as the soil fully mobilized its effective friction angle. In comparative tests on MR sand specimens, shear band formation in contractive RS test (Figure 5.15) resulted in slightly smaller critical shear strength than TxC test (Figure 5.7). However, in dilative specimens of OT and IR sands, very large shear stresses were mobilized (as the effective friction angle was fully mobilized) prior to bifurcation and the mobilized shear stress increased further (after bifurcation) prior to experiencing a second phase transformation (to net contraction) leading to strain softening to the critical state. Under load-controlled conditions, mobilizing such a large shear stress likely would arrest further shear displacement. Furthermore, particle damage and crushing within the shear band causes the permeability to decrease significantly. As a result, pore water pressure dissipation within (and through)

the shear band is slowed considerably. This mechanism may help to explain the occasional occurrence of flow slides in relatively dense (dilative) soils.

6.9 SUMMARY AND CONCLUSIONS

In this chapter, a Plexiglas outer confining ring was used to directly observe shear band formation and evolution during RS tests. Parallel tests performed in TxC did not exhibit distinct shear band formation, while the RS tests produced a discrete shear band where grain crushing readily occurred. This shear band formed as the effective friction angle was fully mobilized (after the peak shear resistance was mobilized in contractive specimens and after the initial phase transformation occurred in dilative specimens). Once a shear band developed in a specimen, the sliding process could be divided into three consecutive stages.

1. Continued shearing caused particle damage and grain crushing within the shear band, and this damage continued as shear displacements increased.
2. Particle damage and grain crushing caused contraction within the shear band. In constant volume tests, this tendency for contraction decreased the normal effective stress and caused a loss of shearing resistance (i.e., strain softening).
3. Strain softening continued until the normal effective stress within the shear band of the constant volume tests decreased sufficiently such that particle damage ceased (this effective stress was as small as a few tens of kilopascals in some cases) and further damage did not occur.

Furthermore, the stress-displacement response of the specimen was affected only by the soil within the shear band, while soil outside the shear band did not experience measurable particle damage, volume change, or strain-softening since no further shear stress increment was applied there after bifurcation occurred.

6.10 FIGURES

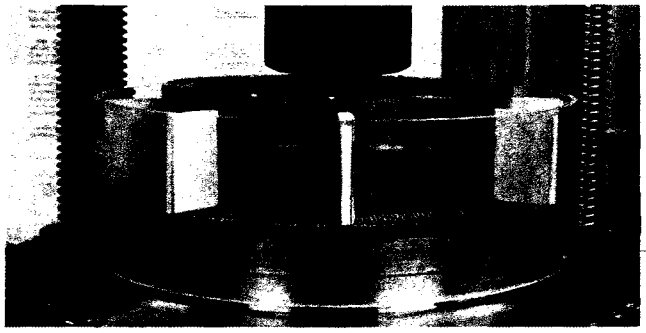

Figure 6.1: Shear box with a Plexiglas outer ring. Cardboard inserts were used to create columns of colored sand.

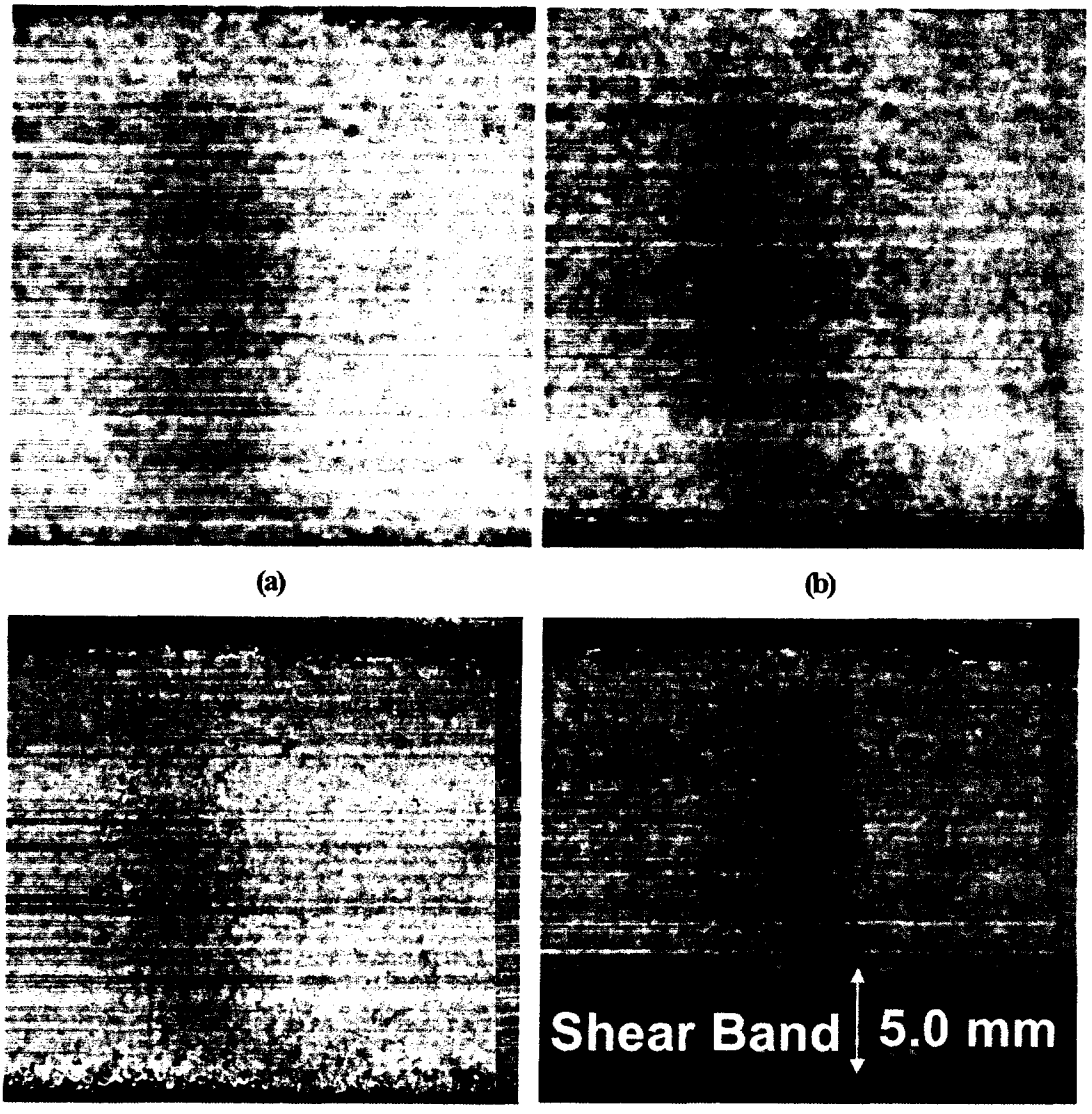

Figure 6.2: Stages of shear band formation corresponding to the stress paths and stress-displacement plots in Figure 6.3. (a) at first phase transformation point (0.95 mm of shear displacement); (b) at initiation of bifurcation (5.3 mm of shear displacement); (c) at second phase transformation (13.6 mm of shear displacement); (d) at end of test (20 m of shear displacement) and illustration of shear band thickness.

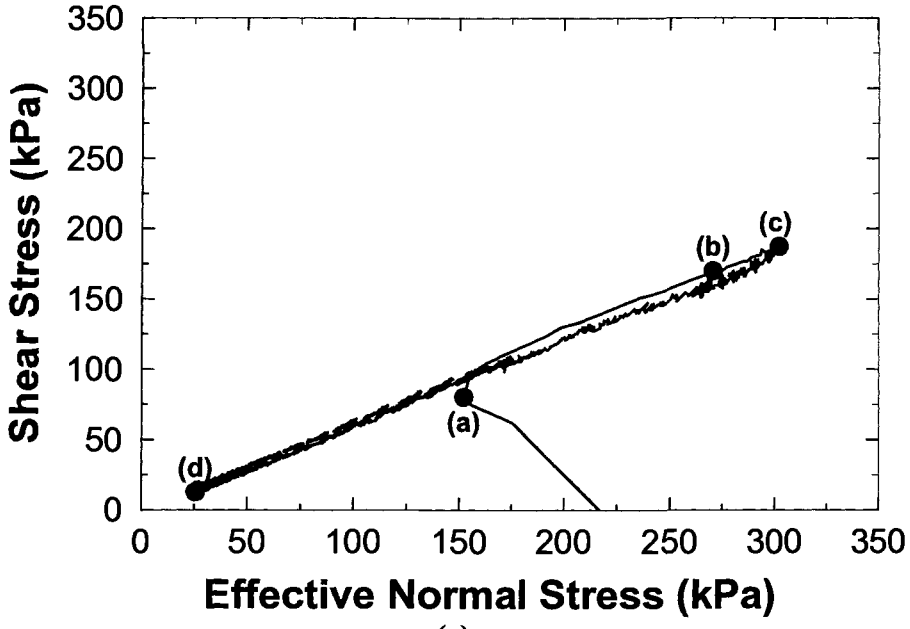

(a)

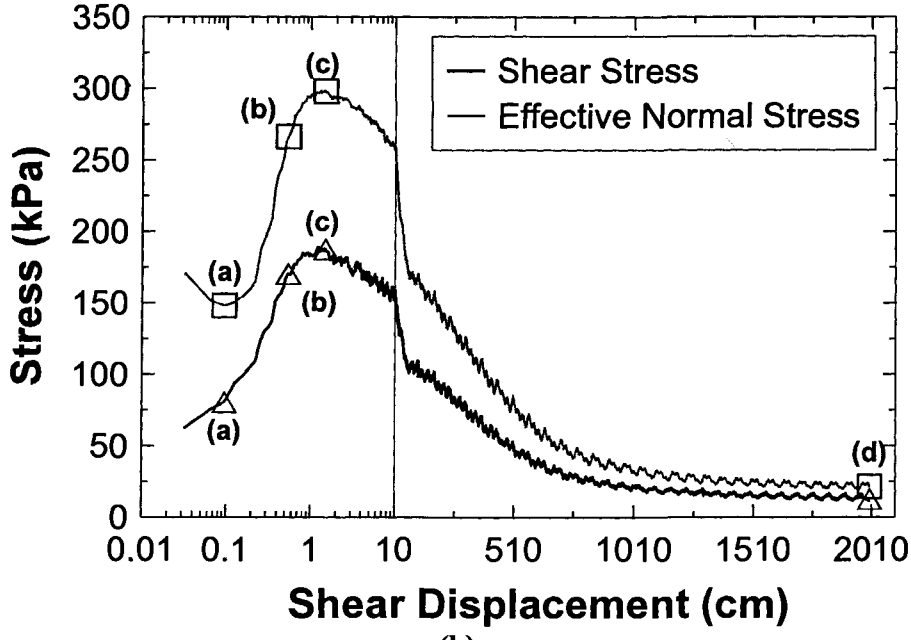

(b)

Figure 6.3: (a) Stress paths and (b) stress-displacement plots in a constant volume RS test on OT sand with consolidation stress of 217 kPa and consolidation void ratio of 0.580 (consolidation relative density of 26%).

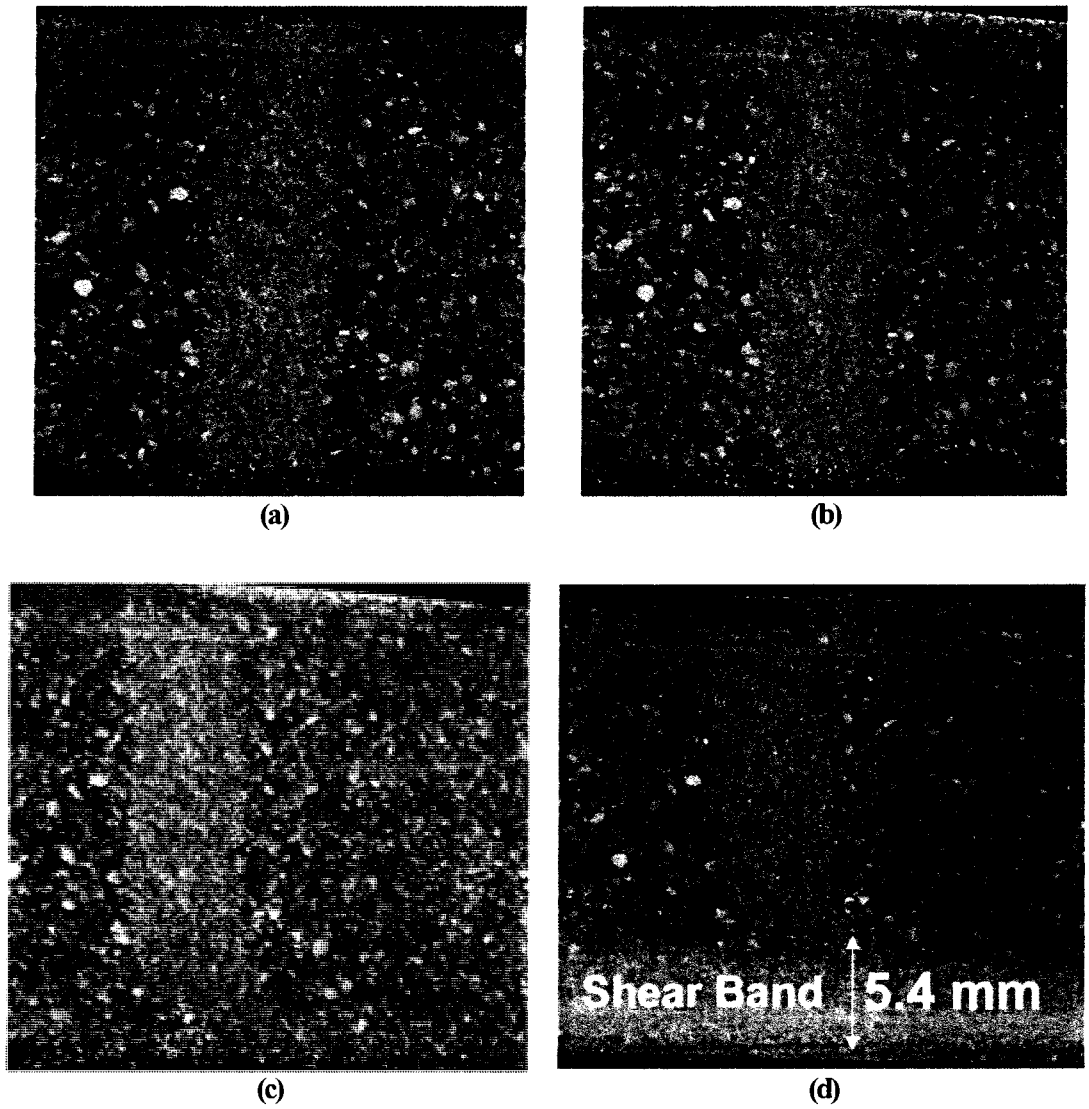

Figure 6.4: Stages of shear band formation corresponding to stress paths and stress-displacement plots in Figure 6.5. (a) At first phase transformation point (1.6 mm of shear displacement); (b) At initiation of bifurcation (5.3 mm of shear displacement); (c) At second phase transformation (11.9 mm of shear displacement); (d) at end of test (20 m of shear displacement) and illustration of shear band thickness.

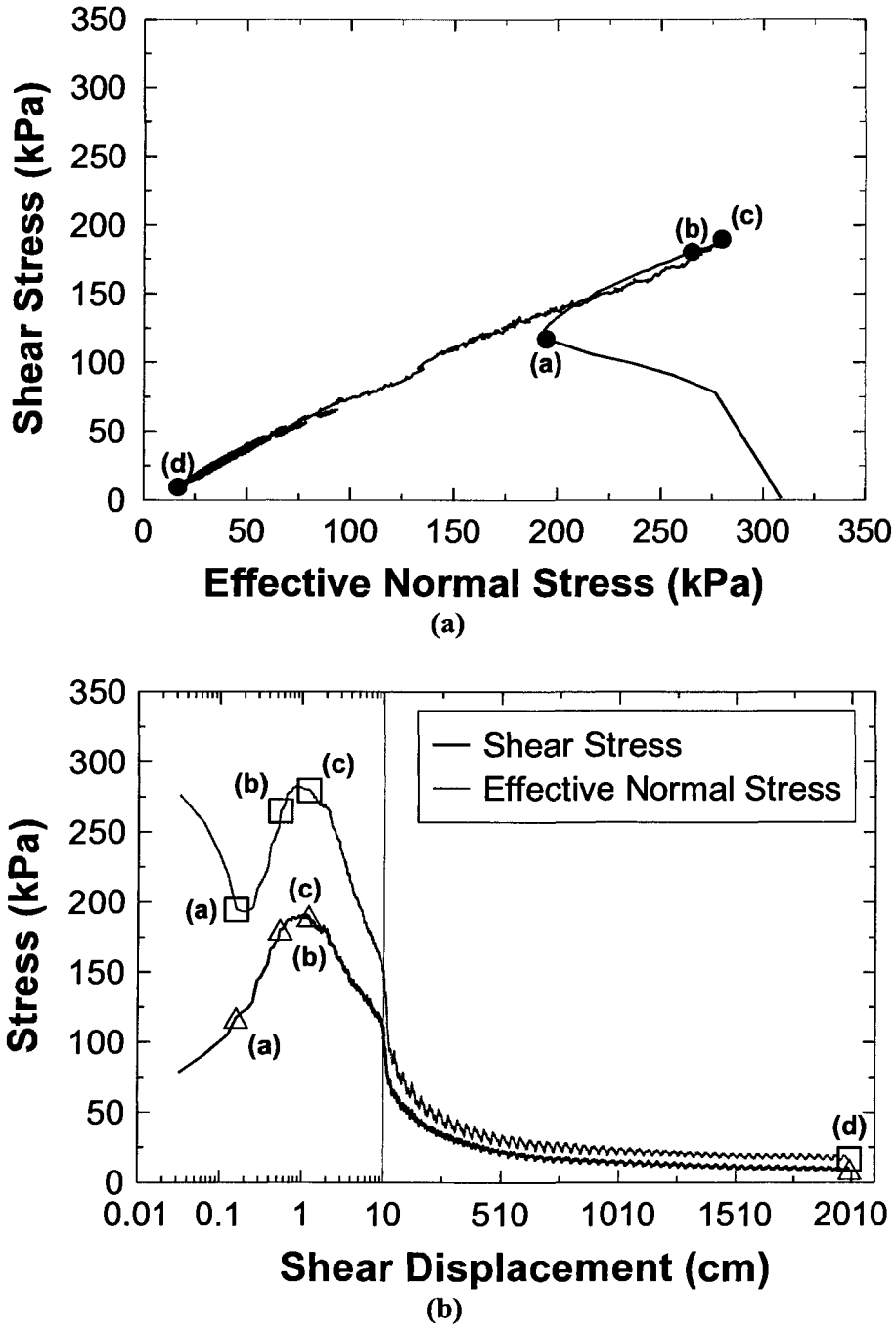

Figure 6.5: (a) Stress paths and (b) stress-displacement plots in a constant volume RS test on IR sand with consolidation stress of 309 kPa and consolidation void ratio of 0.620 (consolidation relative density of 42%).

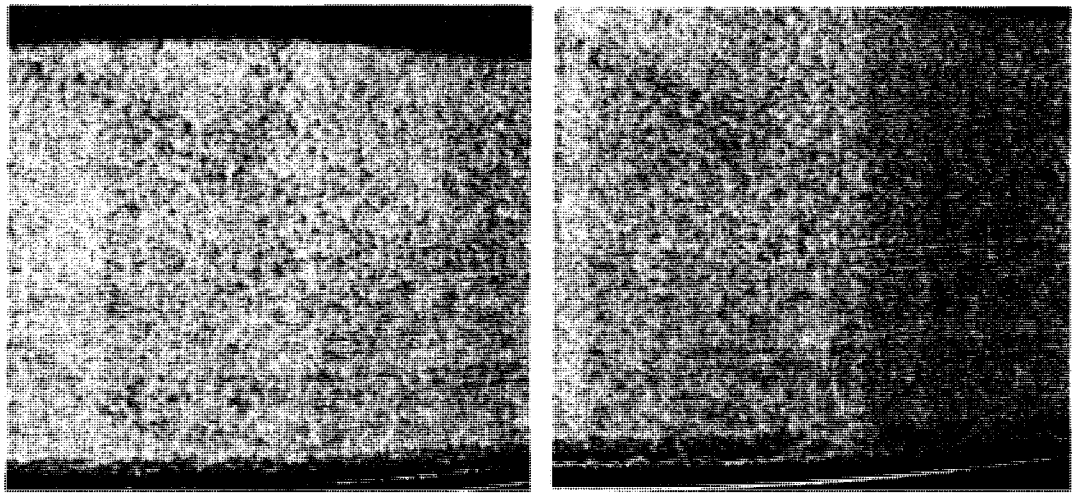

(a) (b)

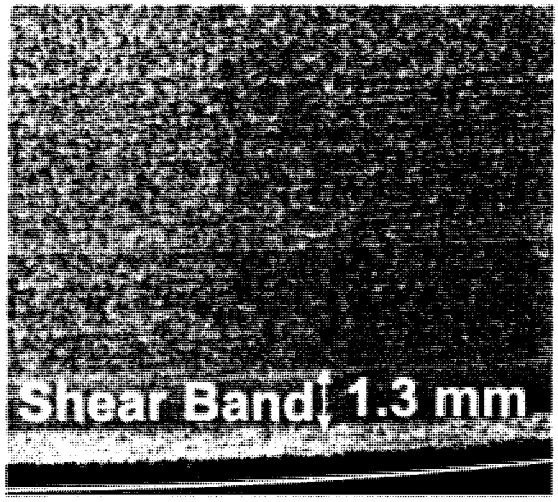

(c)

Figure 6.6: Stages of shear band formation corresponding to stress paths and stress-displacement plots in Figure 6.7: (a) at peak shear resistance (0.9 mm of shear displacement); (b) at initiation of bifurcation (5.3 mm of shear displacement); (c) at end of test (20 m of shear displacement) and illustration of shear band thickness.

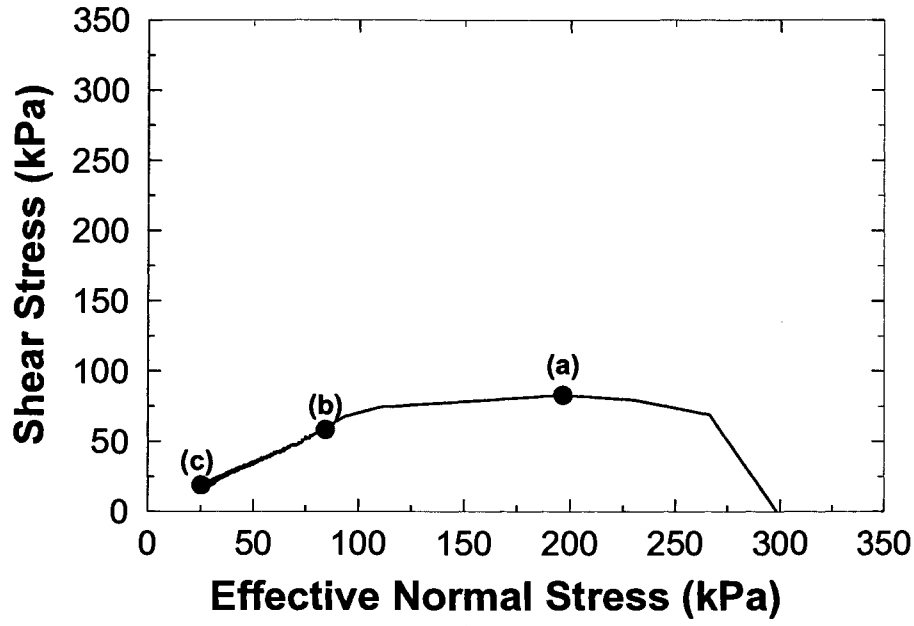

(a)

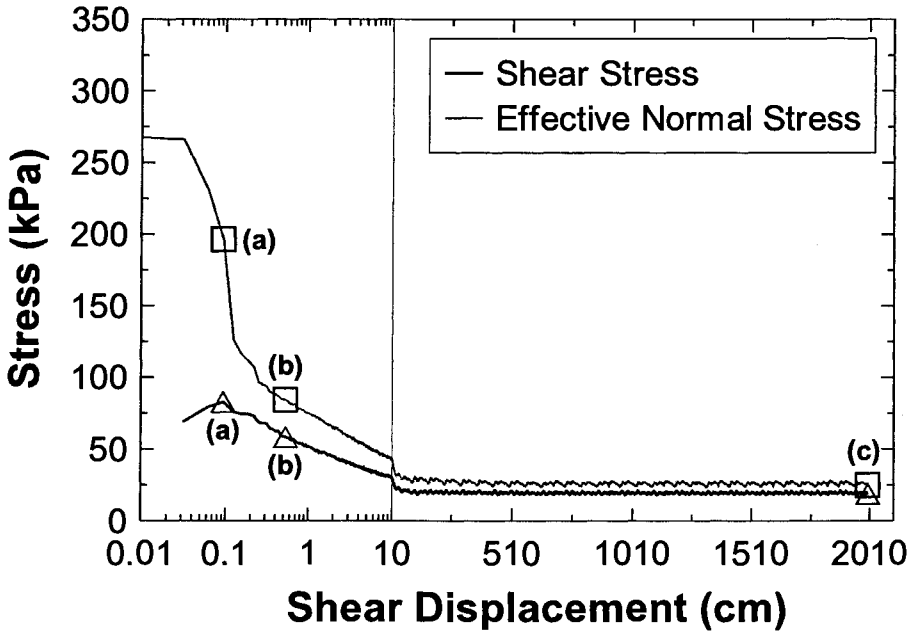

(b)

Figure 6.7: (a) stress paths and (b) stress-displacement plots in a constant volume RS test on MR sand with consolidation stress of 298 kPa and consolidation void ratio of 0.693 (consolidation relative density of 69%).

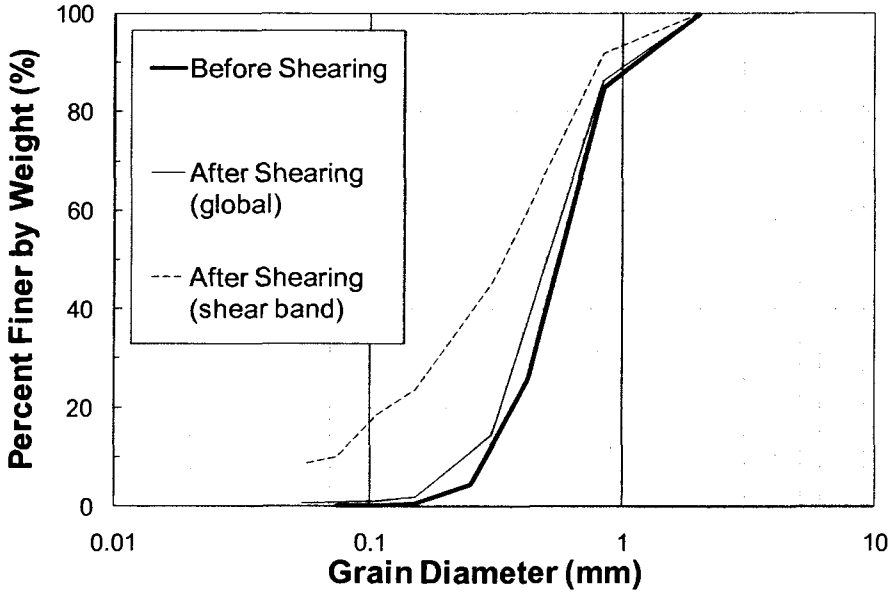

(a)

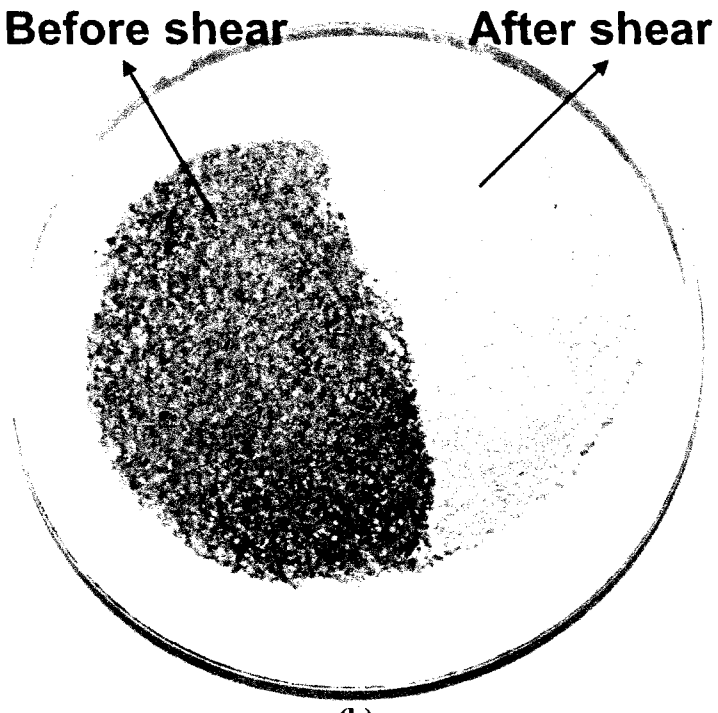

(b)

Figure 6.8: (a) Grain size distributions of IR sand before and after RS testing; (b) photograph of IR sand before and after (from the shear band) RS testing.

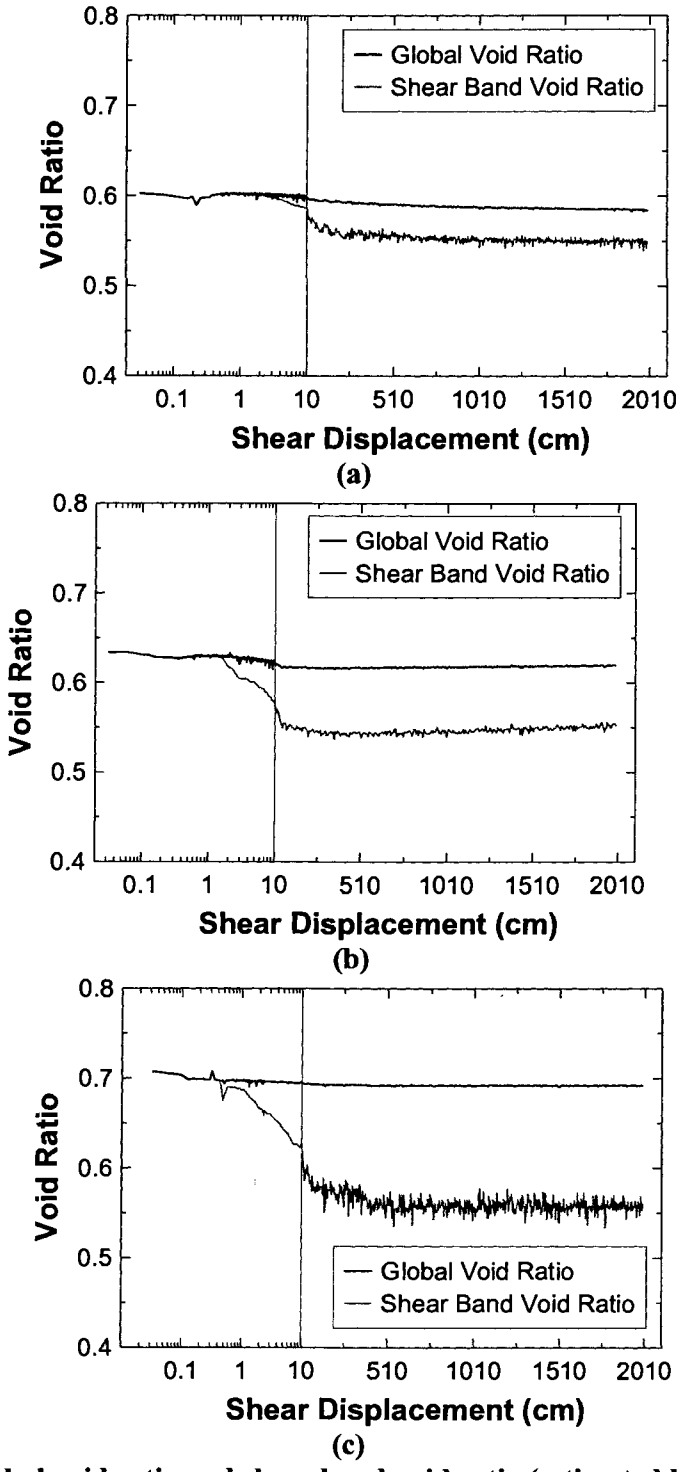

Figure 6.9: Global void ratio and shear band void ratio (estimated by Eq. 6.1) in RS tests on (a) OT sand, (b) IR sand, and (c) MR sand specimens

CHAPTER 7: PARTICLE DAMAGE IN RING SHEAR TESTS

7.1 INTRODUCTION

Many granular materials are comprised of grains that may be damaged by abrasion, shearing off of asperities, and splitting rather than flowing plastically under applied shear stress. Based on the crushing mechanisms, particle damage can be quantified as level I: abrasion or grinding of particle surface asperities; level II: breakage or crushing of particle surface protrusions and sharp particle corners and edges; and level III: fracturing, splitting, or shattering of particles (Mesri and Vardhanabhuti, 2009). Other investigators have also suggested similar classifications (Roberts and de Souza 1958; Hendron 1963; Marsal 1967; Hardin 1985; Rahim 1989; Coop 1990; Pestana and Whittle 1995; Nakata et al. 2001a, b; Chuhan et al. 2002, 2003). In these materials, plasticity arises primarily from particle damage (Robertson and Bolton 2001). There are also many weak-grained crushable soils, such as decomposed granites, carbonate sands, and volcanic ashes for which particle damage can be important even under low confining stresses. Moreover, changes in grain size distribution due to particle damage and crushing may create more drastic changes in internal structure than can be achieved by particle rearrangement alone (Bolton et al. 2008). For these reasons, the effect of particle crushing on the deformation response of coarse-grained soils should not be neglected.

Many researchers have studied particle damage and crushing related to both confined compression and/or shear loading (e.g., Colliat-Dangus et al. 1988; Been et al. 1991; Konrad 1997a,b; Mesri and Vardhanabhuti, *in press*). For example, McDowell et al. (1996) developed a numerical model to express the compression behavior of sand due to grain crushing. McDowell and Bolton (1998) studied the micromechanical behavior of crushable soils and developed a fractal theory of particle crushing based on the assumption that the smallest particles are similar in size and shape (geometrically self-similar) under increasing macroscopic stress. They then used this theory to relate the evolution of particle sizes to the normal compression curve, in terms of the tensile strength and elastic modulus of the particles. Nakata et al. (1999) established a relationship between single-particle crushing properties and a particle breakage factor. As a continuation of this work, Nakata et al. (2001a, b) investigated the relationship between

the isotropic compression curve and typical failure patterns of individual particles. Furthermore, they studied the influence of various soil parameters such as the uniformity coefficient, initial grain size distribution, and void ratio on the compression characteristics of the soil. Interestingly, they showed that the nature of particle damage changes from sudden splitting to gradual breaking of asperities and grinding of particles as the soil becomes more well graded.

In general though, most investigators have found that significantly more particle damage occurs during shear loading than during one-dimensional compression loading (e.g., Vesic and Barksdale 1963) and can occur at much smaller normal stresses during shearing. For example, Wang et al. (2002) performed RS tests on soil samples from the Hiegaesi landslide and found that particle crushing during shear occurred at normal stresses smaller than 40 kPa. Similarly, using ring shear (RS), direct shear, and oedometer tests, Luzzani and Coop (2002) observed that particle breakage caused by shearing was more pronounced than that caused by compression and could occur at effective confining stresses as low as about 50 kPa. They also observed that an extremely large shear strain was required to reach a critical state when particle damage occurred during shearing.

Some researchers have utilized discrete element methods (DEM) to model particle damage and crushing. For example, Robertson (2000) modeled crushable grains as bonded elementary spheres with probabilistic flaws. He concluded that plastic yielding was associated with particle breakage as compaction or dilation developed progressively during shearing. Cheng et al. (2003, 2004) and Cheng (2004) used DEM to illustrate that grain crushing was one of the most important aspects of the plastic behavior of granular soils. Bolton et al. (2008) also used DEM to simulate crushable soils and concluded that the main effect of particle damage, from a micromechanical point of view, was the sudden creation of new degrees of freedom.

In this chapter, the role of particle damage and crushing on the shear behavior of the test sands observed during RS tests are examined.

7.2 PARTICLE CRUSHING IN RING SHEAR TESTS

Table 7.1 shows the tests for which particle crushing was studied. All of these tests were sheared to shear displacements exceeding 20 meters, except test MTOTDR38(2) which was sheared to a displacement of 853 cm. As discussed in Chapter 6, a distinct shear band formed during shear near the specimen base, and within the shear band of each specimen, various degrees of particle damage occurred, while no particle damage was observed above the shear band. While pre- and post- shearing particle size distributions did not show any particle damage in parallel triaxial compression (TxC) tests, serious particle damage and crushing yielded a rock flour (Figure 6.8) in the shear band of the RS tests performed on IR sand when sheared to very large shear displacements. In drained tests, the crushed sand was tightly packed and difficult to remove from the specimen mold, while in constant volume tests the crushed sand particles were loose.

After each RS test, the sand in shear band was collected and its particle size distribution was measured. Figure 7.1 presents the grain size distributions of an OT sand specimen (from test APOTDR40) before and after shearing collected from the shear band. The grain size distributions after shearing include that measured by sieving only and that measured by sedimentation and sieving according to ASTM D422-63. With sieving only, the fines content of the crushed sand was only 6%, but after dispersing the material in sodium hexametaphosphate for 24 hours the fines content increased to 21%. Without dispersing, most of the fines tended to "stick" to coarser grains likely by tightly interlocking and wedging into roughened surfaces of the coarser particles during continued shearing within the narrow shear band and resulted in an artificially coarser grain size distribution. In fact, the same grain size distribution (with fines content of 21%) was obtained when the soil was separated by shaking in water alone. Interestingly, in many cases the soil within the shear band was damaged so severely that sedimentation was not complete after two days, confirming the observation of Nakata et al. (2001b) that as crushing proceeds, it becomes increasingly concentrated in the smaller particle size fraction, where the coordination number is smaller and thus the individual particle tensile stress is larger.

As illustrated in Figure 7.1, particle damage and crushing yields a more well-graded (wider) grain size distribution in which the number of equal-sized nearest neighbors is minimized (Sammis et al. 1987). This reduces stress concentrations by distributing interparticle contact stresses over a larger number of grain contacts. Also, as the shear band forms within the RS specimen, the angle between the shear band and the intergranular slip planes (i.e., β in Eq. 2.2) decreases, promoting relative movement among grains. Consequently at large shear displacements the rate of grain crushing decreases and the potential for particle sliding and rolling increases.

7.3 QUANTIFYING PARTICLE CRUSHING

Several researchers have proposed empirical methods to quantify the magnitude of particle damage and crushing using changes in grain size distribution. Some methods are based on a single particle size, while others are based on the overall change of the grain size distribution. For example, Marsal (1967) proposed a breakage factor to sum the differences in percent passing individual U.S. standard sieves for the initial and final grain size distributions. Lee and Farhoomand (1967) proposed a breakage factor based on changes in the 15% finer particle diameter (D_{15}) before and after testing. Miura and Yamanouchi (1977) and Miura and O'Hara (1979) proposed a method that used the total surface area of the particles assuming spherical particles; but this assumption can lead to significant errors if the sand has angular, elongated, or very iregular particle shapes. Other researchers (e.g. Lade et al. 1996; Tarantino and Hyde 2005; Bolton et al. 2008) also correlated particle damage magnitude with input energy, allowing samples to be compared when tested at different stress levels or when the shear stress changed significantly with shear strain.

Hardin (1985) proposed several particle breakage indices based on changes of the grain size distribution. Hardin's particle breakage parameters are implemented in this study due to their relative simplicity and consideration of the grain size distribution. The latter feature minimizes any small errors in determining individual grain sizes for computing the breakage factors, making this method relatively stable. In this approach, Hardin (1985) defined an initial breakage potential (B_{p0}) as:

$$B_{p0} = \int_0^1 b_{p0} df \qquad \textbf{7.1}$$

where b_{p0} = the pre-shearing potential for breakage that is significant to soil behavior for a given size fraction, df, in an element of soil; and df = the differential of "percent passing." The breakage potential, b_{p0}, for a particle with a given size of D is defined as:

$$b_{p0} = \begin{cases} \log\left(\dfrac{D(\text{mm})}{0.075\,\text{mm}}\right) & \text{for } D \geq 0.075\,\text{mm} \\ 0 & \text{for } D < 0.075\,\text{mm} \end{cases} \qquad \textbf{7.2}$$

where D = grain diameter (in mm) and D = 0.075 mm is the upper limit of silt sizes. Hardin (1985) ignored damage to silt and clay size particles as he postulated that it is less important to soil behavior than damage to coarser particles and because of the larger stresses required to crush silt and clay sized particles. Thus B_{p0} equals the area between the portion of the grain size distribution curve for D > 0.075 mm and a vertical line at 0.075 mm as shown schematically in Figure 7.2a, and Gerolymos and Gazetas (2007) reported typical values of B_{p0} listed in Table 7.2. The final breakage potential, B_{pf} is defined as:

$$B_{pf} = \int_0^1 b_{pf} df \qquad \textbf{7.3}$$

where b_{pf} is the potential for breakage after loading (defined graphically similar to b_{p0}). The amount of total breakage, B_t, is then quantified as the difference between the two breakage potentials:

$$B_t = \int_0^1 \left(b_{p0} - b_{pf}\right) df \qquad \textbf{7.4}$$

where this value equals the area between the grain size distribution curves before and after shearing, as shown schematically in Figure 7.2b. Hardin (1985) reported that total breakage (B_t) is proportional to initial breakage potential (B_{p0}) for soils with the same mineralogy, shape, void ratio, stress state, and loading-induced stress path. Hence Hardin (1985) suggested another index value, the relative breakage (B_r) index to compare the magnitude of particle damage and crushing from multiple tests, independent of the original grain size distribution:

$$B_r = B_t / B_{p0} \qquad \textbf{7.5}$$

The relative breakage index has a lower limit of zero and a theoretical upper limit of unity.

Figure 7.3 presents the range of post-shearing grain size distributions of the tested sands obtained from the shear band of the RS specimens. As illustrated in the figure, particle crushing increases the proportion of finer particles without significantly changing the maximum particle size of the sand. A similar trend was found by probabilistic analysis of particle crushing (McDowell et al. 1996) as well as DEM analyses of breakable particles (Cheng et al. 2005), illustrating the importance of the coordination number on particle damage (i.e., coarser particles have higher coordination numbers and are less susceptible to splitting) and the likelihood that coarser particles are chiefly damaged by abrasion and shearing off of asperities (thus creating fine particles without significantly changing their particle diameter). Based on these grain size distributions, Table 7.1 presents values of initial breakage potential (B_{p0}), final breakage potential (B_{pf}), total breakage (B_t), and relative breakage (B_r) for each test. As indicated in Table 7.1, the initial breakage potentials of OT, IR, and MR sands are 0.471, 0.592, and 0.037 respectively. Figure 7.4 presents the relative breakage index (B_r) versus the consolidation stress for the RS tests in Table 7.1. As suggested earlier, using relative breakage index minimizes the role of original grain size distribution on breakage potential. As seen in

Figure 7.4, some particle crushing occurred at a consolidation stress as low as 28 kPa (in OT sand). Although particle damage was quite variable depending on σ'_n, stress path (drained or constant volume), and specimen preparation method, IR sand generally suffered the most particle damage and crushing, OT sand exhibited a moderate amount of particle damage, while MR sand exhibited the least particle damage. MR sand possibly exhibited low values of B_r because: (1) it has a broader grain size distribution in comparison to the more uniform and coarser IR and OT sands, and thus the particles were better confined and supported by neighboring particles (e.g., Mandl et al. 1977; Hardin 1985; Lade et al. 1996; Gerolymos and Gazetas 2007); and (2) the relative breakage index, B_r only accounts for the grains larger than 0.075 mm, neglecting any particle damage or crushing of silt-sized particles, which apparently occurred in the MR sand (see Figure 7.3c)

Figure 7.4 also illustrates that particle damage severity generally increases with consolidation normal stress and that more damage occurs in drained RS tests than in constant volume tests at a given consolidation normal stress. Constant volume (or undrained) shearing of loose sand results in the tendency to contract and a decrease in effective normal stress; consequently, there is less particle damage and crushing. In contrast, drained shearing results in an increase in shear stress under a constant effective normal stress, thereby causing more particle damage and crushing. Furthermore, moist tamped specimens of IR and OT sands (those indicated by an arrow in Figure 7.4) were consistently less damaged than their air pluviated counterparts in constant volume tests as a result of their very loose fabric (e.g. Casagrande 1979; Vaid and Sivathayalan 2000). These moist tamped specimens contracted more readily and rapidly in constant volume tests, causing the effective normal stress to decrease faster than in air pluviated specimens, thus reducing the severity of particle damage. However, specimen preparation method did not impact breakage in the drained tests. The effect of shear displacement on particle crushing can also be assessed. The sand in test MTOTDR38(1) ($B_r = 0.282$) sheared to a displacement of 2725 cm was more severely damaged than MTOTDR38(2) ($B_r = 0.036$) which was sheared to 853 cm of shear displacement.

Moreover, although all of the RS tests [except MTOTDR38(2)] were sheared to different but still very large, shear displacements (ranging from 21 to 50 m; see

Table 7.1), the amount of particle damage and crushing correlates moderately well with the consolidation normal stress. This implies that, as the shear displacement increases to very large values, the rate of particle damage (within the single shear band) decreases significantly and the grain size distribution approaches a relatively stable ultimate condition that is a function of the effective normal stress corresponding to the critical state of the sand.

7.4 IMAGING OF PARTICLE CRUSHING AND EFFECT OF CRUSHING ON PARTICLE SHAPE

The scanning electron microscope (SEM) photo in Figure 7.5a illustrates that the original OT sand has rounded particles (with a rough surface texture) and a narrow range of grain sizes. Figure 7.5b and Figure 7.6 illustrate that shear-induced damage produces a considerable amount of angular to subangular fine particles, with many fine particles appearing platy to blocky, contrary to the usually prismatic shapes of quartz minerals (Klein and Dutrow 2007). This could be due to the intense shearing and abrading of the particles. To better visualize the coarser particles after being sheared, the sheared sand was washed on a #200 sieve and Figure 7.7 and Figure 7.8 present the coarse fraction only (> 0.075 mm). In contrast to the original OT sand with rounded grains, the coarse-grained sheared sand particles are subangular to angular, have rougher surface textures, considerable damage and a few incipient fractures.

Similarly, Figure 7.9 presents SEM photos of IR sand. The original IR sand has subrounded to angular grains and a relatively narrow grain size range. After being sheared (Figure 7.10), IR sand within the shear band sustained a considerable amount of particle damage by abrading and crushing as indicated by the significant fraction of fines covering the coarser particles and the incipient fracture of one of the coarser particles in the foreground of Figure 7.10b. Similar to OT sand, the high magnification SEM photo (Figure 7.12b) illustrates that the very fine crushed IR sand particles are also platy to blocky. After washing (Figure 7.11 and Figure 7.12a), the sheared, coarse-grained IR sand particles are more angular and rough, and exhibit numerous abrasion scars, but very few incipient fractures. This suggests that the primary source of particle damage in the coarser particles may be attributed to shearing off the asperities resulting from shear-

induced torque applied to individual particles. The post-shear clay-sized particles (particle sizes of less than 5 microns in Figure 7.12b) are likely the result of abrasion of the coarse grains as well as the splitting of the fine particles present in the original sand or produced by abrasion. SEM photos of MR sand (Figure 7.13) illustrate that MR sand has angular to subangular particles distributed over a moderately wide range of particle sizes. After shearing, the particles became more angular, but there were considerably more fine-grained particles attached to the coarser particles. These finer particles appear to have been produced by abrading the asperities of the angular particles during shearing. Larger magnification photos (Figure 7.14) illustrate that the fine particles produced by shearing are generally blocky and tabular, consistent with the crystalline structure of albite (Klein and Dutrow 2007), the dominant mineral present in MR sand. After washing, the coarser particles (> 0.075 mm) shown in Figure 7.15 exhibited severe damage by fracturing and splitting, and numerous incipient fractures were observed. The mode of particle damage observed for MR sand (i.e., particle fracturing and splitting) differs from that observed for OT and IR sands (i.e., abrasion and shearing of asperities) likely as the result of weaker and relatively angular MR sand particles and its contractive fabric. As pointed in Table 2.1, angular particles are inherently more susceptible to splitting and are less influenced by a larger coordination number (Lee and Farhooman, 1967) which is because of the very small contact areas and thus very large contact stresses among the particles. Bolton et al. (2008) used DEM to simulate TxC tests and showed that contractive specimens generally experienced particle splitting (as observed for the MR specimens) while dilative specimens generally experienced asperity damage (as observed for the OT and IR specimens).

7.5 SIGNIFICANCE OF PARTICLE CRUSHING IN GEOTECHNICAL APPLICATIONS

Granular materials within natural slopes, large embankments, foundation subgrades, railroad ballasts, deep mine shafts and deep foundations, as well as in many other geotechnical engineering applications, such as in-situ penetrometer testing, vibratory compaction, and pile driving may experience shear and normal stresses large enough to become damaged (e.g., Mazzucato and Ricceri 1986; Randolph et al. 1994; Yasufuku and

Hyde 1995; Leung et al. 1996; Simonini 1996; Ohta et al. 2001; Lobo-Guerrero et al. 2006; Anderson and Fair 2008). For example, Miura (1985) studied the effect of particle crushing on the tip resistance of piles in sand and found that the tip resistance of piles in sand greatly depends on the extent of particle crushing below the pile tip to a depth of several times the pile diameter. Hattori et al. (1998) carried out plate loading tests on weathered granite in Hiroshima, Japan and observed severe particle crushing in the soil under the plate.

Particle damage increases compressibility, decreases hydraulic conductivity (k), changes the effective friction angle and stress-strain behavior, and leads to a nonlinear failure envelope (e.g., Vesic and Barksdale 1963; Bishop 1966; Lee and Seed 1967; Miura and Yamanouchi 1973; Terzaghi et al. 1996; Feda 2002; this study).

7.5.1 Effect of Particle Crushing on Hydraulic Conductivity

One of the most important effects of particle crushing is its influence on hydraulic conductivity. There are several empirical correlations relating grain size to hydraulic conductivity (e.g., Hazen 1892; Carman 1939; Kenney et al. 1984; Shepherd 1989; Alyamani and Sen 1993; Chapuis and Aubertin 2003), with Hazen's (1892) relation being one of the most widely used:

$$k = 100(D_{10})^2 \qquad 7.6$$

where k = hydraulic conductivity (cm/s) and D_{10} = grain diameter (cm) where 10% of the soil is finer than by weight. While the Hazen (1892) relation was developed using sands with D_{10} between 0.1 and 3.0 mm and coefficients of uniformity less than five, it provides a rough estimate of hydraulic conductivity for a wide range of sands at various void ratios (e.g., Terzaghi et al. 1996). Hazen's (1892) equation is employed here to illustrate changes in hydraulic conductivity before and after RS testing. Using Equation 7.6, pre-shear hydraulic conductivities of 0.176, 0.084, and 0.002 cm/s are computed for OT, IR, and MR sands, respectively.

Figure 7.16 illustrates changes in hydraulic conductivity computed using Equation 7.6 with respect to relative breakage index. As shown in Figure 7.16, hydraulic conductivity

within the shear band can drop to values as low as 10^{-6} cm/s, similar to that of kaolinite (Terzaghi et al 1996). Interestingly, although the relative breakage indices measured from constant volume tests were smaller than those measured from drained tests (see Figure 7.4), the hydraulic conductivities computed for the constant volume tests are smaller than those computed for the drained tests. This likely occurs because the relative breakage index does not account for the fine-grained portion of the sand. Note that the Hazen (1892) equation strictly does not apply to fine-grained materials, and therefore the computed hydraulic conductivities are crude, but the considerable silt and non-plastic clay fraction suggests that the hydraulic conductivities of the shear bands should be fairly small. Such small hydraulic conductivities would hinder the dissipation of any excess pore water pressure developed during earthquake shaking, pile driving, penetration testing, or landslides (e.g., Lee and Farhoomand 1967; Konrad 1998).

7.5.2 Effect of Particle Crushing on Stress-Strain-Strength Response

Under drained conditions, particle damage and crushing results in contraction within the shear band (even for initially dilative sands). However, under undrained or partially drained conditions, particle damage and crushing increases potential compressibility and causes accelerated pore pressure increase within the shear band, thereby reducing liquefaction resistance (Vaid et al. 1985; Sassa et al. 1996, 2005).

Stress-displacement responses for OT, IR, and MR sands, sheared under constant volume conditions are presented in Appendix B. Moist tamped specimens of OT and IR sands (Figs. B.4, B.18, B.31, and B.35) were prepared to high initial void ratios, resulting in initially contractive shear behavior. Particle damage and crushing in these specimens was not significant because of the substantial decrease in effective normal stress during shearing. This behavior is typical of very loose sands that experience flow liquefaction. In contrast, air pluviated specimens of OT and IR sands at their loosest possible void ratios dilated after small displacements. Dilation continued until the shear and normal stresses in the shear band became large enough to damage and fracture the particles. As particle damage increased, plastic volumetric strains increased sufficiently to overcome grain dilation and produce a net contraction. This process yielded a second phase transformation point. Net contraction continued until the effective normal stress became

small enough that particle damage (crushing and abrasion) essentially ceased and a critical state was reached. Similar behavior during landslides in dilative granular soils has been reported by Fleming et al. (1989). Sassa (1994) termed this behavior "sliding surface liquefaction" and used this concept to explain the rapid evolution of some earthquake-induced landslides into long runout debris flows. The shearing resistance in some dilative specimens reached values that would likely have arrested further deformation during landsliding. However, in the field, it seems likely that some local drainage may occur, therefore increasing pore water pressure and decreasing effective stress and if the drained shear resistance is insufficient to arrest the sliding mass momentum, particle damage and sliding surface liquefaction may ensue, leading to an undrained condition, considerable loss in shearing resistance, and long landslide runout.

In contrast to the OT and IR sands, both moist tamped and air pluviated specimens of MR sand (Figs. B.47 and B.58) contracted during shearing as a result of the contractive (softer) initial fabric of this silty sand and easier particle damage (i.e., splitting) during shearing. The tendency of these specimens to contract resulted in a decrease in the effective normal stress and in turn reduced the potential for further particle damage in constant volume tests.

Considerable particle crushing has been observed in some long runout landslides triggered by rapid water table rises from heavy rainfall or snow melt (e.g., Olivares 2001; Wang et al. 2002; Olivares et al. 2003; Leroueil 2003, 2004; Chu et al. 2003) or earthquakes (e.g., Sassa 1992, 1994, 2000; Sassa et al. 1996; Wang et al. 2002; Fukuoka et al. 2004; Sassa et al. 2005), yet there have been only limited field studies to find evidence of this phenomenon. For example, Sassa (2000) and Wang et al. (2002, 2003) describe the Hiegaesi landslide that was triggered by heavy rainfall in August 1988 in Otakura, Japan. The landslide occurred on a 25° slope and was relatively small (1200 m^3) and shallow (about 2.5m), but experienced a long runout of about 70 m. The low apparent friction angle of 11° and long runout suggested a flow-type failure. Sassa (2000) collected soil samples from the landslide mass and found that a distinct shear zone formed at the base of the sliding mass and the soil within the shear zone was finer than that immediately above the shear zone (Figure 7.17), supporting the fact that grain

crushing likely contributed to the long runout of this landslide despite the very low confining stress.

Direct and indirect evidence also suggests that particle damage and crushing played significant roles in several other landslides and rockslides (e.g., Cruden and Krahn 1978; Sassa 1984; Cruden and Hunger 1986; Ui et al. 1986; Fauque and Strecker 1988; Hewitt 1988; Yarnold 1993; Schneider and Fisher 1998; Glicken 1998; Davies et al. 1999). In some of these cases, shear zones developed at depths of up to 40 m (Sassa et al. 2005), potentially facilitating particle damage and crushing.

7.5.3 Effect of Particle Crushing on Volumetric Response

Figure 7.18 presents the vertical compression measured during three drained RS tests (APOTDR5, MTIRDR41, and APMRDR39) normalized by the pre-shear specimen height. During shearing, particle damage and crushing causes plastic volumetric deformations that are superimposed on those resulting from particle rearrangement induced by geometrical interference. At low stress levels (both normal and shear), volumetric response to shear (either contraction or dilation depending on initial state) is mostly controlled by particle sliding and rolling. However, at larger shear and normal stress levels, particle damage gradually occurs and increases as the specimen is sheared to larger shear displacements. Plastic volumetric strains resulting from particle damage can eventually yield net contractive behavior even in initially dilative specimens (e.g., APOTDR5). As crushing continues with increasing shear displacement, the grain size distribution widens and the local contact stresses among the particles decrease. In turn, as the contact stresses decrease the rate of particle damage reduces causing the grain size distribution and volumetric strains to stabilize.

A critical state is reached when grain crushing is essentially complete, such that there is no net volume change (i.e., local dilation is statistically balanced by local contraction). Lobo-Guerrero et al. (2006) reached a similar conclusion based on grain crushing observed in laboratory direct shear tests and DEM simulation.

7.6 SUMMARY AND CONCLUSIONS

Particle damage and grain rearrangement are the two primary mechanisms that cause plastic volumetric deformations in sands. Particle damage and crushing was observed in the shear band of the RS tests, while no particle damage occurred in the soil above the shear band. In contrast, no crushing was observed in parallel TxC tests. The following conclusions can be drawn based on the findings of this chapter.

1. The severity of particle damage was influenced by the grain size distribution, mineralogical composition, shear displacement, drainage conditions, soil fabric (induced by the specimen preparation method) and consolidation stress.
2. Particle damage and crushing during shear occurred at normal stresses as small as about 30 kPa and significantly increased the fines content without changing the maximum particle size of the sand. As damage continued with shear, the particle size distribution became wider (i.e., more well-graded). This process increased particle coordination numbers and reduced particle contact stresses, thereby reducing damage potential. An ultimate particle size distribution was approached at very large shear displacements when particle damage was essentially complete (likely corresponding to the critical state).
3. The primary mechanism of particle damage was a function of particle size and strength. Weaker or finer particles (with a lower coordination number), e.g., MR sand grains, tended to shatter and split under shear. In contrast, stronger and coarser particles (with a larger coordination number), e.g., OT and IR sand grains, tended to accumulate damage by shearing off of asperities and particle abrasion.
4. The post-shear grain shapes of the sands were more angular and slightly more roughened than the original sand grains. The very fine angular particles produced by particle damage during shearing surrounded and interlocked with the coarser, roughened angular particles, forming a fabric in which the matrix consisted of finer particles rather than the original coarser particles.
5. In constant volume RS tests on loose specimens, contraction occurred and reduced the effective confining (normal) stress. This occurrence limited the severity of particle damage and crushing. However, in constant volume tests on dense specimens, dilative response was observed (after a brief initial contractive response) until sufficient

particle damage and crushing occurred in the shear band to result in net contraction as the finer particles produced by particle damage and crushing tended to occupy available void space. Net contraction continued until the effective normal stress and shear stress decreased to a value below which particle damage ceased.

In drained tests on either loose or dense specimens at moderate to large consolidation stresses, specimens experienced considerable particle damage and crushing as a result of the increasing shear stresses applied to the specimen. The fine particles produced by particle damage and crushing occupied the available void space during shearing, resulting in net contraction. At small consolidation stresses, particle damage was limited primarily to abrasion. Thus, particle rearrangement initially controlled the soil response and dilation dominated until sufficient particle damage occurred to result in net contraction.

Particle damage and the resulting increase in fines content leads to increased soil contraction and increased liquefaction susceptibility if undrained conditions prevail. Furthermore, the increase in fines content decreases hydraulic conductivity in the shear band and may slow pore water pressure dissipation.

7.7 TABLES

Table 7.1: Initial breakage potential (B_{p0}), final breakage potential (B_{pf}), total breakage (B_t), and relative breakage (B_r) in the RS tests in this study

Test ID	Shear Displacement (cm)	B_{p0}	B_{pf}	B_t	B_r
MTOTDR2	3240	0.471	0.460	0.011	0.023
APOTDR5	2163	0.471	0.456	0.015	0.031
MTOTDR38(1)	2725	0.471	0.338	0.133	0.282
MTOTDR38(2)	853	0.471	0.455	0.016	0.036
APOTDR40	2544	0.471	0.317	0.154	0.327
APOTDR78	2783	0.471	0.319	0.152	0.322
APOTCV17	2680	0.471	0.346	0.125	0.265
MTOTCV21	2136	0.471	0.435	0.036	0.076
APOTCV24	3384	0.471	0.359	0.112	0.237
APOTCV29	5018	0.471	0.321	0.150	0.318
APOTCV52	2178	0.471	0.343	0.128	0.272
MTOTCV54	2903	0.471	0.408	0.063	0.133
APOTCV54	3031	0.471	0.312	0.159	0.337
MTOTCV63	2434	0.471	0.407	0.064	0.136
APOTCV82.5	2422	0.471	0.364	0.106	0.226
MTIRDR41	3371	0.592	0.440	0.152	0.256
MTIRDR54	2729	0.592	0.293	0.299	0.505
APIRDR71	2171	0.592	0.256	0.336	0.567
APIRDR85	2152	0.592	0.250	0.342	0.577
MTIRCV18	3553	0.592	0.526	0.066	0.111
APIRCV42	2406	0.592	0.488	0.104	0.175
MTIRCV75	2621	0.592	0.574	0.018	0.030
APIRCV81	2333	0.592	0.439	0.153	0.258
APIRCV82	2406	0.592	0.437	0.155	0.261
MTMRDR40	3696	0.037	0.026	0.010	0.282
APMRDR39	4400	0.037	0.024	0.013	0.353
APMRCV22	2700	0.037	0.034	0.003	0.081
APMRCV43	2519	0.037	0.029	0.008	0.211
MTMRCV49	2529	0.037	0.032	0.005	0.143

Table 7.2: Typical values for the initial breakage potential, B_{p0} (Gerolymos and Gazetas 2007)

Predominant grain size	Range of particle size (mm)	Typical range of B_{p0}
Fine-grained sand	0.125 – 0.250	0.0 – 0.5
Medium-grained sand	0.250 – 0.500	0.5 – 1.0
Coarse-grained sand	0.500 – 1.000	1.0 – 1.5
Fine-grained gravel	4 – 8	1.5 – 2.0
Medium-grained gravel	8 – 16	2.0 – 2.5
Coarse-grained gravel	16 – 32	2.5 – 3.0

7.8 FIGURES

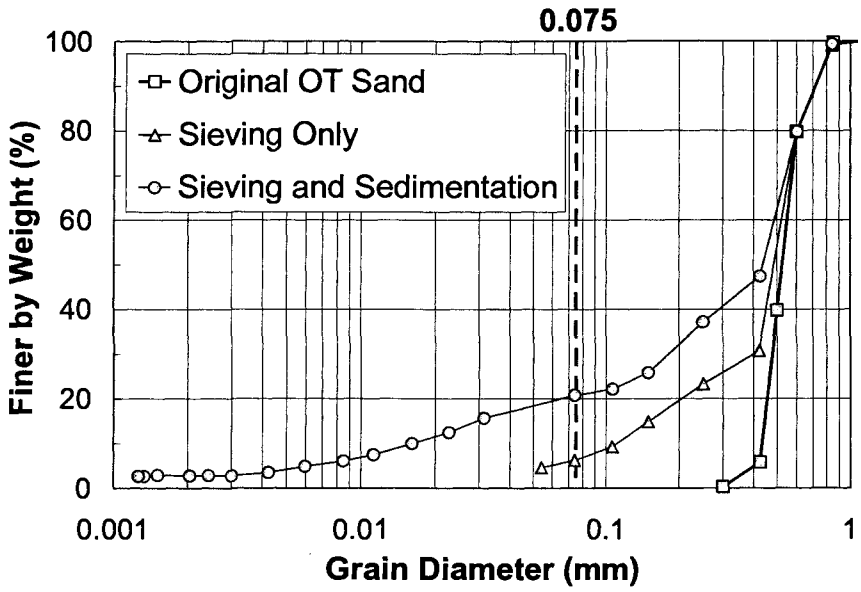

Figure 7.1: Grain size distributions of OT sand specimen (collected from the shear band of test APOTDR40) before and after shearing determined by sieving only (triangles) and by sedimentation and sieving (circles) according to ASTM D422-63.

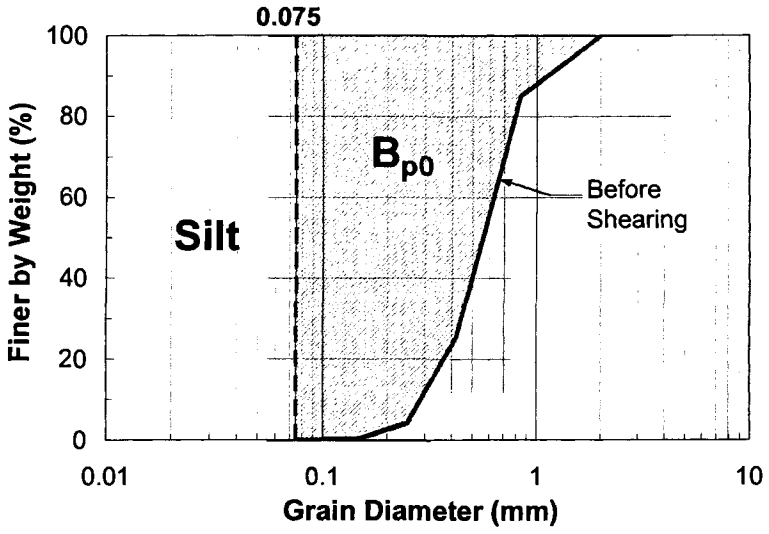

(a)

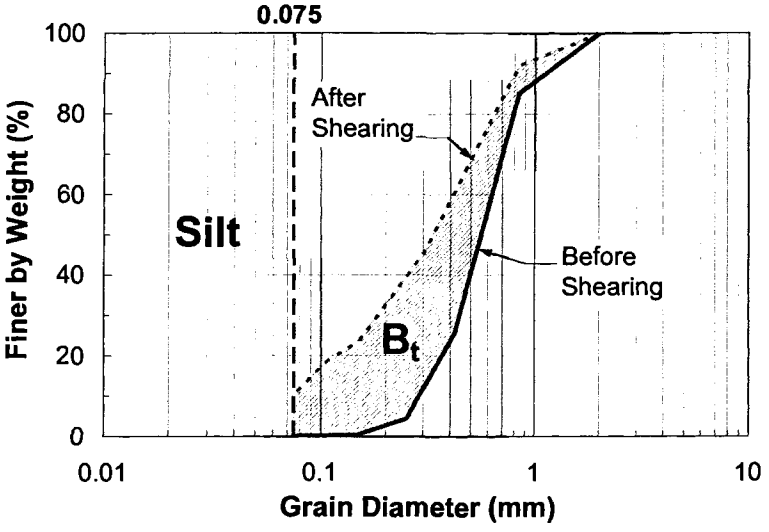

(b)

Figure 7.2: Definitions of (a) initial breakage index B_{p0}; and (b) total breakage B_t (after Hardin 1985)

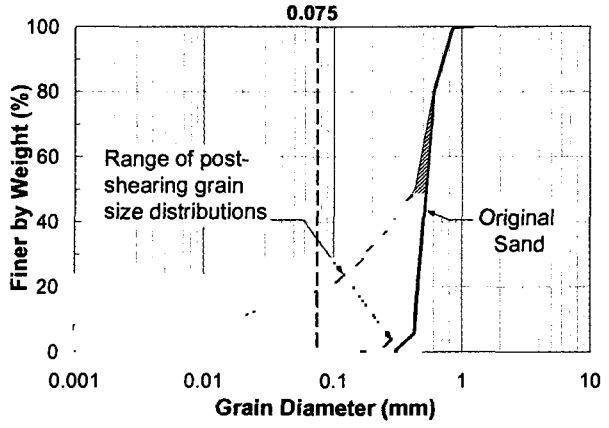

(a)

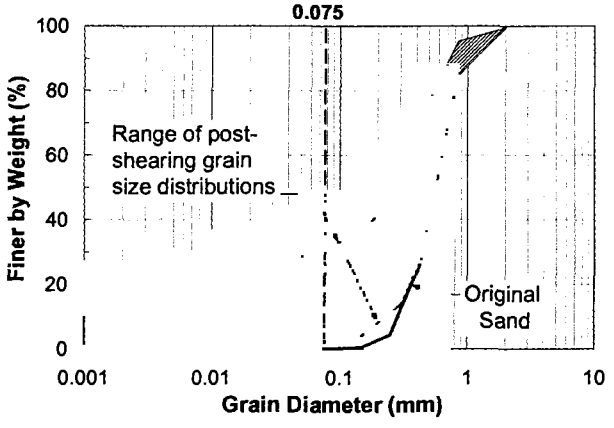

(b)

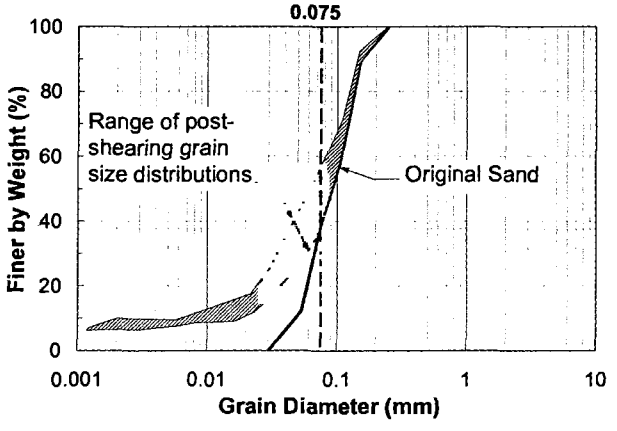

(c)

Figure 7.3: Range of grain size distributions before and after RS tests on (a) OT sand, (b) IR sand, and (c) MR sand.

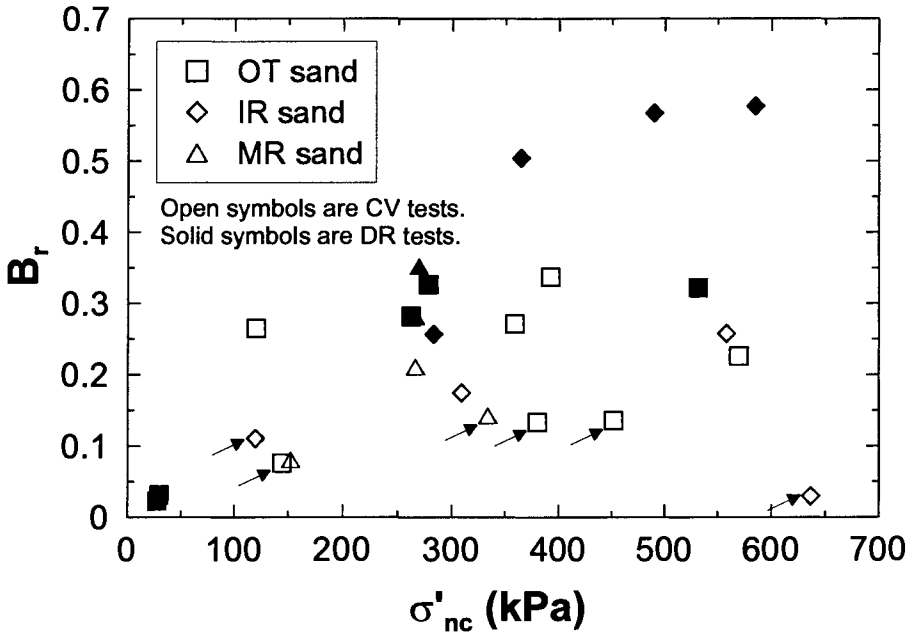

Figure 7.4: Relative breakage versus consolidation normal stress for RS specimens (CV = constant volume; DR = drained). The arrows indicate specimens prepared by moist tamping and sheared under constant volume conditions.

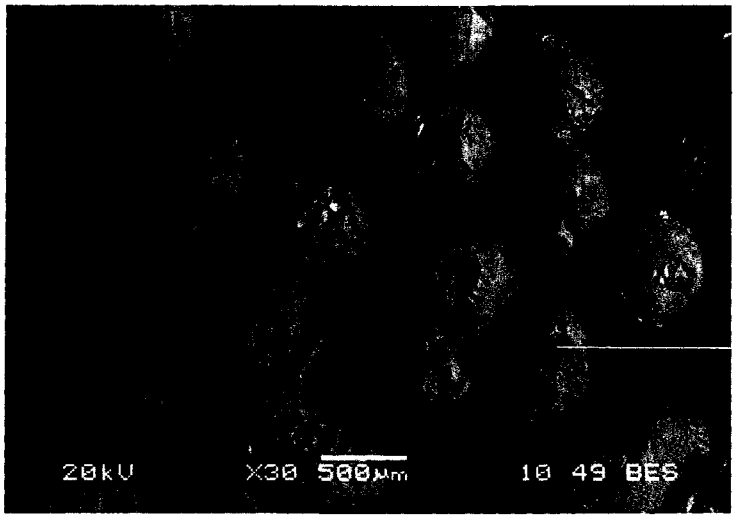

(a)

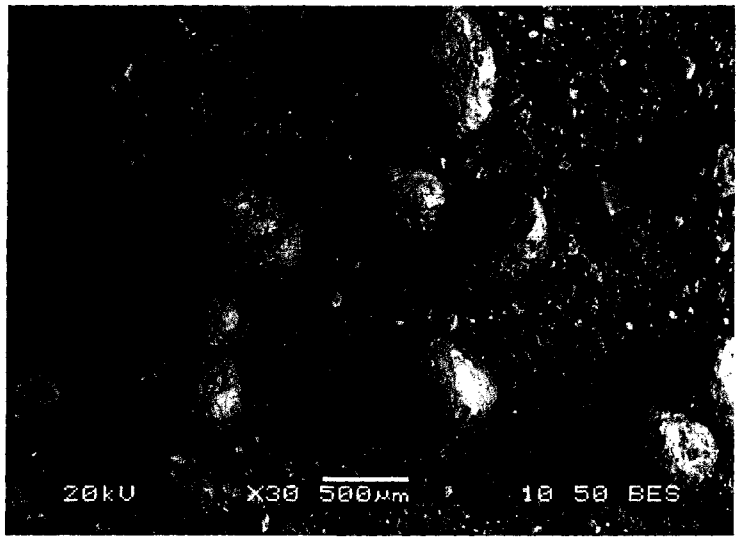

(b)

Figure 7.5: SEM photos of OT sand particles obtained from the shear band of RS test (MTOTDR40): (a) before (30x magnification), and (b) after (30x magnification) being sheared.

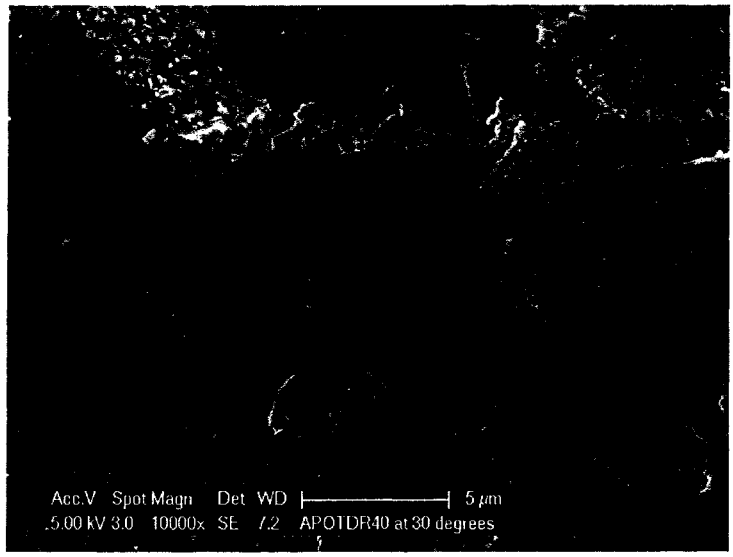

(a)

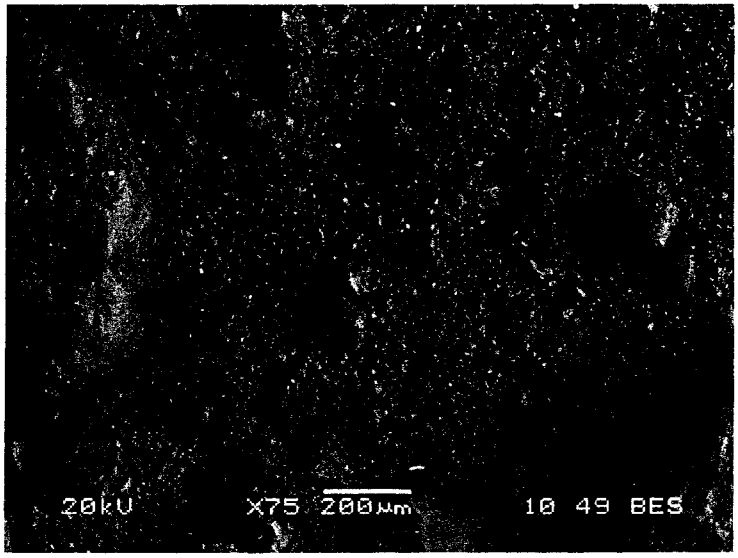

(b)

Figure 7.6: SEM photos of OT sand particles obtained from the shear band of RS test (MTOTDR40): (a) after (10000x magnification), and (b) after (75x magnification - after washing the fines) being sheared.

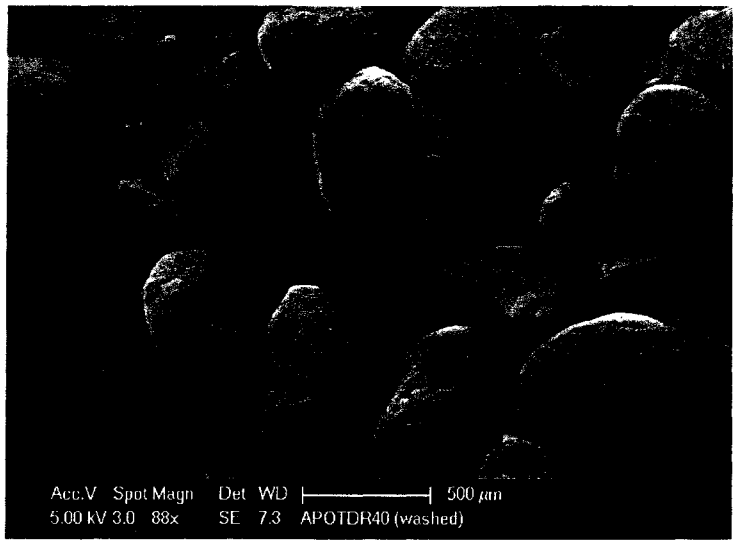

(a)

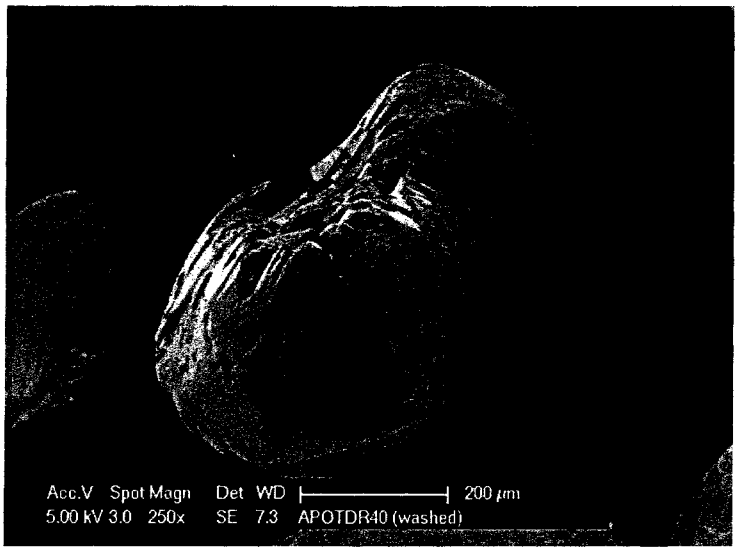

(b)

Figure 7.7: SEM photos of OT sand particles obtained from the shear band of RS test (MTOTDR40): (a) after (88x magnification - after washing the fines), and (b) after (250x magnification - after washing the fines) being sheared.

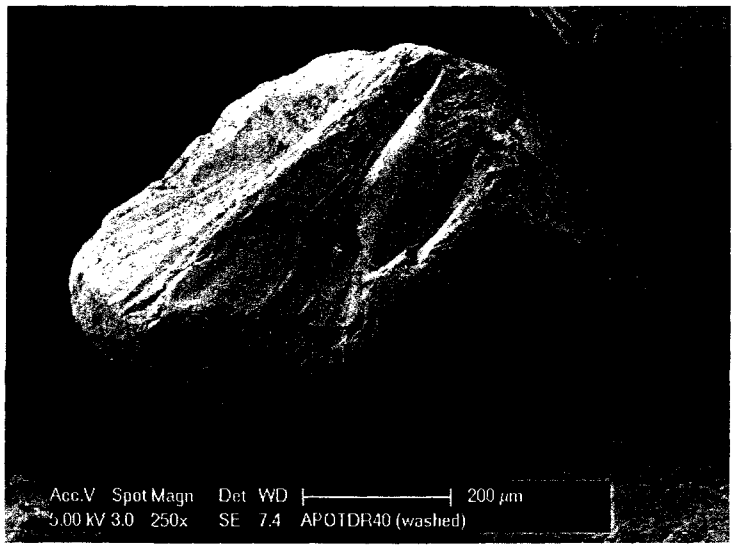

(a)

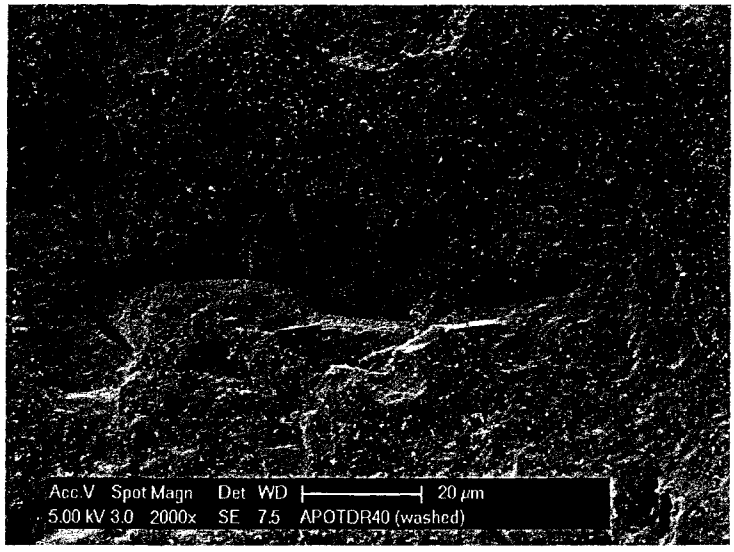

(b)

Figure 7.8: SEM photos of OT sand particles obtained from the shear band of RS test (MTOTDR40): (a) after (250x magnification - after washing the fines), and (b) after (2000x magnification - after washing the fines) being sheared.

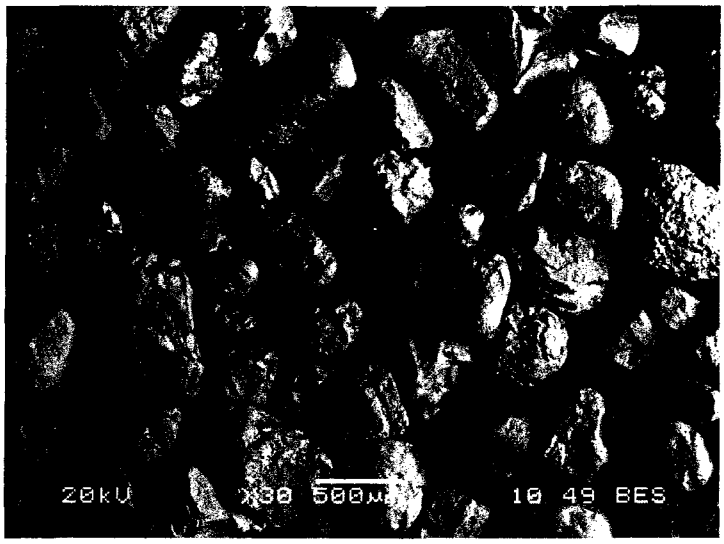

(a)

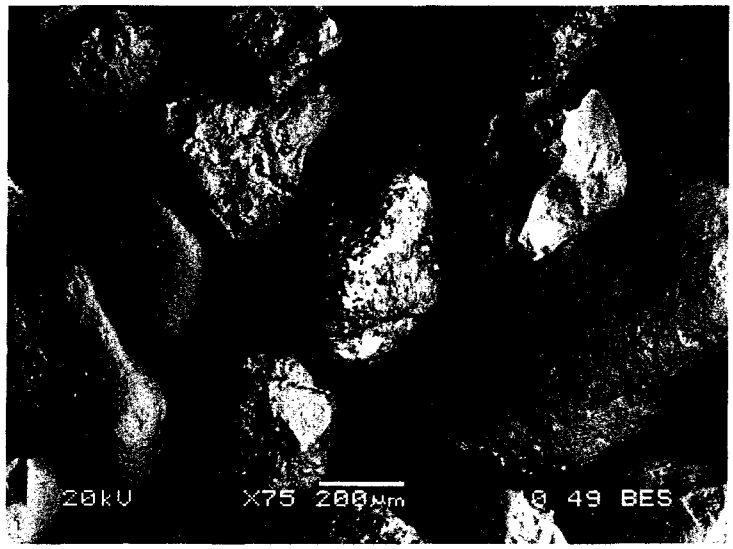

(b)

Figure 7.9: SEM photos of IR sand particles obtained from the shear band of RS test (MTIRDR41): (a) before (30x magnification), and (b) before (75x magnification) being sheared.

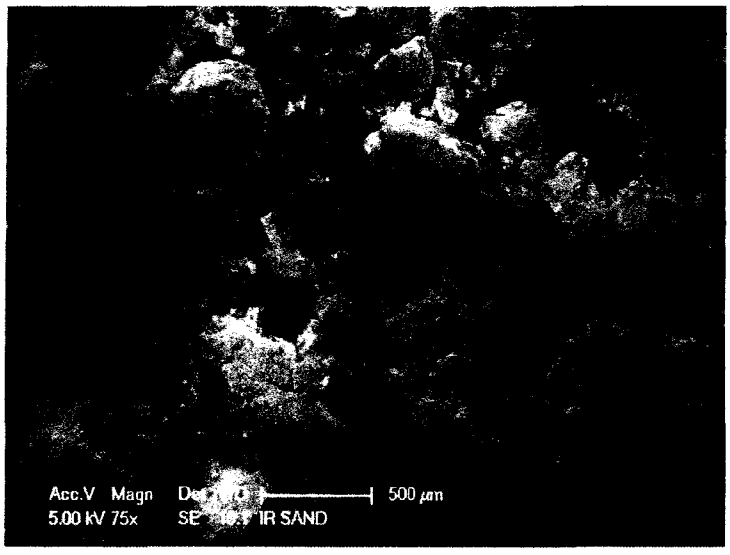

(a)

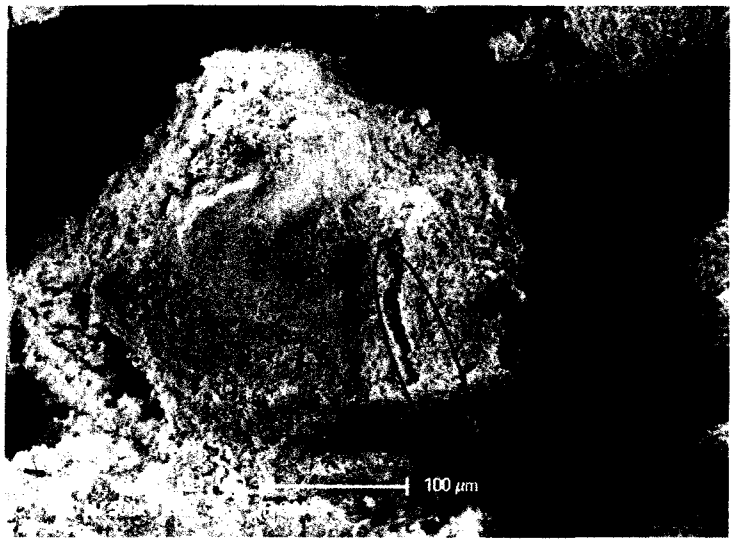

(b)

Figure 7.10: SEM photos of IR sand particles obtained from the shear band of RS test (MTIRDR41): (a) after (75x magnification), and (b) after (500x magnification) being sheared.

(a)

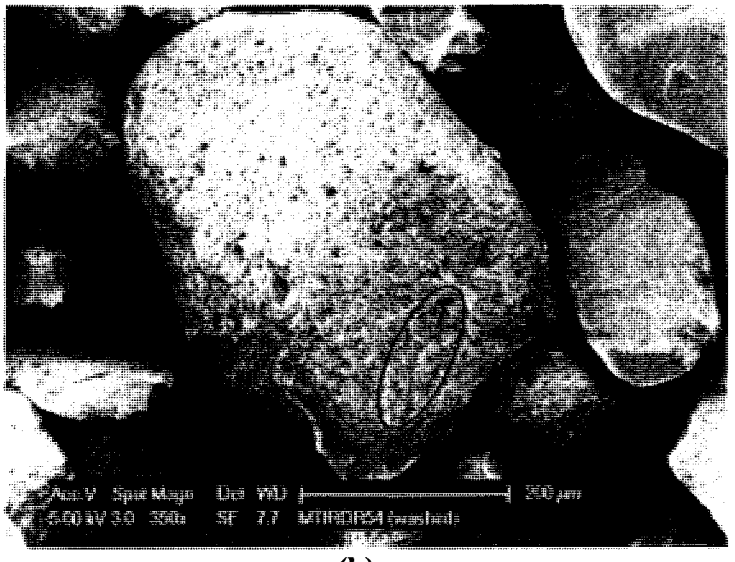

(b)

Figure 7.11: SEM photos of IR sand particles obtained from the shear band of RS test (MTIRDR41): (a) after (88x magnification - after washing the fines), and (b) after (350x magnification - after washing the fines) being sheared.

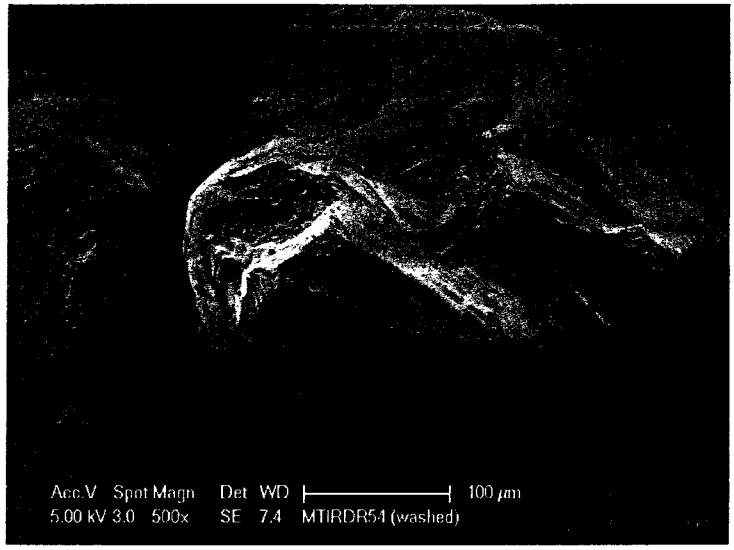

(a)

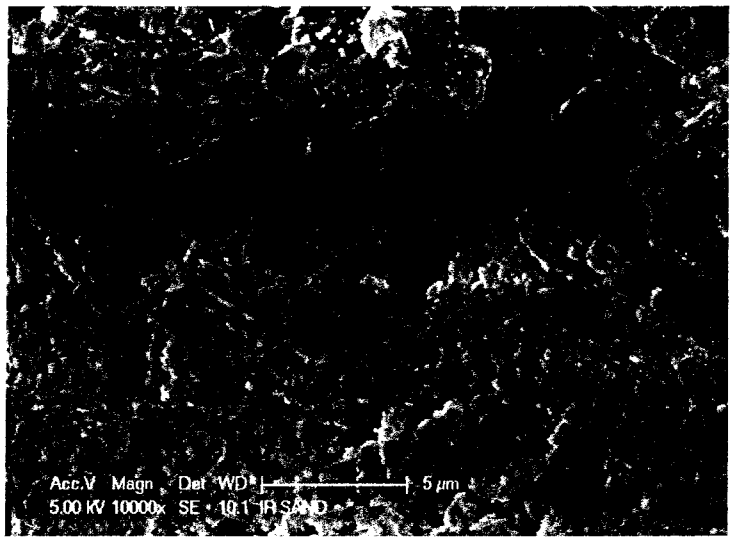

(b)

Figure 7.12: SEM photos of IR sand particles obtained from the shear band of RS test (MTIRDR41): (a) after (500x magnification - after washing the fines), and (b) after (10000x magnification) being sheared being sheared.

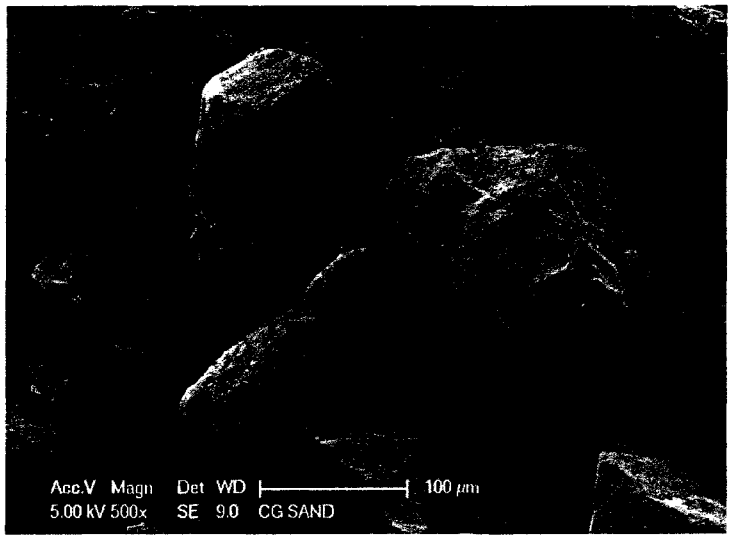

(a)

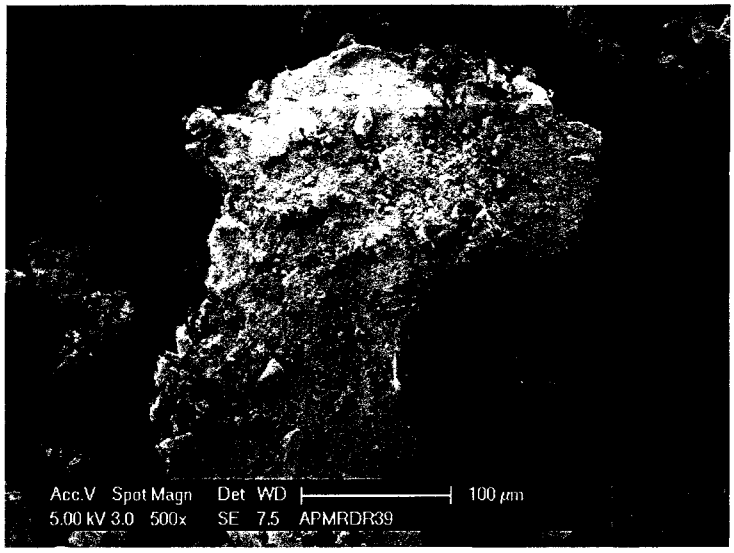

(b)

Figure 7.13: SEM photos of MR sand particles obtained from the shear band of RS test (APMRDR39): (a) before (500x magnification), and (b) after (500x magnification) being sheared.

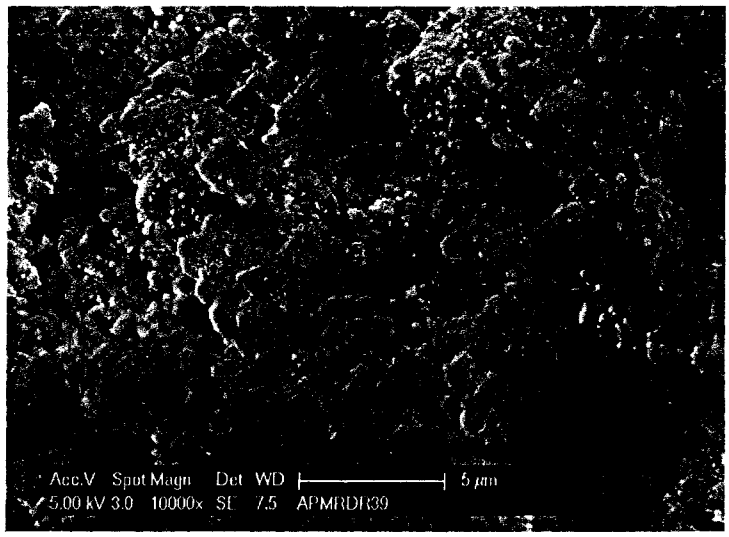

(a)

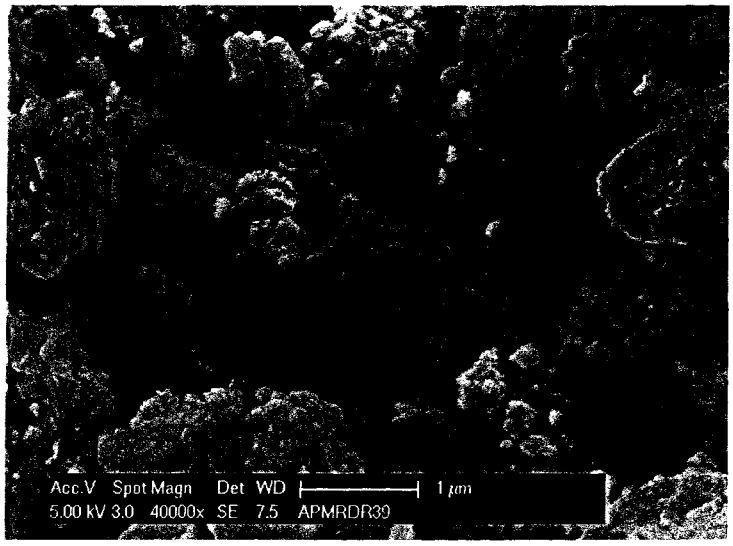

(b)

Figure 7.14: SEM photos of MR sand particles obtained from the shear band of RS test (APMRDR39): (a) after (10000x magnification), and (b) after (40000x magnification) being sheared.

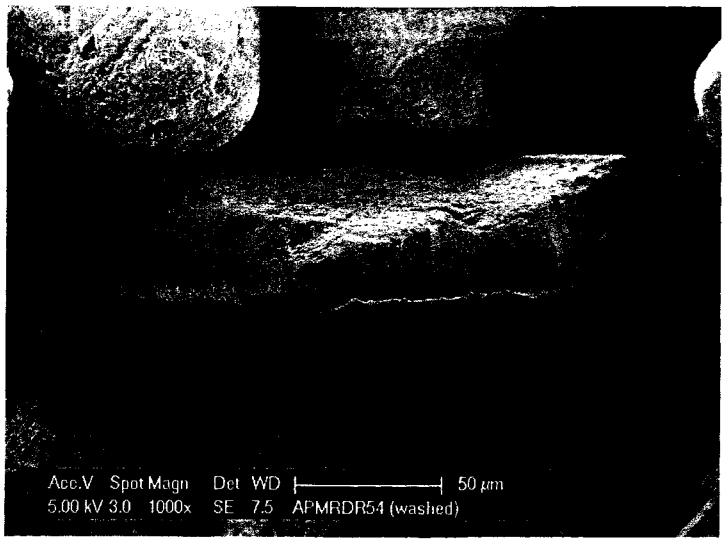

(a)

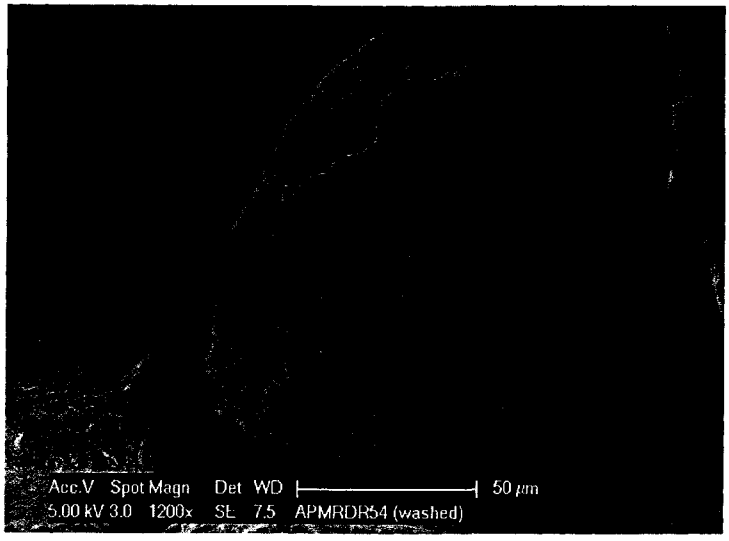

(b)

Figure 7.15: SEM photos of MR sand particles obtained from the shear band of RS test (APMRDR39): (a) after (1000x magnification - after washing the fines), and (b) after (1200x magnification - after washing the fines) being sheared.

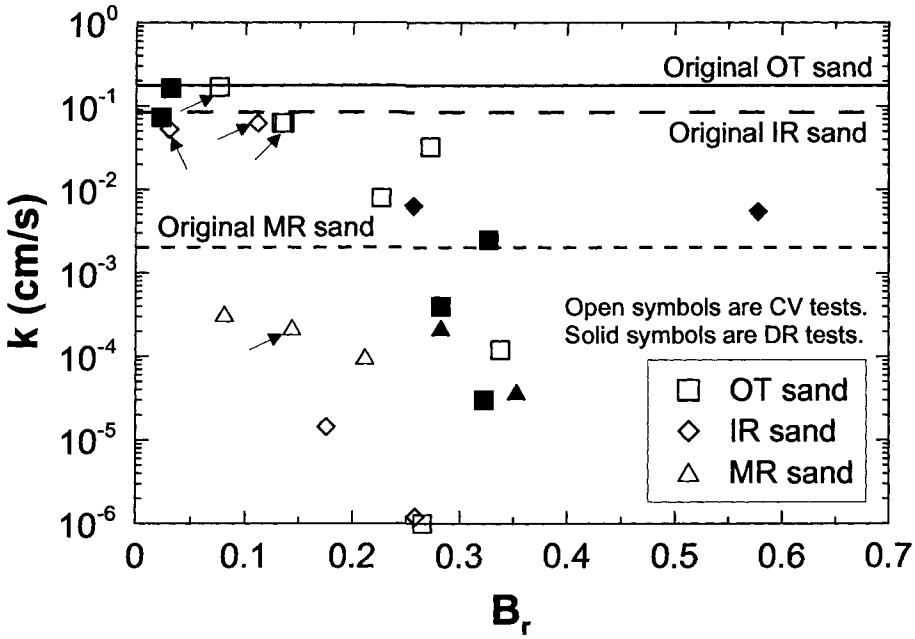

Figure 7.16: Change of hydraulic conductivity resulting from RS testing estimated using Equation 7.6 with respect to relative breakage index. Open and solid symbols are CV and DR tests, respectively. Similar to Figure 7.4, the arrows indicate specimens prepared by moist tamping and sheared under constant volume conditions.

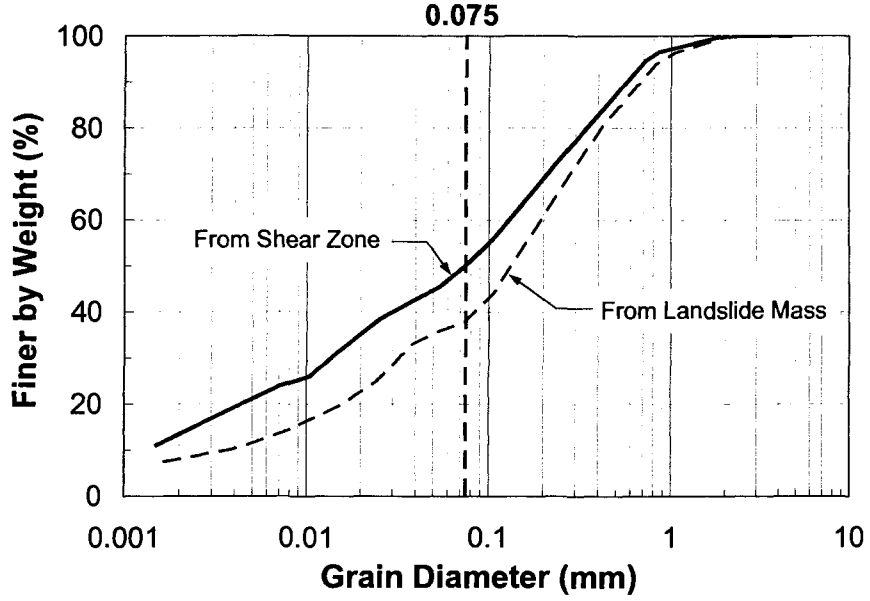

Figure 7.17: Grain size distribution of the soil samples collected from the sliding zone and the other areas of the Hiegaesi landslide mass (after Sassa 2000)

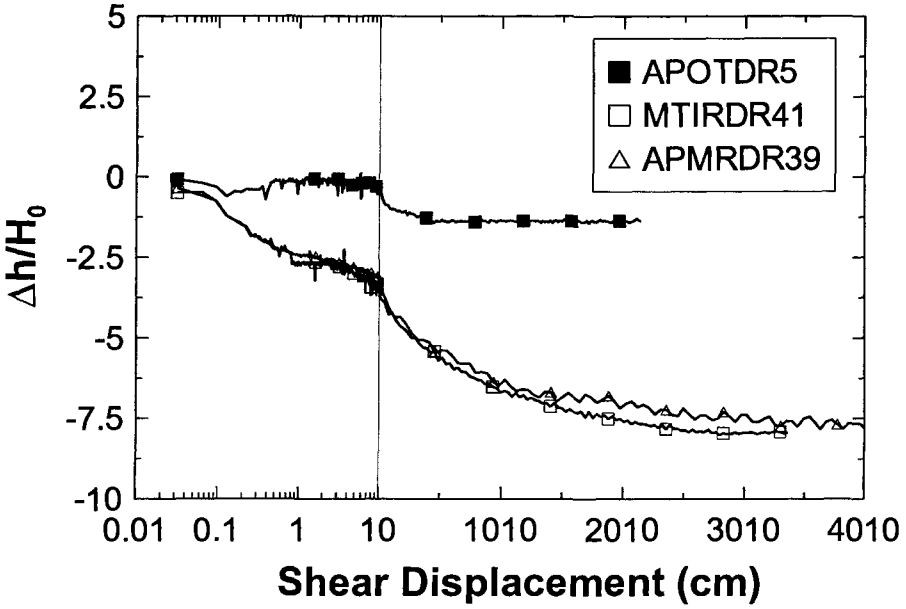

Figure 7.18: Volumetric strain measured during drained RS tests on OT, IR, and MR sands

CHAPTER 8: THE CRITICAL STATES OF SANDS

8.1 INTRODUCTION

Casagrande (1936) first observed that loose and dense sand specimens sheared under drained conditions achieved an essentially constant porosity and constant shearing resistance that was independent of the initial condition. The void ratio at this state was termed the "critical void ratio" by Taylor (1948). Roscoe et al. (1958) extended Casagrande's concept of critical void ratio to the critical void ratio state at which any further increment of shear deformation would not result in any void ratio change in a drained test or would not result in any change in effective stress and shear resistance in an undrained test. Later, Schofield (1980) performed a suite of drained triaxial compression (TxC) tests that reached failure at the same void ratio and observed that brittle, dilative shear failure occurred at low pressure but that the rate of dilation decreased as the mean effective stress increased up to a critical pressure.

Critical state soil mechanics (CSSM) combines Casagrande's concept of critical void ratio and Drucker et al. (1957) concept of plasticity to form a useful framework for modeling soil behavior. The central idea of CSSM is that the behavior of a sand deposit depends on a unique combination of its initial density and stress level. In sands, critical state typically occurs at large strains when the volume, pore water pressure, and shear and normal stresses remain constant. Casagrande (1975) hypothesized that at the critical void ratio state, the soil develops a "flow structure" where soil grains roll over each other with minimum resistance. Despite the possibility that void redistribution, pore water pressure migration and dissipation, and water layer formation may invalidate critical state concepts under some field conditions, CSSM provides a useful framework to interpret laboratory test results and field case histories, as well as to interpret the failure criteria and postfailure behavior of many constitutive models. Owing to its importance in interpreting liquefaction susceptibility of sandy soils, investigations of critical state have focused on loose sands and conclusions have generally been drawn from global results of triaxial compression (TxC) tests on loose sands (e.g., Poulos et al. 1985; Riemer and Seed 1992).

The ring shear (RS) apparatus was initially designed to investigate the residual shear resistance of clays (e.g., Bishop et al. 1971; Bromhead 1979); however, because of its ability to reach large shear displacements – a typical requirement for reaching the critical state – monotonically-loaded RS tests are used in this chapter to evaluate the critical state of sands. The results are compared with the critical states interpreted from monotonically-loaded TxC shear tests. Monotonic loading test results are relatively simple to understand and model and the large-displacement strength from both monotonically- and cyclically-loaded tests are similar (Ishihara 1993; Jefferies and Been 2006).

8.2 CRITICAL STATE LINES FOR ORIGINAL AND CRUSHED GRADATIONS

Figure 8.1 through Figure 8.3 illustrate the evolution of void ratio versus σ'_n for some of the RS and TxC tests performed on OT, IR, and MR sand specimens. Shear band void ratios (e_{sb} from Eq. 6.1) are used in plotting the RS results while total specimen (global) void ratios (e_{global}) are used for the TxC tests. For these plots, the σ'_n on the failure surface (σ'_{nf}) was used rather than the mean effective stress (σ'_{mean}) because the principal stresses are not controlled or measured in RS tests. In TxC, the shear and effective normal stresses for a theoretical failure plane at $(45 - \phi'_{cs,o}/2)$ with respect to the major principal stress direction can be computed readily as:

$$\sigma'_{nf} = \frac{1}{2}(\sigma'_1 + \sigma'_3) - \frac{1}{2}(\sigma'_1 - \sigma'_3)\sin\phi'_{cs,o} \qquad \textbf{8.1}$$

$$\tau_f = \frac{1}{2}(\sigma'_1 - \sigma'_3)\cos\phi'_{cs,o} \qquad \textbf{8.2}$$

where σ'_1 and σ'_3 are the major and minor effective principal stresses, respectively, and $\phi'_{cs,o}$ is the effective stress friction angle at critical state (or failure) of the uncrushed sand.

In Figure 8.1 through Figure 8.3, the numbers in the parentheses indicate the magnitude of shear displacements in centimeters. The limiting axial displacement of 2.5 cm for the TxC tests correspond to a shear displacement of about 2.8 cm on the failure plane oriented at an angle of $(45 - \phi'_{cs,o}/2)$ with respect to the major principal plane where $\phi'_{cs,o} = 28^{\circ}$, 29°, and 31° for the OT, IR, and MR sands, respectively (see Figure 9.5 in Chapter 9). In Figure 8.1, TxC specimen APOTUN54 dilated following an initial contraction until the specimen reached the device's loading capacity at an axial displacement of 1.4 cm (or 1.6 cm of shear displacement), while specimen MTOTUN52 contracted throughout shear until reaching the practical displacement capacity of the triaxial device (about 2.5 cm axial displacement or 2.8 cm shear displacement). In contrast, RS specimen APOTCV85 initially contracted and dilated similar to the TxC specimen, but then exhibited a second phase transformation to contractive response as a result of particle damage and crushing within the shear band. Specimen MTOTCV54 contracted throughout shear, and particle damage contributed substantially to this contractive response. Similar trends can be observed for the IR and MR sands in Figure 8.2 and Figure 8.3.

As discussed above, accumulated particle damage within the shear band in constant volume tests causes contraction and reduces σ'_n as displacement increases. Thus, it may be possible to construct hypothetical state lines that correspond to equal shear displacements. These hypothetical equal displacement state lines represent conditions of incomplete particle rearrangement and/or particle damage. As expected, some physical responses occur at similar levels of shear displacement, as summarized in Table 8.1. For example, the data in Figure 8.2 suggest that an equal displacement state line could be drawn through the points corresponding to shear band formation (at a shear displacement $\sim$ 0.53 cm). Similar equal displacement lines could be constructed for other displacements.

After sufficient shear displacement occurs (> 20 m in some specimens) to exhaust particle damage (as a result of the decreased interparticle stresses), the particle size distribution of the sand stabilizes and the soil reaches a large-displacement critical state line (CSL) for the crushed sand, termed the crushed sand critical state line (CSL_c), which represents the locus of critical states for the crushed sand (CS_c) gradation. It is noted that

the initially contractive specimens experience a greater rate of contraction and generally less particle damage (compared to the dilative specimens of each sand), and therefore reach this final state at smaller displacements.

Using the approach described above, Figure 8.4 through Figure 8.6 present all of the (e, σ'_n) data for ring shear tests and the (e, σ'_n) data for the contractive TxC specimens. Equal displacement state lines for several levels of shear displacements, as well as at the crushed sand critical state (CS_c) are drawn in the figures. The equal displacement state lines (of the form: $e = \Gamma - \lambda \log \sigma'_n$) become increasingly steeper as shear displacement and particle damage increase. Particle damage and crushing within the shear band creates fine angular grains and results in the steeper state lines (Castro 1969; Been and Jefferies 1985; Hird and Hassona 1990; Hagiwara et al. 1995; Kramer 1996). Furthermore, the more efficient particle packing resulting from the broader grain size distribution (i.e., increasing coefficient of uniformity, C_U) causes the state lines to shift downward in e – log σ'_n space, similar to observations by De Matos (1988) and Dawson et al. (1994). At very large shear displacements (> 10 m), the equal displacement lines converge and become roughly parallel. This implies that the specimen is reaching a constant volume state at which the rate of dilation and rate of particle damage approach zero and the particle size distribution stabilizes, eventually reaching the CSL_c. Note that although a very dense sand structure was formed in the shear band at very large displacements, the likely unrealistic small void ratios computed for the MR sand (Figure 8.6) could result from pronounced uncertainties involved in using Equation 6.1 to compute e_{sb} due to the very fine gradation and the corresponding thin shear band of the MR sand.

Reviewing the very loose moist tamped TxC specimens of OT and IR sands as well as the air pluviated TxC specimens of MR sands (i.e., specimens exhibiting a contractive response; see Appendix A), these specimens achieved critical state prior to the end of shearing (corresponding to shear displacements less than 2.8 cm). This critical state likely represents a state of complete particle rearrangement without significant particle crushing, or the critical state of the original sand gradation (CS_o), and the locus of the CS_o data is termed the CSL_o. The RS tests also likely reached a CS_o prior to considerable particle damage, but after shear band formation. As indicated in Table 8.1, shear band formation occurred at shear displacements of about 0.53 cm (or a shear strain

of about 20% based on the original specimen height) for all of the sands while particle damage and crushing became significant at shear displacements of about 6.0 cm in dilative specimens and about 30.0 cm in contractive specimens of both OT and IR sands. (Note that these shear displacements were determined visually during tests performed using the transparent outer ring, and therefore likely represent upper bounds for the initiation of particle damage.)

As a preliminary comparison, the state of the RS specimens at a shear displacement of 2.8 cm and the critical states from the contractive TxC results are plotted in Figure 8.4 through Figure 8.6 to evaluate the CSL_o. However, due to the rigid boundaries in the RS tests (as opposed to the flexible membrane in TxC tests) the intermediate principal stress (σ'_2) is larger in the RS tests than in the TxC tests, and thus, a smaller displacement would be required to reach the CS_o in the RS tests than in the TxC tests (Green 1971; Lade and Duncan 1973).

Therefore, soil state at shear band formation in RS tests would correspond to an upper bound for the CSL_o, and the soil state at 2.8 cm of shear displacement in RS tests would correspond to a lower bound CSL_o. At these small displacements, differences between the e_{global} and e_{sb} remain small (Figure 6.9) allowing direct comparison of the TxC and RS results using e_{global} of the original grain size distribution. In Figure 8.5 the RS state line at shear banding and at 2.8 cm (triaxial-equivalent shear displacement) for IR sand are nearly identical. For very loose specimens, complete particle rearrangement may occur shortly after shear banding at shear displacements much smaller than 2.8 cm. In contrast, the RS state lines at shear banding from OT and MR sands are parallel to and plot above the state line at 2.8 cm of shear displacement indicating a range of possible CSL_o locations. The coincidence for IR sand may be attributed to the smoother surface texture of the IR sand (compared to OT and MR sands) which requires less displacement to disengage particle interlocking and achieve complete particle rearrangement.

Figure 8.5 and Figure 8.6 also illustrate that the small shear displacement (about 0.53 - 2.8 cm) state lines derived from TxC and RS tests coincide for the IR and MR sands. This coincidence confirms the assertion by Poulos et al. (1985) that only small displacements are required to achieve complete particle rearrangement and a conventional critical state condition in some highly contractive sand specimens. Thus for these sands, the state line

at shear displacement of 2.8 cm could be reasonably assumed to represent the CSL_o. In contrast to IR and MR sands, the small displacement (i.e., 2.8 cm) state line of the OT sand obtained from TxC is parallel to but plots above the small-displacement state line obtained from RS tests. It is possible that this difference resulted because of the less compressible mineralogy and rougher surface textures (e.g. Mesri and Vardhanabhuti 2009) of OT sand particles that promoted larger σ'_2 on the solid lateral boundaries of RS apparatus (in comparison to the deformable membrane in the TxC shear device). This would cause a larger volumetric contraction and effective stress reduction during RS tests (e.g. Lade and Duncan 1973; Sayao and Vaid 1996). It is also possible (and perhaps likely) that the apparent critical state reached in the TxC tests on OT sand were only transient states of constant volume where a temporary balance was reached between volumetric compression arising from particle reorientation and rearrangement and volumetric dilation resulting from particles climbing over each other (e.g. Chandler 1985, Baharom and Stallebrass 1998, Coop et al. 2004, Lobo-Guerrero and Vallejo 2006). However, the lower state line (in $e - \log \sigma'_n$ space) from the RS tests suggests more complete particle rearrangement; therefore, this state line may represent the CSL_o of the OT sand. Note that scatter in the CSL_o likely results from the small differences between e_{sb} and e_{global} for some specimens even at small displacement, particularly for MR sand because of its very fine gradation and thin shear band, as well as the possibility of internal shear banding in the TxC tests.

To better illustrate the evolution of state lines with shear displacement, Figure 8.7 and Figure 8.8 present the variation of λ and Γ with shear displacement. Both λ and Γ (in all three sands) increase at a much larger rate after about 2.5 – 2.8 cm of shear displacement and this further confirms that CS_o was reached at about 2.8 cm of shear displacement in RS tests. The state line slopes (λ) of OT, IR and MR sands reach plateaus of approximately 0.18, 0.27, and 0.34 after 2100 cm, 250 cm and 50 cm of shear displacements, respectively. These values of λ are similar to those reported for clays [e.g., Speswhite kaolin clay has $\lambda = 0.25$ (Lawrence 1980)]. Because λ is chiefly influenced by particle angularity, the stabilization of λ implies that particle crushing is complete. However, Γ values for the OT, IR and MR sands essentially stabilize after larger shear displacements of 2100 cm, 1750 cm, and 750 cm, respectively. This implies that

additional shear displacement was required for particle reorientation and rearrangement to be complete after particle crushing ceased. The state lines reached after both λ and Γ stabilize represent CSL_c and satisfies all of the requirements of the critical state. The critical state after crushing reflects the mineralogy of the sands (e.g., MR sand vs. OT and IR sands) and is independent of drainage conditions and specimen preparation methods.

8.3 UNIQUENESS OF THE CRITICAL STATE LINE

Many researchers have questioned the uniqueness of the CSL as a result of the role of consolidation stress, stress path, particle crushing, sample preparation method, strain rate, and drainage conditions. These factors are discussed in the following sections with respect to the RS tests performed in this study.

8.3.1 Effect of Sample Preparation Method

Numerous researchers (e.g., Kuerbis and Vaid 1989; Vaid et al. 1990; Vaid and Sivathayalan 2000; Papadimitriou et al. 2005) have found that sample preparation methods (i.e., initial sand fabric) strongly influences the CSL, and some have found similar differences when comparing CSLs from reconstituted specimens and undisturbed samples (e.g., Castro and Troncoso 1989; Marcuson et al. 1990). In contrast, other researchers (e.g., Been et al. 1991; Ishihara 1993; Negussey and Islam 1994; Zlatovic and Ishihara 1997; Murthy et al. 2007) have shown that specimens prepared by slurry-deposition, moist tamping, and water pluviation have a unique CSL. In fact, Verdugo et al. (1995) proposed to divide the initial fabric of a soil into two groups: (1) fabrics that could be completely erased at large strains (attained in TxC); and (2) fabrics that could not be fully erased at large strains (again in TxC).

In the RS tests performed for this study, both moist tamped and air pluviated specimens yielded essentially unique CSLs for both the original sand gradation (CSL_o) and crushed sand (CSL_c). Thus, the differences observed from TxC testing can be explained by considering that the triaxial device is unable to impose shear displacements large enough to completely erase the initial fabric of reconstituted and natural sands that develop an anisotropic and nonhomogeneous structure with preferred particle arrangement and particle contact orientations during deposition (e.g., Oda 1972; Symes et

al. 1984; Mitchell 1993). In contrast, the RS can shear a soil to sufficient displacements to completely erase the initial soil fabric (as suggested by Poulos 1981), resulting in a unique CSL_o and CSL_c.

8.3.2 Effect of Drainage Conditions and Stress Path

The variation in drainage conditions is closely related to the stress path effect, since altering drainage conditions subjects samples to entirely different effective stress paths. Similar to what other researchers (e.g., Been et al. 1991; Riemer and Seed 1992; Sasitharan et al. 1993; Hagiwara et al. 1995; Li and Wang 1998; Been and Jefferies 2006; Murthy et al. 2007) have observed, the $e - \log \sigma'_n$ pairs from drained and undrained TxC (or RS) tests at the critical state of the original or crushed sands all yield a unique state line. Thus CSL_o and CSL_c appear to be independent of the drainage conditions for the sands tested here.

Separate but parallel drained and undrained CSLs were found by Finno and Rechenmacher (2003) in biaxial compression tests on angular masonry and concrete sands and by Santamarina and Cho (2001) in TxC tests on a very angular blasting sand. A larger amount of shear displacement may be required to reach a critical state in angular sands, and the tests reported by these researchers may not have reached the critical state.

8.3.3 Effect of Mode of Shearing

Numerous researchers (e.g., Miura and Toki 1982; Symes et al 1985; Shibuya and Hight 1987; Vaid et al. 1990; Riemer and Seed 1992; Negussey and Islam 1994; Vaid and Thomas 1995; Vaid et al. 1995) have shown that the stress-strain behavior of sands may differ significantly during undrained shearing, often with sands exhibiting dilative behavior during compression and contractive behavior in extension. Using hollow cylinder test results, Yoshimine and Ishihara (1998) and Yoshimine et al. (1998) suggested that the effective principal stress (major, minor, and intermediate) directions and magnitudes influenced the CSL. These differences typically led to CSLs interpreted from TxE tests being parallel to but below the CSL from TxC tests, suggesting that for a given void ratio the critical shear strength would be lower in extension than in compression. Furthermore, Riemer and Seed (1997) found that the critical strength in

simple shear was lower than that measured in both of the TxC and TxE, and attributed the differences to the different strain paths followed in the different tests. In contrast, other researchers (e.g., Castro et al. 1985; Poulos 1997; Infante-Sedano 1998; Jefferies and Been 2006) have suggested that the CSL from different modes of shearing would match. Particularly, Poulos (1997) and Jefferies and Been (2006) asserted that the differences between the CSLs from different modes of shear arise from the difficulty of maintaining a uniform specimen and not considering the void ratio within the shear band. The effect of mode of shear can be separated into (1) the effect of fabric anisotropy and principal stress orientations with respect to the anisotropic fabric (e.g. Ochiai and Lade 1983; Lam and Tatsuoka 1988; Lade and Kirkgard 2000; Abelev and Lade 2003, 2004; Lade and Abelev 2003; Lade 2006), and (2) the influence of σ'_2 (Kjellman 1936; Habib 1953; Broms and Casbarian 1965; Bishop 1966; Lade and Duncan 1973; Yamada and Ishihara 1979; Haruyama 1981; Sayao and Vaid 1996; Lade et al. 2008).

In the results presented in this study, similar CSL_o were obtained from the TxC and RS tests on IR and MR sands, suggesting that complete particle rearrangement and reorientation (i.e., zero dilation) was achieved for these sands. This further implies that the anisotropic fabric was destroyed at the critical state and thus critical state was independent of the orientation of the principal stresses. For OT sand, however, the results suggest that complete particle rearrangement may not have reached in the TxC tests, within its shear displacement capacity and σ'_2 may have caused larger volumetric contraction in the RS tests and thus different CSL_o from TxC and RS tests. The effect of mode of shear, and particularly the influence of σ'_2 on critical state behavior has been debated among several researchers (e.g. Cornforth 1964; Stroud 1971; Haruyama 1981; Lade 1984; Bolton 1986; Corfdir and Sulem 2008) and further research in this area would be useful in resolving this issue.

8.3.4 Effect of Consolidation Stress

Konrad (1990a) performed undrained TxC tests on an angular to subangular dune sand and found separate but parallel state lines (UF and LF lines) corresponding to different consolidation stresses. Riemer and Seed (1997) attributed the scatter in defining CSL from undrained TxC tests to the effect of the consolidation stress level. Yamamuro and

Lade (1998) found that CSLs from drained and undrained TxC tests on Nevada sand with 7% fines coincided at confining stresses between 200 and 1000 kPa, but at lower stresses, the two lines diverged.

The effect of consolidation stress on CSL appears to be related to its influence on the amount of particle damage and crushing. In the RS tests performed for this study, it was found that both CSL_o and CSL_c for the tested sands were independent of the applied consolidation stress over a wide range of consolidation stresses (28 – 708 kPa).

8.3.5 Effect of Rate of Shearing

To examine if the rate of shearing (i.e., imposed strain rate) influenced the RS results, as well as the comparison between RS and TxC results (performed at strain rates of 18.6 and 0.127 cm/min, respectively), the strain rate was varied during RS test MTOTCV54 after the specimen reached a critical state (at 2000 cm of shear displacement). Figure 8.9 presents the measured effective normal stress and shear stress at the shear band for a variety of strain rates (ranging from about 4 times slower to 6 times faster than the standard strain rate imposed for the tests in this study). These results indicate that the rate of shearing (in the range of 4.7 to 111.6 cm/min) did not influence the shear resistance and effective normal stress at the critical state, supporting the conclusion of Hungr and Morgenstern (1984) that the strain rate has no effect on the shearing response of granular materials. This also implies that load-controlled and displacement-controlled tests should yield similar critical state conditions (as found experimentally by Castro et al. 1982 and Been et al. 1991).

Furthermore, these results support the RS test results from other researchers (e.g., Novosad 1964; Schimming et al. 1966; Scarlett and Todd 1969; Savage 1982; Hungr and Morgenstern 1984; Lemos 1986; Negussey et al. 1988; Sassa 1984, 1985, 2000; Fukuoka 1991; Sassa et al. 1991; Tika et al. 1996; Infante-Sedano 1998) which indicate that the effect of rate of shearing on the large-displacement strength of granular soils is negligible.

8.3.6 Other Issues

8.3.6.1 Bilinear CSL

Numerous researchers (e.g., Lee and Seed 1967; Been et al. 1991; Verdugo and Ishihara 1996; Riemer and Seed 1997; Wang 1997; Konrad 1998; Jefferies and Been 2006) have suggested that the CSL may be curved, in part as the result of particle damage and crushing, and a bilinear CSL may be used to capture this curvature. In contrast to these results, the RS tests performed for this study suggest that the state lines (including the CSL_o and CSL_c) are straight in e – log σ'_n space, even when particle crushing occurs. The primary difference in these RS tests is that particle damage and crushing occurs within the shear band for both loose and dense sands at almost all magnitudes of consolidation stress, while in TxC, shear-induced particle damage commonly occurs only under very large consolidation stresses (greater than 1 MPa) within the range of the possible shear displacements in TxC tests.

8.3.6.2 Flow structure

Casagrande (1976) and Poulos (1981) speculated that a flow structure forms during shearing at the critical state. To examine this hypothesis, shearing was stopped and restarted in a few RS tests after reach CS_c. These stop-restart cycles resulted in no change in the specimen height and resulted in only a small peak shear resistance during the restart (probably due to inertial effects) prior to resuming shearing at the critical state. This implies that a flow structure does form at the CSL_c as originally elongated and newly-created, angular crushed particles become aligned along the direction of shear displacement at very large displacement magnitudes.

8.3.6.3 Phase transformation and quasi-critical state

The phase transformation (PT) is the state at which the sand response changes from contractive to dilative (Ishihara et al. 1975). Quasi-critical state (also termed quasi-steady state or pseudo-steady state) is the state at which the shear stress, reaches a local minimum during undrained shearing (Alarcon-Guzman et al. 1988) and is commonly observed in TxC tests performed on loose to medium dense specimens (Verdugo and

Ishihara 1996; Vaid and Sivathayalan 2000). Quasi-critical states measured in TxC tests commonly have been treated as the critical state, because the mobilized stress ratios that are observed during these responses are similar (e.g. Verdugo and Ishihara 1996; Vaid and Sivathayalan 2000) and this occasionally has resulted in the nonunique CSLs reported by various investigators (Jefferies and Been 2006).

Figure A.21 and Figure B.40 show phase transformation stress paths observed in TxC and RS tests on OT sand, respectively. Although TxC specimen MTOTUN103 was at a more contractive state than for example RS specimen MTOTCV87 (in terms of relative density and consolidation pressures), the TxC specimen dilated after an initial contraction and exhibited a quasi-critical state and phase transformation. On the other hand, both RS (APOTCV17) and TxC (APOTUN54) air pluviated specimens (Figure B.40 and Figure A.32, respectively) dilated after a phase transformation without any quasi-critical state.

Similar to RS tests MTOTCV87 and APOTCV17, quasi-critical state behavior was not observed in any of the RS tests. The behavior of very loose to medium dense sand was either completely contractive or exhibited a phase transformation without a quasi-critical state. Infante-Sedano (1998) observed the same behavior in his RS tests. These results suggest that the quasi-critical state could be an artifact of the triaxial boundary conditions, the area correction factor (Zhang and Garga 1997), specimen and shearing non-uniformity (Been et al. 1991; McRobertson and Sladen 1992; Thomson and Wong 2008), and volume change in an otherwise undrained test (Newland and Allely 1959). However, it is possible that the range of consolidation densities and pressures of the RS testing program was insufficient to observe a quasi-critical state. Because of its potential impact on interpreting and predicting field behavior, this subject requires further research.

8.4 IMPLICATIONS OF PARTICLE DAMAGE ON CRITICAL STATE

Depending on the field conditions and triggering mechanism(s), significant particle damage and crushing may develop during shearing. The implications of particle damage on critical state are summarized below.

8.4.1 Critical State without Significant Particle Crushing

This state is reached after particles are sufficiently reoriented and rearranged such that a state of constant shear stress, constant volume, and zero dilation is achieved. The behavior is manifested in conventional mass liquefaction behavior (i.e., flow liquefaction) where the contractive tendency of very loose soil triggers excess pore water pressure during undrained shearing. If the soil is very loose, grain crushing is not necessary to trigger flow liquefaction and the rapid generation of excess pore water pressure. The consequent rapid decrease of effective stress and shearing resistance precludes significant particle damage (Hutchinson 1986; Spence and Guymer 1997).

In the laboratory, the CSL of the original sand gradation (CSL_o) can be obtained at relatively small shear displacements (i.e., about 0.5 to 3 cm in the sands tested for this study) for very loose and compressible sand fabrics. In these cases, small-displacement apparatuses like triaxial, simple shear and direct shear devices may be able to achieve a critical state, as observed for the very loose specimens of moist tamped OT and IR sands or the more compressible fabric of air pluviated MR sand.

8.4.2 Critical State with Significant Particle Crushing

As discussed earlier in Chapter 7, particle damage and crushing can occur in loose to dense sands after shear band formation. Within a shear band, intense shear displacement causes particle abrasion and fracture in addition to particle reorientation and rearrangement. As particle damage occurs, excess pore water pressures develop within the shear band and can trigger "sliding surface liquefaction" (Sassa 1996, 2000; Sassa and Wang 2005) especially in initially dense soils. Particle damage within the shear band creates finer soil particles and widens the grain size distribution, steepening the CSL and moving it downward in $e - \log \sigma'$ space. As a result, significant additional shear displacement is required to exhaust particle damage (i.e., when the particle contact stresses become very low) and allow for particle reorientation and rearrangement within the evolving grain size distribution. In the laboratory, small displacement apparatuses like triaxial, simple shear and direct shear devices do not impose sufficient shear displacements to reach a critical state when particle damage occurs (Okada et al. 2000).

Only large displacement tests, such as RS, can impose sufficient displacement to achieve a critical state.

Numerous investigators have documented flow failures and debris flows in initially dense soils. The common factors among all of these failures are the sudden, long run-out of the sliding mass and the very flat post-failure slopes which suggest considerable loss of shearing resistance. In addition, considerable particle crushing has been observed in some long runout landslides triggered by rapid water table rises from heavy rainfall or snow melt (e.g., Olivares 2001; Wang et al. 2002; Olivares et al. 2003; Leroueil 2003, 2004; Chu et al. 2003) or earthquakes (e.g., Sassa 1992, 1994, 2000; Sassa et al. 1996; Wang et al. 2002; Fukuoka et al. 2004; Sassa et al. 2005).

8.5 SUMMARY AND CONCLUSIONS

The determination and overall validity of the critical state in sand is of considerable importance, as it provides the basis for failure criteria of many constitutive models and in general, is a useful framework to interpret laboratory tests and field observations. By far, the triaxial device has been most widely employed to study the critical state of sands. However, the limited displacement that the triaxial device is capable of imposing on a specimen often is insufficient to reach a critical state where the sand is continuously deforming at constant volume, constant normal effective stress, and constant shear stress. As a result, studies using the triaxial device have yielded contradictory conclusions regarding the uniqueness of CSL and the role of various factors such as soil fabric, stress path, mode of shear, and consolidation stress (among others) on the CSL.

The results of the RS tests demonstrate that shear band formation and particle damage play an important role in the contractive response of sands, and suggest two types of critical states. The CSL_o (CSL of the original sand gradation without crushing) is achieved through particle reorientation/rearrangement. In this case, liquefaction and undrained post-peak strain-softening leading to the critical state occurs only in very loose contractive sands and can be achieved at small shear displacements (about 0.5 to 3 cm in this study) (within the capacity of nearly all laboratory testing devices, including the triaxial and simple shear devices). In contrast, the CSL_c (CSL including particle damage and crushing) involves shear band formation and particle damage/crushing within the

shear band (i.e., "sliding surface" liquefaction). In this case, very large displacements (on the order of meters) are required to reach a critical state and this level of shear displacement in laboratory element tests can only be achieved using a RS device. Furthermore, particle damage and crushing results in markedly contractive behavior, and even dense sands that experience crushing respond by contracting and strain-softening to a final critical state. The CSL_c reflects the mineralogy of the sands and is independent of the drainage conditions, specimen preparation methods, consolidation stress, fabric, and strain rate. However, whether the intermediate principal stress influences the critical state is not clear and requires further research.

8.6 TABLES

Table 8.1: Range of shear displacements corresponding to peak resistance, first phase transformation, shear banding, second phase transformation, and critical state of crushed sand.

Sand	Mode of shear	Shear displacement range corresponding to particular physical response (cm)				
		Peak resistance (1)	1st PT (2)	Shear band formation	2nd PT (2)	Crushed critical state
OT	TxC	0.07(0.6%) – 0.25 (2.2%)	0.29(2.7%) – 0.97(9%)	n/a	n/a	n/a
	RS	0.06 – 0.16	0.10 – 0.32	0.53	0.60 – 1.36	120 - 220
IR	TxC	0.07(0.7%) – 0.13 (1.2%)	0.33(3%) – 0.54(5%)	n/a	n/a	n/a
	RS	0.09 – 0.19	0.10 – 0.35	0.53	0.73 – 1.31	700 - 2000
MR	TxC	0.05(0.5%) – 0.09 (0.8%)	0.54(5%) – 0.76(7%)	n/a	n/a	n/a
	RS	0.06 – 0.51	n/a	0.53	n/a	350 - 1200

(1) Contractive specimens only; numbers in parentheses are axial strains in TxC
(2) Dilative specimens only

8.7 FIGURES

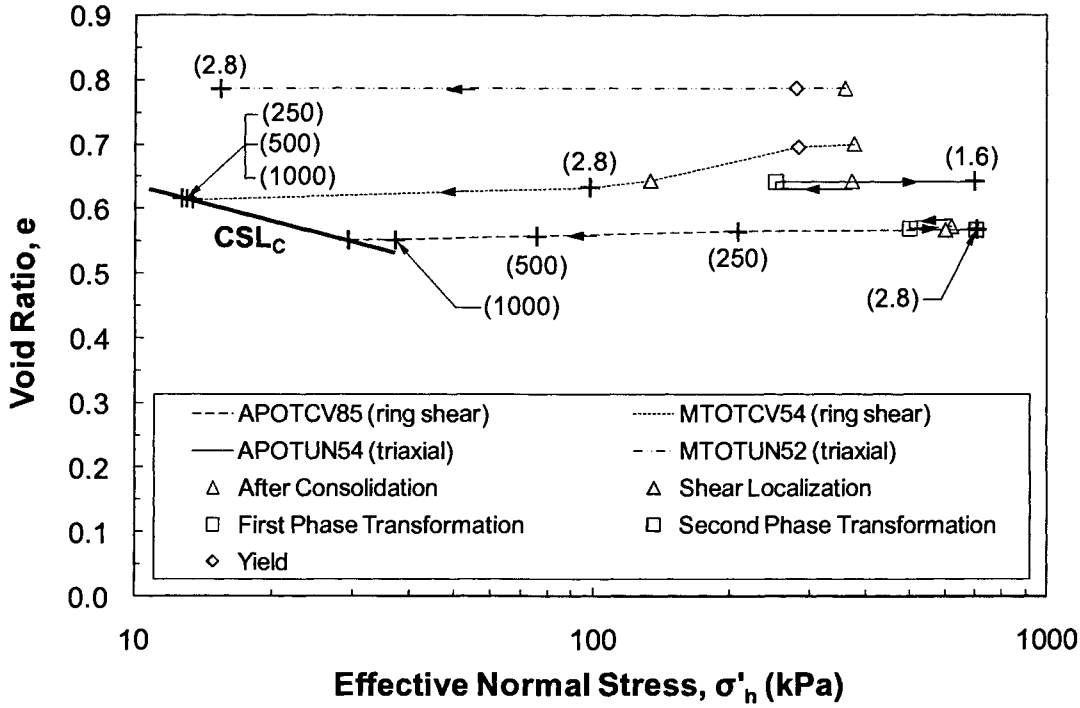

Figure 8.1: Void ratio – σ'_n responses in RS tests on OT sand (numbers in parentheses are shear displacements in centimeters)

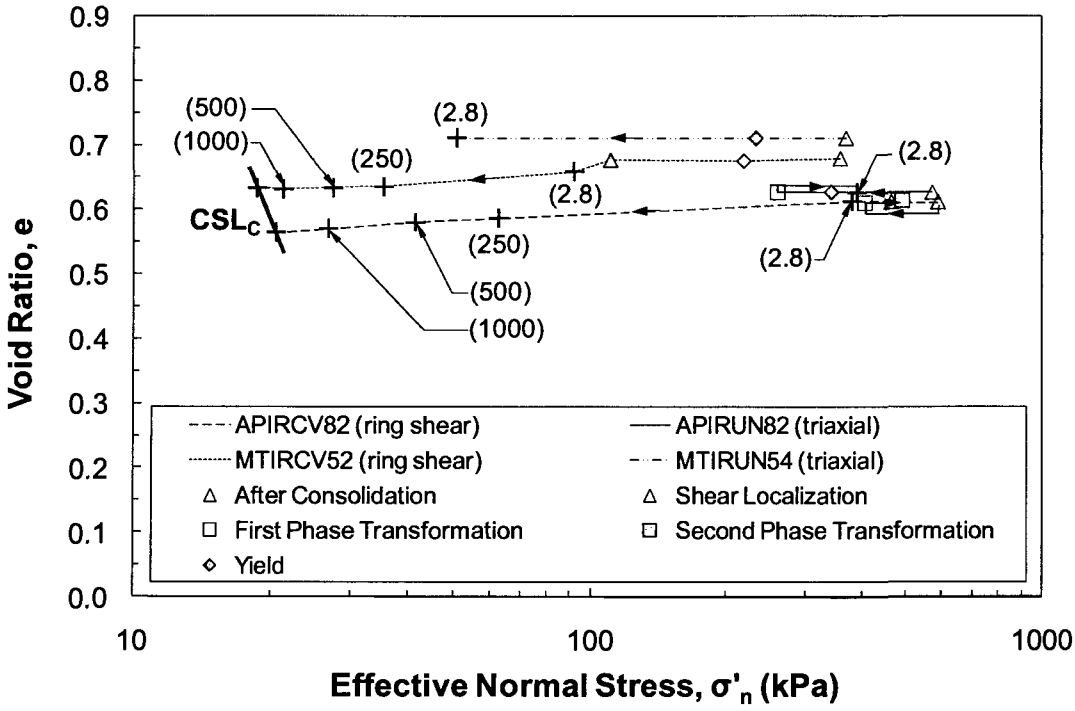

Figure 8.2: Void ratio – σ'_n responses in RS tests on IR sand (numbers in parentheses are shear displacements in centimeters)

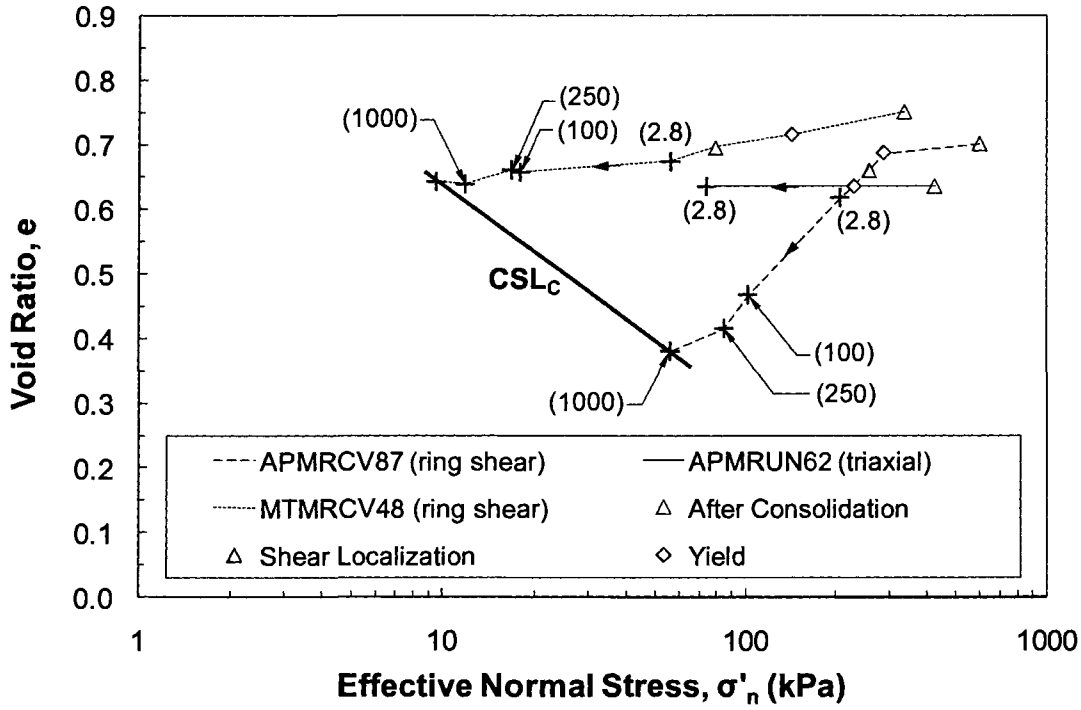

Figure 8.3: Void ratio – σ'_n responses in RS tests on MR sand (numbers in parentheses are shear displacements in centimeters)

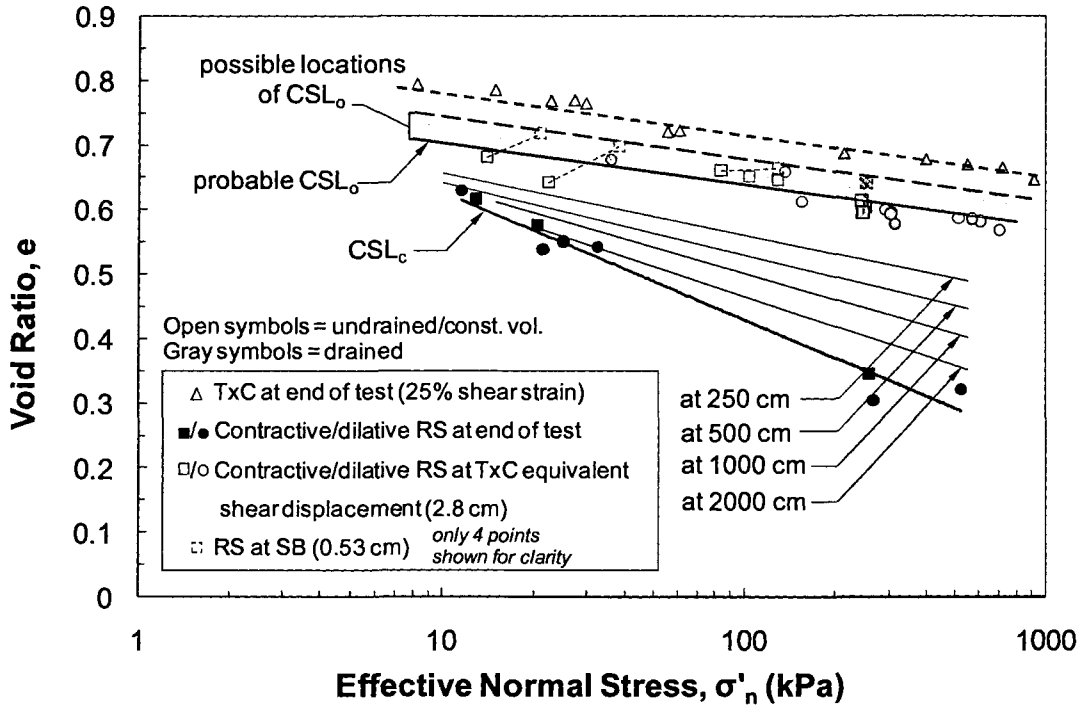

Figure 8.4: State lines from TxC (at shear displacement of 2.8 cm) and RS (at shear displacements of 0.53, 2.8, 250, 500, 1000, 2000, and 3000 cm) tests on OT sand. e_{global} and e_{sb} are used for the TxC and RS tests, respectively.

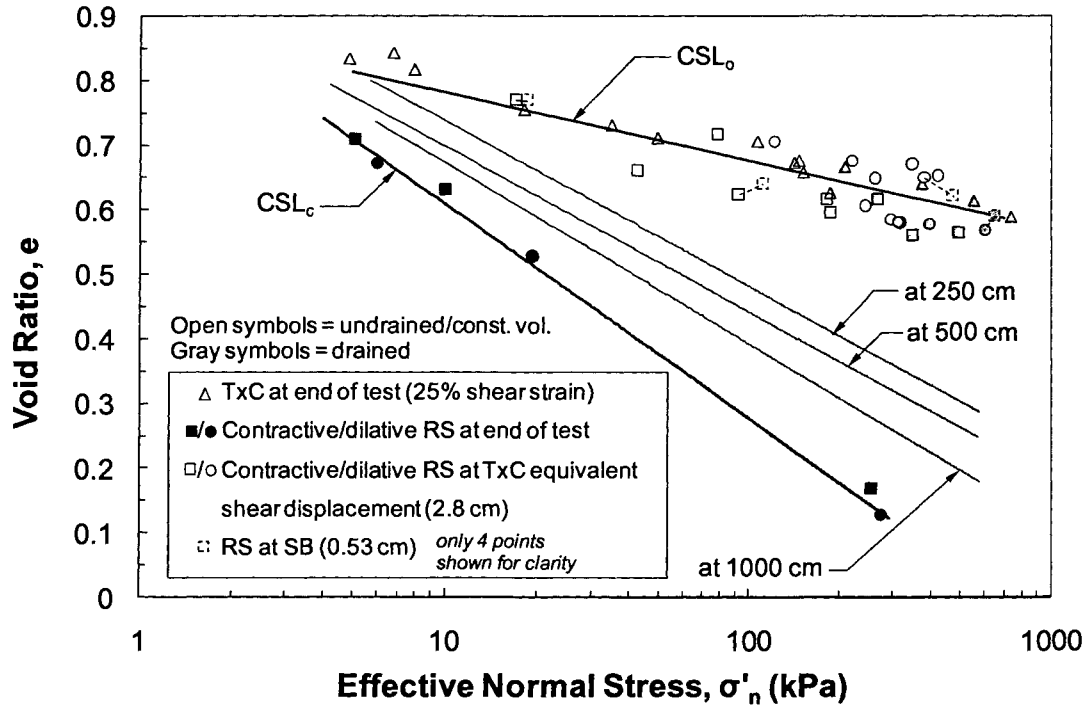

Figure 8.5: State lines from TxC (at shear displacement of 2.8 cm) and RS (at shear displacements of 0.53, 2.8, 250, 500, 1000, and 3000 cm) tests on IR sand. e_{global} and e_{sb} are used for the TxC and RS tests, respectively.

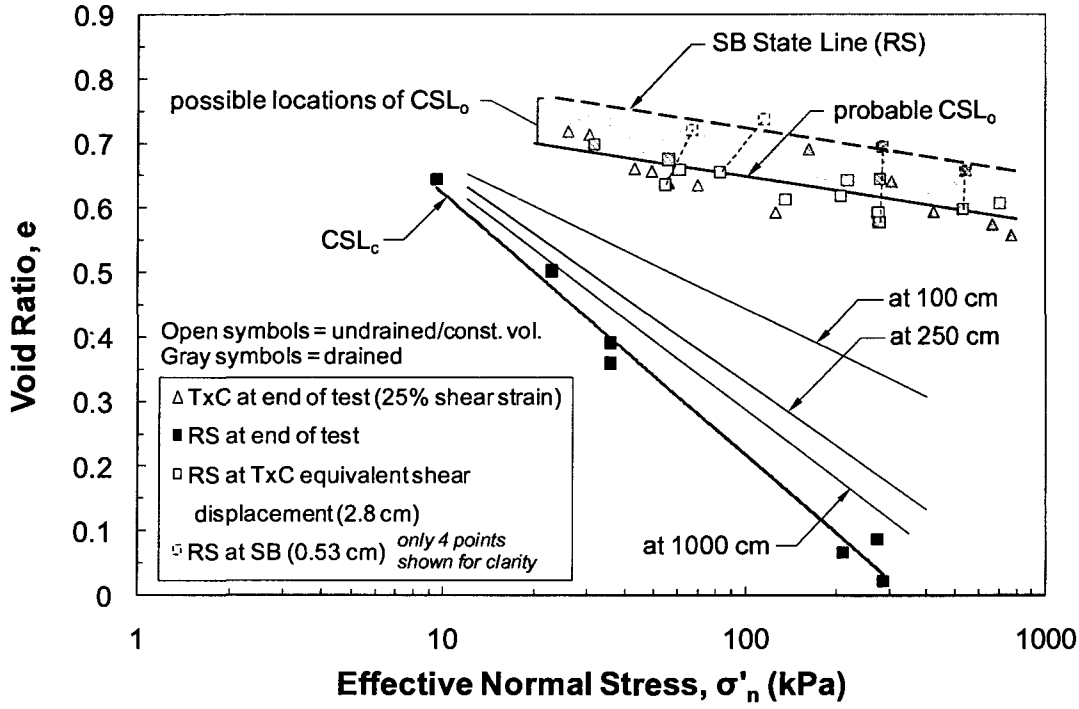

Figure 8.6: State lines from TxC (at shear displacement of 2.8 cm) and RS (at shear displacements of 0.53, 2.8, 100, 250, 1000, and 3000 cm) tests on MR sand. e_{global} and e_{sb} are used for the TxC and RS tests, respectively. (Note that the unrealistically small void ratios (< 0.1) could have been affected by the more pronounced uncertainties involved in using Equation 6.1 due to the very fine gradation and thin shear band of MR sand.)

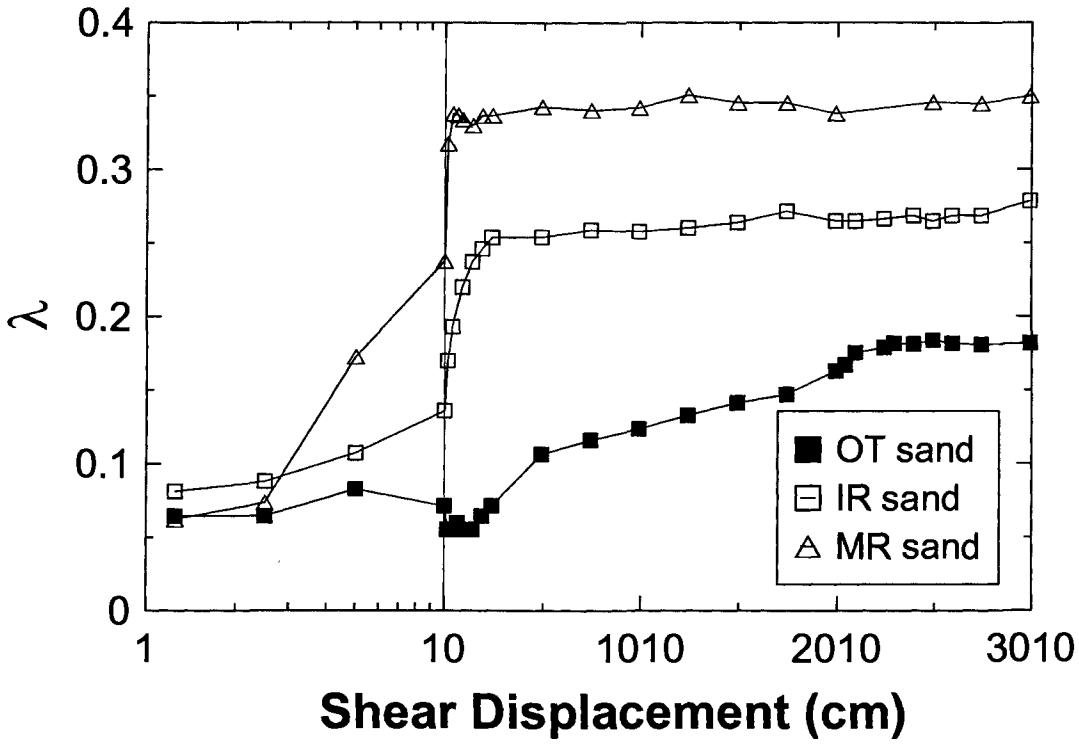

Figure 8.7: Evolution of slope (λ) of the state lines with shear displacement during RS tests

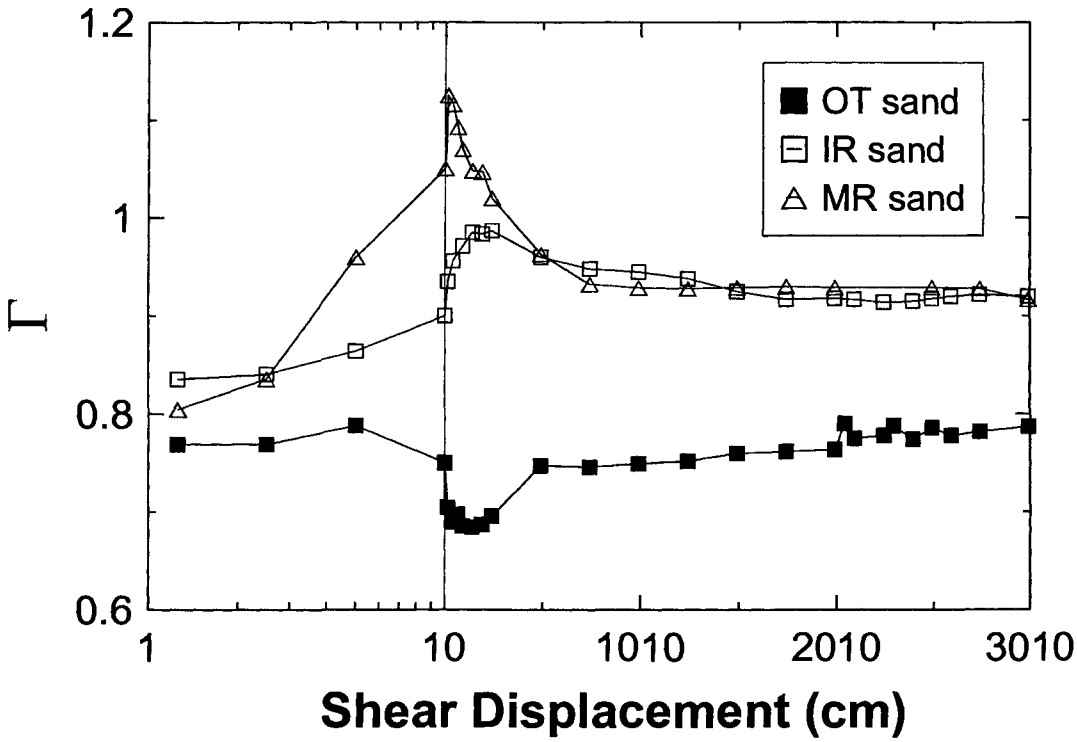

Figure 8.8: Evolution of the intercept (Γ) of the state lines with shear displacement during RS tests

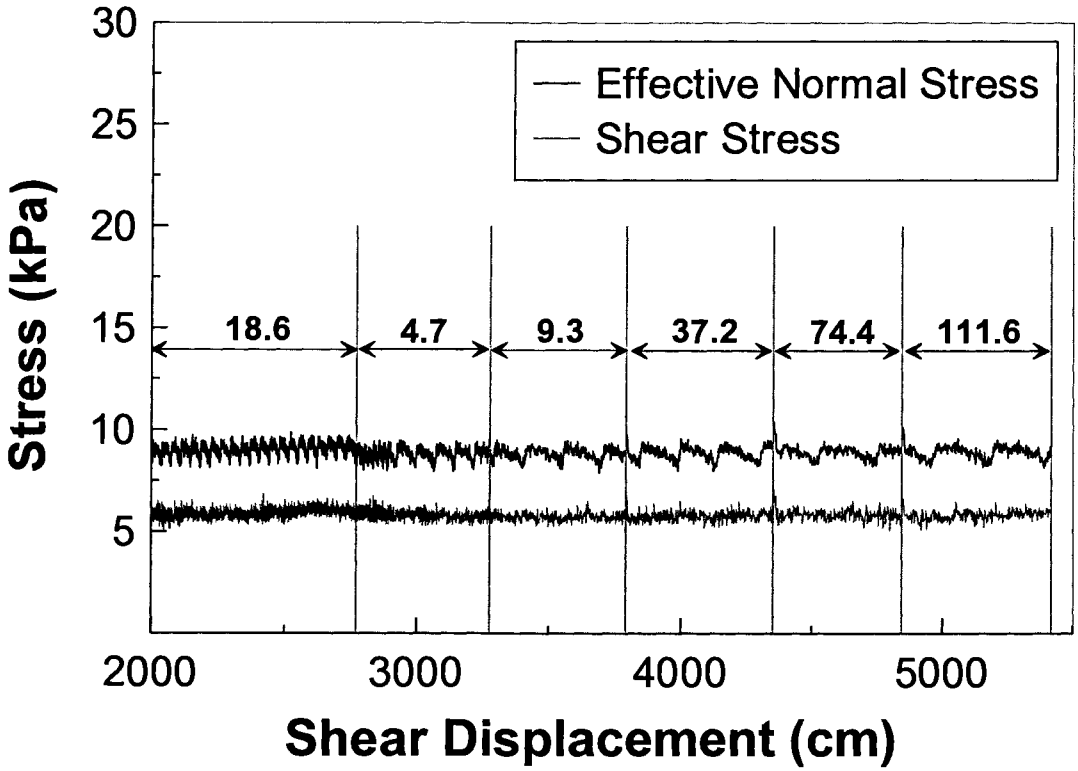

Figure 8.9: Effect of rate of shearing on the critical state stresses in RS test MTOTCV54. (The numbers between the displacement intervals indicate the shearing rate in cm/min.)

CHAPTER 9: FRICTION ANGLE OF SANDS

9.1 INTRODUCTION

Granular soils mobilize shear resistance through interparticle sliding friction and geometrical interference among particles (Taylor 1948; Rowe 1962; Lee and Seed 1967; Terzaghi et al. 1996). Interparticle sliding friction is the friction mobilized via sliding of one particle against the surface of another particle and is characterized by the interparticle friction angle (ϕ'_μ). The interparticle friction angle is essentially a material constant independent of confining pressure and density (Rowe 1962; Lee and Seed 1967), and ranges from approximately 20° to 40° depending on the surface roughness of the particles. This roughness is related to the strength, texture, and hardness of the particle surface, which in turn are determined by the crystal structure of the minerals and intercrystalline bonding (Terzaghi et al. 1996). Surface roughnesses that influence interparticle friction commonly have a smaller amplitude than those constituting particle angularity (Barrett 1980). Consistent and reproducible measurements of ϕ'_μ are difficult to achieve, thus use of this parameter in practice is virtually nonexistent (Negussey et al. 1988), but Table 9.1 presents values of ϕ'_μ measured for some common minerals.

In addition to interparticle sliding friction, an assemblage of particles subjected to shear stress mobilizes shear resistance by particles pushing against, climbing over, and damaging (i.e., abrading, fracturing, and crushing) adjacent particles. This source of shear resistance is termed geometrical interference or interlocking, and is designated by a geometrical interference friction angle (ϕ'_g) which ranges from 0° at large effective confining pressures where particle movement occurs through sliding and particle crushing, to 30° or more at low effective confining pressures where particle movement involves pushing adjacent particles out of the way and climbing over them. Geometrical interference can be further divided into the resistance produced by dilation or particle climbing (ϕ'_d) and resistance developed by particle rearrangement and damage/crushing (ϕ'_p) (Terzaghi et al. 1996). Thus, the components of the mobilized friction angle, ϕ'_{mob}, are:

$$\phi'_{mob} = \phi'_{\mu} + \phi'_{g} = \phi'_{\mu} + \phi'_{d} + \phi'_{p} \quad 9.1$$

The dilation angle depends on the initial density and confining stress level (Been et al. 1985; Wan and Guo 1999) as well as the surface roughness of the particles (Dietz and Lings 2006). For example, Sture et al. (1998) measured large dilation angles near 30° in a reconstituted sand tested at extremely low confining stresses (0.05 to 0.5 kPa) during triaxial compression (TxC) shear tests conducted during a space shuttle mission. This observation helps to explain friction angles as large as 70° to 80° measured by Matsuoka et al. (2001) for rockfills at low stresses. As the initial void ratio of a granular soil increases, the contribution of dilation (ϕ'_d) decreases and particles resist shear mainly by particle pushing or crushing, causing the soil mass to contract. At a particular large void ratio at which the volume of the soil remains constant during shear (i.e., the critical void ratio), ϕ'_d becomes zero and the effective stress friction angle at failure is designated as the constant volume friction angle (ϕ'_{cv}). At a constant volume condition, particle rearrangement and damage/crushing (ϕ'_p) typically contributes 5° to 6° (Terzaghi et al. 1996) to the mobilized friction angle of a sand (i.e., $\phi'_{cv} = \phi'_{\mu} + \phi'_p$).

Numerous researchers have studied the friction angles mobilized at peak shear stress (e.g., Cornforth 1964; Bishop 1966; Green 1971; Olson and Mattson 2008) and at critical state (e.g., Horne 1969; Golightly 1989; Santamarina and Cho 2001; Luzzani and Coop 2002; Kato et al. 2003; Guo and Su 2007; Malvick et al. 2008). The influence of several factors such as particle shape (Chan and Page 1997; Sukumaran and Ashmawy 2001), initial soil fabric (Been et al. 1991), interparticle friction (Thornton 2000; Liu and Matsuoka 2003), fines content (Sladen et al. 1985; Ni et al. 2004; Murthy et al. 2007) and particle damage/crushing (Bishop and Green 1965; Lee and Seed 1967; Tarantino and Hyde 2005) on these friction angles have been debated based primarily on the results of triaxial compression (TxC) tests. Of course, the shear displacements that can be achieved in the triaxial device are quite limited, contributing to some of the disagreements in the literature. In this chapter, the effective stress friction angle mobilized in sands is examined using both ring shear (RS) and TxC tests to evaluate some of the factors listed above.

9.2 DEFINING FRICTION ANGLES

In this study friction angles were defined from TxC tests using water saturated specimens. However, because of difficulties in saturating and measuring pore water pressures in the RS device, all of the RS specimens were prepared and sheared dry or moist. It is important to note that although water can influence the shear strength (i.e., ϕ'_g) of granular soils composed of particles that are susceptible to weathering or slaking, water has no significant effect on ϕ'_μ (Terzaghi et al. 1996). Since no weathering or slaking conditions were present in the RS tests, the mobilized friction angles are independent of the presence of water. In the TxC tests, the friction angles on the failure plane were defined as follows:

$$\sin\phi' = \frac{3M}{6+M} \qquad 9.2$$

where M is stress ratio [= $(\sigma'_1 - \sigma'_3)/(\sigma'_1 + 2\sigma'_3)/3$] and σ'_1 and σ'_3 are the major and minor principal effective stresses, respectively.

In the RS tests, the shear stress (τ) and effective normal stress (σ'_n) on the horizontal plane are measured directly. By assuming that the horizontal plane is the plane of maximum obliquity (Mandl et al. 1977; Skempton 1985; Negussey et al. 1988), the friction angle can be determined as:

$$\tan\phi' = \left(\frac{\tau}{\sigma'_n}\right) \qquad 9.3$$

Figure 9.1a shows typical constant volume and drained RS stress paths normalized by the consolidation stress (σ'_{nc}) of contractive moist tamped specimens of IR sand. In the constant volume test, the friction angle mobilized at Point A where the specimen yields and the shear stress starts to decrease is termed the yield friction angle (ϕ'_{yield}). The yield friction angle is affected by the intermediate principal stress (e.g., Cornforth 1964; Bishop 1966; Green and Bishop 1969; Green 1971; Reades 1972; Lade and Duncan 1973) and consolidation shear stress (Olson et al. 2006). A shear band forms (Point B) at 0.53

cm shear displacement for IR sand in both drained and constant volume tests (Figure 6.4). Significant particle crushing after Point D was observed visually in numerous RS tests performed with a transparent outer ring, and this crushing led to further contraction and decrease in the stresses and void ratios locally within the shear band.

Figure 9.1b shows typical stress paths of constant volume and drained RS tests on denser specimens of air pluviated IR sand. In the constant volume test, after initial contraction, the sand exhibited a first phase transformation (Point A') and began to dilate. In both constant volume and drained tests, dilation continued until shear strains localized (into a shear band) and peak friction angles (Point B) of 39.2° (in constant volume test) and 36.4° (in drained test) were mobilized in the original sand before crushing of the particles. This friction angle results from both dilation and particle interlocking, which are influenced by density and confining stress, in addition to interparticle friction. After Point B, particles start to become damaged and crushed within the shear band, leading to local contraction. By Point C, sufficient particle damage has occurred to disengage interlocking such that local contraction exceeds dilation and a second phase transformation (from dilation to contraction) occurs.

TxC tests performed on loose or dense sand specimens yielded stress paths similar to those illustrated in Figure 9.1 up to its displacement capacity shortly after Point B; thus the TxC tests did not reach a second phase transformation (Point C) and a critical state incorporating grain crushing (Point E).

In both loose and dense specimens, particle crushing continues until a critical state at Point E. A friction angle of $\phi'_{cs} = 38°$ was mobilized at critical state after all significant particle crushing was complete. And since at Point E, the specimen volume (both globally and locally) becomes constant, ϕ'_{cs} also is referred to as the constant volume friction angle (ϕ'_{cv}). Horne (1969) suggested a direct relation between ϕ'_{μ} and ϕ'_{cs} and postulated the uniqueness of ϕ'_{cs} for a granular material. However, because of the difficulties in measuring ϕ'_{μ} consistently and reliably, it is difficult to establish a direct correspondence between ϕ'_{μ} and ϕ'_{cs}. The ϕ'_{cs} of 38° for the IR sand is larger than what would be expected for a quartz sand. This larger friction angle possibly occurs because the large shear displacements (> 10 m) imposed in the shear band of the RS tests results in the sand particles being severely damaged. The damaged and crushed particles are very

angular and considerably finer than the original grains, filling the void spaces among the larger grains thereby increasing the local density as well as the number of particle contacts. This evolution in grain size distribution and particle shape leads to an increase in ϕ'_{cs}. The mobilized friction angle stabilizes at a critical state value as particle crushing ceases (as a result of the small interparticle contact stresses) and sand in the shear band approaches its critical void ratio. Therefore, $\phi'_{cs,c}$ is used to indicate the ϕ'_{cs} of the sand after all significant particle crushing is complete.

Since the increase in ϕ'_{cs} (after Point D) was caused by particle crushing, the friction angle mobilized at Point D (at an average shear displacement of 7 cm in the RS tests) in Figure 9.1 at which the geometrical interference friction (ϕ'_g) was minimum (implying that although particle damage/crushing had started and suppressed dilation sufficiently to trigger a second phase transformation in the dense specimens, it had yet to occur sufficiently to influence the particle size distribution and overall particle shape). Therefore, the mobilized friction angle (ϕ'_{mob}) at point D could be very close to critical state friction angle of the original (uncrushed) sand gradation, termed $\phi'_{cs,o}$. The value of $\phi'_{cs,o}$ (= 32°) for the IR sand agrees with typical critical state friction angles reported for quartz sands (e.g., Bolton 1986). The friction angle mobilized at Point D also was very close to the friction angle mobilized at the first phase transformation (Point A') of the RS and TxC tests where the first phase transformation occurred. Other researchers also observed close agreement between the friction angles mobilized at phase transformation (ϕ'_{PT}) from undrained TxC tests on medium-dense sands and $\phi'_{cs,o}$ obtained from RS (Bishop 1966; Castro et al. 1982; Negussey et al. 1988) or TxC (Vaid and Chern 1985; Vaid et al. 1990) tests.

The larger $\phi'_{cs,c}$ (from a wider gradation and angular crushed particles) in comparison to $\phi'_{cs,o}$ indicates that ϕ'_{cs} cannot be uniquely determined from ϕ'_{μ} (which is a function of particle mineralogy and roughness), but depends on particle shape as well. More specifically, granular materials comprised of angular particles usually mobilize higher macroscopic shear resistance at a given confining stress than those comprised of rounded particles because particle angularity causes interlocking (and additional restraint to particle rotation), and makes particle rearrangement more difficult (larger ϕ'_p). Other

researchers have made similar observations. For example, Chan and Page (1997) and Sukumaran and Ashmawy (2001) reported that the value of $\phi'_{cs,o}$ decreases with increasing particle roundness, and this may result in a variation in $\phi'_{cs,o}$ of as much as 8° (Koerner 1970). Liu and Matsuoka (2003) also concluded that grain shape affected both shear resistance and the stress-dilatancy relation measured in direct shear tests.

These observations are similar to results observed during TxC tests performed on sands at high confining pressures (e.g., Bishop 1966; Lee and Seed 1967; Murphy 1970; Colliat-Dangus et al 1988; Yamamuro and Lade 1996). These studies have shown that the mobilized friction angle decreases after reaching an initial peak, suggesting that dilation is being suppressed. Near the end of most of these tests, the mobilized friction angle recovers slightly, but the triaxial device is unable to shear specimens to large enough displacements to cause complete particle damage and grain crushing (i.e., widening of the grain size distribution and contraction within the shear band) and greatly influence ϕ'_{cs}.

9.3 FRICTION ANGLES MEASURED IN TXC TESTS

Table 9.2 indicates $\phi'_{cs,o}$ mobilized in the TxC tests and Figure 9.2 through Figure 9.4 show how $\phi'_{cs,o}$ was defined for some of the TxC tests on each sand. Figure 9.5 shows the variation of $\phi'_{cs,o}$ with the consolidation void ratio (e_c) and consolidation mean stress (σ'_c) and illustrates that $\phi'_{cs,o}$ ($= \phi'_{\mu} + \phi'_{p}$) becomes larger as the percentage of feldspar and calcite constituents (which exhibit larger ϕ'_{μ} than quartz) increases from OT to IR to MR sands. It is also apparent that $\phi'_{cs,o}$ decreases with increasing e_c for IR and OT sands while for MR sand $\phi'_{cs,o}$ appears to be independent of e_c. It is likely that the more compressible fabric of the silty MR sand was completely erased by the end of the TxC test, while the OT and IR sands were still influenced by the initial fabric. In addition, $\phi'_{cs,o}$ appears to be independent of σ'_c for the sands tested here because different depositional energies (tamping force/drop height) were used to prepare the laboratory specimens of each sand, leading to separate compression lines for each specimen. However, note that a relatively uniform depositional method and energy may form a particular field deposit. In this case a unique relationship would exist between e_c and σ'_c, and $\phi'_{cs,o}$ would depend on σ'_c through its unique relation with e_c.

Some of the TxC $\phi'_{cs,o}$ are smaller (< 25°) than what has been reported in the literature for $\phi'_{cs,o}$ (and even ϕ'_{μ} according to Table 9.1) of sands with similar mineralogies. Terzaghi et al. (1996) suggested that at very large void ratios (i.e., specimens with Dr < -15%, achieved artificially by moist tamping), some particles cannot keep up with the movement of adjacent particles and the contraction rate remains greater than zero throughout shearing. In this case, the contribution of ϕ'_p disappears, and even ϕ'_{μ} may not be fully mobilized, causing $\phi'_{cs,o}$ to be less than ϕ'_{μ}.

Figure 9.6 illustrates the variation of ϕ'_{yield} from TxC tests with e_c and σ'_c. These data indicate that ϕ'_{yield} decreases with e_c (as reported by Bishop 1971; Alarcon-Guzman et al. 1988; Lade 1993; Yamamuro and Lade 1997); however, there is no clear trend between ϕ'_{yield} and σ'_c. As anticipated, $\phi'_{cs,o}$ and ϕ'_{yield} are inversely related to e_c because the mobilized friction angle depends on the number of particle contacts, which in turn is a function of the void ratio. As yield occurs at small to moderate strain (and displacement) levels, the initial fabric of the soil (as reflected in e_c) strongly influences ϕ'_{yield}.

However, similar to $\phi'_{cs,o}$, and ϕ'_{yield} (observed in individual tests) is also independent of σ'_c because the different depositional methods used to prepare the specimens yielded different initial void ratios (Ishihara et al. 1975; Stewart et al. 1983; Verdugo and Ishihara 1996; Zlatovic and Ishihara 1997; Vaid et al. 1999). Thus after consolidation, consolidation void ratios (at the same consolidation stress) varied and yielded different mobilized friction angles. Again, note that in some geologic settings where a contractive sand deposit is laid down in a fairly uniform manner (i.e., with similar initial void ratios), ϕ'_{yield} would become a function of σ'_c, too.

The state parameter (Been and Jefferies 1985) can be used to combine the effects of both e_c and σ'_c on $\phi'_{cs,o}$ and ϕ'_{yield}, and it has been stated by Manzari and Dafalias (1997) and Li and Dafalias (2000) that mobilized friction angle is a function of state parameter. As anticipated, Figure 9.7 illustrates that both $\phi'_{cs,o}$ (except for MR sand) and ϕ'_{yield} decrease with increasing ψ. As discussed earlier, the fabric of MR sand was likely erased by the end of the TxC tests and therefore its $\phi'_{cs,o}$ was independent of ψ.

9.4 FRICTION ANGLES MEASURED IN RS TESTS

As discussed earlier, the friction angle mobilized at Point D (Figure 9.1) (i.e. prior to significant particle damage) is likely close to the critical state friction angle of the original uncrushed sand ($\phi'_{cs,o}$). Table 9.3 presents values of $\phi'_{cs,o}$ obtained from Point D in the RS stress paths as well as other details of those tests. Figure 9.8 through Figure 9.12 graphically illustrate the stress paths from some of the RS tests, as well as values of $\phi'_{cs,o}$ and $\phi'_{cs,c}$. Figure 9.13 shows how $\phi'_{cs,o}$ changes with e_c and σ'_{nc}. These data suggest that e_c (and hence the pre-shear fabric) does not strongly affect $\phi'_{cs,o}$, and some other factors should be controlling its variation.

In contrast to e_c, Figure 9.13b indicates that $\phi'_{cs,o}$ decreases with consolidation stress and becomes essentially constant at moderate (> 100 - 200 kPa) stresses. Infante-Sedano (1998) also found stress-dependent critical state friction angles at stresses below 100 kPa, which became constant at larger stress levels in RS tests on Unimin 2010 sand. Similar behaviors were also observed for Hostun River (Lancelot et al. 2006), Karlsruhe (Kolymbas and Wu 1990), and Toyoura (Fukushima and Tatsuoka 1984) sands. At small stresses (< 100 kPa), $\phi'_{cs,o}$ of 32°, 36°, and 38° were mobilized in OT, IR and MR sands, respectively. However average $\phi'_{cs,o}$ of 31.0°, 32°, and 34° were obtained at σ'_{nc} > 100 - 200 kPa for respectively OT, IR, and MR sands. These ranges agree with the range of $\phi'_{cs,o}$ for sands from 32° to 37° (Bolton 1986; Santamarina and Cho 2001; Fukuoka et al. 2004; Malvick et al. 2008). The higher values correspond to sands that have a significant proportion of feldspar, while lower values correspond to quartz sands. The angular MR sand particles develop greater interlocking (ϕ'_p) and lead to larger friction angles than those mobilized by the rounded, rotund grains of the OT and IR sands. In addition to the effect of particle angularity, feldspar and calcite minerals present in MR sand lead to the larger values of ϕ'_μ, and due to the lower hardness and larger grain textures of these minerals (Terzaghi et al. 1996), they develop more effective interlocking and yield larger values of $\phi'_{cs,o}$. DEM simulations by Thornton (2000) and Liu and Matsuoka (2003) have also shown that $\phi'_{cs,o}$ tends to increase with ϕ'_μ.

Figure 9.14 shows the variation of $\phi'_{cs,c}$ corresponding to the end of RS tests at very large shear displacements with e_c and σ'_{nc}. As discussed before, particle damage occurred

in the shear band of most of the RS tests and $\phi'_{cs,c}$ corresponds to the critical state of the crushed sand. These data illustrate that $\phi'_{cs,c}$ at the end of the RS tests of the crushed sand is fairly independent of e_c, suggesting that the preshear sand fabric was erased at very large shear displacements where $\phi'_{cs,c}$ was measured. Furthermore, the data scatter (particularly for MR sand) implies that other parameters likely affect $\phi'_{cs,c}$. As discussed earlier for $\phi'_{cs,o}$, $\phi'_{cs,c}$ also decreased with increasing σ'_{nc}, becoming fairly constant at σ'_{nc} larger than 100 - 200 kPa. The values of $\phi'_{cs,c}$ at $\sigma'_{nc} < 100$ kPa averaged 44° for OT and IR sands and 47° for MR sand. As σ'_{nc} increased, $\phi'_{cs,c}$ decreased as potential particle interaction was suppressed (Haruyama 1969) without dropping to its lowest value at σ'_{nc} = 100 – 200 kPa. The decrease in $\phi'_{cs,c}$ with increasing σ'_{nc} occurs because of the larger relative particle sliding and particle damage (which reduces particle interaction and interlocking) and thus smaller ϕ'_p and $\phi'_{cs,c}$ at larger stresses. At larger σ'_{nc} (>200 kPa) $\phi'_{cs,c}$ increased slightly in OT and IR sands because of the larger fines content and more angular crushed particles produced by severe particle crushing. This trend was not observed in MR sand, possibly because of its initially wider particle size distribution and larger original fines content. At $\sigma'_{nc} > 200$ kPa, average $\phi'_{cs,c}$ of 34°, 38°, and 41° were obtained for OT, IR, and MR sands, respectively. Particle crushing creates a wide grain size distribution for which friction angle becomes relatively insensitive to stress level (e.g., Insley and Hillis 1965; Bishop 1966). Since the crushed sand particles are more angular and there is a considerable increase in the fines content (up to 40%), the number of particle contacts increases and $\phi'_{cs,c}$ becomes larger than the $\phi'_{cs,o}$ for each sand. Similar trends of increasing ϕ'_{cs} with increasing non-plastic silt content was also observed by Sladen et al. (1985), Ni et al. (2004), and Murthy et al. (2007).

To further demonstrate the effect of crushing, Figure 9.15 shows the variation of $\phi'_{cs,c}$ obtained at very large shear displacements in RS tests with respect to the relative breakage factor, B_r (Hardin 1985). The procedure to define B_r for the RS tests was explained in Chapter 7. As shown in Figure 9.15, $\phi'_{cs,c}$ decreases with increasing breakage, B_r. This is because, at low σ'_{nc} particles experience less crushing and more relative particle movement and interaction in the form of particles pushing each other and rolling, thus mobilizing a larger ϕ'_p and $\phi'_{cs,c}$. This behavior is responsible for the curvature of the

critical state Mohr-Coulomb envelope at larger stresses, as observed by numerous investigators (e.g., Vesic and Barksdale 1963; Bishop and Green 1965; Bishop 1966; Lee and Seed 1967; Vesic and Clough 1968; Bishop 1972; Billam 1972; Lo and Roy 1973; Miura and Yamanouchi 1977; Touati 1982; Colliat-Dangus et al. 1988; Golightly 1989; Tarantino and Hyde 2005). At larger σ'_{nc} and B_r values (> 0.2), $\phi'_{cs,c}$ became approximately constant. This occurs possibly because the reduction in $\phi'_{cs,c}$ caused by crushing and suppressing relative particle movement was compensated by the increase in $\phi'_{cs,c}$ resulting from the creating of additional angular particles during crushing. At very large shear displacements where $\phi'_{cs,c}$ was measured, dilation became very small, and $\phi'_{cs,c}$ was primarily the result of interparticle sliding and particle interaction. The influence of shear displacement on $\phi'_{cs,c}$ is similar to the effect of σ'_{nc} as they are both directly related to particle crushing and damage. In TxC tests where maximum shear displacements are limited, the effect of particle damage on $\phi'_{cs,c}$ has been studied by increasing the confining stress. For example, Lo and Roy (1973) performed constant volume TxC tests on aluminum oxide, quartz, and limestone particles at confining stresses ranging from 172 kPa to 11 MPa and showed that the ultimate stress ratio, σ'_1/σ'_3, decreased with increasing confining stress. Similarly, Golightly (1989) performed triaxial tests on Dogs Bay sand and showed that the mobilized friction angle decreased with increasing confining stress. Kato et al. (2003) tested Masado (decomposed granitic sand) and Chiibishi sand (a weak carbonate sand) at constant-volume conditions and found that the stress ratio at an axial strain of 30% decreased markedly over a range of confining pressures from 50 kPa to 40 MPa. In the RS tests performed in this study however, the large shear displacements contributed significantly to the amount of particle crushing, masking the effect of confining stress. In addition, the larger values of $\phi'_{cs,c}$ for MR sand in comparison to those of OT and IR sands, even after severe particle crushing, indicates that $\phi'_{cs,c}$ is clearly influenced by ϕ'_{μ}. This is similar to the conclusions described before for $\phi'_{cs,o}$ but contrasts the findings by Skinner (1969) and Abriak and Mahboubi (1992) who suggested that ϕ'_{cs} is independent of ϕ'_{μ}.

Figure 9.16 presents ϕ'_{yield} measured in constant volume RS tests on contractive specimens with respect to e_c and σ'_{nc}, and Figure 9.17 shows $\phi'_{cs,c}$ and ϕ'_{yield} as a function

of state parameter (where ψ was determined with respect to the CSL_o of each sand). Similar to the TxC tests (Figure 9.6 and Figure 9.7b), ϕ'_{yield} decreases with increasing e_c and ψ; however, a mild decrease in ϕ'_{yield} with σ'_{nc} is observed only for MR sand. Also the narrow range of ϕ'_{yield} (14° – 24°) falls within the range reported by Olson and Mattson (2008) for DSS and RS tests and encompasses the range of 14° to 19° for Leighton Buzzard, and Nerlerk sands (Sladen et al. 1985) and 17° to 23° reported by Terzaghi et al. (1996) for Banding sand (data from Castro 1969). Similar to the influence of σ'_{nc} on $\phi'_{cs,c}$, Figure 9.17a indicates that $\phi'_{cs,c}$ initially decreases as ψ increases and reaches a relatively constant value at larger ψ.

These data illustrate that $\phi'_{cs,c}$ (and $\phi'_{cs,o}$) independent of e_c and σ'_{nc} (for $\sigma'_{nc} > 200$ kPa) in RS tests (Figure 9.13 and Figure 9.14) and suggests that $\phi'_{cs,c}$ (and $\phi'_{cs,o}$) depends on particle mineralogy and angularity (Bolton 1986; Yang and Mu 2008). Furthermore, $\phi'_{cs,c}$ (and $\phi'_{cs,o}$) is independent of initial soil fabric/specimen preparation method (Bishop et al. 1971), consistent with the basic concept of critical state soil mechanics (Schofield and Wroth 1968) and similar to the findings of some other researchers (e.g., Horne 1969; Vaid and Chern 1985; Kuerbis et al. 1988; Negussey et al. 1988; Vaid et al. 1990; Vaid and Sasitharan 1992; Vaid and Sivathayalan 1996; Verdugo and Ishihara 1996; Riemer and Seed 1997; Luzzani and Coop 2002; Sivathayalan and Vaid 2002; Guo and Su 2007). One of the reasons that some researchers (e.g., Fannin et al. 2005) reported nonunique values of $\phi'_{cs,o}$ for a particular sand in TxC is that the triaxial device is unable to impose sufficient displacement to reach critical state conditions for some sands, particularly when particle crushing occurs.

Subsequently, ϕ'_{yield} (Figure 9.18) and $\phi'_{cs,o}$ (Figure 9.19) measured in RS tests were up to 10° larger than those measured in TxC for each of the tested sands. In addition to differences in mode of shearing, the different lateral boundaries in TxC (deformable boundary) and RS (rigid boundary) resulted in different σ'_2 and likely impacted ϕ'_{mob} (e.g., Cornforth 1964; Ko and Scott 1967; Green and Bishop 1969; Green 1971; Bishop 1972; Lade and Duncan 1973; Reades and Green 1976; Miyamori 1976; Yamada and Ishihara 1979; Ergun 1981; Ochiai and Lade 1983; Bolton 1986; Lam and Tatsuoka 1988; Sayao and Vaid 1996; Jefferies and Shuttle 2002; Jefferies and Been 2006; Lade et al. 2008). In

contrast to the rigid RS boundaries, the deformable membrane boundaries used in TxC tests allowed some movement and contraction (negative dilatancy) of the sand particles, resulting in a smaller mobilized ϕ'_p in comparison to RS tests. Accordingly, the differences between ϕ'_{yield} and $\phi'_{cs,o}$ measured in TxC and those mobilized in RS tests were largest for MR sand because of its greater fines content, more compressible fabric (mineralogy), and particle shape and therefore the greater potential influence of σ'_2.

Based on the RS tests, Figure 9.20 presents the conceptual evolution of mobilized friction angle (ϕ'_{mob}) with shear displacement for sands at varying levels of confining stress and the contributions from different frictional components. At small shear displacements, particles rearrange without significant crushing until dilation (ϕ'_d) becomes zero and particle rearrangement is complete (ϕ'_p = constant) at the critical state of the original sand gradation where $\phi'_{cs,o}$ is mobilized. As shearing continues, particle damage and crushing become significant, causing the particle gradation to evolve and the particles to rearrange (i.e., contract). After large shear displacement, the tendency for particle damage and crushing and particle rearrangement is exhausted (as a result of the low particle contact stresses) and crushed soil reaches a new critical state condition. At this condition, $\phi'_d = 0$ and $\phi'_{cs,c}$ is mobilized; however, because of the wider gradation, more angular particles, and greater particle interaction, ϕ'_p is larger than that mobilized at $\phi'_{cs,o}$. In addition, as the confining stress increases from about 50 kPa to 200 kPa, the influence of particle interaction decreases and ϕ'_{cs} decreases. This decrease is largest for $\phi'_{cs,c}$ because of the wider particle size distribution, more angular particles, and hence larger contribution of particle interaction to $\phi'_{cs,c}$.

9.5 SUMMARY AND CONCLUSIONS

In this chapter, yield and critical state friction angles of sands were investigated using RS and TxC tests on air pluviated and moist tamped specimens of three different sands. Critical state friction angles were observed in RS tests on both contractive and dilative specimens, while yield friction angles were defined from contractive tests only. These tests illustrate that $\phi'_{cs,o}$ and ϕ'_{yield} measured in TxC are independent of effective stress but

inversely related to consolidation void ratio. This suggests that the initial soil fabric was not erased after reaching the displacement limit of the triaxial device.

No clear relationship was observed between ϕ'_{yield} and σ'_{nc} in the RS tests; however, ϕ'_{yield} decreased with e_c and ψ. The range of ϕ'_{yield} (14° - 24°) measured in RS agrees with those measured in DSS and RS tests performed in other studies (Riemer 1992; Yoshimine et al. 1999; Wang and Sassa 2002). Dense specimens tested in RS dilated until local contraction resulting from particle crushing surpassed local dilation and yielded a second phase transformation from dilative to contractive volumetric response. The minimum friction angle measured after the second phase transformation was approximately equal to the critical state friction angle of the original uncrushed sand ($\phi'_{cs,o}$) and was independent of initial soil fabric but decreased slightly until the consolidation stress (σ'_{nc}) exceeded about 150 kPa. Average values of $\phi'_{cs,o} = 31°$, 32°, and 34° were measured for OT, IR and MR sands, respectively. Furthermore, $\phi'_{cs,o}$ was very similar to the effective friction angle mobilized at the first phase transformation, ϕ'_{PT}.

As shearing continued in the RS tests, the mobilized friction angle increased as the sand particles became severely damaged and more angular. Furthermore, fine particles produced by particle abrasion and shattering of the original grains, filled the void spaces among the larger grains, increasing the density and mobilized friction angle. The mobilized friction angle stabilized at a critical state value ($\phi'_{cs,c}$) as particle crushing ceased and the local void ratio in the shear band became constant (critical void ratio). At this condition, the initial sand fabric was destroyed and $\phi'_{cs,c}$ was independent of the initial fabric. Note that $\phi'_{cs,c}$ at low stresses (i.e., $\sigma'_{nc} < 100$ kPa) increased but at larger stresses, average values of $\phi'_{cs,c} = 34°$, 38°, and 41° were mobilized in OT, IR, and MR sands, respectively.

Overall, the RS results confirm that $\phi'_{cs,c}$ (and $\phi'_{cs,o}$) depends primarily on particle mineralogy and shape, as well as the intermediate principal stress and is independent of stress path and fabric.

9.6 TABLES

Table 9.1: ϕ'_μ of some common minerals (after Terzaghi et al. 1996)

Mineral	ϕ'_μ (°)
Quartz	22-35
Feldspar	36-38
Hornblende	31
Calcite	31-34
Anthracite	31
Chalk	30

Table 9.2: TxC test specifications and friction angles

Test No.[1]	σ'_c *(kPa)*	Dr_c *(%)*[2]	ϕ'_{yield} *(°)*[3]	$\phi'_{cs,o}$ *(°)*	*Test No.*	σ'_c *(kPa)*	Dr_c *(%)*	ϕ'_{yield} *(°)*	$\phi'_{cs,o}$ *(°)*
MTOTUN83	571	-16	1.5	23.6	MTIRUN55	381	28	23.5	29.3
MTOTUN52	361	-38	14.4	21.6	MTIRUN43	298	0	18.6	27.2
MTOTUN103	711	-7	16.9	25.0	MTIRUN54	373	15	19.3	28.0
MTOTUN102	704	-32	13.0	22.6	MTIRUN26	177	4	18.2	28.0
MTOTUN42	290	-41	13.2	21.2	MTIRDR74	511	30	-	28.6
MTOTUN92	635	-32	14.2	22.2	MTIRDR37	252	22	-	28.6
MTOTUN82	566	-30	15.1	23.0	MTIRDR54	372	29	-	29.6
MTOTUN63	435	-15	16.7	24.0	MTIRDR20	137	27	-	29.6
MTOTDR55	380	8	-	28.1	APIRUN82	566	44	-	29.2
MTOTDR21	143	18	-	30.0	APMRUN32	221	68	15.1	31.0
MTOTDR88	610	1	-	28.0	APMRUN62	425	85	16.2	29.2
MTOTDR39	266	7	-	28.5	APMRUN92	636	93	16.9	30.5
MTOTDR71	487	8	-	27.7	APMRUN47	326	84	16.2	30.0
APOTUN54	369	13	-	30.1	APMRUN39	272	83	16.7	30.0
MTIRUN29	199	-30	15.5	25.5	APMRUN58	397	80	14.6	30.0
MTIRUN17	117	-27	19.3	26.0	APMRUN23	161	67	15.4	30.0
MTIRUN52	359	17	23.5	28.0	APMRDR29	200	73	-	31.0
MTIRUN54	373	9	-	27.6	APMRDR29	200	69	-	31.0
MTIRUN83	569	33	22.5	28.5	APMRDR16	109	60	-	30.2
MTIRUN112	773	27	20.4	28.0	APMRDR81	560	80	-	30.0
MTIRUN109	752	44	-	29.0	APMRDR64	443	72	-	30.6
MTIRUN12	85	-21	19.3	27.0	APMRDR41	281	79	-	30.6

[1] MT and AP in test number indicate moist tamping or air pluviation preparation methods, respectively. OT, IR, and MR indicate OT, IR and MR sands, respectively. UN and DR indicate undrained or drained conditions, respectively.

[2] Relative density after consolidation.

[3] ϕ'_{yield} was defined only in contractive undrained tests.

Table 9.3: RS test specifications and friction angles

Test No.[1]	σ'_{nc} (kPa)	Dr_c (%)[2]	ϕ'_{yield} (°)[3]	$\phi'_{cs,o}$ (°)[4]	$\phi'_{cs,c}$ (°)[4]	Test No.	σ'_{nc} (kPa)	Dr_c (%)	ϕ'_{yield} (°)	$\phi'_{cs,o}$ (°)	$\phi'_{cs,c}$ (°)
MTOTCV54(1)	389	7	19.2	32.0	-	MTIRDR54	364	10	-	33.0	37.0
MTOTCV21	149	-6	17.0	31.0	-	APIRCV82	590	49	-	32.0	38.0
MTOTCV87	624	-5	14.0	31.0	34.0	APIRCV81	553	35	-	32.0	38.0
MTOTCV63	448	3	16.0	31.0	34.0	APIRCV17	137	14	-	32.0	35.0
MTOTCV54(2)	376	-8	15.0	31.5	-	APIRCV94	646	28	-	33.0	39.0
APOTCV83	541	47	-	31.5	-	APIRCV78	541	29	-	33.0	37.5
APOTCV85	620	37	-	31.5	34.0	APIRCV41	309	42	-	33.0	38.0
APOTCV28	217	26	-	31.0	33.5	APIRCV45	323	48	-	33.0	38.0
APOTCV54	392	31	-	31.0	34.0	APIRCV39	272	34	-	33.0	38.0
MTOTDR40	279	3	-	31.5	34.0	APIRDR52	360	58	-	32.0	37.0
APOTDR40(1)	279	24	-	31.0	33.3	APIRDR42	301	56	-	33.0	38.0
MTOTDR4	28	33	-	31.5	44.0	APIRDR5	48	59	-	36.1	44.0
MTOTDR38(1)	287	-3	-	31.0	34.5	APIRDR38	277	53	-	33.0	38.0
MTOTDR38(2)	289	-2	-	31.0	34.5	APIRDR72	490	40	-	32.0	37.0
APOTDR5	29	23	-	32.0	44.0	APIRDR85	550	56	-	32.0	38.0
APOTCV17	120	6	-	28.3	31.0	APIRDR76	540	50	-	32.0	38.0
APOTDR40(2)	278	1	-	31.0	34.0	APMRCV57	378	59	21.0	-	40.0
APOTDR78	562	48	-	31.0	34.0	APMRCV43	298	69	22.5	34.0	-
MTOTCV52	383	12	-	31.0	-	APMRCV87	602	70	-	34.0	41.0
APOTCV52	357	28	-	31.0	33.3	APMRCV89	624	57	-	33.5	-
MTIRCV46	318	-8	15.0	-	38.0	APMRCV97	708	88	-	33.3	46.0
MTIRCV53	351	3	17.0	33.0	38.0	APMRCV22	151	65	23.0	32.0	43.0
MTIRCV58	403	44	-	33.0	38.0	APMRDR39	271	63	-	33.3	41.0
MTIRCV75	628	39	23.0	33.0	38.0	APMRDR4	29	56	-	38.0	47.0
MTIRCV52	360	26	24.0	32.5	37.5	APMRDR40	276	67	-	33.0	39.0
MTIRCV56	396	17	20.0	-	37.0	APMRDR77	523	73	-	34.0	41.0
MTIRCV18	124	4	21.0	33.0	33.0	APMRCV48	355	87	-	33.0	-
MTIRDR41	278	29	-	33.0	37.5	MTMRCV48	334	60	22.0	-	39.5
MTIRDR75	516	29	-	33.0	39.0	MTMRDR40	266	51	-	33.0	41.0

[1] MT and AP in test number indicate moist tamping or air pluviation preparation methods, respectively. OT, IR, and MR indicate OT, IR and MR sands, respectively. CV and DR indicate constant volume or drained conditions, respectively.

[2] Relative density after consolidation.

[3] ϕ'_{yield} was defined only in contractive undrained tests.

[4] $\phi'_{cs,o}$ (or $\phi'_{cs,c}$) are not reported in tests where $\phi'_{cs,o}$ and $\phi'_{cs,c}$ were not clearly distinguishable from each other.

9.7 FIGURES

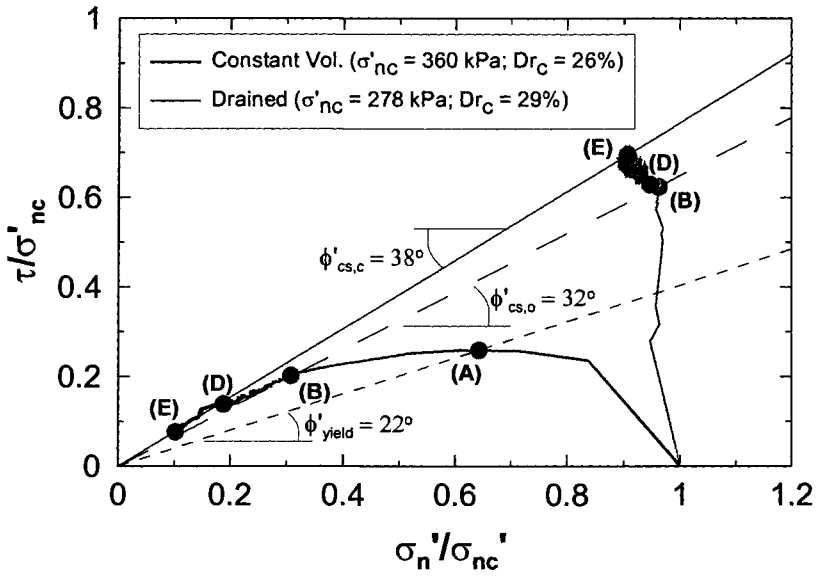

(a)

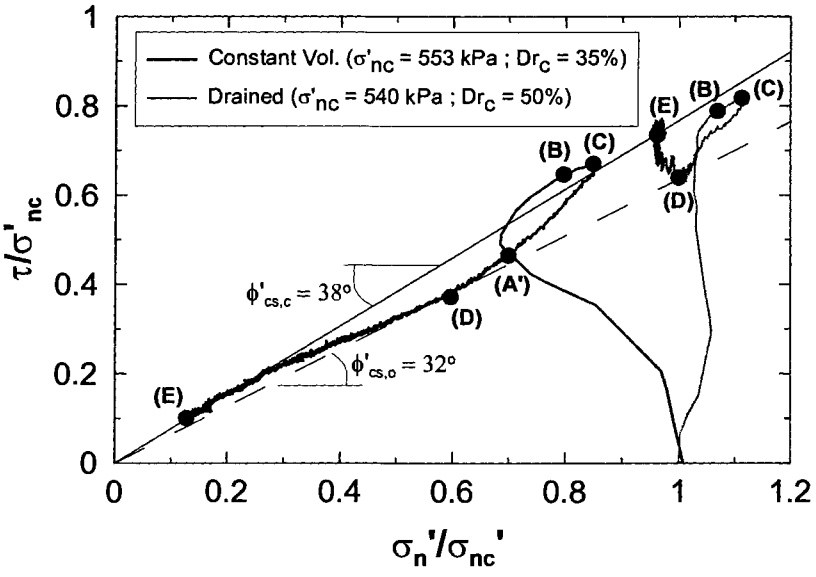

(b)

Figure 9.1: Typical RS stress paths on (a) loose (MTIRCV52 and MTIRDR41) and (b) dense (APIRCV81 and APIRDR76) IR sand specimens normalized to the consolidation stress.

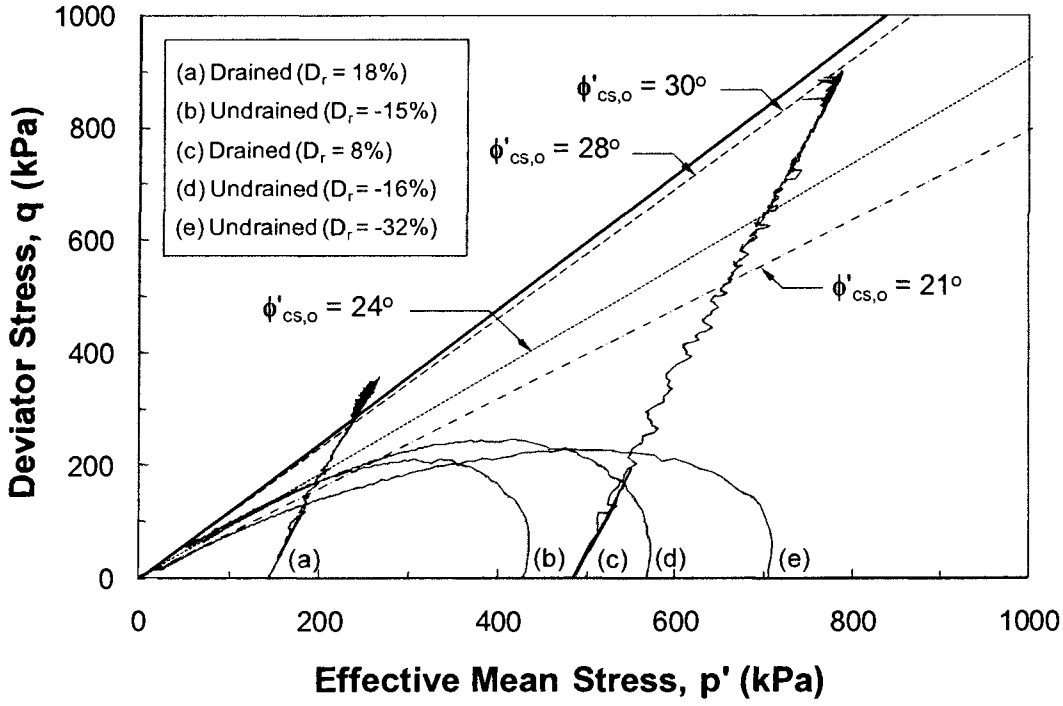

Figure 9.2: Stress paths of some TxC tests on OT sand specimens

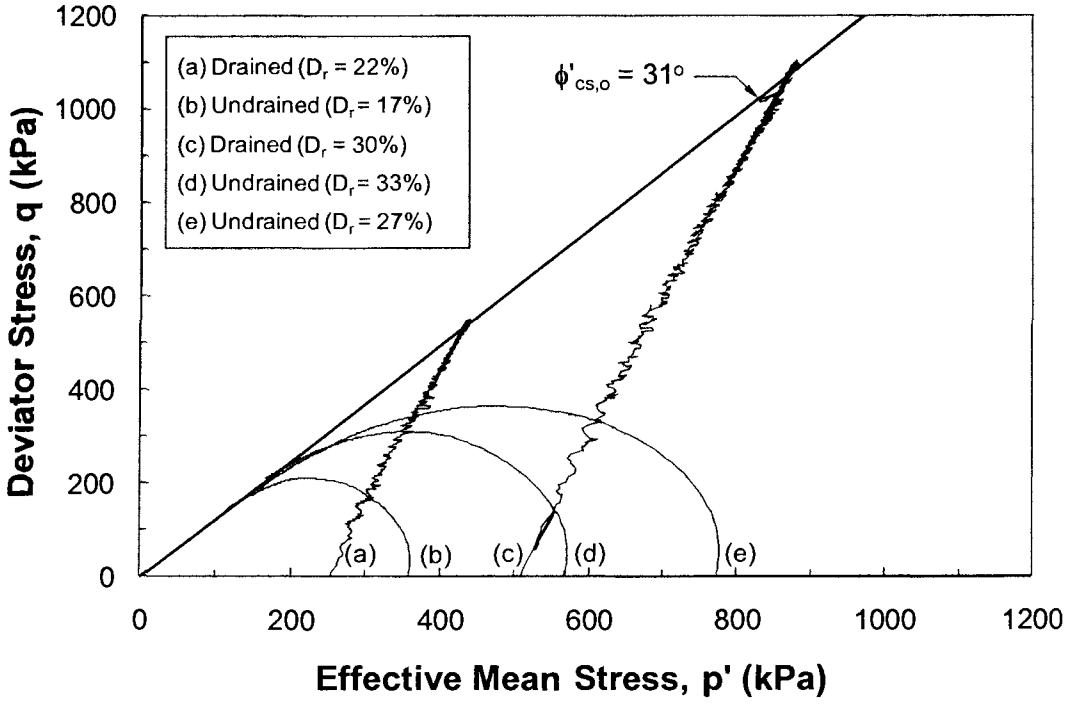

Figure 9.3: Stress paths of some TxC tests on IR sand specimens

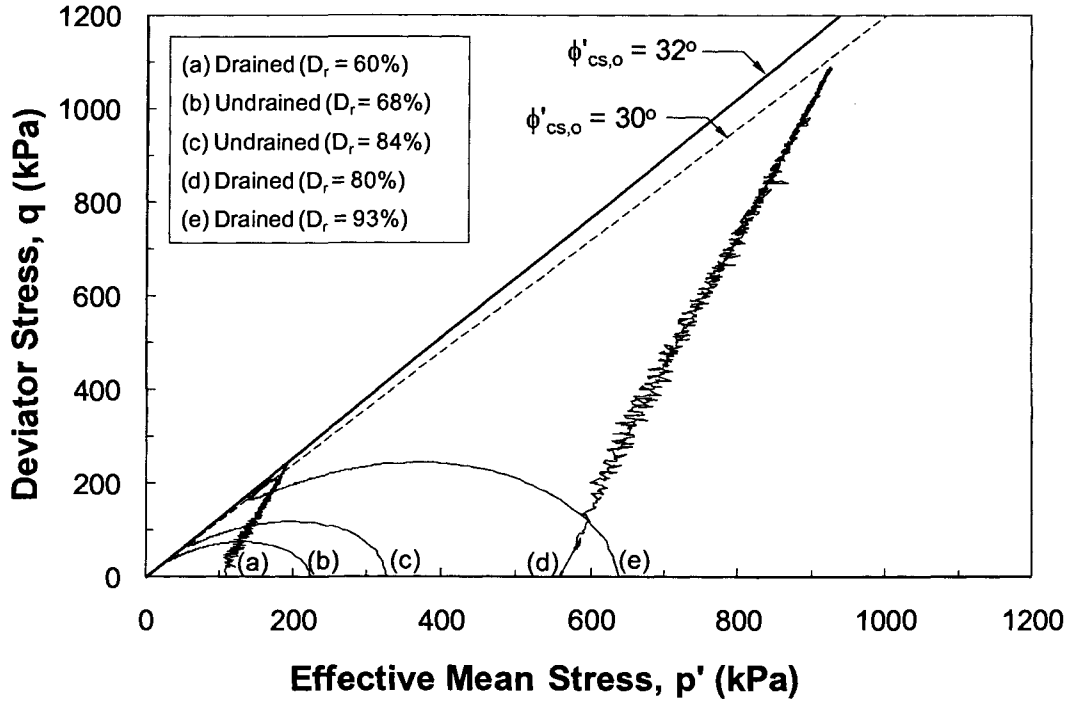

Figure 9.4: Stress paths of some TxC tests on MR sand specimens

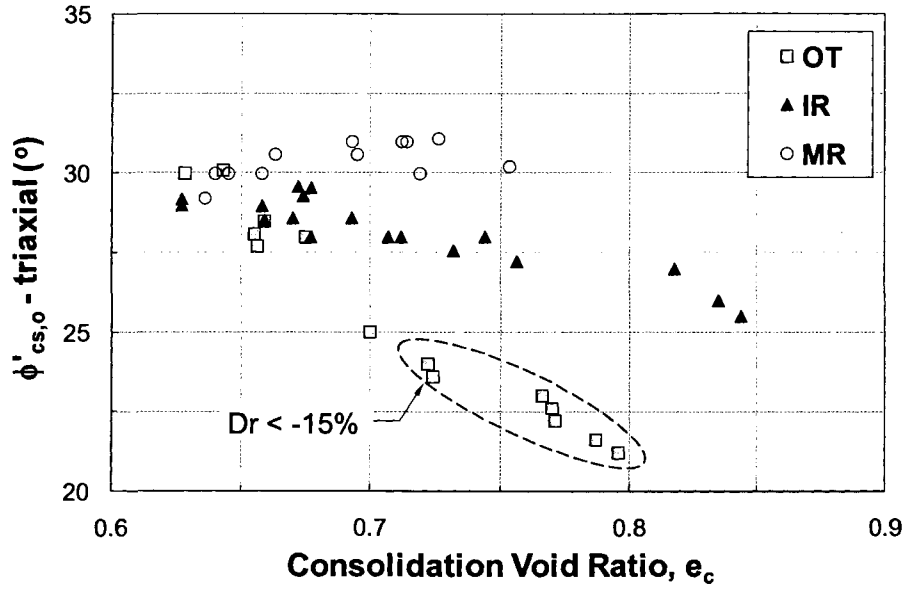

(a)

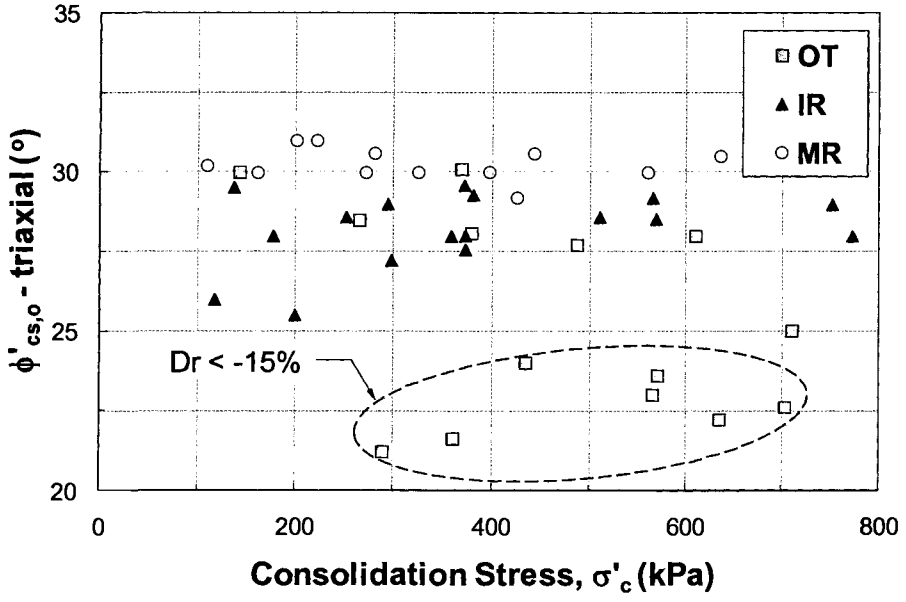

(b)

Figure 9.5: Variation of $\phi'_{cs,o}$ from TxC tests with (a) e_c and (b) σ'_c

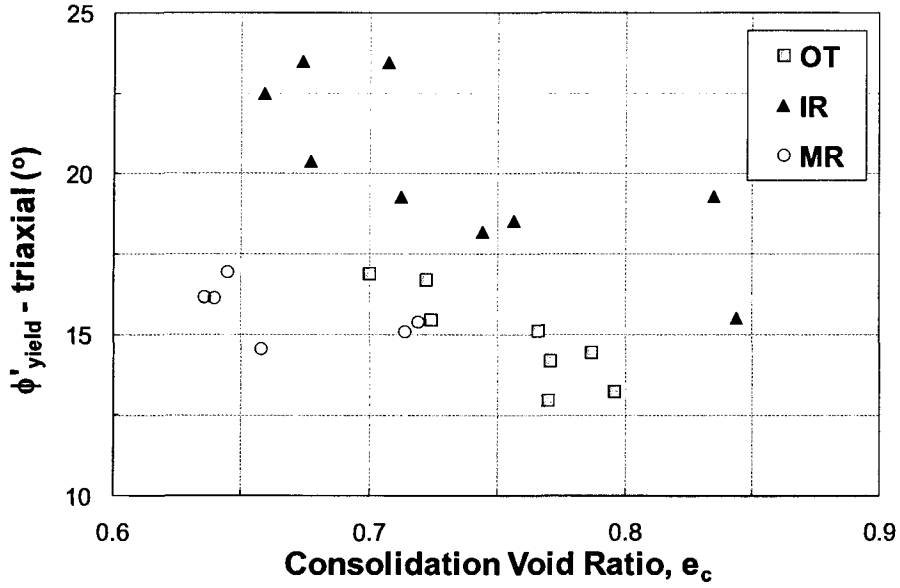

(a)

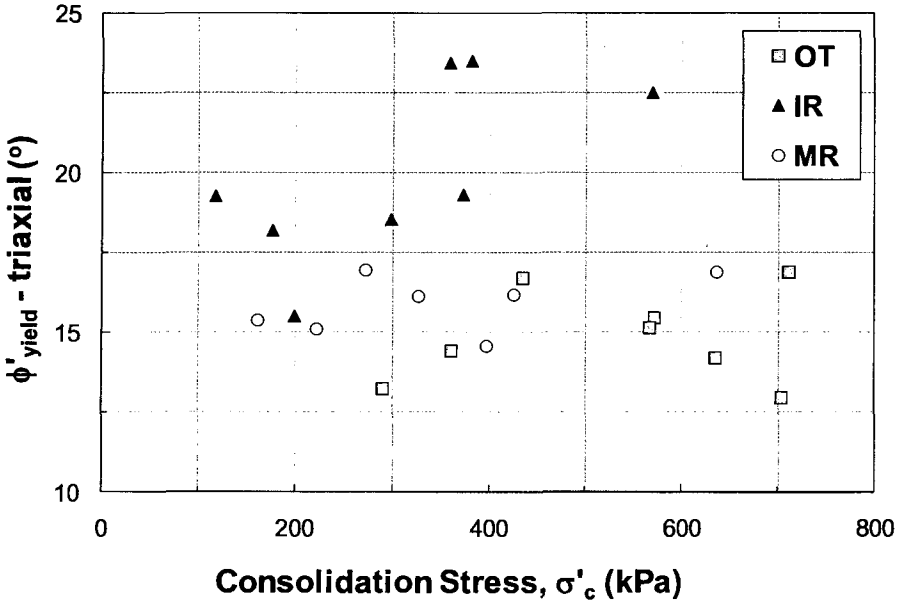

(b)

Figure 9.6: Variation of ϕ'_{yield} observed in TxC tests with (a) e_c and (b) σ'_c

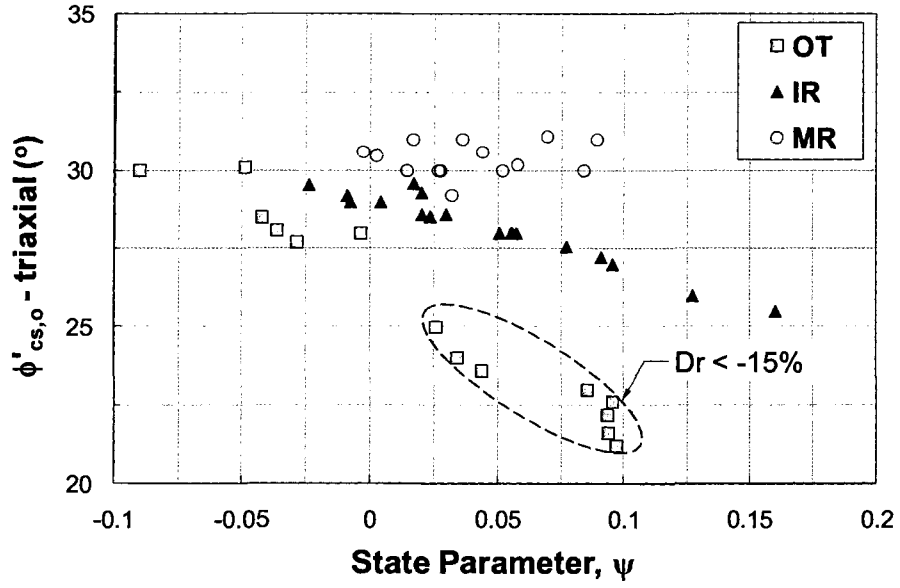

(a)

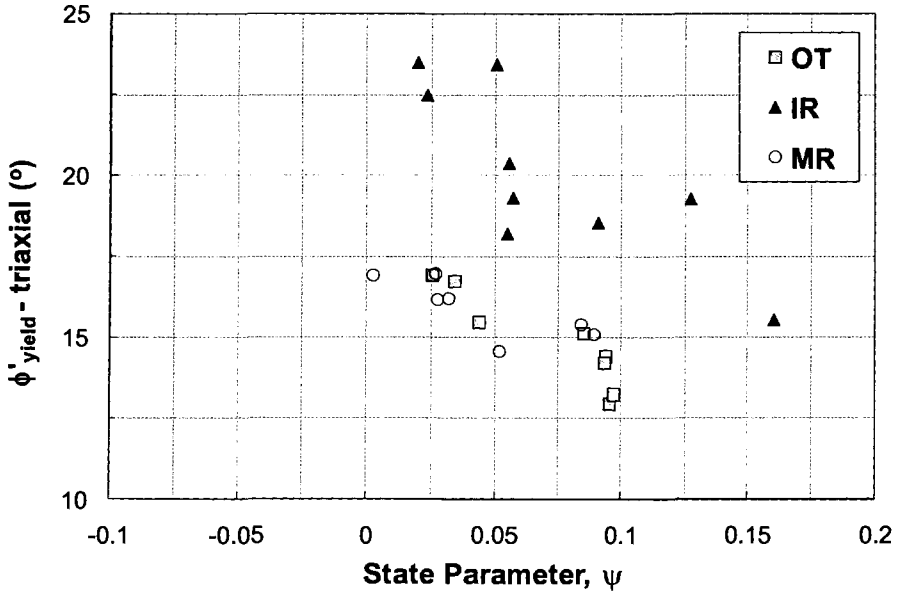

(b)

Figure 9.7: Variation of (a) $\phi'_{cs,o}$ and (b) ϕ'_{yield} with ψ observed in TxC tests

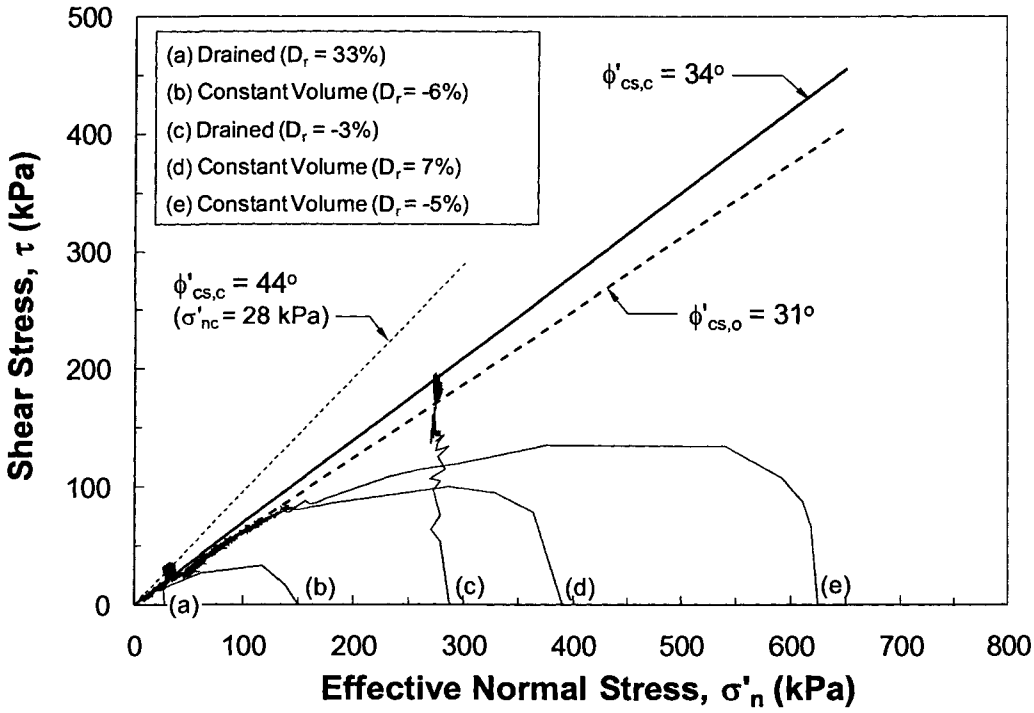

Figure 9.8: Stress paths from some of the RS tests on moist tamped OT sand specimens

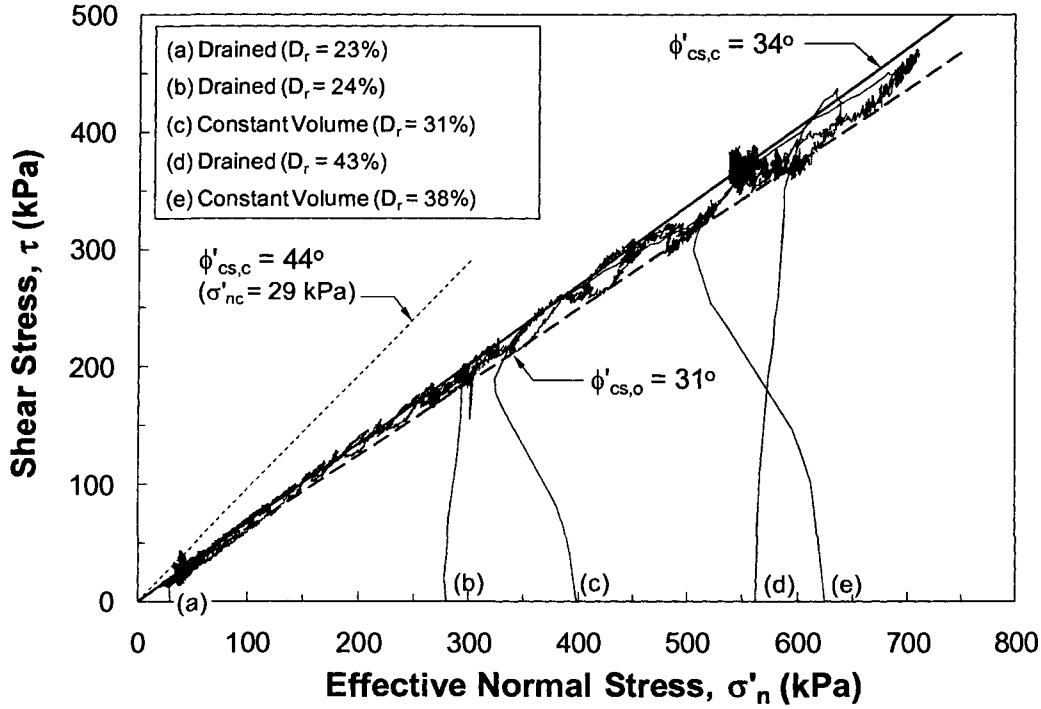

Figure 9.9: Stress paths from some of the RS tests on air pluviated OT sand specimens

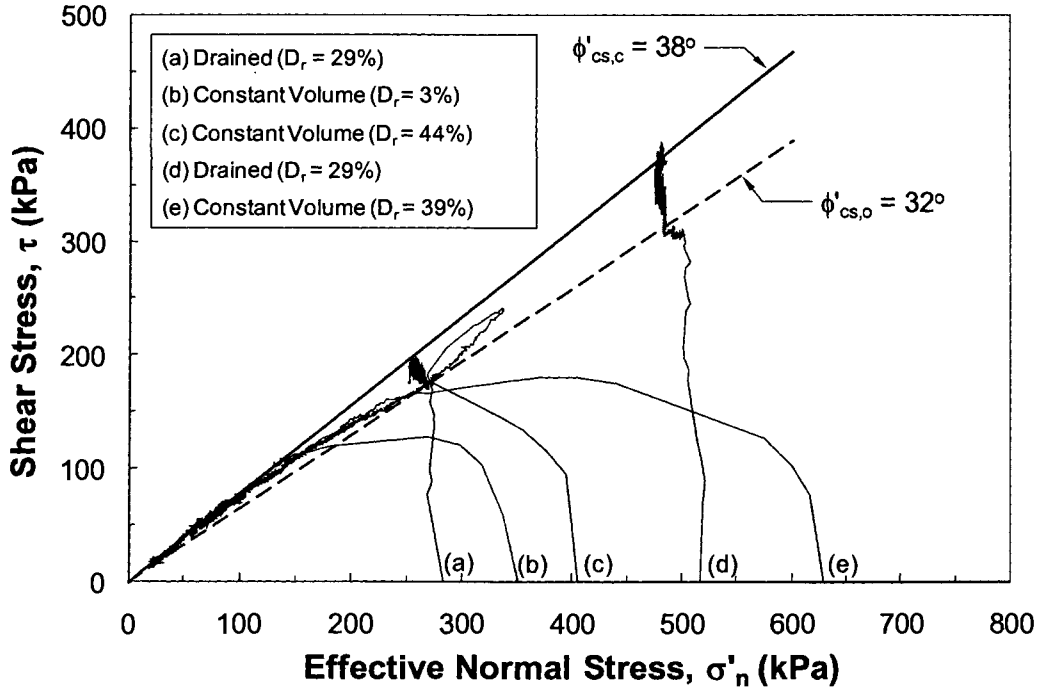

Figure 9.10: Stress paths from some of the RS tests on moist tamped IR sand specimens

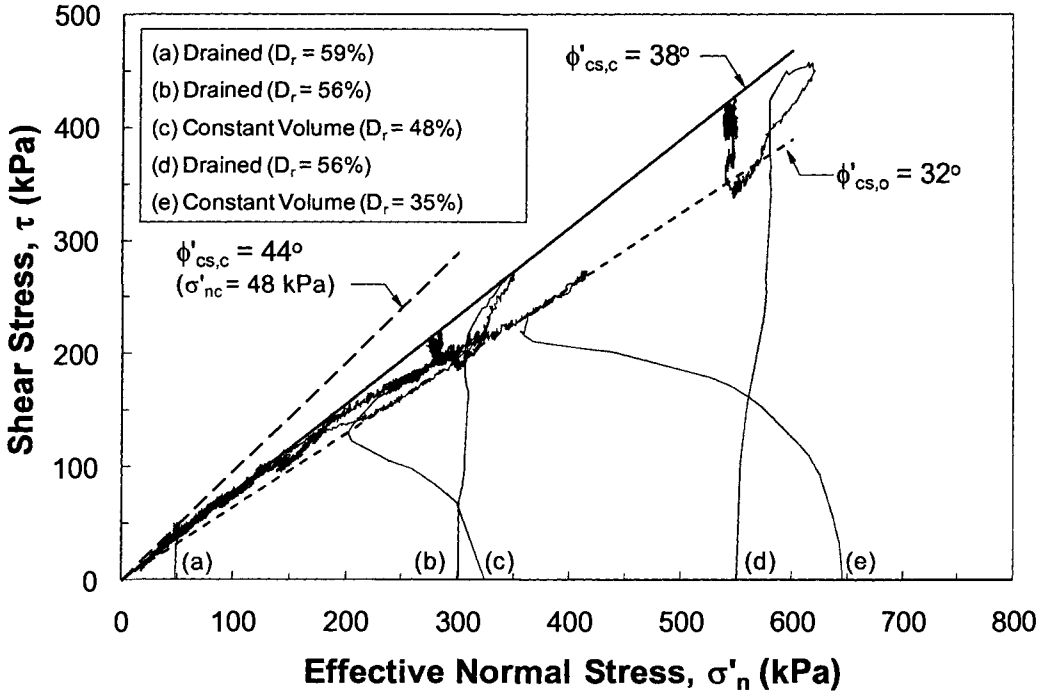

Figure 9.11: Stress paths from some of the RS tests on air pluviated IR sand specimens

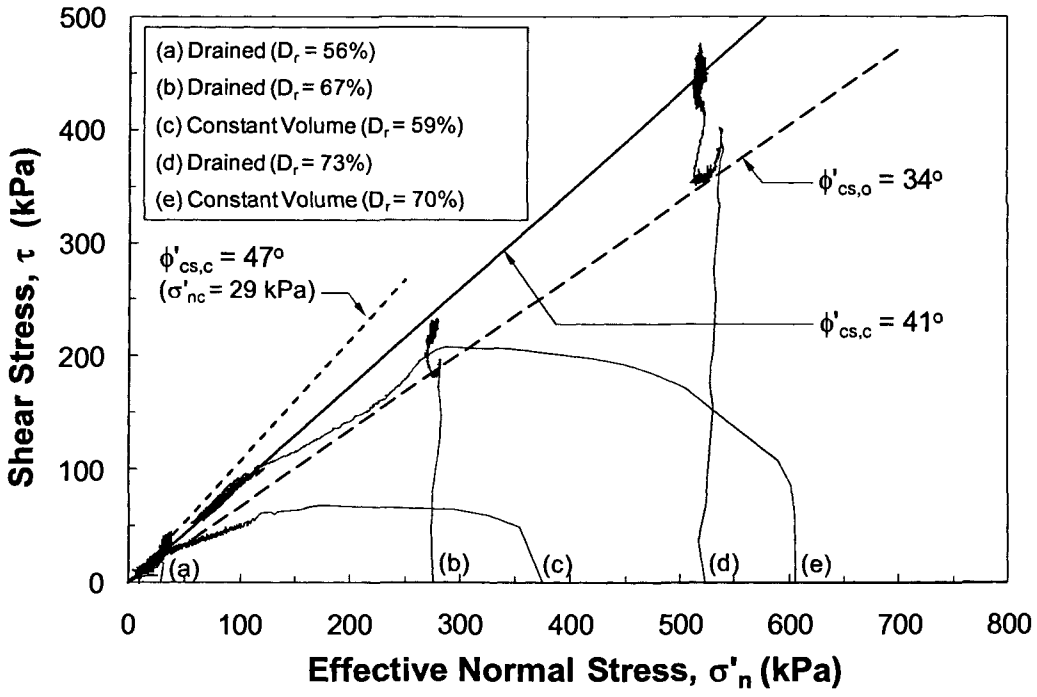

Figure 9.12: Stress paths from some of the RS tests on air pluviated MR sand specimens

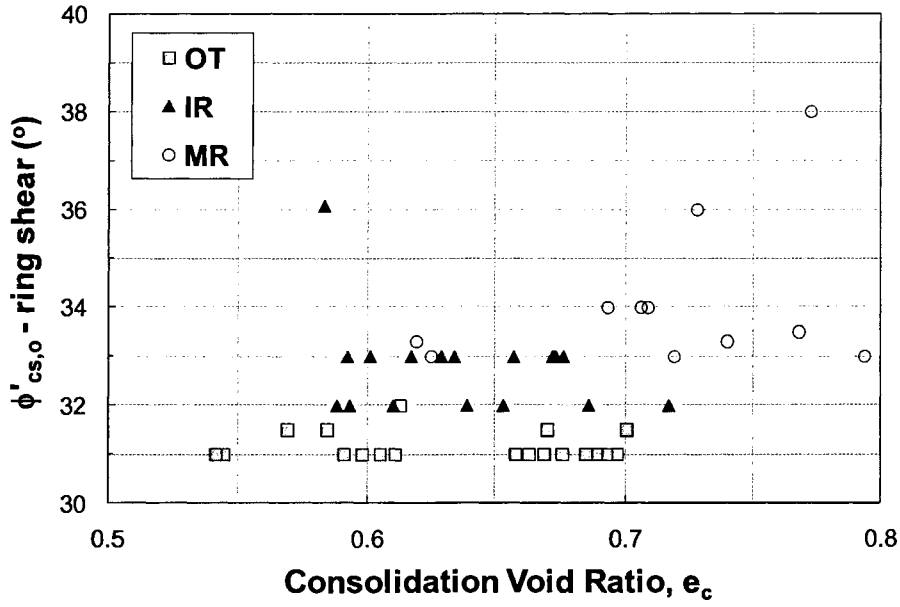

(a)

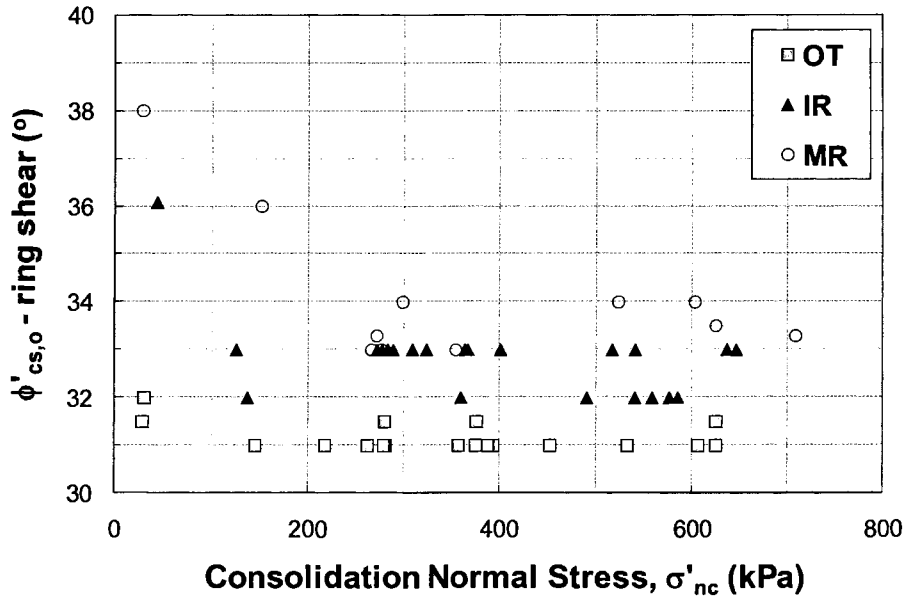

(b)

Figure 9.13: Variation of $\phi'_{cs,o}$ from RS tests with (a) e_c and (b) σ'_{nc}

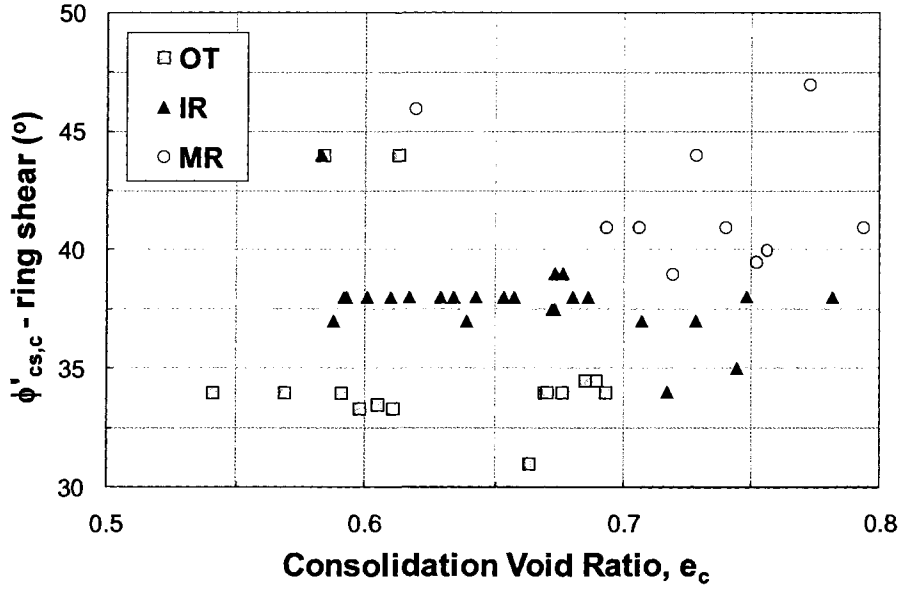

(a)

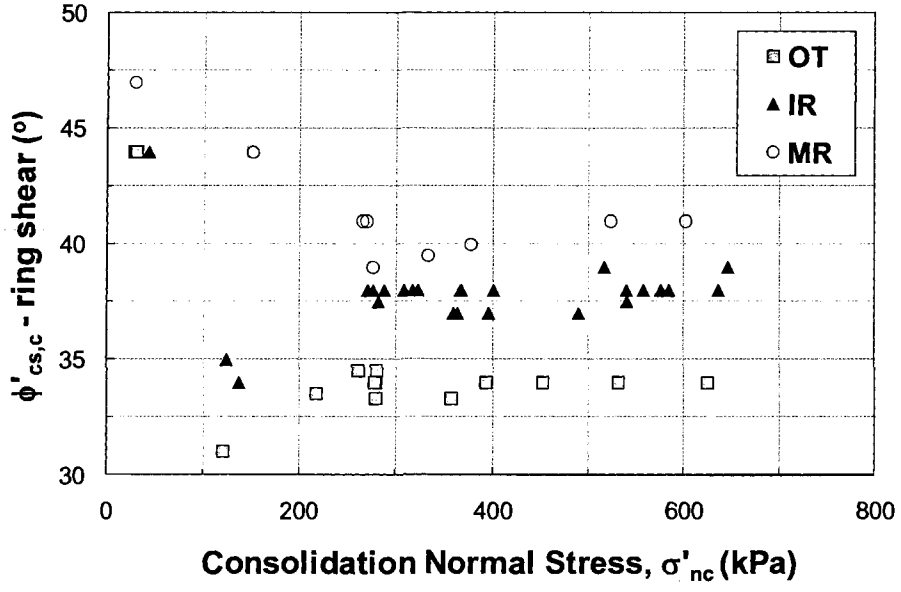

(b)

Figure 9.14: Variation of $\phi'_{cs,c}$ at very large shear displacements from the RS tests versus (a) e_c and (b) σ'_{nc}.

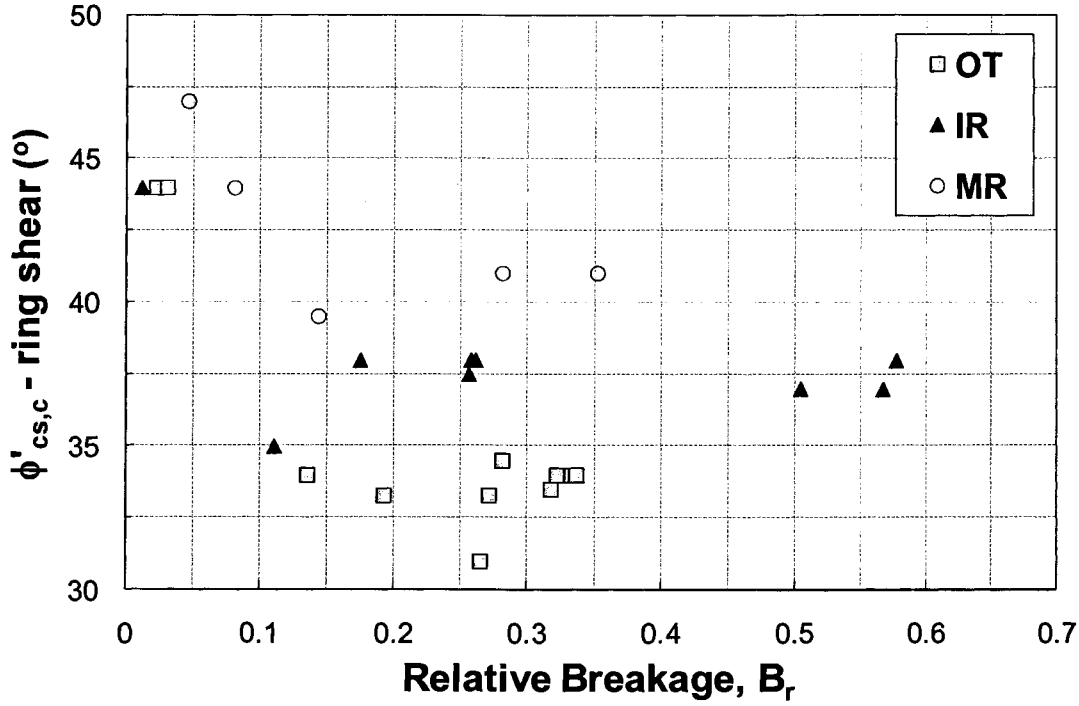

Figure 9.15 : Variation of $\phi'_{cs,c}$ at very large shear displacements from the RS tests versus B_r

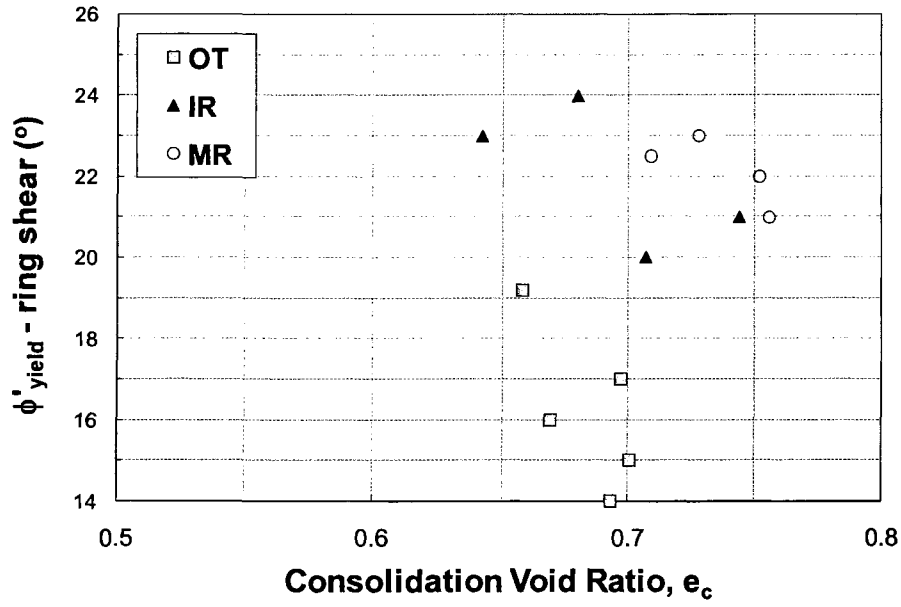

(a)

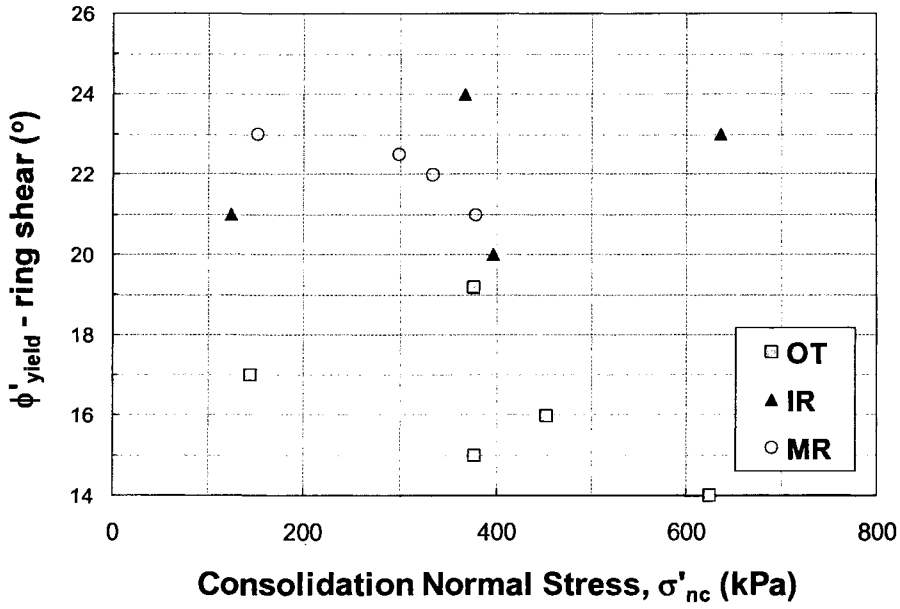

(b)

Figure 9.16: Variation of ϕ'_{yield} from the RS tests versus (a) e_c and (b) σ'_{nc}

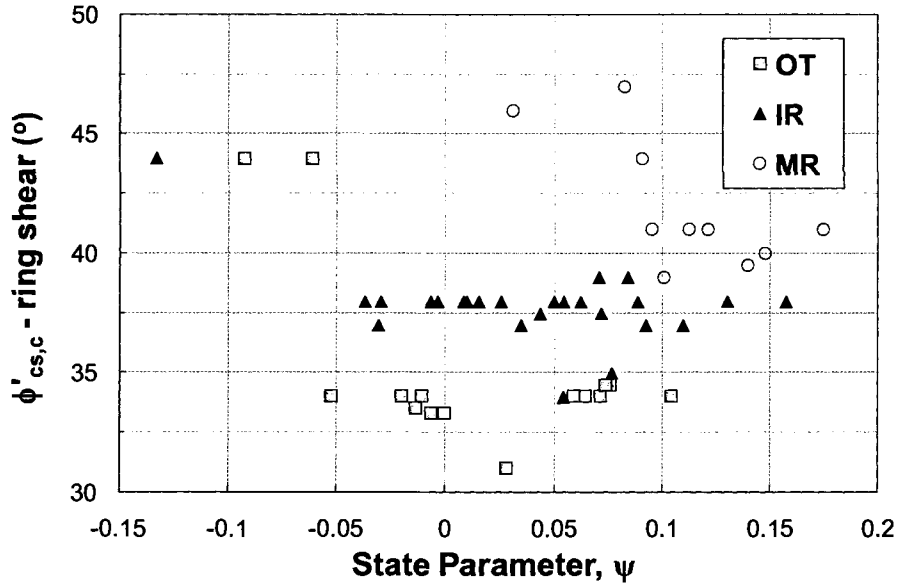

(a)

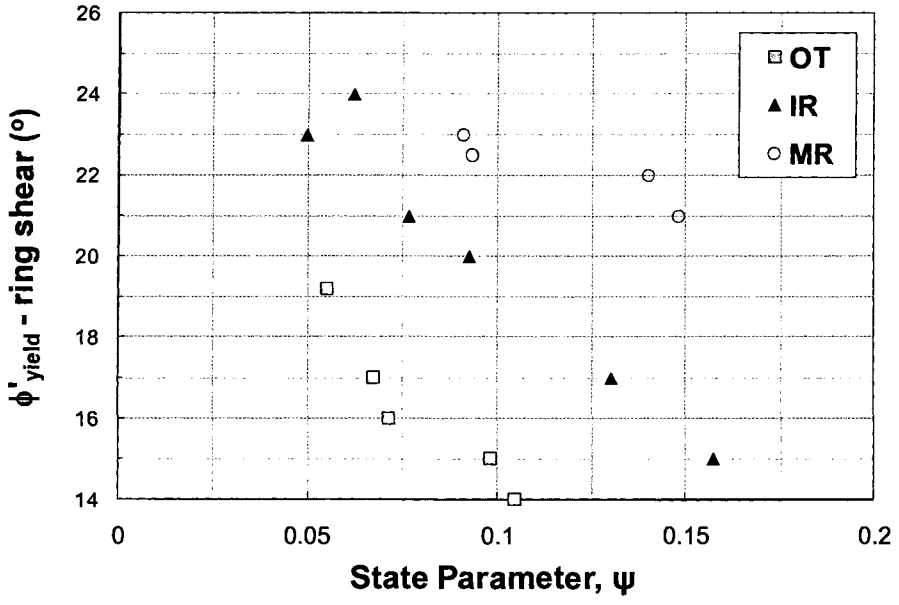

(b)

Figure 9.17: Variation of (a) $\phi'_{cs,c}$ and (b) ϕ'_{yield} obtained from RS tests with ψ

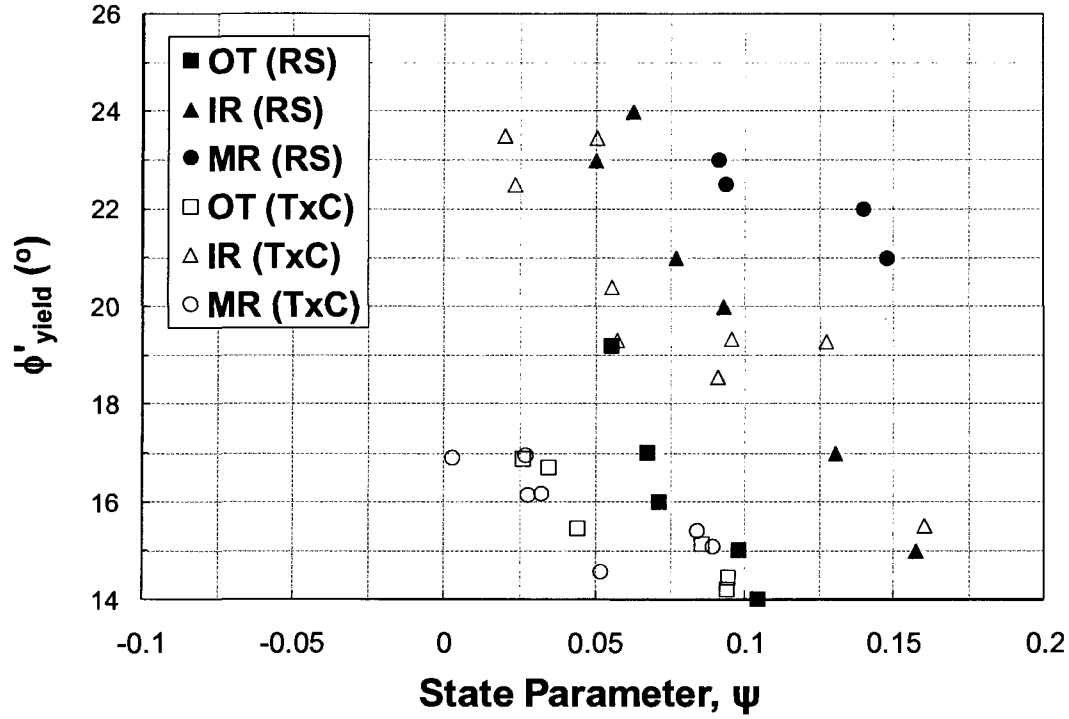

Figure 9.18: ϕ'_{yield} from TxC and RS tests versus state parameter

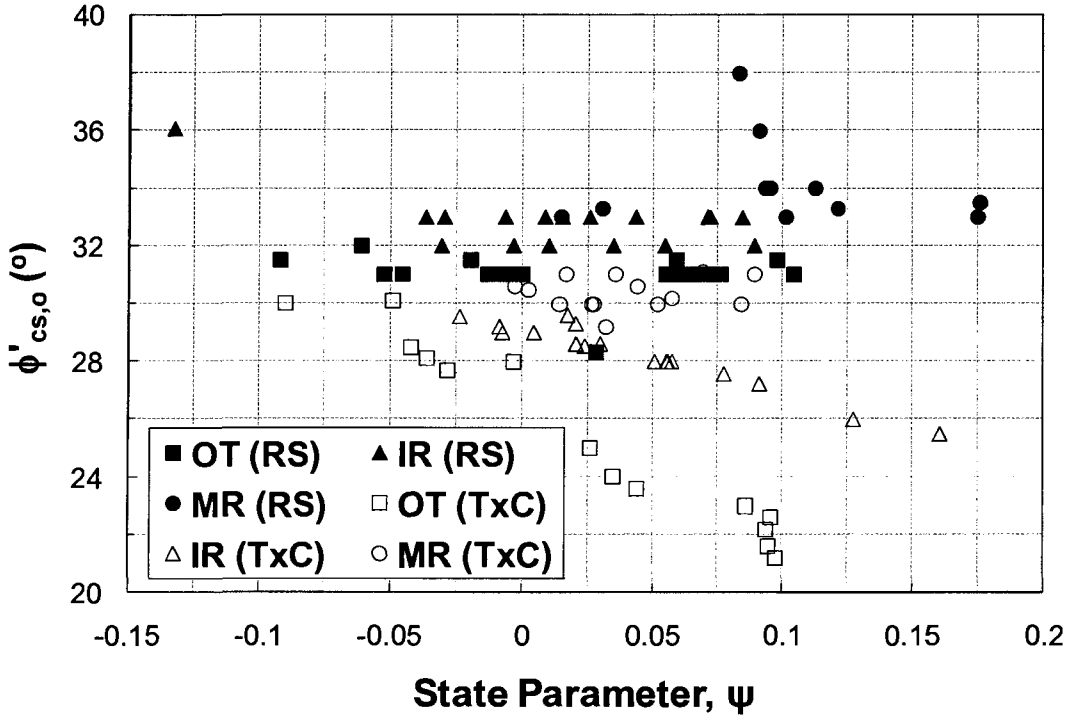

Figure 9.19: $\phi'_{cs,o}$ from TxC and RS tests versus state parameter

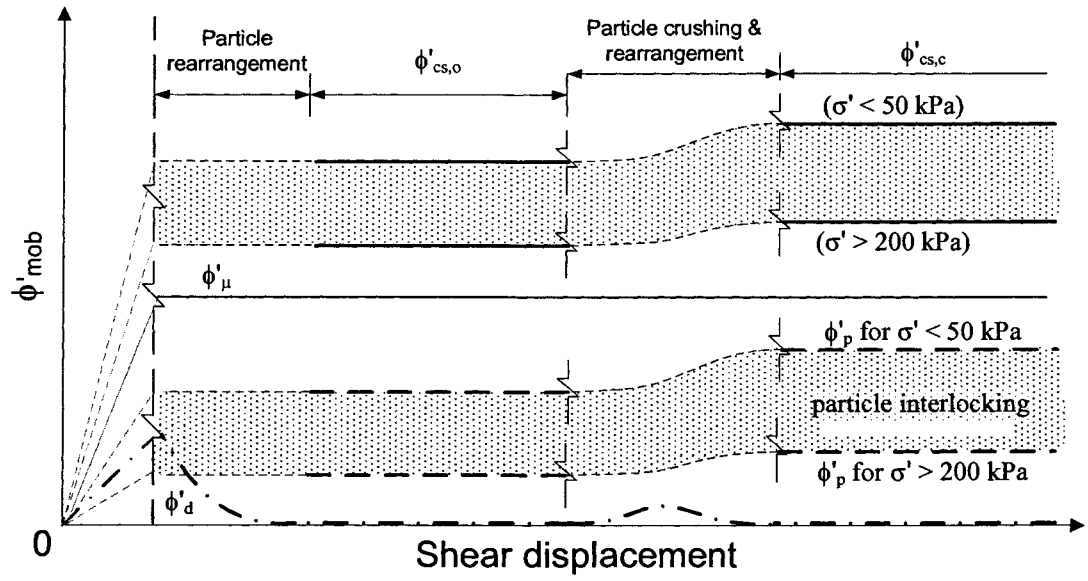

Figure 9.20: Contributions to the mobilized friction angle of granular materials

CHAPTER 10: YIELD AND LIQUEFIED STRENGTH RATIOS

10.1 INTRODUCTION

Researchers have normalized yield and critical shear strengths [s_u(yield) and s_u(critical), respectively] mobilized during undrained shearing of saturated, contractive soils to various consolidation stresses [mean (σ'_c), normal (σ'_{nc}), or vertical (σ'_{vc})] to define shear strength ratios. The resulting yield and critical strength ratios [s_u(yield)/σ'_c and s_u(critical)/σ'_c, respectively] have been studied by several researchers using both shear strengths measured in laboratory shear tests and back-calculated from field case histories. For example, Bjerrum et al. (1961) normalized undrained yield shear strengths of sands involved in Norwegian flow slides with respect to the consolidation stress (σ'_c) and found that the yield strength ratio decreased with increasing consolidation void ratio. Hanzawa (1980) measured undrained yield strengths of relatively undisturbed samples of Persian Gulf sand in isotropically-consolidated triaxial compression (TxC) tests, and found that s_u(yield)/σ'_c was approximately 0.31. Hanzawa also measured s_u(yield)/σ'_c = (0.11 – 0.27), (0.23 – 0.41), and (0.18 – 0.32) for Valgrinda, Sengenyama, and Kisarazu sands. Been and Jefferies (1985) performed TxC tests on reconstituted specimens of Kogyuk sand and measured s_u(yield)/σ'_c = 0.21 to 0.51, with the yield strength ratio increasing with decreasing consolidation void ratio. Similarly, Vaid and Sivathayalan (1996) measured s_u(critical)/σ'_c = 0.10 to 0.25 in direct simple shear (DSS) tests on Fraser River sand and found that critical strength ratio increased with decreasing void ratio.

Olson and Stark (2003a) collected a database of isotropically-consolidated TxC test results for 46 sands, silty sands, and sandy silts and found that s_u(yield)/σ'_c ranged from about 0.29 to 0.42 while s_u(critical)/σ'_c ranged from about 0.02 to 0.22. More recently, Olson and Mattson (2008) updated the database of the test results collected by Olson and Stark (2003a) (adding data from 13 new sands) and also added DSS, ring shear (RS), and triaxial extension (TxE) tests to the database.

Of course, there are difficulties with using laboratory tests to assess shear strengths mobilized in the field, including: (1) retrieving and preparing undisturbed samples of sand; (2) testing equipment limitations (e.g., limited displacement capacity, stress and

strain nonuniformities, variable cross-sectional dimensions in TxC and TxE, local volume changes, end cap and membrane restraining effects); and (3) inability of element tests to capture void redistribution, water layer formation, hydroplaning, or other scale effects. The limited displacement capacity of TxC and DSS tests suggests that potential particle rearrangement and particle breakage may be incomplete at the end of the test. These difficulties have led other researchers to evaluate yield and critical strength ratios measured in situ or back-calculated from field liquefaction flow failures (e.g., Castro and Troncoso 1987; Jefferies et al. 1990; Stark and Mesri 1992; Ishihara 1993; Baziar and Dobry 1995; Olson and Stark 2002, 2003b; Idriss and Boulanger 2006). Nevertheless, laboratory tests provide a useful framework for understanding field behavior, and the development of an improved RS device allows sands to be sheared to very large displacements and reach critical state.

In this chapter, the theoretical background for the yield and critical strength ratios are briefly reviewed and the results from very large displacement (> 20 m) RS tests on the three test sands are presented. Using the RS results, the factors that affect strength ratios are discussed and strength ratios mobilized in RS tests are compared to those measured in the parallel TxC tests.

10.2 DEFINITIONS AND THEORETICAL BACKGROUND

Figure 10.1 schematically illustrates (e – log σ') behavior of saturated, contractive sand during consolidation and undrained shear. Point A in Figure 10.1 represents a soil immediately after deposition at an initial void ratio of e_o and initial effective stress of σ'_o. As more soil is deposited, Point A consolidates to a void ratio of e_c at an effective stress of σ'_c (Point B). The line connecting points A and B is the normal compression line (NCL), which for many sandy soils can be approximated as a straight line in a semi-log diagram as follows:

$$e = N - C_C \log \sigma' \qquad \text{for} \qquad \sigma' < \sigma'_b \qquad 10.1$$

where N is the void ratio of the soil at an effective stress of one unit of stress, C_C is the NCL slope in e - log σ' space, and σ'_b is the stress after which considerable particle damage and crushing may happen [ranging from around 400 kPa for carbonate sands (Coop 1990) to about 8 MPa for quartz sands (Roberts and de Souza 1958; Hendron 1963; Pestana and Whittle 1995; Yet 1998; Nakata et al. 2001a, b; Chuhan et al. 2003)].

If sheared under undrained or constant volume conditions, the effective stress decreases as the initially loose soil tends to contract at a constant void ratio (e_c). During this process, the shearing resistance reaches a peak at Point C. The peak shear strength mobilized at Point C is termed the yield shear strength, s_u(yield), and represents the triggering condition for static liquefaction (Vaid and Chern 1983; Vasquez-Herrera et al. 1988; Konrad 1993; Terzaghi et al. 1996; Olson and Stark 2003a). Liquefaction is triggered when the stress state in the soil reaches or attempts to exceed the yield envelope under undrained conditions (Hanzawa et al. 1980; Olson 2006) as a result of a monotonic or cyclic loading under undrained conditions (Terzaghi et al. 1996).

After mobilizing s_u(yield), excess pore water pressure increases at a greater rate, and strain softening occurs. Strain-softening continues until the soil has exhausted its dilatancy potential and all net particle reorientation/rearrangement and breakage are complete. At this critical condition (Point D), the soil deforms with a constant volume, constant shear stress, and constant effective stress (Casagrande 1936; Taylor 1948). The shearing resistance mobilized at this condition is the critical shear strength, s_u(critical) (Terzaghi et al. 1996). In the field, void redistribution, water layer formation, soil mixing, and hydroplaning may occur, violating the constant volume condition. Therefore, Olson and Stark (2002) termed the shear strength mobilized in the field the liquefied shear strength, s_u(liq).

The locus of the void ratio and effective stress pairs at yield (C-C') and critical state (D-D') are termed yield state line (YSL) and critical state line (CSL), respectively (Figure 10.1). These lines can be expressed as below:

$$\text{YSL:} \quad e_y = \Gamma_y - \lambda_y \log \sigma' \qquad 10.2$$

$$\text{CSL:} \quad e_{cs} = \Gamma_{cs} - \lambda_{cs} \log \sigma' \qquad 10.3$$

where e_y and e_{cs} are the void ratios on the YSL and CSL, Γ_y and Γ_{cs} are the void ratios of the yield and critical state lines at an effective stress of one unit of stress, respectively, and λ_y and λ_{cs} are the slopes of the YSL and CSL in e-log σ' space, respectively. Note that YSL may be parallel to CSL (e.g., Terzaghi et al. 1996), however this may not be universally applicable to all sands.

In Figure 10.1, the difference between the consolidation void ratio (e_c) and the critical void ratio corresponding to the consolidation stress (σ'_c) is commonly referred to as the state parameter, ψ (Roscoe and Poorooshasb 1963; Wroth and Bassett 1965; Been and Jefferies 1985), and indicates soil behavior as a combined function of density and effective stress. For later comparisons, the term critical state parameter, ψ_{cs}, is used to represent the original definition of ψ. Negative values of ψ_{cs} generally correspond to dilative behavior while positive values of ψ_{cs} generally correspond to contractive response, with the severity of strain softening increasing with increasing ψ_{cs}. In addition to ψ_{cs} it is possible to define similar parameters that correspond to other states, such as the yield state parameter, ψ_y.

Olson and Stark (2002, 2003a) define yield and liquefied strength ratios, respectively, as the yield and liquefied shear strengths normalized by the initial vertical effective stress, σ'_{vo} (which equals the consolidation stress, σ'_{nc}, in RS tests and major principal consolidation stress, σ'_{1c}, in TxC tests). In the isotropically consolidated (i.e., equal all-around consolidation) TxC tests performed in this chapter, the mean consolidation [$\sigma'_c = (\sigma'_{1c} + \sigma'_{2c} + \sigma'_{3c})/3$, and σ'_{2c} and σ'_{3c} are the intermediate and minor principal consolidation stresses], normal consolidation (σ'_{nc}), and major principal consolidation stresses are the same, and are simply termed the consolidation stress, σ'_c. Using ψ_{cs}, an expression can be derived for strength ratio at critical state as follows:

$$\psi_{cs} = e_c - e_{cs} = \left(\Gamma_{cs} - \lambda_{cs} \log \sigma'_{cs}\right) - \left(\Gamma_{cs} - \lambda_{cs} \log \sigma'_c\right) = \lambda_{cs} \log \frac{\sigma'_c}{\sigma'_{cs}} \qquad 10.4$$

where σ'_{cs} is the effective stress on the CSL corresponding to e_c. Values of ψ_y can be defined similarly. Rearranging Equation 10.4 we get:

$$\sigma'_c = \sigma'_{cs} 10^{\psi_{cs}/\lambda_{cs}} \qquad 10.5$$

For the RS tests discussed later, the stresses at failure (i.e., at the critical state) are the critical shear strength, s_u(critical), and the effective normal stress, σ'_n. The effective friction angle in RS tests can be defined in terms of these stresses as (similar to Equation 3.6):

$$\phi'_{cs} = \tan^{-1}\left(\frac{s_u(critical)}{\sigma'_{cs}}\right) \qquad 10.6$$

And the strength ratio corresponding to the critical state in the RS tests would become:

$$\frac{s_u(critical)}{\sigma'_c} = 10^{-\psi_{cs}/\lambda_{cs}} \tan\phi'_{cs} \qquad 10.7$$

Similar to the RS test, s_u(critical)/σ'_c is defined in TxC as:

$$s_u(critical) = \frac{q_{cs}}{2}\cos\phi'_{cs} \qquad 10.8$$

where $q_{cs} = (\sigma'_1 - \sigma'_3)_{cs}$ and ϕ'_{cs} is critical friction angle defined as (similar to Equation 4.16):

$$\phi'_{cs} = \sin\left(\frac{3\dfrac{q}{\sigma'_{mean}}}{6+\dfrac{q}{\sigma'_{mean}}}\right)_{cs} \qquad 10.9$$

Therefore:

$$\frac{s_u(critical)}{\sigma'_c} = 10^{-\psi_{cs}/\lambda_{cs}} \frac{1.5\sin 2\phi'_{cs}}{3-\sin\phi'_{cs}} \qquad 10.10$$

Although Equations 10.4 through 10.10 were defined at the critical state, these equations can be rewritten for any general state (indicated by subscript "s") parameter, as illustrated below:

$$\psi_s = e_c - e_s = (N - C_c \log\sigma'_c) - (\Gamma_s - \lambda_s \log\sigma'_c) = (N-\Gamma_s) - (C_c - \lambda)\log\sigma'_c \qquad 10.11$$

Then the general equation for s_u/σ'_c at a particular state (including yield and critical states) becomes:

$$\frac{S_u}{\sigma'_c} = 10^{-\psi_s/\lambda_s} f(\phi'_s) = 10^{\left[\frac{(C_c-\lambda_s)}{\lambda_s}\log\sigma'_c - \frac{(N-\Gamma_s)}{\lambda_s}\right]} f(\phi'_s) \qquad 10.12$$

where $f(\phi'_s)$ is a function of the effective stress friction angle at that particular state (ϕ'_s) and can follow the forms in Equations 10.6 and 10.9 when measured in RS or TxC, respectively. Equation 10.12 shows that the shear strength ratio decreases with increasing state parameter and decreasing ϕ'_s. Rutledge (1947) first normalized the undrained shear strength of clays to the preconsolidation pressure and since then a number of researchers have normalized the undrained shear strength of normally consolidated, unaged, and uncemented sandy soils (e.g., Roscoe and Poorooshasb 1963; Wroth and Bassett 1965; Been and Jefferies 1985; Stark and Mesri 1992; Ishihara 1993; Pillai and Salgado 1994; Baziar and Dobry 1995; Fear and Robertson 1995; Terzaghi et al. 1996; Vaid and Sivathayalan 1996; Olson and Stark 2003b; Jefferies and Been 2006; Olson and Mattson 2008).

As discussed in Chapter 9 the critical state friction angle, ϕ'_{cs} for both critical state of the original sand gradation (CS_o) and critical state of the crushed sand gradation (CS_c), decreases with increasing σ'_n until σ'_n approaches 100 – 200 kPa, and thereafter remains constant. Average friction angles of 31°, 32°, and 34° corresponding to the CS_o were obtained for OT, IR and MR sands, respectively, while larger friction angles of 34°, 38°, and 41° were obtained at the CS_c (after complete particle reorientation and crushing) for OT, IR, and MR sands, respectively. Thus at either critical states (CS_o and CS_c), the friction angle would not vary and change the strength ratio. However, before reaching the critical state, ϕ'_s varies depending on the severity of particle rearrangement and crushing. Particle rearrangement increases the density (i.e. decreases void ratio) and thus increases ϕ'_s and particle crushing would increase ϕ'_s by producing more angular grains. These effects would all depend on the amount of shear displacement, stress, and initial density of the sand deposit. For example, the friction angle at yield was observed to vary from 14° to 19° for OT sand. This agrees with the range of yield friction angles for DSS and RS tests reported by Olson and Mattson (2008), but such a variation in the yield friction angle for example for test MTIRCV18 would theoretically lead to a change of 38% in $s_u(\text{yield})/\sigma'_c$ (assuming $\psi_y = 0.078$ in RS test MTIRCV18, and $\lambda_y = 0.081$ in Eq. 10.12).

10.3 PARALLELISM OF NCL AND CSL

As can be deduced from Equation 10.12 and discussed by others (Finn 1998; Olson 2001; Jefferies and Been 2006), if the NCL is parallel to the CSL (i.e., ψ_{cs} is independent of consolidation stress), the critical strength ratio becomes constant since ϕ'_{cs} is constant. The same is true for the yield strength ratio if the NCL is parallel to YSL. For nearly all clays, it is reasonable to assume that the NCL and CSL are roughly parallel (Rutledge 1947). As a result, a given normally consolidated clay deposit will exhibit a constant ψ and s_u/σ'_{vo} independent of σ'_{vo} (Terzaghi et al. 1996). Of course, sand can be deposited in numerous ways, and the depositional method and energy affects the NCL slope and intercept, N (i.e., a dense sand typically has smaller values of C_c and N than an identical loose sand). Olson and Stark (2002) postulated that for sands loose enough to be

susceptible to flow liquefaction, the NCL is likely to be roughly parallel to the CSL, particularly for silty sands with fines contents of 12% or more.

Figure 10.2 through Figure 10.4 present the CSLs and NCLs for OT, IR, and MR sands tested in this study. Both the CSL of the original gradation prior to crushing (CSL_o) and the CSL after crushing is complete (CSL_c) as defined by in Chapter 8 are shown in the figures. NCLs of the original and crushed sands (NCL_o and NCL_c, respectively) were defined by oedometer tests following ASTM D2435 standard procedure. As illustrated in these figures, the NCL_o slope is slightly smaller than the CSL_o slope for the relatively incompressible OT and IR sands, and parallel to CSL_o in the compressible MR sand. However, as shearing continues and the sand particles crush, the state lines become steeper and the difference between the slopes of NCL and state lines becomes larger until each sand reaches its CSL_c. However, Coop (1990) performed RS tests on carbonate sands (which are very susceptible to crushing) and showed that the CSL_c ($e = -0.775\log(\sigma') + 3.372$) and NCL_c ($e = -0.771\log(\sigma') + 4.800$) were parallel. This occurred because the carbonate sands easily crushed during both compression and shear leading to steep NCL_c and CSL_c.

In addition to large displacements, very large confining stresses can also contribute to parallel compression and critical state lines (Yamamuro and Lade 1996; Verdugo and Ishihara 1996). For example, Yamamuro and Lade (1996) tested Cambria sand at very large stresses where considerable particle crushing happened. Their tests included isotropic consolidation and undrained TxC tests. Although they were limited by the shear displacement capacity of the triaxial device, but they found that at very large confining stresses (> 10 MPa) the NCL_c would become considerably steeper than NCL_o and eventually parallel to CSL_c obtained from TxC tests.

Figure 10.5 summarizes these data and compares their slopes to data collected by Olson (2001) and that for Duncan Dam analyzed by Olson (2006). As reported by some investigators (e.g., Verdugo and Ishihara 1996; Leong et al. 2000), NCL_o and CSL_o are not parallel for relatively incompressible clean sands. However, for compressible sandy soils, such as sands with compressible mineralogies (e.g., carbonate sands, micaceous sands), silty sands (with more than about 12% fines content), sandy silts, silts, and tailings sands, the CSL_o is approximately parallel to the NCL_o when the sand is deposited

loosely (Olson 2001). In addition, many of the sands involved in well-documented liquefaction flow failures contained a significant percentage of non-siliceous and even clayey fines. For example, only six of 33 flow failure case histories documented by Olson and Stark (2002) involved clean sands with less than 5% fines, and 20 of 33 cases involved sandy soils with more than 12% fines. Table 10.1 provides some details regarding the mineralogy of the soils involved in several liquefaction flow failures. The compressible mineralogy in these cases (similar to the MR sand) results in a steeper NCL_o that is more likely to be parallel to the CSL_o. Besides sand particle mineralogy and fines content, sand particle shape also affects the slopes of NCL (Mesri and Vardhanabhuti, *in press*) and CSL (Poulos 1981).

10.4 YIELD STRENGTH RATIO

The yield strength ratio can be used to estimate the undrained shear strength that is available prior to the initiation of undrained instability and liquefaction (Olson and Stark 2003a). Using data back-calculated from liquefaction case histories Olson (2001) proposed relationships between $s_u(yield)/\sigma'_{vo}$ and overburden-stress normalized cone penetration test (CPT) tip resistance and standard penetration test (SPT) blow count to evaluate the triggering of liquefaction in contractive sandy soils. This concept has been found universally applicable for sands (Olson and Stark 2003a). Figure 10.6 presents $s_u(yield)/\sigma'_c$ measured in RS and TxC for the OT, IR, and MR sands. Only $s_u(yield)$ from fully contractive specimens are included in the figure. The critical state parameters for the RS and TxC specimens, ψ_{cs}, are based on CSL_o. Table 10.2 summarizes the ranges of $s_u(yield)/\sigma'_c$ for each of the sands. As illustrated in Figure 10.6, $s_u(yield)/\sigma'_c$ decreases with increasing state parameter for each sand. And at similar state parameters, $s_u(yield)/\sigma'_c$ is larger in the plane strain RS tests possibly because of the larger intermediate principal stress mobilized in these tests (e.g., Cornforth 1964; Ko and Scott 1967; Green and Bishop 1969; Miyamori 1976; Reades and Green 1976; Yamada and Ishihara 1979; Ergun 1981; Ochiai and Lade 1983; Sayao and Vaid 1996).

10.5 CRITICAL STRENGTH RATIO

Figure 10.7 through Figure 10.9 present $s_u(critical)/\sigma'_c$ measured in the RS and TxC tests on OT, IR and MR sands, respectively. The RS data include critical strength ratios corresponding to the original (CS_o) and crushed gradations (CS_c at end of shearing), but ψ_{cs} corresponds to CSL_o. Only critical strengths measured in fully contractive TxC and RS specimens are plotted as CS_o. Table 10.2 summarizes the ranges of $s_u(critical)/\sigma'_c$ measured for the three sands based on CS_o and CS_c measured in RS and CS_o measured in TxC. The constrained radial deformation and thus the larger intermediate principal stress mobilized in the plane strain RS tests was possibly the reason (e.g., Cornforth 1964; Sutherland and Mesdary 1969; Stroud 1971; Haruyama 1981; Lade 1984; Lam and Tatsuoka 1988; Sayao and Vaid 1996) for the larger $s_u(critical)/\sigma'_c$ from the RS tests (at CS_o) in comparison to the $s_u(critical)/\sigma'_c$ mobilized in the TxC shear tests at similar ψ_{cs}.

As illustrated in Figure 10.7 through Figure 10.9, $s_u(critical)/\sigma'_c$ decreases with increasing state parameter. As the displacement continues and the sands shear toward the CS_c, the variability in the trends decreases considerably. The reason for this is that although both the NCL and CSL slopes increase, the ratio of ψ_{cs}/λ_{cs} increases and $s_u(critical)/\sigma'_c$ decreases as described in Equation 10.10. Also note that initially dilative RS specimens ($\psi_{cs} < 0$) mobilized $s_u(critical)/\sigma'_c$ values consistent with initially contractive specimens at CS_c, indicating that CSL_c was reached through particle crushing-induced contraction.

10.6 COMPARISON WITH PREVIOUS LABORATORY AND FIELD OBSERVATIONS

Figure 10.10 and Figure 10.11 compare yield and critical strength ratios measured in this study with the data compiled by Olson and Mattson (2008), and Table 10.2 includes the Olson and Mattson (2008) data ranges. These comparisons confirm that the yield and critical strength ratios are consistent with yield and critical strengths measured in previous laboratory studies. The $s_u(yield)/\sigma'_c$ values measured in TxC fall near or at the bottom of the range of previously measured data as expected given the very loose relative densities required for eliciting a contractive response in OT and IR specimens.

Olson (2001) backcalculated yield and liquefied strength ratios from liquefaction flow failure case histories and found that $s_u(yield)/\sigma'_c$ mobilized during static liquefaction flow failures varied from about 0.23 to 0.31. These data are included in Table 10.2. The upper bound (0.31) of the field $s_u(yield)/\sigma'_c$ agrees well with the laboratory shear data, but the lower bound (0.23) is larger than the lower bound $s_u(yield)/\sigma'_c$ of the laboratory data. This is because of the extremely loose moist tamped specimens (such as TxC test MTOTUN42 with a $Dr_c = -41\%$) which were tested to obtain contractive response. These very low Dr values are lower than what could occur in field settings, thus the laboratory yield strength ratios would be lower than the field data for these tests. As illustrated in Figure 10.11 and Table 10.2, the critical strength ratios mobilized in the RS and TxC compression tests performed during this study agree closely with the ranges of $s_u(critical)/\sigma'_c$ mobilized in the DSS/RS and TxC tests compiled by Olson and Mattson (2008).

The $s_u(liq)/\sigma'_c$ from liquefaction field case histories (0.05 – 0.12) fall within the range of $s_u(critical)/\sigma'_c$ from TxC and RS tests at CS_o. This is because the soil in most of the back-calculated field cases (Olson 2001) were loose [$(N_1)_{60} < 5$] and upon liquefaction reached CS_o without significant particle crushing. However, $s_u(critical)/\sigma'_c$ from RS tests at CS_c is smaller than $s_u(critical)/\sigma'_c$ at CS_o and closer to the lower bound of $s_u(liq)/\sigma'_c$ from liquefaction field case histories of Olson (2001). This is because particle crushing occurred (particularly in dense specimens at very large shear displacements), further reducing $s_u(critical)$ in the RS experiments. Similar behavior has been observed in some other field flow failures. For example, particle crushing occurred in the shear zone of the Nikawa landslide that was triggered by the 1995 Hyogoken-Nambu earthquake (Sassa 1995). The soil in the shear zone of this landslide was a partially saturated mass and medium dense to very dense [$(N_1)_{60} \approx 14 - 80$] deposit of sand to silty sand, not readily susceptible to mass liquefaction (Gerolymos and Gazeras 2007). However, grain crushing generated excess pore water pressure in the shear zone of this landslide and resulted in a runout of more than 100 m (Sassa et al. 1996). Also, as discussed earlier in Chapter 7, field observations confirmed that grain crushing happened in the sliding zone of the Hiegaesi Landslide located in southern region of Fukushima Prefecture, Japan. This long runout landslide was triggered by the heavy rainfalls in August 1998 (Wang et al. 2002).

The Higashi Takezawa and the Terano landslides which were both triggered by the 2004 Niigata earthquake (M6.8) involved particle crushing as well. These landslides contained stiff silt layers overlain by sand. The sand was a marine deposit from the Tertiary period and shaking under a large overburden stress facilitated grain crushing, thereby generating excess water pressure (Sassa et al. 2005). These cases and the laboratory RS test results of this study illustrate that s_u(critical or liq)/σ'_{vo} may be inversely related to shear displacement in addition to being inversely related to state parameter (Olson and Stark 2003b).

Lastly, other phenomena such as void ratio redistribution, nonuniformities of pore-water pressure, drainage, and water layers and/or hydroplaning likely occur in some model and centrifuge tests (e.g. Liu and Qiao 1984; Fiegel and Kutter 1994; Kokusho 2000; Kulasingam et al. 2004) and may occur during some flow failures (e.g. Seed et al. 1975; Marcuson et al. 1979; Ishihara 1984; Whitman 1985; Seed 1987; Stark and Mesri 1992; Harder and Stewart 1996). These factors are implicitly incorporated into liquefied shear strengths and strength ratio calculations back-calculated from liquefaction flow failure case histories (Seed 1987; Olson and Stark 2002). Although some of these phenomena may occur to some extent in element scale laboratory studies (e.g. Riemer 1992; Finno et al. 1996; Ayoubian and Robertson 1998), their possiblty was not quantified or studied in the laboratory element tests of this study. More research is needed to quantify these effects and their potential impact on field and laboratory studies of liquefied (or critical) shear strength.

10.7 SUMMARY AND CONCLUSION

In this chapter, s_u/σ'_c was defined using simple mathematical definitions of the compression and shearing behavior of sands. The resulting relationship indicated that not only the slopes of the NCL and CSL, but also their intercepts with the void ratio axis (at $\sigma' = 1$) and ϕ' affect the values of s_u/σ'_c. However, for a particular deposit a s_u/σ'_c independent of the initial stress and void ratio is obtained only if NCL and CSL are parallel. This would happen in compressible sands (silty or softer mineralogy) which constitute many of the sands involved in well-documented liquefaction flow failures. However, if particle crushing takes place as shearing continues, the state line becomes

steeper and the difference between the slopes of NCL and state line increases. This causes the s_u/σ'_c and its range of variability to decrease particularly at large shear displacements at which particle rearrangement and crushing have been largely exhausted.

The TxC and RS tests show that $s_u(\text{yield})/\sigma'_c$ and $s_u(\text{critical})/\sigma'_c$ both decrease with increasing state parameter with the later also decreasing with larger shear displacements. The $s_u(\text{yield})/\sigma'_c$ from TxC (0.16 – 0.32) and RS (0.15 – 0.31) tests are close to those from earlier laboratory experiments on loose sands and with the back-calculated $s_u(\text{yield})/\sigma'_c$ from liquefaction flow failures. Similarly the $s_u(\text{critical})/\sigma'_c$ from TxC tests (0.01 – 0.23) and RS (at CS_o) tests (0.04 – 0.21) on loose specimens agree very well with the range of values from earlier laboratory experiments on loose sands and with the back-calculated $s_u(\text{liq})/\sigma'_c$ from liquefaction failures of loose sand deposits. This indicates that in loose sands flow liquefaction likely occurs without significant particle crushing and a critical state is reached mostly through particle rearrangement and reorientation.

However, $s_u(\text{critical})/\sigma'_c$ mobilized in specimens that experienced severe particle damage and crushing (particularly in dense sands) has a narrower range and is, on average, smaller than those mobilized at the critical state of loose sands without particle crushing. This shows that liquefaction flow may happen in dense sands mainly through particle damage and crushing, i.e., sliding surface liquefaction. The relatively small $s_u(\text{critical})/\sigma'_c$ may partly explain the rapid and large runout (> 100 m) of some relatively dense field deposits triggered by a large earthquake, heavy rainfall or snowmelt (Sassa 1995; Sassa 2000; Wang et al. 2002). This also implies that a large s_u/σ'_c determined at the end of a TxC test on a dilative sand may not always be conservative, but only a RS device can achieve such large displacements and capture the entire shear strength – displacement behavior of the sand.

10.8 TABLES

Table 10.1: Mineralogical compositions of soils involved in some liquefaction flow failures

Case history	Mineralogy	Reference
Fraser River Delta slides	40% quartz, 11% feldspar, 45% rock fragments, 4% other minerals.	Chillarage et al. (1997)
Rocky Mountain Coal Mine Waste Dumps	50 to 70% carbonaceous shale, 20 to 40% siltstone, 0 to 20% sandstone, 0 to 10% coal, and some other minerals.	Dawson (1994)
La Marquesa dam	Silty-clayey sands weathered from granodiorite (biotite mica and hornblende)	de Alba et al. (1988)
La Palma dam	Silty-clayey sands weathered from granodiorite (biotite mica and hornblende)	de Alba et al. (1988)
Calaveras dam	Mainly non-siliceous materials cemented with calcium carbonate and calcium sulphate	Hazen (1918)
Jamuna bridge	Micaceous fine sand with FC = 2 to 10% and mica content of 15 to 30%	Yoshimine et al. (1999)
Nerlerk berm	Fine sand with 84% quartz, 13% feldspar plagioclase, 1% other minerals	Jefferies and Been (2006)

Table 10.2: $s_u(yield)/\sigma'_c$ and $s_u(critical)/\sigma'_c$ from RS (or DSS) and TxC tests

Parameter	Sand/Reference	TxC	RS	Field case histories (Olson 2001)
$s_u(yield)/\sigma'_c$	OT Sand	0.16 – 0.25	0.18 – 0.27	0.23 – 0.31
	IR Sand	0.19 – 0.32	0.15 – 0.28	
	MR Sand	0.17 – 0.19	0.18 – 0.31	
	Olson & Mattson (2008)	0.18 – 0.43	0.13 – 0.29*	

State		CS_o	CS_o	CS_c	
s_u(critical or liq)/σ'_c	OT Sand	0.01 – 0.06	0.04 – 0.11	0.01 – 0.07	0.05 – 0.12
	IR Sand	0.02 – 0.23	0.04 – 0.21	0.01 – 0.04	
	MR Sand	0.08 – 0.11	0.11 – 0.21	0.02 – 0.06	
	Olson & Mattson (2008)	0.01 – 0.32	0.01 – 0.22*		

* From RS (Wang and Sassa 2002) and DSS (Riemer 1992; Yoshimine 1996; Yoshimine et al. 1999) tests.

10.9 FIGURES

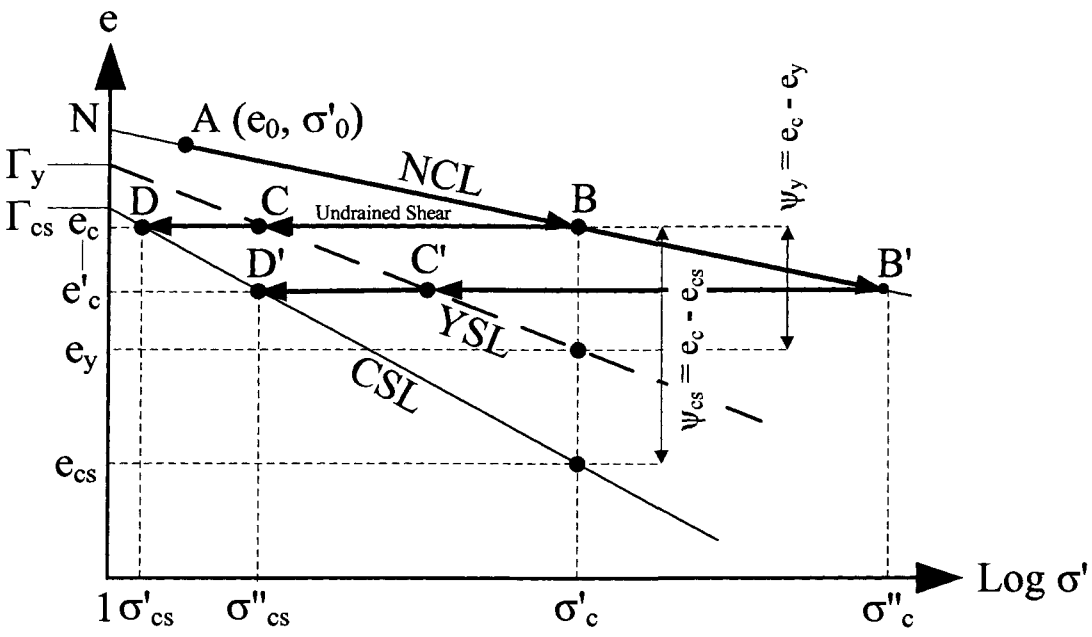

Figure 10.1: Schematic one-dimensional normal compression line (NCL), yield state line (YSL), and critical state line (CSL) in void ratio – log effective stress (e – log σ') space

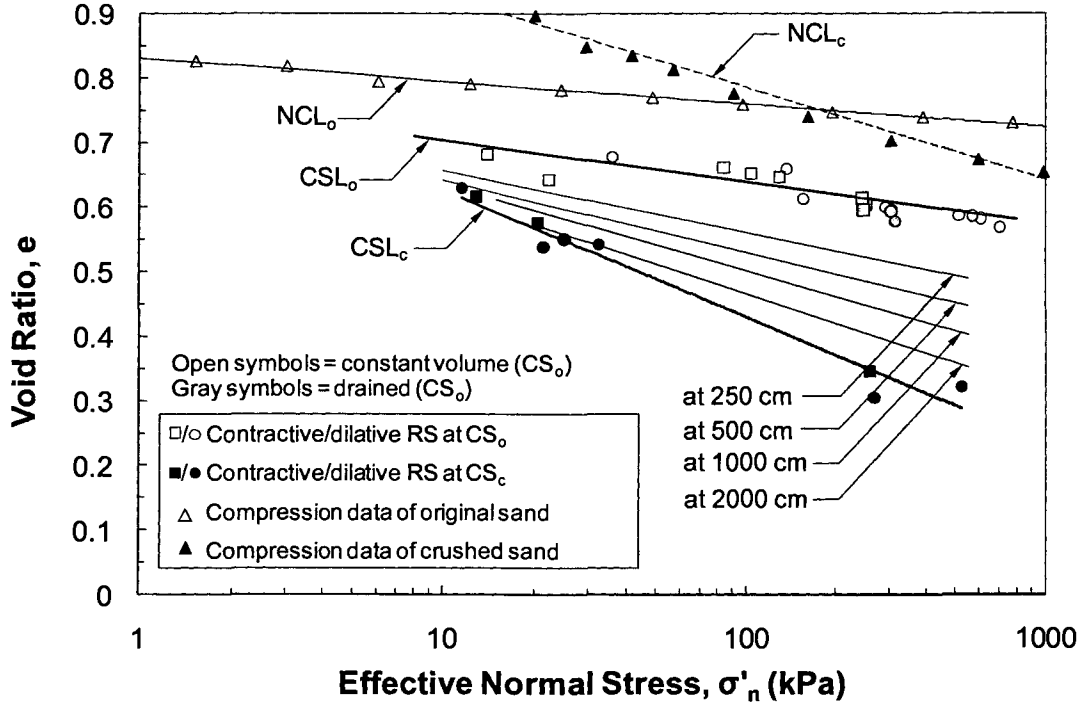

Figure 10.2: CSL and NCL of the original and crushed OT sand

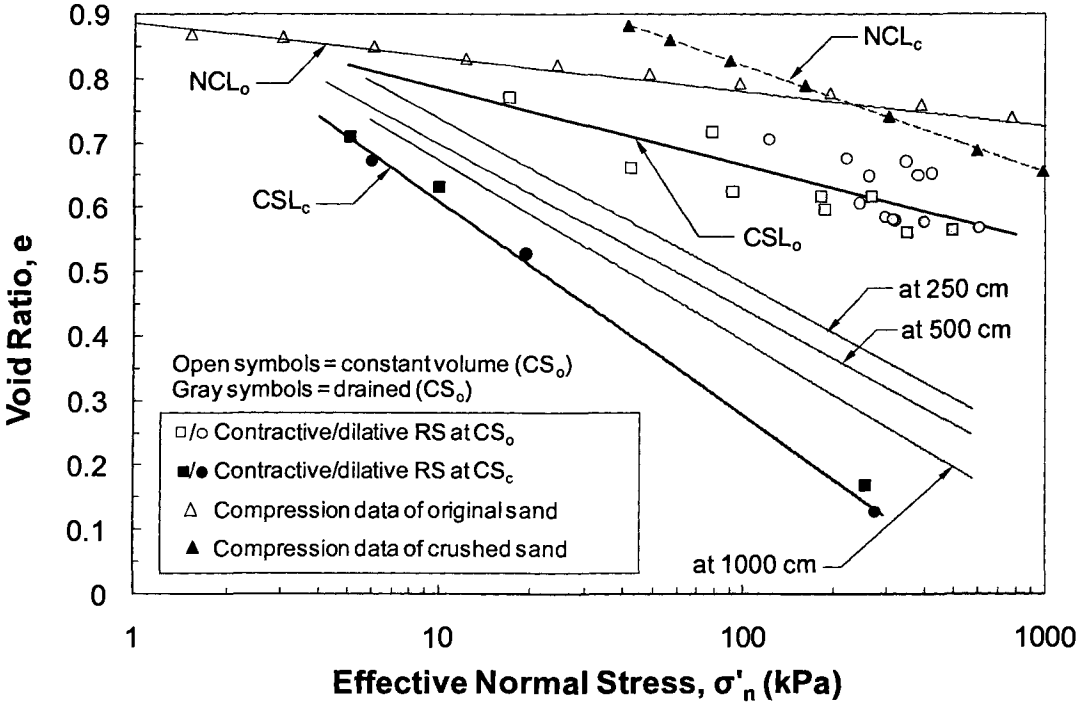

Figure 10.3: CSL and NCL of the original and crushed IR sand

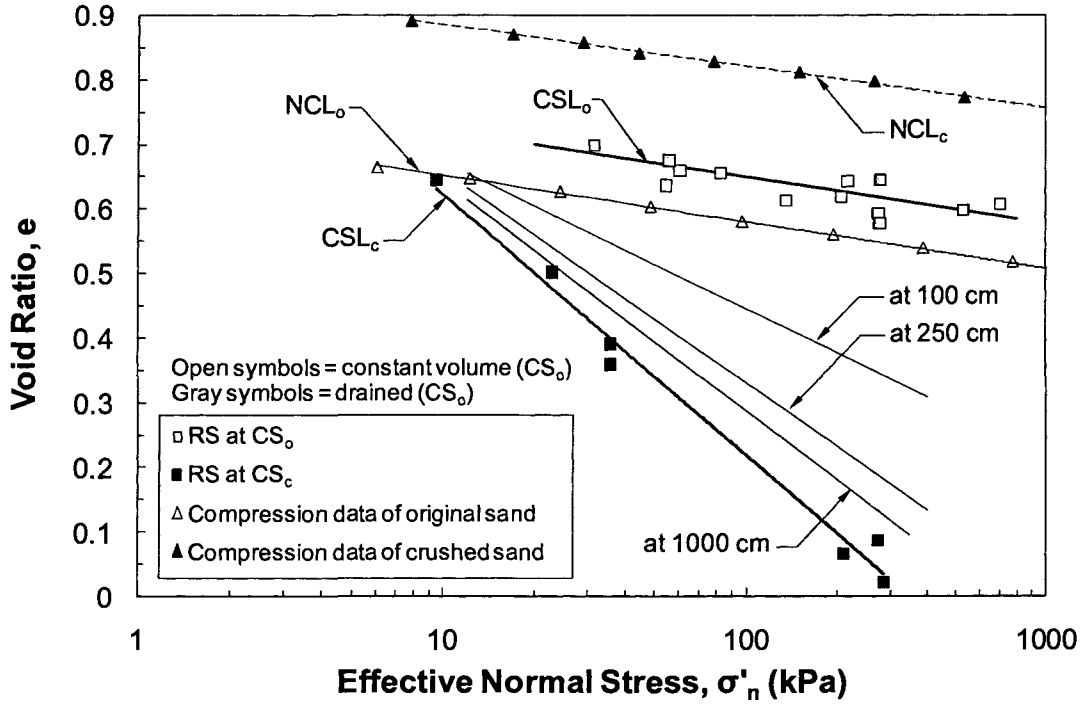

Figure 10.4: CSL and NCL of the original and crushed MR sand

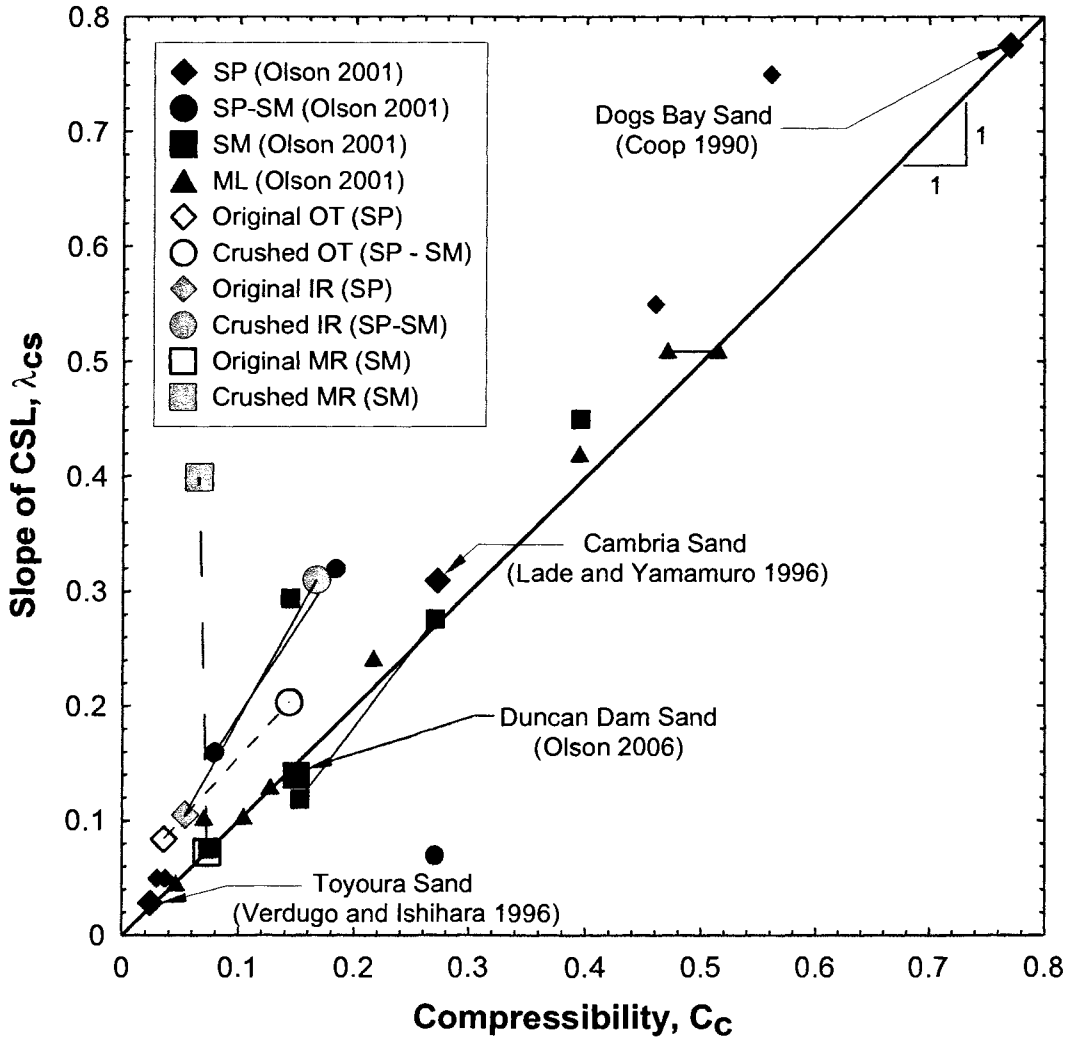

Figure 10.5: Comparison of compressibility and CSL slopes for OT, IR, and MR sands from this study, Dogs Bay Carbonate sand (Coop 1990), Cambria sand (Lade and Yamamuro 1996), Toyoura sand (Verdugo and Ishihara 1996), Duncan Dam sand (Olson 2006) and sands in Olson (2001) laboratory database. SP, SP-SM, SM, and ML are soil type descriptors as defined in the Unified Soil Classification System (USCS; ASTM D2487).

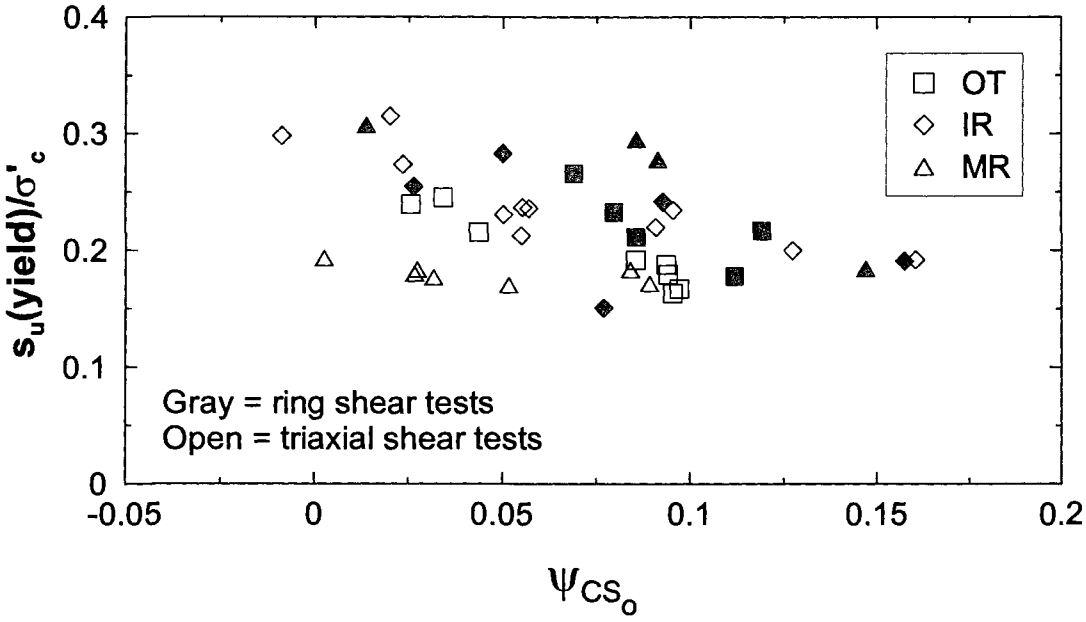

Figure 10.6: Yield strength ratios from contractive TxC and RS tests

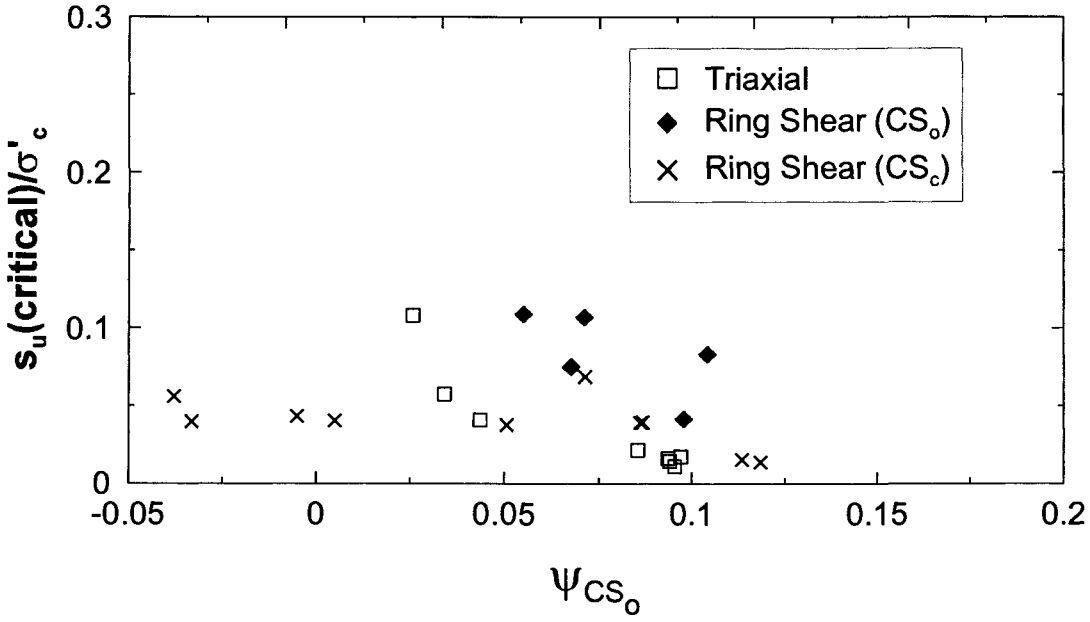

Figure 10.7: Critical strength ratios from fully contractive TxC, fully contractive RS (for CS_o and CS_c), and initially dilative (for CS_c) RS tests on OT sand

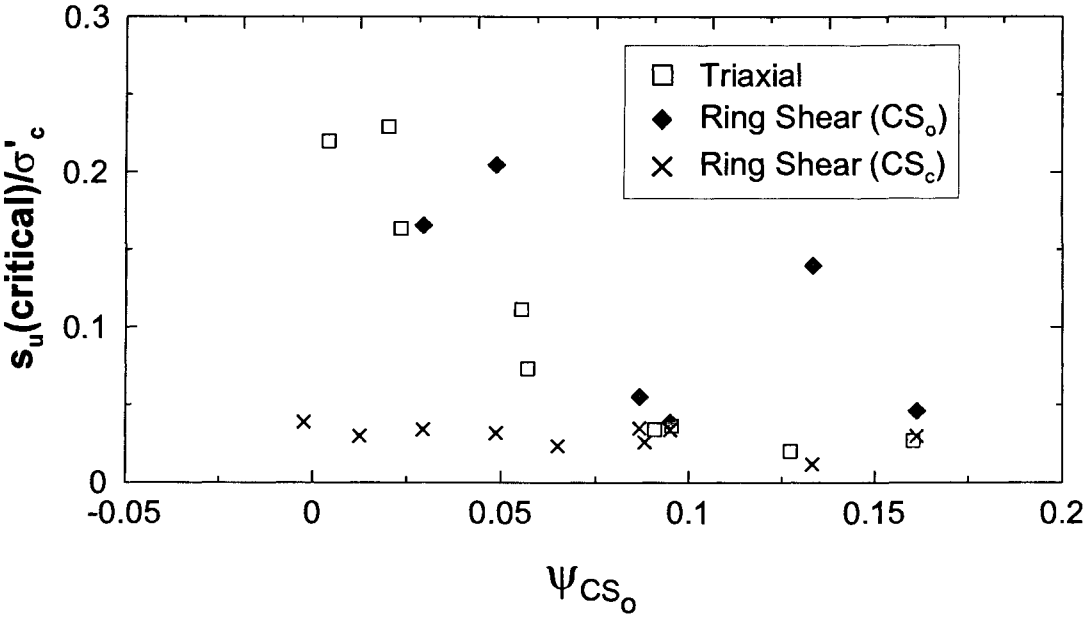

Figure 10.8: Critical strength ratios from fully contractive TxC, fully contractive RS (for CS_o and CS_c), and initially dilative (for CS_c) RS tests on IR sand

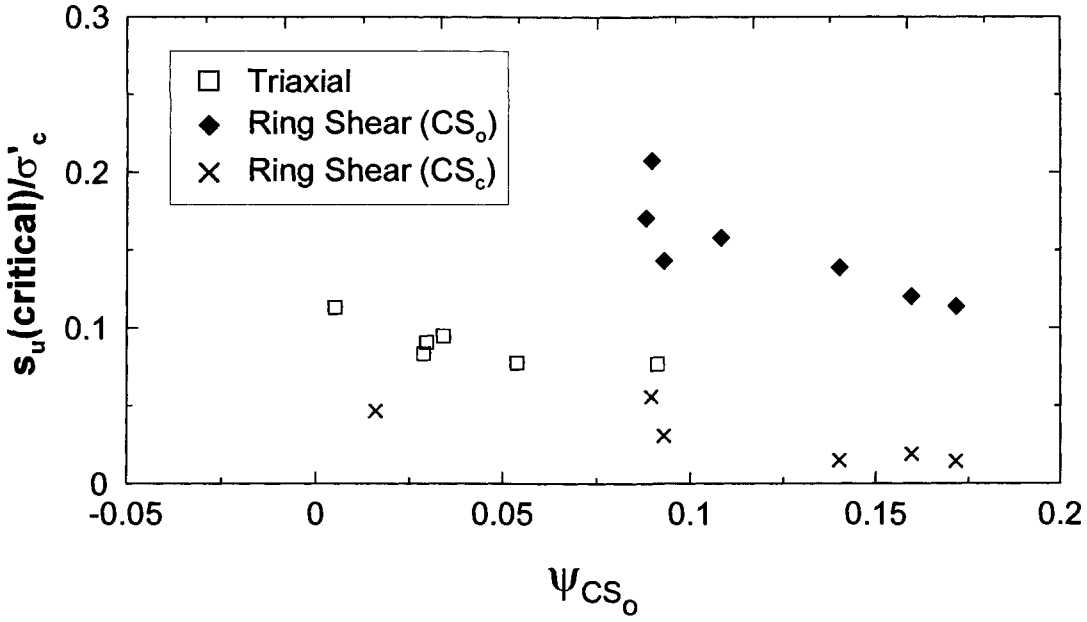

Figure 10.9: Critical strength ratios from TxC and RS tests on MR sand (note that both TxC and RS tests on MR sand were fully contractive)

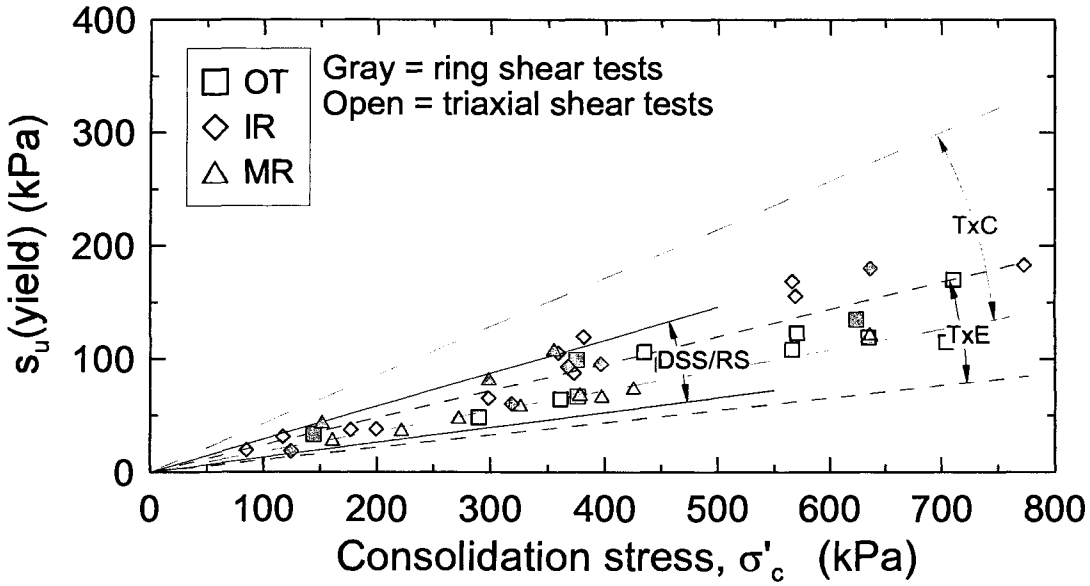

Figure 10.10: Comparison of range of yield strength ratios from TxC and RS tests of this study with those collected by Olson and Mattson (2008) for TxC, DSS/RS, and TxE.

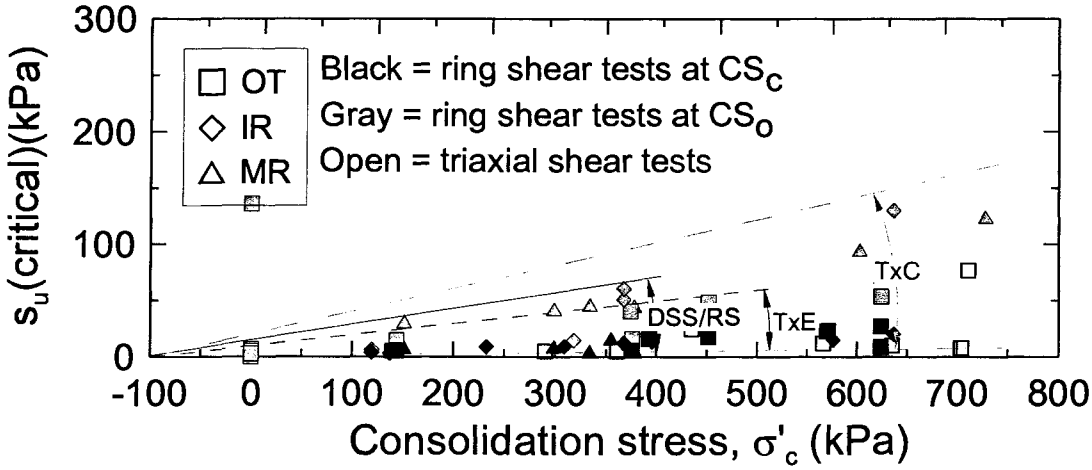

Figure 10.11: Comparison of range of critical strength ratios from TxC and RS tests of this study with those collected by Olson and Mattson (2008) for TxC, DSS/RS, and TxE.

CHAPTER 11: CONCLUSIONS

This thesis presents the shearing behavior of three sands using triaxial compression (TxC) and ring shear (RS) tests. The large shear displacement and critical state behavior of sand is of particular interest. The following sections summarize the findings of this work and highlight important conclusions.

11.1 LARGE SHEAR DISPLACEMENT TESTING OF SANDS

Several laboratory devices have been used to measure the large displacement behavior of sands, most common of which are the direct simple shear (DSS), TxC, and RS devices. The primary requirement is that the device should be able to shear a soil to large displacements without significant stress or strain non-uniformities in an undrained (or constant volume) and drained conditions. Based on this requirement and its other merits, the RS device appears to be best suited (of the devices reviewed) to define the large displacement behavior of sands. The other merits of the RS test include: (1) the ability to reach virtually unlimited shear displacements without creating substantial non-uniformities in stress and strain distributions at small to moderate shear displacement levels; (2) the ability to shear a soil on its depositional planes; (3) the ability to rotate principal stresses in a manner similar to that expected under field conditions; and (4) a constant specimen cross-sectional area and geometry during shearing. However, like all laboratory devices, the RS test has some limitations, such as potential stress and strain non-uniformities associated with some specimen dimensions, potential soil extrusion during shearing, difficulties in performing undrained testing, and friction that develops along the walls of the specimen confining rings.

Aware of these limitations, a new RS device was designed by the author and his advisor and constructed at the University of Illinois that minimizes their impact. Specifically, the device can perform either constant volume or drained tests. The confining ring dimensions were selected to reduce stress and strain non-uniformities to a negligible amount at smaller shear displacements, noting that these non-uniformities become irrelevant at larger shear displacements. Auxiliary load and torque cells measure any wall friction that develops along the confining rings, allowing computing the normal

effective stress and shearing resistance at the shear plane. In addition, the device utilizes quad rings along the confining rings to prevent soil extrusion and a specialized computer controlled servo-motor can perform RS tests under strain- or stress-controlled loading. Comparative RS and TxC shear tests on a silty, fine-grained sand demonstrated the capabilities of the new RS device and illustrated that the large displacement friction angles obtained from constant volume and drained RS tests were essentially identical and were consistent with the effective stress friction angles measured in drained and undrained TxC tests (based on correlations between plane strain and TxC effective stress friction angles).

Comparative RS and TxC tests appear to indicate that the TxC test may not produce a true critical state for many sands, even in loose samples, because the test is terminated at limited displacements before particle reorientation and crushing are complete. Furthermore, the limited displacement capacity of the TxC makes it difficult to model confidently some liquefaction flowslides and debris flows with runouts of tens or hundreds of meters. In contrast, the RS device can achieve the very large shear displacements, which may be required to reach a true critical state in some sands where particle reorientation and crushing occur. As a result, the RS device may be very useful in analyzing some liquefaction flow failures and other rapid, large runout landslides that develop discrete shear zones.

11.2 STRAIN LOCALIZATION AND SHEAR BANDING

A Plexiglas outer confining ring was used to directly observe shear band formation and evolution during RS tests. Parallel tests performed in TxC did not exhibit visible shear band formation, while the RS tests produced a discrete shear band where grain crushing readily occurred. This shear band formed as the effective friction angle was fully mobilized (after the peak shear resistance was mobilized in contractive specimens and after the initial phase transformation occurred in dilative specimens). Once a shear band developed in a specimen, the sliding process could be divided into three consecutive stages.

1. Continued shearing caused particle damage and grain crushing within the shear band, and this damage continued as shear displacements increased.

2. Particle damage and grain crushing caused contraction within the shear band. In constant volume tests, this tendency for contraction decreased the normal effective stress and caused a loss of shearing resistance (i.e., strain softening).
3. Strain softening continued until interparticle contact stresses decreased sufficiently such that particle damage ceased and further damage did not occur.

Furthermore, the stress-displacement response of the specimen was controlled only by the soil within the shear band, while soil outside the shear band did not experience measurable particle damage, volume change, or strain-softening since no further shear stress increment was applied there after bifurcation occurred.

11.3 PARTICLE DAMAGE AND CRUSHING

Particle damage and grain rearrangement are the two primary mechanisms that cause plastic volumetric deformations in sands. Particle damage and crushing was observed in the shear band of the RS tests, while no particle damage occurred in the soil above the shear band. In contrast, no crushing was observed in parallel TxC tests. The following conclusions can be drawn based on the findings of this chapter.

1. The severity of particle damage was influenced by the grain size distribution, mineralogical composition, shear displacement, drainage conditions, soil fabric (induced by the specimen preparation method) and consolidation stress.
2. Particle damage and crushing during shear occurred at normal stresses as small as about 30 kPa and significantly increased the fines content (up to 21%) without changing the maximum particle size of the sand. As damage continued with shear, the particle size distribution became wider (i.e., more well-graded). This process increased particle coordination numbers and reduced particle contact stresses, thereby reducing damage potential. An ultimate particle size distribution was approached at very large shear displacements when particle damage was essentially complete (likely corresponding to the critical state).
3. The primary mechanism of particle damage was a function of particle size and strength. Weaker or finer particles (with a lower coordination number), e.g., MR sand grains, tended to shatter and split under shear. In contrast, stronger and coarser

particles (with a larger coordination number), e.g., OT and IR sand grains, tended to accumulate damage by shearing off of asperities and particle abrasion.

4. The post-shear grain shapes of the sands were more angular and slightly more roughened than the original sand grains. The very fine angular particles produced by particle damage during shearing surrounded and interlocked with the coarser, roughened angular particles, forming a fabric in which the matrix consisted of finer particles rather than the original coarser particles.
5. In constant volume RS tests on loose specimens, contraction occurred and reduced the effective confining (normal) stress. This occurrence limited the severity of particle damage and crushing. However, in constant volume tests on dense specimens, dilative response was observed (after a brief initial contractive response) until sufficient particle damage and crushing occurred in the shear band to result in net contraction as the finer particles produced by particle damage and crushing tended to occupy available void space. Net contraction continued until the effective normal stress and shear stress decreased to a value below which particle damage ceased.

In drained tests on either loose or dense specimens at moderate to large consolidation stresses, specimens experienced considerable particle damage and crushing as a result of the increasing shear stresses applied to the specimen. The fine particles produced by particle damage and crushing occupied the available void space during shearing, resulting in net contraction. At small consolidation stresses, particle damage was limited primarily to abrasion. Thus, particle rearrangement initially controlled the soil response and dilation dominated until sufficient particle damage occurred to result in net contraction.

Particle damage and the resulting increase in fines content leads to increased soil contraction and increased liquefaction susceptibility if undrained conditions prevail. Furthermore, the increase in fines content decreases hydraulic conductivity in the shear band and may slow pore water pressure dissipation.

11.4 CRITICAL STATE OF SANDS

The determination and overall validity of the critical state in sand is of considerable importance, as it provides the basis for failure criteria of many constitutive models and in general, is a useful framework to interpret laboratory tests and field observations. By far,

the triaxial device has been most widely employed to study the critical state of sands. However, the limited displacement that the triaxial device is capable of imposing on a specimen often is insufficient to reach a critical state where the sand is continuously deforming at constant volume, constant normal effective stress, and constant shear stress. As a result, studies using the triaxial device have yielded contradictory conclusions regarding the uniqueness of the critical state line (CSL) and the role of various factors such as soil fabric, stress path, mode of shear, and consolidation stress (among others) on the CSL.

The results of the RS tests demonstrate that shear band formation and particle damage play an important role in the contractive response of sands, and suggest two types of critical states. The CS_o (critical state of the original sand gradation without crushing) is achieved solely through particle reorientation/rearrangement and/or dilation. In this case, liquefaction and undrained post-peak strain-softening leading to the critical state occurs only in very loose, contractive sands and can be achieved at small shear displacements (about 0.5 to 3 cm in this study) within the capacity of nearly all laboratory testing devices, including the triaxial and simple shear devices. In contrast, the CS_c (critical state including particle damage and crushing) involves shear band formation and particle damage/crushing within the shear band (i.e., "sliding surface" liquefaction). In this case, very large displacements (on the order of meters) are required to reach a critical state and this level of shear displacement can only be achieved in a RS device. Furthermore, particle damage and crushing results in markedly contractive behavior, and even dense sands that experience crushing respond by contracting and strain-softening to a final critical state. The CSL_c reflects the mineralogy of the sand and is independent of drainage conditions, specimen preparation methods, consolidation stress, fabric, and strain rate. However, the role of intermediate principal stress on critical state is not clear and requires further research.

11.5 YIELD AND CRITICAL STATE FRICTION ANGLES

Yield (ϕ'_{yield}) and critical state ($\phi'_{cs,o}$) friction angles of sands measured in RS and TxC tests on air pluviated and moist tamped specimens illustrated that $\phi'_{cs,o}$ and ϕ'_{yield} measured in TxC are independent of σ'_n but inversely related to e_c. This suggests that the

initial soil fabric was not erased after reaching the displacement limit of the triaxial device. Similarly, no clear relationship was observed between ϕ'_{yield} and σ'_{nc} in the RS tests; and, ϕ'_{yield} measured in RS tests decreased with e_c and ψ. The range of ϕ'_{yield} (14° - 24°) measured in RS agrees with those measured in DSS and RS tests performed by others. Dense specimens tested in RS dilated until local contraction resulting from particle crushing suppressed local dilation and yielded a second phase transformation from net dilative to contractive volumetric response. The minimum friction angle measured after the second phase transformation was approximately equal to the critical state friction angle of the original uncrushed sand, $\phi'_{cs,o}$, and was independent of initial soil fabric but decreased slightly until σ'_{nc} exceeded about 150 kPa. Average values of $\phi'_{cs,o}$ of 31°, 32°, and 34° were measured for OT, IR and MR sands, respectively. Furthermore, $\phi'_{cs,o}$ was very similar to the effective friction angle mobilized at the first phase transformation, ϕ'_{PT}.

As shearing continued in the RS tests, the mobilized friction angle increased as the sand particles became severely damaged and more angular. Furthermore, fine particles produced by particle abrasion and shattering of the original grains were very angular, filling the void spaces among the larger grains, increasing the density and mobilized friction angle. The mobilized friction angle stabilized at a critical state value ($\phi'_{cs,c}$) as particle crushing ceased and the local void ratio in the shear band became constant (at the critical void ratio). At this condition, the initial sand fabric was destroyed and $\phi'_{cs,c}$ was independent of the initial fabric. Average values of $\phi'_{cs,c}$ = 34°, 38°, and 41° were measured for OT, IR, and MR sands, respectively at σ'_{nc} > 200 kPa. Overall, the RS results indicate that $\phi'_{cs,c}$ (and $\phi'_{cs,o}$) depends primarily on particle mineralogy and shape, as well as the intermediate principal stress and is independent of stress path and fabric.

11.6 YIELD AND CRITICAL SHEAR STRENGTH RATIOS

The shear strength ratio (s_u/σ'_c) mobilized in sands depends not only on the slopes of the NCL and CSL, but also their intercepts with the void ratio axis. Furthermore, s_u/σ'_c is a function of ϕ'_s. However for a particular deposit, s_u/σ'_c is independent of the initial stress and void ratio if the NCL and CSL are parallel. This parallelism occurs in more

compressible sands (silty or non-siliceous mineralogy) that constitute many of the sands involved in well-documented liquefaction flow failures. However, if particle crushing takes place as shearing continues, the state line becomes steeper and the difference between the slopes of NCL and state line increases. This causes the s_u/σ'_c and its range of variability to decrease, particularly at large shear displacements at which particle rearrangement and crushing have been largely exhausted.

The TxC and RS tests show that $s_u(\text{yield})/\sigma'_c$ and $s_u(\text{critical})/\sigma'_c$ both decrease with increasing state parameter with the latter also decreasing with larger shear displacements. The $s_u(\text{yield})/\sigma'_c$ from TxC (0.16 – 0.32) and RS (0.15 – 0.31) tests agree closely with values from earlier laboratory experiments on loose sands and with the back-calculated $s_u(\text{yield})/\sigma'_c$ from liquefaction flow failures. Similarly the $s_u(\text{critical})/\sigma'_c$ range from TxC tests (0.01 – 0.23) and RS (at CS_o) tests (0.04 – 0.21) on loose specimens agree very well with the range of values from earlier laboratory experiments on loose sands and with the back-calculated $s_u(\text{liq})/\sigma'_c$ from liquefaction failures of loose sand deposits. This suggests that flow liquefaction occurs in very loose sands without significant particle crushing and a critical state is reached primarily through particle rearrangement and reorientation. However, $s_u(\text{critical})/\sigma'_c$ at very large shear displacements (> 20 m) at which significant particles may crush within discrete shear zones (particularly in dense sands) has a narrower range and is on average smaller than those mobilized at the critical state of loose sands without particle crushing (TxC and RS tests at 2.8 cm). This suggests that sliding surface liquefaction (Sassa 2000) can occur in dense sands mainly through particle damage and crushing. The relatively small $s_u(\text{critical})/\sigma'_c$ may partly explain the rapid and large runout (> 100 m) of some relatively dense field deposits when triggered by a large earthquake, heavy rainfall or snowmelt (Sassa 1995; Sassa et al. 2000; Wang et al. 2002).

CHAPTER 12: FUTURE RESEARCH

12.1 FURTHER IMPROVEMENT OF THE RING SHEAR APPARATUS

The RS apparatus at the University of Illinois was designed and constructed within the scope and purpose of this Ph.D. research project. Further improvements and capabilities can be added to this device as described below:

12.1.1 Undrained Testing

Undrained testing of saturated specimens can be performed by adding a pore pressure transducer to the outer ring close to the lower portion of the specimen where the shear band forms. Extra sensors can also be installed to monitor the pore water pressure in circumference of the shear band. Several drainage paths may be needed for drained testing of saturated sands.

12.1.2 Measuring Lateral Horizontal Stresses

The outer and/or inner confining rings can be instrumented with strain gauges and calibrated in order to measure the lateral horizontal stresses exerted on the inner surfaces of the confining rings particularly at the shear band. This will enable not only measuring the horizontal at-rest stresses but also the horizontal stress (which is likely a principal stress) during shear and particle crushing. It should be ensured that the side walls are as smooth as possible to reduce the effect of the side shear stresses.

12.1.3 Automated Application of Normal Stress and Constant Volume

The normal stress and deformations in the current RS apparatus are controlled with dead weights and manual adjustments. A mechanical screw jack operated by a computer-controlled servo motor can be implemented to control the normal load during consolidation and drained shearing and the specimen height during constant volume shearing. This would also significant improve specimen preparation method.

12.1.4 Cyclic Testing

Cyclic testing can be performed with the current servo motor. However, a large capacity resistor would be required to dissipate (as heat) the inertial energy of braking and changing the direction of load.

12.1.5 Integrated Data Acquisition and Motion Control

In the current design of the machine, two separate software control the motion of the servo motor and acquire the data from the data-logger. An single code can be made (possibly with LabView) to collect the data and control the motions of the servo motor and any additional devices (vertical screw jack, or an extra shearing motor). This is in particular necessary in performing cyclic tests where simultaneous application of load and data acquisition (without any time lag) is required.

12.2 DIRECT MEASUREMENT OF SHEAR BAND VOID RATIO

In the current study, shear band void ratio was estimated indirectly using an analytical procedure and global height of the RS specimen. As described in the thesis, this method has specific uncertainties and is approximate. However, the shear band void ratio can be defined more accurately by solidifying (possibly by freezing, resin impregnation, etc.) the shear band, cutting it into pieces with specific volumes and weighing the mass of the sand. Special inlets and outlets may need to be installed on the specimen chamber for easy flow of the solidifying fluid in and out of the specimen. The exact height of the shear band within the specimen can also be measured with this method.

12.3 PARTICLE MOVING MECHANISMS

The micromechanical mechanisms of dilation, particle crushing, particle rearrangement, relative particle movements, and interlocking can be studied using high resolution videos of shearing from the tests with Plexiglas outer ring. This will improve understanding of the kinematics of shear banding, particle crushing and particle movement at critical state.

12.4 EFFECT OF PARTICLE MINERALOGY

Different liquefaction behaviors were observed in this study for quartz (OT sand) and non-quartz (MR sand) sands. Further research and testing of sand with different and mixed mineralogies would be valuable to increase our knowledge of how sand mineralogy affects shear behavior.

12.5 EFFECT OF INTERMEDIATE PRINCIPAL STRESS

Here the different CSLs (OT sand), friction angles and strengths measured in some TxC and RS tests may be related to differences in intermediate principal stress. However, it is not possible to test this postulate with the current ring shear device. By instrumenting the confining rings to measure σ'_2, its influence on sand behavior can be studied. This could have significant implications on applying laboratory experimental results to field soil behavior.

12.6 EXISTENCE OF A QUASI-CRITICAL STATE IN RING SHEAR TESTS

Quasi-critical state (i.e. quasi-steady state) type of behavior has been widely observed in triaxial tests, however as discussed in this thesis, no quasi-critical state behavior was observed in the ring shear tests performed here. Furthermore, there has not been any clear observation of this behavior in the field and therefore it is questionable whether quasi-critical state is a real soil behavior or a test-induced response. A ring shear testing program that covers a wide range of carefully selected initial stresses and densities can be devised to better evaluate the occurrence of a quasi-critical state in the ring shear device.

12.7 PARTICLE SIZE EVOLUTION DURING SHEAR

Although the particle size distribution of the sand within the shear band was defined at the end of most of the RS tests performed in this study, the evolution of particle size distribution and particle crushing before reaching the crushed critical state was not examined. Series of RS tests sheared to different levels of shear displacements can be performed on several sands (with different mineralogies and particle size distributions) and the evolution of particle size distribution of the sand from the shear band can be

defined. The effects of consolidation stress, stress path, mineralogy, and particle size on initiating particle crushing and the displacement at which a critical state is reached can be studied through these experiments.

12.8 EFFECTS OF VOID REDISTRIBUTION AND HYDROPLANING

As discussed earlier, the effects of void redistribution, hydroplaning, and particle migration on laboratory soil behavior are not clear. A ring shear testing program (using the Plexiglas outer ring) could be developed to examine these effects, and undisturbed sampling of the post-shear specimen (by solidifying the specimen) could be performed to verify observations made during testing.

REFERENCES

Abelev, A. V. and Lade, P. V. (2003). "Effects of cross-anisotropy on three-dimensional behavior of sand. Part I: Stress-strain behavior and shear banding." Journal of Engineering Mechanics, 129: 160-166.

Abelev, A. V. and Lade, P. V. (2004). "Characterization of failure in cross-anisotropic soils." Journal of Engineering Mechanics, ASCE 130(5): 599–606.

Abriak, N. and Mahboubi, A., (1992). "Influence du frottement local sur le frottement global." Scientific Report of GRECO Geomaterials (Lyon, France: INSA).

Agung, M.W., Sassa, K, Fukuoka, H. and Wang, G. (2004). "Evolution of shear-zone structure in undrained ring-shear tests." Landslides, 1: 101-112.

Alarcon-Guzman, A., Leonards, G.A. and Chameau, J.L., (1988). "Undrained monotonic and cyclic strength of sands." ASCE Journal of Geotechnical Engineering Division, 114(10), 1089-1109.

Alshibli, K. A., and Sture, S. (1999). "Shear band thickness measured by digital image techniques," Journal of Computing in Civil Engineering, 13(2): 103-109.

Alshibli, K. A., and Sture, S. (2000). "Shear band formation in plane strain experiments of sand." Journal of Geotechnical and Geoenvironmental Engineering, 126(6): 495 – 503.

Alshibli, K. A., Batiste, S., and Sture, S. (2003). "Strain localization in sand: Plane strain versus Triaxial Compression." Journal of Geotechnical and Geoenvironemental Engineering, ASCE, 129(6): 483 – 494.

Alshibli, K. A. and Akbas, I. S. (2007). "Strain localization in clay: plane strain versus triaxial loading conditions," Geotechnical and Geological Engineering, 25: 45-55.

Alyamani, M. S. and Sen, Z. (1993). "Determination of hydraulic conductivity from complete grain-size distribution curves," Groundwater, 31(4): 551-555.

Anderson, W. F. and Fair, P. (2008). "Behavior of railroad ballast under monotonic and cyclic loading," Journal of Geotechnical and Geoenvironmental Engineering, ASCE, 134(3): 316-327.

ASTM, Standard D2435 (2004). "Standard Test Methods for One-Dimensional Consolidation Properties of Soils Using Incremental Loading." Annual Book of ASTM Standards, 4(8), ASTM International, West Conshohocken, PA.

ASTM, Standard D422 (1963). "Standard Test Method for Particle Size Analysis of Soils." Annual Book of ASTM Standards, 4(8), ASTM International, West Conshohocken, PA.

ASTM, Standard D4254 (2000). "Standard Test Methods for Minimum Index Density and Unit Weights of Soils and Calculation of Relative Density." Annual Book of ASTM Standards, 4(8), ASTM International, West Conshohocken, PA.

ASTM, Standard D4767 (2004). "Standard Test Method for Consolidated Undrained Triaxial Compression Test for Cohesive Soils." Annual Book of ASTM Standards, 4(8), ASTM International, West Conshohocken, PA.

ASTM D6467, (1999). "Standard test method for torsional ring shear test to determine drained residual shear strength of cohesive soils." American Society for Testing and Materials.

ASTM, Standard D854 (2000). "Standard Test Method for Specific Gravity of Soil Solids by Water Pycnometer," Annual Book of ASTM Standards, 4(8), ASTM International, West Conshohocken, PA.

Ayoubian, A., and Robertson, P.K. (1998). "Void ratio redistribution in undrained triaxial extension tests on Ottawa sand." Canadian Geotechnical Journal, 35: 351–359.

Baharom, B. and Stallebrass, S.E. (1998). "A constitutive model combining the microscopic and macroscopic behavior of sands in shear and volumetric deformation." Proceedings of the 4th European Conference on Numerical Methods in Geotechnical Engineering, Udine, Springer-Verlag Wien, New York: 263-273.

Baldi, G. and Nova, R. (1984). "Membrane penetration effects in triaxial testing." Journal of Geotechnical Engineering, ASCE 110(3): 403–420.

Bardet, J. P., and Proubet, J. (1991). "A Numerical Investigation of the Structure of Persistent Shear Bands in Granular Media," Geotechnique, 41(4): 599 – 613.

Barrett, P.J. (1980). "The shape of rock particles, a critical review." Sedimentology, 27: 291-303.

Baziar, M. H., and Dobry, R. (1995). "Residual strength and large-deformation potential of loose silty sands," Journal of Geotechnical Engineering, ASCE, 121(12): 896 – 906.

Been, K., and Jefferies, M. G. (1985). "A state parameter for sands," Geotechnique, 35(2): 99-112.

Been, K., and Jefferies, M. G. (1993). "Towards systematic CPT interpretation." C. P. Wroth Memorial Symposium, Predictive Soil Mechanics, Thomas Telford London: 99-112.

Been, K., Jefferies, M.G. and Hachey, J. (1991). "The critical state of sand." Geotechnique, 41(3), 365-381.

Berre, T. (1982). "Triaxial testing at the Norwegian Geotechnical Institute." ASTM Geotechnical Testing Journal, 5(1/2): 3–17.

Billam, J. (1972). "Some aspects of the behavior of granular materials at high pressures," Stress-Strain Behavior of Soils: Proc., Roscoe Memorial Symposium, Cambridge University, Cambridge, U.K.: 69-80.

Bishop, A. W. (1966). "The strength of soils as engineering materials," Geotechnique, 16: 89-130.

Bishop, A. W. (1971). Technical note: "The influence of progressive failure on the choice of the method of stability analysis." Geotechnique, 21(2): 168-173.

Bishop, A. W. (1972). "Shear strength parameters for undisturbed and remoulded soil specimens." In Stress–strain behaviour of soils: Proceedings of the Roscoe Memorial Symposium, Cambridge, 29-31 March 1971 (ed. R. H. G. Parry), Henley-on-Thames: Foulis: 3 – 58.

Bishop, A. W., and Green, G. E. (1965). "The influence of end restraint on the compression strength of a cohesionless soil," Geotechnique, 15(3): 243-266.

Bishop, A. W., and Henkel, D. J. (1962). "The measurement of soil properties in the triaxial test," 2nd Edition, London: Edward Arnold.

Bishop, A. W., Green, G. E., Garga, V. K., Andersen, A., and Browns, J. D. (1971). "A new ring shear apparatus and its application to the measurement of residual strength." Geotechnique, 21(4): 273–328.

Bjerrum, L. and Landva, A. (1966). "Direct simple shear tests on a Norwegian quick clay." Geotechnique, 16(1): 1-20.

Bjerrum, L., Kringstad, S. and Kummeneje, O. (1961) "The shear strength of a fine sand" Proceedings of the 5th International Conference on Soil Mechanics and Foundation Engineering, 1: 29-37.

Black, D. K., and Lee, L. L. (1973). "Saturating laboratory samples by back pressures." Journal of the Soil Mechanics and Foundation Division, ASCE, 99(SM1): 75–93.

Bolton, M. D. (1986). "The strength and dilatancy of sands," Geotechnique, 36: 65-78.

Bolton, M. D., Nakata, Y., and Cheng, Y. P. (2008). "Micro- and macro-mechanical behavior of DEM crushable materials," Geotechnique, 58(00): 1-10.

Bromhead, E. N. (1979). "A simple ring shear apparatus." Ground Engineering, 12(5):40-44.

Broms, B. B., Casbarian, A. O., (1965). "Effects of rotation of the principal stress axes and of the intermediate principal stress on the shear strength." In: Proceedings of the 6th ICSMFE, Montreal 1; 179–183.

Carman, P. C. (1939). "Permeability of saturated sands, soils and clays," Journal of Agricultural Science, 29: 263-273.

Carr, J. F. and Walker, D. M. (1967). "An annular shear cell for granular materials." Powder Technology, Elsevier Publishing Company, Amesterdam, Netherlands, 1(6): 369-373.

Casagrande, A. (1936). "Characteristics of cohesionless soils affecting the stability of slopes and earth fills." Journal of the Boston Society of Civil Engineers. January: reprinted in Contributions to Soil Mechunics 1925-1940, BSCE. pp. 25 J-276.

Casagrande, A. (1940). "Characteristics of cohesionless soils affecting the stability of slopes and earth fills." *Contributions to Soil Mechanics, 1925-1940*, Boston Society of Civil Engineers, October, (Originally published in the Journal of the Boston Society of Civil Engineers, January, 1936), 257-276.

Casagrande, A. (1965). "Second Terzaghi Lecture: the role of calculated risk in earthwork and foundation engineering." Journal of the Soil Mechanics and Foundations Division, ASCE, 91(SM4), 1-40.

Casagrande, A. (1975). "Liquefaction and cyclic deformation of sands — a critical review." *In* Proceedings of the 5th Pan-American Conference on Soil Mechanics and Foundation Engineering, Buenos Aires. Vol. 5: 79–133.

Casagrande, A., (1976). "Liquefaction and cyclic deformation of sands – a critical review." Harvard Soil Mechanics Series, No.88. Harvard University, Cambridge, Massachusetts.

Casagrande, A. (1979). "Liquefaction and Cyclic Deformation of Sands: A Critical Review," Proceedings of the 5th Pan-American Conference on Soil Mechanics and Foundation Engineering, Buenos Aires, Argentina, Harvard University, MA.

Castro, G (1969) "Liquefaction of sands" Ph.D. Dissertation, Harvard University, Cambridge, Massachusetts.

Castro, G. and Poulos, S.J. (1977). "Factors affecting liquefaction and cyclic mobility." ASCE Journal of Geotechnical Engineering Division, 103(GT6): 501-516.

Castro G., and Troncoso, J. (1989). "Effects of 1989 Chilean earthquake on three tailings dams." In: Proceedings, 5th Chilean Conference on Seismology and Earthquake Engineering, Santiago.

Castro, G., Enos, J.L., France, J.W. and Poulos, S.J. (1982) "Liquefaction Induced by Cyclic Loading" Report to National Science Foundation, Washington DC, No. NSF/CEE-82018.

Castro, G., Poulos, S. J., and Leathers, F. D. (1985). "A reexamination of the slide of the Lower San Fernando Dam." Journal of Geotechnical Engineering, 111(9): 1093-1107.

Castro, G., Keller, T.O., and Boynton, S.S. (1989). "Re-evaluation of the Lower San Fernando Dam: Report 1, an investigation of the February 9, 1971 slide." *U.S. Army Corps of Engineers Contract Report GL-89-2*, Vols. 1 and 2, U.S. Army Corps of Engineers Waterways Experiment Station, Vicksburg, Mississippi.

Castro, G., Seed, R. B., Keller, T. O., and Seed, H. B. (1992). "Steady-state strength analysis of Lower San Fernando Dam Slide," Journal of Geotechnical Engineering Division, ASCE, 118: 406-427.

Chan, L. C. Y. and Page, N. W. (1997). "Particle fractal and load effects on internal friction in powders." Powder Technology, 90: 259-266.

Chandler, H.W. (1985) "A plasticity theory without Drucker's postulate, suitable for granular materials." Journal of Mechanics and Physics of Solids, 33: 215-226.

Chang, N. Y., Hseih, N. P., Samuelson, D. L., and Horita, M. (1981). "Static and cyclic behaviour of Monterey #0 sand." *In* Proceedings of the 3rd Microzonation Conference, Seattle, Washington: 929-944.

Chapuis, R. P. and Aubertin, M. (2003). "On the use of the Kozeny-Carman equation to predict the hydraulic conductivity of soils," Canadian Geotechnical Journal, 40: 616-628.

Chen, L. C. Y. and Page, N. W. (1997). "Particle fractal and load effects on internal friction in powders," Powder Technology, 90(3): 259-266.

Chen, H. W., and van Zyl, D. J. A. (1988). "Shear strength and volume change behavior of copper tailings under saturated conditions." In Hydraulic fill structures. Edited by D.J.A. van Zyl and S. G. Vick. American Society of Civil Engineers, Geotechnical Special Publication 21: 430-451.

Cheng, Y. P. (2004). "Micromechanical investigation of soil plasticity." Ph.D. thesis, Cambridge University.

Cheng, Y. P., Bolton, M. D., and Nakata, Y. (2004). "Crushing and plastic deformation of soils simulated using DEM." Geotechnique, 54(2): 131-141.

Cheng Y. P., Bolton, M. D., and Nakata, Y. (2005). "Grain crushing and critical states observed in DEM simulations." Powders and Grains, Taylor and Francis Group, London: 1393 – 1397.

Cheng, Y. P., Nakata, Y., and Bolton, M. D. (2003). "Discrete element simulation of crushable soil." Geotechnique, 53(7): 633-642.

Chester, J. S., Lenz, S. C., Chester, F. M., and Lang, R. A. (2004). "Mechanisms of compactions of quartz sand at diagenetic conditions," Earth Planet Science Letters, 220: 435-451.

Cheuk, C. Y., White, D. J., and Dingle, H. R. C. (2008). "Upper bound plasticity analysis of a partially-embedded pipe under combined vertical and horizontal loading," Soils and Foundations, 48(1): 133-144.

Chillarige, A. V., Robertson, P. K., Morgenstern, N. R., and Christian, H. A. (1997). "Evaluation of the in-situ state of Fraser River sand." Canadian Geotechnical Journal, 34(4), 510-519.

Chik, Z. (2004). "The Effect of Fragmentation on the Engineering Properties of Granular Materials: Laboratory and Fractal Analysis." Ph.D.Thesis, Department of Civil and Environmental Engineering, University of Pittsburgh.

Chu, J. and Leong, W. K. (2002). "Effect of fines on instability behavior of loose sand." Geotechnique, 52(10): 751 – 755.

Chu, J., and Lo, S.-C.R. (1993). "On the measurement of critical state parameter of dense granular soils." ASTM Geotechnical Testing Journal, 16: 27–35.

Chu, J. and Wanatowski, D. (2009). "Effect of loading mode on strain softening and instability behavior of sand in plane-strain tests," Journal of Geotechnical and Geoenvironmental Engineering, ASCE, 135(1): 108-120.

Chu, J., Leroueil, S., and Leong, W. K. (2003). "Unstable behavior of sand and its implication for slope instability." Canadian Geotechnical Journal, 40: 873 – 885.

Chuhan, F. A., Kjeldstad, A., Bjørlykke, K., and Høeg, K. (2002). "Porosity loss in sand by grain crushing-experimental evidence and relevance to reservoir quality." Marine and Petroleum Geology, 19: 39-53.

Chuhan, F. A., Kjeldstad, A., Bjørlykke, K., and Høeg, K. (2003). "Experimental compression of loose sands: relevance to porosity reduction during burial in sedimentary basins." Canadian Geotechnical Journal, 42(5): 995-1011.

Cole, E. R. (1967). "The behavior of soils in the simple shear apparatus," Ph.D. Thesis, Cambridge University, Cambridge, U.K.

Coumoulos, D. G. (1968). "A radiographic study of soils," Ph.D. Thesis, Cambridge University, Cambridge, U.K.

Colliat-Dangus, J.-L., Desrues, J., and Foray, P. (1988). "Triaxial testing of granular soil under elevated cell pressure." In Advanced Triaxial Testing of Soil and Rocks. American Society for Testing and Materials, Special Technical Publication No. 977: 290-310.

Coop, M. R. (1990). "The mechanics of uncemented carbonate sands." Geotechnique, 40(4): 607-626.

Coop, M.R., Sorensen, K.K., Bodas Freitas, T and Georgoutsos, G. (2004) "Particle breakage during shearing of a carbonate sand." Geotechnique, 54(3): 157-163.

Corfdir, A., and Sulem, J. (2008). "Comparison of extension and compression triaxial tests for dense sand and sandstone." Acta Geotechnica, 3(3): 241-246.

Cornforth, D. H. (1964). "Some experiments on the influence of strain conditions on the strength of sand." Geotechnique, 14(2): 143-167.

Cruden, D. M., and Hungr, O. (1986). "The debris of the Frank Slide and theories of rockslideavalanche mobility." Canadian Journal of Earth Sciences, 23: 425-432.

Cruden, D.M. and Krahn, J. (1978) "Franc rockslide, Alberta, Canada." Rockslides and Avalanches, I., Voight B. Ed., Elsevier, 97-112.

Davies, T. R., McSaveney, M. J., and Hodgson, K. A. (1999). "A fragmentation-spreading model for long-runout rock avalanches." Canadian Geotechnical Journal, 36: 1096 – 1110.

Dawson, R.F., Morgenstern, N.R. and Gu, W.H. (1994). "Liquefaction flowslides in western Canadian Coal mine waste dumps, phase II: Case Histories." Canada Center for Mineral and Energy Technology, SSC file number XSG42-00138 (608), 112p.

De Alba, P.A., Seed, H.B., Retamal, E., and Seed, R.B. (1988). "Analyses of dam failures in 1985 Chilean earthquake." Journal of Geotechnical Engineering, ASCE, 114(12): 1414- 1434.

De Matos, M. M. (1988). "Mobility of soil and rock avalanches." Ph.D. Thesis, University of Alberta, Edmonton, Alberta.

Dennis, N.D. (1988). "Influence of specimen preparation techniques and testing procedures on undrained steady state shear strength." *In* Advanced Triaxial Testing of Soil and Rock. American Society for Testing and Materials, Special Technical Publication No. 977: 642–654.

Desrues, J., Lanier, J. and Stutz, P. (1985). "Localization of the deformation in tests on sand sample." Engineering Fracture Mechanics, 21(4): 909-921.

Desrues, J., Chambon, R., Mokni, M., and Mazerolle, F. (1996). "Void ratio evolution inside shear bands in triaxial sand specimens studied by computed tomography." Geotechnique, 46(3): 529-546.

Dietz, M. S., and Lings, M. L. (2006). "Postpeak strength of interfaces in a stress-dilatancy framework." Journal of Geotechnical and Geoenvironmental Engineering, 132(11): 1474-1484.

Djordjevic, N. and Morrison, R. (2006). "Exploratory modelling of grinding pressure within a compressed particle bed." Minerals Engineering, 19(10): 995-1004.

Drescher, A. and de Josselin de Jong, G. (1972). "Photo-elastic verification of a mechanical model for flow of a granular material" Journal of Mechanics and Physics of Solids, 20: 337-351.

Drucker, D.C., Gibson, R.E. and Henkel, D.J. (1957). "Soil mechanics and working hardening theories of plasticity." Transactions of ASCE, 122: 338–346.

Dyvik, R., Berre, T., Lacasse, S., and Raadim, B. (1987). "Comparison of truly undrained and constant volume direct simple shear tests," Geotechnique, 37(1): 3-10.

Eckersley, D. (1990). "Instrumented Laboratory Flowslides." Geotechnique, 40(3): 489-502.

Ergun, M. U. (1981). "Evaluation of three-dimensional shear testing." *Proc. of 10th International Conference on Soil Mechanics and Foundation Eng.*, Stockholm: 593-596.

Fannin, R.J., Wilkinson, J.M.T. and Eliadorani, A. (2005). "Shear strength of cohesionless soils at low stress." Geotechnique, 55(6):467–478.

Fauque, L., and Strecker, M. R. (1988). "Large rock avalanches (Sturzstrume, sturzstroms) at Sierra Aconquija, northern Sierras Pampeanas, Argentina." Eclogae geologicae Helvetiae, 81(3): 579 – 592.

Fear, C.E., and Robertson, P.K. (1995). "Estimating the undrained strength of sand: a theoretical framework." Canadian Geotechnical Journal, 32: 859–870.

Feda, J. (2002). "Notes on the effect of grain crushing on the granular soil behavior," Engineering Geology, 63: 93-98.

Fiegel, G. F. and Kutter, B. L. (1994). "Liquefaction induced lateral spreading of mildly sloping ground." Journal of Geotechnical Engineering, ASCE, 120(12): 2236-2243.

Finn, W. D. L. (1971). "Seismic safety of embankment dams developments in research and practice 1988-1998," Speciality Conference on Geotechnical Earthquake

Engineering and Soil Dynamics III, Seattle, Geotechnical Special Publication. No. 75: 813 – 853.

Finn, W.D.L. (1998). "Seismic safety of embankment dams: developments in research and practice 1988-1998." Proc., Geotechnical Earthquake Engineering and Soil Dynamics III, ASCE Geotechnical Special Publication No. 75, Vol. 2: 812-853.

Finn, W.D.L., Ledbetter, R.H. and Wu, G. (1994). "Liquefaction in silty soils: design and analysis" Geotechnical Special Publication No.44: Ground Failures under Seismic Conditions; Ed. S. Prakash & P. Dakoulas, American Society of Civil Engineers, 51-76.

Finn, W. D. L. and Vaid, Y. P. (1977). "Liquefaction potential from drained constant volume cyclic simple shear tests." Proceedings of the 6th World Conference on Earthquake Engineering, New Delhi, 6: 7-12.

Finno, R.J. and Rechenmacher, A.L., (2003). "Effects of consolidation history on critical state of sand," Journal of Geotechnical and Geoenvironmental Engineering, 129(4): 350–360.

Finno, R. J., Harris, W. W., Mooney, M. A., and Viggiani, G. (1996). "Strain localization and undrained steady state of sand." Journal of Geotechnical Engineering, ASCE, 122(6): 462 – 473.

Finno, R. J., Harris, W. W., Mooney, M. A., and Viggiani, G. (1997). "Shear bands in plane strain compression of loose sand," Geotechnique, 47(1): 149-165.

Fleming, R. W., Ellen, S. D., and Algus, M. A. (1989). "Transformation of dilative and contractive landslide debris into debris flows – an example from Marin County, California." Engineering Geology, 27: 201-223.

Franke, E., Kiekbusch, M. and Schuppener, B. (1979). "A new direct simple shear device." Geotechnical Testing Journal, 2(4): 190-199.

Frost, J. D. and Jang, D.-J. (2000). "Evolution of sand microstructure during shear." Journal of Geotechnical and Geoenvironmental Engineering, 126(2): 116-130.

Frost, J. D. and Park, J.-Y. (2003). "A critical assessment of the moist tamping technique." Journal of Geotechnical Testing, 26(1): 1 - 14.

Fukuoka, H. (1991). "Variation of the friction angle of granular materials in the high speed high stress ring shear apparatus." Bulletin of the Disaster Prevention Research Institute, Kyoto University, 41(362), part 4: 243 – 279.

Fukuoka, H., Wang, G., Sassa, K., Wang, F. W. and Matsumoto, T. (2004). "Earthquake induced rapid long-traveling flow phenomenon: May 2003 Tsukidate Landslide." Landslides, 1(2):151-155.

Fukuoka H., Sassa K., Wang G., Sasaki R. (2006). "Observation of shear development in ringshear apparatus with a transparent shear box." Landslides, 3:239–251.

Fukushima, S. and Tatsuoka, F. (1984). "Strength and deformation characteristics of saturated sand at extremely low pressures," Soils and Foundations, 24(4): 30-48.

Gajo A., Muir Wood D. (1999). "A kinematic hardening constitutive model for sands: the multiaxial formulation." International Journal for Numerical and Analytical Methods in Geomechanics, 23: 925-965.

Garga, V. K. and Infante-Sedano, J. A. (2002). "Steady state strength of sands in a constant volume ring shear apparatus." Geotechnical Testing Journal, 25(4): 414-421.

Garga, V. K., and Zhang, H. (1997). "Volume changes in undrained triaxial tests on sands," Canadian Geotechnical Journal, 34: 762-772.

Gerolymos, N. and Gazetas, G. (2007). "A model for grain-crushing-induced landslides - Application to Nikawa, Kobe 1995." Soil Dynamics and Earthquake Engineering, 27: 803-817.

Gilbert, P. A. (1984). "Investigation of density variation in triaxial test specimen of cohesionless soil subjected to cyclic and monotonic loading." Tech. Rep. GL-84-10, U.S. Army Engineers Waterways Experiment Station, Vicksburg, Miss.

Gilbert, P. A. and Marcuson, W. F. (1988). "Density Variation in specimens subjected to cyclic and monotonic loads." ASCE Journal of Geotechnical Engineering Division 114(1): 1-20.

Glicken, H. X. (1998). "Rockslide-debris avalanche of May 18, 1980, Mount St. Helens volcano, Washington." Bulletin of the Geological Society of Japan. 49: 55-105.

Golightly, C. R. (1989). "Engineering properties of carbonate sands." Ph.D. Thesis, University of Bradford, UK.

Green, G. E. (1971). "Strength and Deformation of Sand Measured in an Independent Stress Control Cell," Proceedings of the Roscoe Memorial Symposium: "Stress-Strain Behavior of Soils," Cambridge University, pp. 285–323.

Green, G. E. and Bishop A. W. (1969). "A note on the drained strength of sand under generalized strain conditions." Geotechnique, 19(1): 144–149.

Guo, P. and Su, X. (2007). "Shear strength, interparticle locking, and dilatancy of granular materials." Canadian Geotechnical Journal, 44(5): 579 – 591.

Habib, P. (1953). "Influence of the variation of the average principal stress upon the shearing strength of soils [in French]." Proceedings of the 3rd International Conference on Soil Mechanics and Foundation Engineering, 1: 131-136.

Hagerty, M. M., Hite, D. R., Ulrich, C. R., and Hagerty, D. J. (1993). "One-dimensional high pressure compression of granular media," Journal of Geotechnical Engineering, 119(1): 1-18.

Hagiwara, T., Kitazawa, K., and Kusakabe, O. (1995). "Steady state and related concepts of natural deposited granular materials." Earthquake Geotechnical Engineering Conference, Ed. Ishihara:221-226.

Hall, E. B., and Gordon, B. B. (1963). "Triaxial testing with large-scale pressure equipment." Symposium on Laboratory Shear Testing of Soils, ASTM STP 361: 315-328.

Han, C. and Drescher, A. (1993). "Shear bands in biaxial tests on dry coarse sand." Soils and Foundations, 33(1): 118-132.

Han, C. and Vardoulakis, I. (1991). "Plane strain compression experiments on water-saturated fine-grained sand." Geotechnique, 41(1): 49-78.

Hanzawa, H. (1980) "Undrained strength and stability analysis for a quick sand." Soils and Foundations, 20(2): 17–29.

Harder, L. F. and Stewart, J. P. (1996). "Failure of Tapo Canyon Tailings Dam." Journal of Performance of Constructed Facilities, ASCE, 10(3): 109-114.

Hardin, B. O. (1985). "Crushing of soil particles" Journal of Geotechnical Engineering, Proceedings of ASCE, 111(10): 1177-1192.

Harris, W. W. (1994). "Localization of loose granular soils and its effect on undrained steady state strength," Ph.D. Thesis, Northwestern University, Evanston, IL.

Haruyama, M. (1969). "Effect of surface roughness on the shear characteristics of granular materials." Soils and Foundations, 9(4): 48-67.

Haruyama, M. (1981). "Anisotropic deformation-strength characteristics of an assembly of spherical particles under 3D stresses." Soils and Foundations, 21(4): 41-55.

Hazen, A. (1918). "A study of the slip in the Calaveras Dam." Engineering News-Record, 81(26): 1158-1164.

Head, K. H. (1986). "Manual of soil laboratory testing." Vol. 3, Effective stress tests. Pentech Press, London, 491 pp.

Healy, K. A. (1963) "The response of soil to dynamic loads" Report No. 13: The dependence of dilation in sand on rate of shear strain. US Army Waterways Experiment Station, Vicksburg, MS.

Hendron, A. J. (1963). "The behavior of sand in one-dimensional compression." Ph.D. Thesis, Department of Civil and Environmental Engineering, University of Illinois at Urbana-Champaign, Urbana, Ill.

Henkel, D. J. and Gilbert, G. D. (1952). "The effect of the rubber membrane on the measured triaxial compression strength of clay samples." Geotechnique, 3(1): 20-29.

Hewitt, K. (1988). "Catastrophic landslide deposits in the Karakoram Himalaya." Science (Washington, D. C.), 242: 64-67.

Hird, C. C. and Hassona, F. A. K. (1990). "Some factors affecting the liquefaction and flow of saturated sands in laboratory tests." Engineering Geology, 28: 149-170.

Horne, M. R. (1969). "The behavior of an assembly of rotund, rigid, cohesionless particles." III Proceedings of Royal Society, Series A, 310: 21-34.

Hosono, Y., and Yoshimine, M. (2004). "Liquefaction of sand in simple shear condition." International Conference on Cyclic Behavior of Soils and Liquefaction Phenomena, Germany: 129-136.

Hryciw, R.D., Vitton, S., and Thomann, T.G. (1990). "Liquefaction and flow failure during seismic exploration," Journal of Geotechnical Engineering, ASCE, **116**(12): 1881–1899.

Hsu, S. T., and Liao, H. J., (1998). "Uplift Behavior of Cylindrical Anchors in Sand," Canadian Geotechnical Journal, 35(1): 70-80.

Huang, A.-B., Hsu, H., and Chang, J.-W. (1999). "The behavior of a compressible silty fine sand." Canadian Geotechnical Journal, 36: 88-101.

Hungr, O., and Morgenstern, N. R. (1984). "High velocity ring shear tests on sand." Geotechnique, 34(3): 415–421.

Hutchinson, J. N. (1986). "A sliding consolidation model for flow slides." Candadian Geotechnical Journal 23: 115-126.

Hutchinson, J. N. and Bhandari, R. K. (1971). "Undrained loading, a fundamental mechanism of mudflows and other movements" Geotechnique, 21(4): 353-358.

Hvorslev, M. J. (1939). "Torsion shear tests and their place in the determination of shearing resistance of soils" Proceedings of the American Society of Testing and Materials, 39: 999-1022.

Hvorslev, M. J. and Kaufman, R. I. (1952). "Torsion shear apparatus and testing procedures." Bulletin No. 38, Vicksburg, Mississippi, USAE Waterways Experiment Station.

Idriss, I. M., and Boulanger, R. W. (2006). "Semi-empirical procedures for evaluating liquefaction potential during earthquakes." Journal of Soil Dynamics and Earthquake Engineering, Elsevier, 26: 115-130.

Infante-Sedano, J. A. (1998). "Constant volume ring shear test for sand." M.Sc. thesis, University of Ottawa, Ottawa, Canada.

Insley, A. E., and Hillis, S. F. (1965). "Triaxial shear characteristics of a compacted glacial till under unusually high confining pressure." Proc. of the Sixth International Conference on Soil Mechanics and Foundation Engineering: 244-248.

Ishihara, K. (1984). "Post-earthquake failure of a tailings dam due to liquefaction of the pond deposit." Proc., Inter. Conf. on Case Histories in Geotechnical Engineering, Rolla, Missouri, May 6-11, 3: 1129-1143.

Ishihara, K. (1993) "Liquefaction and flow failure during earthquakes." Géotechnique, 43(3): 351–415.

Ishihara, K., Tatsuoka, F. and Yasua, S. (1975). "Undrained deformation and liquefaction of sand under cyclic stresses," Soils and Foundations, 15(1): 29-44.

Ishihara, K. and Verdugo, R. and Acacio, A.A. (1991). "Characterization of cyclic behavior of sand and post-seismic analyses." Proceedings of the 9th Asian Regional

Conference on Soil Mechanics and Foundation Engineering. Bangkok, Thailand. 2: 45-68.

ISO (1996). "Soil quality – Determination of aggregate strength – Part 1: Tensile strength measurement (crushing test)," Draft International Standard ISO/DIS 11273-1, ISO/TC 190/SC 5.

Iverson, N.R., Hooyer, T.S. and Hooke, R. LeB. (1996). "A laboratory study of sediment deformation: stress heterogeneity and grain-size evolution." Annals of Glaciology, 22: 167-175.

Iverson N.R., Baker, R.W. and Hooyer T.S. (1997). "A ring-shear device for the study of till deformation: tests on tills with contrasting clay contents." Quaternary Science Review, 16(9): 1057-1066.

Iverson N. R., Hooyer, T. S. and Baker, R.W. (1998) "Ring shear studies of till deformation: Coulomb-plastic behavior and distributed strain in glacier beds" Journal of Glaciology, 44(148): 634-642.

Iverson, R.M., Logan, M., Denlinger, R.P. (2004). "Granular avalanches across irregular three dimensional terrain. 2: Experimental tests." Journal of Geophysical Research, Earth Surf., 109(1), F01015.

Iwashita, K. and Oda, M., (1998). "Rolling resistance at contacts in the simulation of shear band development by DEM." Journal of Engineering Mechanics, ASCE 124(3): 285–292.

Jang, D. J. (1997). "Quantification of sand structure and its evolution during shearing using image analysis," Ph.D. thesis, Georgia Institute of Technology, Atlanta.

Jang, D. –J., and Frost, J. D. (2000). "Use of image analysis to study the microstructure of a failed sand specimen." Canadian Geotechnical Journal, 37: 1141 – 1149.

Jefferies, M. G. (1993). "Nor-sand: A simple critical state model for sand." Geotechnique, 43: 91-103.

Jefferies, M. and Been, K. (1987). "Use of critical state representations of sand in the method of stress characteristics." Canadian Geotechnical Journal, 24: 441-446.

Jefferies, M., and Been, K. (2006). "Soil liquefaction: a critical state approach," Taylor and Francis, 512 pp.

Jefferies, M. and Shuttle, D. A. (2002). "Dilatancy In General Cambridge-Type Models", Geotechnique, 52(9): 625-638.

Jefferies, M., Been, K., and Hachey, J. E. (1990). "The influence of scale on the constitutive behavior of sand." Proc. 43rd Canadian Geotechnical Conference, Quebe City, 1: 263-273.

Kato, Y., Nakata, Y., Hyodo, M., and Murata, H., (2003). "Effect of Particle Characteristics on Drained Shear Properties of Sand." Deformation Characteristics of Geomaterials, Di Benedetto et al., Eds.: 707–713.

Kenney, T., Lau, D., and Ofoegbu, G. (1984). "Permeability of compacted granular materials." Canadian Geotechnical Journal, 21: 726-729.

Kjellman, W. (1936). "Report on an apparatus for consummate investigation of the mechanical properties of soils." Proceedings of the 1st International Conference on Soil Mechanics and Foundation Engineering, Cambridge, Mass., 2: 16-20.

Klein, C., and Dutrow, B. (2007). Manual of Mineral Science, 23rd Ed., John Wiley & Sons, Inc, 675pp.

Ko, H.Y., and Davidson, L.W. (1973). "Bearing capacity of footings in plain strain." Journal of Soil Mechanics and Foundation Div., 99(1):1–23.

Ko, H. Y. and Scott, R. F. (1967). "Deformation of sand in shear." Journal of Soil Mechanics and Foundations, 93: 283–310.

Koerner, R. M. (1970). "Behaviour of single mineral soils in triaxial shear." Journal Soil Mechanics Foundation Div., ASCE 96: 1373-1390.

Koester, J. P. (1994). "The influence of fines type and content on cyclic strength." Ground failures under seismic conditions, Geotechnical Special Publication, No. 44, ASCE, Reston, Va: 17-33.

Kokusho, T. (2000). "Mechanism for water film generation and lateral flow in liquefied sand layer." Soils and Foundations, 40(5):99-111.

Koltz, E. U., and Coop, M. R. (2001). "An investigation of the effect of soil state on the capacity of driven piles in sands," Geotechnique, 51(9): 733-751.

Kolymbas D., and Wu. W. (1990). "Recent results of triaxial tests with granular materials." Powder Technology, 60:99–119.

Konrad, J.-M. (1990a). "The minimum undrained strength of two sands," Journal of Geotechnical Engineering, ASCE, 116(6): 932-947.

Konrad, J.-M. (1990b). "Minimum undrained strength vs. steady state strength of sands," Journal of Geotechnical Engineering, ASCE, 116(6): 948-963.

Konrad, J.-M. (1993). "Undrained response of loosely compacted sands during monotonic and cyclic compression tests." Geotechnique, 43(1): 69–89.

Konrad, J.-M. (1997a). "Sand state from cone penetrometer tests: a framework considering grain crushing stress," Geotechnique, 48(2): 201-215.

Konrad, J.-M. (1997b). "In situ sand state from CPT: Evaluation of a unified approach at two CANLEX sites." Canadian Geotechnical Journal, 34: 120-130.

Konrad, J. –M. (1998). "Sand state from cone penetrometer tests: a framework considering grain crushing stress." Geotechnique, 48(2): 201-215.

Konrad, J.M. and Pouliot, N. (1997). "Ultimate state of reconstituted and intact samples of deltaic sand." *Canadian Geotechnical Journal*, 34: 737-748.

Kramer, S. L. (1985). "Liquefaction of sands due to non-seismic loading." Ph.D. Dissertation, University of California, Berkeley, California.

Kramer, S.L. (1989). "Uncertainty in steady state liquefaction evaluation procedures." Journal of Geotechnical Engineering, ASCE, 115(10): 1402–1419.

Kramer, S.L. (1996). Geotechnical Earthquake Engineering. Prentice Hall, New Jersey, 653p.

Kramer, S.L., and Seed, H.B. (1988) "Initiation of soil liquefaction under static loading conditions." Journal of Geotechnical Engineering, ASCE, 114(4): 412–430.

Kramer S.L., Bennets B.A. and Wang C.H. (2002) "Sand behavior at large strain in ring simple shear" U.S.-Japan Seminar on Seismic Disaster Mitigation in Urban Area by Geotechnical Engineering: 291-303.

Kramer, S. L., Wang, C. H. and Byers, M. B. (1999). "Experimental measurements of the residual strength of particular materials" In: Proceedings of the International Workshop on the Physics and Mechanics of Soil Liquefaction Baltimore Maryland, September 1998, Lade, P.V. & Yamamuro, J.A. eds., Balkema: 249-259.

Kuerbis, R., Negussey, D., and Vaid, Y.P. (1988). "Effect of gradation and fines content on the undrained response of sand." In Hydraulic fill structures. Edited by D.J.A.

Van Zyland S.G. Vick. Geotechnical Special Publication 21, American Society of Civil Engineers, New York: 330–345.

Kuerbis, R.H. and Vaid, Y.P, (1989) "Undrained behavior of clean and silty sand" Proceedings , 12th International Conference on Soil Mechanics and Foundation Engineering, Rio de Janeiro, Brazil, August.

Kulasingam, R., Malvick, E. J., Boulanger, R. W., and Kutter, B. L. (2004). "Strength loss and localization at silt interlayers in slopes of liquefied sand." Journal of Geotechnical and Geoenvironmental Engineering, 130(11): 1192-1202.

La Rochelle, P., Leroueil, S., Trak, B., Blais-Leroux, L., and Tavenas, F. (1988). "Area corrections in triaxial tests." Advanced Triaxial Testing of Soil and Rock, ASTM, Philadelphia, STP977: 715-731.

Ladd, R. S. (1974). "Specimen preparation and liquefaction of sands," ASCE Journal of Soil Mechanics and Foundation Division, 100: 1180-1184.

Ladd, R. S. (1978). "Preparing test specimens using undercompaction." Geotechnical Testing Journal, 1(1): 16-23.

Lade, P. V. (1982). "Localization effects in triaxial tests on sand." In Proc. IUTAM Conf. on Deformation and Failure of Granular Media, Delft: 461-471.

Lade, P. V. (1984). "Failure criterion for frictional materials." In: Desai CS, Gallagher RH (eds) Mechanics of engineering materials. John Wiley and Sons Ltd, Chapter 20.

Lade, P.V. (1993) "Initiation of static instability in the submarine Nerlerk berm." Canadian Geotechnical Journal, 30: 895–904.

Lade, P. V. (2003). "Analysis and prediction of shear banding under 3D conditions in granular materials," Soils and Foundations, 43(4): 161–172.

Lade, P. V. (2006). "Assessment of test data for selection of 3D failure criterion for sand." International Journal for Numerical and Analytical Methods in Geomechanics, 30: 307-333.

Lade, P. V. and Abelev, A. V. (2003). "Effects of cross-anisotropy on three-dimensional behavior of sand. Part II: Volume change behavior and failure." Journal of Engineering Mechanics, 129: 167 – 174.

Lade, P. V. and Duncan, J. M., (1973). "Cubical triaxial tests on cohesionless soils." ASCE Journal of Soil Mechanics and Foundation Div., 99(SM10): 793–812.

Lade, P. V. and Kirkgard, M. M., (2000). "Effects of stress rotation and changes of b-values on cross-anisotropic behavior of natural K_0-consolidated soft clay." Soils and Foundations 40(6): 93–105.

Lade, P.V. and Yamamuro, J.A. (1996). "Undrained sand behavior in axisymmetric tests at high pressures" Journal of Geotechnical Engineering, Proc. ASCE, 122(2): 120-129.

Lade, P. V., Nam, J., Hong, W. P. (2008). "Shear banding and cross-anisotropic behavior observed in laboratory sand tests with stress rotation." Canadian Geotechnical journal, 45: 74-84.

Lade, P.V., Yamamuro, J.A., and Bopp, P.A. (1996) "Significance of particle crushing in granular materials." Journal of Geotechnical Engineering, ASCE, 122(4): 309–316.

Lade, P.V., and Yamamuro, J.A. (1996). "Undrained sand behavior in axisymmetric tests at high pressures." Journal of Geotechnical Engineering, ASCE, 122(2): 120–129.

Lade, P.V. and Yamamuro, J. A. (1997). "Effects of non-plastic fines on static liquefaction of sands" Canadian Geotechnical Journal, 34: 918-928.

Lade, P. A., Liggio, C. D., and Yamamuro, J. A. (1998). "Effect of non-plastic fines on minimum and maximum void ratios of sand," Geotechnical Testing Journal, ASTM, 21(4): 336-347.

La Gatta, D. P. (1970). "Residual strength of clay and clay-shales by rotation shear tests." Harvard Soil Mechanics Series, No. 86, Cambridge, Massachusetts.

Lancelot, L., Shahrour, I., and Al Mahmoud, M. (2006). "Failure and dilatancy properties of sand at relatively low stresses." Journal of Engineering Mechanics, ASCE, 132(12): 1396-1399.

Lang, Y., Ote, K., Fukuoka. H., and Sassa K. (1991). "Image-processing the velocity distribution of particles in ring shear tests." In: Proceedings of the Conference of Japan Society of Erosion Control Engineering: 302–305 (in Japanese).

Lam, W. K., and Tatsuoka, F. (1988). "Effects of initial anisotropic fabrics and σ_2 on strength and deformation characteristics of sand." Soils and Foundations, 28(1): 89-106.

Lambe T.W. and Whitman R.V. (1979) "Soil Mechanics" New York, John Wiley and Sons.

Law, K. T., and Ling, Y. H. (1992). "Liquefaction of granular soils with noncohesive and cohesive fines." Proc. 10th World Conf. on Earthquake Engineering: 1491-1496.

Lawrence, D. (1980). "Some properties associated with kaolin soils." M. Phil. Thesis, Cambridge University, Cambridge, U.K.

Lee, K. (1970). "Comparison of plane strain and triaxial tests on sand." Journal of Soil Mechanics and Found Div., ASCE, 96(3):901–923

Lee, D. M. (1992). "The angle of friction of granular fills," Ph.D. Dissertation, University of Cambridge.

Lee, K. L. and Farhoomand, I. (1967). "Compressibility and crushing of granular soil in anisotropic triaxial compression," Canadian Geotechnical Journal, 4(1): 68-86.

Lee, K. L. and Seed, H. B. (1967). "Drained strength characteristics of sands." ASCE Journal of the Soil Mechanics and Foundations Division, 93(SM6): 117-141.

Lemos, L. J. L. (1986). "The effect of rate on the residual strength of soil." PhD thesis, University of London.

Leong, W. K., Chu, J., and Teh, C. I. (2000). "Liquefaction and instability of a granular fill material." Geotechnical Testing Journal, 23(2): 178–192.

Leroueil, S. (2003). "Soil mechanics in the context of slopes." Proc. XIX CGT, DISTR, Torino, Italy: 1-45.

Leroueil, S. (2004). "Geotechnics of slopes before failure." Proc., IX Int. Symp. on Landslides: Evaluation and Stabilization, Rio de Janeiro, Balkema, Rotterdam, The Netherlands: 863-884.

Leung, C. F., Lee, F. H., and Yet, N. S. (1996). "The role of particle breakage in pile creep in sand." Canadian Geotechnical Journal, 33(6): 888-898.

Li, X. S. and Dafalias, Y. F. (2000). "Dilatancy for cohesionless soils." Geotechnique, 50(4): 449–460.

Li, X. S., and Wang, Y. (1998). "Linear representation of steady state line for sand," Geotechnique, 124(12): 1215-1217.

Liu, S. H. (2006). "Simulating a direct shear box test by DEM," Canadian Geotechnical Journal, 43: 155-168.

Liu, S.H., and Matsuoka, H. (2003). "Microscopic interpretation on a stress–dilatancy relationship of granular materials," Soils and Foundations, 43(3): 73–84.

Liu, H. and Qiao, T. (1984). "Liquefaction Potential of Saturated Sand Deposits Underlying Foundation of Structure", Proceedings, 8th World Conference on Earthquake Engineering, San Francisco, California, Vol. III, July, pp. 199-206.

Lo, K. Y. and Roy, M. (1973). "Response of particulate materials at high pressures." Soils and Foundations, 13(1): 61–76.

Lobo-Guerrero, S. and Vallejo, L. E. (2005) "Crushing a weak granular material: experimental numerical analyses." Geotechnique, Technical Note, 55(3): 245-249.

Lobo-Guerrero, S. and Vallejo, L. E. (2006). "Modeling granular crushing in ring shear tests: experimental and numerical analyses." Soils and Foundations, 46(2): 147 – 158.

Luzzani, L. and Coop, M.R. (2002). "On the relationship between particle breakage and the critical state of sands." Soils and Foundations, 42(2): 71-82.

Malvick, E. J., Kutter, B. L. and Boulanger, R. W. (2008). "Postshaking shear strain localization in a centrifuge model of a saturated sand slope." Journal of Geotechnical & Geoenvironmental Engineering (ASCE), 134(2): 164-174.

Mandl, G., de Jong, L. N. J. and Maltha, A. (1977). "Shear zones in granular material: An experimental study of their structure and mechanical genesis." Rock Mechanics 9: 95–144.

Manzari M.T. and Dafalias Y.F. (1997). "A critical state two-surface plasticity model for sands." Geotechnique, 47(2): 255-272.

Marcuson, W. F. III and Gilbert, P. A., (1972). "Earthquake Liquefaction Potential at Patoka Dam, Indiana," U.S. Army Waterways Experiment Station, Miscellaneous paper S-72–42.

Marcuson, W.F., III, Ballard, R.F., Jr., and Ledbetter, R.H. (1979). "Liquefaction failure of tailings dams resulting from the Near Izu Oshima earthquake, 14 and 15 January, 1978." Proc. 6th Pan-American Conf. on Soil Mechanics and Foundation Engineering, Lima Peru, Vol. 2, 69-80.

Marcuson, W. F. III, Hynes, M. E., and Franklin, A. G. (1990). "Evaluation and use of residual strength in seismic safety." Analysis of Embankments, Earthquake Spectra, 6(3): 529-572.

Marsal, R. J. (1967). "Large scale testing of rockfill materials." ASCE Journal of Soil Mechanics and Foundation Division, 93(SM2): 27-43.

Martin, G.R., Finn, W.D.L., and Seed, H.B. (1978). "Effects of system compliance on liquefaction tests." Journal of the Geotechnical Engineering Division, ASCE, 104(4): 463–479.

Matsuoka, H., Liu, S., Sun, D. and Nishikata, U. (2001). "Development of a new in situ direct shear test." Geotechnical Testing Journal 24(1): 92-101.

Mazzucato, A. and Ricceri, G. (1986). "Load test on model pile driven into sand," Proc. Int. Conf. Deep Found., China Building Industry Press, Beijing, China, 1: 154-159.

McDowell G.R., and Bolton M.D. (1998). "On the micromechanics of crushable aggregates." Geotechnique, 48(5): 667-679.

McDowell G. R., Bolton M.D., and Robertson D. (1996). "The fractal crushing of granular materials." Journal of Mech. Phys Solids, 12(44): 2079-2102.

McDowell, G. R., and Khan, J. J. (2003). "Creep of granular materials," Granular Matter, 5: 115-120.

McRobertson, E.C., and Sladen, J. A. (1992). "Observations on static and cyclic sand-liquefaction analysis." Canadian Geotechnical Journal, 29(4): 650-655.

Mesri, G. (1987). "Fourth law of soil mechanics: a law of compressibility," Proceedings of International Symposium on Geotechnical Engineering of Soft Soils, Mexico City, Mexico, Vol. 2: 179 – 187.

Mesri, G. and Vardhanabhuti, B. (2007). "Coefficient of earth pressure at rest for sands subjected to vibration." Canadian Geotechnical Journal, 44: 1242-1263.

Mesri, G. and Vardhanabhuti, B. (2009). "Compression of granular materials," Canadian Geotechnical Journal, *in press*.

Mitchell, J. K. (1993). "Fundamentals of soil behavior." Second edition, New York, John Wiley & Sons Inc.

Miura, N. (1985). "Point resistance of piles in sand," Proc. 11th ICSMFE, San Francisco, 3: 1445-1448.

Miura, S., and Toki, S. (1982). "A sample preparation method and its effect on static and cyclic deformation strength properties of sand." Soils and Foundations, 22(1): 61-77.

Miura, N. and O'Hara, S. (1979). "Particle crushing of a decomposed granite soil under shear stresses." Soils and Foundations, 19(3): 1-14.

Miura, N. and Yamanouchi, T. (1977). "Effect of particle crushing on the shear characteristics of a sand." Proceedings of the Japanese Society of Civil Engineers, No. 260: 109-118.

Miyamori, T. (1976). "Deformation and strength of a sand in three-dimensional stress state." Proc. JSCE, 225: 81–91 (in Japanese).

Muir Wood, D. and Maeda, K. (2008). "Changing grading of soil: effect on critical states," Acta Geotechnica, 3: 3-14.

Mohammad, R., and Dobry, R. (1986). "Undrained monotonic and cyclic triaxial strength of sand." ASCE Journal of Geotechnical Engineering Division, 112(10): 941-958.

Molenkamp, F. and Luger, H. J. (1981). "Modeling and minimization of membrane penetration effects in tests on granular soils." *Geotechnique*, 31(4): 471-486.

Mooney, M. A. (1996). "An experimental study of strain localization and the mechanical behavior of sand," Ph.D. Thesis, Northwestern University, Evanston, IL.

Mooney, M. A., Finno, R. J. and Viggiani, M. G. (1998). "A unique critical state for sand?" ASCE Journal of Geotechnical Engineering Division 112(10): 941-958.

Mooney, M. A., Finno, R. J., Viggiani, G., and Harris,W. W., (1996). "Issues of Uncertainty Regarding Localized Strains in Granular Soils," Proceedings, Uncertainty '96, Vol. 1, American Society of Civil Engineers, Reston, VA, pp. 312–325.

Mueller, C. G. (2000). "Load and Deformation Response of Tieback Walls" Ph.D. Thesis, University of Illinois at Urbana-Champaign, 554pp.

Mulilis, J. P., Chan, C. K., and Seed, H. B. (1975). "The effects of method of sample preparation on the cyclic stress-strain behavior of sands." Rep. No. EERC 75-18, University of California, Berkeley.

Mulilis, J.P., Seed, H. B., Chan, C. K. and Mitchell, J. K. (1977). "Effect of sample preparations on sand liquefaction." ASCE Journal of Geotechnical Engineering Division, 103(GT2): 91-108.

Mulilis, J. P., Townsend, F. C., and Horz, R. C., (1978). "Triaxial testing techniques and sand liquefaction." Dynamic Geotechnical Testing, ASTM STP 654, American Society for Testing and Materials, pp. 265-279.

Murthy, T. G., Loukidis, D., Carraro, J.A.H., Prezzi, M. and Salgado, R. (2007). "Undrained monotonic response of clean and silty sands." Geotechnique, 57(3): 273-288.

Murphy, D.J. (1970). "Soils and rocks: Composition, confining level and strength," PhD Dissertation, Duke University.

Nakata Y., Hyde A. F. L., Hyodo M., Murata H. (1999). "A probabilistic approach to sand particle crushing in the triaxial test." Geotechnique, 49(5): 567–83.

Nakata, Y., Kato, Y., Hyodo, M., Hyde, A. F. L., and Murata, H. (2001a). "One-dimensional compression behavior of uniformly graded sand related to single particle crushing strength." Soils and Foundations, 41(2): 39-51.

Nakata, Y., Hyodo, M., Hyde, A. F. L., Kato, Y., and Murata, H. (2001b). "Microscopic particle crushing of sand subjected to high pressure one-dimensional compression." Soils and Foundations, 41(2): 69-82.

Nakata, Y., Hyodo, M., Murata, H., Hyde, A. F. L., and Ham, T. G. (2003). "Effect of water on particle breakage for decomposed granite soils," Deformation Characteristics of Geomaterials, H. Di Benedetto, T. Doanh, H. Geoffroy, and C. Sauzeat, eds., Taylor & Francis, London: 701-705.

Negussey, D., and Islam, M.S. (1994). "Uniqueness of steady state and liquefaction potential." Canadian Geotechnical Journal, 31(1): 132–139.

Negussey, D., Wijewickreme, W. K. D. and Vaid, Y. P. (1988). "Geomembrane interface friction." Canadian Geotechnical Journal, 126: 165-169.

Newland, P.L., and Alley, B.H. (1957). "Volume changes in drained triaxial tests on granular materials." Geotechnique, 7(1): 17–34.

Newland, P.L., and Alley, B.H. (1959). "Volume changes during undrained triaxial tests on saturated dilatant granular materials." Géotechnique, 9(3): 174–182.

Ni, J., Li, Z. and Mendoza, C. (2004). "Blown-sand transport rate." Earth Surface Processes and Landforms 29: 1-14.

Novosad, J. (1964). "Studies on Granular Materials. II. Apparatus for measuring the dynamic angle of internal and external friction of granular materials." Collection of Czechoslovak Chemical Communications, 29: 2697-2701.

Ochiai, H., and Lade, P.V., (1983). "Three-Dimensional Strength of Sand with Anisotropic Fabric." (in Japanese), Proceedings of the 18th Japan National Conference on Soil Mechanics and Foundation Engineering, Kotiyarma, Japan: 251-254.

Oda, M. (1972). "Initial fabrics and their relations to mechanical properties of granular material." Soils and Foundations, 12(1):17–36.

Oda, M., Iwashita, K., and Kazama, H., (1997). "Micro-Structure Developed in Shear Bands of Dense Granular Soils and Its Computer Simulation-Mechanism of Dilatancy and Failure," IUTAM Symposium on Mechanics of Granular and Porous Materials, N. A. Fleck and A. C. F. Cocks, Eds.: 353–364.

Olivares, L. (2001). "Static liquefaction: an hypothesis for explaining transition from slide to flow in pyroclastic soils." In: Proceedings of Conference on transition from slide to flow-mechanisms and remedial measure, Karadeniz Technical University, Trabzon.

Olivares L., Damiano E., and Picarelli L. (2003). "Wetting and flume tests on a volcanic ash." In: Picarelli L (ed) Proceedings of the international conference on fast slope movements—prediction and prevention for risk mitigation, Napoli, Vol 1. Patron, Bologna: 399-404.

Olson, S. M. (2001). "Liquefaction analysis of level and sloping ground using field case histories and penetration resistance." Ph.D. thesis, University of Illinois at Urbana-Champaign, Urbana, Ill.

Olson, S. M. (2006). "Liquefaction analysis of Duncan Dam using strength ratios," Canadian Geotechnical Journal, 43(5): 484-499

Olson, S.M. and Stark, T.D. (2002). "Liquefied strength ratio from liquefied flow failure case histories." Canadian Geotechnical Journal, 39: 629-647.

Olson, S. M. and Stark, T. D. (2003a). "Use of laboratory data to confirm yield and liquefied strength ratio concepts." Canadian Geotechnical Journal, 40(6): 1164-1184.

Olson, S.M. and Stark, T.D. (2003b). "Yield strength ratio and liquefaction analysis of slopes and embankments." Journal of Geotechnical and Geoenvironmental Engineering, ASCE, 129(8): 727-737.

Olson, S. M., and Mattson, B. B. (2008). "Mode of shear effects on yield and liquefied strength ratios." Canadian Geotechnical Journal, 45: 574 – 587.

Olson, S.M., Sacks, A., Mattson, B., and Servigna, D. (2006). "Evaluating liquefaction of sloping ground." Proceedings, 8th National Earthquake Engineering Conference (1906 Centennial), April 18-21, San Francisco, CA.

Okada, Y., Sassa, K. and Fukuoka, H. (2000) "Excess pore pressure generation of sandy soil during shearing" Proceedings, 8th International Symposium on Landslides, E. Bromhead, N. Nixon and M.L. Ibsen Eds., Cardiff, 3: 1147-1153.

Okada, Y., Sassa K. and Fukuoka, H. (2004) "Excess pore pressure and grain crushing of sands by means of undrained and naturally drained ring shear tests" Engineering Geology, 75: 325-343.

Ohta, H., Yoshikoshi, H., Mori, Y., Yonetani, S., Itho, M., and Ishiguro, T. (2001). "Behavior of rockfill dam during construction." Proc. 15th International Conference on Soil Mechanics and Geotechnical Engineering, Istanbul, 2: 1227-1231.

Olivares, L. (2001). "Static liquefaction: An hypothesis for explaining transition from slide to flow in pyroclastic soils." Proc. ISSMGE CT-11, Transition from Slide to Flow: Mechanisms and Remedial Measures, Trabzon, TC-11 and ATC-9, Kyoto, Japan.

Olivares, L., Andreozzi, L., Damiano, E., Avolio, B., and Picarelli, L. (2003). "Hydrologic response of a steep slope in unsaturated pyroclastic soils," Proc. Int. Conference on "Fast Slope Movements — Prediction and Prevention for Risk Mitigation", Patron Editore, Napoli: 391–397.

Ovando-Shelley, E., and Perez, B. E. (1997). "Undrained behavior of clayey sands in load controlled triaxial tests." Geotechnique, 47(1): 97-111.

Papadimitriou, A., Dafalias, Y. F., and Yoshimine, M. (2005). "Plasticity modeling of the effect of sample preparation method on sand response." Soils and Foundations, 45(2): 109-123.

Papageorgiou, G. (2001). "Liquefaction of tailings." Ph.D. thesis, University of the Witwatersrand, Johannesburg, South Africa.

Pestana, J.M. and Whittle, A.J. (1995). "Compression model for cohesionless soils" Geotechnique, 45(4): 611-631.

Peters, J., Lade, P., and Bro, A. (1988). "Shear band formation in triaxial and plane strain tests." Advanced triaxial testing of soil and rock, ASTM, STP977, R. Donaghe, R. Chaney, and M. Silver, eds., ASTM: 604-627.

Pillai, V.S., and Salgado, F.M. (1994). "Post-liquefaction stability and deformation analysis of Duncan Dam." Canadian Geotechnical Journal, 31: 967–978.

Pitman, T.D., Robertson, P.K., and Sego, D.C. (1994). "Influence of fines on the collapse of loose sands." Canadian Geotechnical Journal, 31: 728–739.

Poorooshasb, H. B., Holubec, I., and Sherbourne, A. N. (1967). "Yielding and flow of sand in triaxial compression, Part II." Canadian Geotechnical Journal, 4(5): 376–397.

Poorooshasb, H. B. (1989). "Description of flow of sand using state parameters." Computers and Geotechnics, 8: 195-218.

Poulos, S.J. (1988). "Liquefaction and related phenomena." in Advanced Dam Engineering for Design, Construction, and Rehabilitation, R.B. Jansen, ed., Van Nostrand Reinhold, New York: 292-320.

Poulos, J., (1981). "The steady state of deformation." ASCE Journal of Geotechnical Engineering Division, 107(GT5): 553-562.

Poulos, J. (1997). "Comments on Laboratory Determination of Undrained Steady State Shear Strength," NSF Workshop: Post-Liquefaction Shear Strength of Granular Soils Workshop, April 17, Urbana Illinois, USA: 147-153.

Poulos, S. J., Castro, G., and France, J. (1985). "Liquefaction evaluation procedure." Journal of Geotechnical Engineering, ASCE, 111(6): 772-792.

Poulos, S.J. Castro, G., and France, W. (1988). Closure to discussion of "Liquefaction evaluation procedure." Journal of Geotechnical Engineering, ASCE, 114(2): 251-259.

Prakash, S., Guo, T., and Kumar, S. (1998). "Liquefaction of silts and silt-clay mixtures." Geotechnical Earthquake Engineering and Soil Dynamics III, GTP No. 75 Dakoulal, P. Yegian M. and Holtz, R. D. ASCE, Seattle, WA: 337-348.

Rahim, A. (1989). "Effect of morphology and mineralogy on compressibility of sands." Ph.D. Thesis, Indian Institute of Technology Kanpur, Kanpur, India.

Rahman, M. M. and Gnanendran, C. T. (2008). "On equivalent granular void ratio and steady state behavior of loose sand with fines." Canadian Geotechnical Journal, 45:1439 – 1456.

Raju, V.S., and Sadasivan, S.K. (1974). "Membrane penetration in triaxial tests on sand." Journal of the Geotechnical Engineering Division, ASCE, 100(4): 482–489.

Raju, V.S., and Venkatramana, K. (1980). "Undrained triaxial tests to assess liquefaction potential of sands - effects of membrane penetration." *In* Proceedings of the International Symposium on Soils under Cyclic Transient loading, Rotterdam, 2: 483–494.

Rahman, M. M. and Gnanendran, G. T. (2008). "On equivalent granular void ratio and steady state behavior of loose sand with fines," Canadian Geotechnical Journal, 45: 1439 – 1456.

Randolph, M. F., Dolwin, J. and Beck, R. (1994). "Design of driven piles in sand." Geotechnique, 44(3): 427-448.

Reades, D. W. (1972). Stress–strain characteristics of sand under three dimensional loading. PhD thesis, University of London.

Reades, D. W. and Green, G. E. (1976). "Independent stress control and triaxial extension tests on sand." Geotechnique, 26(4): 551–576.

Rechenmacher, A.L. (2000). "Effects of Consolidation History and Shear Rate on the Critical State of Two Sands." Ph.D. Thesis, Northwestern University, Evanston, IL.

Rechenmacher, A. L. and Finno, R. J., (2004). "Digital image correlation to evaluate shear banding in dilative sands," Geotechnical Testing Journal, 27(1): pp. 13–22

Rice, J. (1976). "The localization of plastic deformation." In Proc. 16th International Congress on Theoretical and Applied Mechanics, Delft, North Holland, Amsterdam, 1: 207.

Riemer, M. F. (1992). "The effects of testing conditions on the constitutive behavior of loose, saturated sands under monotonic loading," Ph.D. Thesis, University of California, Berkeley, California.

Riemer, M. F. and Seed, R. B. (1992). "Observed effects of testing conditions on the residual strength of loose, saturated sands at large strains," Proceedings from the 4th Japan-U.S. Workshop on Earthquake Resistant Design of Lifeline Facilities and Countermeasures for Soil Liquefaction: Tokai University Pacific Center, Honolulu, Hawaii: 223-237.

Riemer, M. F. and Seed, R. B. (1997). "Factors affecting apparent position of steady-state line." Journal of Geotechnical and Geo-environmental Engineering, 123(3): 281-288.

Roberts, J. E., and De Souza, J. M. (1958). "The compressibility of sands." In Proceedings of American Society of Testing and Materials, Special Technical Publication 58: 1269 – 1277.

Robertson, P.K. (1994). "Suggested terminology for liquefaction." *In* Proceedings of the 47th Canadian Geotechnical Conference, Halifax, N.S.: 277–286.

Robertson, D. (2000). "Computer simulations of crushable aggregates." Ph.D. Thesis, Cambridge University.

Robertson, D. and Bolton, M.D. (2001) "DEM simulations of crushable grains and soils." In: 4th International Conference on Micromechanics of Granular Media Powders and Grains, 21-25 May 2001, Sendai, Japan.

Robertson, P.K., and Campanella, R.G. (1985). "Liquefaction potential of sands using the CPT." ASCE Journal of Geotechnical Engineering, 111(3): 384-403.

Roscoe, K. H. (1970). "The influence of strains in soil mechanics," Geotechnique, 20(2): 129-170.

Roscoe, K. H. and Poorooshasb, H. B. (1963). "A theoretical and experimental study of strains in triaxial tests on normally consolidated clays." Geotechnique, 13: 12-38.

Roscoe, K. H., Schofield, A. N., and Wroth, M. A. (1958). "On the yielding of soils." Geotechnique, 8: 22 – 53.

Roscoe, K.H. and Burland, J. B. (1968). "On the generalized stress strain behaviour of wet clay." In *Engineering Plasticity*, eds. J. Heyman and F.A. Leckie, Cambridge, England: Cambridge University Press: 535-609.

Rowe, P. W., (1969). "The relation between the shear strength of sands in triaxial compression, plane strain and direct shear." Geotechnique, 19(1): 75-86.

Rowe, P. W. (1962). "The stress dilatancy relation for static equilibrium of an assembly of particles in contact." Proceedings Royal Society, 269: 500-527.

Rowe, W.P., and Barden, L. (1964). "Importance of free ends in triaxial testing." Journal of the Soil Mechanics and Foundations Division, ASCE, 90(SM1): 1–27.

Rudnicki, J. W., and Rice, J. R. (1975). "Conditions for the localization of deformation in pressure-sensitive dilatant materials." Journal of Mechanics and Physic Solids., 23: 371-394.

Rutledge, P. C. (1947). "Cooperative triaxial shear research program." Progress Rep. on Soil Mech. Fact Finding Survey, U.S. Army Corps of Engineers, Waterways Experiment Station, Vicksburg, Miss.

Saada, A. S. (1988). "Hollow cylinder torsional devices: Their advantages and limitations." Symposium on Advanced Triaxial Testing of Soil and Rock, ASTM Geotechnical Testing Journal, STP 977: 766-795.

Saada A. S., and Townsend F. C. (1981). "State of the Art. Laboratory strength testing of soils." In: Yong, Townsend (eds) Laboratory shear strength of soils, ASTM, STP 740: 7–77.

Sammis, C., King, G. and Biegel R. (1987). "The Kinematics of gouge deformation." Pure Applied Geophysics, 125(5): 777-812.

Santamarina, J. C., and Cho, G. C. (2001). "Determination of critical state parameters in sandy soils - simple procedure." Geotechnical Testing Journal, 24: 185–192.

Sasitharan, S., Robertson, P.K., Sego, D.C., and Morgenstern, N.R. (1993). "Collapse behavior of sand." Canadian Geotechnical Journal, 30: 569–577.

Sasitharan, S., Robertson, P. K., Sego, D.C. and Morgenstern, N. R. (1994). "State boundary surface for very loose sand and its practical implications." Canadian Geotechnical Journal, 31: 321-334.

Sassa, K. (1984) "The mechanism starting liquefaction landslides and debris flows." IV International Symposium on Landslides (ISL 1984), Toronto, Canada, 2, 349-354.

Sassa, K. (1985). "The mechanism of debris flow." Proceedings of the 11th International Conference on Soil Mechanics and Foundation Engineering, San Francisco, 3: 1173 – 1176.

Sassa, K. (1992), "Access to the dynamics of landslides during earthquakes by a new cyclic loading ring shear apparatus." Proceedings of the 6th International Symposium on Landslides, Balkema, 3: 1919-1937.

Sassa, K. (1994). "Development of a new cyclic loading ring shear apparatus to study earthquake-induced-landslides." Report for Grain-in-Aid for Development Scientific

Research by the Ministry of Education, Science and Culture, Japan (Project No.03556021), 106p.

Sassa, K. (1995). "Access to the dynamics of landslides during earthquakes by a new cyclic loading high-speed ring shear apparatus (keynote paper)." In: 6th International Symposium on Landslides, "Landslides", A. A. Balkema. Christchurch: 1919-1937.

Sassa, K. (1996), "Prediction of earthquake induced landslides." Special Lecture at 7th International Symposium on Landslides "Landslides", Trondheim, Balkema, 1: 115-132.

Sassa, K., (2000). "Mechanism of flows in granular soils" International Conference on Geotechnical and Geological Engineering (GeoEng 2000), Melbourne, Australia, 1671-1702.

Sassa, K. and Wang, G.-H. (2005). "Mechanism of landslide-triggered debris flows: liquefaction phenomena due to the undrained loading of the torrent deposits." In Debris flows hazards and related phenomena. Edited by M. Jakob and O. Hungr. Springer-Verlag, Heidelberg, Germany. Chap. 5.

Sassa, K., Fukuoka, H., Lee, J. H. and Zhang, D. X. (1991). "Measurement of the apparent friction angle during rapid loading by the high-speed high-stress ring shear apparatus - interpretation of the relationship between landslide volume and the apparent friction during motion." Proceedings of the 6th International Symposium Landslides, Christchurch, N.Z. 1: 545 - 552.

Sassa, K., Fukuoka, H., Scarascia-Mugnozza, G. and Evans, S. (1996). "Earthquake-induced-landslides: distribution, motion and mechanisms." Special Issue of Soils and Foundations: 53-64.

Sassa, K., Wang, G. H. and Fukuoka, H. (2003). "Performing undrained shear tests on saturated sands in a new intelligent type of ring shear apparatus." Geotechnical Testing Journal, 26(3): 257-265.

Sassa, K., Fukuoka, H., Wang, G.H. and Ishikawa, N. (2004). "Undrained dynamic loading ring shear apparatus and its application to landslide dynamics." Landslides 1(1): 7-19.

Sassa K., Fukuoka H., Wang F., and Wang G. (2005). "Dynamic properties of earthquakeinduced large-scale rapid landslides within past landslide masses." Landslides, 2: 125-134.

Savage, S.B. and Sayed, M. (1984). "Stresses developed by dry cohesionless granular materials sheared in an annular shear cell." Journal of Fluid Mechanics, 142: 391-430.

Savage, S. B. (1982). "Granular flows at high shear rates." In Theory of dispersed multiphase flow (ed. R. E. Meyer), Mathematical Research Center, University of Wisconsin: 339 - 358.

Sayão, A.S.F., and Vaid, Y.P. (1996). "Influence of intermediate principal stress on the deformation response of sand. Canadian Geotechnical Journal, 33: 822.828.

Scarlett, B. and Todd, A. C. (1969) "The critical porosity of free flowing solids." Journal of Engineering for Industry (Transactions of ASME), Series A, 91(1): 478-488.

Schimming, B. B., Haas, A. M., and Saxe, H. C., (1966). "Study of Dynamic and Static Failure Envelopes." Journal of the Soil Mechanics and Foundations Division, ASCE, 92(SM2):105–124.

Schneider, J.-L., and Fisher, R. V. (1998). "Transport and emplacement mechanisms of large volcano debris avalanches: evidence from the northwestern sector of Cantal Volcano (France)." Journal of Volcanology and Geothermal Research, 83: 141 – 165.

Schofield, A. N. (1980). "Cambridge Geotechnical Centrifuge Operations." Geotechnique, 30(3): 227 – 268.

Schofield, A. N. and Wroth, C. P. (1968). "Critical state soil mechanics," McGraw-Hill, London.

Seed, H. B. (1979). "Soil liquefaction and cyclic mobility evaluation for level ground during earthquake." Journal of Geotechnical Engineering, ASCE, 105(2): 201-225.

Seed, H.B. (1987). "Design problems in soil liquefaction." Journal of Geotechnical Engineering Division, ASCE, 113(8): 827–845.

Seed, H. B. and Lee, K .L. (1967). "Undrained strength characteristics of cohesionless soils." Journal of Soil Mechanics and Foundation Division, ASCE, 93(6): 333-360.

Seed, H.B., Lee, K.L., and Idriss, I.M. (1969). "Analysis of Sheffield Dam failure." Journal of the Soil Mechanics and Foundations Division, ASCE, 95(SM6), 1453-1490.

Seed, H. B., Martin P. P., and Lysmer J. (1975). "The generation and dissipation of pore water pressures during soil liquefaction." Rep. No. UCB/EERC 75-26, Earthq. Eng. Research Ctr., UC Berkely, CA.

Seed, H.B., Idriss, I.M., and Arango, I. (1983). "Evaluation of liquefaction potential using field performance data." ASCE, Journal of Geotechnical Engineering, 109(3): 458–482.

Seed, H.B., Tokimatsu, K., Harder, L.F. and Chung, R.M. (1985). "The influence of SPT procedure in soil liquefaction resistance evaluations" Journal of Geotechnical Engineering, American Society of Civil Engineers, 111(12): 1425-1445.

Seed, H.B., Seed, R.B., Harder, L.F., and Jong, H.-L. (1989). "Re-evaluation of the Lower San Fernando Dam: Report 2, examination of the post-earthquake slide of February 9, 1971." *U.S. Army Corps of Engineers Contract Report GL-89-2*, U.S. Army Corps of Engineers Waterways Experiment Station, Vicksburg, Mississippi.

Seed, R.B., and Harder, L.F., Jr. (1990). "SPT-based analysis of cyclic pore pressure generation and undrained residual strength." In Proceedings of the H.B. Seed Memorial Symposium, Bi-Tech Publishing Ltd., 2: 351–376.

Sembenelli, P. and Ramirez, A. L. (1969). "Measurement of residual strength of clay with a rotating shear machine." Proceedings of the 7th International Conference on Soil Mechanics, Mexico, 3: 528-529.

Shepherd, R. G. (1989). "Correlations of permeability and grain size," Groundwater, 27(5): 633-638.

Simonini, P. (1996). "Analysis of behavior of sand surrounding pile tips," Journal of Geotechnical Engineering, 122(11): 897-905.

Shibua, S., and Hight, D. W. (1987). "A bounding surface for granular materials." Soils and Foundations, 27(4): 123-136.

Shoaei, Z. and Sassa, K. (1994). "Basic study on the shear behavior of landslides during earthquakes." Bulletin of the Disaster Prevention Research Institute, Kyoto University, 44(1), No. 378: 1-43.

Silver, M.L., Tatsuoka, F., Phukunhaphan, A. and Avramidis, A.S. (1980). "Cyclic undrained strength of sand by triaxial test and simple shear test." Proceedings, 7th World Conference on Earthquake Engineering, Istanbul, 3: 281-288.

Sivathayalan, S., and Vaid, Y.P. (2002). "Influence of generalized initial state and principal stress rotation on the undrained response of sands." Canadian Geotechnical Journal, 39: 63-76

Skempton, A.W. (1985). "Residual strength of clays in landslides, folded strata and the laboratory." Geotechnique, 35(1): 3-18.

Sladen, J.A., and Handford, G. (1987). "A potential systematic error in laboratory testing of very loose sands." Canadian Geotechnical Journal, 24(3): 462-466.

Sladen, J.A., D'Hollander, R.D., and Krahn, J. (1985) "Back analysis of the Nerlerk berm liquefaction slides." Canadian Geotechnical Journal, **22**: 579–588.

Skinner, A. E. (1969). "A note on the influence of interparticle friction on the shearing strength of a random assembly of spherical particles," Geotechnique, 19(1): 150-157.

Skopek, O., Morgenstern, N.R., Robertson, P.K., and Sego, D.C. (1994). "Collapse of dry sand." Canadian Geotechnical Journal, 31: 1008–1014.

Spence, K.J. and Guymer, I. (1997). "Small-scale laboratory flowslides" Geotechnique, 47(5), 915-932.

Stark, T. D. and Contreras, I. A., (1996). "Constant volume ring shear apparatus." Geotechnical Testing Journal, 19(1): 3-11.

Stark, T. D. and Mesri, G. (1992). "Undrained shear strength of liquefied sands for stability analysis." Journal of Geotechnical Engineering, 118(11): 1727-1747.

Stark, T. D. and Vettel, J. J. (1992). "Bromhead ring shear test procedure." Geotechnical Testing Journal, ASTM, 15(1): 24-32.

Stewart, H. R., Jefferies, M. G., and Goldby, H. M. (1983). "Berm construction for the Gulf Canada Mobile Arctic Caisson." In Proceedings of the Annual Offshore Technology Conference, 2-5 May 1983, Vol. 2: 339 – 346.

Stroud, M. A. (1971). "The behavior of sand at low stress levels in the simple shear apparatus," Ph.D. thesis, University of Cambridge, Cambridge, U.K.

Sture, S., Costes, N.C., Batiste, S.N., Lankton, M.R., Alshibli, K.A., Jeremic, B., Swanson, R.A. and Frank, M., (1998). "Mechanics of Granular Materials at Very Low Effective Stresses." ASCE, Journal Aerospace Engineering, 11(3): 67-72.

Sukumaran, B., and Ashmawy, A.K. (2001). "Quantitative characterization of the geometry of discrete particles." Geotechnique, 51(7): 171-179.

Sutherland, H. B., and Mesdary, M. S. (1969). "The influence of the intermediate principal stress on the strength of sand." Proceedings of the 7th International Conference on Soil Mechanics and Foundation Engineering, Mexico City, Vol. 1: 391-399.

Symes, M. J., Gens, S., Hight, D. W. (1984). "Undrained anisotropy and principal stress rotation." Geotechnique, ASCE, 34(1): 11- 27.

Symes, M. J., Shibuya, S., Hight, D. W., and Gens, A. (1985). "Liquefaction with principal stress rotation." Proceedings, 11th International Conference on Soil Mechanics and Foundation Engineering, San Francisco, 1: 1919-1922.

Takei, M., Kusakabe, O., and Hayashi, T. (2001). "Time-dependent behavior of crushable materials in one-dimensional compression test," Soils and Foundations, 41(1): 97-121.

Tarantino, A. and Hyde, A. F. L. (2005). "An experimental investigation of work dissipation in crushable materials." Geotechnique, 55(8): 575-584.

Tatsuoka, F., and Silver, M. L. (1981). "Undrained stress-strain behavior of sand under irregular loading." Soils and Foundations, 21(1): 51–66.

Tatsuoka, F., Muramatsu, M., and Sasaki, T. (1982). "Cyclic undrained stress-strain behavior of dense sands by torsional simple shear." Soils and Foundations, 22(2): 55-70.

Tatsuoka, F., Nakamura, S., Huang, C-C., and Tani, K. (1990). "Strength anisotropy and shear band direction in plane strain tests of sand." Soils and Foundations, 30(1): 35-54.

Tatsuoka, F., Masuda, T., Siddiquee, M. S. A., and Koseki, J. (2003). "Modeling the stress-strain relations of sand in cyclic plane strain loading," Journal of Geotechnical and Geoenvironmental Engineering, 129(6): 450-467.

Taylor, D. W. (1952). "A direct shear tests with drainage control." Symposium on Direct Shear Testing of Soils, ASTM STP 131: 63-74.

Taylor, D. (1948). "Fundamentals of soil mechanics." New York: Wiley.

Terzaghi, K., Peck, R. B., and Mesri, G. (1996). "Soil mechanics in engineering practice," John Wiley & Sons, Inc., 3rd Edition, 549pp.

Thevanayagam, S. and Mohan, S. (1998). "Intergranular void ratio-steady state strength relations for silty sands." Geotechnical Earthquake Engineering and Soil Dynamics III, 1: 349-360.

Thomson, P. R. and Wong, R. C. K. (2008). "Specimen nonuniformities in water-pluviated and most-tamped sands under undrained triaxial compression and extension." Canadian Geotechnical Journal, 45: 939-956.

Thornton, C. (2000). "Numerical simulations of deviatoric shear deformation of granular media." Géotechnique, 50(1): 43-53.

Tika, T.E., Vaughan P.R. and Lemos, L.J. (1996). "Fast shearing of pre-existing shear zones in soil." Geotechnique, 46(2): 197-233.

Tokimatsu, K., and Yoshimi, Y. (1983) "Empirical correlation of soil liquefaction based on SPT N-value and fines content." Soils and Foundations, 23(4):57–74.

Torabi, A., Braathen, A., Cuisiat, F., and Fossen, H. (2007). "Shear zones in porous sand: Insights from ring-shear experiments and naturally deformed sandstones." Tectonophysics, 437: 37-50.

Touati, A., (1982). "Comportement mécanique des sols pulvérulents sous fortes contraintes." PhD thesis, École nationale des ponts et chaussés.

Towhata, I. (2008). "Geotechnical Earthquake Engineering" Springer-Verlag Berlin Heidelberg, 676 pp.

Troncoso, J. H., and Verdugo, R. (1985) "Silt content and dynamic behavior of tailing sands." In Proceedings of the 11th International Conference on Soil Mechanics and Foundation Engineering, San Francisco, Calif., August, 3: 1311–1314.

Tsoungui, O., Vallet, D., and Charmet, J. C. (1999). "Numerical model of crushing of grains inside two-dimensional granular materials," Powder Technology, 105: 190-198.

Ueng, T., Tzou, Y., and Lee, C. (1988). "The effect of end restraint on volume change and partical breakage of sands in triaxial tests." *In* advanced triaxial testing of soil and rock. American Society for Testing and Materials, Special Technical Publication 977: 679–691.

Ui, T., Kawachi, S., and Neall, V. E. (1986). "Fragmentation of debris avalanche material during flowage – evidence from the Pungarehu Formation, Mount Egmont, New Zealand." Journal of Volcanology and Geothermal Research, 27: 255 – 264.

Vaid, Y. P., and Chern, J. C. (1983). "Effect of static shear on resistance to liquefaction," Soils and Foundations, 23(1): 47-60.

Vaid, Y.P., and Chern J.C. (1985). "Cyclic and monotonic undrained response of saturated sands." Session No. 52, Advances in the Art of Testing Soils Under Cyclic Conditions, Annual Convention and Exposition, Detroit, MI.

Vaid, Y. P., and Finn, W. D. L. (1979). "Static Shear and Liquefaction Potential," Journal of Geotechnical Division, ASCE, 105(GT10): 1233-1246.

Vaid, Y.P. and Negussey, D. (1988). "Preparation of reconstituted sand specimens." Advanced Triaxial Testing of Soil and Rock, ASTM STP 977, Donaghe, Chaney and Silver Eds., ASTM International, West Conshohocken, PA: 405-417.

Vaid, Y.P. and Sasitharan, S. (1992). "The strength and dilatancy of sand." Canadian Geotechnical Journal, 29: 522-526.

Vaid, Y. P., and Sivathayalan, S. (1996). "Static and cyclic liquefaction potential of Fraser Delta sand in simple shear and triaxial tests." Canadian Geotechnical Journal., 33 (4): 281-289.

Vaid, Y. P. and Sivathayalan, S. (1999). "Fundamental factors affecting liquefaction susceptibility of sands," Physics and Mechanics of Soil Liquefaction, Proc. Int. Workshop on the Physics and Mechanics of Soil Liquefaction, Baltimore, Maryland, USA:105-120.

Vaid, Y. P. and Sivathayalan, S. (2000). "Fundamental factors affecting liquefaction susceptibility of sands," Canadian Geotechnical Journal, 37: 592-606.

Vaid, Y. P. and Thomas, J. (1995). "Liquefaction and postliquefaction behavior of sand." Journal of Geotechnical Engineering, 121(2): 163-173.

Vaid, Y.P., Chern, J.C. and Tumi, H. (1985). "Confining pressure, grain angularity and liquefaction." ASCE Journal of Geotechnical Engineering Division, 111(10): 1229-1235.

Vaid, Y.P., Chung, E. K. F. and Kuerbis, R.H. (1990). "Stress path and steady state." Canadian Geotechnical Journal, 27(1): 1-7.

Vaid, Y. P., Sivathayalan, S., and Stedman, D. (1999). "Influence of specimen-reconstituting method of the undrained response of sand." Geotechnical Testing Journal, 22: 187-195.

Vaid, Y. P., Uthayakumar, M., Sivathayalan, S., Robertson, P. K. and Hofmann, B. (1995). "Laboratory testing of Syncrude sand." Proceedings of the 48th Canadian Geotechnical Conference, 1: 223-232.

Vardoulakis, I. (1996). "Deformation of water-saturated sand: I. uniform undrained deformation and shear banding." Geotechnique, 46(3): 441-456.

Vardoulakis, I. and Aifantis, E. (1991). "A gradient flow theory of plasticity for granular materials." Acta Mech. 87(3–4): 197-217.

Vardoulakis, I. and Graf, B. (1985) "Calibration of constitutive models for granular materials using data from biaxial experiments" Geotechnique, 35: 299-317.

Vargas-Monge, W. (1997). "Ring shear tests on large deformation of sand." Ph.D. Thesis, University of Tokyo, Tokyo, Japan.

Vasquez-Herrera A., Dobry R., and Ng, T. T. (1988). "Pore pressure build-up and liquefaction failure of anisotropically consolidated sand due to cyclic straining." Proceedings of conference on hydraulic fill structures, Fort Collins. American Society of Engineers, New York: 346–366.

Verdugo, R. 1992. Characterization of sandy soil behavior under large deformation. Ph.D. thesis, University of Tokyo.

Verdugo, R. and Ishihara, K. (1996). "The steady state of sandy soils." Soils and Foundations, 36(2): 81-91.

Verdugo, R., Castillo, P., and Briceno, L. (1995). "Initial Soil Structure and Steady-State Strength." The First International Conference on Earthquake Geotechnical Engineering, K. Ishihara (ed.), Balkema, 1: 209-214.

Vesic, A. B., and Barksdale, R. D. (1963). "On shear strength of sand at very high pressures," Report published by the Georgia Institute of Technology, Atlanta; Summarized in Discussion of Test Methods and New Equipment, *Symposium on Laboratory Shear Testing of Soils*, ASTM STP 361: 301-305.

Vesic A.S., Clough, G.W. (1968). "Behavior of granular materials under high stresses." Soil Mechanics and Foundations Divisions, proceeding of the Journal of Geotechnical Engineering 94 (SM 3): pp. 661–688.

Viggiani, G., Kuentz, M. and Desrues, J. (2001). "An experimental investigation of the relationships between grain size distribution and shear banding in sand." In: Vermeer, P.A., Diebels, S., Ehlers, W., Herrmann, H.J., Luding, S. and Ramm, E., Editors, 2001. *Continuous and Discontinuous Modelling of Cohesive-Frictional Material*, Springer, Stuttgart: 111–126

Wafid, M.A., Sassa K., Fukuoka H., and Wang G.H. (2004). "Evolution of shear-zone structure in undrained ring-shear tests." Landslide, 1(2):101–112.

Wan, R. G., and Guo, R. G. (1999). "A pressure and density dependent dilatancy model for granular materials." Soils and Foundations, 39(6): 1–12.

Wanatowski, D. and Chu, J. (2007). "Static liquefaction of sand in plane strain," Canadian Geotechnical Journal, 44(3): 299-313.

Wang, Y. (1997). "Characterization of dilative shear failure in sand." M. Phil thesis, Hong Kong University of Science and Technology, Hong Kong, China.

Wang, F. W. and Sassa, K. (1998). "Experimental study on the factors affecting high-mobility of landslides by ring-shear tests." Proc. 8th Int. Association of Engineering Geology and the Environment, Int. Congress, Rotterdam:Balkema, 3: 1819-1826.

Wang, G. and Sassa, K. (2002). "Post-failure mobility of saturated sands in undrained load-controlled ring shear tests." Canadian Geotechnical Journal, 39(4):821–837.

Wang, F. W., Sassa, K., Wang, G. (2002). "Mechanism of a long-runout landslide triggered by the August 1998 heavy rainfall in Fukushima Prefecture, Japan" Engineering Geology, 63: 169-185.

Wang, G., Sassa, K. and Fukuoka, H. (2003). "Downslope volume enlargement of a debris slide – debris flow in the 1999 Hiroshima, Japan, rainstorm." Engineering Geology, 69: 309-330.

Watanabe, K., Koseki, J., and Tateyama, M. (2003). "Application of High-Speed Digital CCD Cameras to Observe Static and Dynamic Deformation Characteristics of Sand," Geotechnical Testing Journal, ASTM, 28(5): 1-13.

Whitman, R.V. (1985). "On liquefaction." Proceedings of the eleventh international conference on soil mechanics and foundation engineering, San Fransisco, 4: 1923-1926.

Wood, D.M. (1984). "On stress parameters." Geotechnique, 34: 282–287.

Wroth, C.P. and Bassett, R.H., (1965). "A stress–strain relationship for the shearing behaviour of a sand." Geotechnique, 15: 32–56.

Wroth, C. P. and Basset, R. H. (1965). "A stress-strain relationship for the shearing behavior of a sand," Geotechnique, 15(1): 32-56.

Yamada, Y., and Ishihara, K. (1979). "Anisotropic deformation characteristics of sand under three dimensional stress conditions." Soils and Foundations, 19(2): 79-94.

Yamamuro, J. A. and Lade, P. V. (1996). "Drained sand behavior in axisymmetric tests at high pressures." Journal of Geotechnical Engineering, 122(2): 109–119.

Yamamuro, J.A., and Lade, P.V. (1997) "Static liquefaction of very loose sands." Canadian Geotechnical Journal, 34: 905–917.

Yamamuro, J.A. and Lade, P.V. (1998). "Steady state concepts and static liquefaction of silty sands" Journal of Geotechnical and Geo-environmental Engineering, ASCE, 124(9): 868-877.

Yang, J., and Mu, F. (2008). "Use of state-dependent strength in estimating end bearing capacity of piles in sand." Journal of Geotechnical & Geoenvironmental Engineering ASCE, 134(7): 1010-1014.

Yang, S. L., Sandven, R. and Grande, L. (2006). "Steady-state lines of sand-silt mixtures," Canadian Geotechnical Journal, 43: 1213-1219.

Yarnold, J. C. (1993). "Rock-avalanche characteristics in dry climates and the effect of flow into lakes: insights from mid-Tertiary sedimentary breccias near Artillery Peak, Arizona." Geological Society of America Bulletin, 105:345–360.

Yasufuku, N. and Hyde, A. F. L. (1995). "Pile end-bearing capacity in crushable sands." Geotechnique, 45(4): 663-676.

Yet, N. S. (1998). "Time-dependent behavior of pile in sand." Ph.D. Thesis, National University of Singapore.

Yoshida, T., (1994). "Strain Localization and Shear Banding during Failure of Sands." Doctoral Thesis at University of Tokyo (in Japanese).

Yoshida, T., Tatsuoka, F., Kamegai, Y., Siddiquee, M. S. A. & Park, C.-S. (1994). "Shear banding in sands observed in plane strain compression." Proc. 3rd Int. Workshop on Localization and Bifurcation Theory for Soils and Rocks, Aussois, France. Rotterdam:Balkema: 165-179.

Yoshimi, Y. and Oh-oka, H. (1975). "Influence of degree of shear stress reversal on the liquefaction potential of saturated sand." Soils and Foundations, The Japanese Geotechnical Society, 15(3): 27-40.

Yoshimine, M. (1996). "Undrained flow deformation of saturated sand under monotonic loading condition," Ph.D. Thesis, University of Tokyo, Tokyo, Japan.

Yoshimine, M., and Ishihara, K. (1998). "Flow potential of sand during liquefaction." Soils and Foundations, 38: 189-198.

Yoshimine, M., Ishihara, K., and Vargas-Monge, W. (1998). "Effects of principal stress direction and intermediate principal stress on undrained shear behavior of sand." Soils and Foundations, 38(3): 179-188.

Yoshimine, M., Ozay, R., Sezen, A., and Ansal, A. (1999). "Undrained plane strain shear tests on saturated sand using a hollow cylinder torsional shear apparatus." Soils and Foundations, 39(2): 131-136.

Zhang, H., and Garga, V.K. (1997). "Quasi-steady state: a real behavior?" Canadian Geotechnical Journal, 34: 749-761.

Zlatovic, S. and Ishihara, K. (1995). "On the influence of non-plastic fines on residual strength" Proceedings, IS-TOKYO'95, First International Conference, Earthquake Geotechnical Engineering, Tokyo, K. Ishihara, Ed. A.A.Balkema: 239-244.

Zlatovic, S., and Ishihara, K. (1997). "Normalized behavior of very loose non-plastic soils: Effects of fabric." Soils and Foundations, 37(4): 47-56.

APPENDIX A. TXC TEST RESULTS

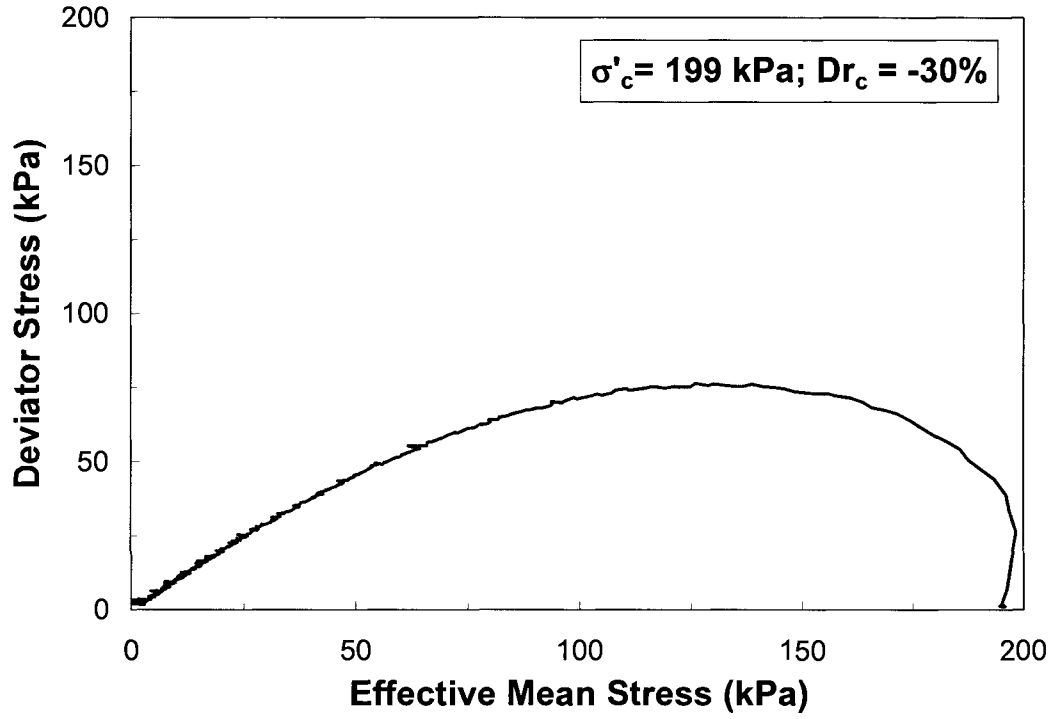

(a)

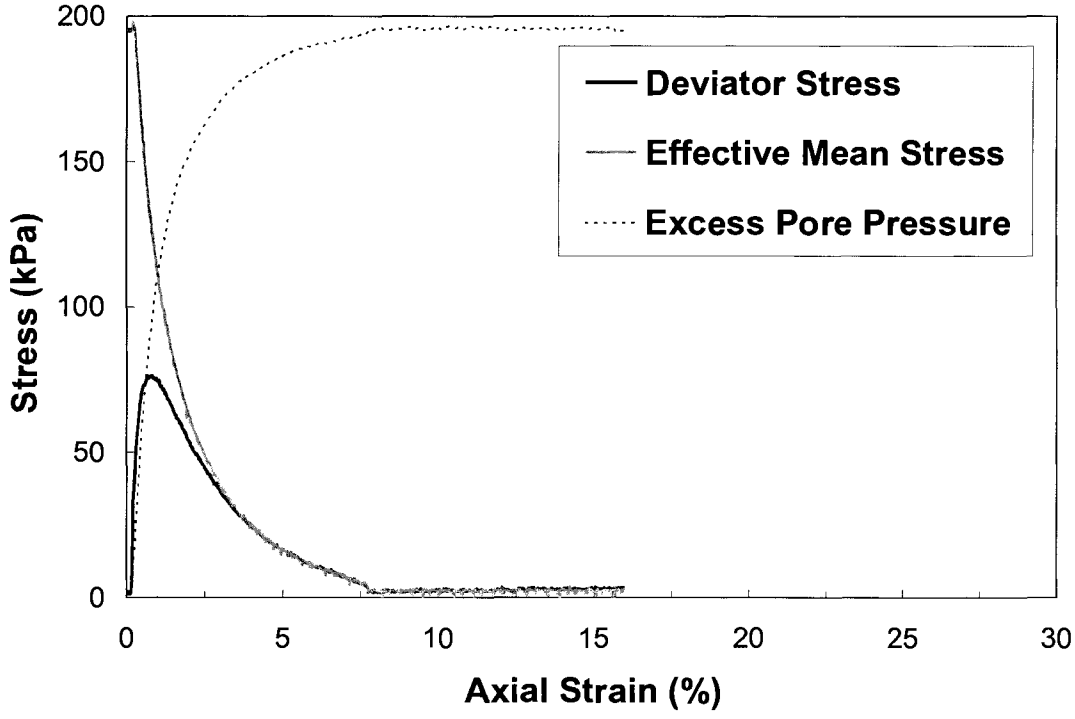

(b)

Figure A.1: (a) stress path, and (b) stress-displacement plots in TxC test MTIRUN29

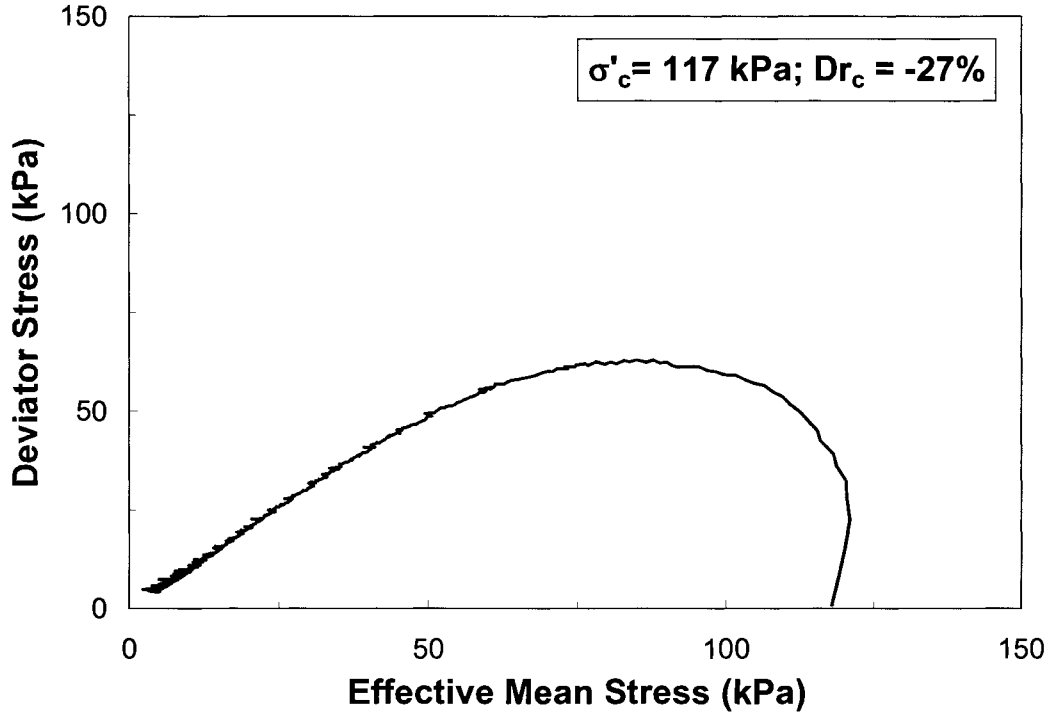

(a)

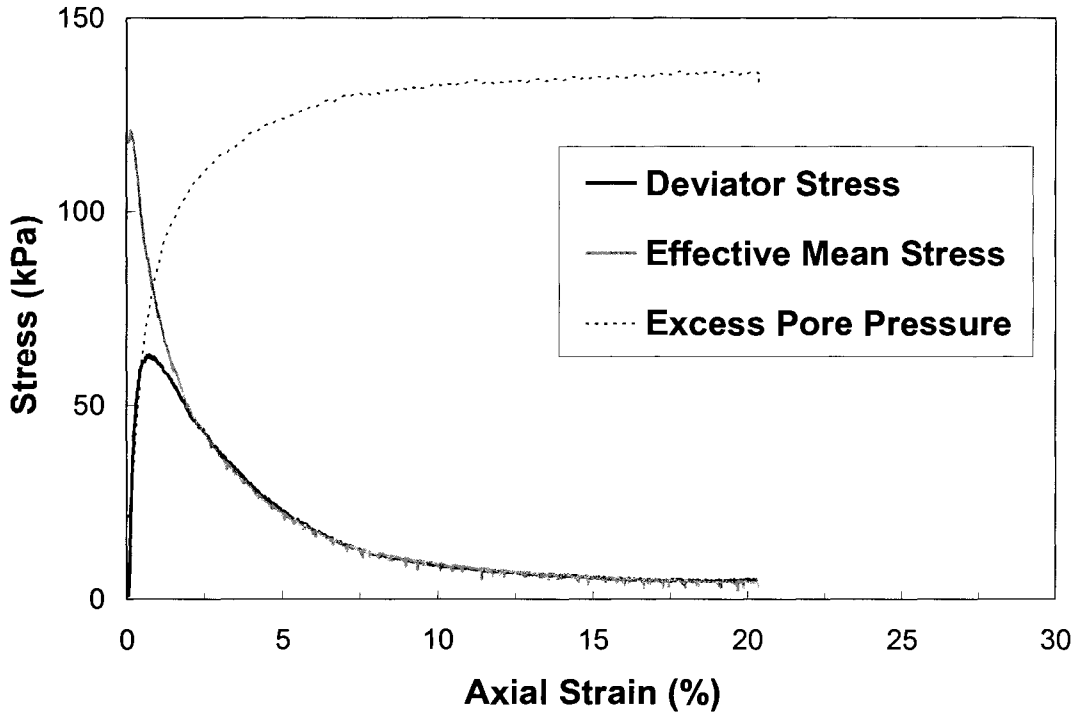

(b)

Figure A.2: (a) stress path, and (b) stress-displacement plots in TxC test MTIRUN17

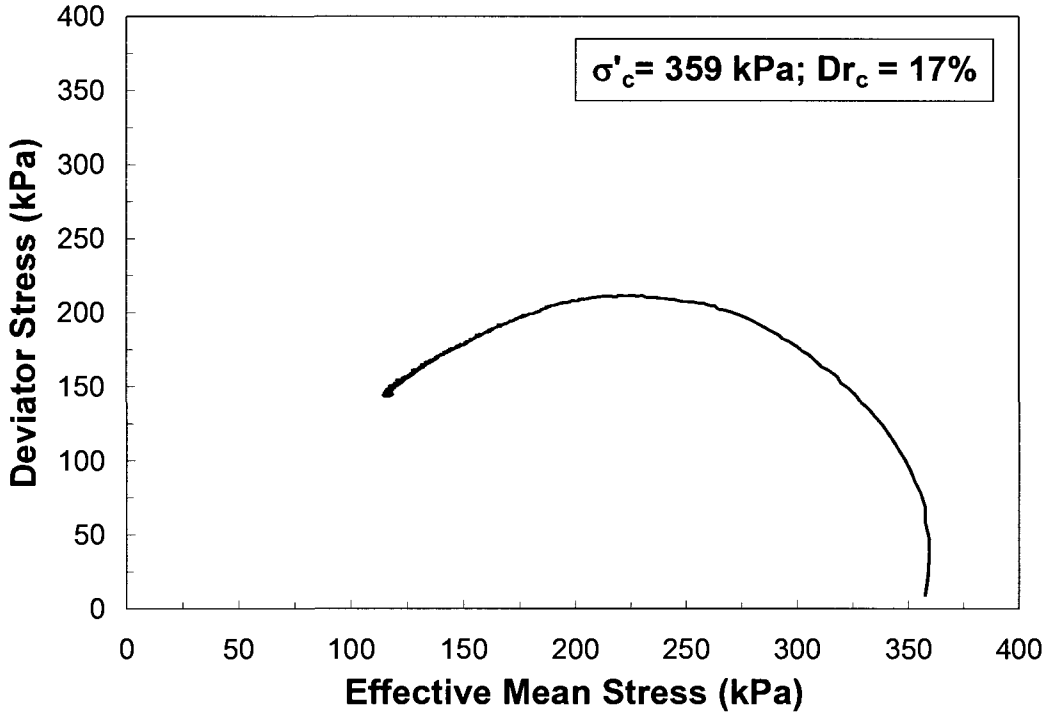

(a)

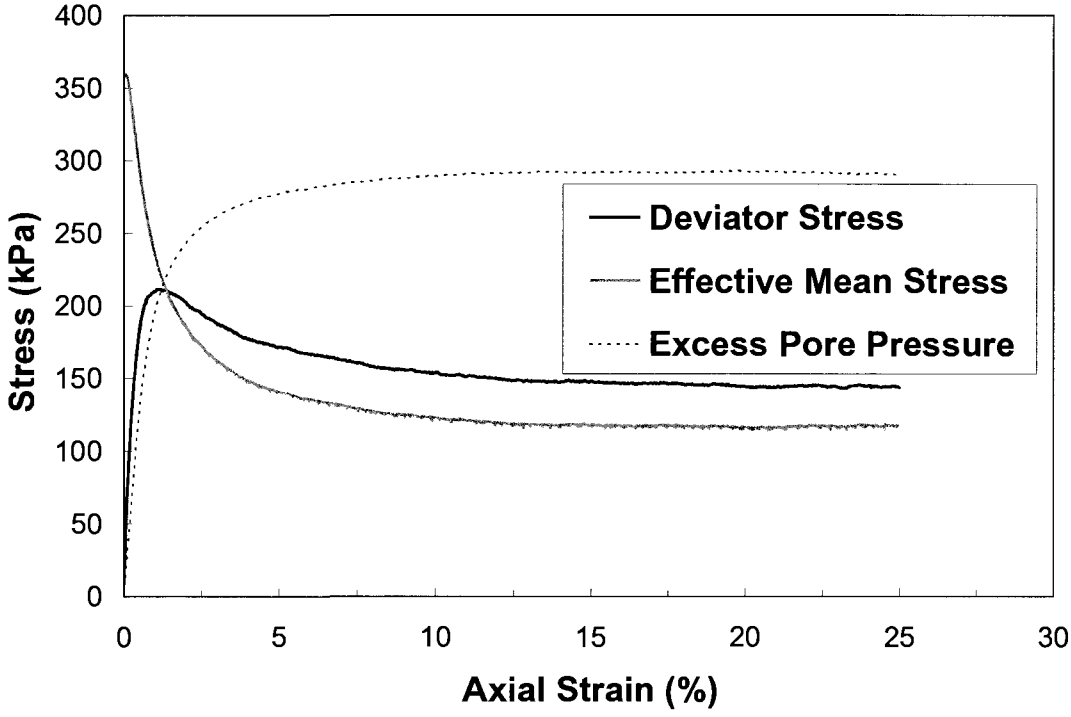

(b)

Figure A.3: (a) stress path, and (b) stress-displacement plots in TxC test MTIRUN52

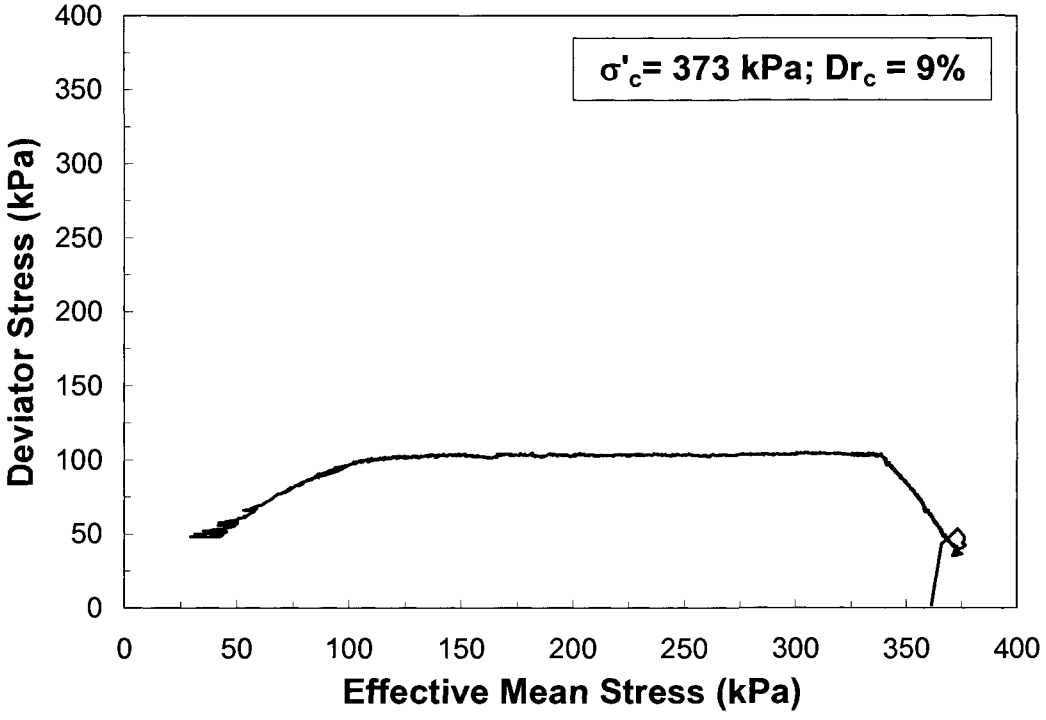

(a)

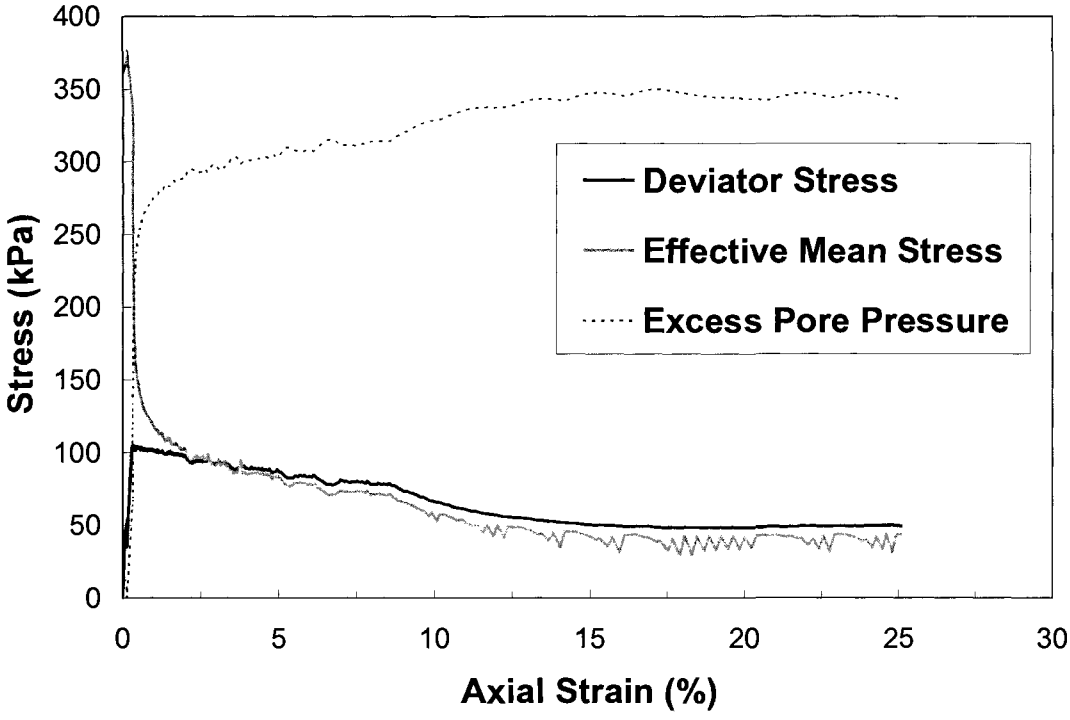

(b)

Figure A.4: (a) stress path, and (b) stress-displacement plots in TxC test MTIRUN54

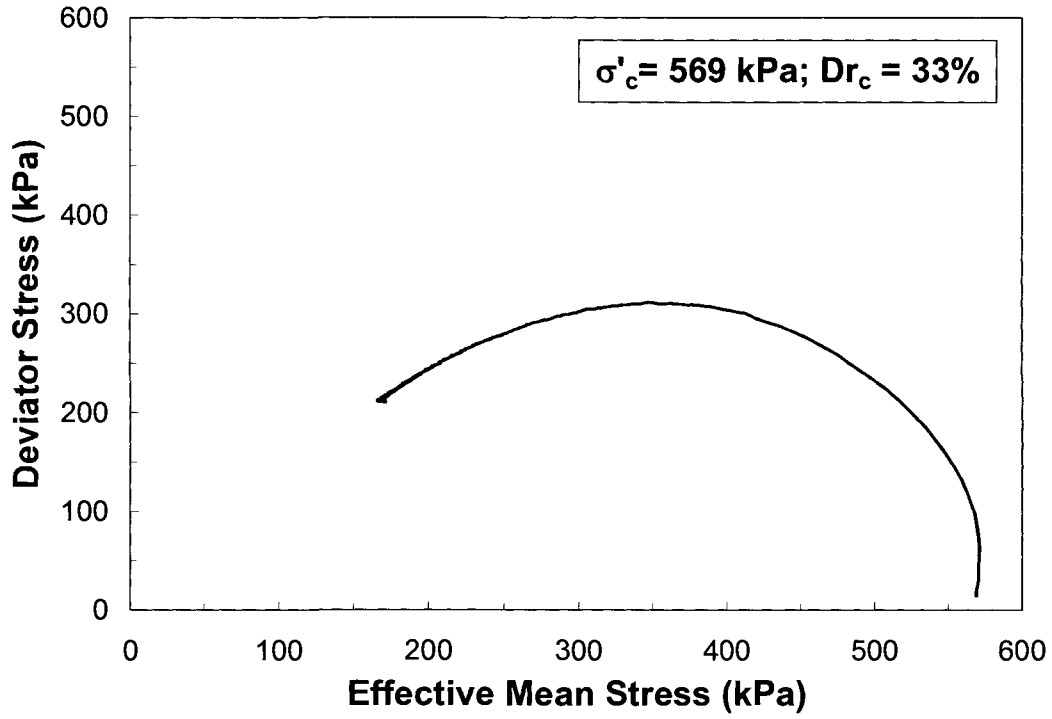

(a)

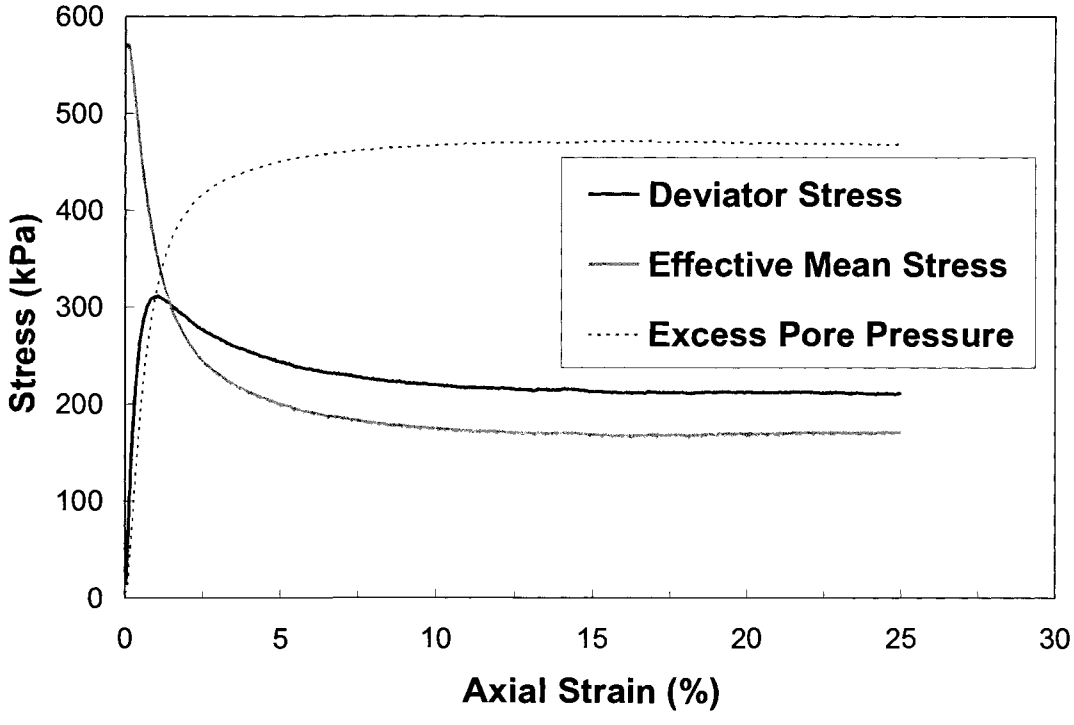

(b)

Figure A.5: (a) stress path, and (b) stress-displacement plots in TxC test MTIRUN83

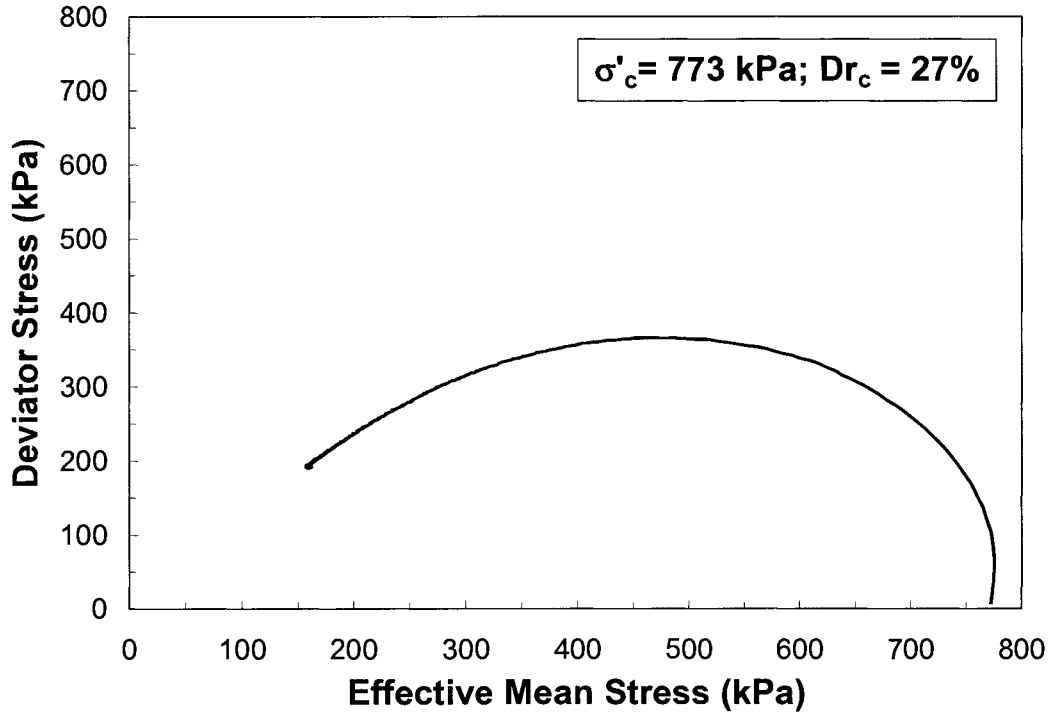

(a)

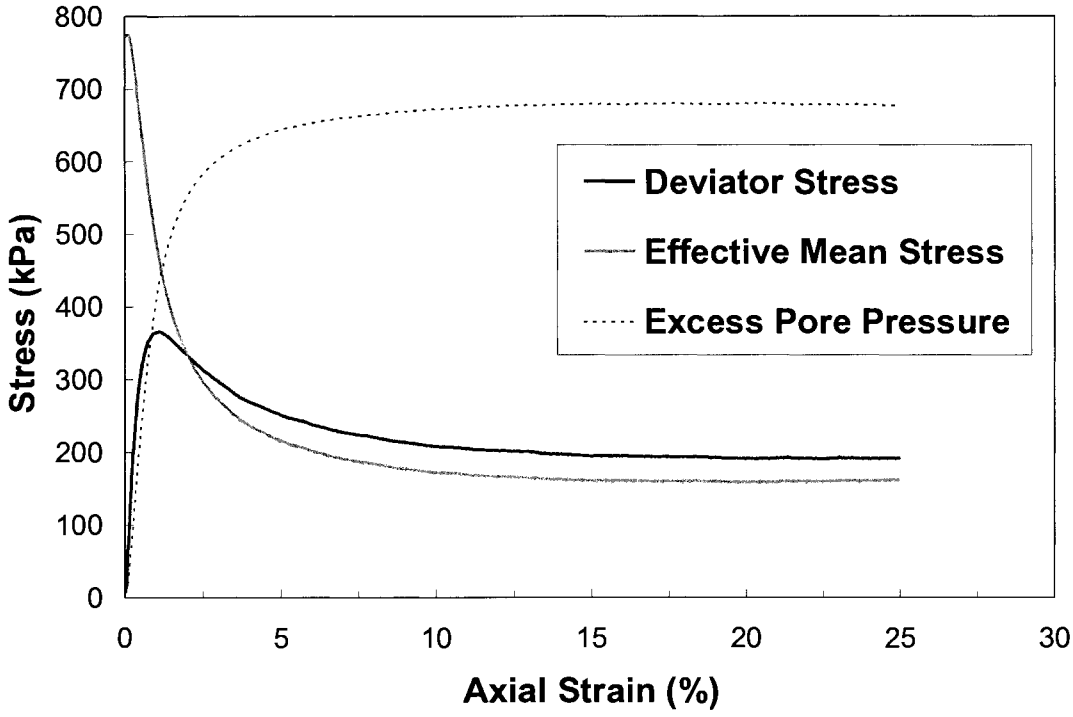

(b)

Figure A.6: (a) stress path, and (b) stress-displacement plots in TxC test MTIRUN112

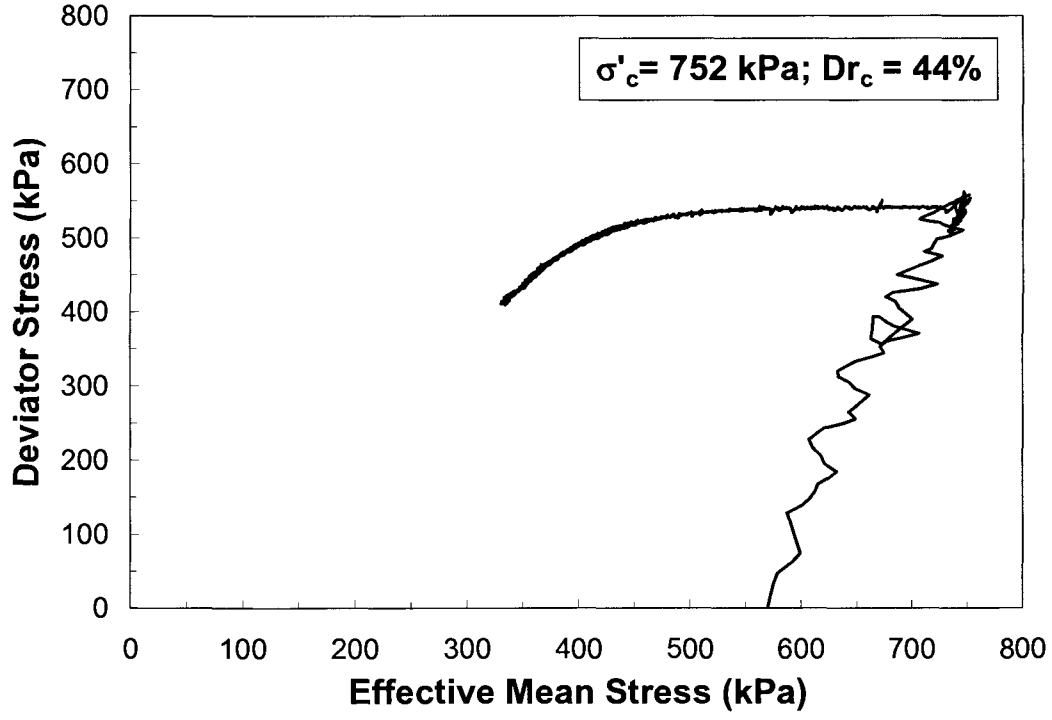

(a)

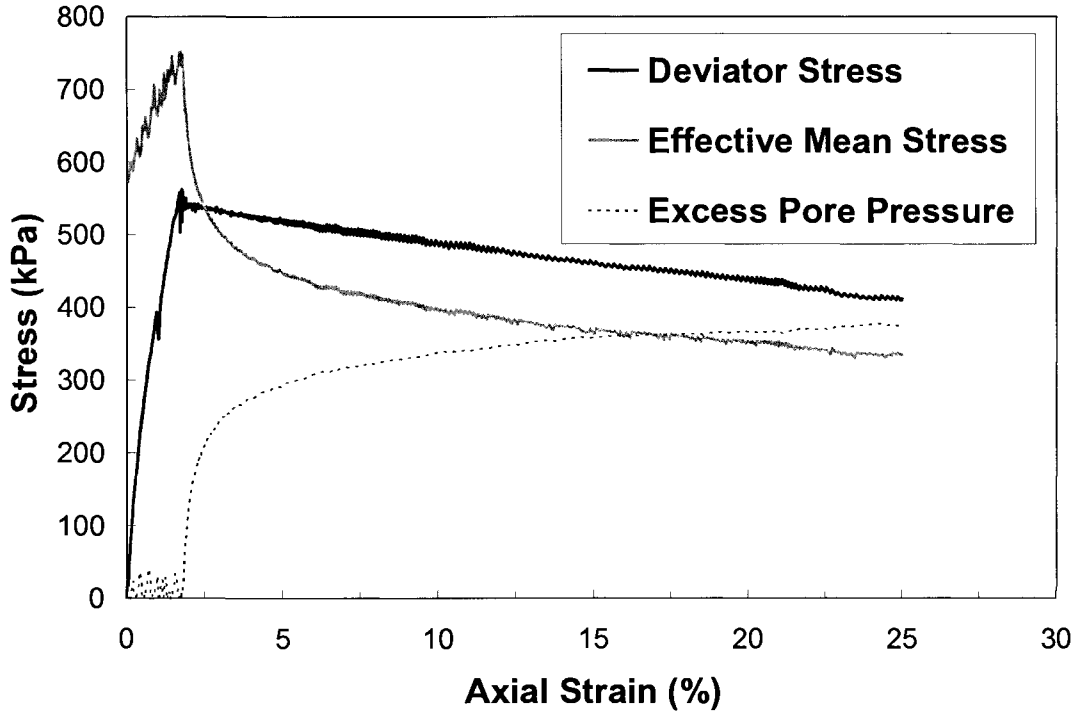

(b)

Figure A.7: (a) stress path, and (b) stress-displacement plots in TxC test MTIRUN109

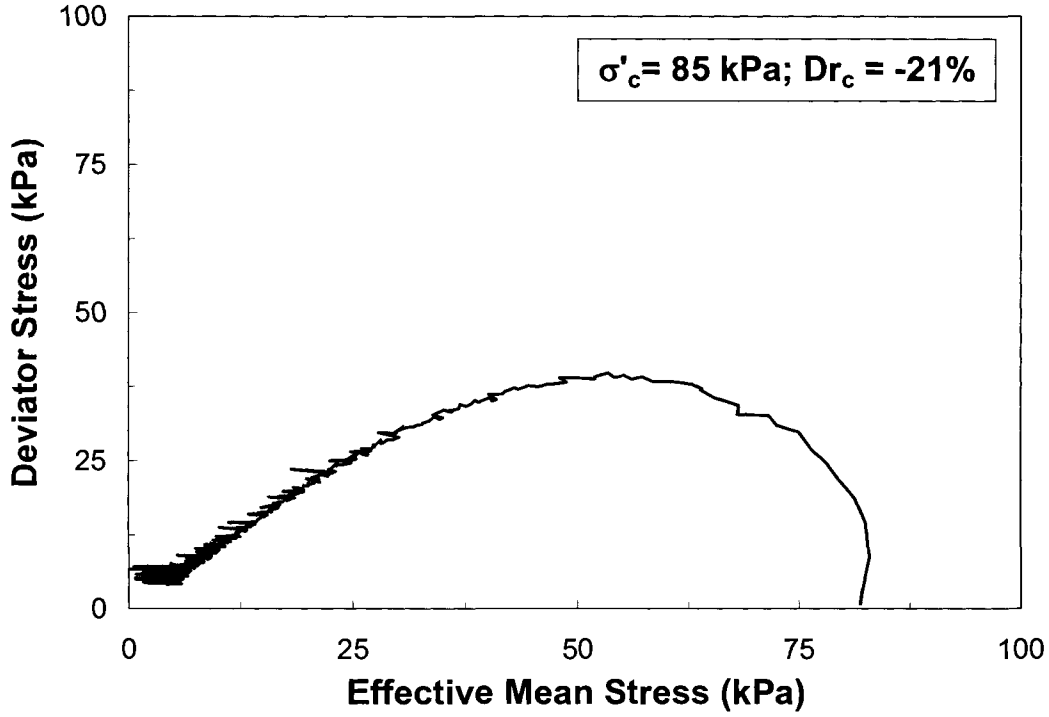

(a)

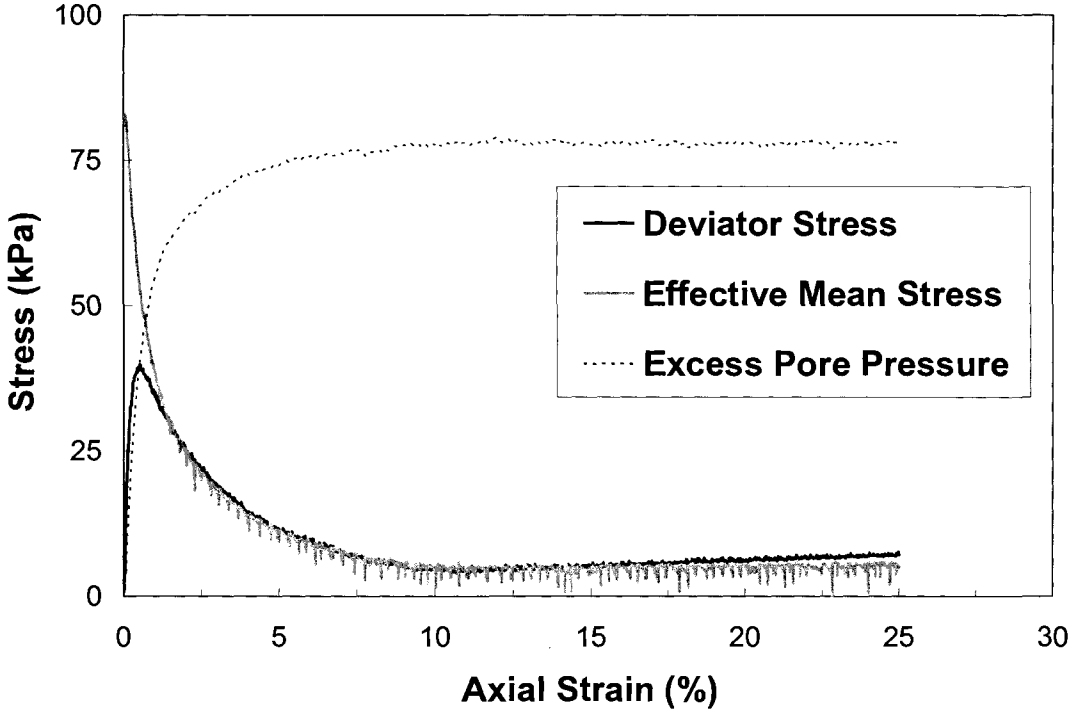

(b)

Figure A.8: (a) stress path, and (b) stress-displacement plots in TxC test MTIRUN12

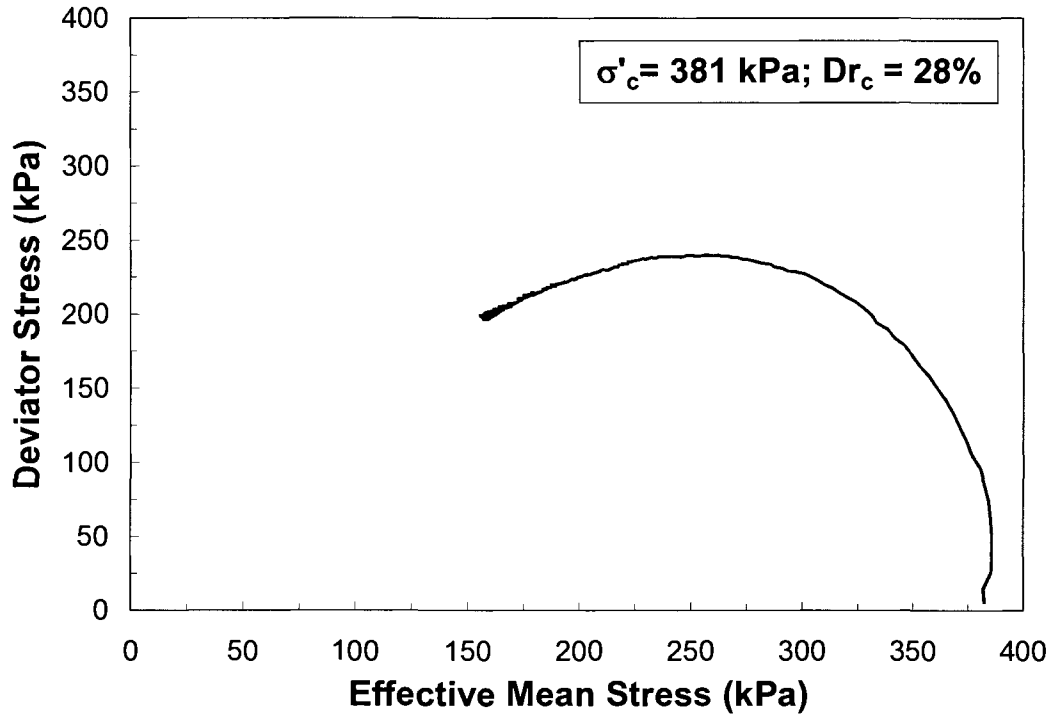

(a)

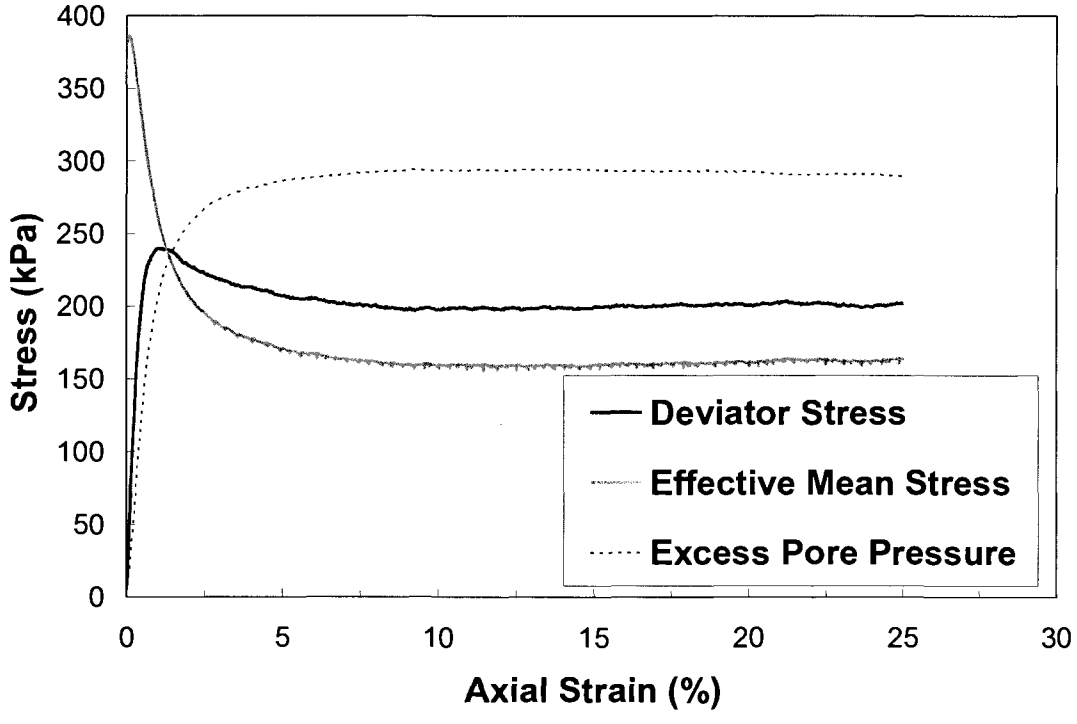

(b)

Figure A.9: (a) stress path, and (b) stress-displacement plots in TxC test MTIRUN55

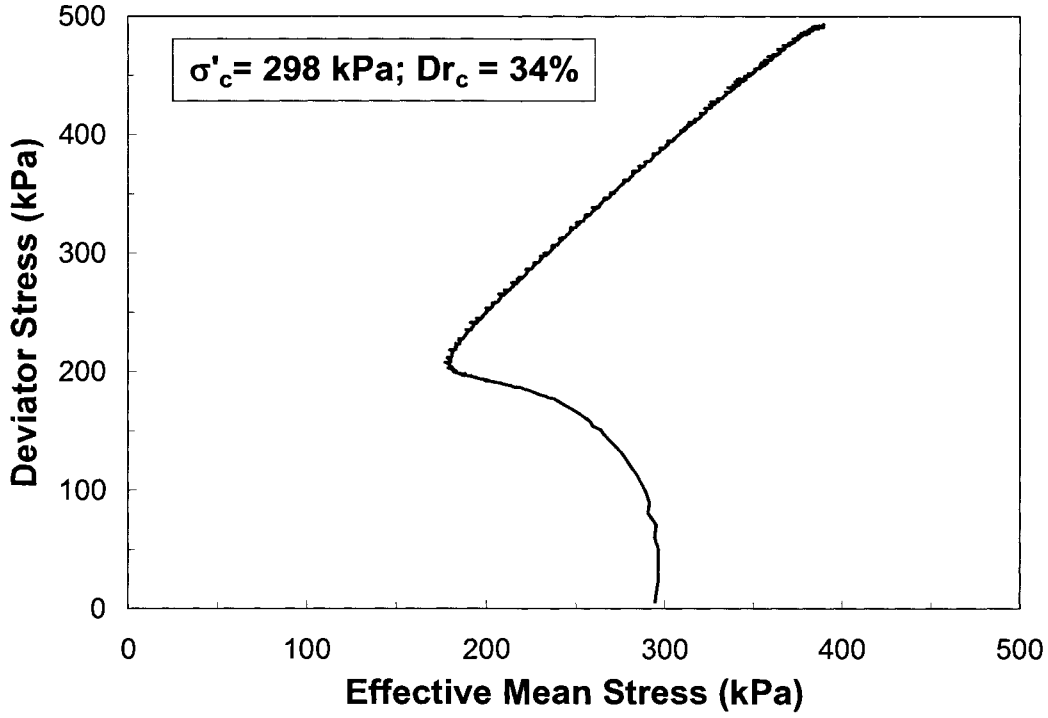

(a)

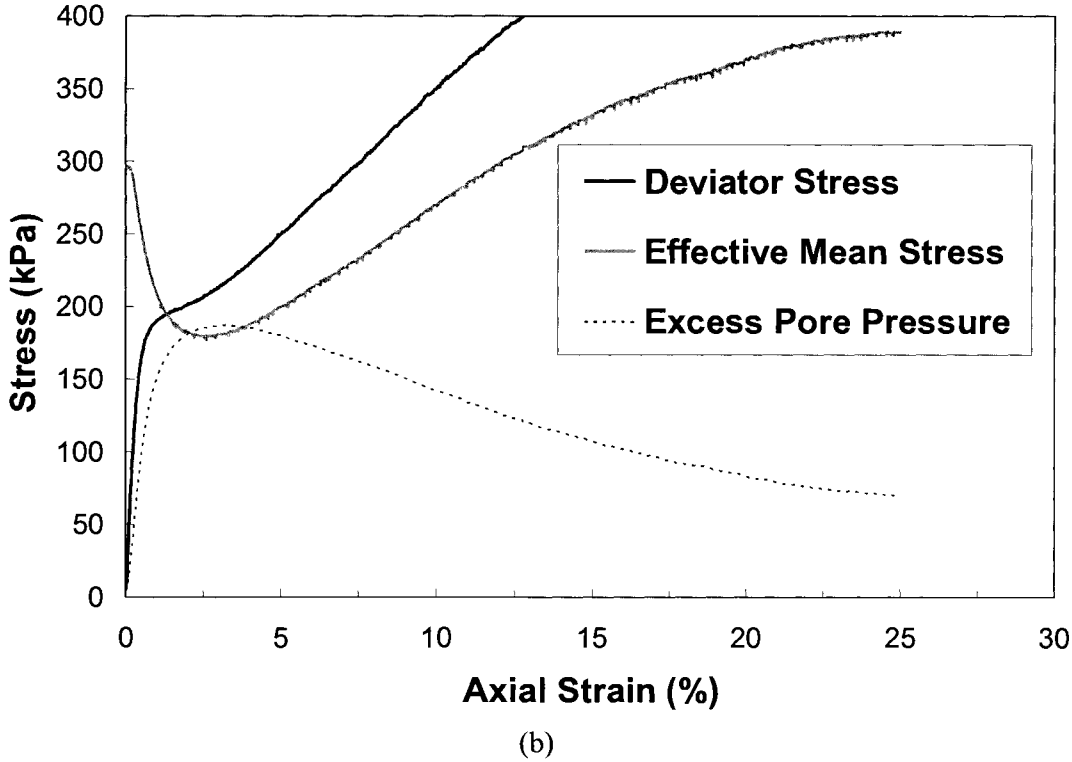

(b)

Figure A.10: (a) stress path, and (b) stress-displacement plots in TxC test MTIRUN43

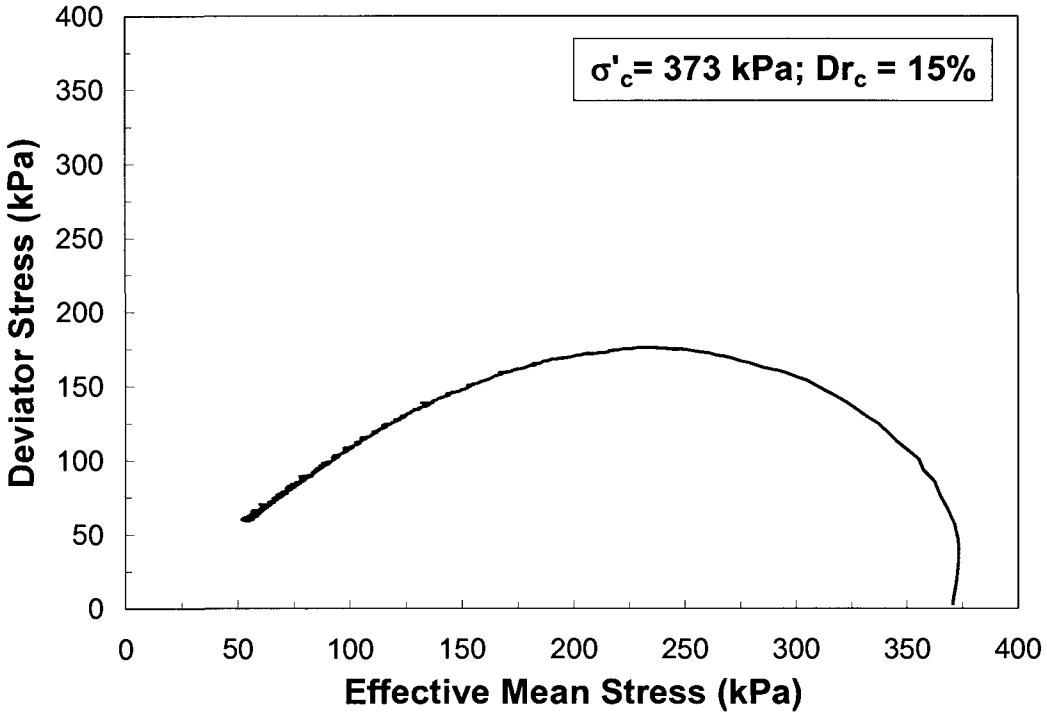

(a)

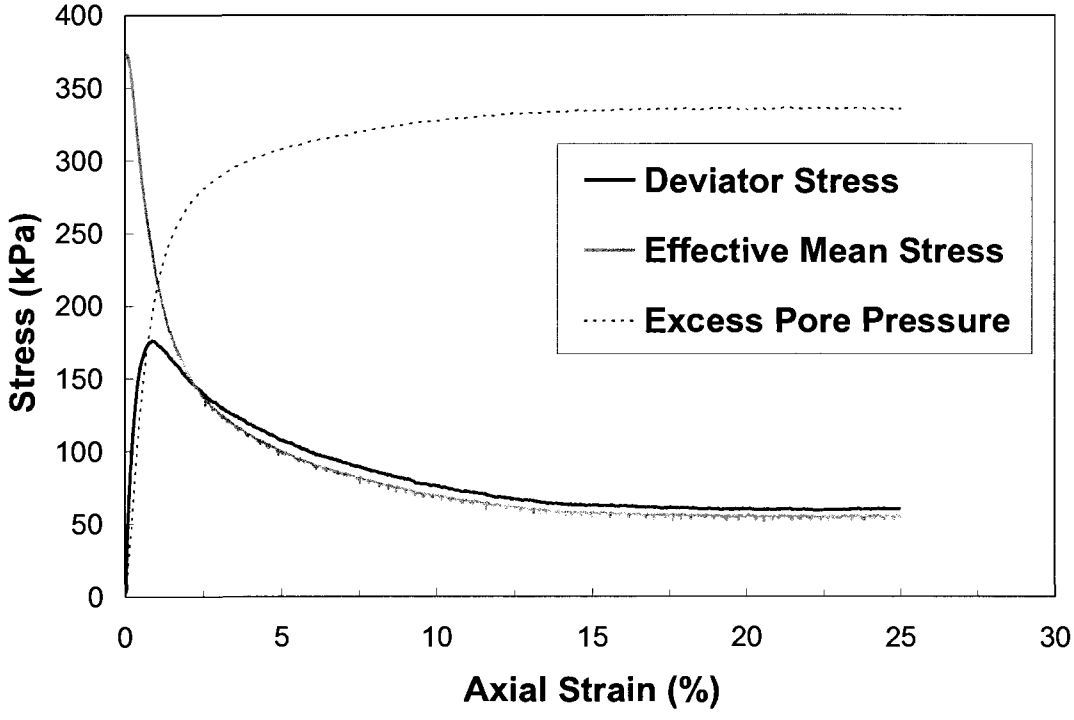

(b)

Figure A.11: (a) stress path, and (b) stress-displacement plots in TxC test MTIRUN54

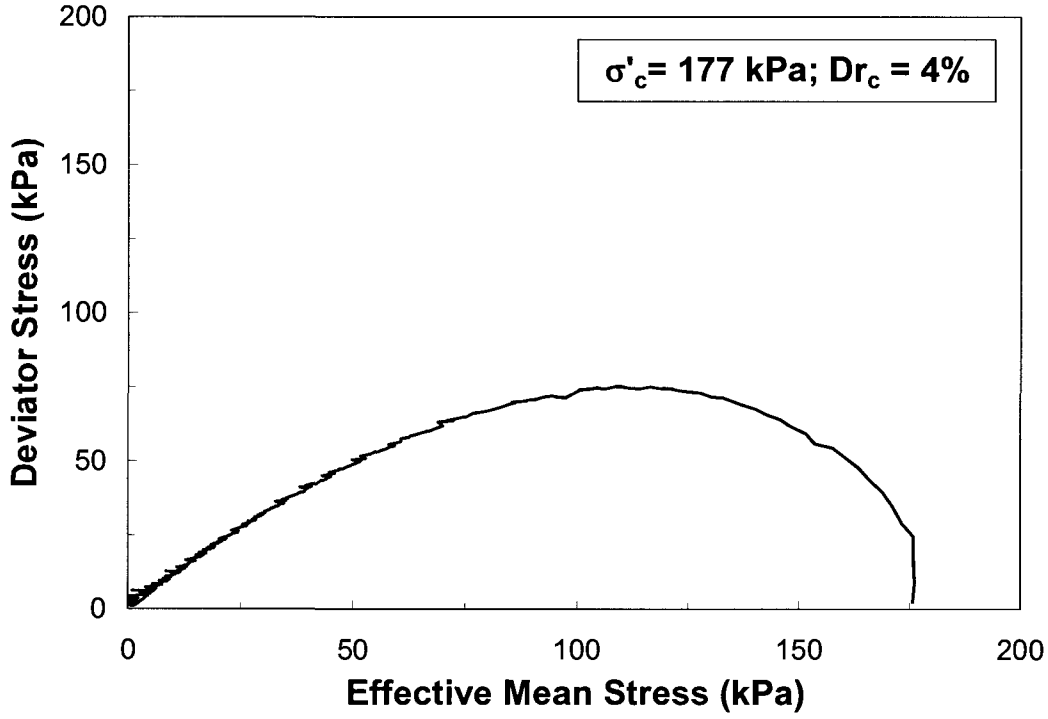

(a)

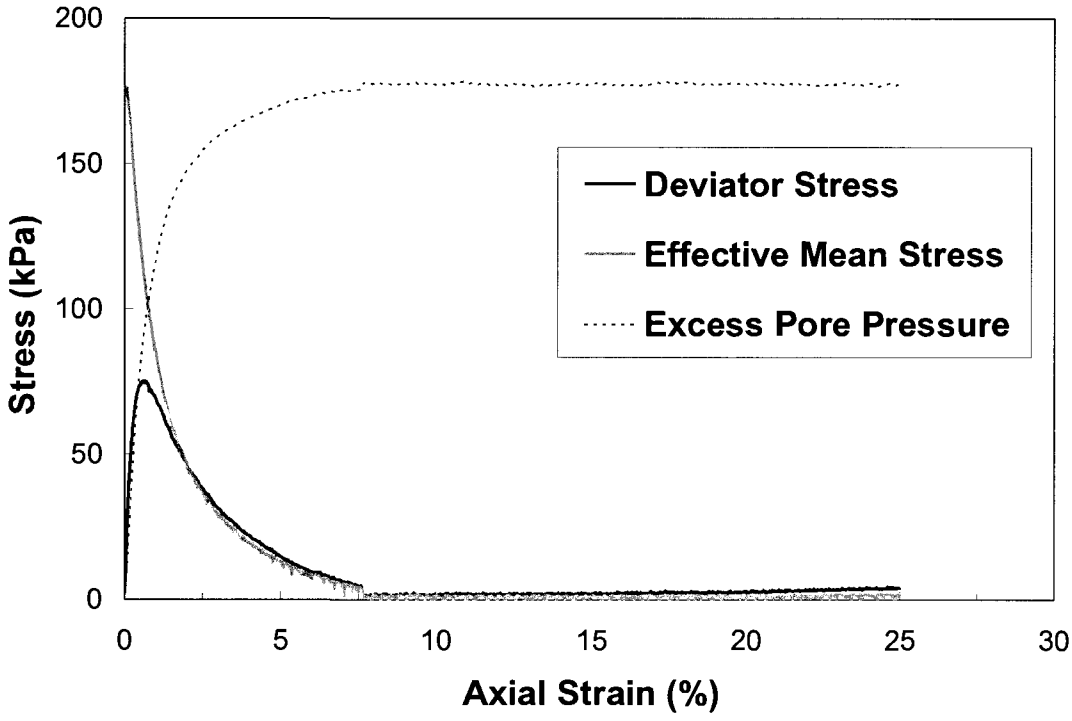

(b)

Figure A.12: (a) stress path, and (b) stress-displacement plots in TxC test MTIRUN26

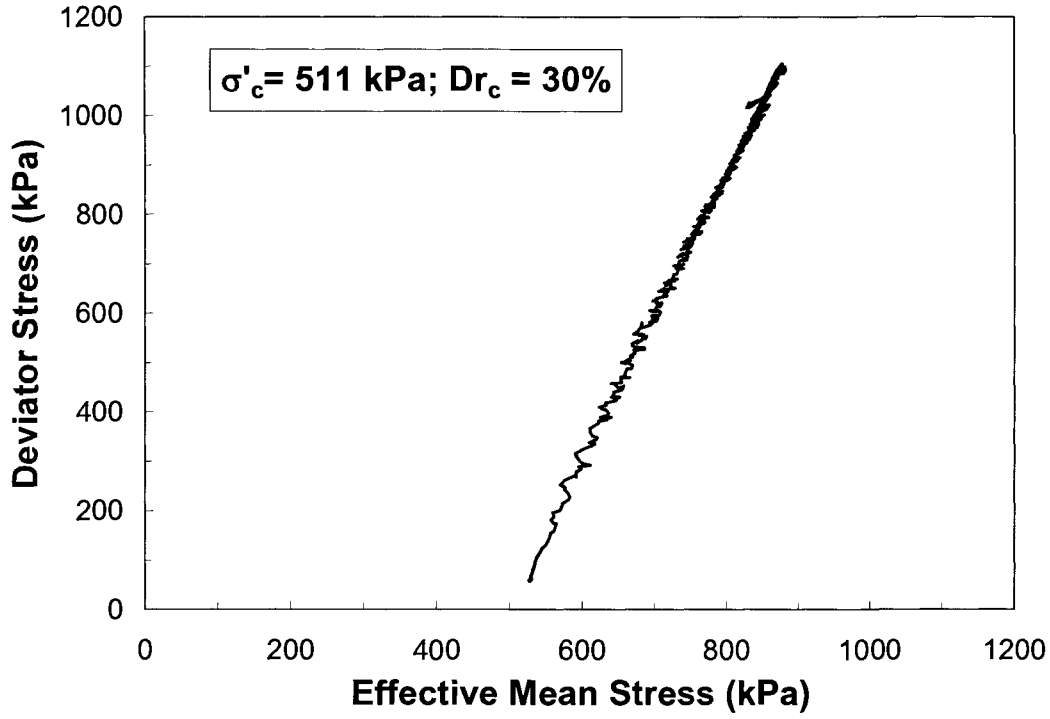

(a)

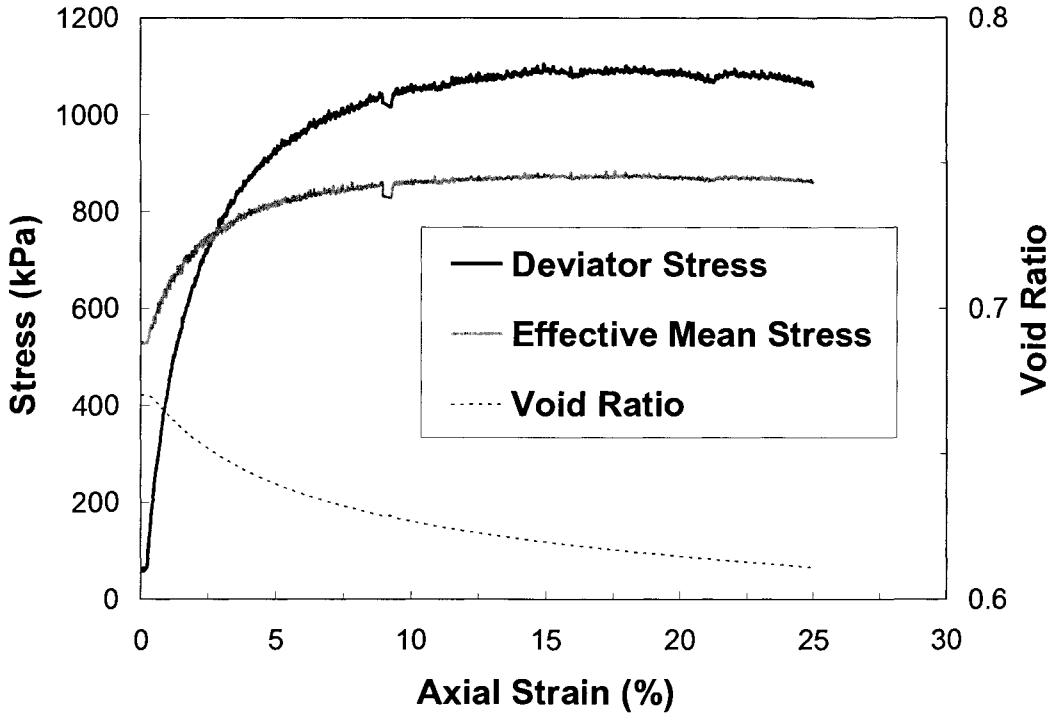

(b)

Figure A.13: (a) stress path, and (b) stress-displacement plots in TxC test MTIRDR74

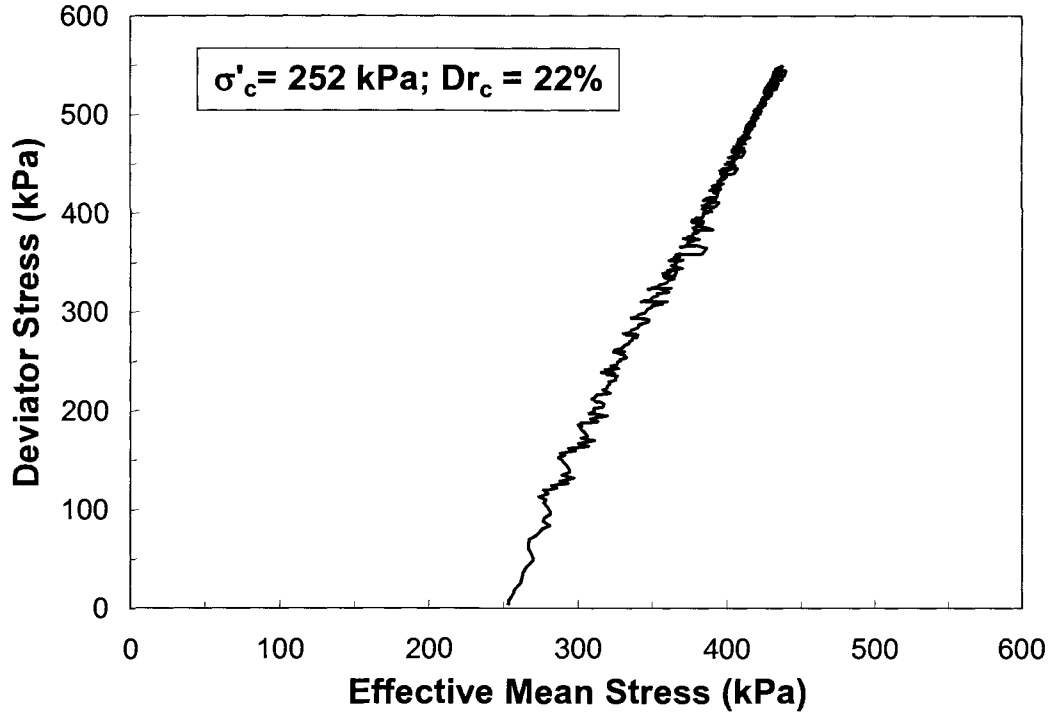

(a)

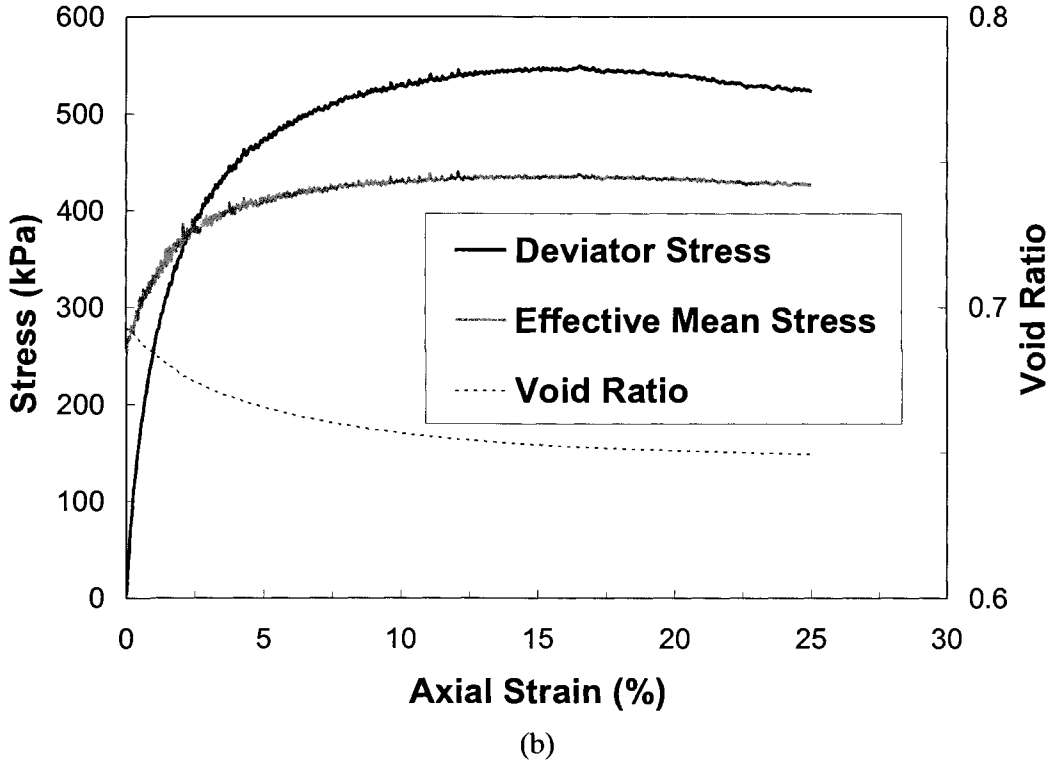

(b)

Figure A.14: (a) stress path, and (b) stress-displacement plots in TxC test MTIRDR37

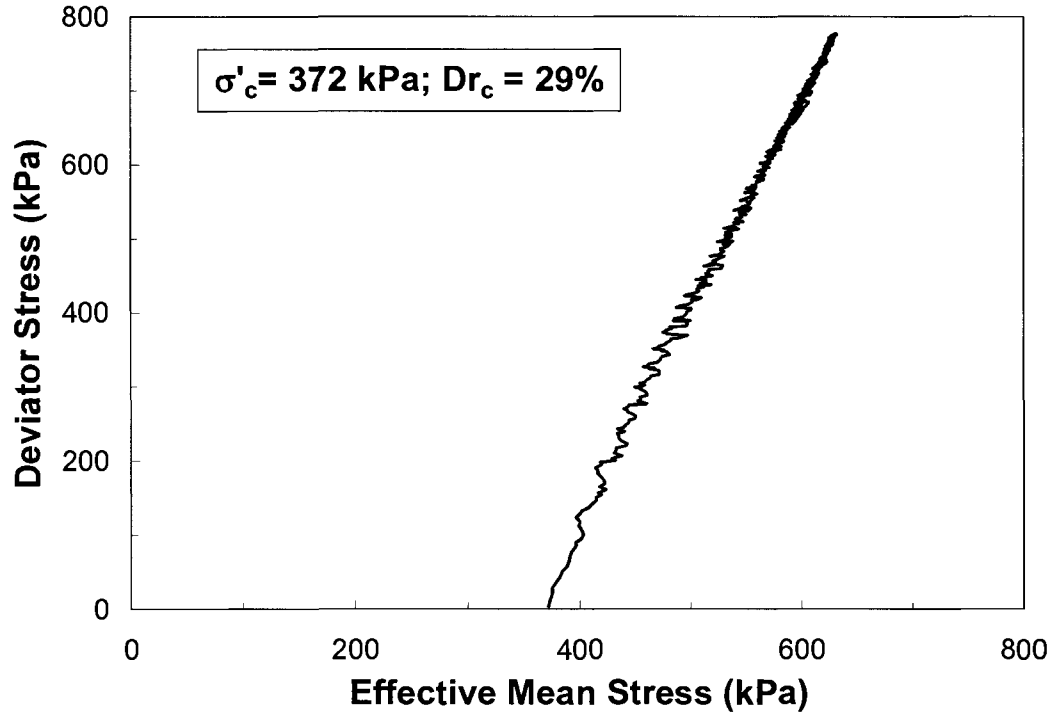

(a)

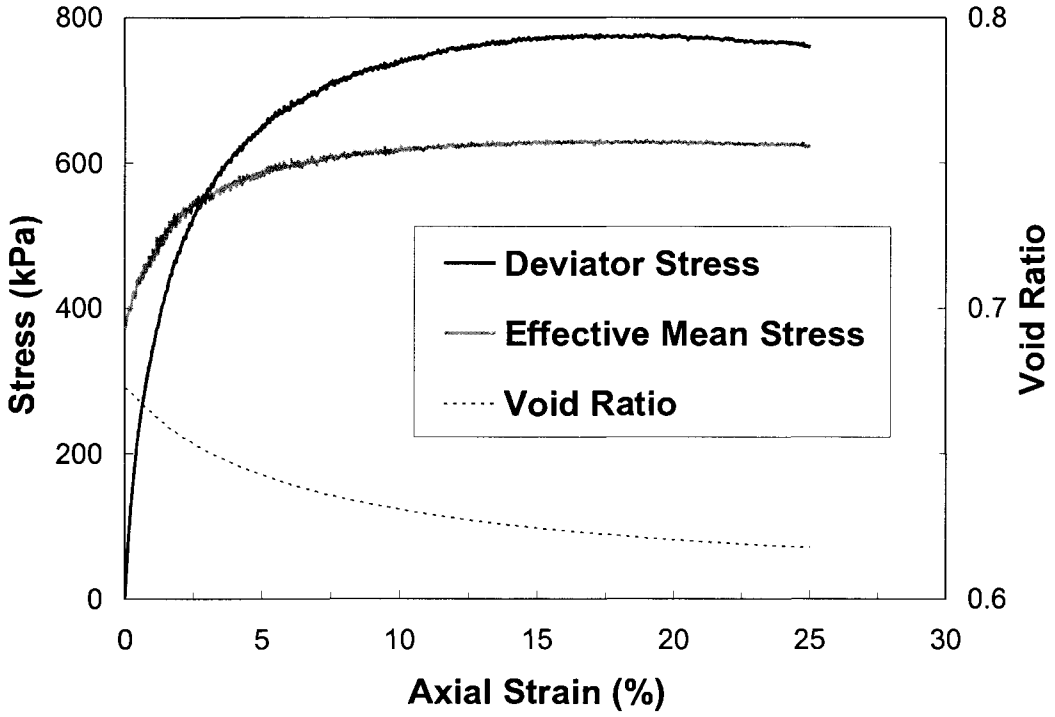

(b)

Figure A.15: (a) stress path, and (b) stress-displacement plots in TxC test MTIRDR54

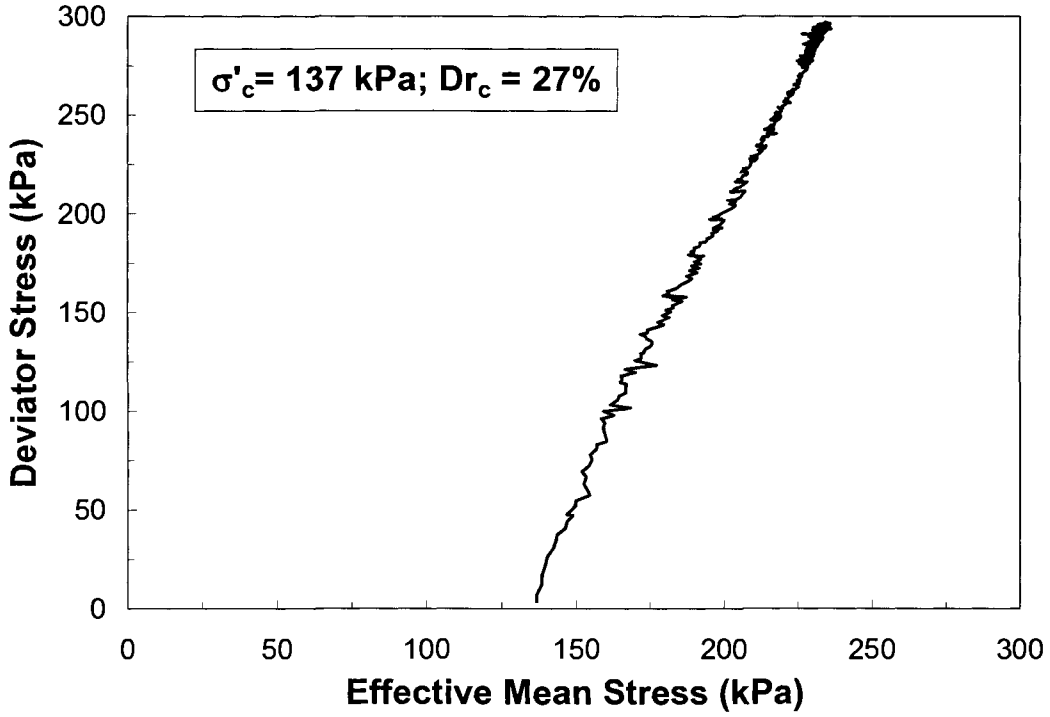

(a)

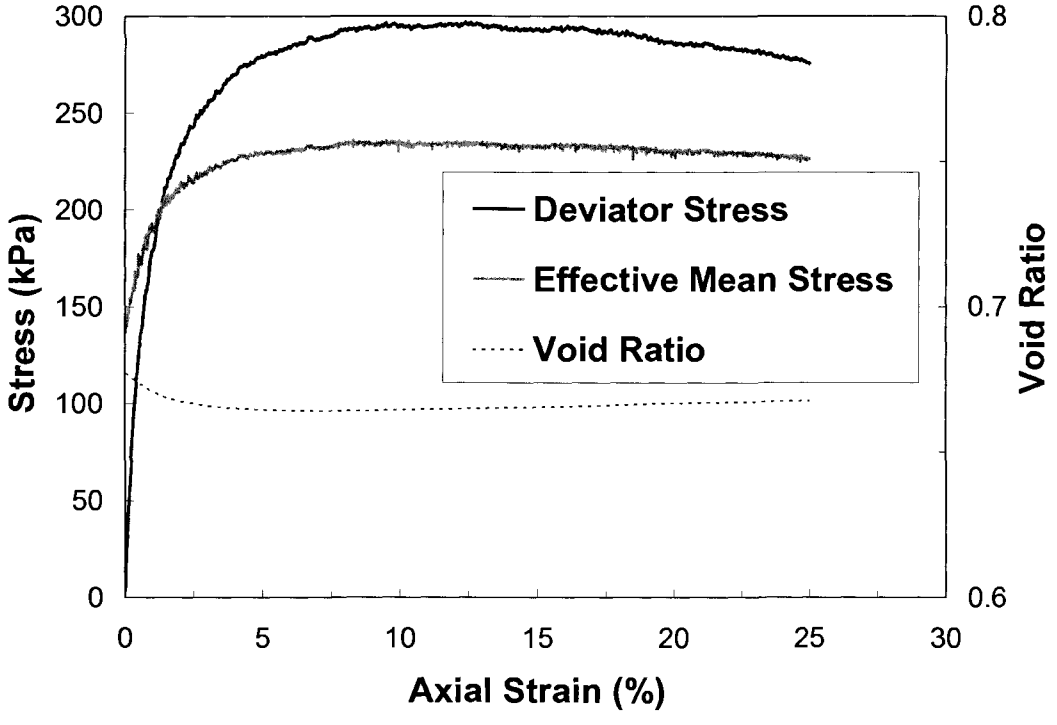

(b)

Figure A.16: (a) stress path, and (b) stress-displacement plots in TxC test MTIRDR20

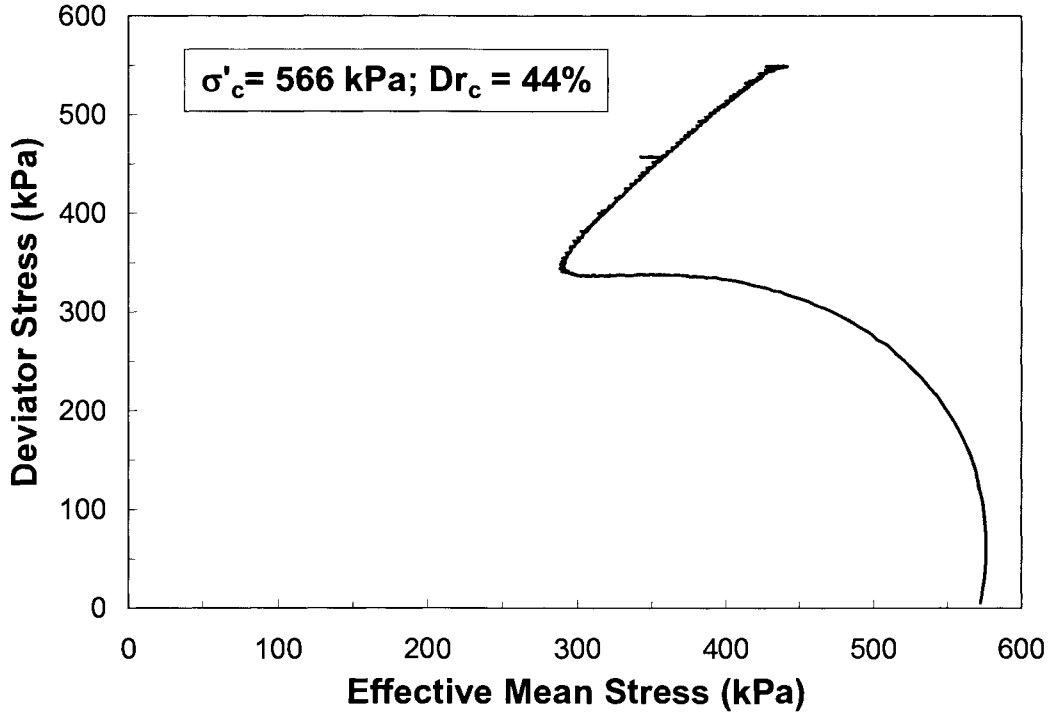

(a)

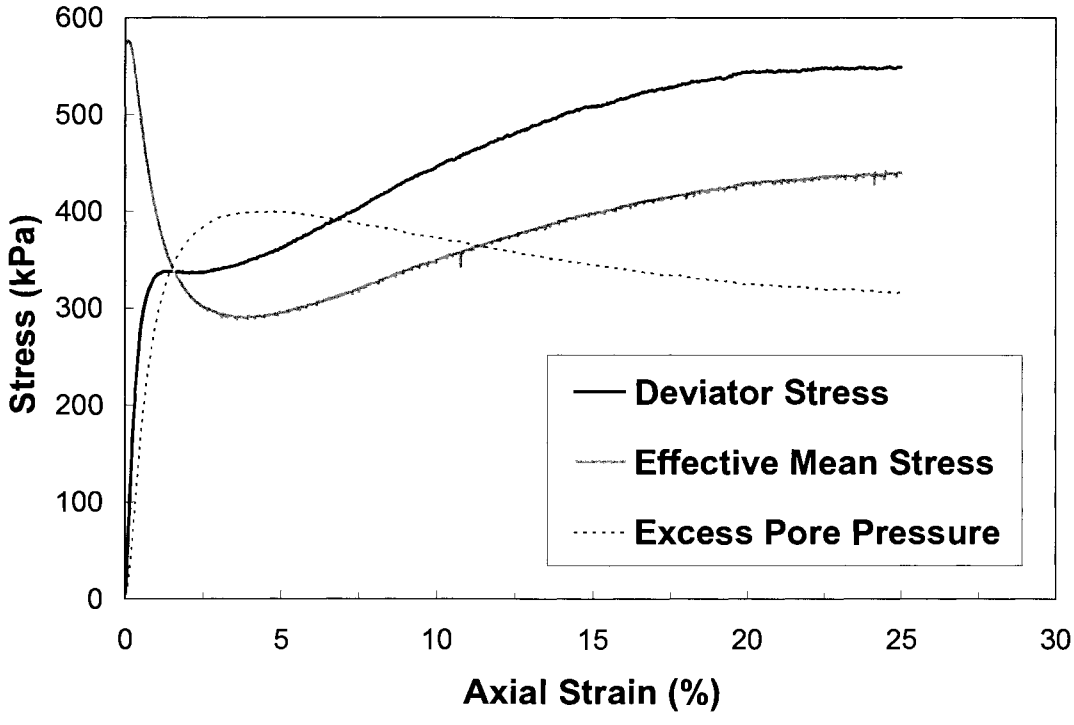

(b)

Figure A.17: (a) stress path, and (b) stress-displacement plots in TxC test APIRUN82

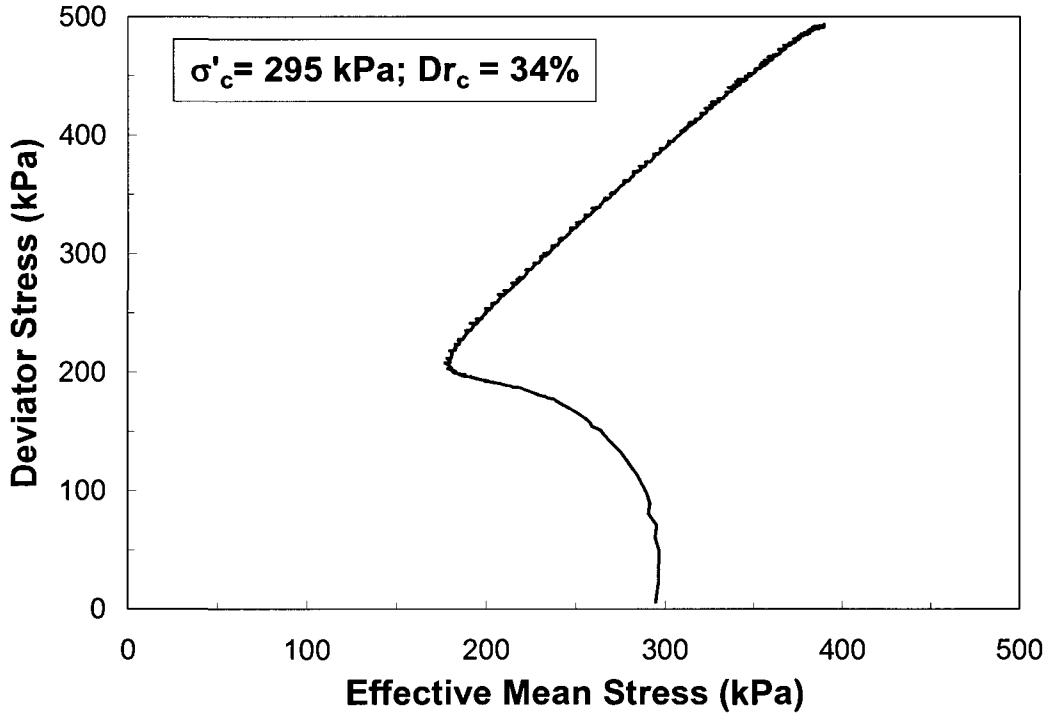

(a)

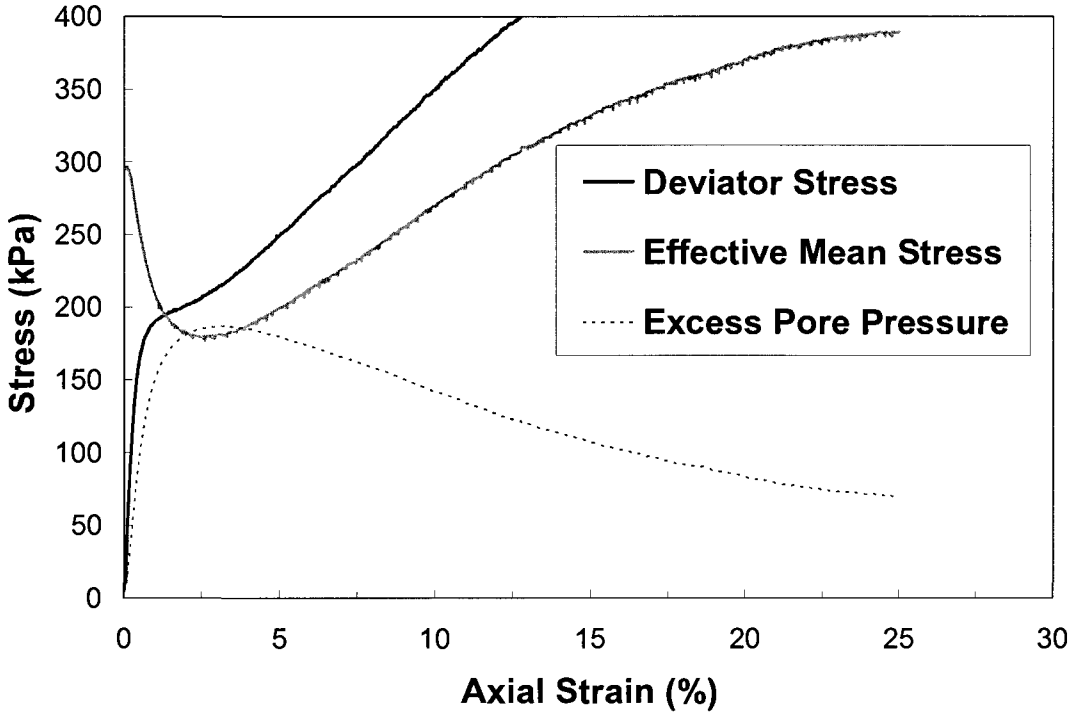

(b)

Figure A.18: (a) stress path, and (b) stress-displacement plots in TxC test APIRUN43

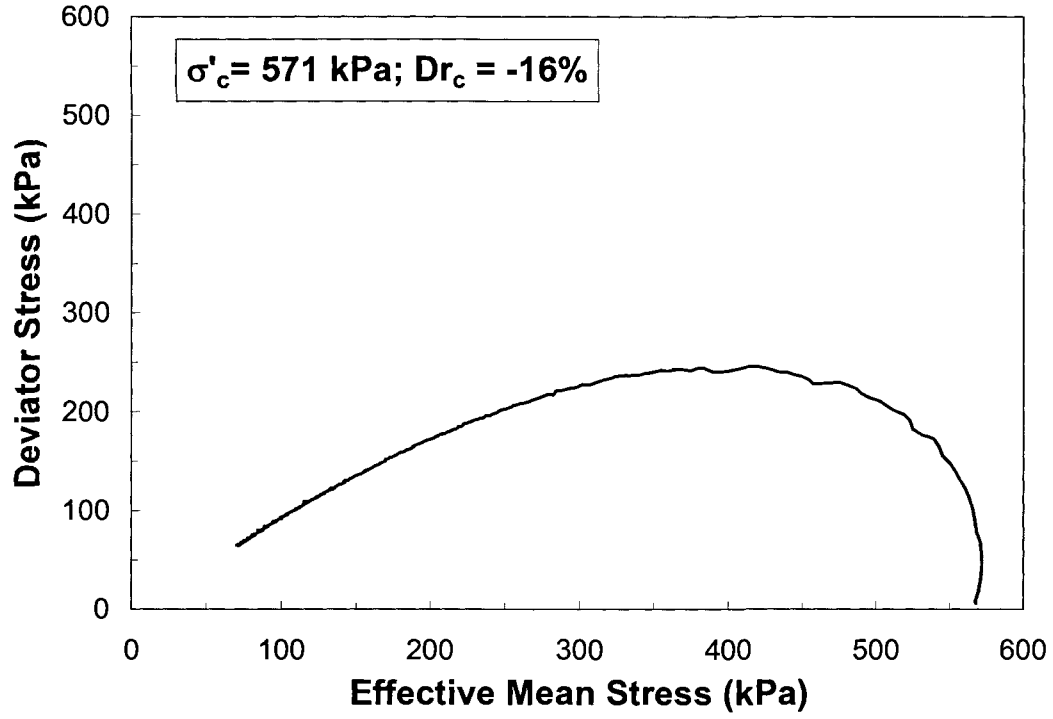

(a)

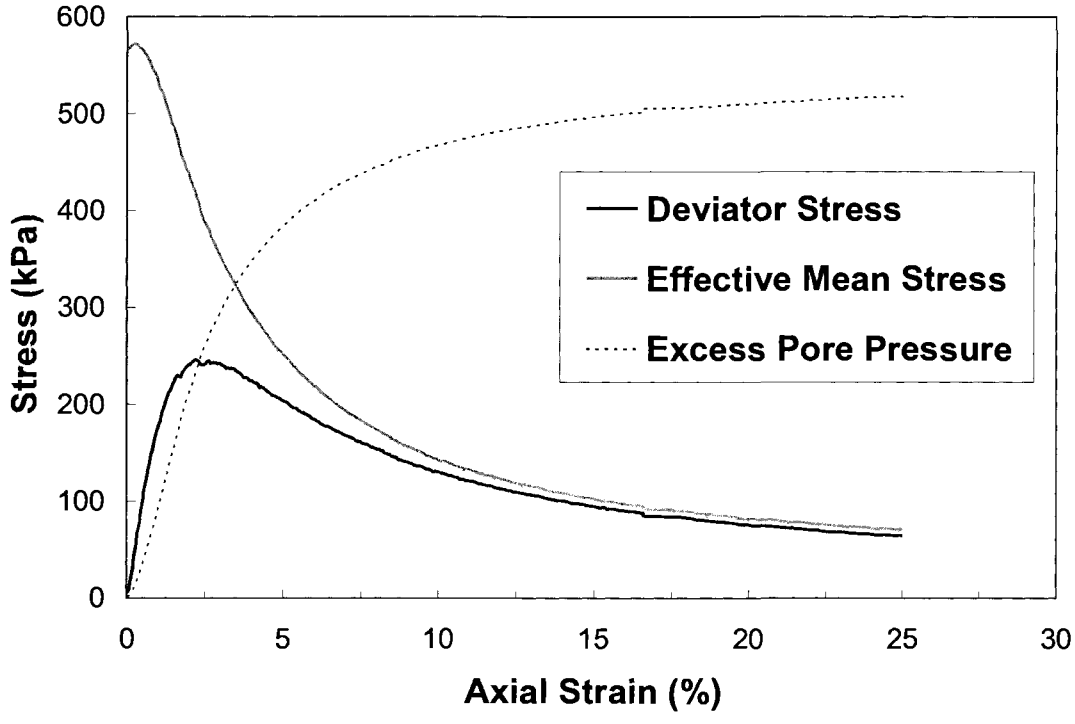

(b)

Figure A.19: (a) stress path, and (b) stress-displacement plots in TxC test MTOTUN83

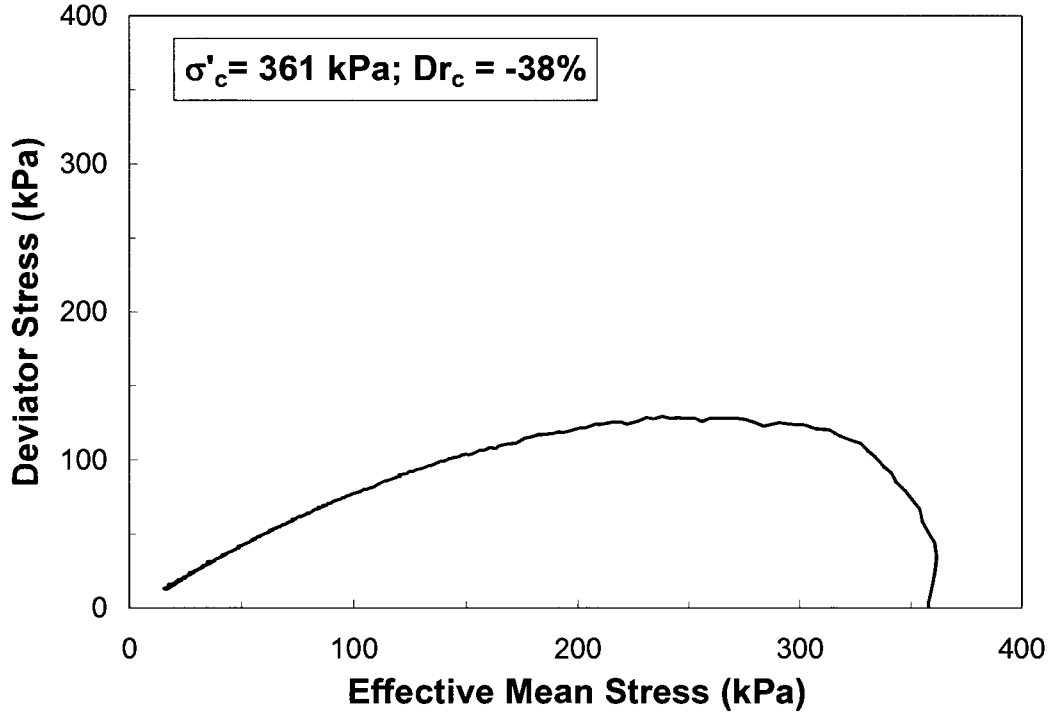

(a)

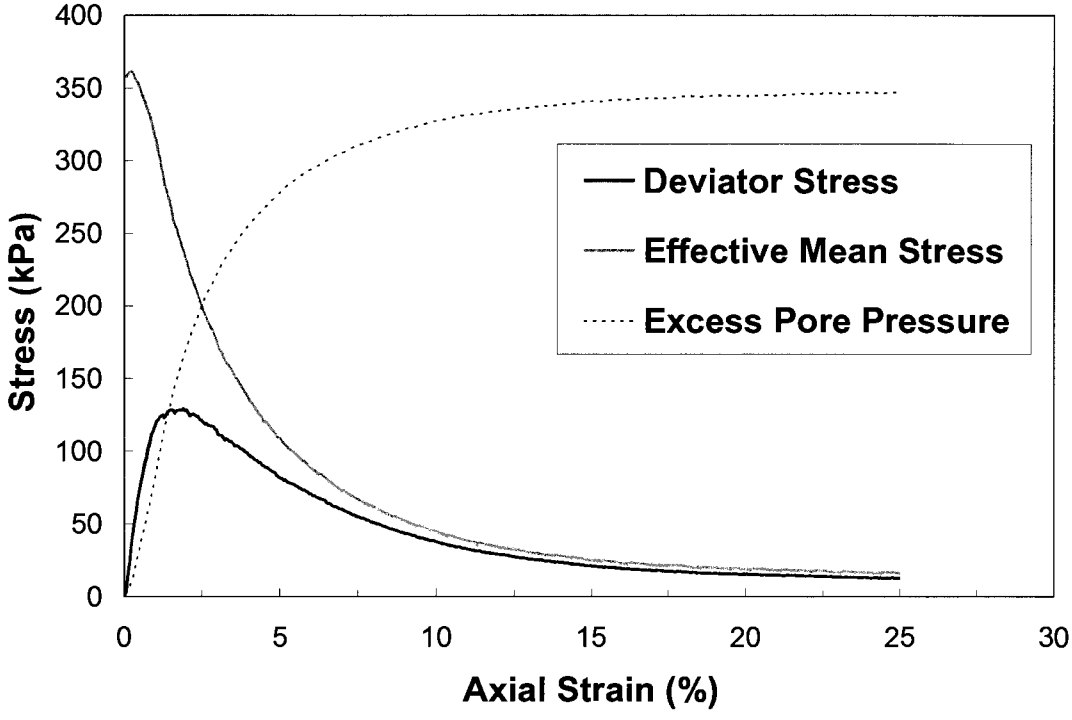

(b)

Figure A.20: (a) stress path, and (b) stress-displacement plots in TxC test MTOTUN52

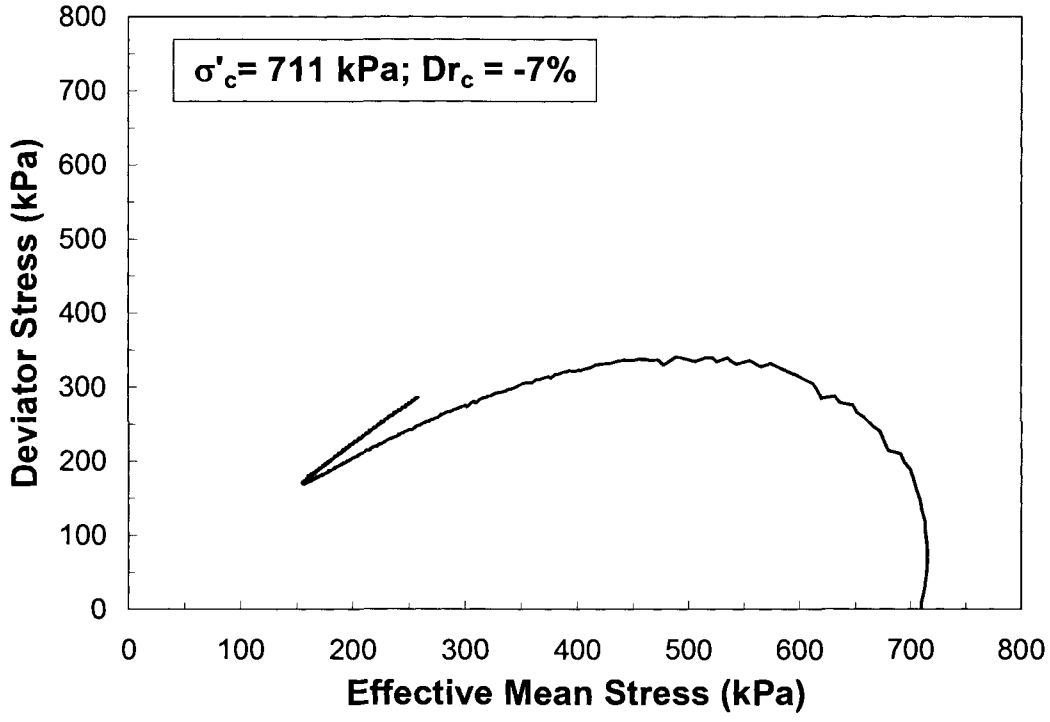

(a)

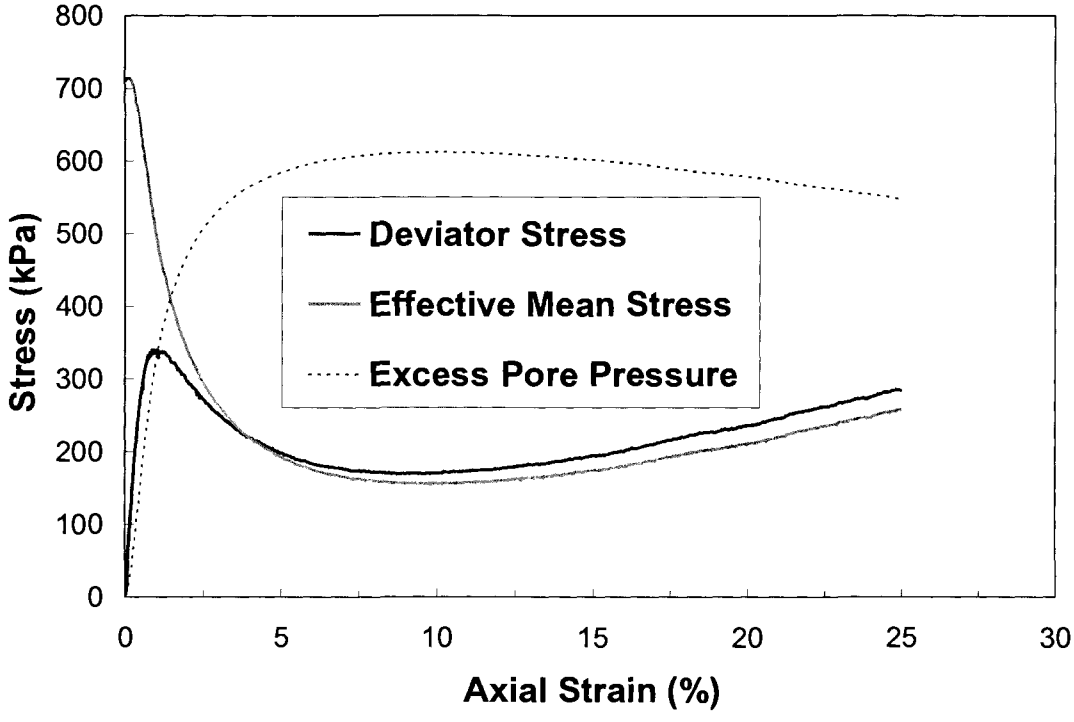

(b)

Figure A.21: (a) stress path, and (b) stress-displacement plots in TxC test MTOTUN103

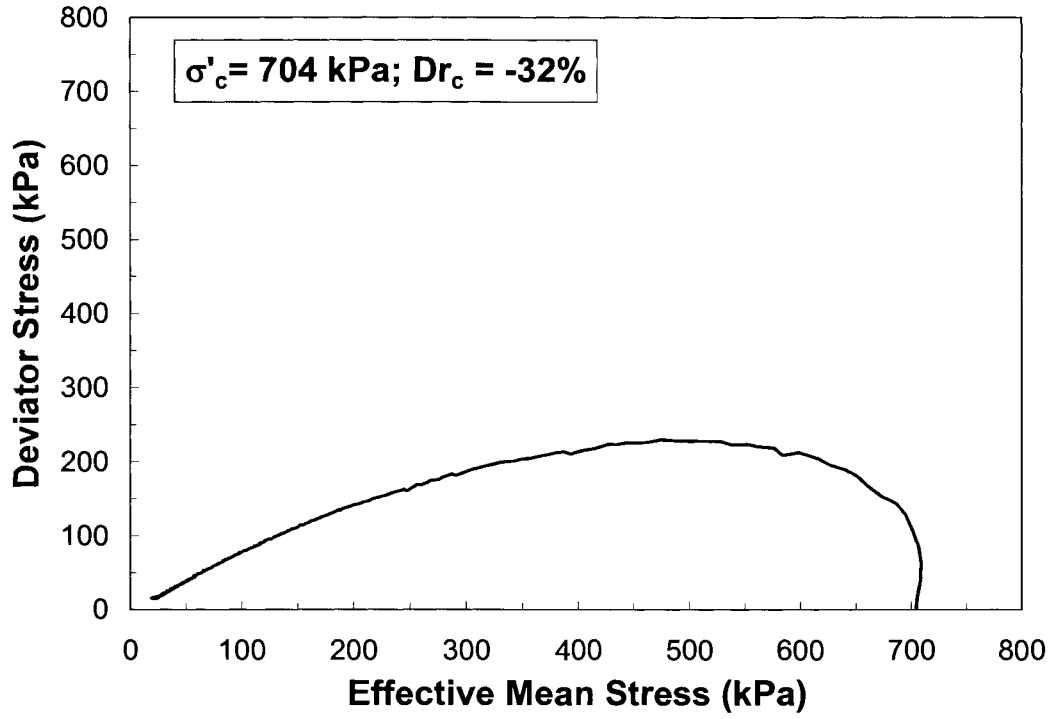

(a)

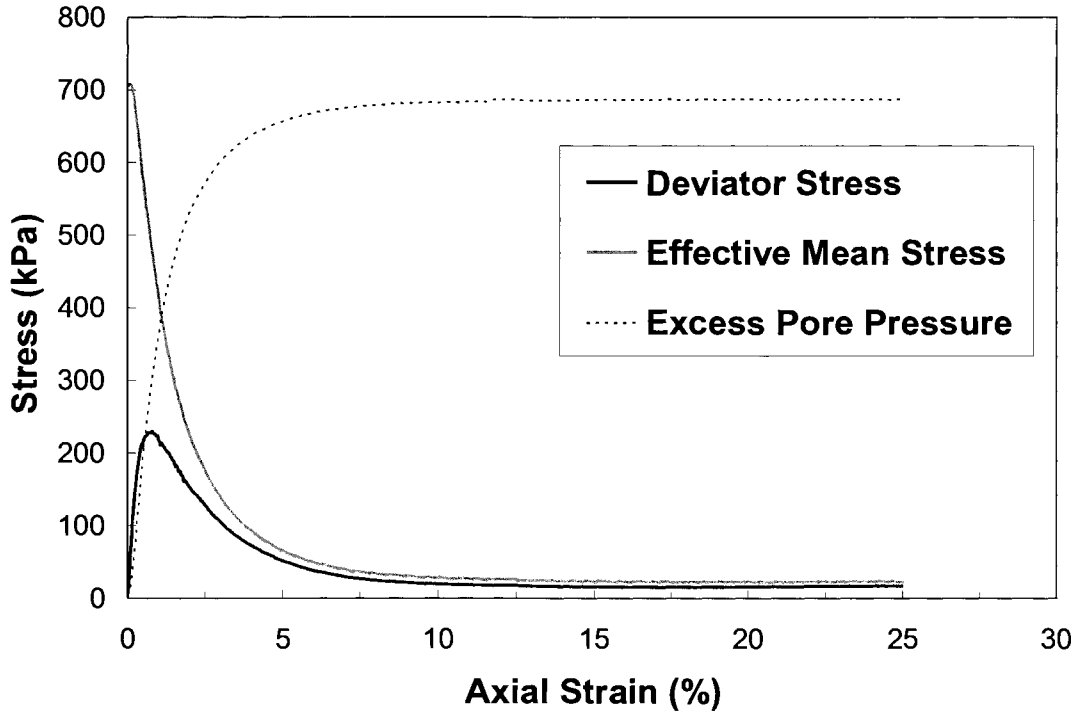

(b)

Figure A.22: (a) stress path, and (b) stress-displacement plots in TxC test MTOTUN102

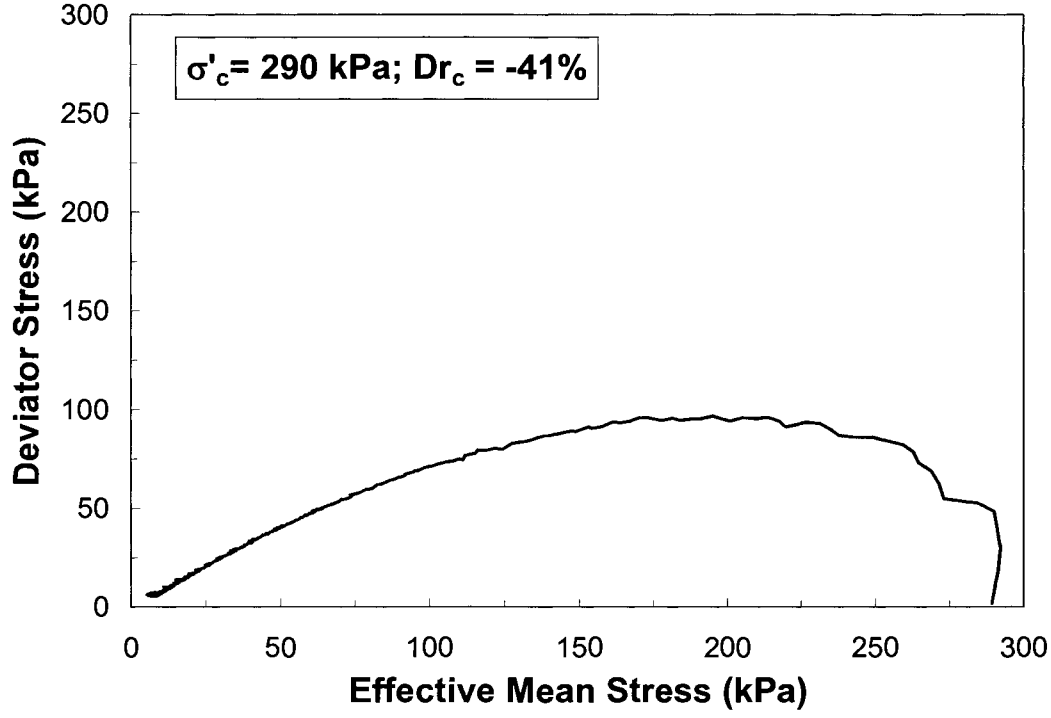

(a)

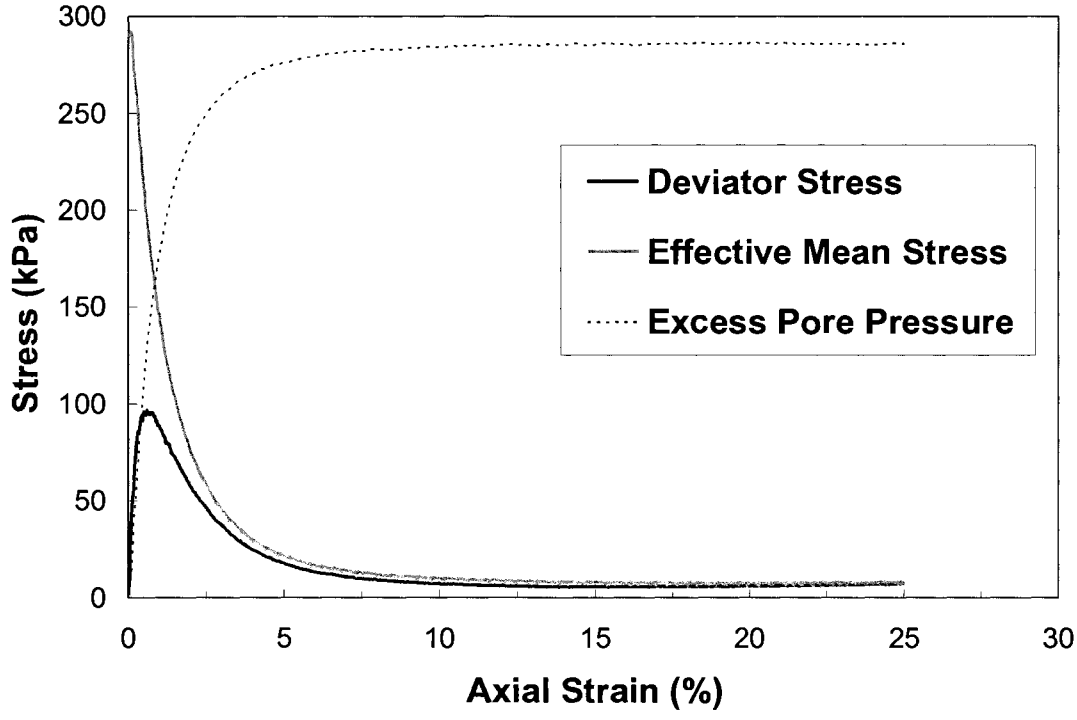

(b)

Figure A.23: (a) stress path, and (b) stress-displacement plots in TxC test MTOTUN42

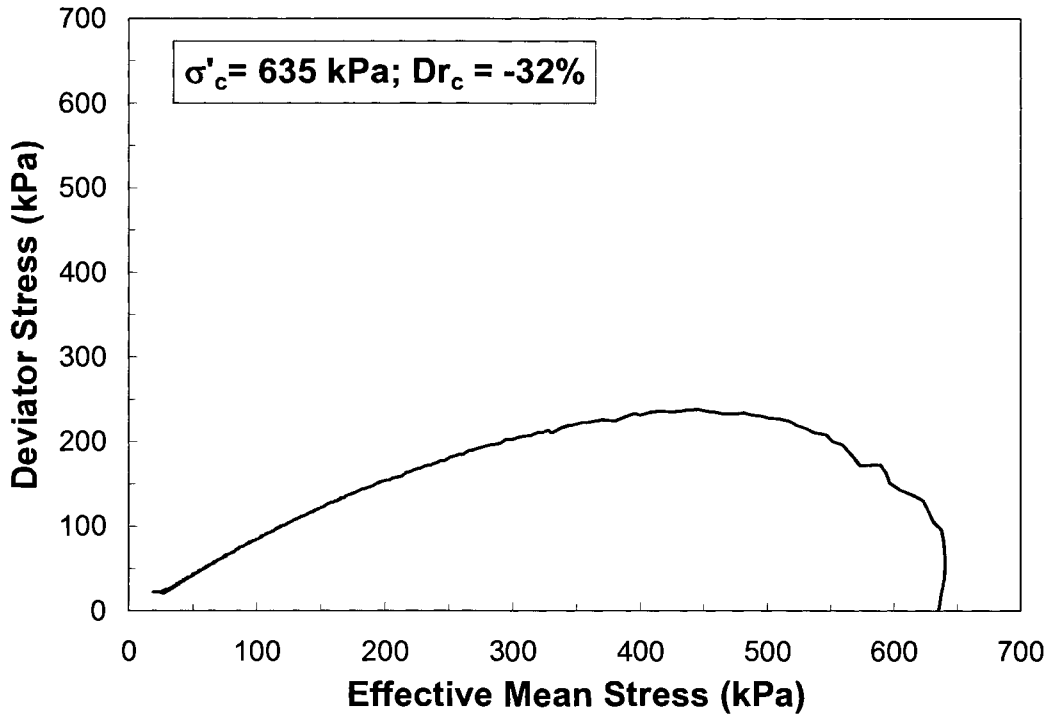

(a)

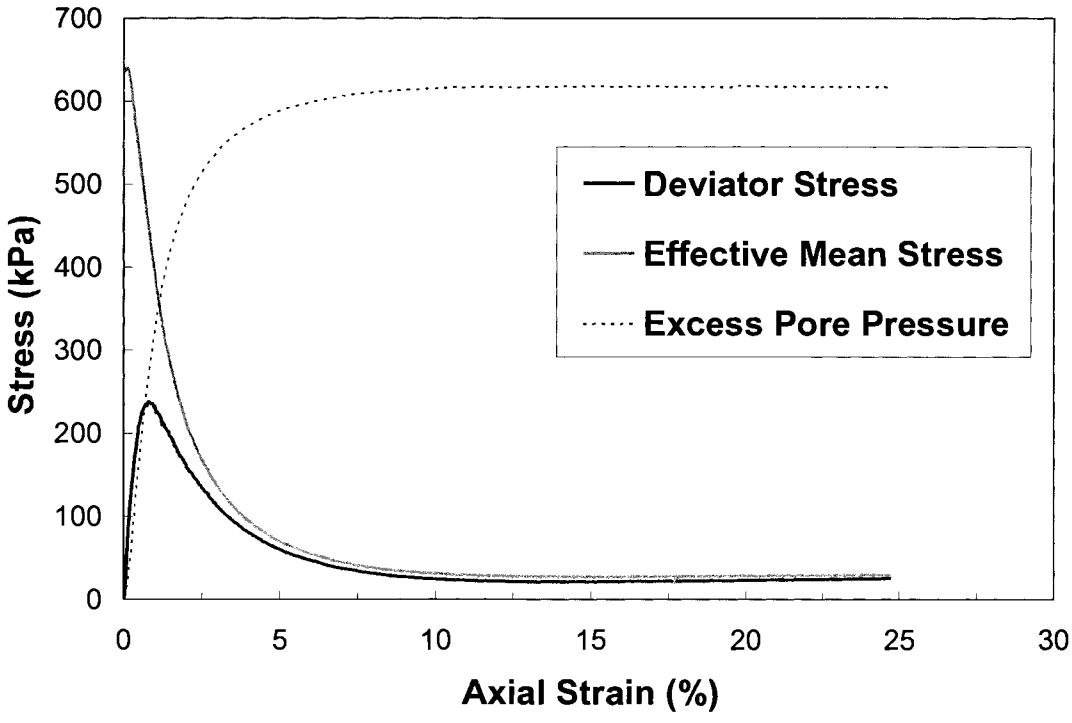

(b)

Figure A.24: (a) stress path, and (b) stress-displacement plots in TxC test MTOTUN92

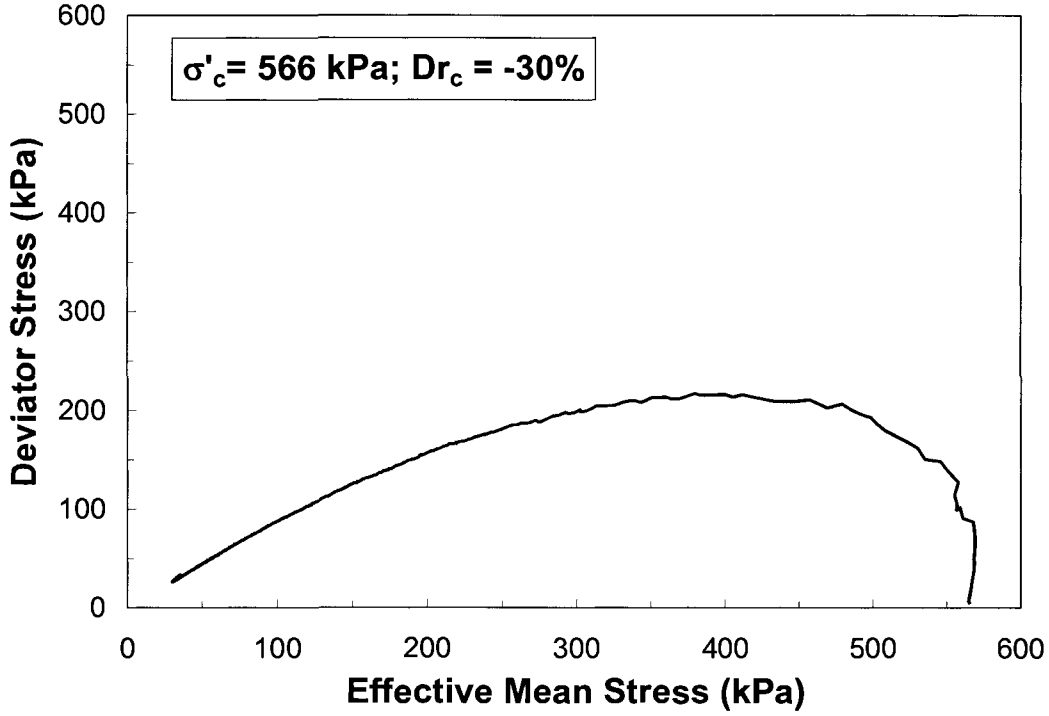

(a)

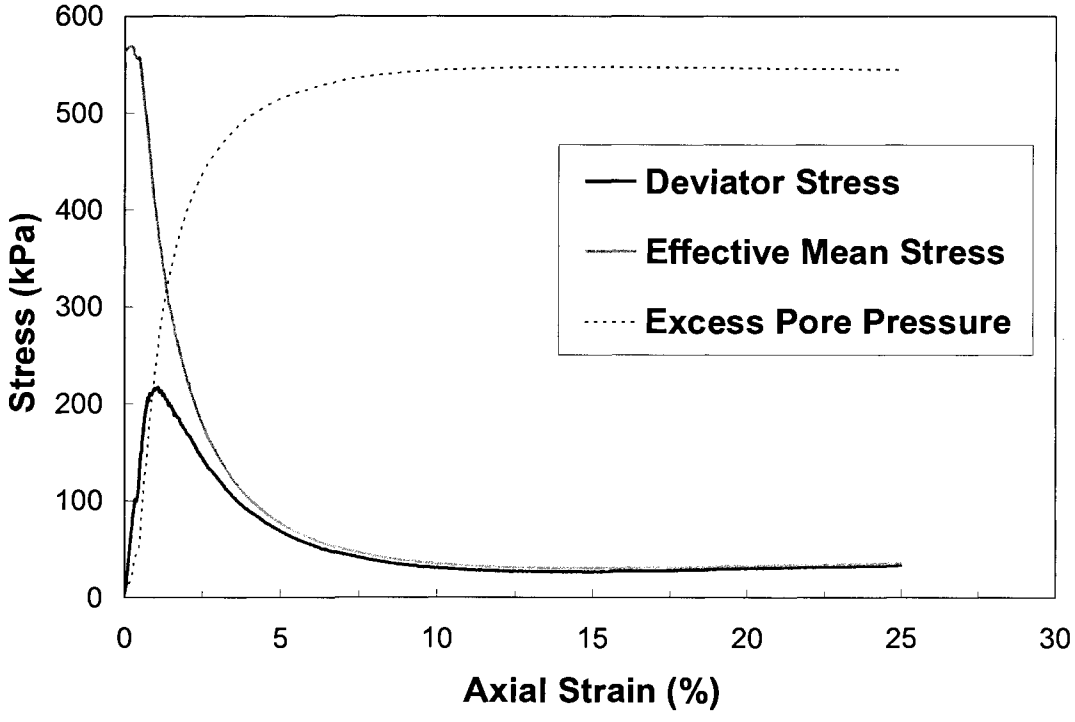

(b)

Figure A.25: (a) stress path, and (b) stress-displacement plots in TxC test MTOTUN82

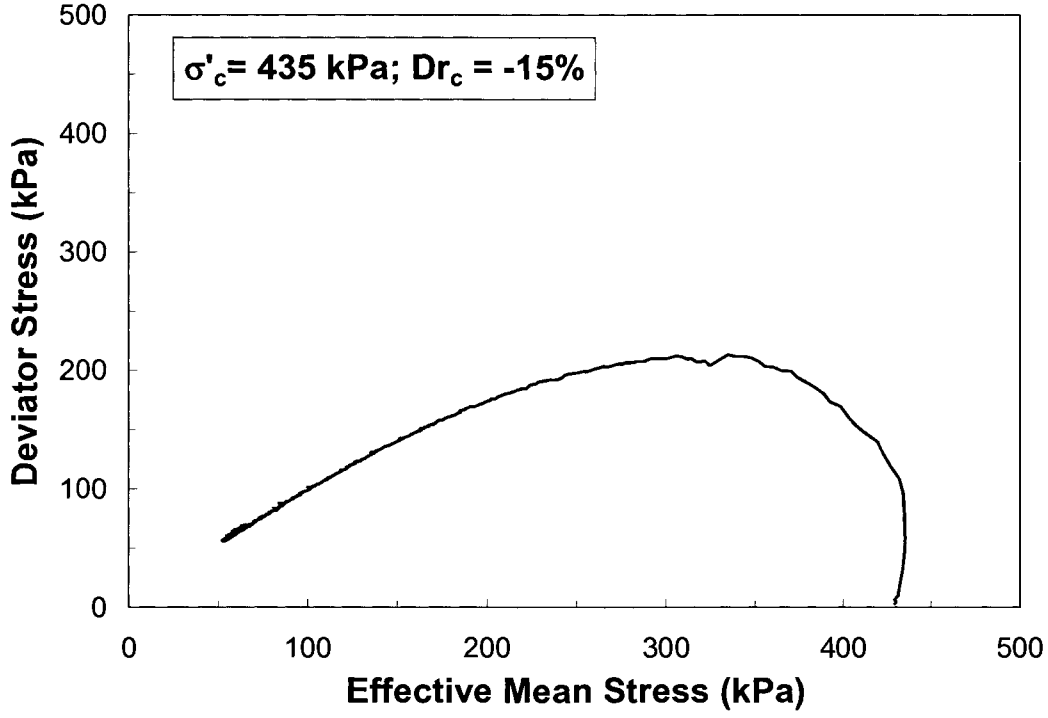

(a)

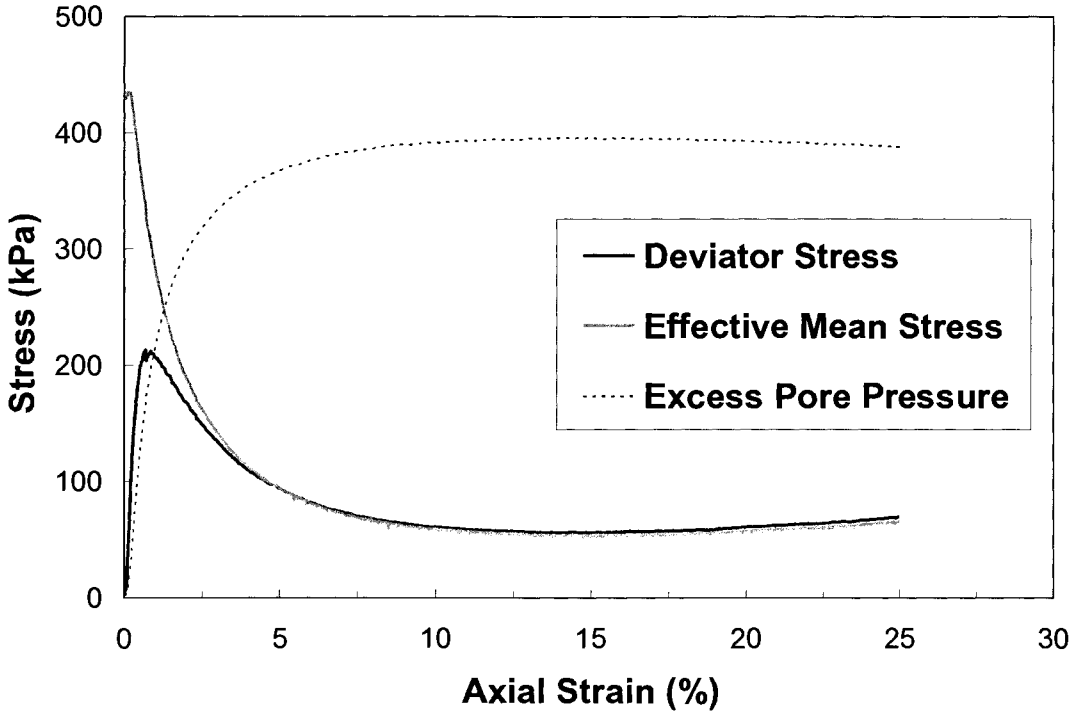

(b)

Figure A.26: (a) stress path, and (b) stress-displacement plots in TxC test MTOTUN63

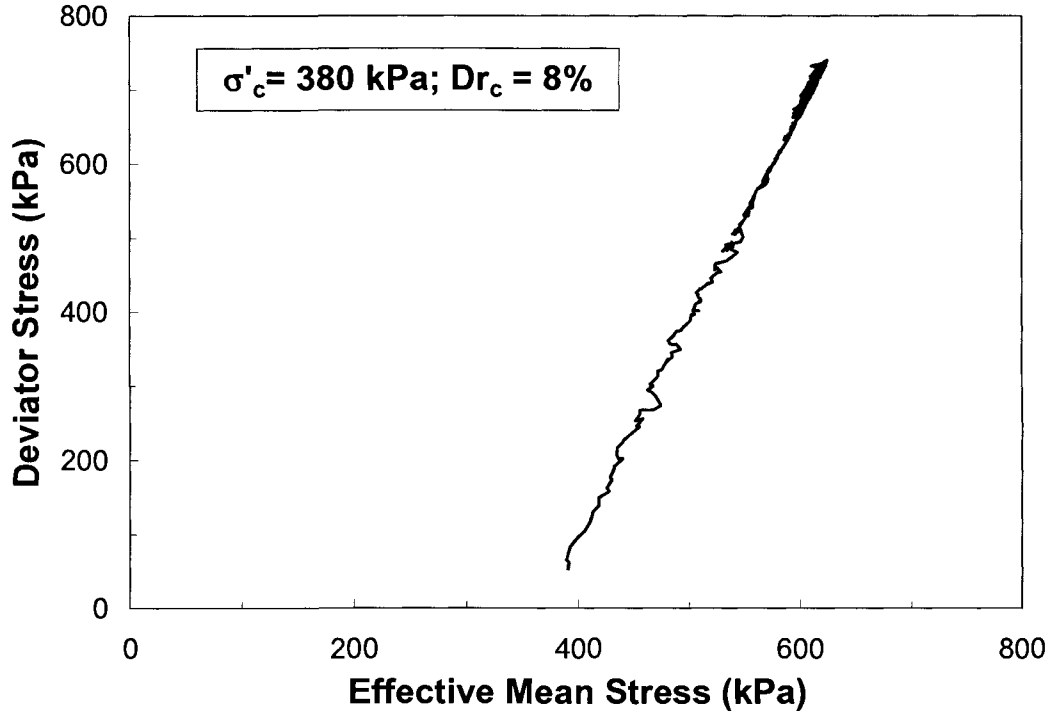

(a)

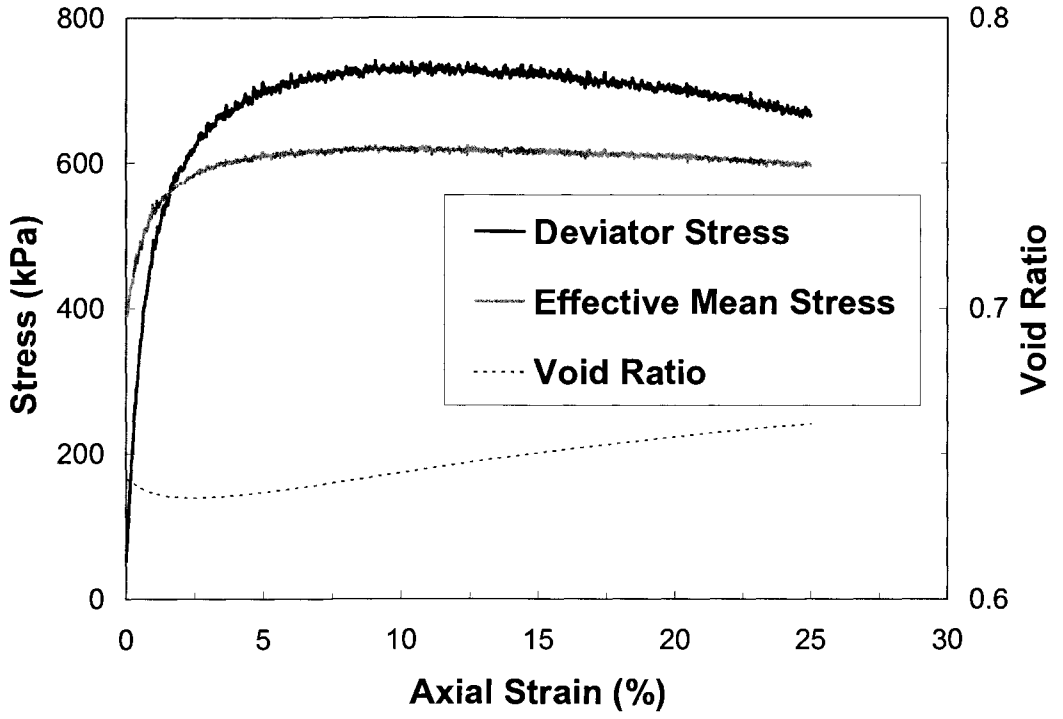

(b)

Figure A.27: (a) stress path, and (b) stress-displacement plots in TxC test MTOTDR55

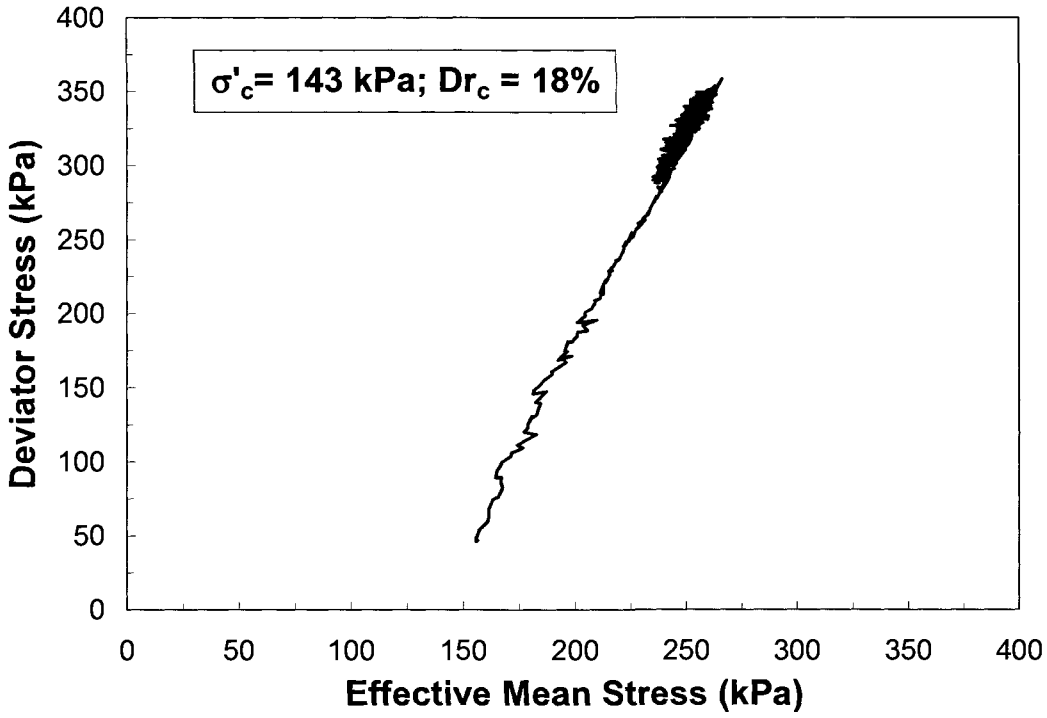

(a)

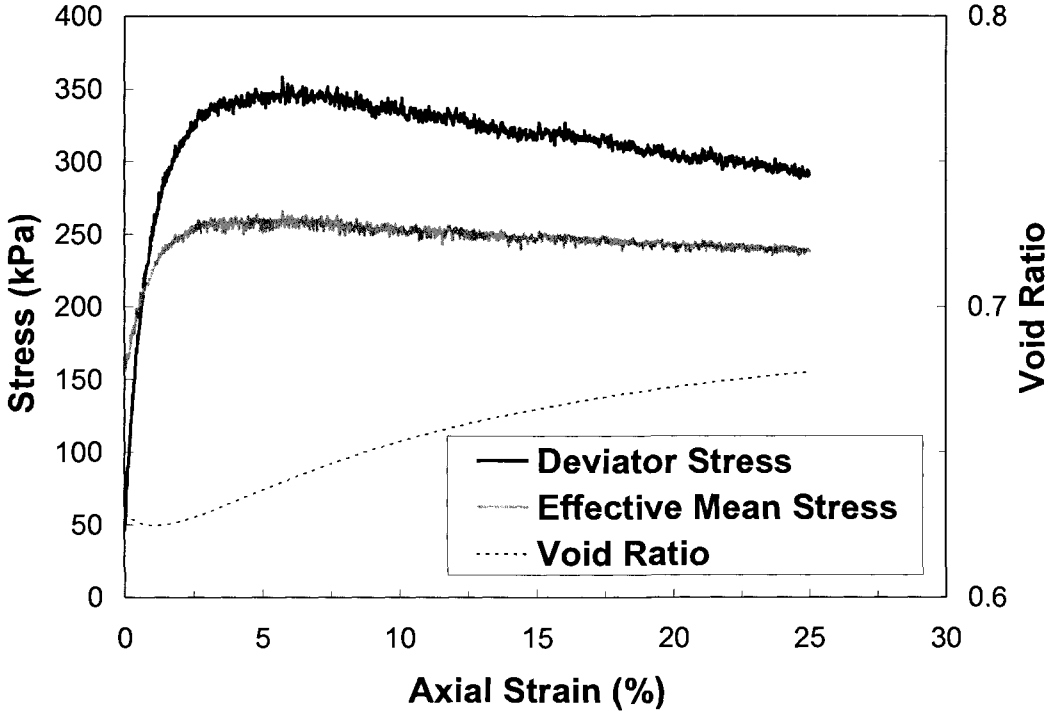

(b)

Figure A.28: (a) stress path, and (b) stress-displacement plots in TxC test MTOTDR21

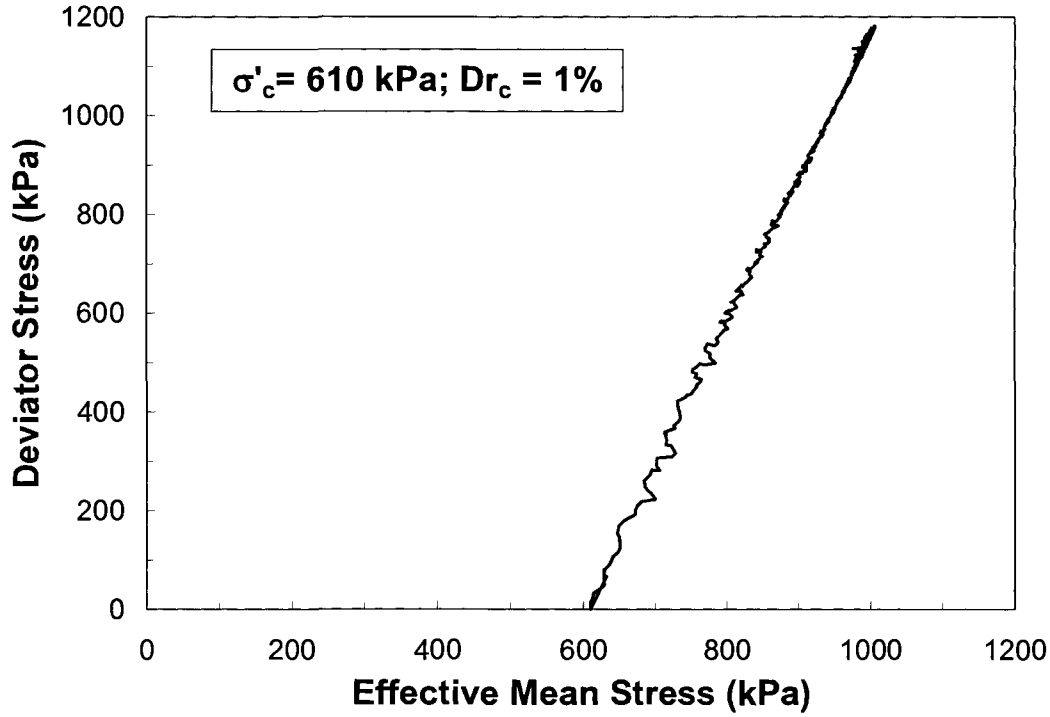

(a)

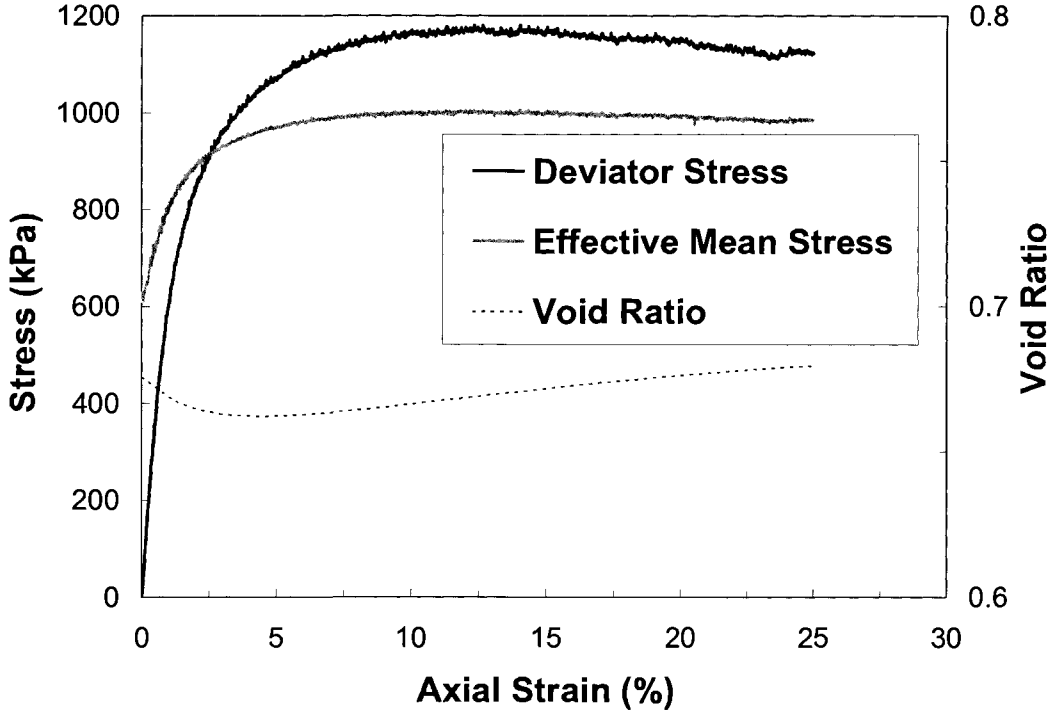

(b)

Figure A.29: (a) stress path, and (b) stress-displacement plots in TxC test MTOTDR88

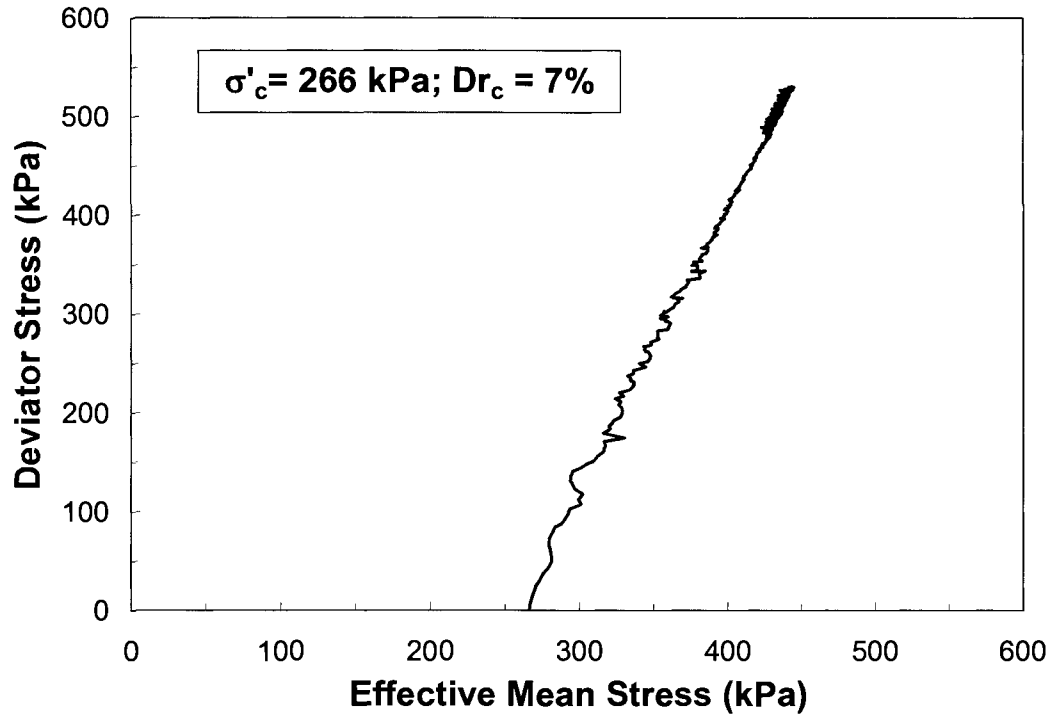

(a)

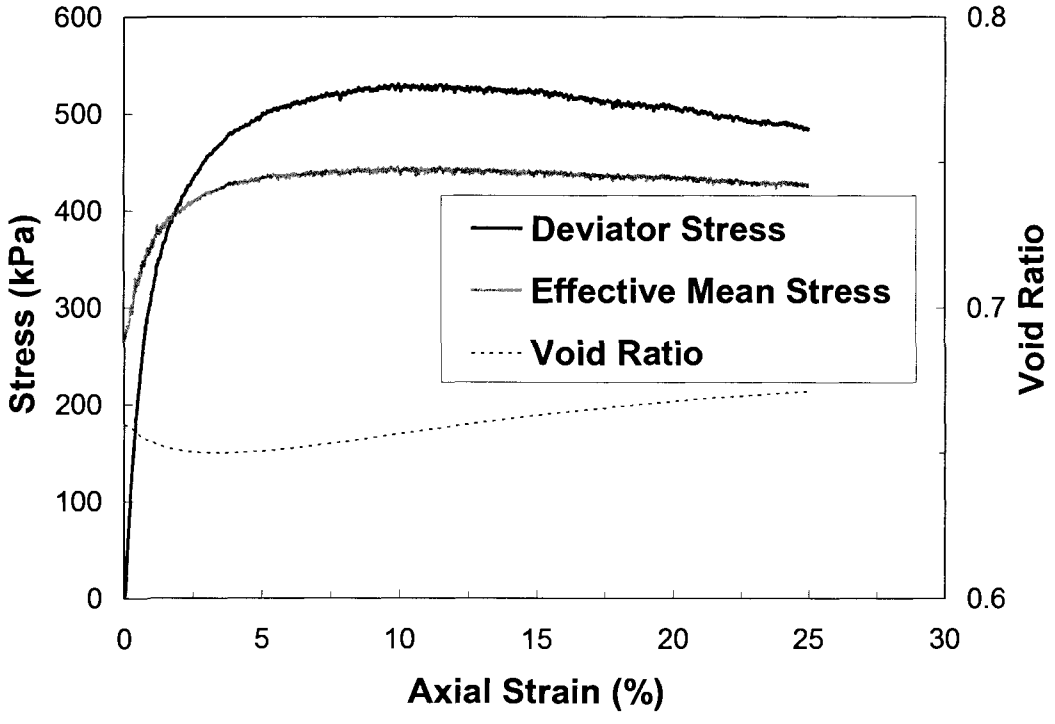

(b)

Figure A.30: (a) stress path, and (b) stress-displacement plots in TxC test MTOTDR39

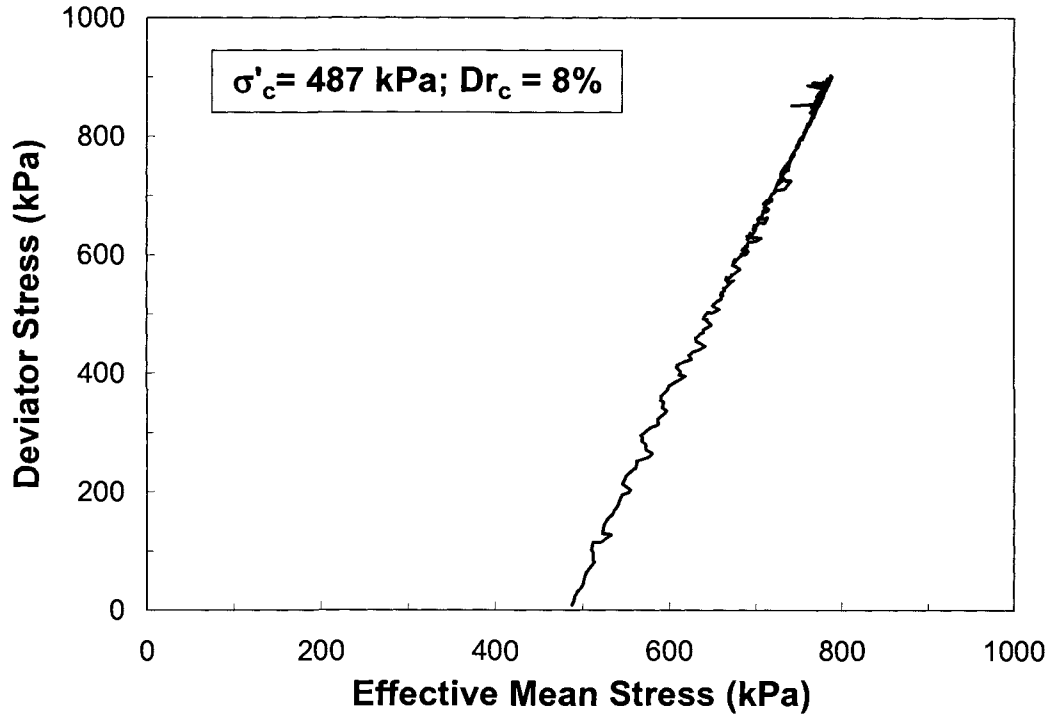

(a)

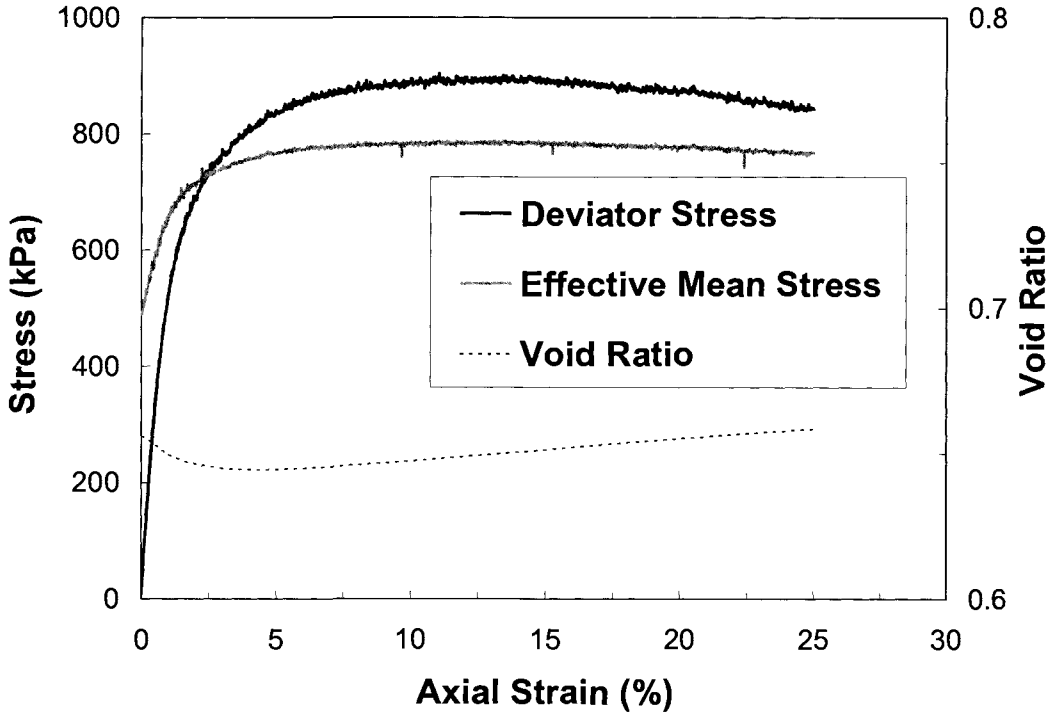

(b)

Figure A.31: (a) stress path, and (b) stress-displacement plots in TxC test MTOTDR71

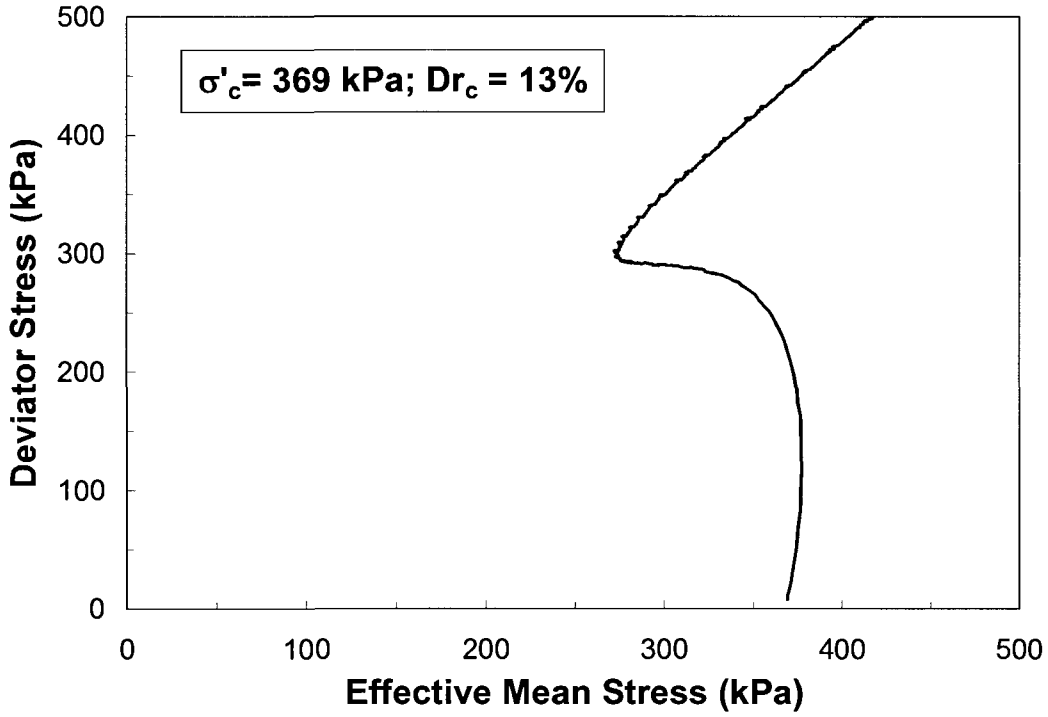

(a)

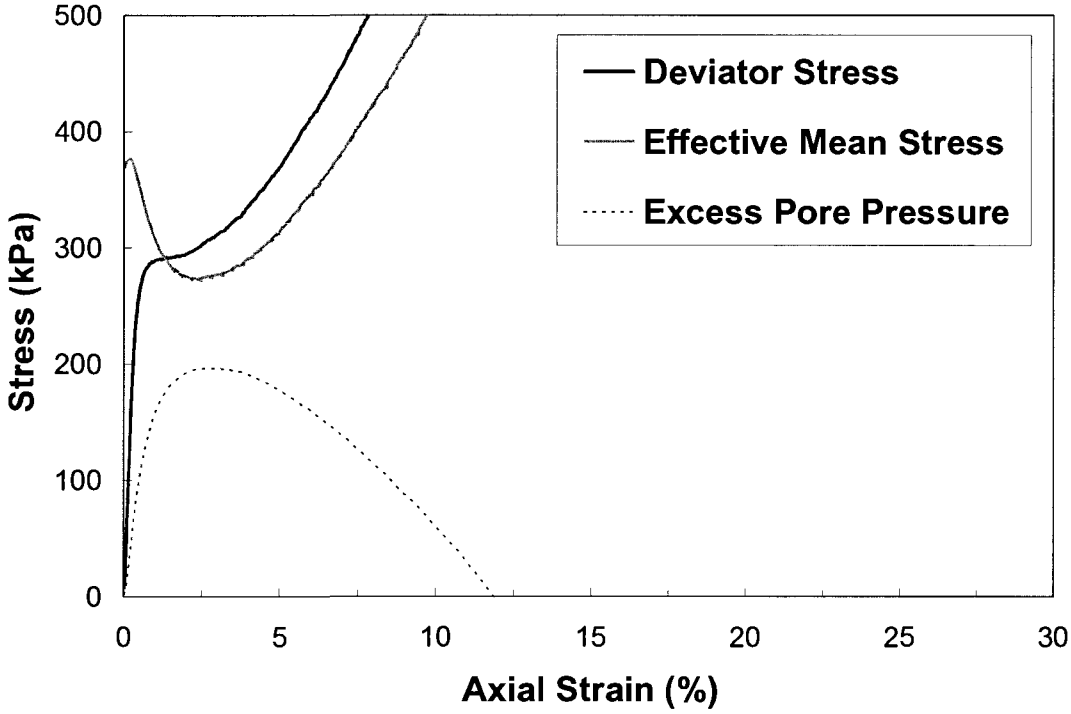

(b)

Figure A.32: (a) stress path, and (b) stress-displacement plots in TxC test APOTUN54

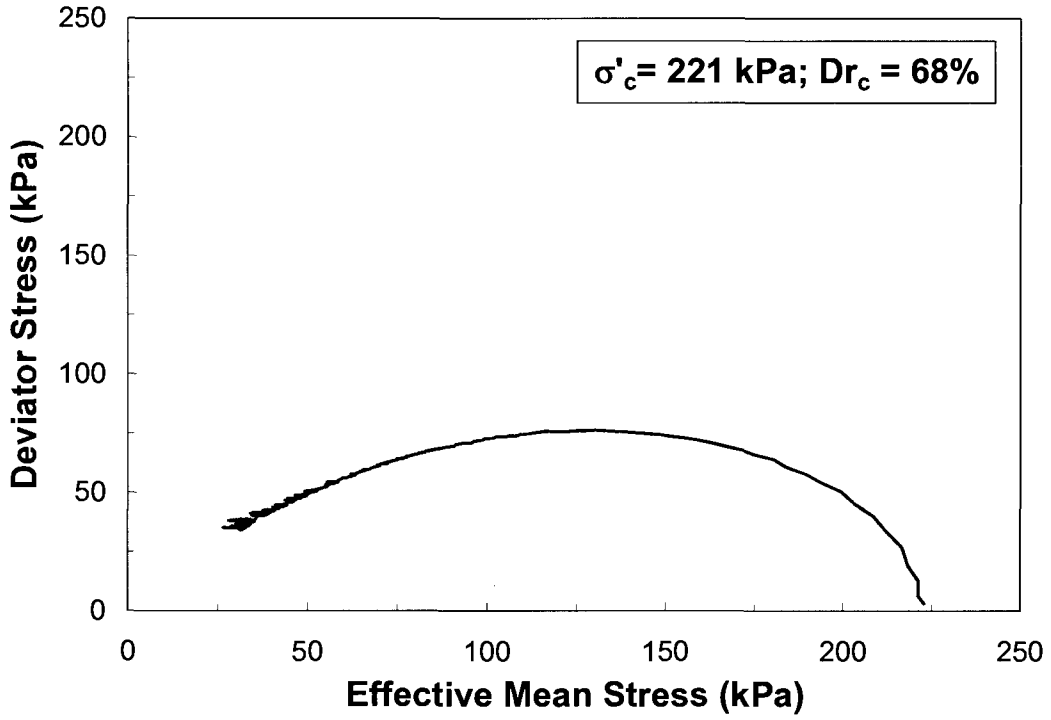

(a)

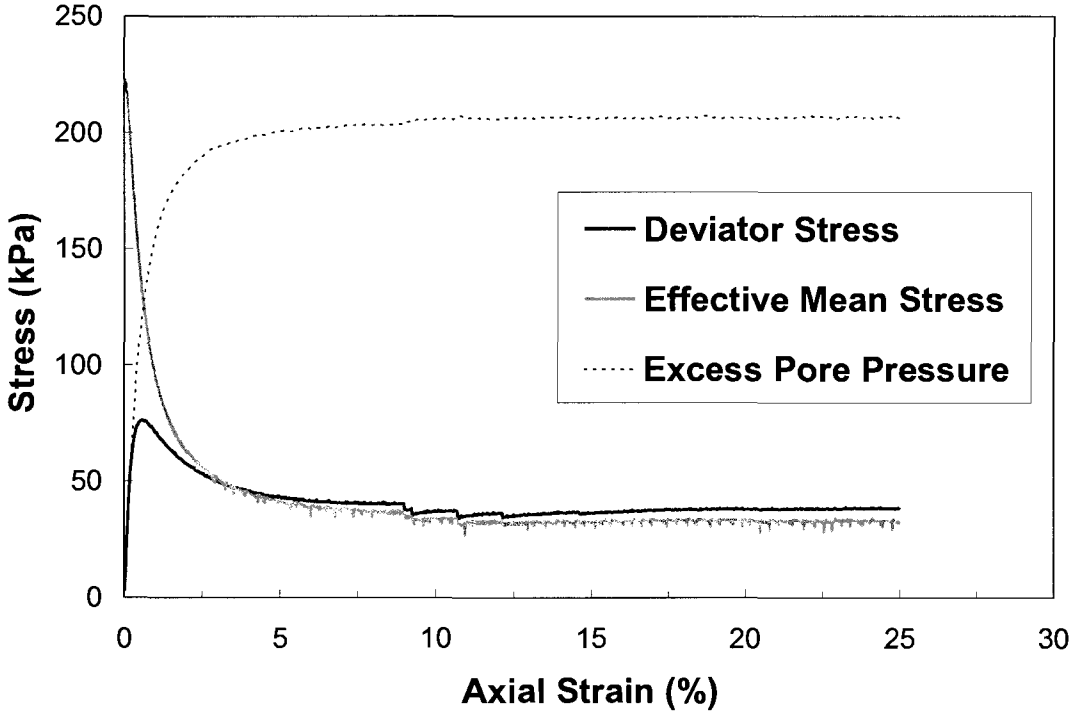

(b)

Figure A.33: (a) stress path, and (b) stress-displacement plots in TxC test APMRUN32

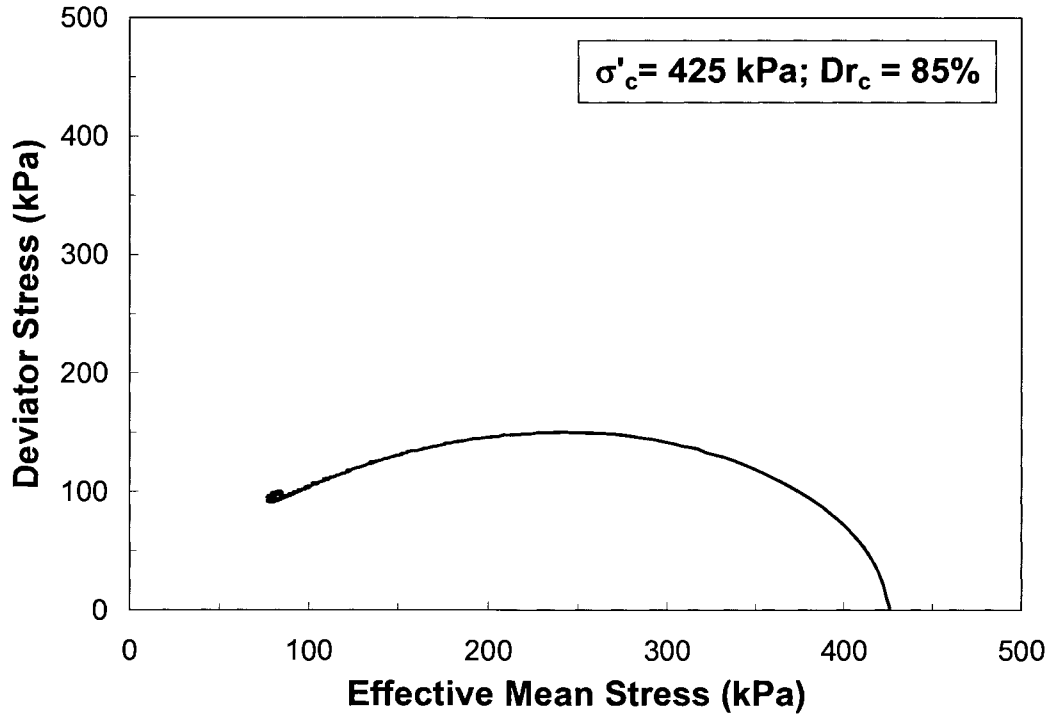

(a)

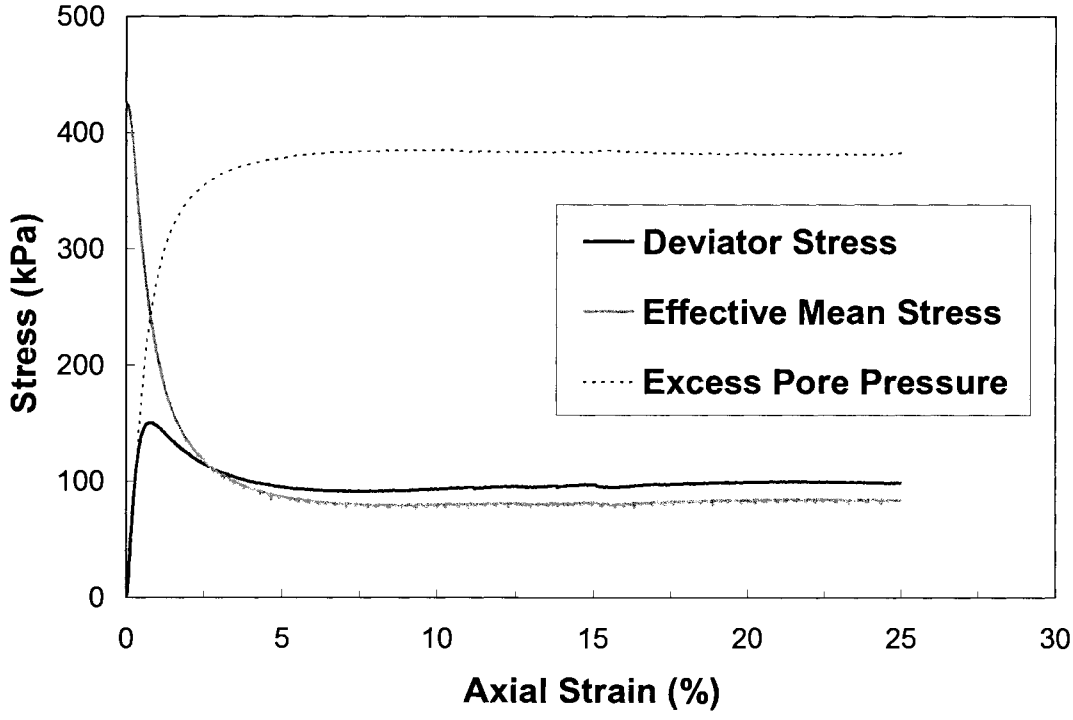

(b)

Figure A.34: (a) stress path, and (b) stress-displacement plots in TxC test APMRUN62

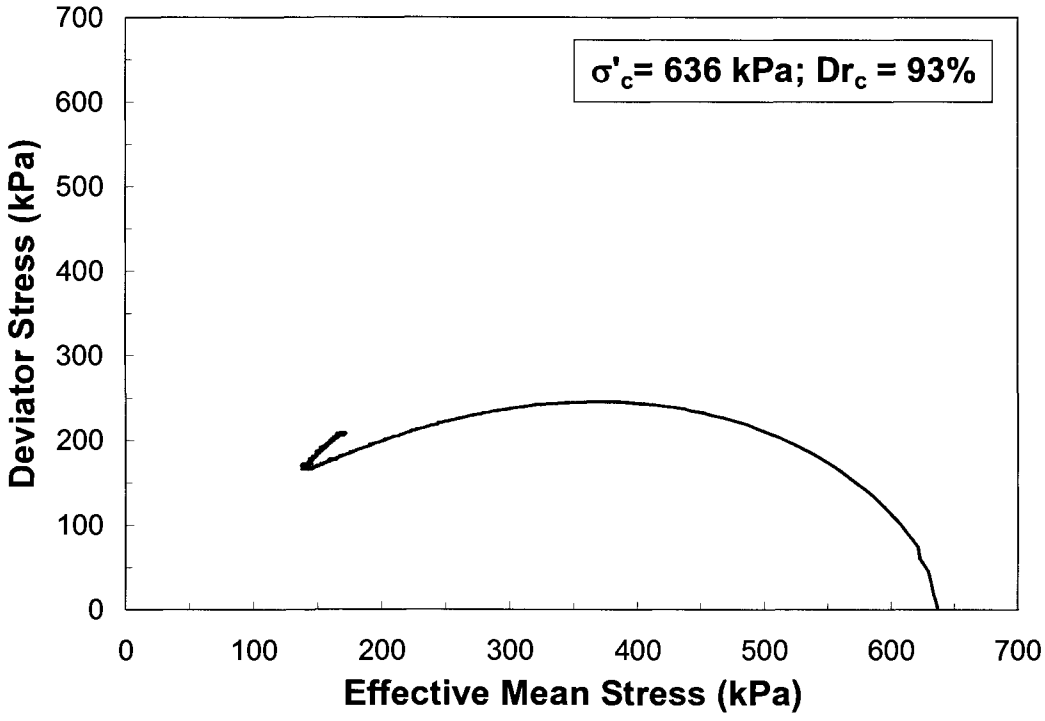

(a)

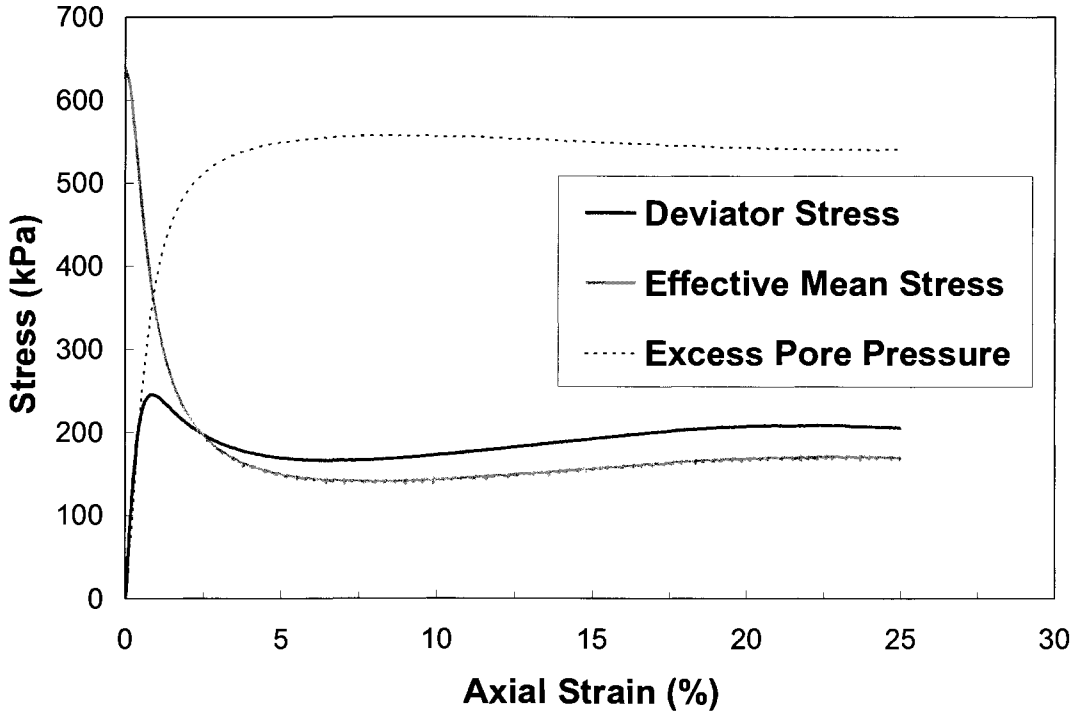

(b)

Figure A.35: (a) stress path, and (b) stress-displacement plots in TxC test APMRUN92

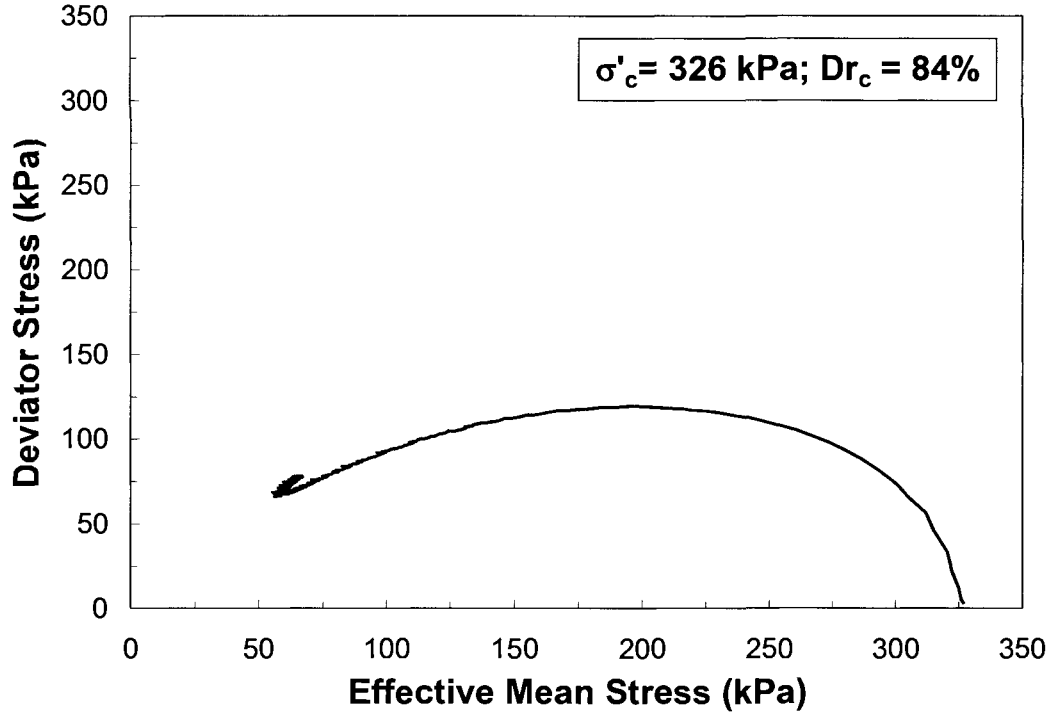

(a)

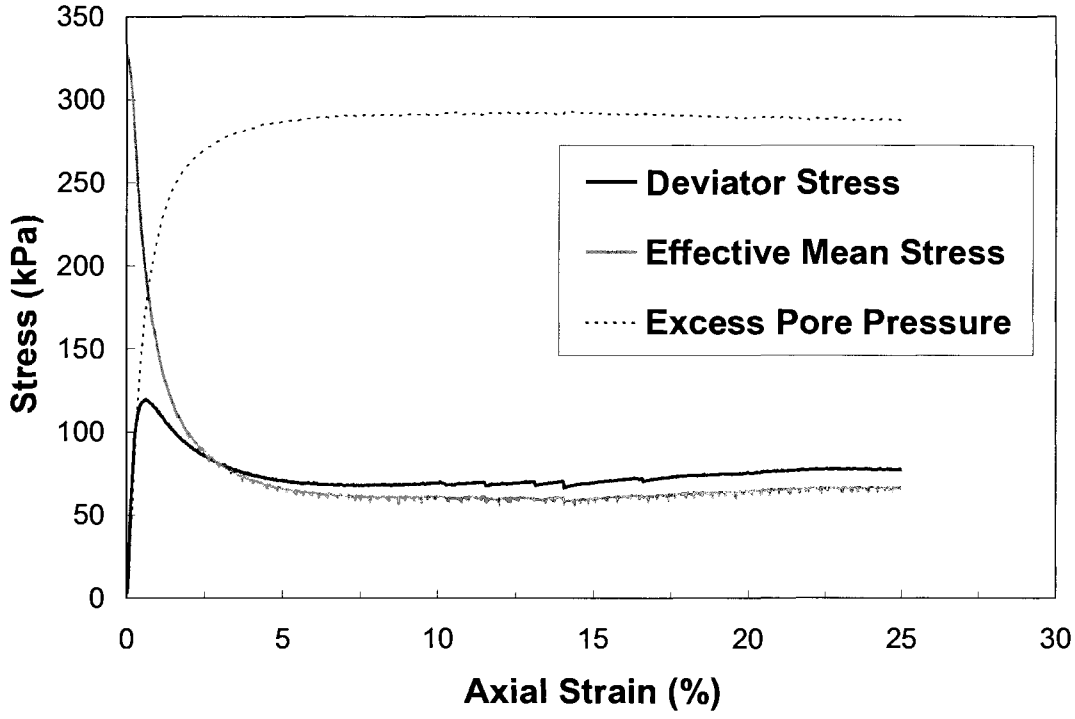

(b)

Figure A.36: (a) stress path, and (b) stress-displacement plots in TxC test APMRUN47

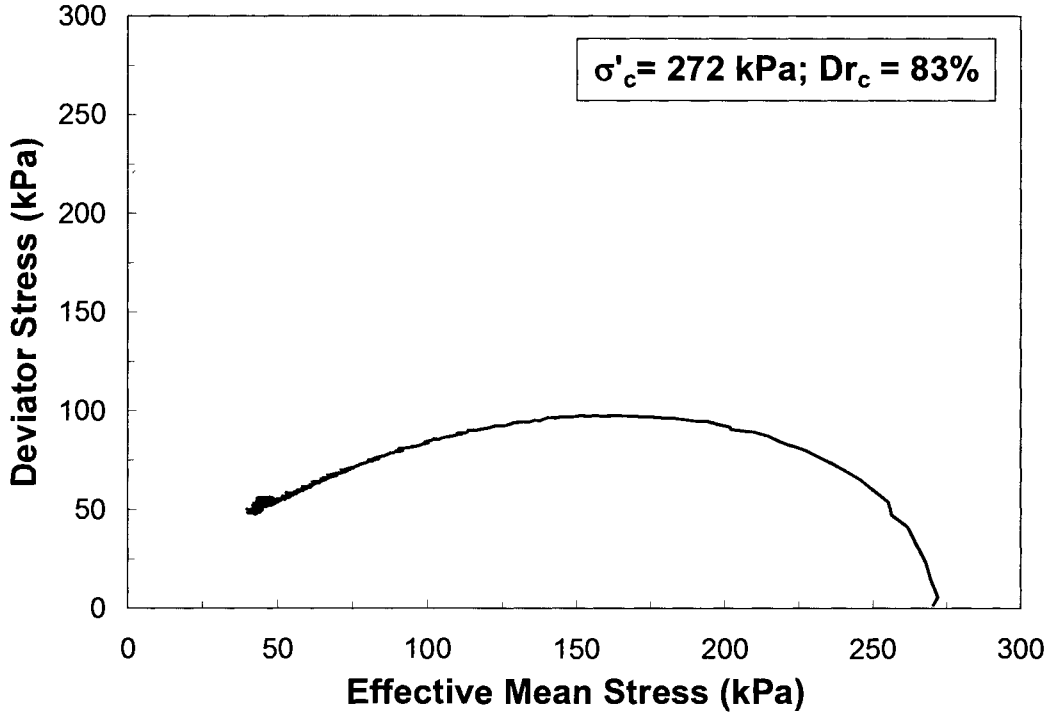

(a)

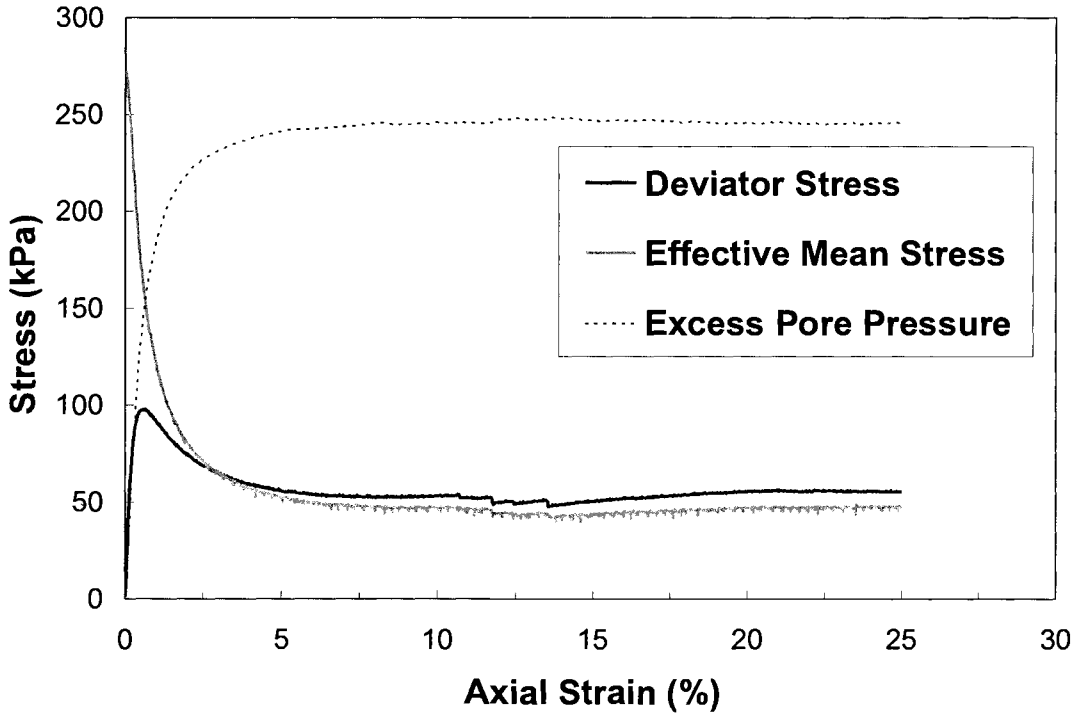

(b)

Figure A.37: (a) stress path, and (b) stress-displacement plots in TxC test APMRUN39

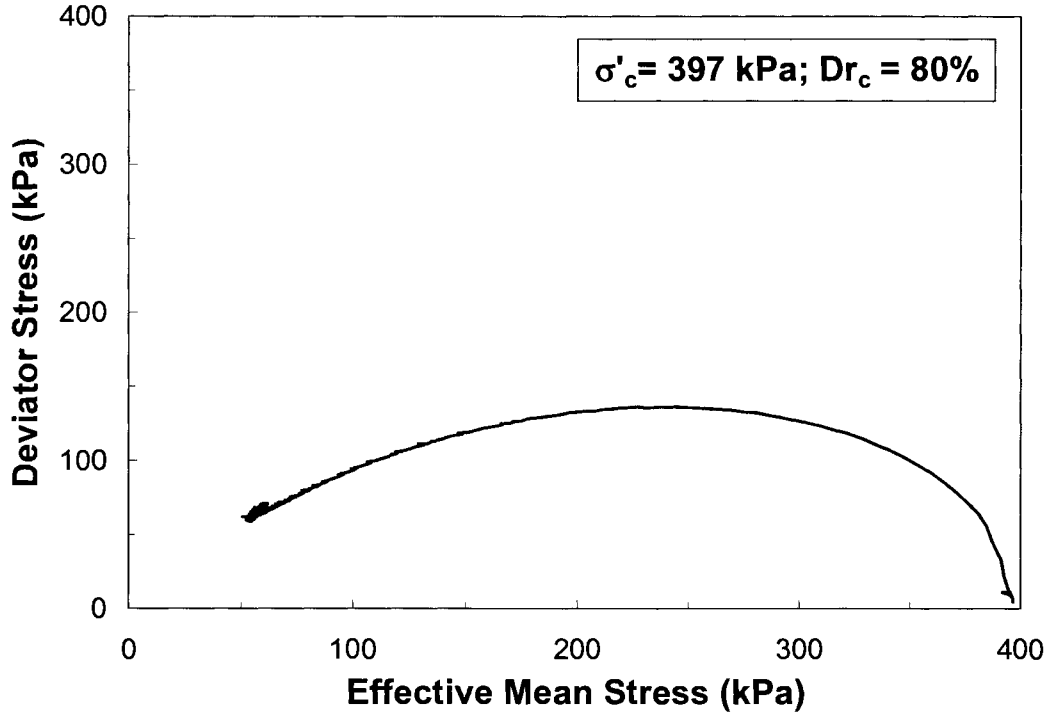

(a)

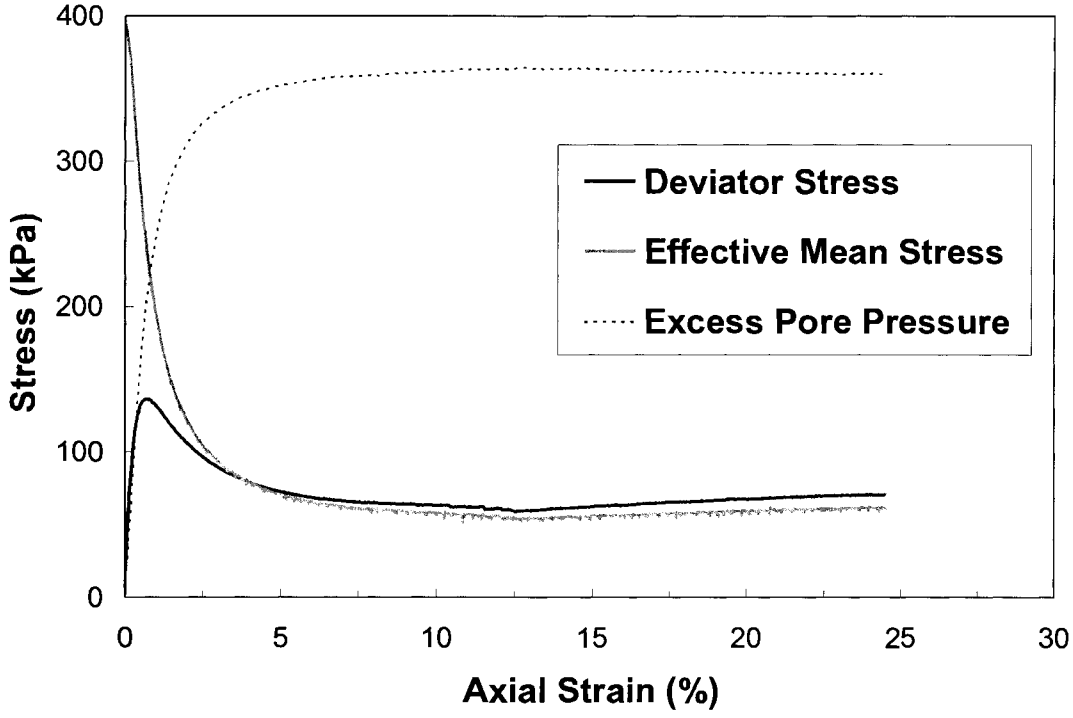

(b)

Figure A.38: (a) stress path, and (b) stress-displacement plots in TxC test APMRUN58

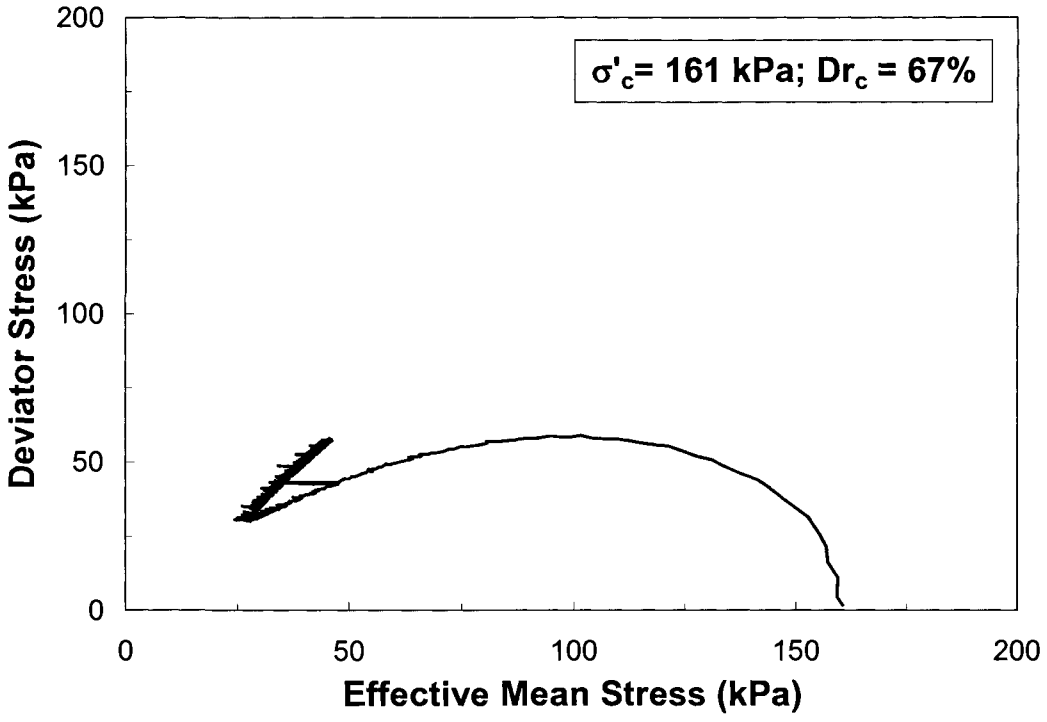

(a)

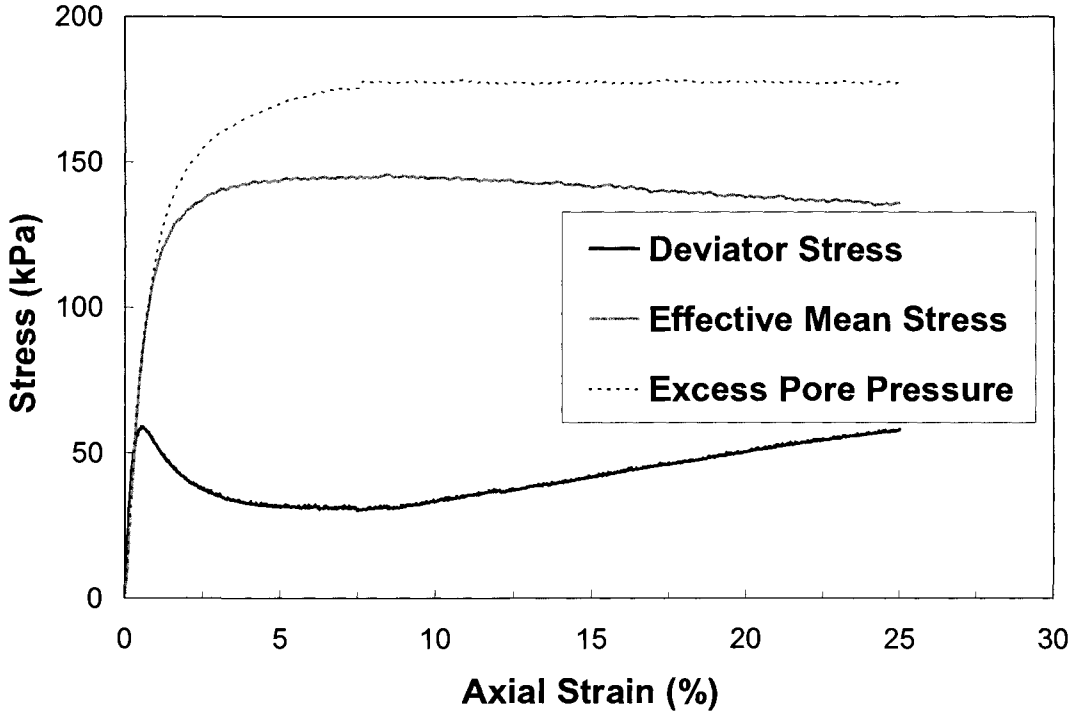

(b)

Figure A.39: (a) stress path, and (b) stress-displacement plots in TxC test APMRUN23

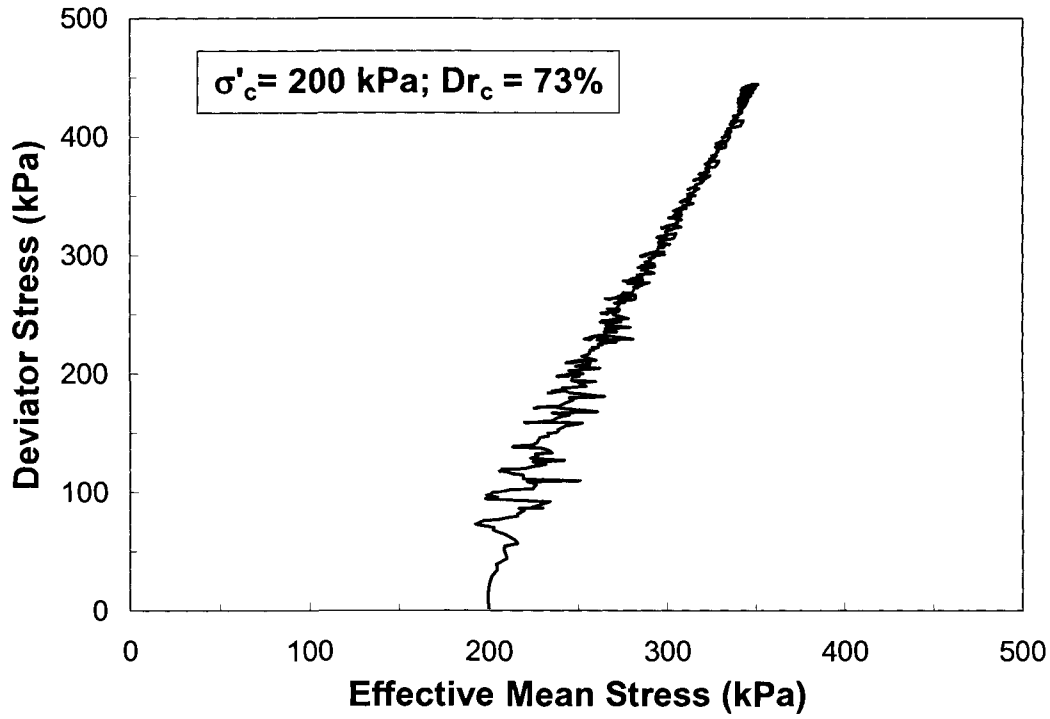

(a)

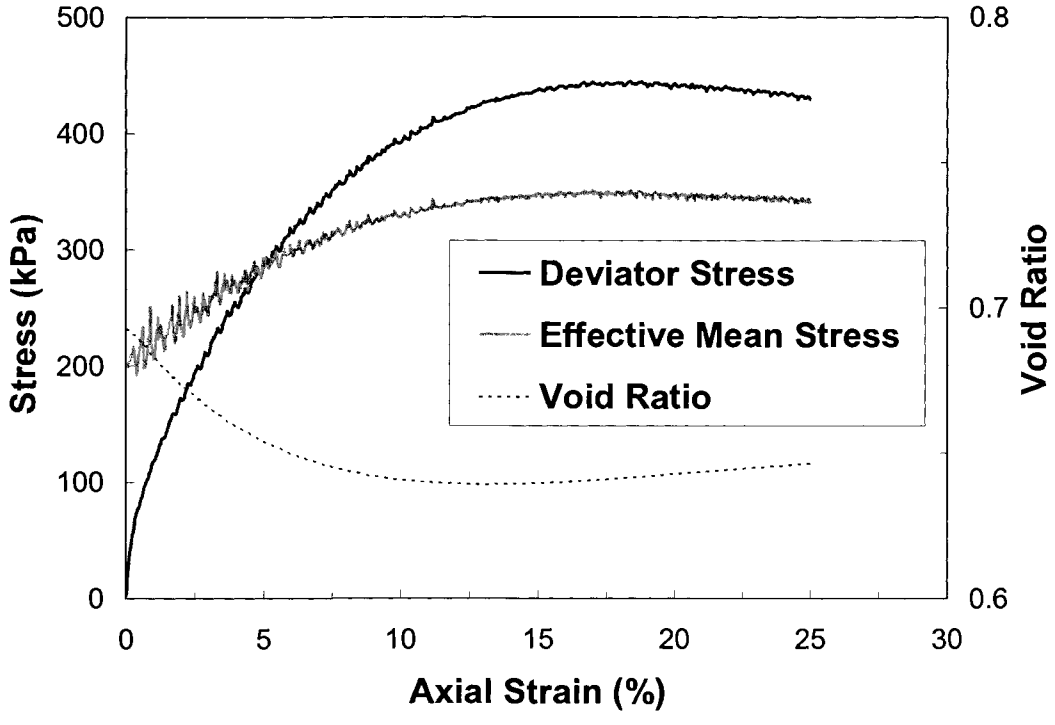

(b)

Figure A.40: (a) stress path, and (b) stress-displacement plots in TxC test APMRDR29

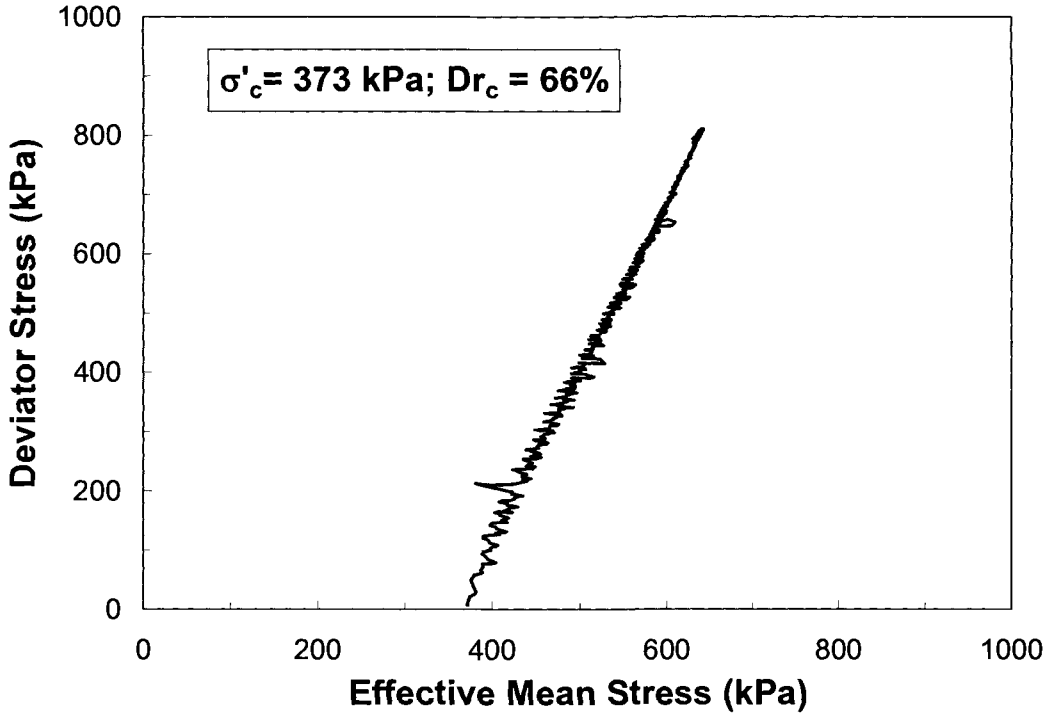

(a)

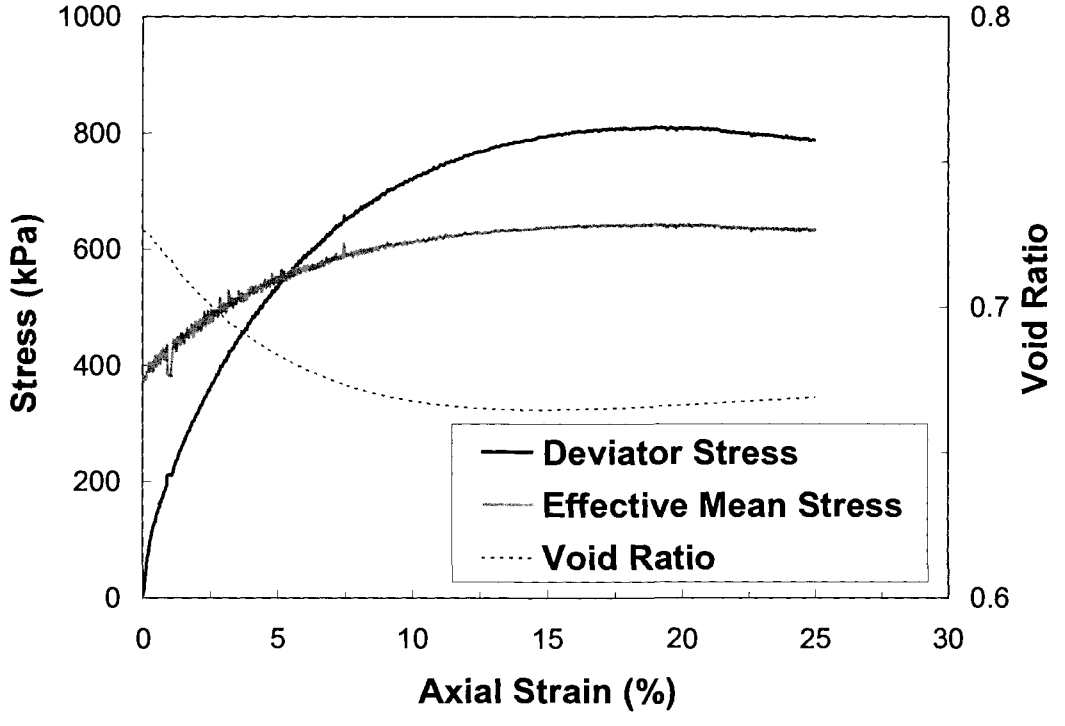

(b)

Figure A.41: (a) stress path, and (b) stress-displacement plots in TxC test APMRDR54

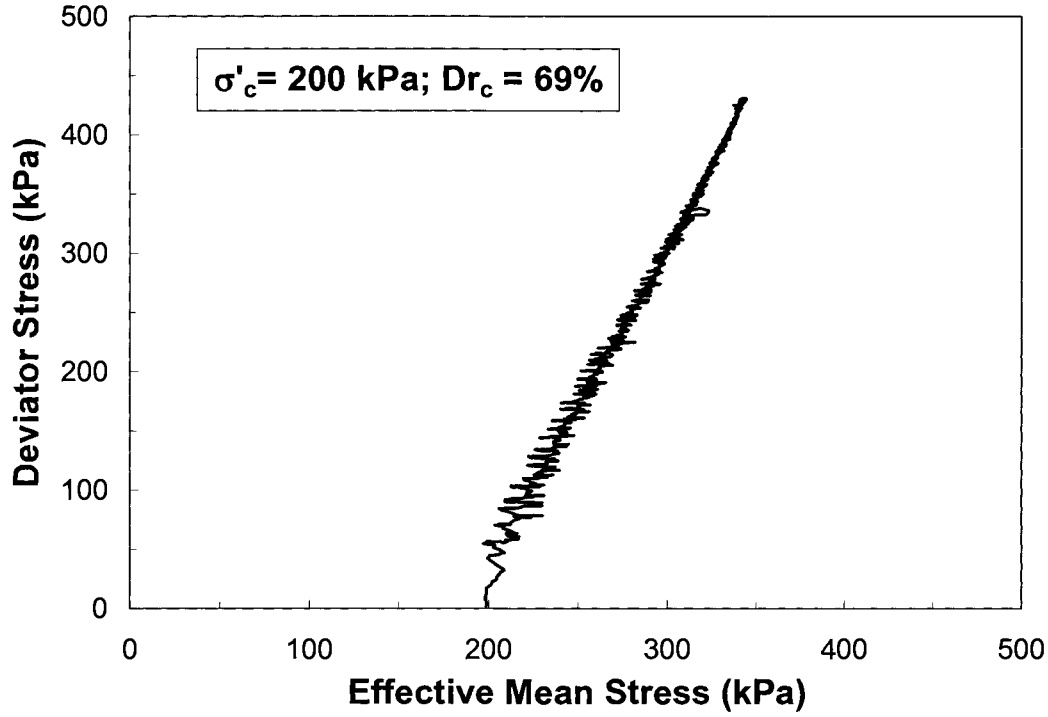

(a)

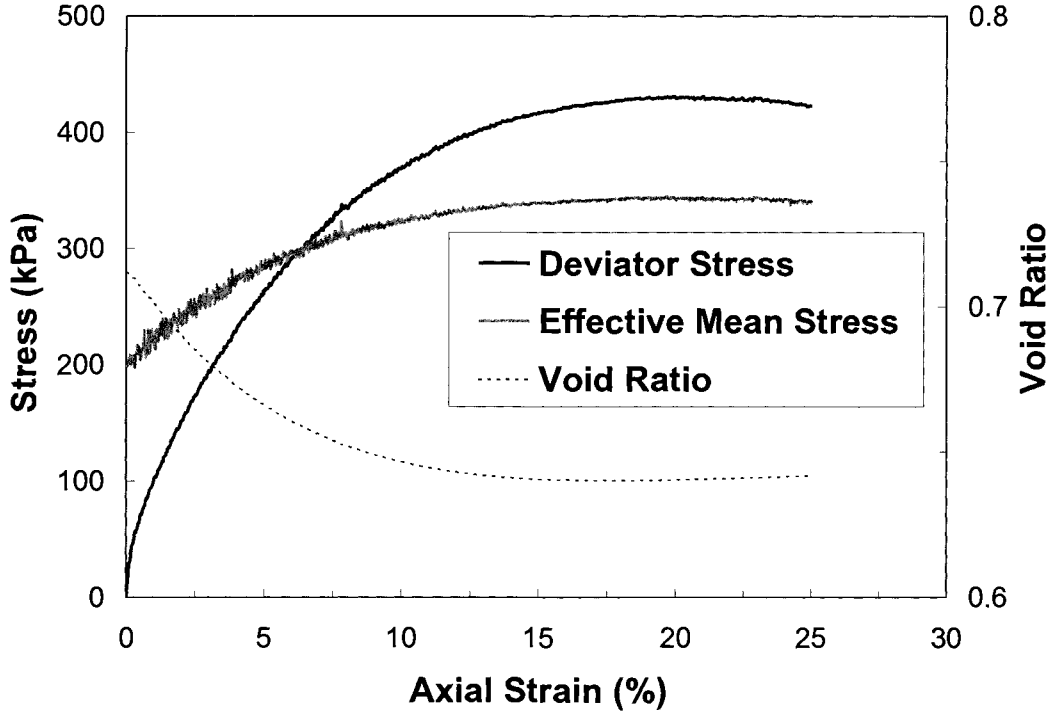

(b)

Figure A.42: (a) stress path, and (b) stress-displacement plots in TxC test APMRDR29

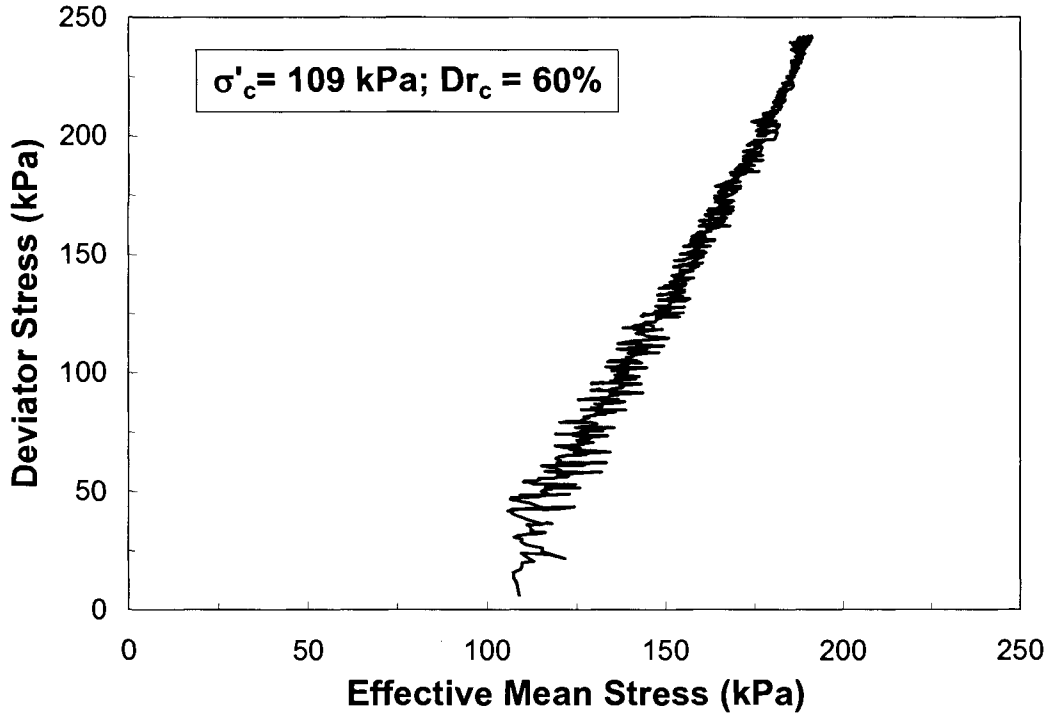

(a)

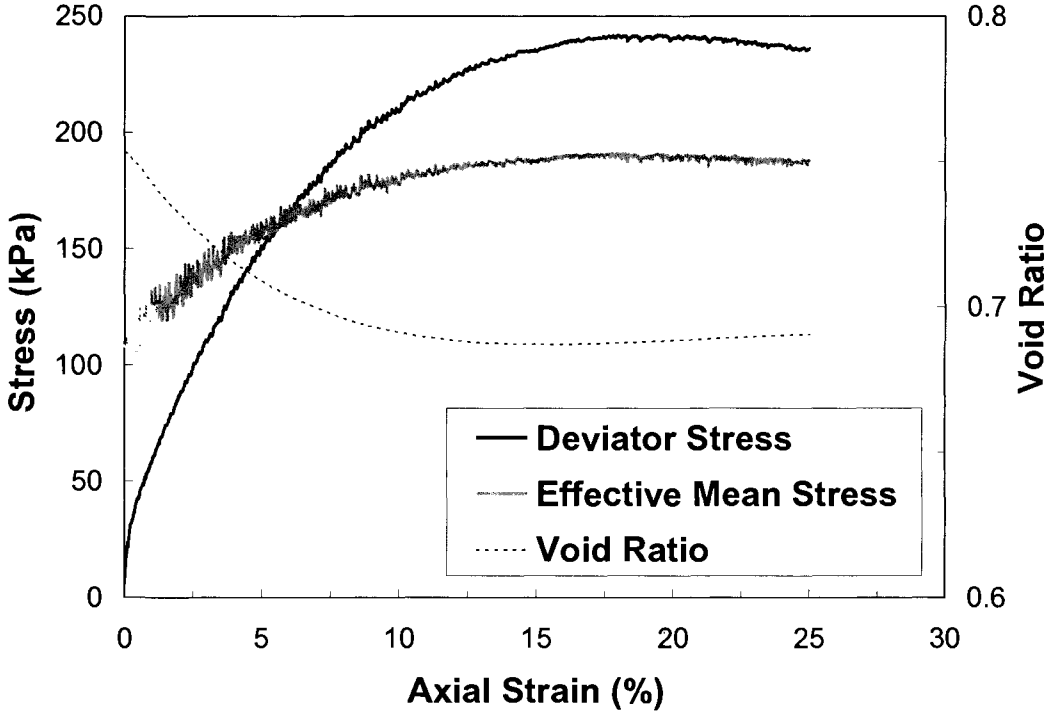

(b)

Figure A.43: (a) stress path, and (b) stress-displacement plots in TxC test APMRDR16

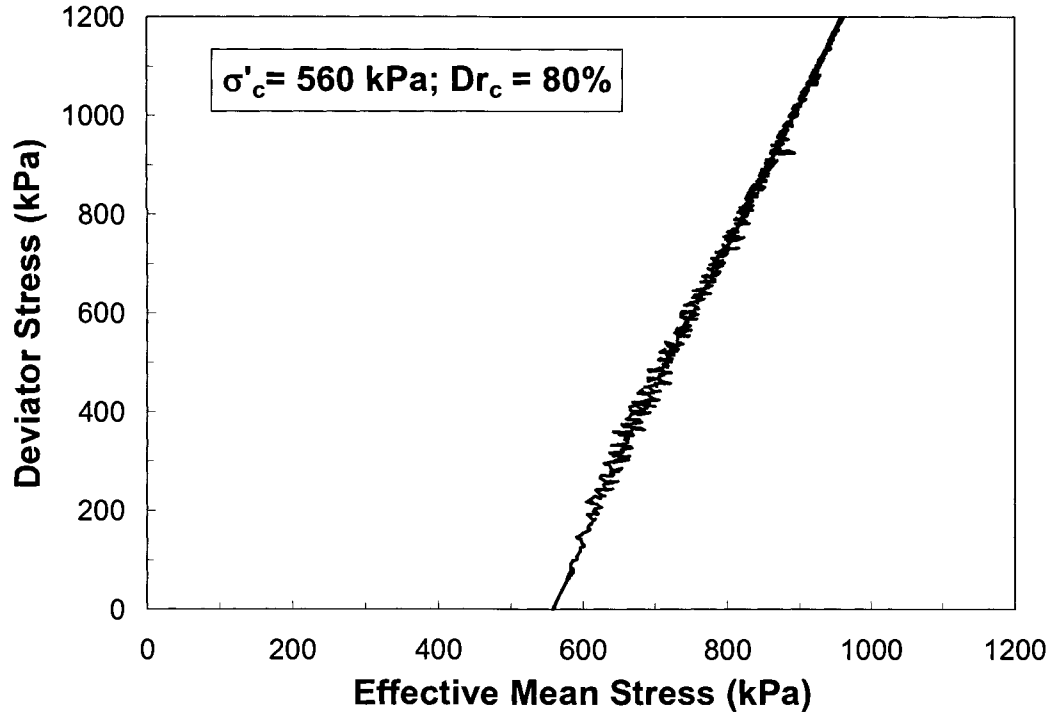

(a)

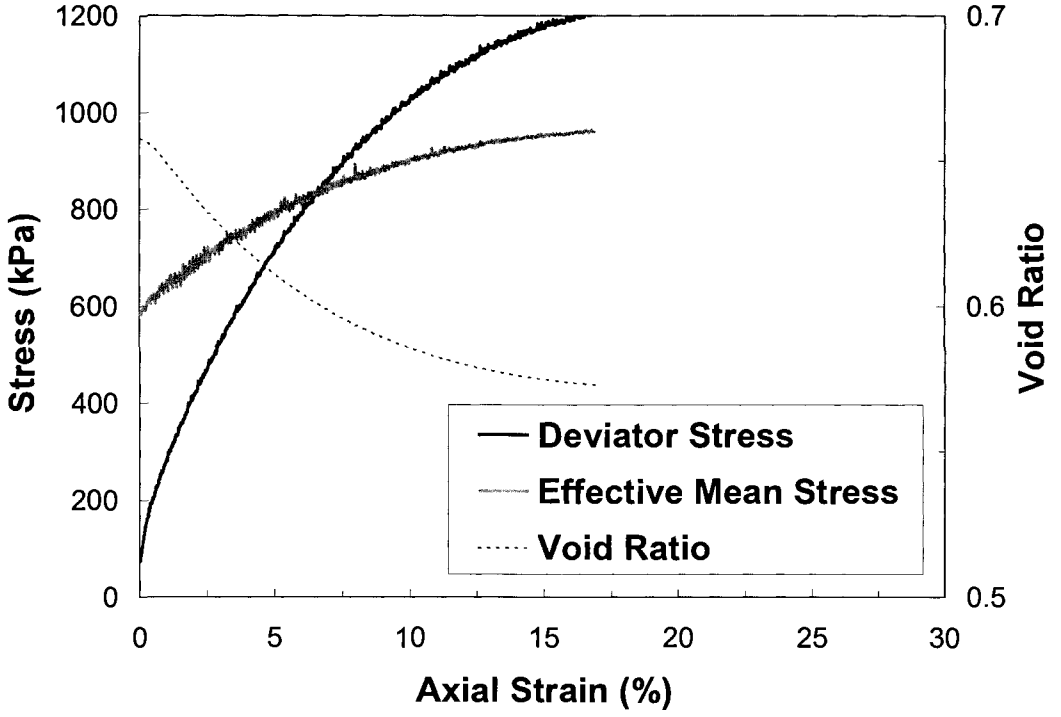

(b)

Figure A.44: (a) stress path, and (b) stress-displacement plots in TxC test APMRDR81

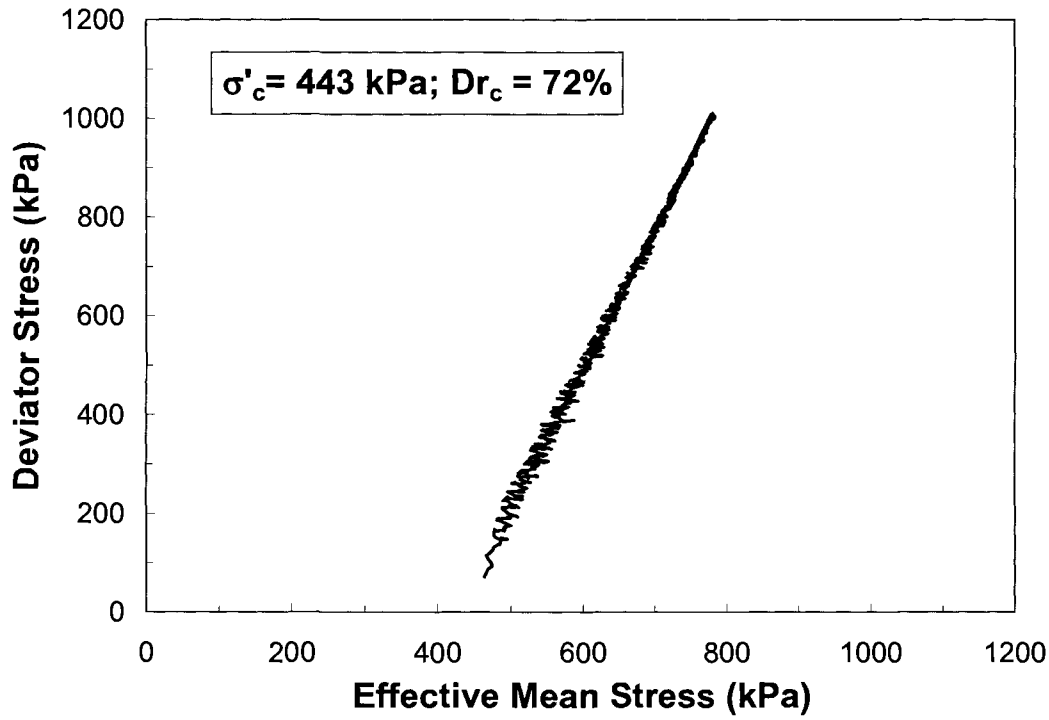

(a)

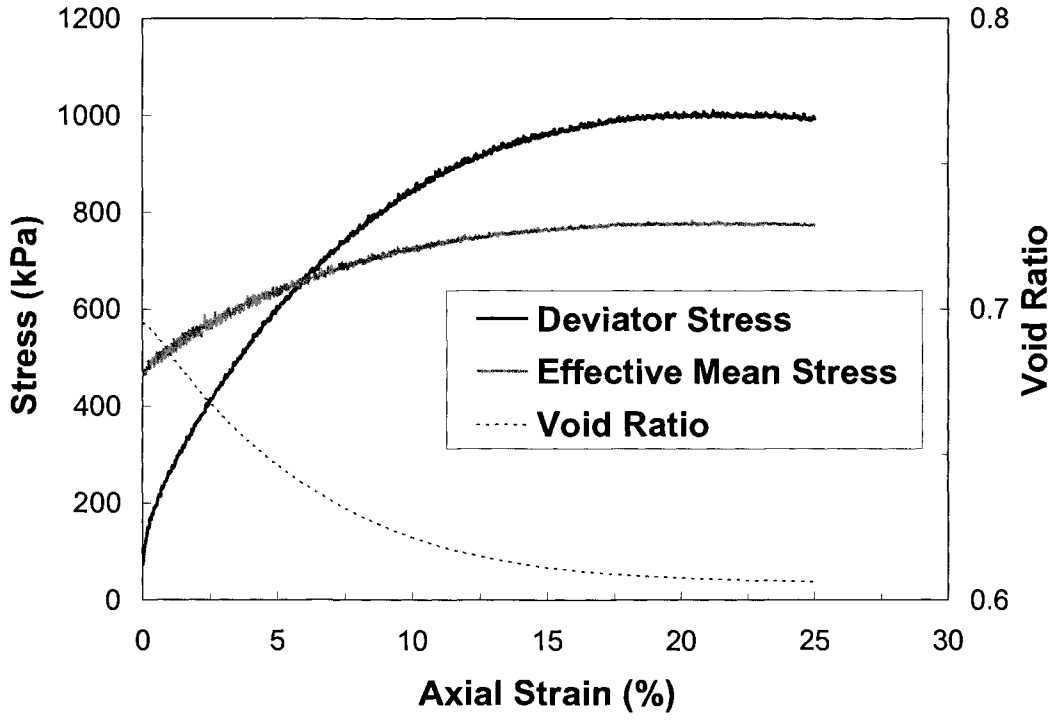

(b)

Figure A.45: (a) stress path, and (b) stress-displacement plots in TxC test APMRDR64

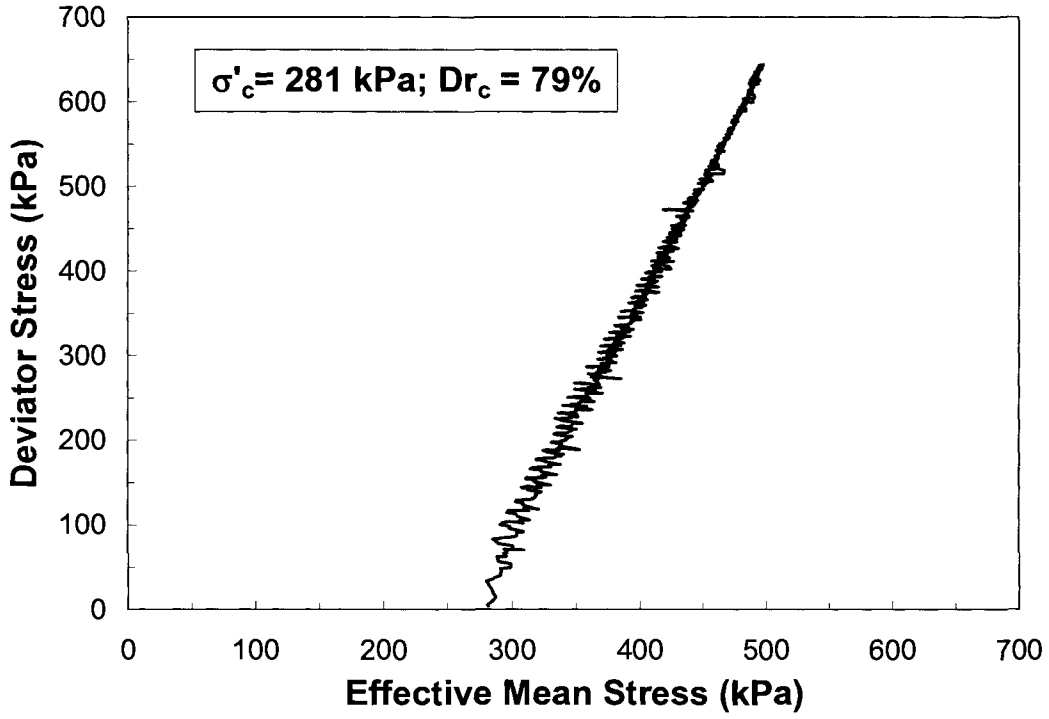

(a)

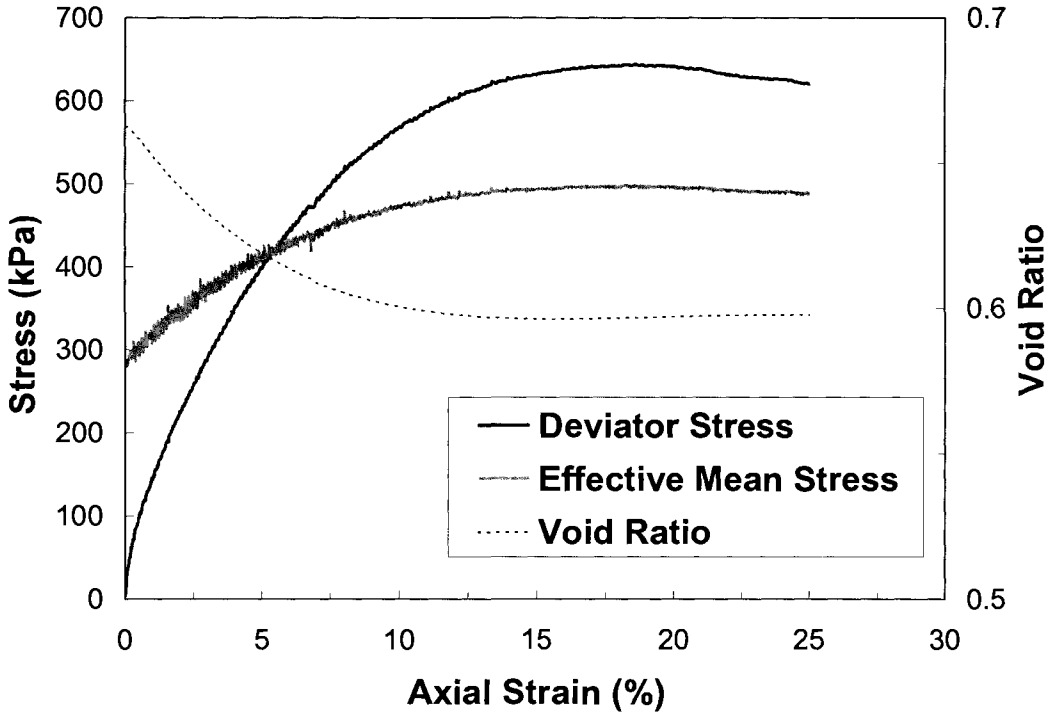

(b)

Figure A.46: (a) stress path, and (b) stress-displacement plots in TxC test APMRDR41

APPENDIX B. RING SHEAR TEST RESULTS

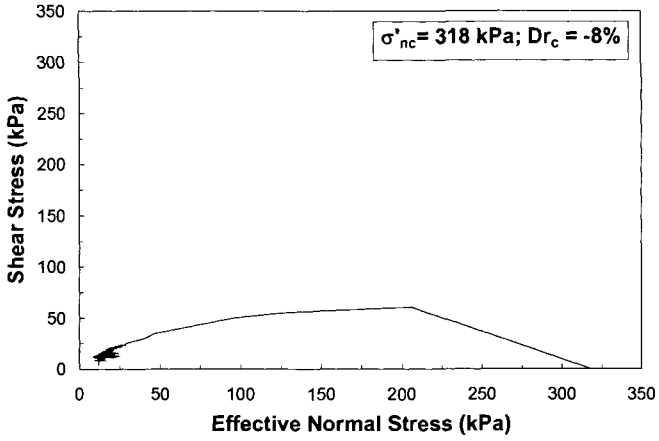

(a)

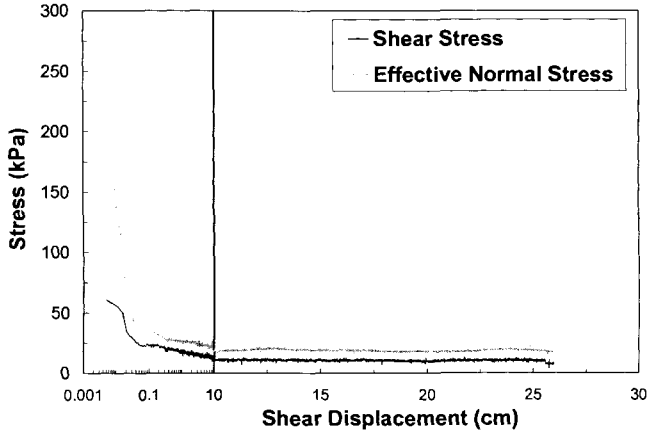

(b)

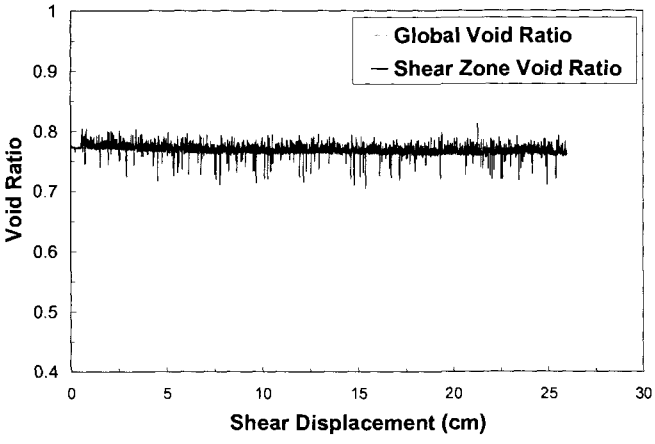

(c)

Figure B.1: (a) stress path, (b) stress-displacement, and (c) void ratio – displacement plot in ring shear test MTIRCV46

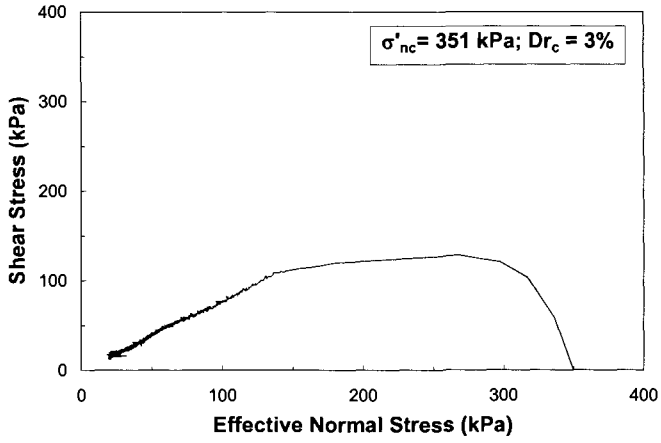

(a)

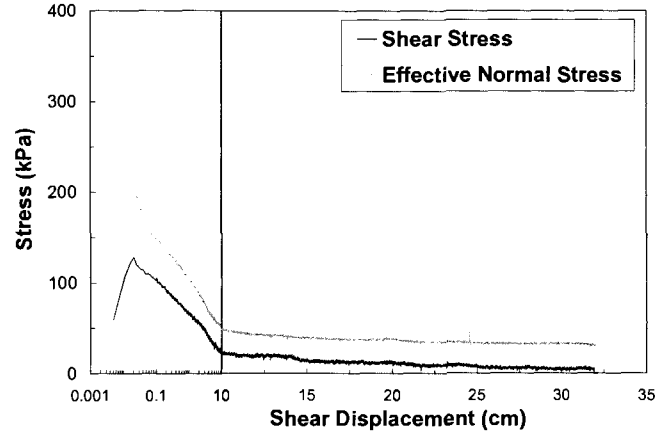

(b)

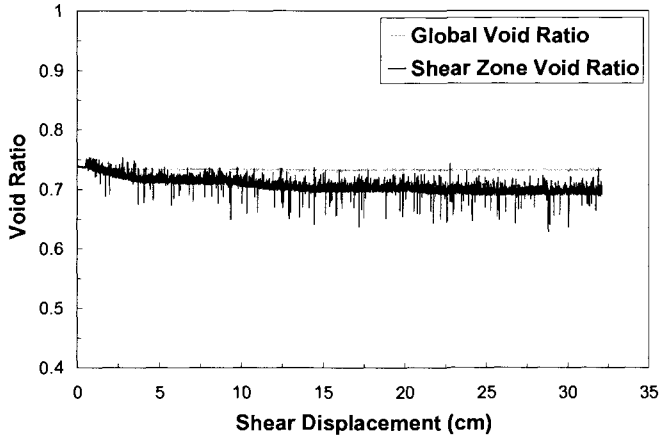

(c)

Figure B.2: (a) stress path, (b) stress-displacement, and (c) void ratio – displacement plot in ring shear test MTIRCV53

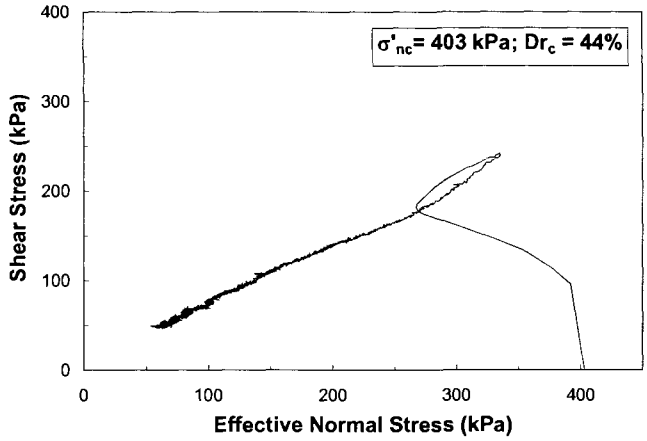

(a)

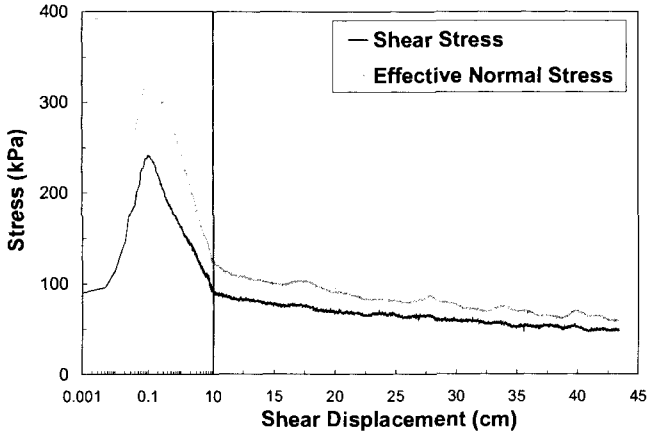

(b)

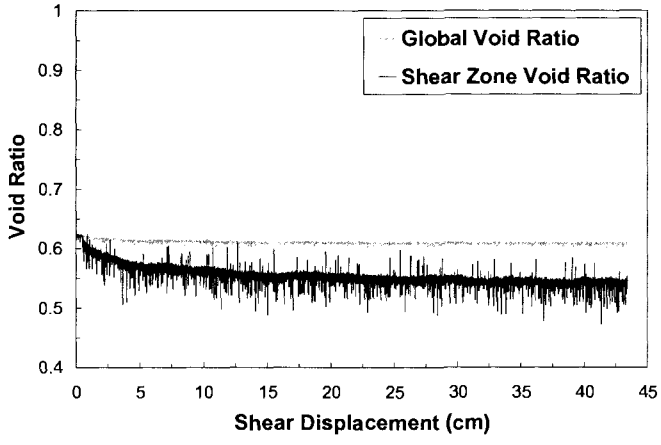

(c)

Figure B.3: (a) stress path, (b) stress-displacement, and (c) void ratio – displacement plot in ring shear test MTIRCV58

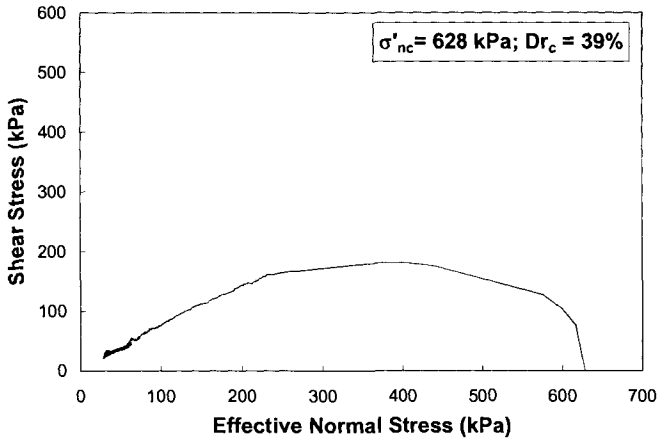

(a)

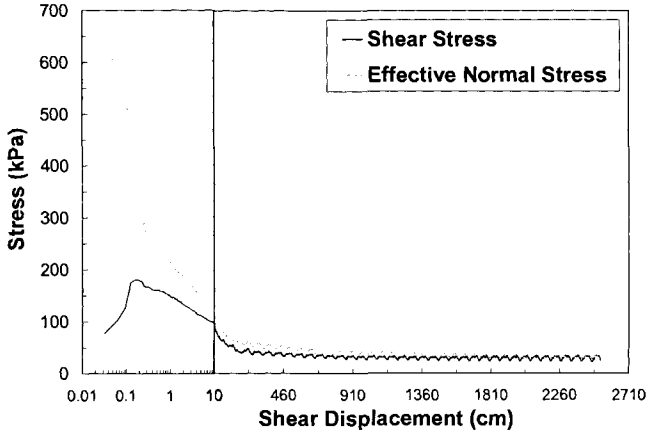

(b)

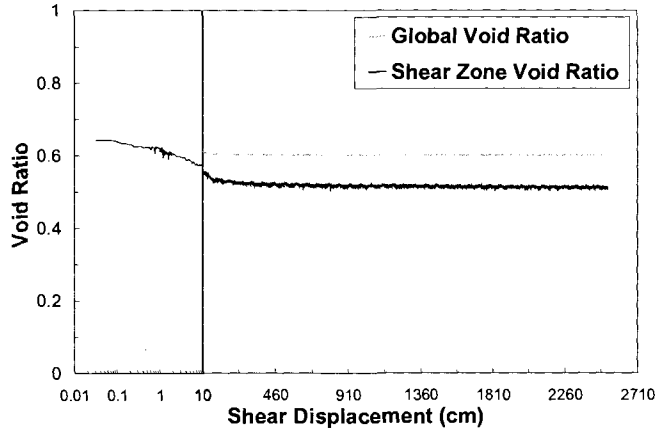

(c)

Figure B.4: (a) stress path, (b) stress-displacement, and (c) void ratio – displacement plot in ring shear test MTIRCV75

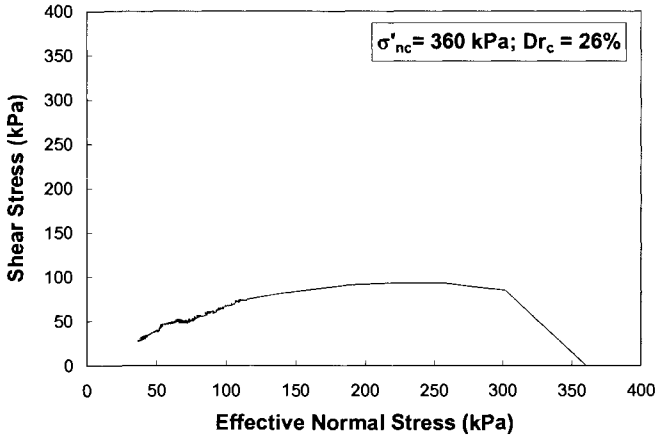

(a)

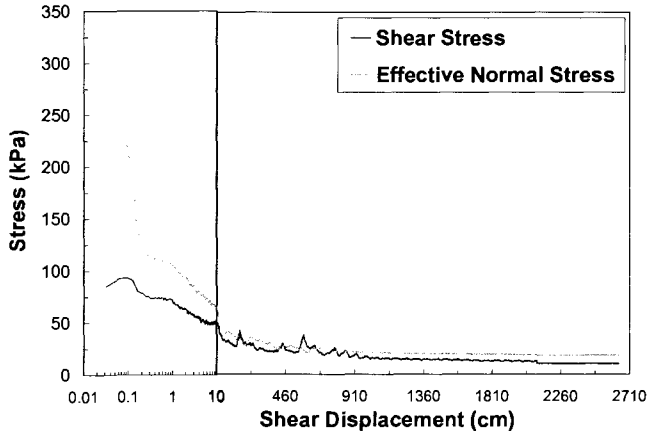

(b)

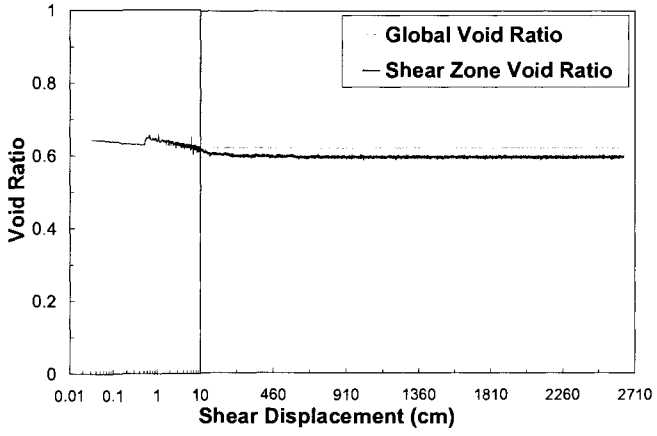

(c)

Figure B.5: (a) stress path, (b) stress-displacement, and (c) void ratio – displacement plot in ring shear test MTIRCV52

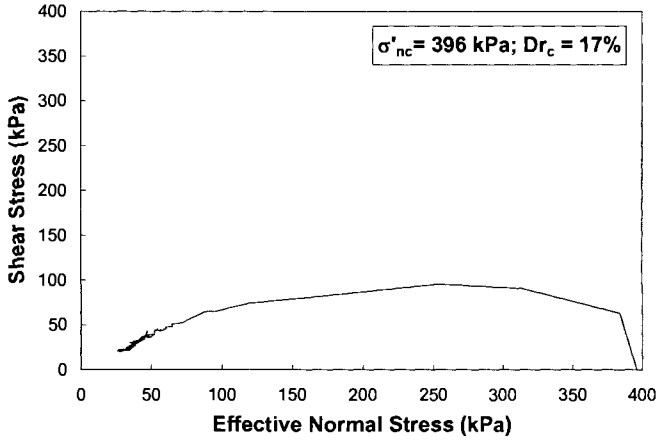

(a)

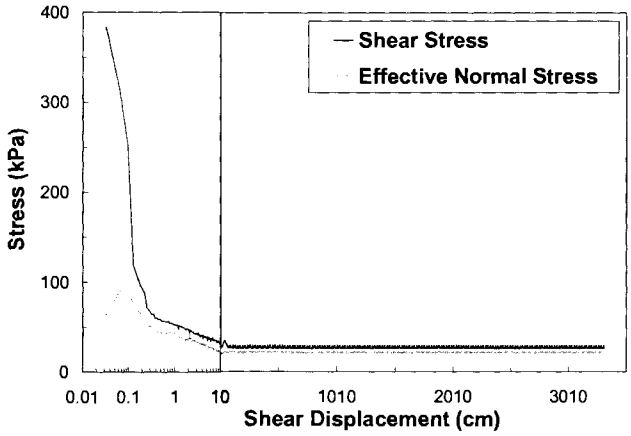

(b)

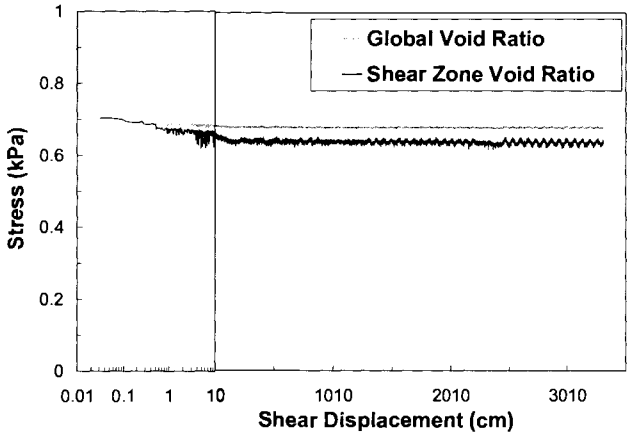

(c)

Figure B.6: (a) stress path, (b) stress-displacement, and (c) void ratio – displacement plot in ring shear test MTIRCV56

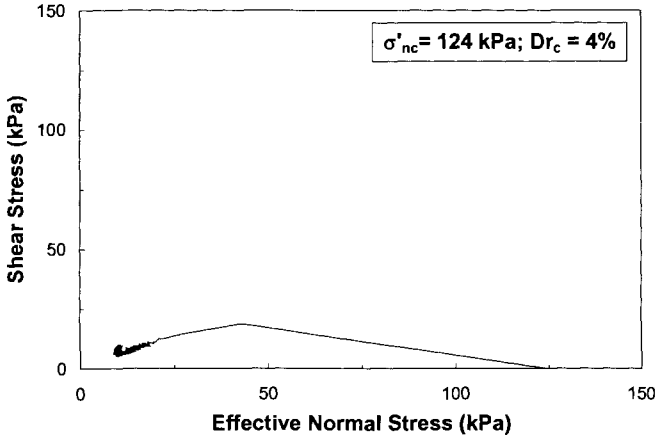

(a)

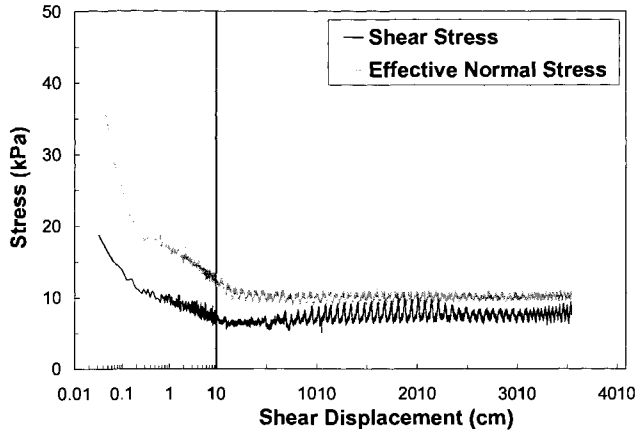

(b)

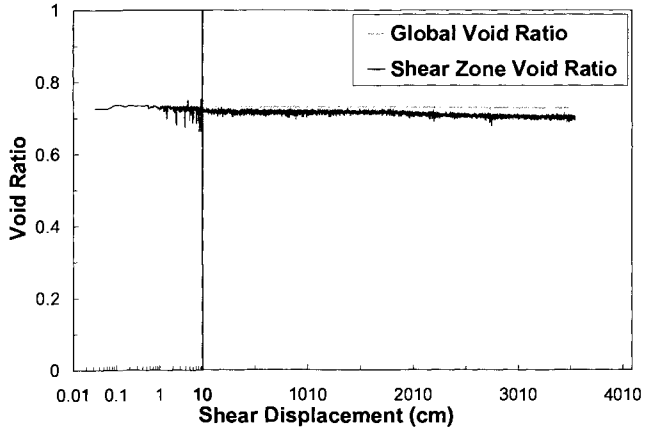

(c)

Figure B.7: (a) stress path, (b) stress-displacement, and (c) void ratio – displacement plot in ring shear test MTIRCV18

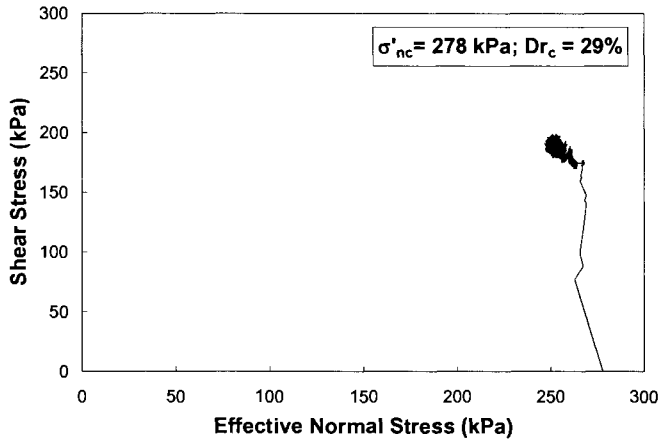

(a)

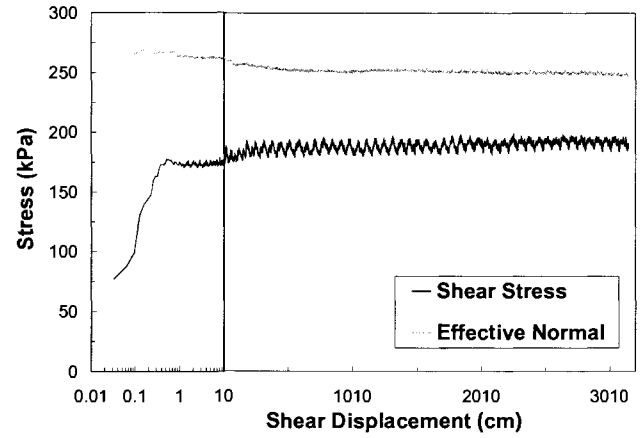

(b)

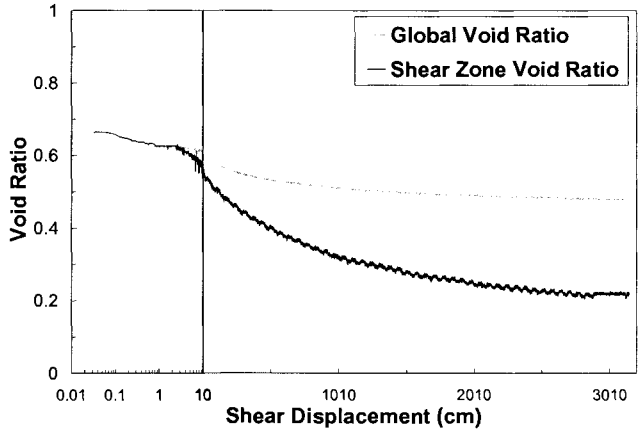

(c)

Figure B.8: (a) stress path, (b) stress-displacement, and (c) void ratio – displacement plot in ring shear test MTIRDR41

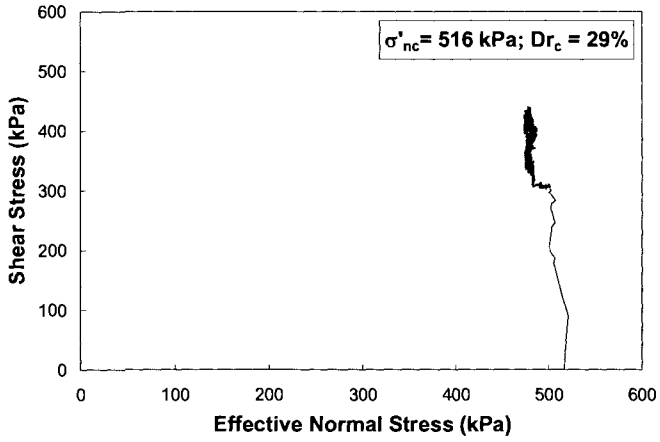

(a)

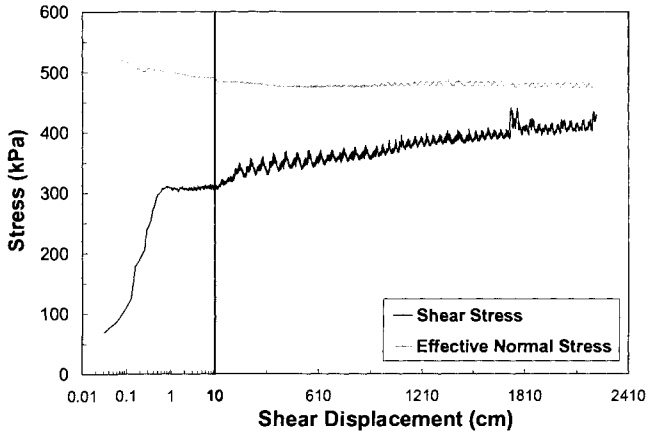

(b)

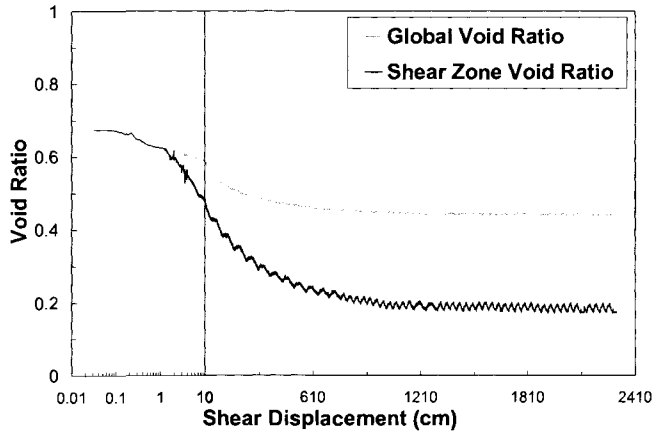

(c)

Figure B.9: (a) stress path, (b) stress-displacement, and (c) void ratio – displacement plot in ring shear test MTIRDR75

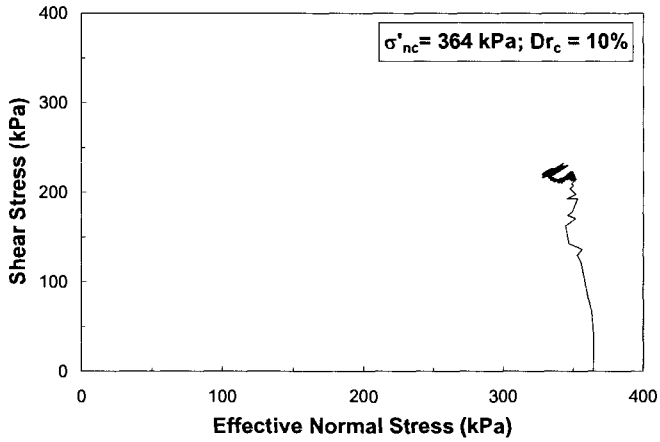

(a)

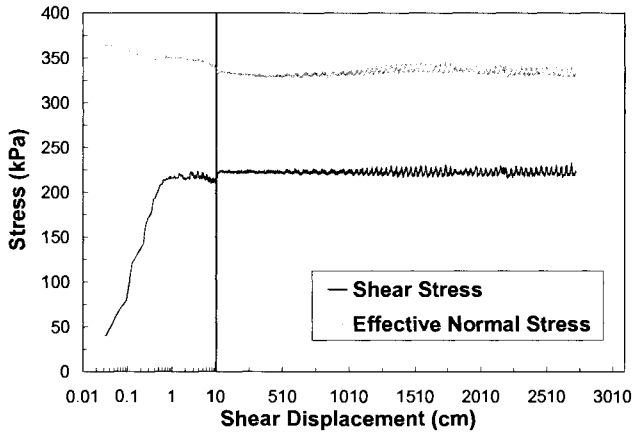

(b)

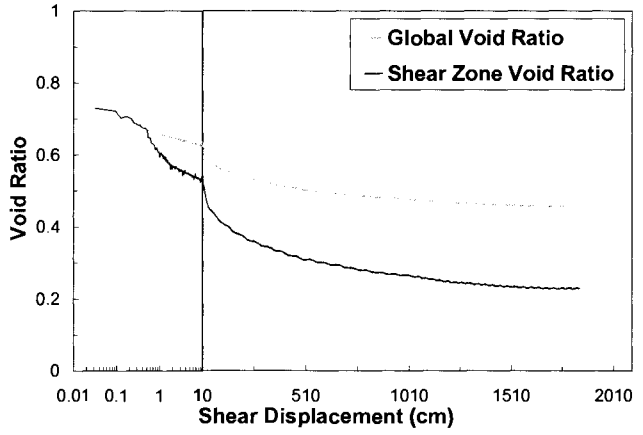

(c)

Figure B.10: (a) stress path, (b) stress-displacement, and (c) void ratio – displacement plot in ring shear test MTIRDR54

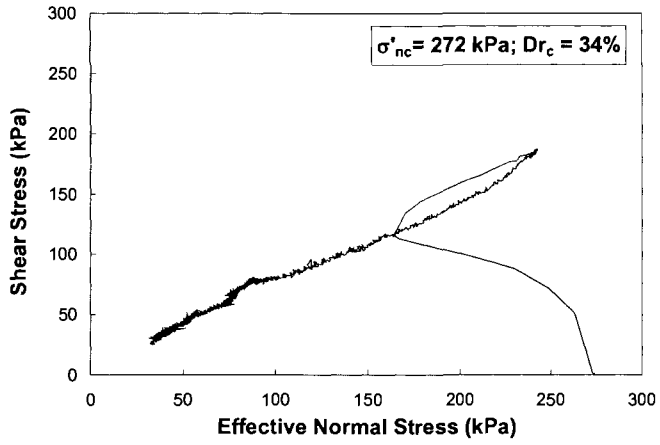

(a)

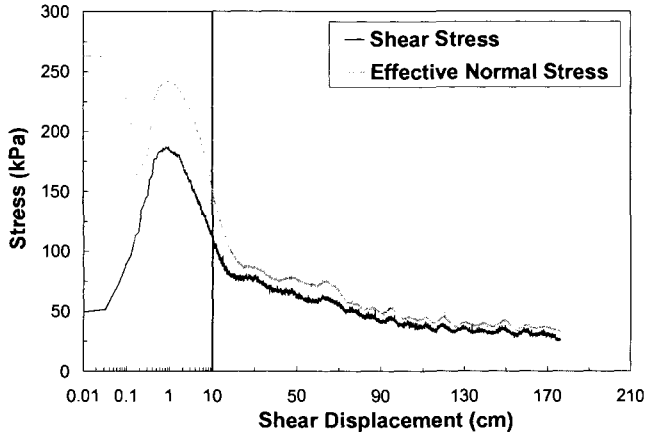

(b)

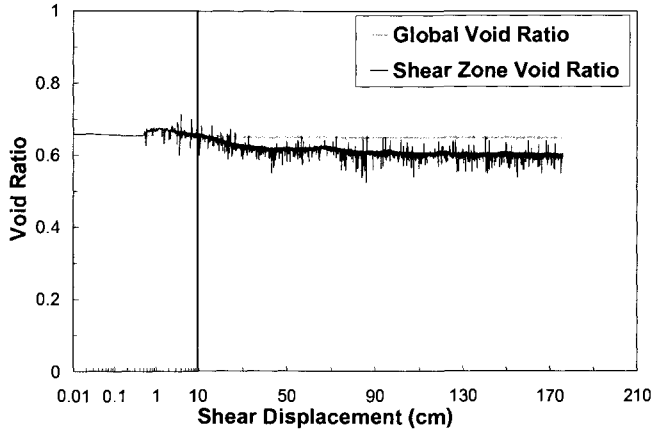

(c)

Figure B.11: (a) stress path, (b) stress-displacement, and (c) void ratio – displacement plot in ring shear test APIRCV39

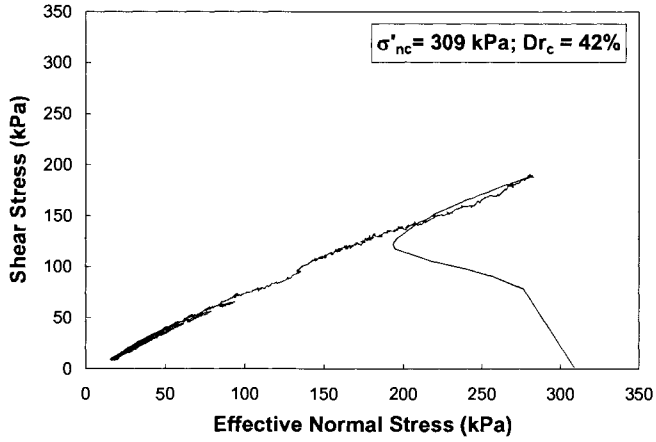

(a)

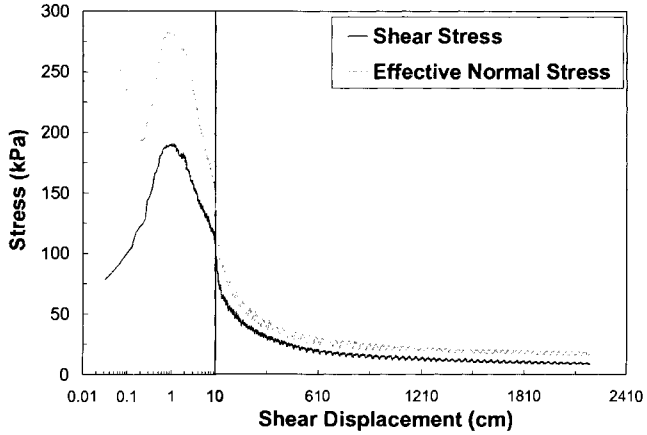

(b)

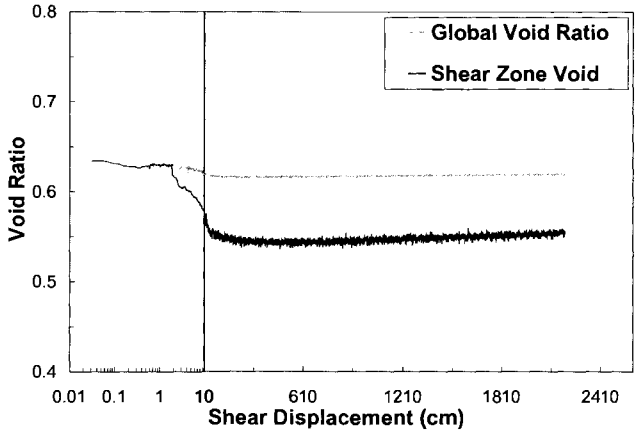

(c)

Figure B.12: (a) stress path, (b) stress-displacement, and (c) void ratio – displacement plot in ring shear test APIRCV42

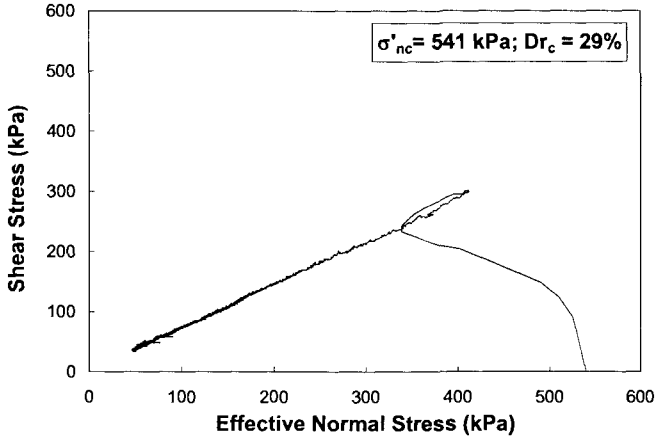

(a)

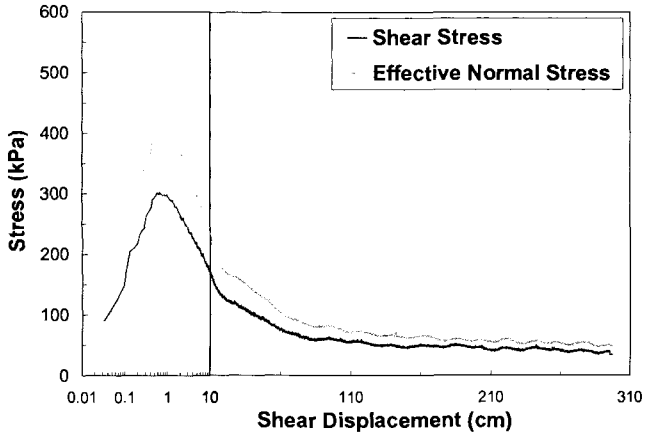

(b)

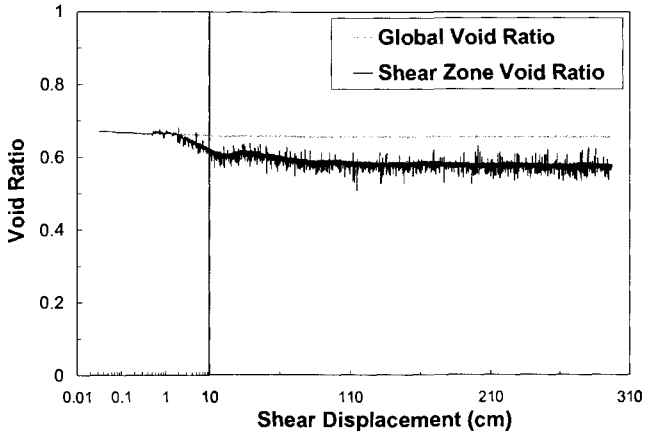

(c)

Figure B.13: (a) stress path, (b) stress-displacement, and (c) void ratio – displacement plot in ring shear test APIRCV78

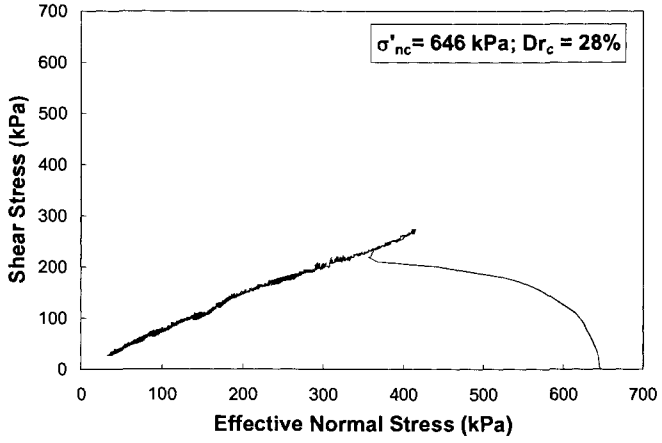

(a)

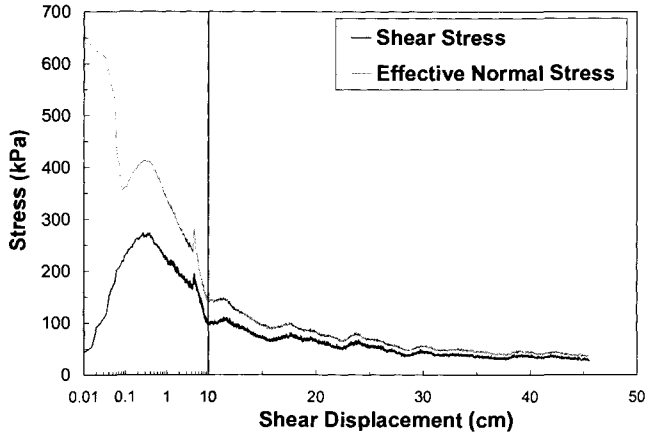

(b)

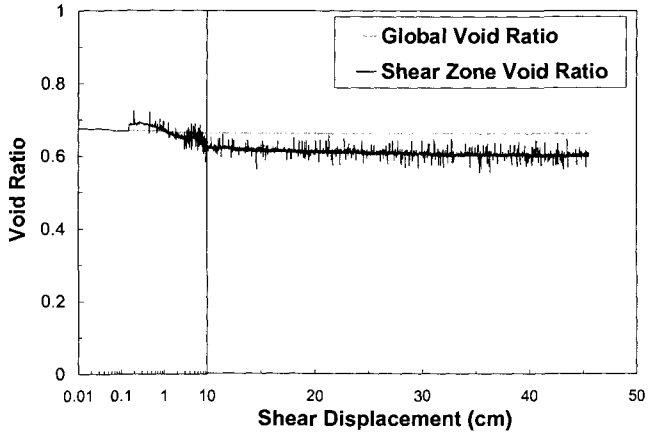

(c)

Figure B.14: (a) stress path, (b) stress-displacement, and (c) void ratio – displacement plot in ring shear test APIRCV94

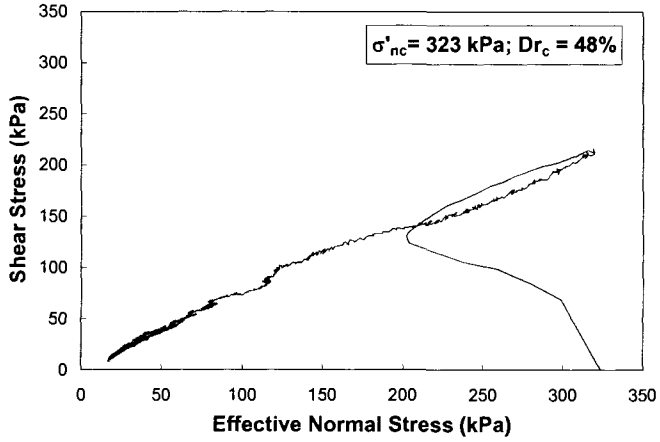

(a)

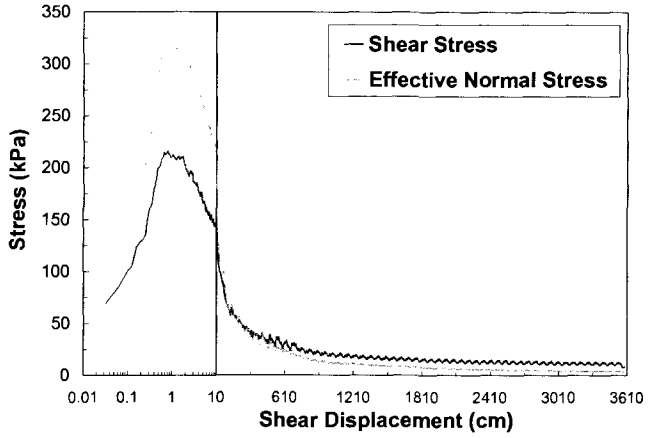

(b)

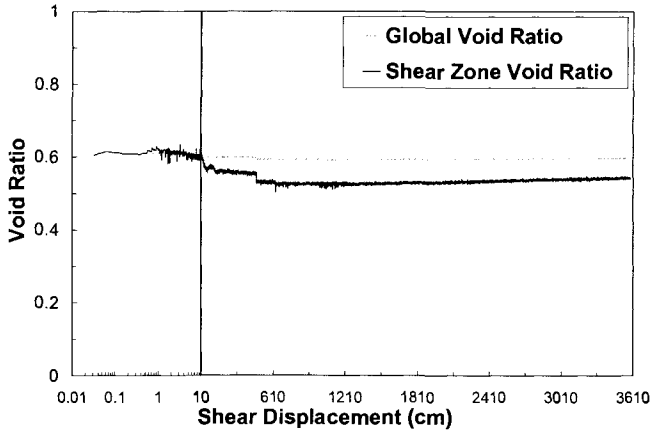

(c)

Figure B.15: (a) stress path, (b) stress-displacement, and (c) void ratio – displacement plot in ring shear test APIRCV45

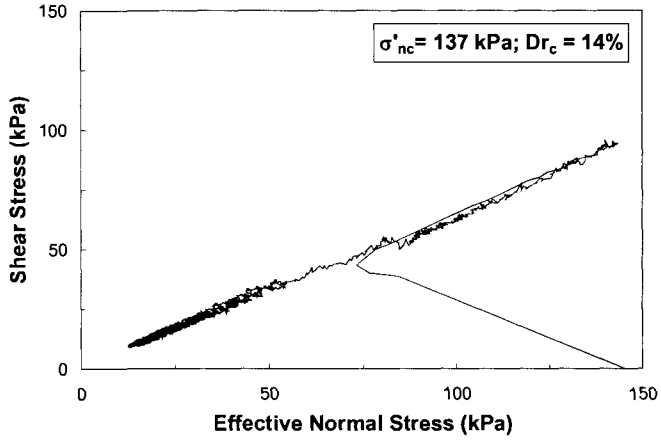

(a)

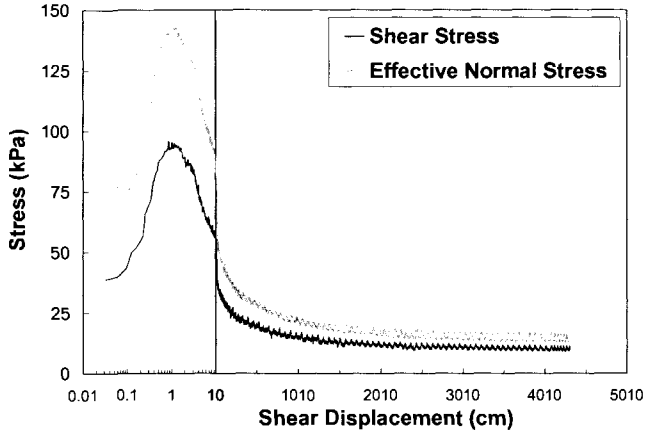

(b)

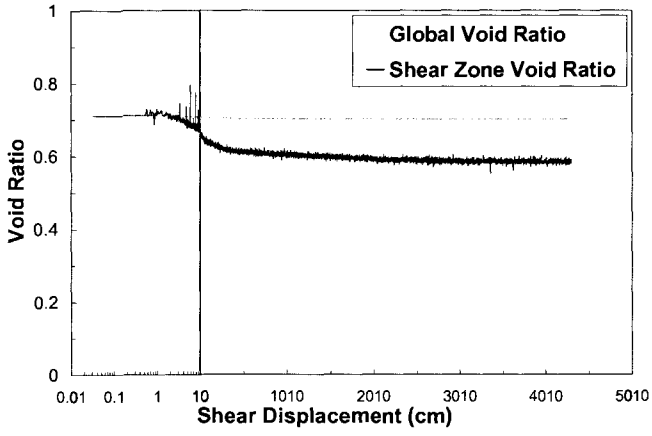

(c)

Figure B.16: (a) stress path, (b) stress-displacement, and (c) void ratio – displacement plot in ring shear test APIRCV17

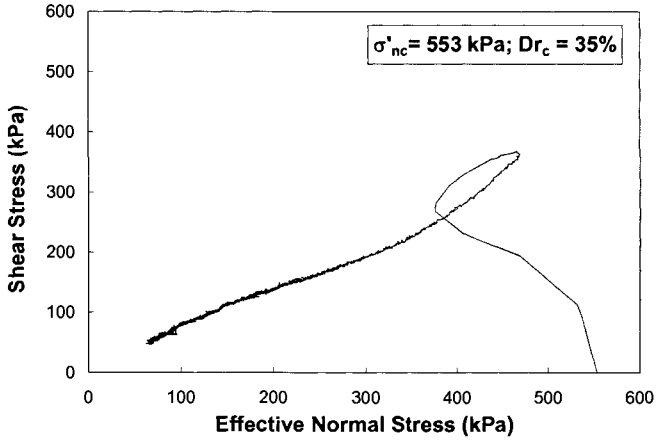

(a)

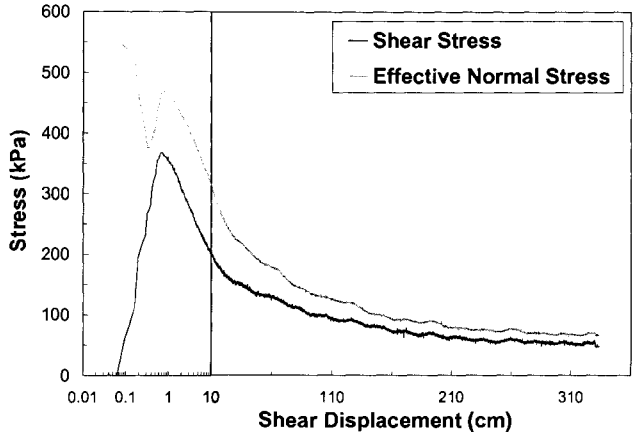

(b)

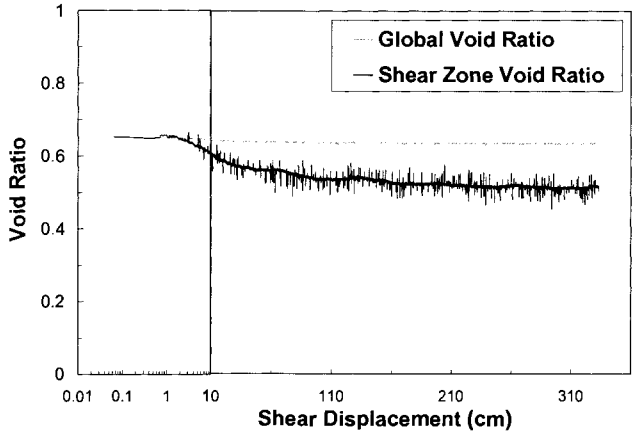

(c)

Figure B.17: (a) stress path, (b) stress-displacement, and (c) void ratio – displacement plot in ring shear test APIRCV81

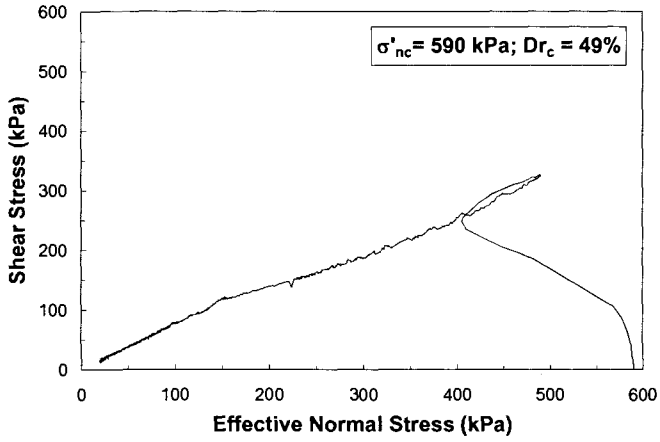

(a)

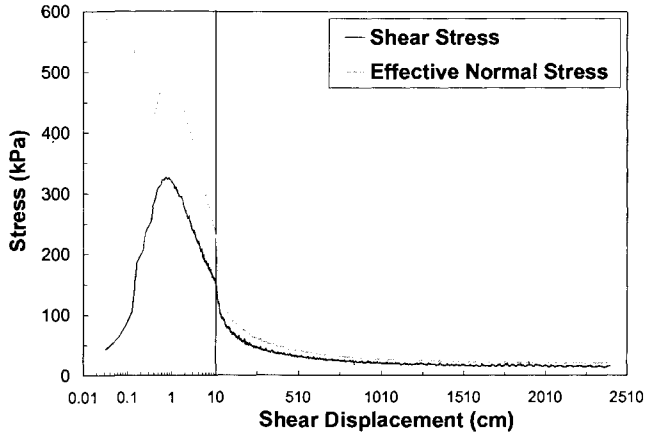

(b)

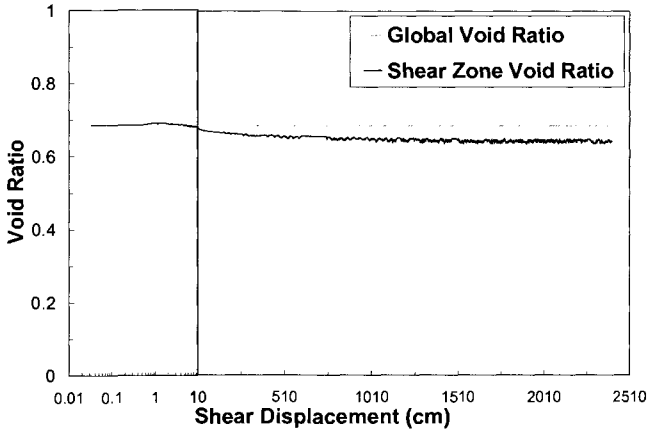

(c)

Figure B.18: (a) stress path, (b) stress-displacement, and (c) void ratio – displacement plot in ring shear test APIRCV82

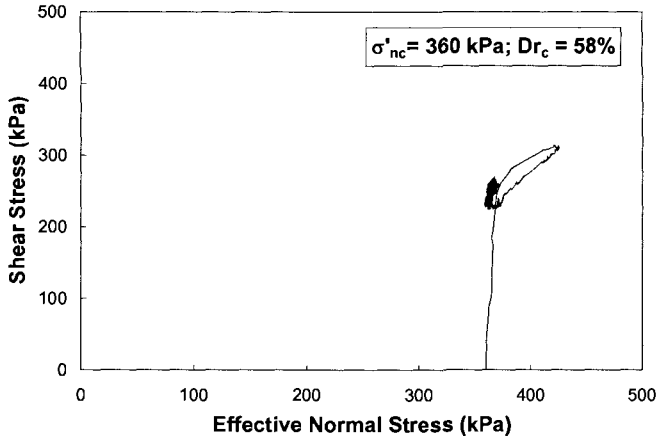

(a)

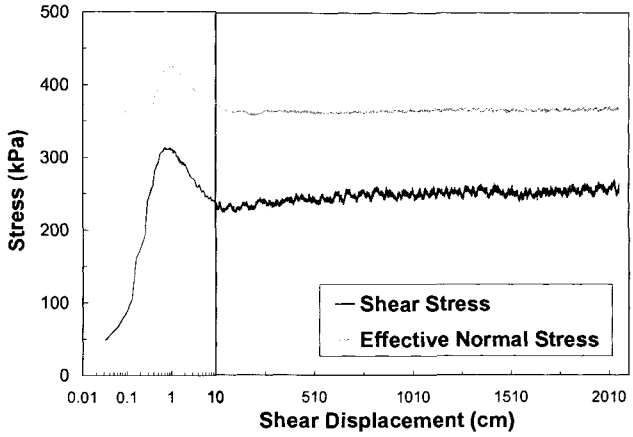

(b)

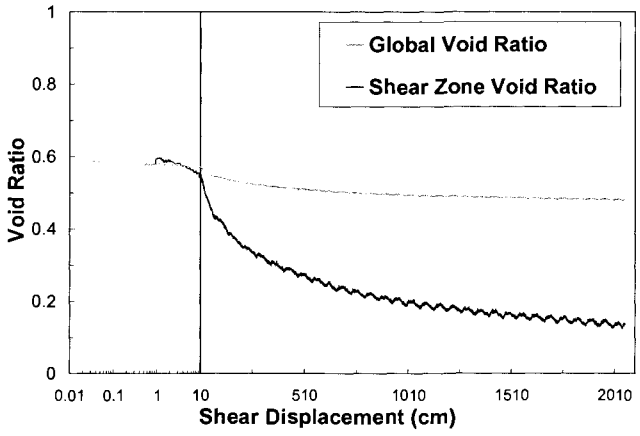

(c)

Figure B.19: (a) stress path, (b) stress-displacement, and (c) void ratio – displacement plot in ring shear test APIRDR52

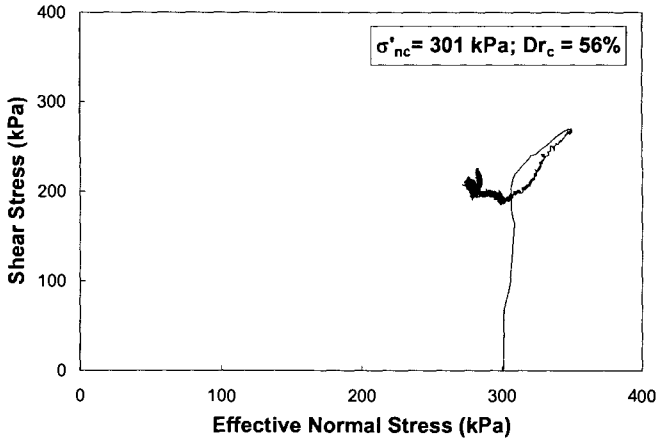

(a)

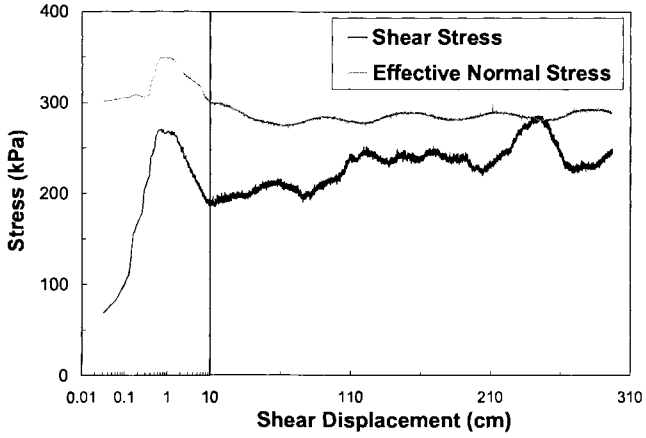

(b)

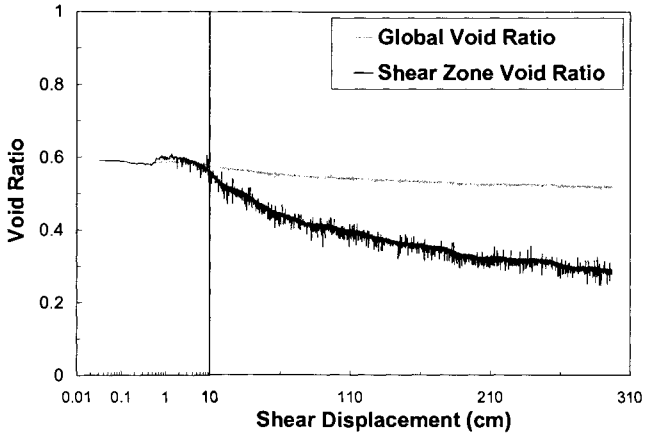

(c)

Figure B.20: (a) stress path, (b) stress-displacement, and (c) void ratio – displacement plot in ring shear test APIRDR42

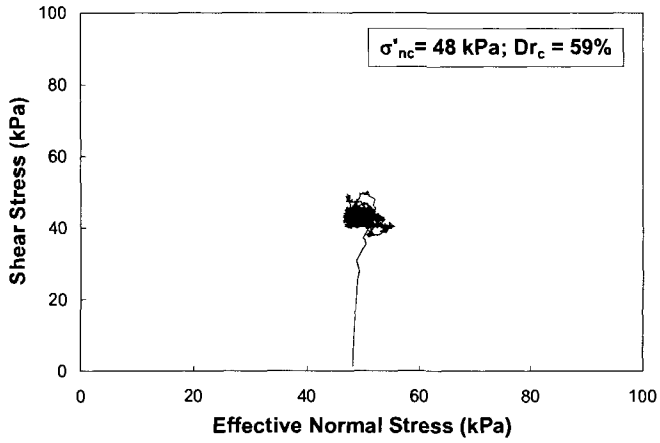

(a)

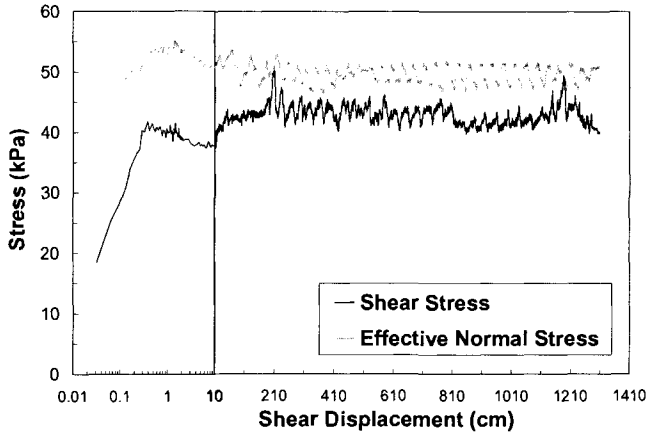

(b)

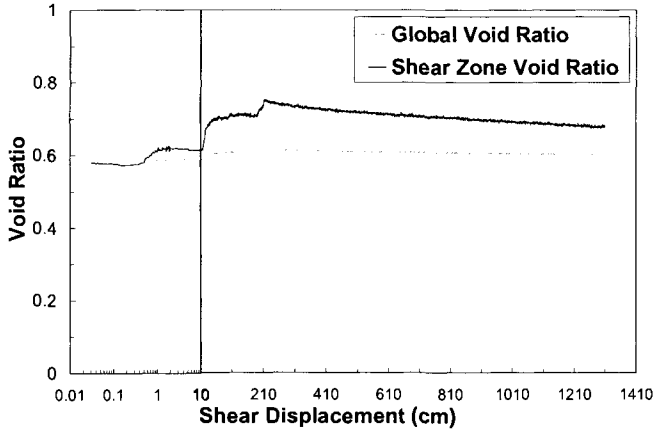

(c)

Figure B.21: (a) stress path, (b) stress-displacement, and (c) void ratio – displacement plot in ring shear test APIRDR5 (large stress fluctuations are due to comparatively larger noise and less resolutions of the force and torque cells at low normal stresses)

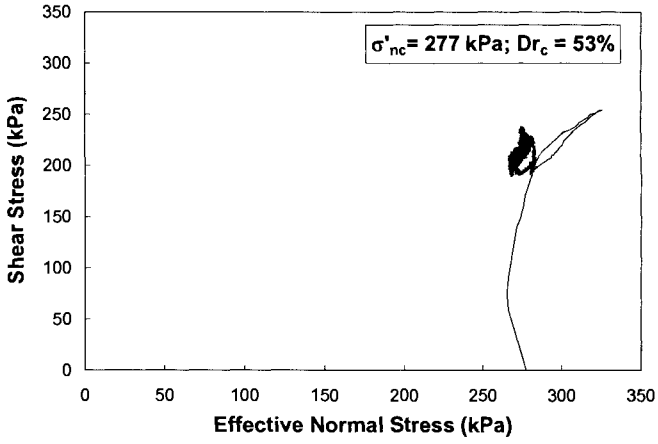

(a)

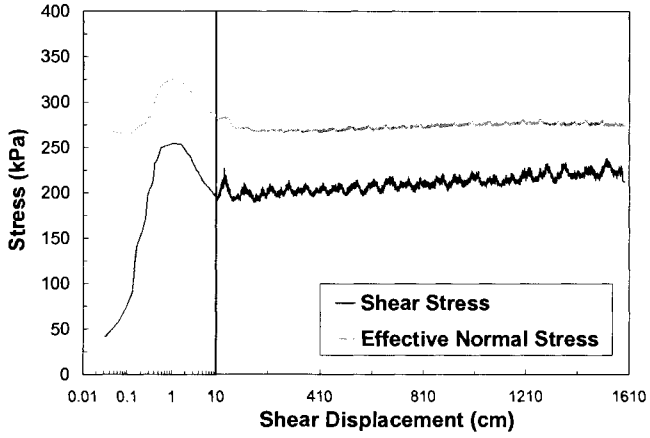

(b)

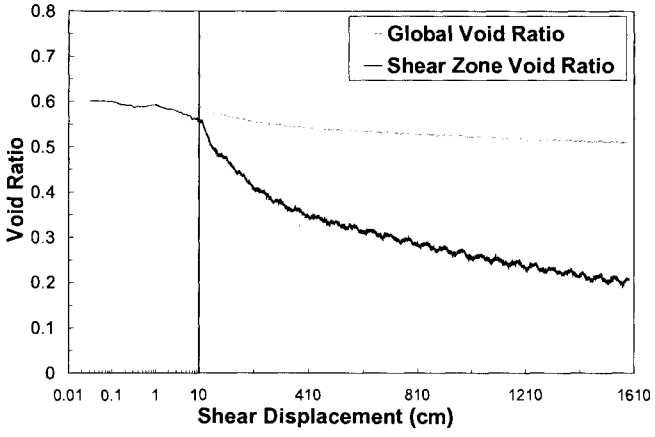

(c)

Figure B.22: (a) stress path, (b) stress-displacement, and (c) void ratio – displacement plot in ring shear test APIRDR38

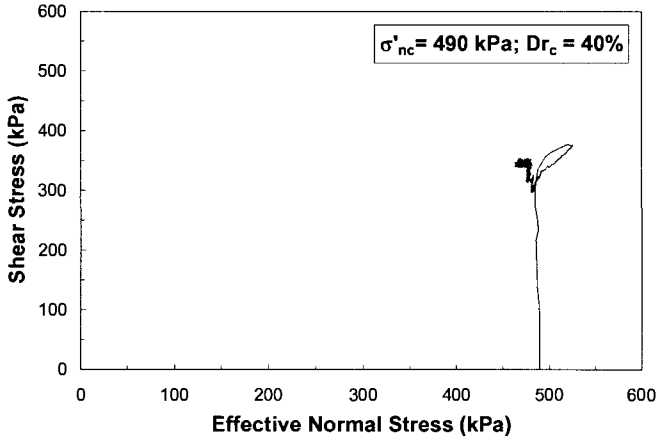

(a)

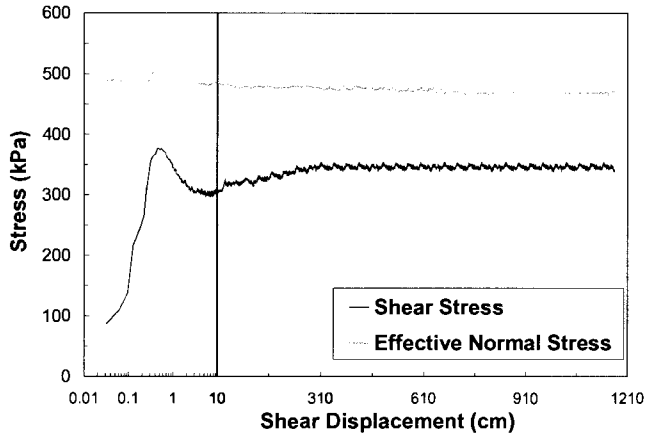

(b)

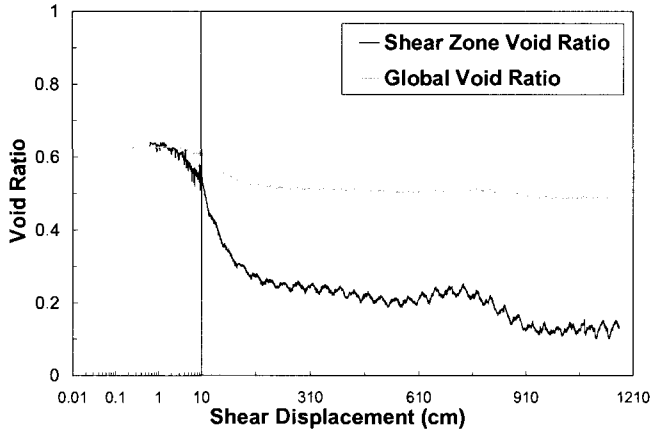

(c)

Figure B.23: (a) stress path, (b) stress-displacement, and (c) void ratio – displacement plot in ring shear test APIRDR72

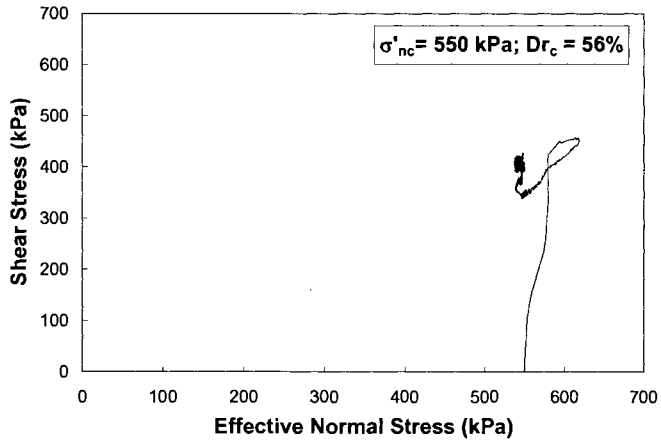

(a)

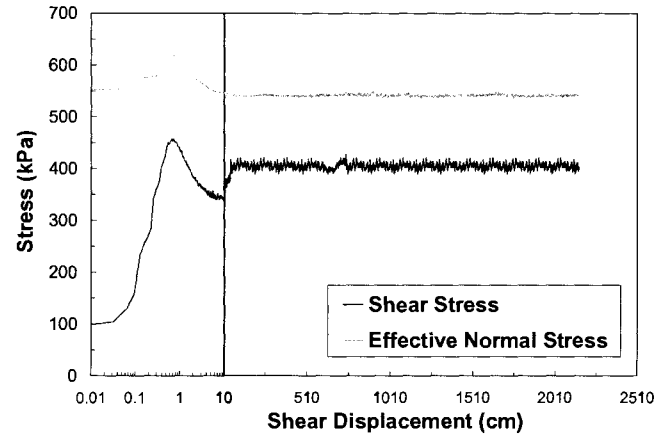

(b)

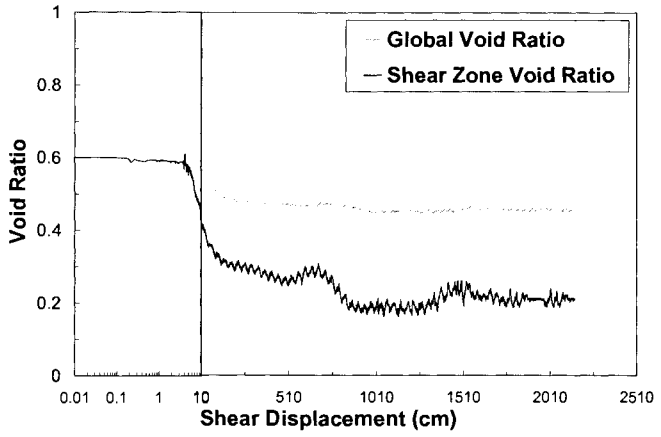

(c)

Figure B.24: (a) stress path, (b) stress-displacement, and (c) void ratio – displacement plot in ring shear test APIRDR85

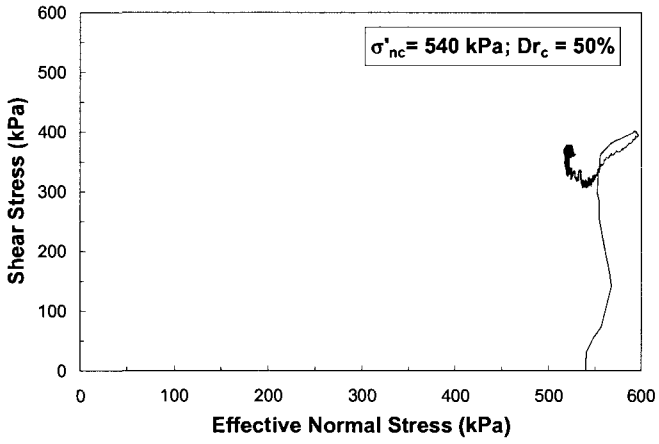

(a)

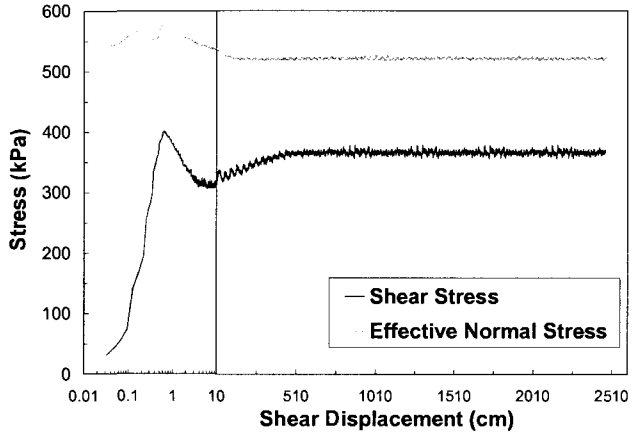

(b)

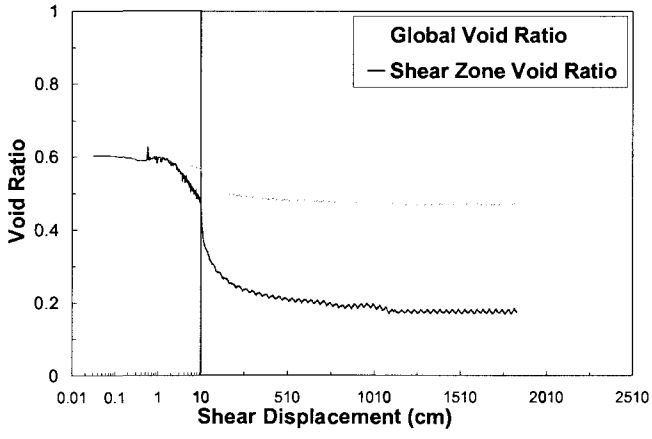

(c)

Figure B.25: (a) stress path, (b) stress-displacement, and (c) void ratio – displacement plot in ring shear test APIRDR76

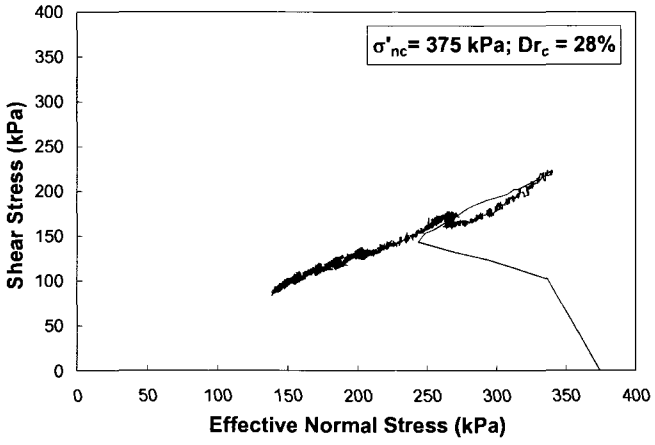

(a)

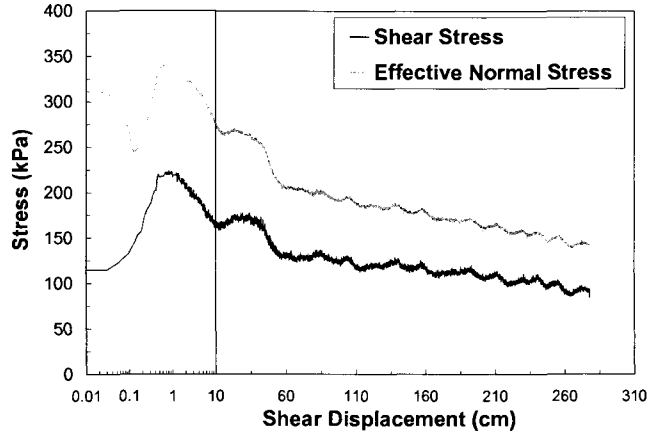

(b)

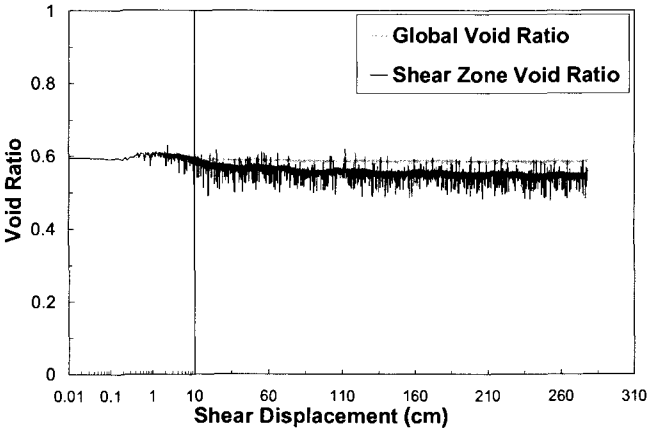

(c)

Figure B.26: (a) stress path, (b) stress-displacement, and (c) void ratio – displacement plot in ring shear test APOTCV52

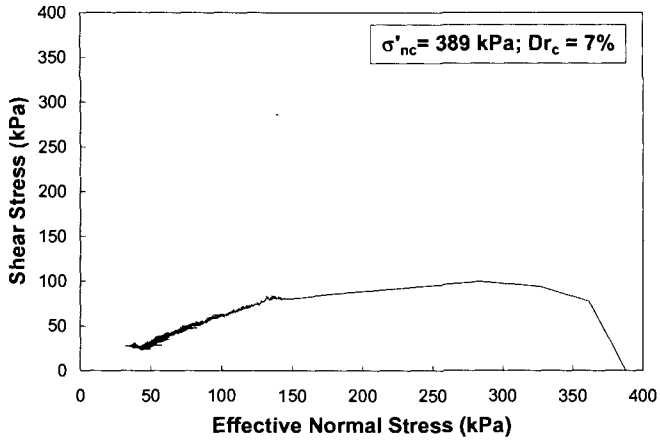

(a)

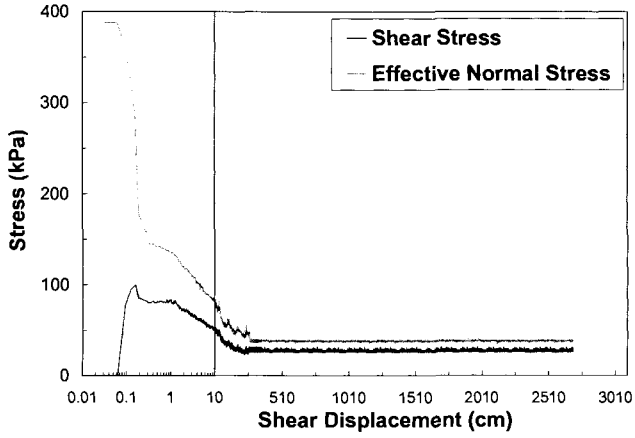

(b)

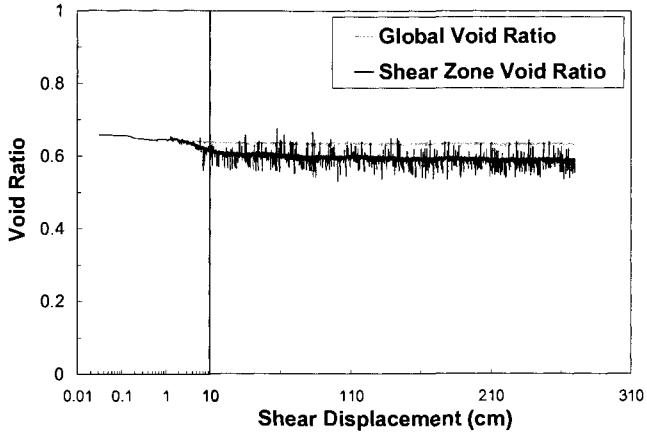

(c)

Figure B.27: (a) stress path, (b) stress-displacement, and (c) void ratio – displacement plot in ring shear test MTOTCV54(1)

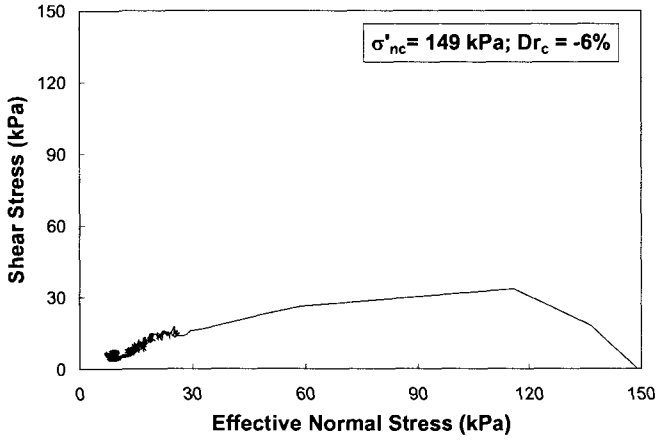

(a)

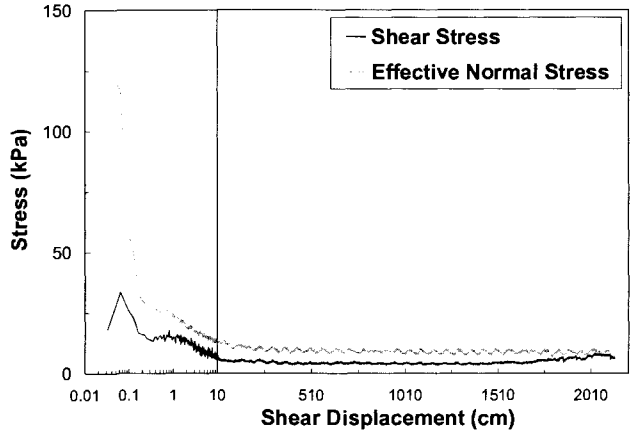

(b)

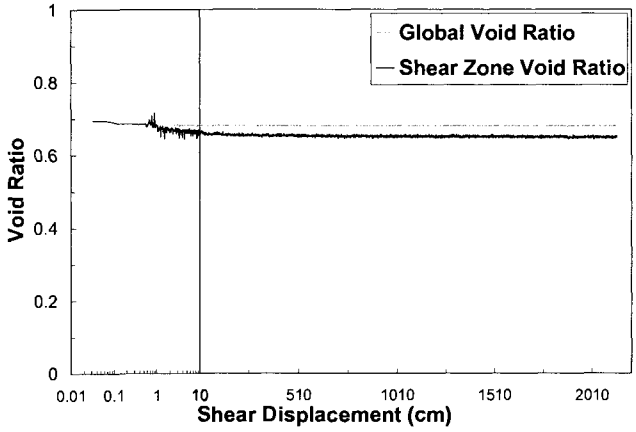

(c)

Figure B.28: (a) stress path, (b) stress-displacement, and (c) void ratio – displacement plot in ring shear test MTOTCV21

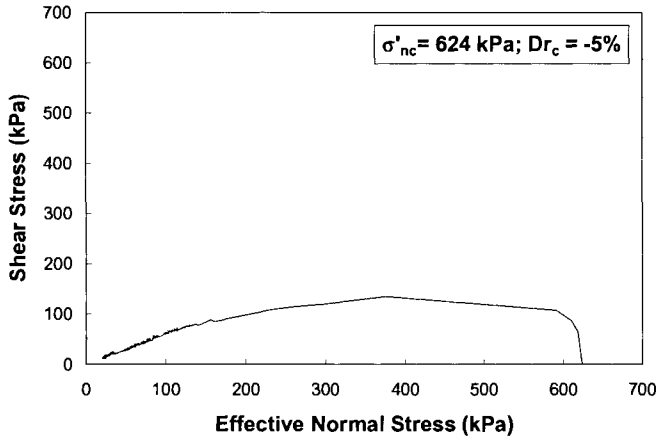

(a)

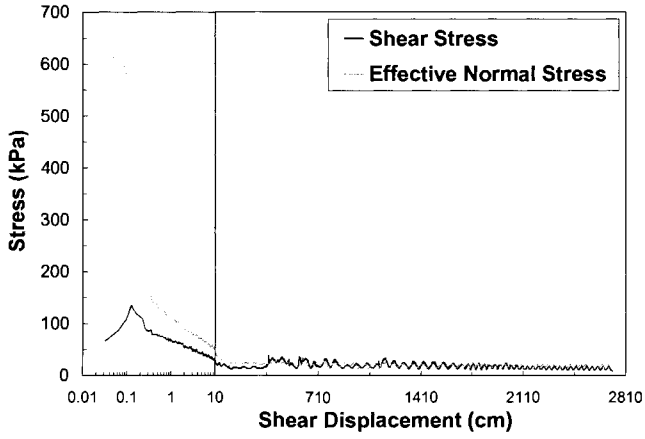

(b)

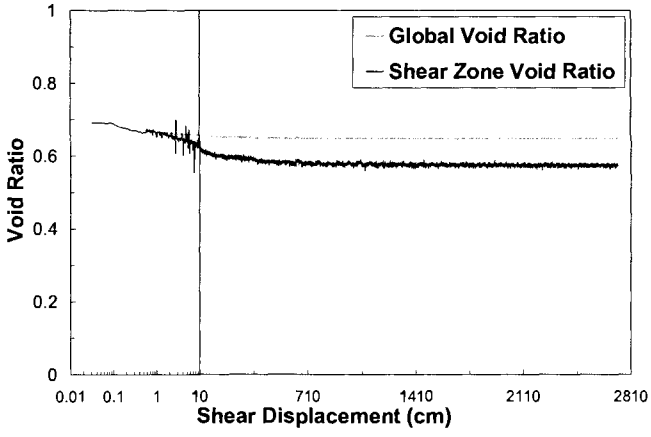

(c)

Figure B.29: (a) stress path, (b) stress-displacement, and (c) void ratio – displacement plot in ring shear test MTOTCV87

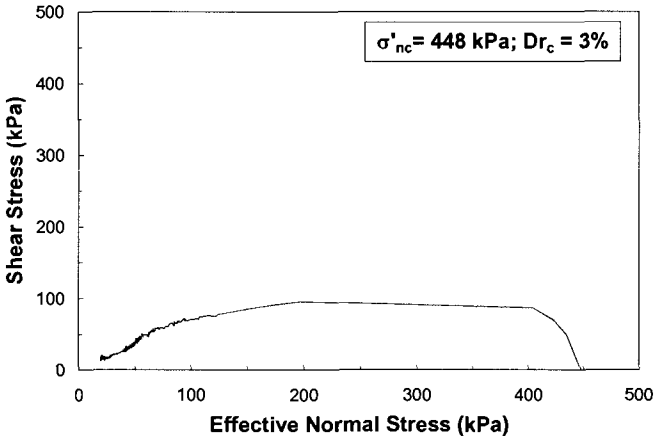

(a)

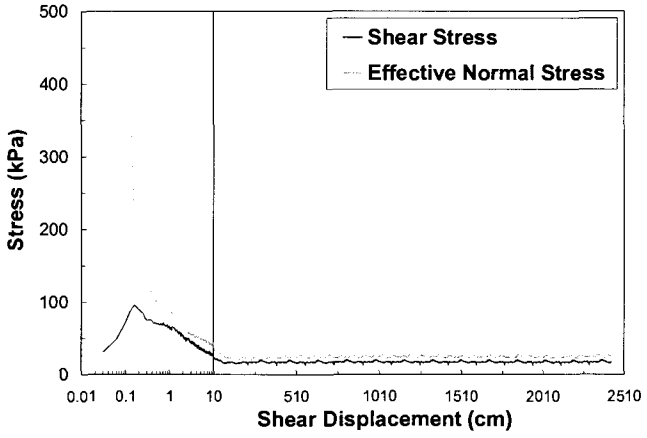

(b)

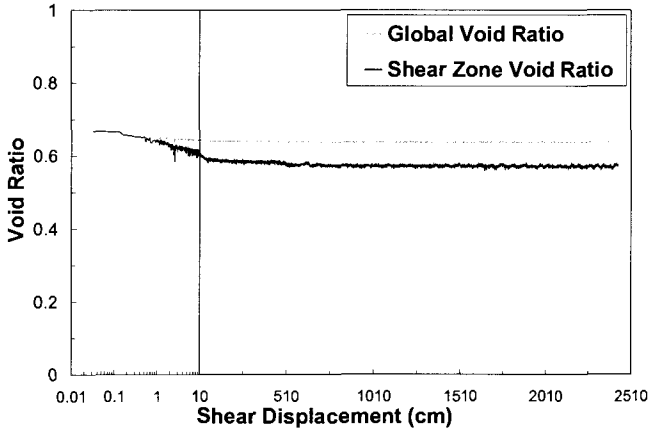

(c)

Figure B.30: (a) stress path, (b) stress-displacement, and (c) void ratio – displacement plot in ring shear test MTOTCV63

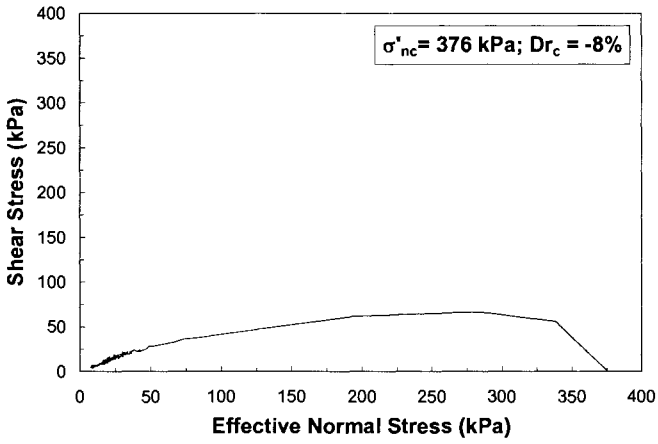

(a)

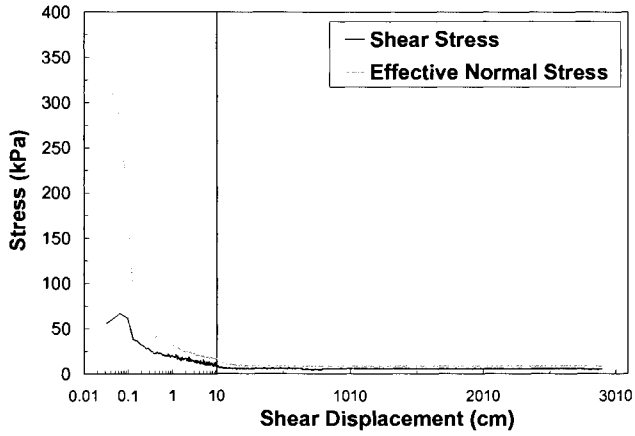

(b)

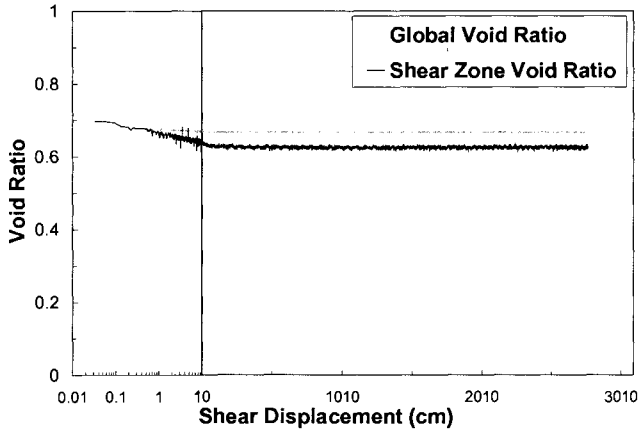

(c)

Figure B.31: (a) stress path, (b) stress-displacement, and (c) void ratio – displacement plot in ring shear test MTOTCV54

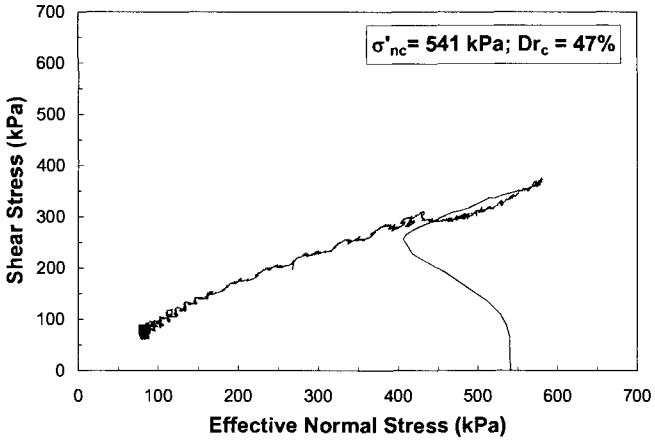

(a)

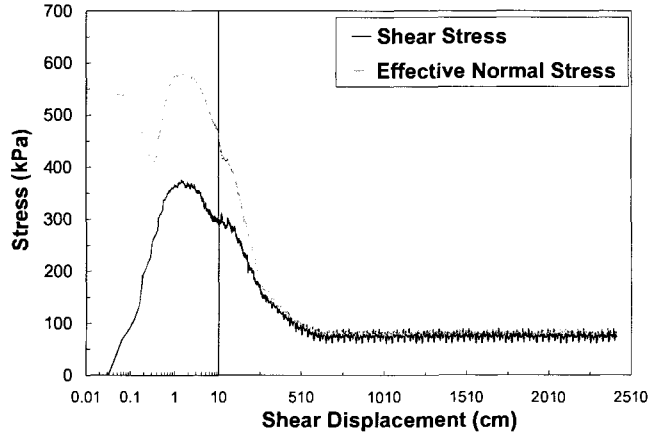

(b)

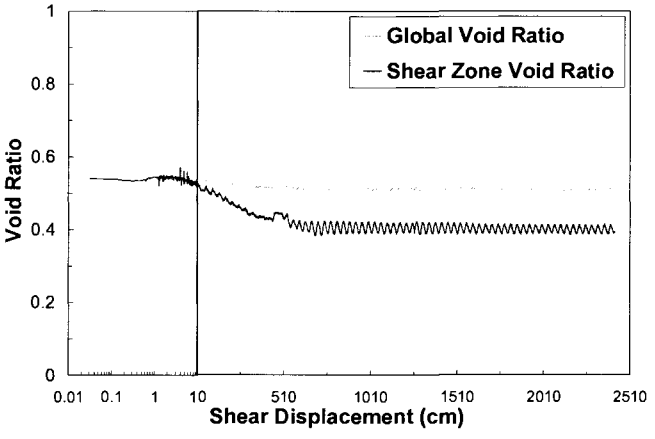

(c)

Figure B.32: (a) stress path, (b) stress-displacement, and (c) void ratio – displacement plot in ring shear test APOTCV83

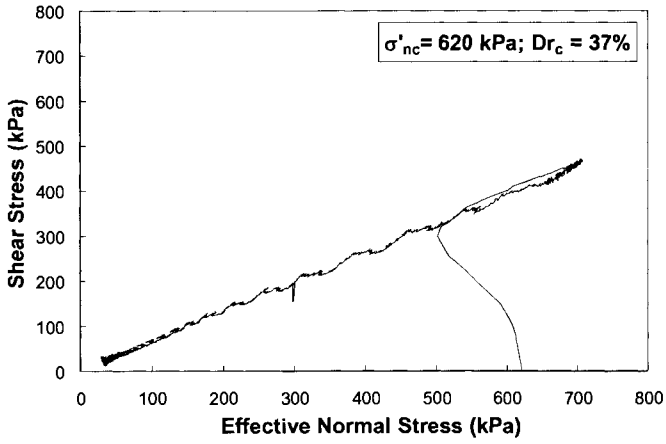

(a)

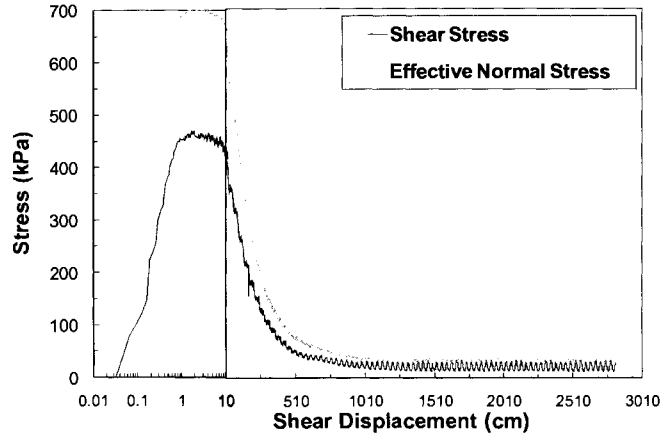

(b)

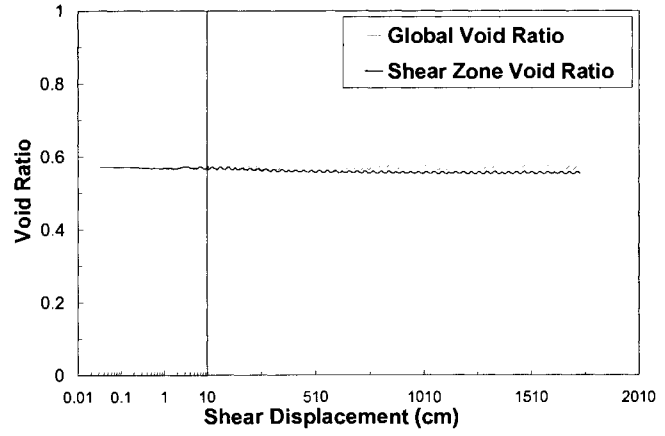

(c)

Figure B.33: (a) stress path, (b) stress-displacement, and (c) void ratio – displacement plot in ring shear test APOTCV85

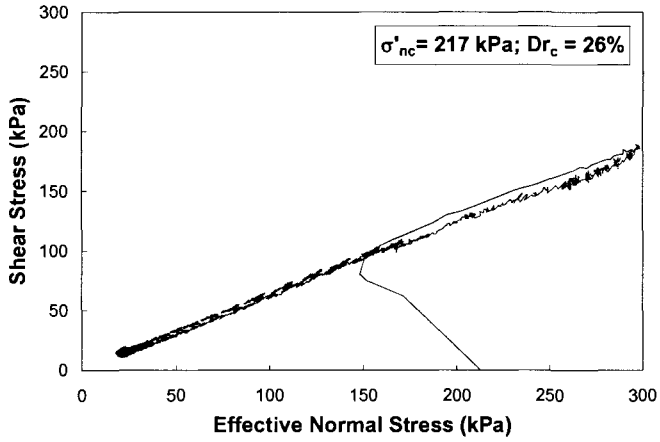

(a)

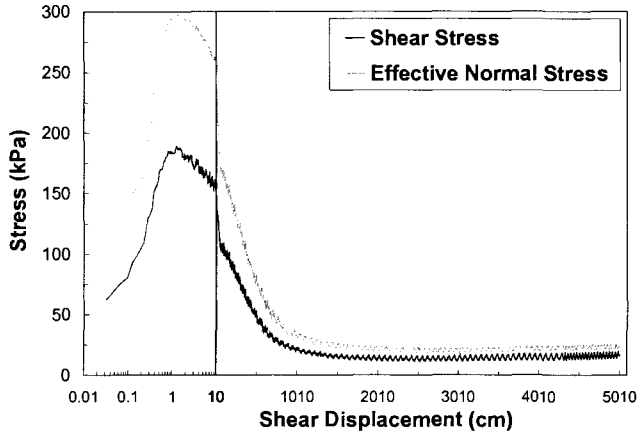

(b)

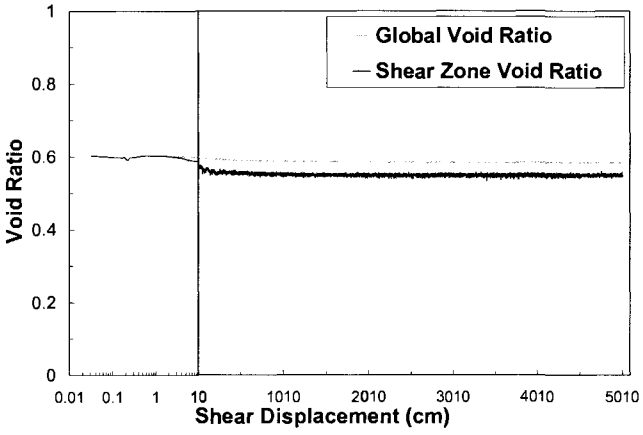

(c)

Figure B.34: (a) stress path, (b) stress-displacement, and (c) void ratio – displacement plot in ring shear test APOTCV28

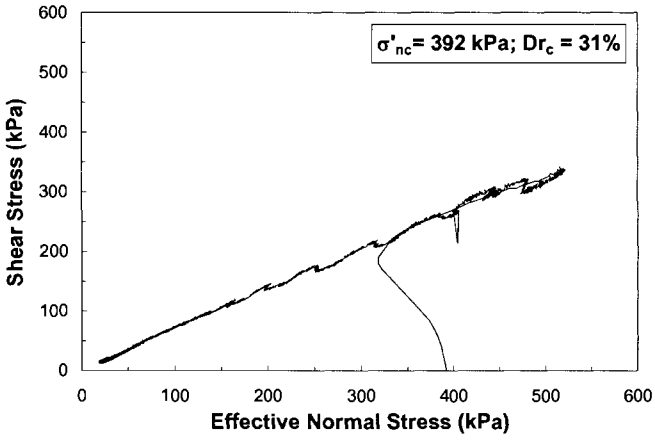

(a)

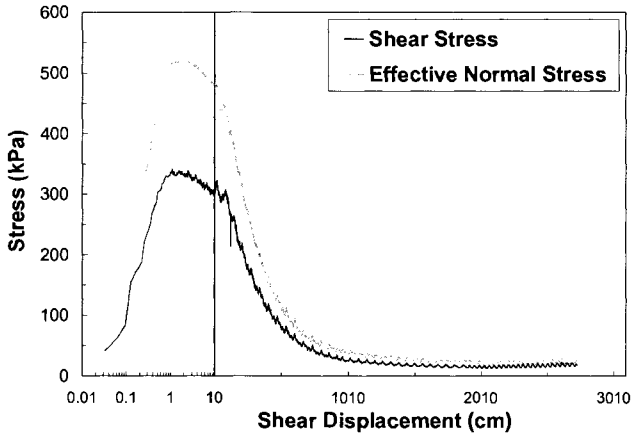

(b)

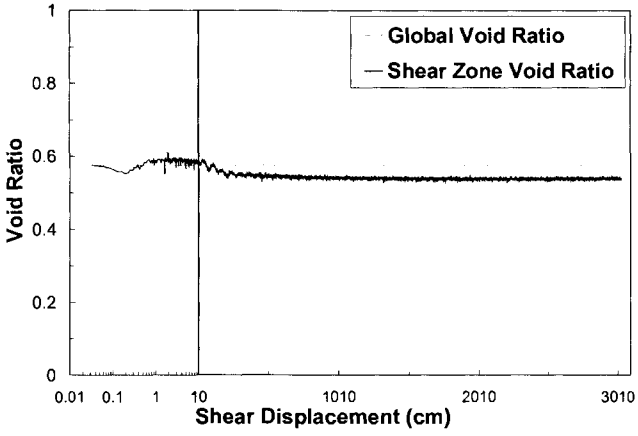

(c)

Figure B.35: (a) stress path, (b) stress-displacement, and (c) void ratio – displacement plot in ring shear test APOTCV54

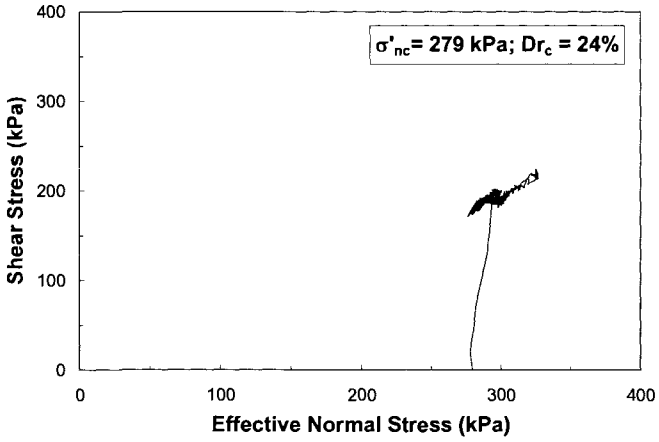

(a)

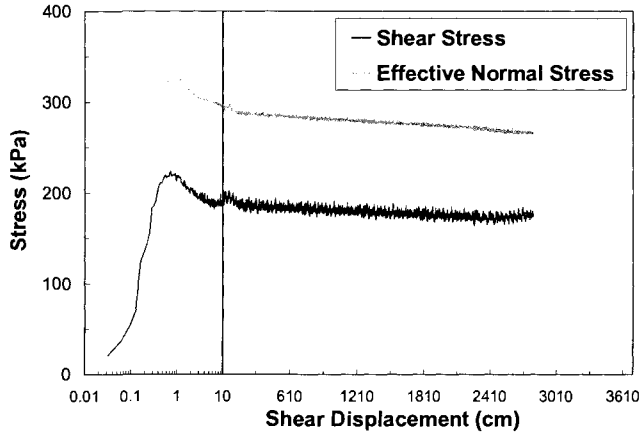

(b)

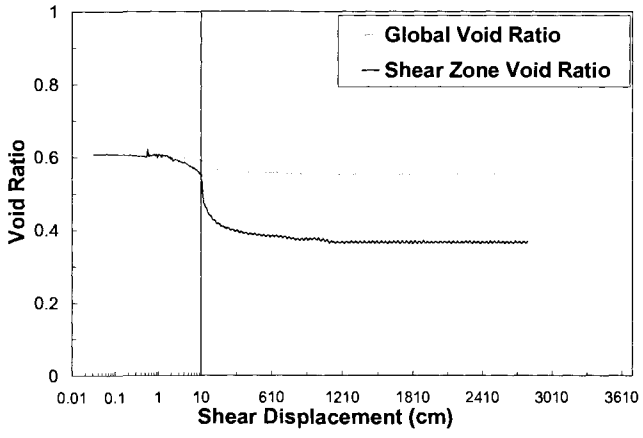

(c)

Figure B.36: (a) stress path, (b) stress-displacement, and (c) void ratio – displacement plot in ring shear test APOTDR40(1)

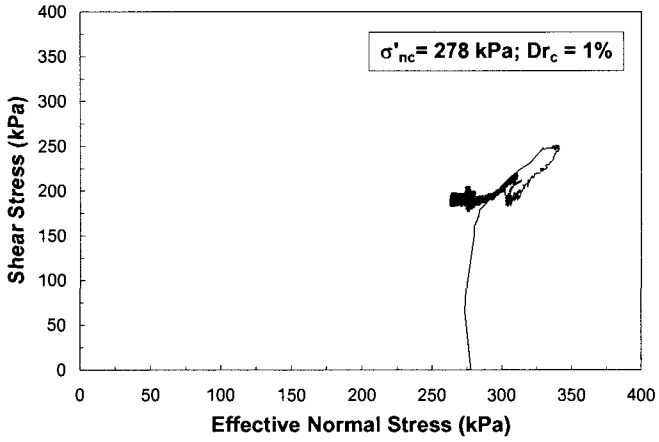

(a)

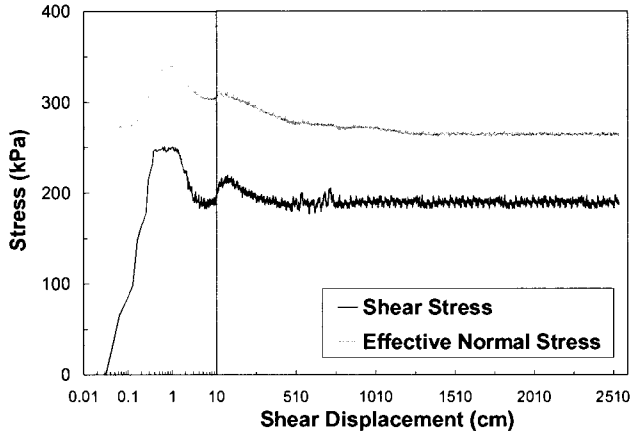

(b)

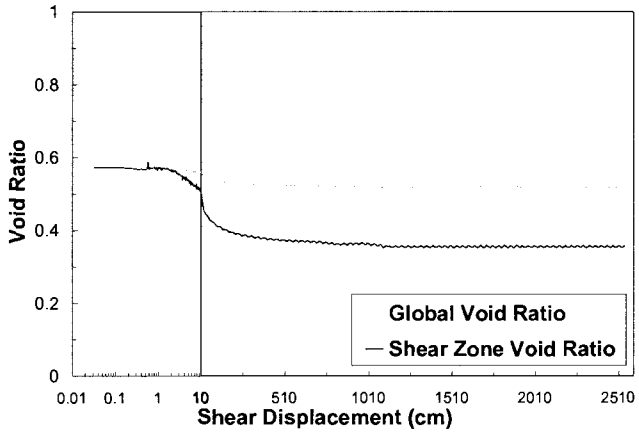

(c)

Figure B.37: (a) stress path, (b) stress-displacement, and (c) void ratio – displacement plot in ring shear test APOTDR40(2)

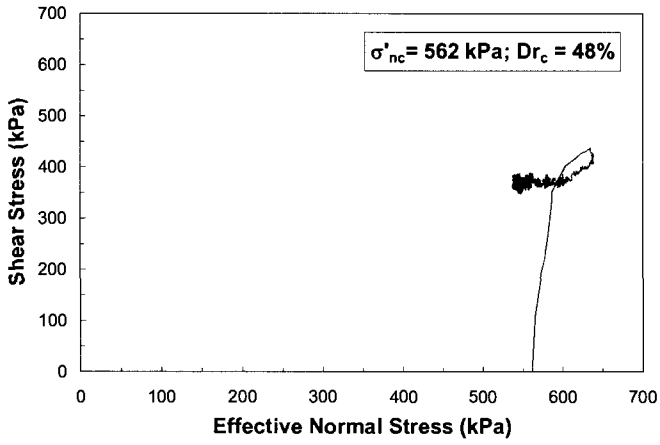

(a)

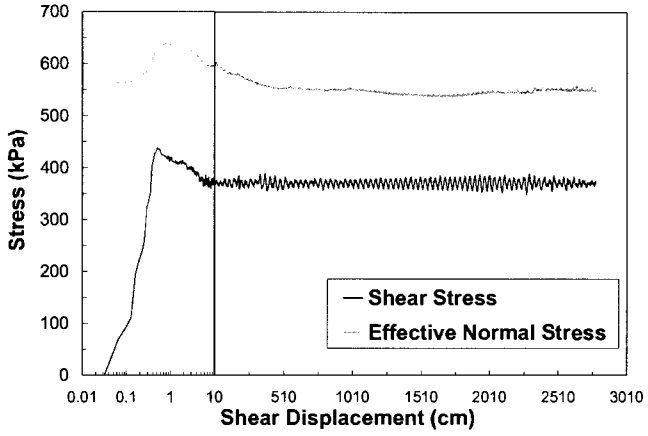

(b)

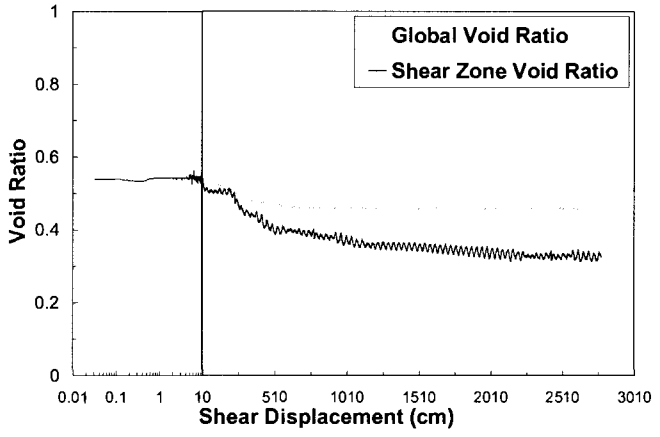

(c)

Figure B.38: (a) stress path, (b) stress-displacement, and (c) void ratio – displacement plot in ring shear test APOTDR78

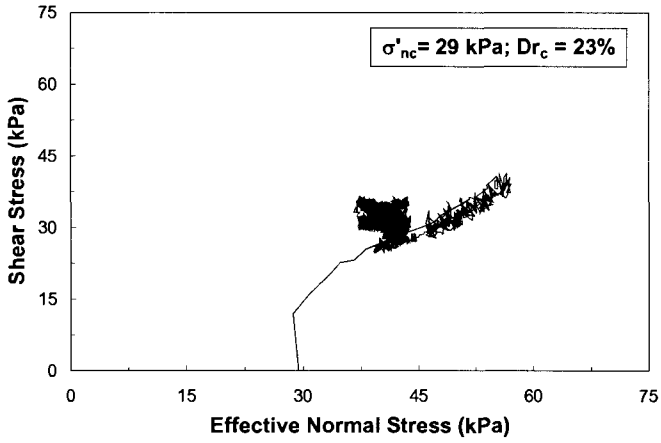

(a)

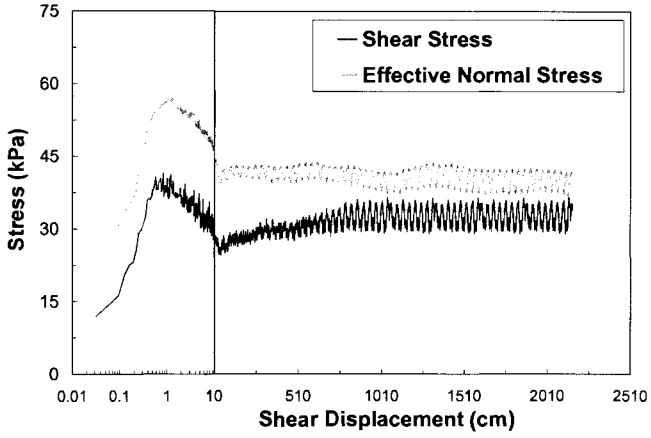

(b)

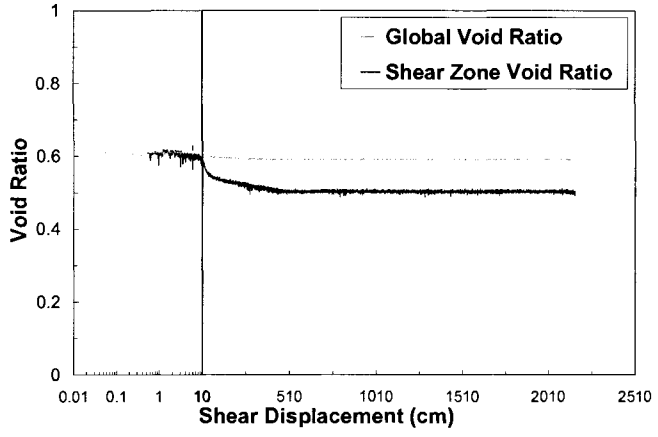

(c)

Figure B.39: (a) stress path, (b) stress-displacement, and (c) void ratio – displacement plot in ring shear test APOTDR5 (large stress fluctuations are due to comparatively larger noise and less resolutions of the force and torque cells at low normal stresses)

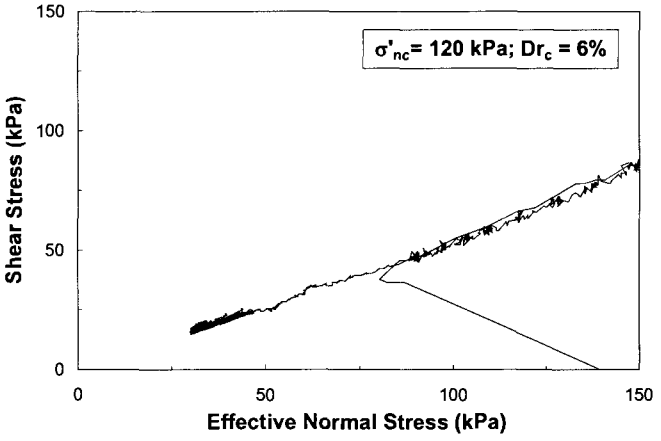

(a)

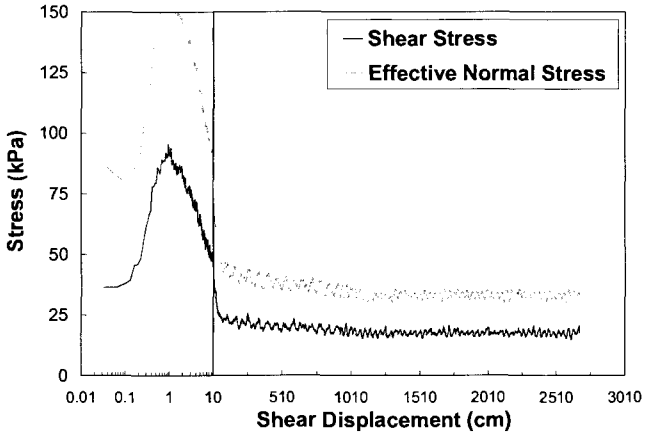

(b)

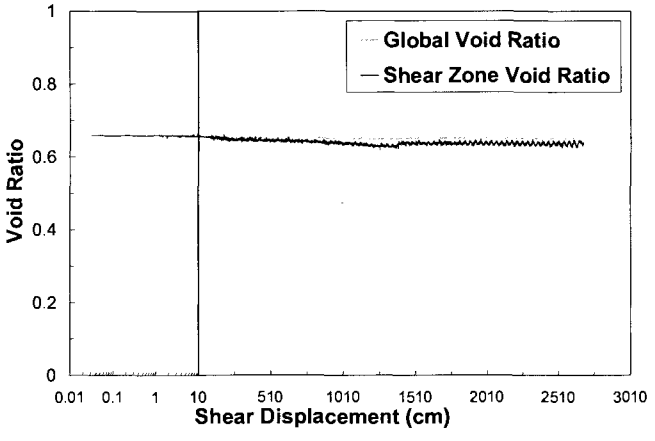

(c)

Figure B.40: (a) stress path, (b) stress-displacement, and (c) void ratio – displacement plot in ring shear test APOTCV17

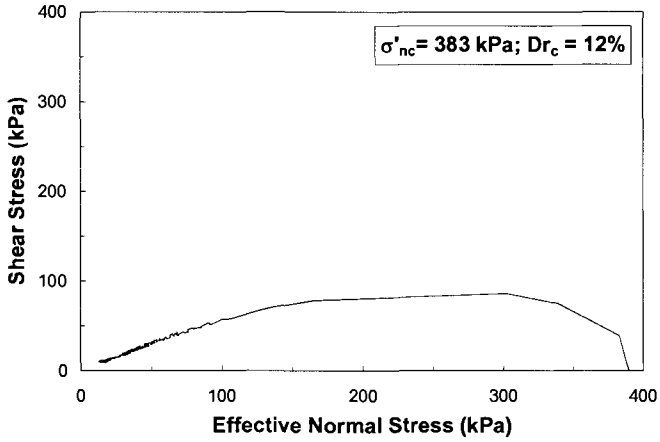

(a)

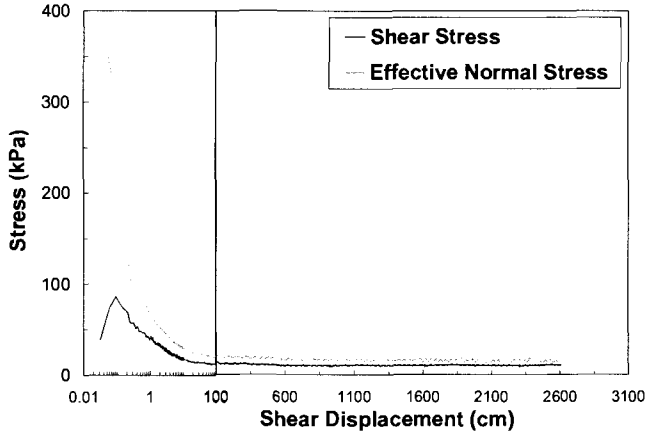

(b)

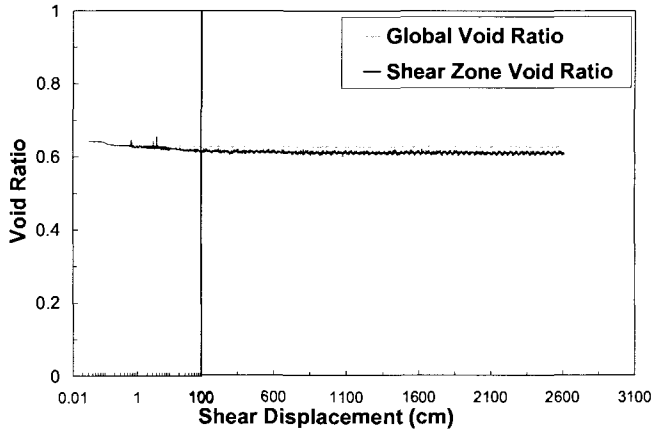

(c)

Figure B.41: (a) stress path, (b) stress-displacement, and (c) void ratio – displacement plot in ring shear test MTOTCV52

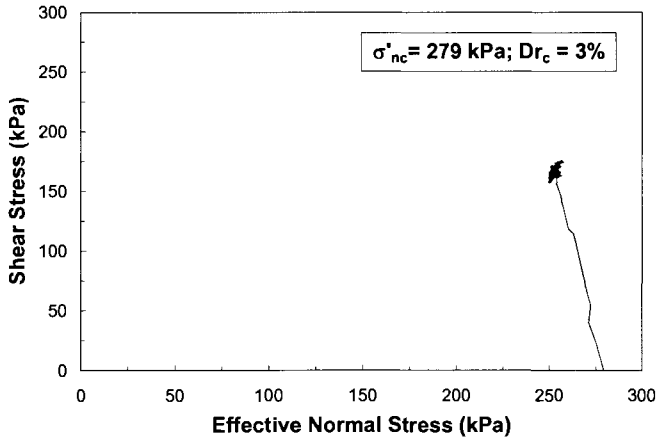

(a)

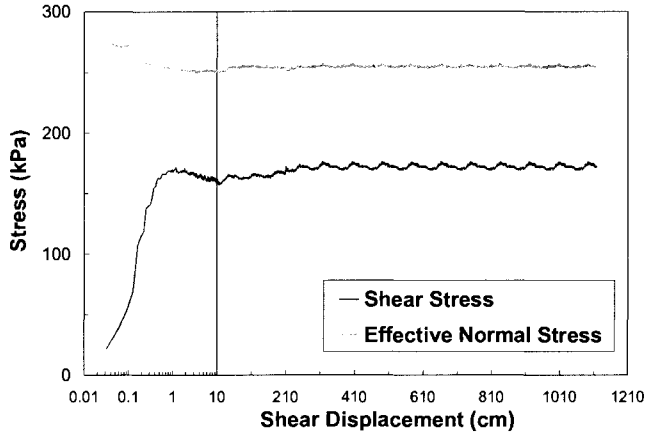

(b)

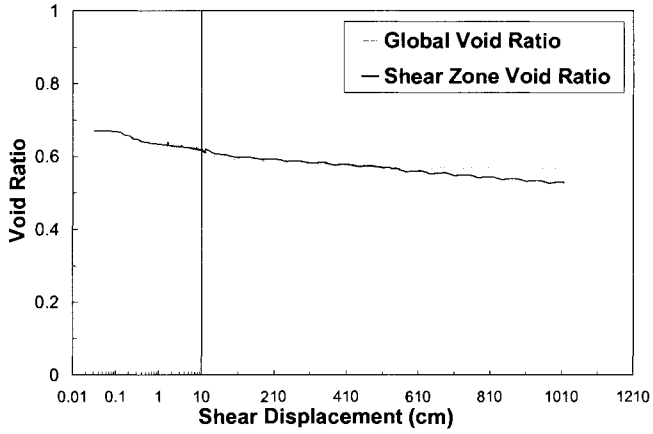

(c)

Figure B.42: (a) stress path, (b) stress-displacement, and (c) void ratio – displacement plot in ring shear test MTOTDR40

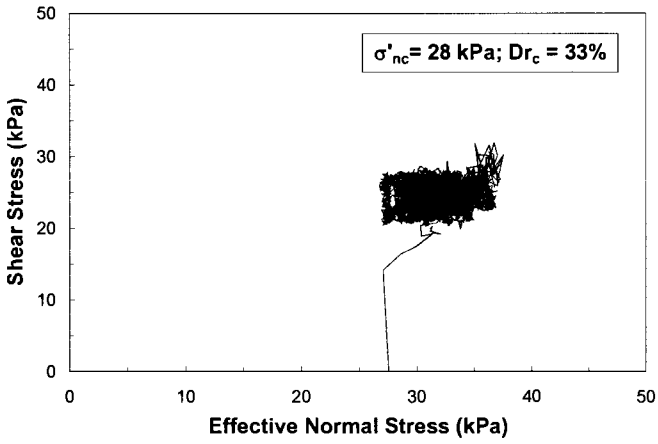

(a)

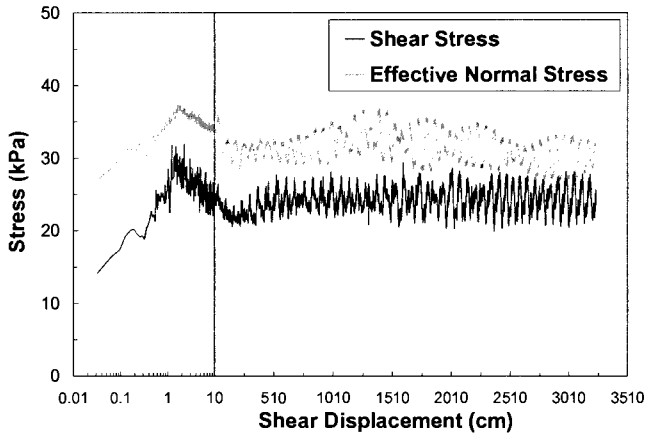

(b)

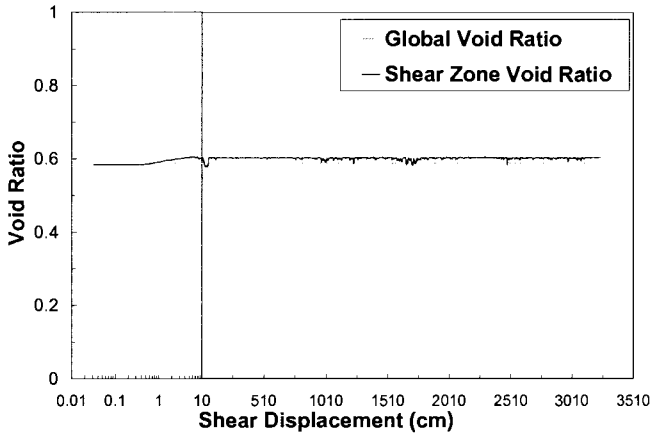

(c)

Figure B.43: (a) stress path, (b) stress-displacement, and (c) void ratio – displacement plot in ring shear test MTOTDR4 (large stress fluctuations are due to comparatively larger noise and less resolutions of the force and torque cells at low normal stresses)

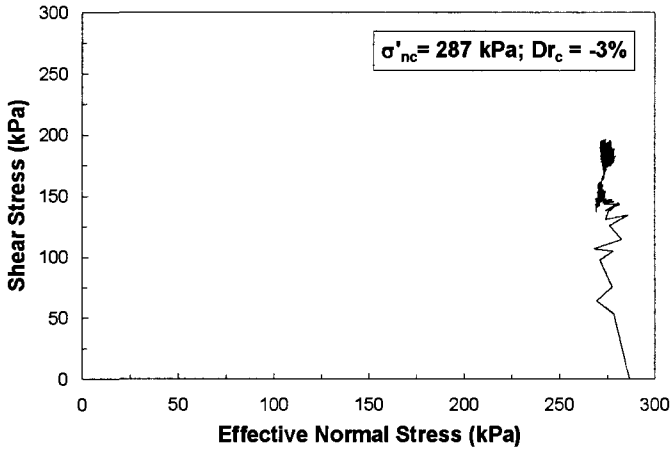

(a)

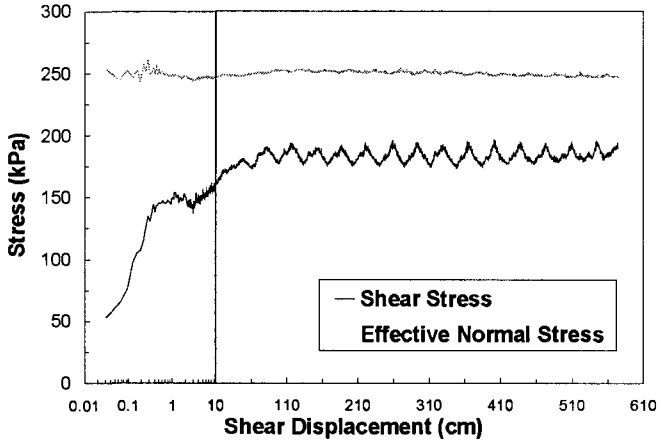

(b)

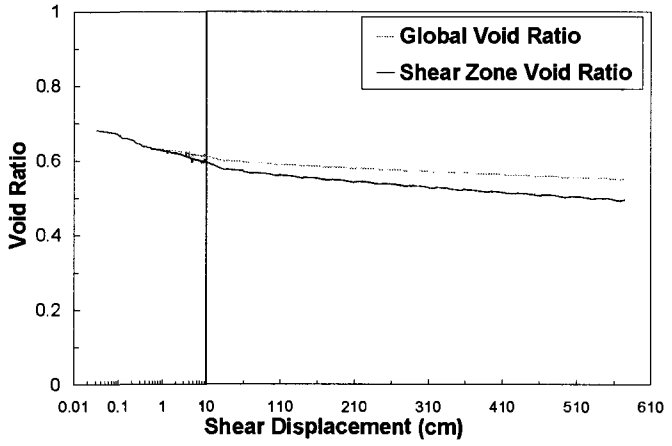

(c)

Figure B.44: (a) stress path, (b) stress-displacement, and (c) void ratio – displacement plot in ring shear test MTOTDR38(1)

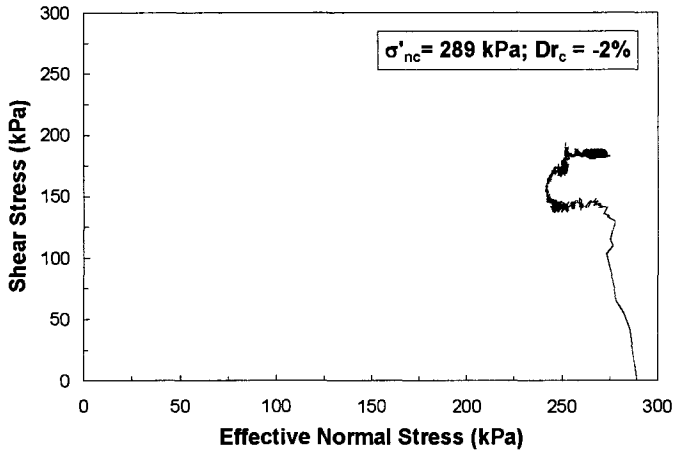

(a)

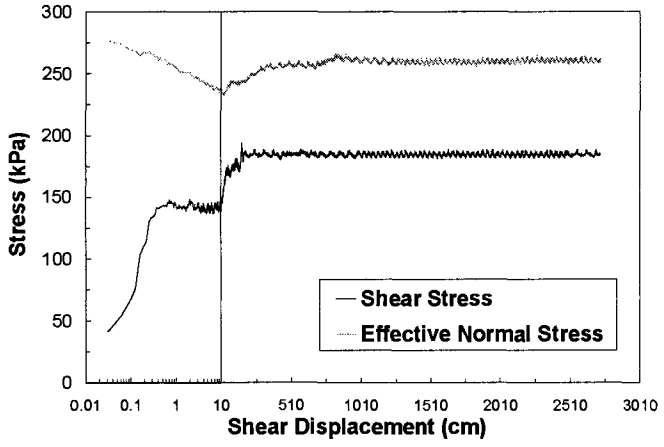

(b)

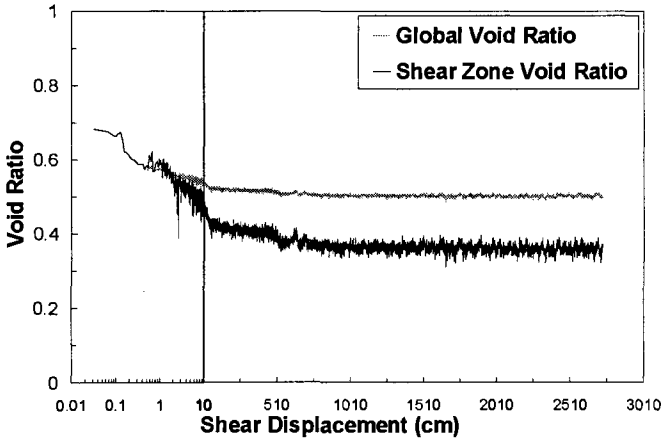

(c)

Figure B.45: (a) stress path, (b) stress-displacement, and (c) void ratio – displacement plot in ring shear test MTOTDR38(2)

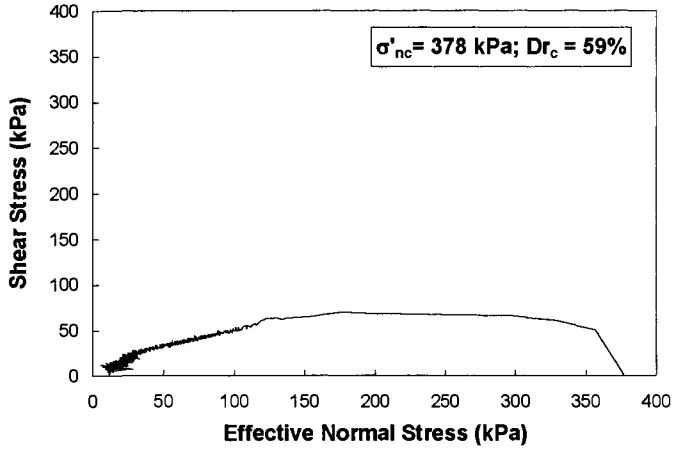

(a)

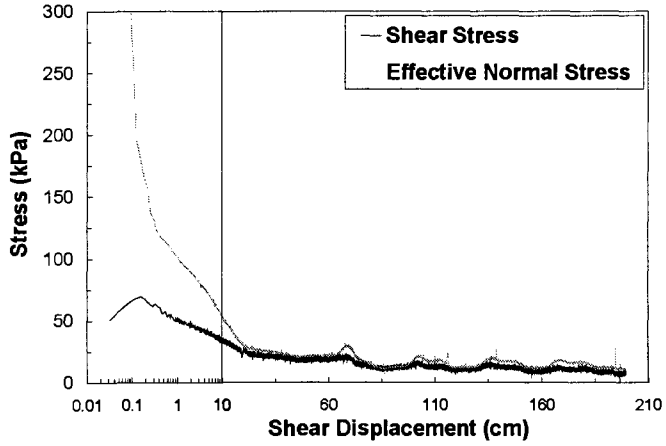

(b)

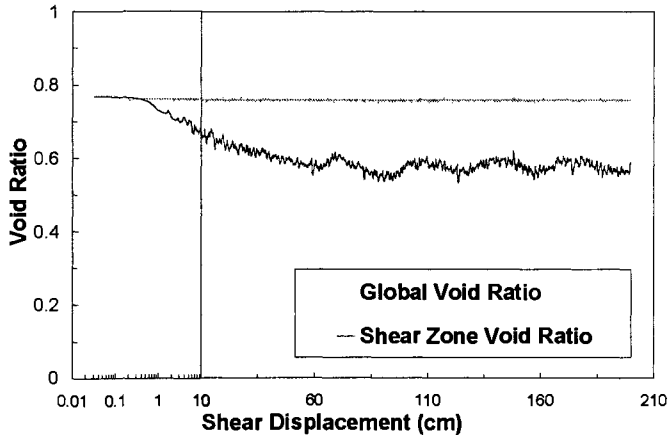

(c)

Figure B.46: (a) stress path, (b) stress-displacement, and (c) void ratio – displacement plot in ring shear test APMRCV57

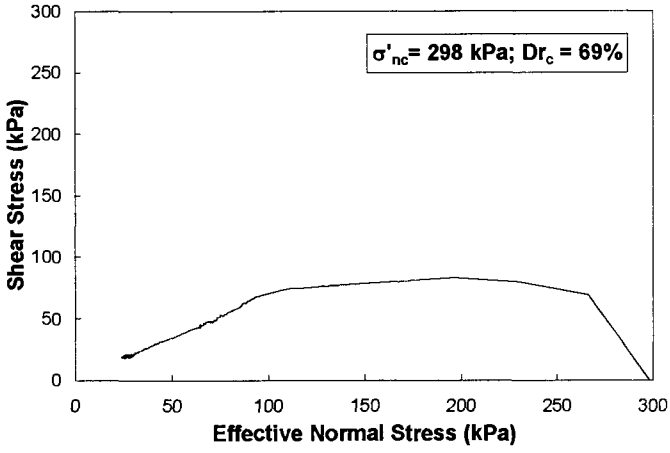

(a)

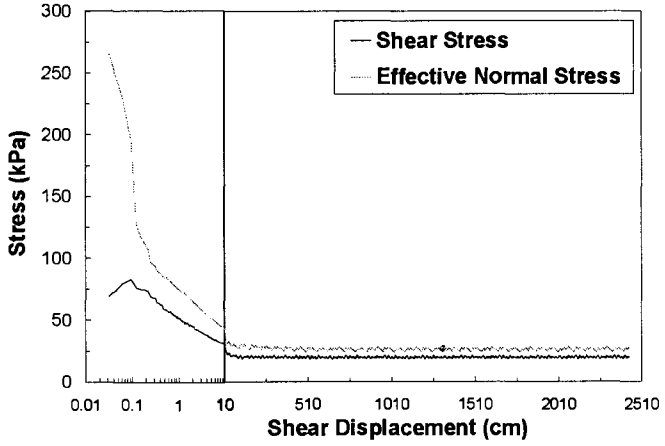

(b)

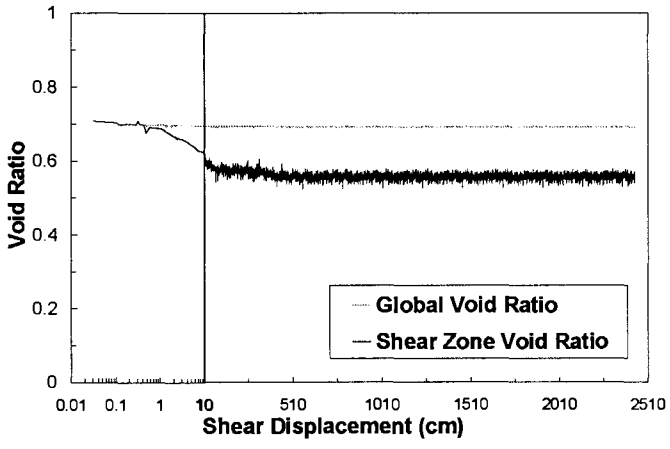

(c)

Figure B.47: (a) stress path, (b) stress-displacement, and (c) void ratio – displacement plot in ring shear test APMRCV43

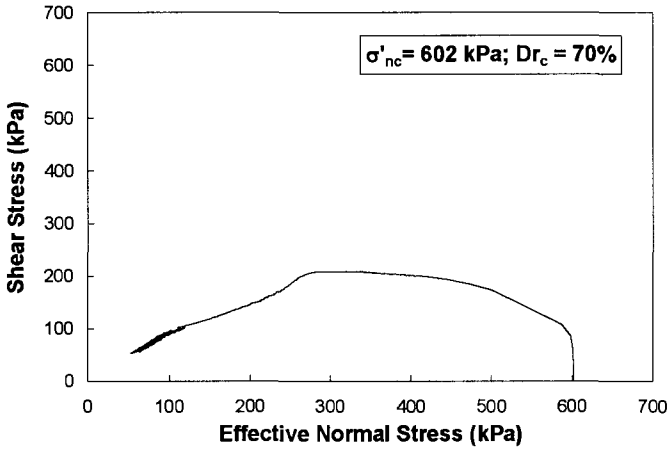

(a)

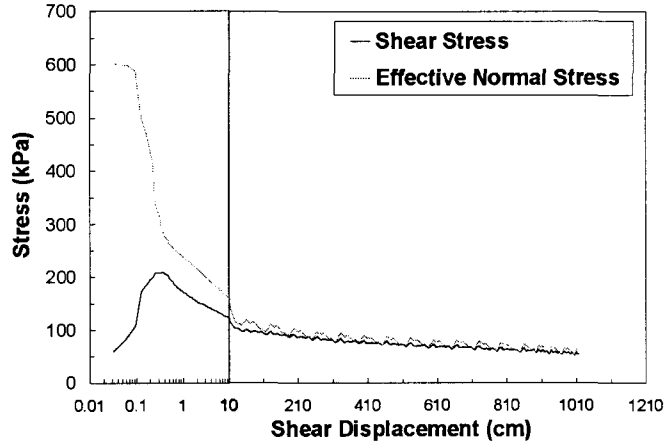

(b)

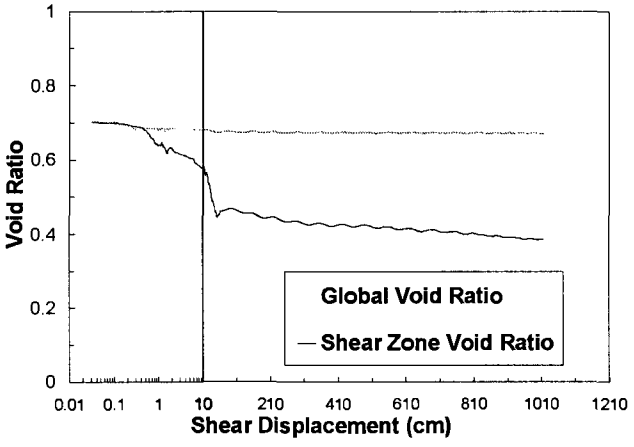

(c)

Figure B.48: (a) stress path, (b) stress-displacement, and (c) void ratio – displacement plot in ring shear test APMRCV87

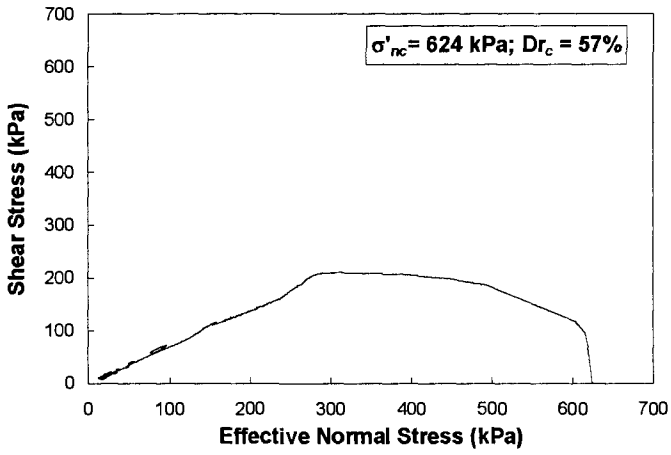

(a)

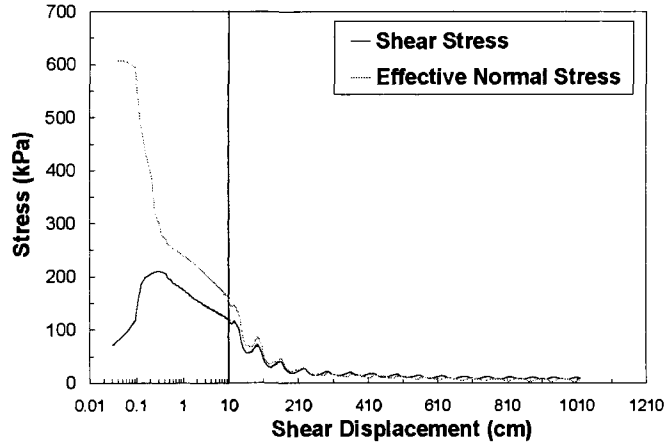

(b)

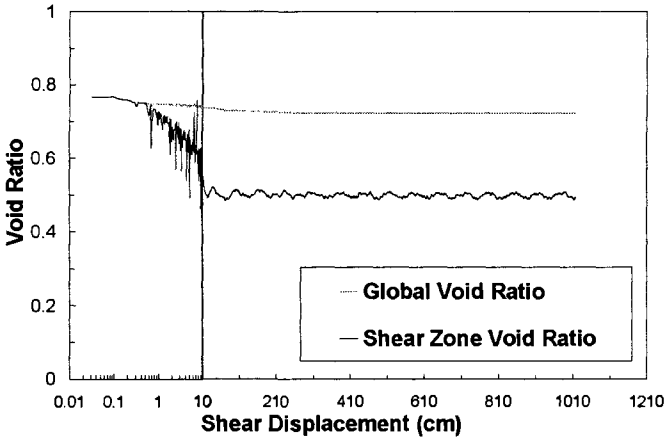

(c)

Figure B.49: (a) stress path, (b) stress-displacement, and (c) void ratio – displacement plot in ring shear test APMRCV89

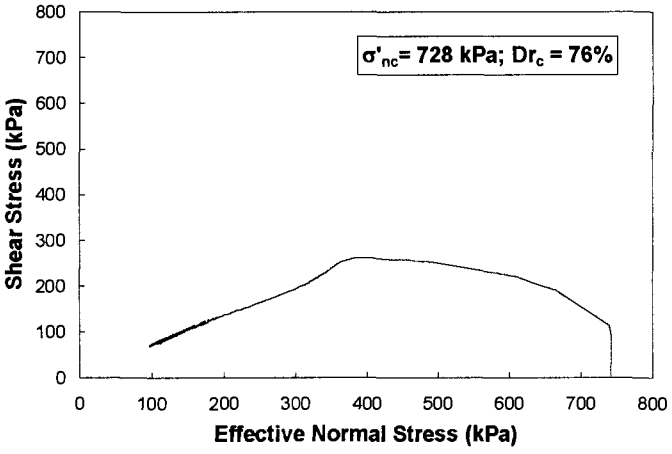

(a)

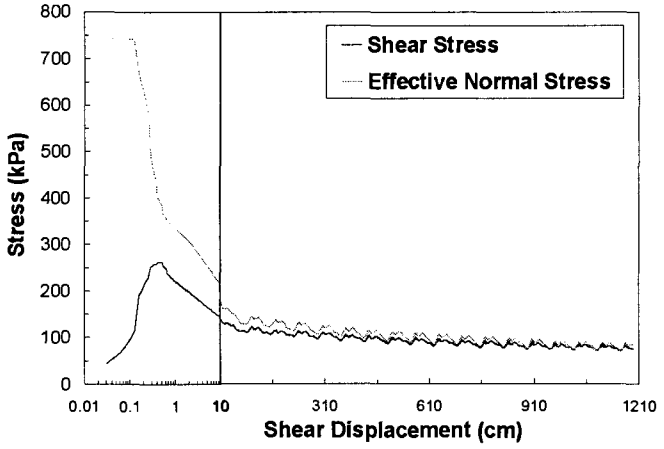

(b)

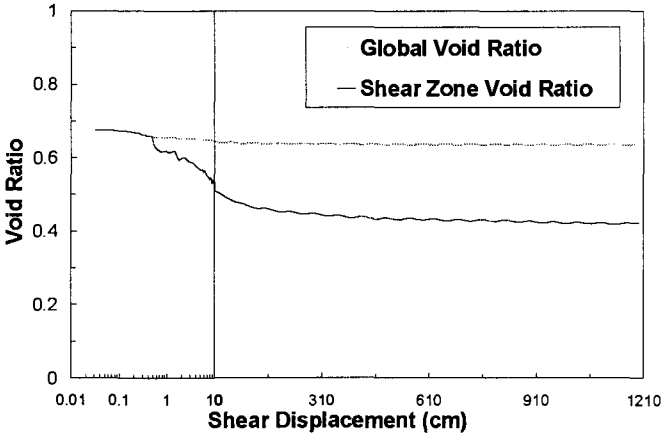

(c)

Figure B.50: (a) stress path, (b) stress-displacement, and (c) void ratio – displacement plot in ring shear test APMRCV103

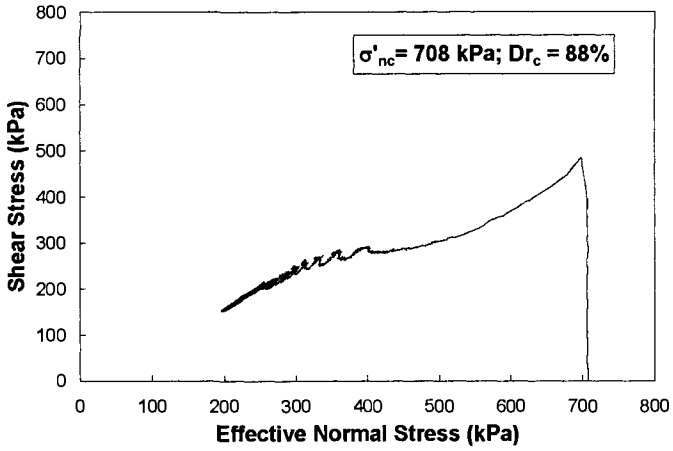

(a)

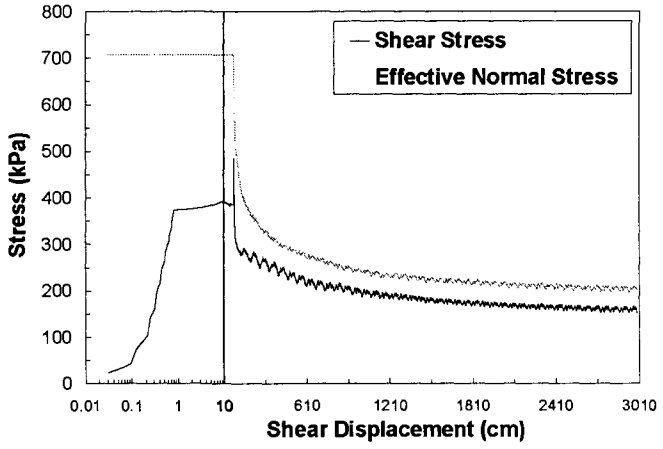

(b)

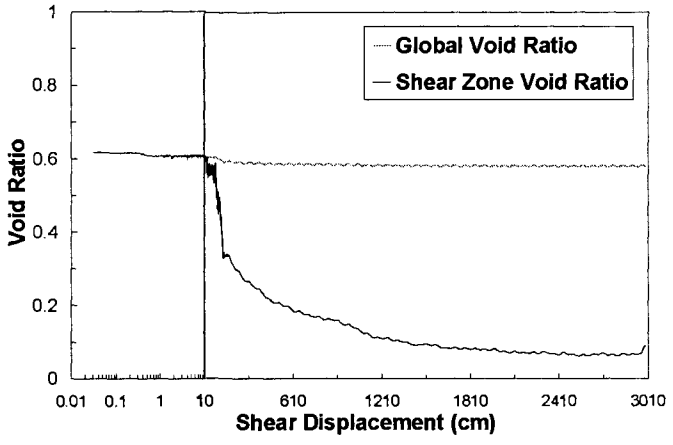

(c)

Figure B.51: (a) stress path, (b) stress-displacement, and (c) void ratio – displacement plot in ring shear test APMRCV97

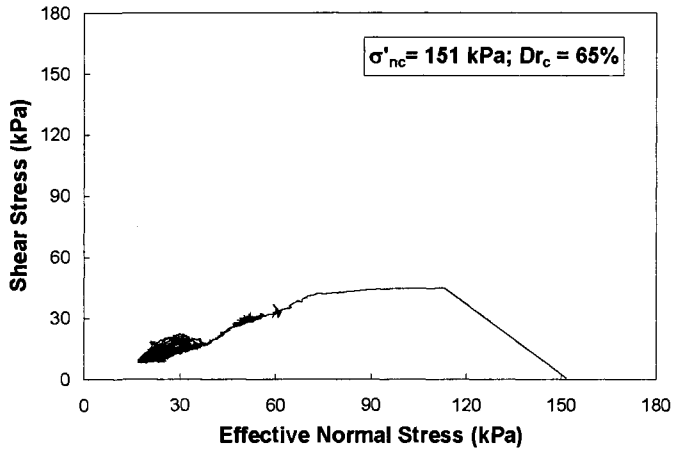

(a)

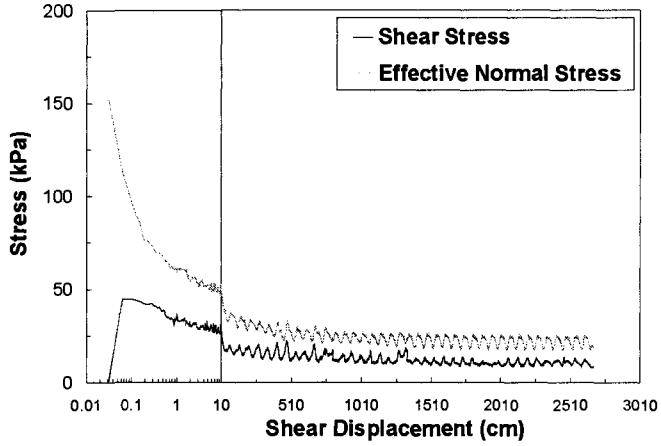

(b)

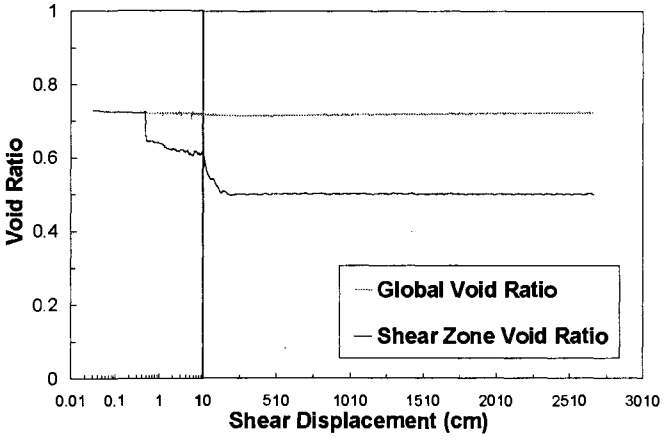

(c)

Figure B.52: (a) stress path, (b) stress-displacement, and (c) void ratio – displacement plot in ring shear test APMRCV22

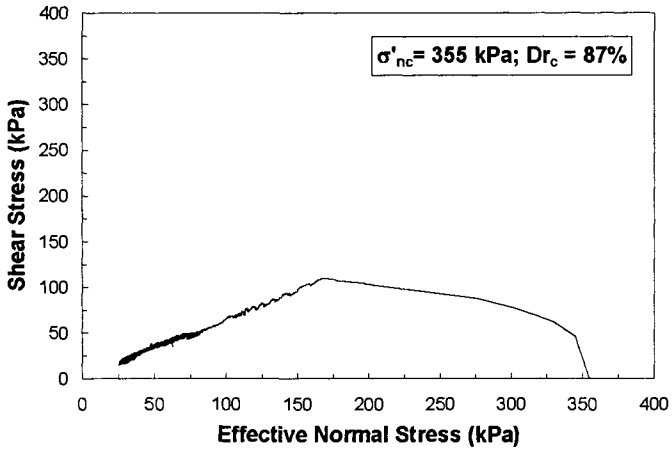

(a)

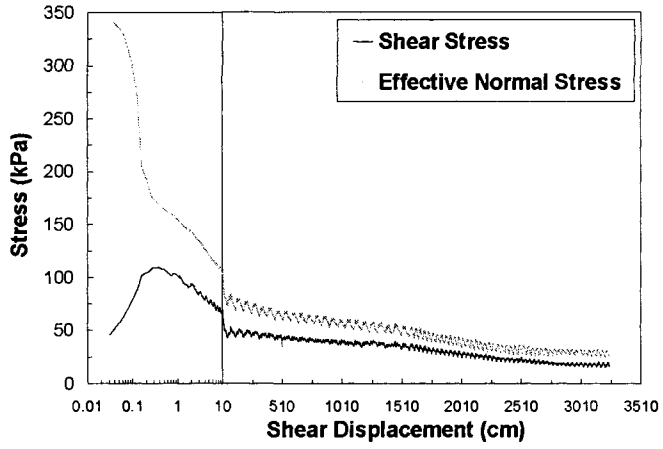

(b)

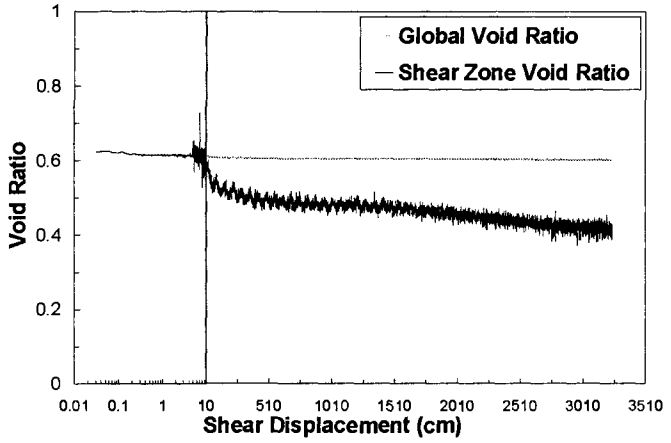

(c)

Figure B.53: (a) stress path, (b) stress-displacement, and (c) void ratio – displacement plot in ring shear test APMRCV48

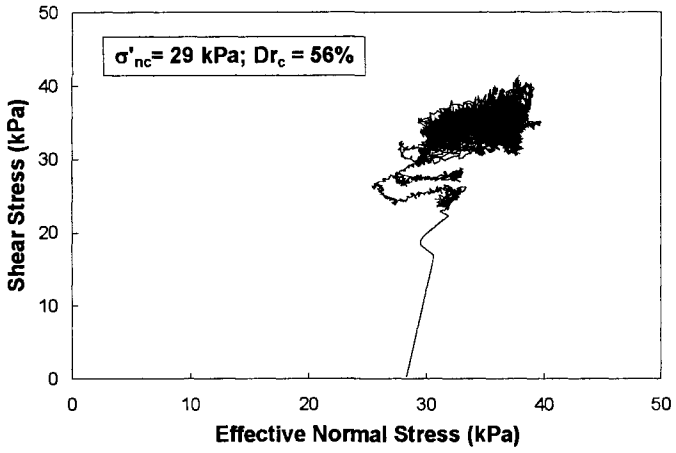

(a)

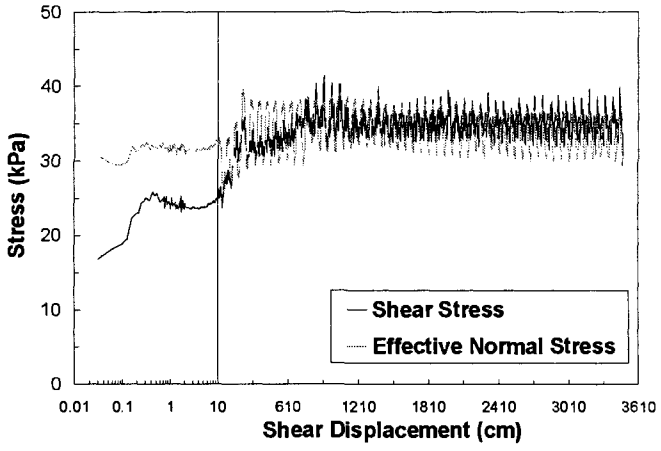

(b)

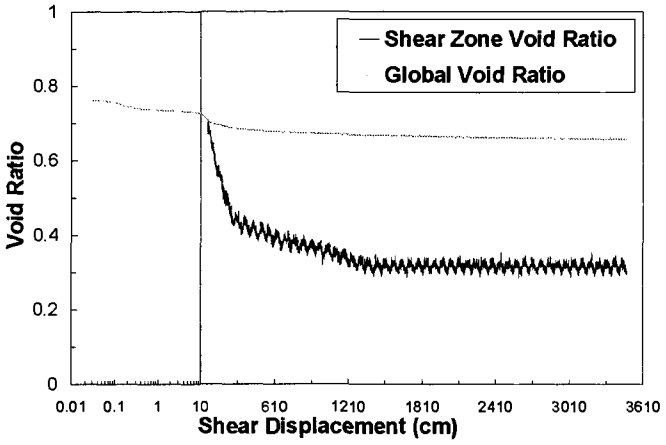

(c)

Figure B.54: (a) stress path, (b) stress-displacement, and (c) void ratio – displacement plot in ring shear test APMRDR4 (large stress fluctuations are due to comparatively larger noise and less resolutions of the force and torque cells at low normal stresses)

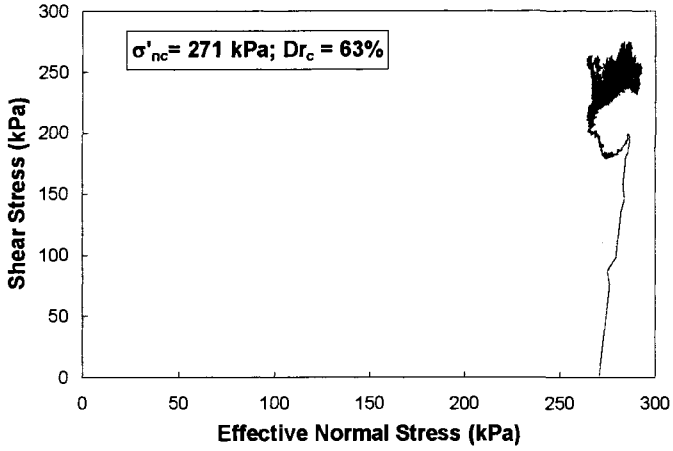

(a)

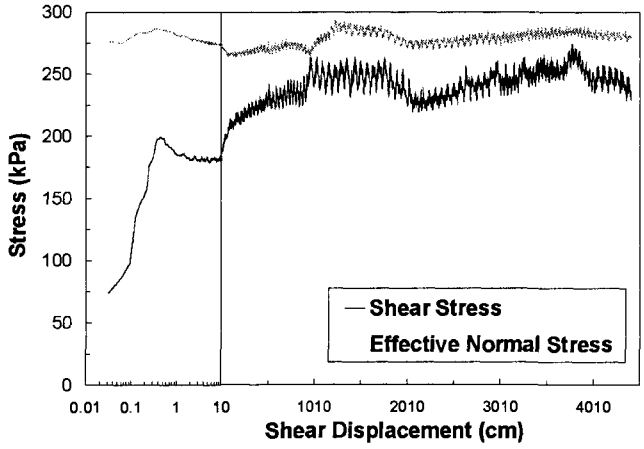

(b)

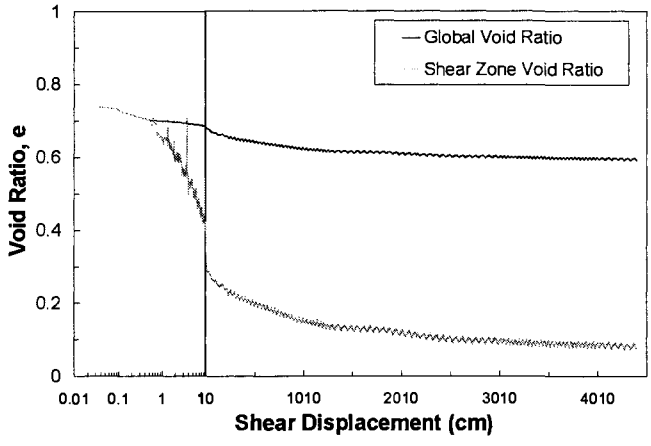

(c)

Figure B.55: (a) stress path, (b) stress-displacement, and (c) void ratio – displacement plot in ring shear test APMRDR39

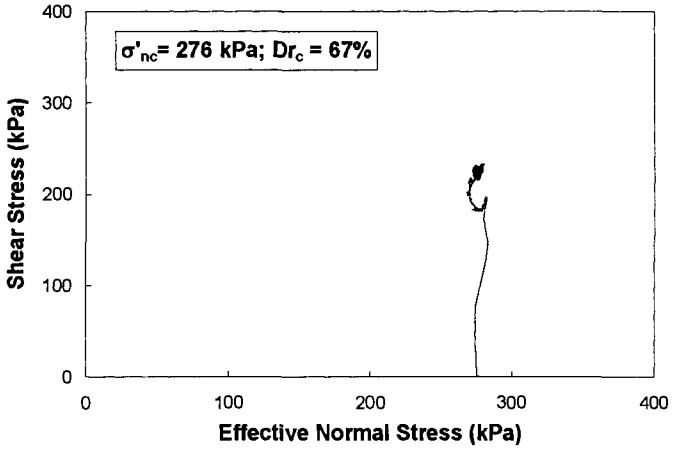

(a)

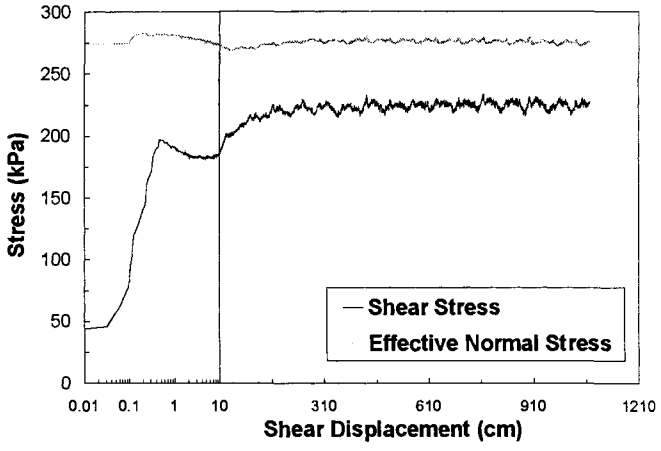

(b)

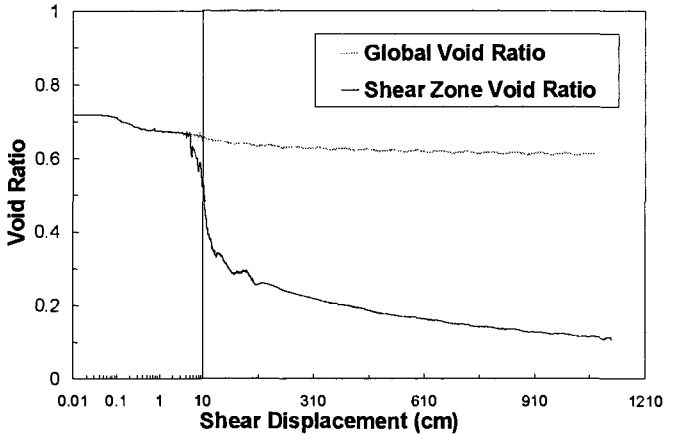

(c)

Figure B.56: (a) stress path, (b) stress-displacement, and (c) void ratio – displacement plot in ring shear test APMRDR40

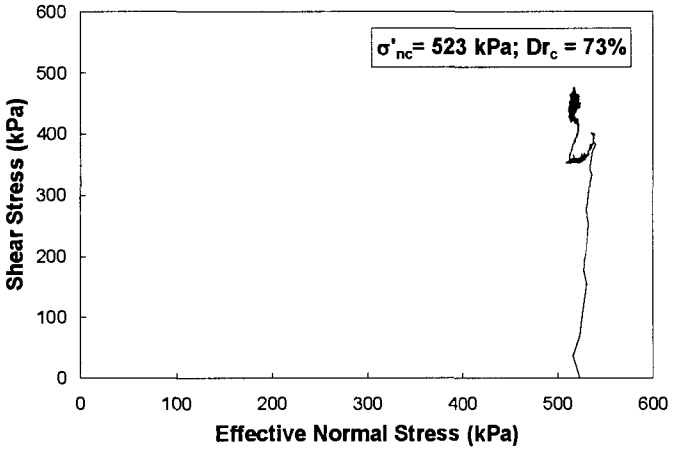

(a)

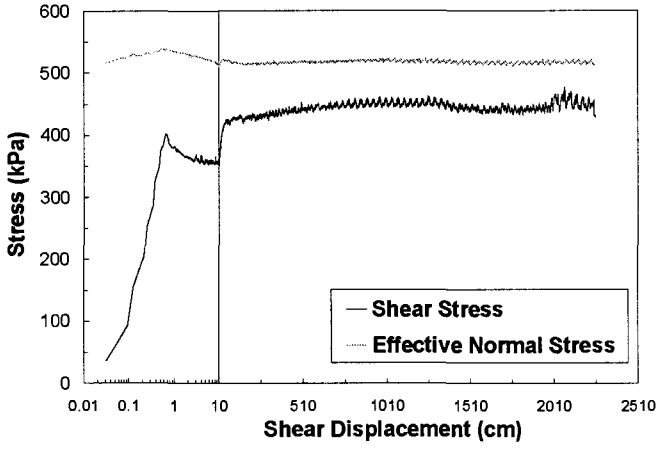

(b)

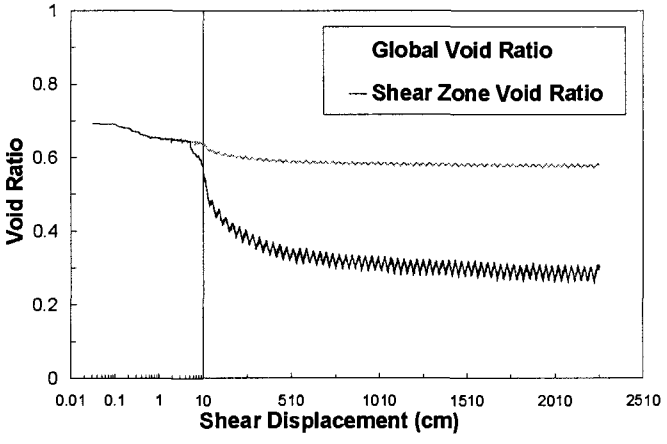

(c)

Figure B.57: (a) stress path, (b) stress-displacement, and (c) void ratio – displacement plot in ring shear test APMRDR77

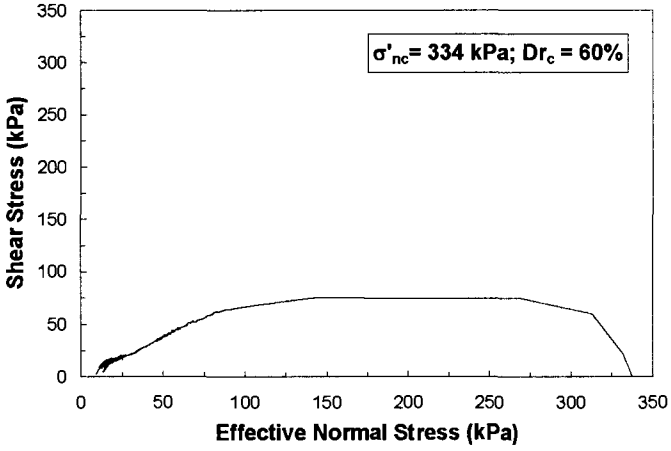

(a)

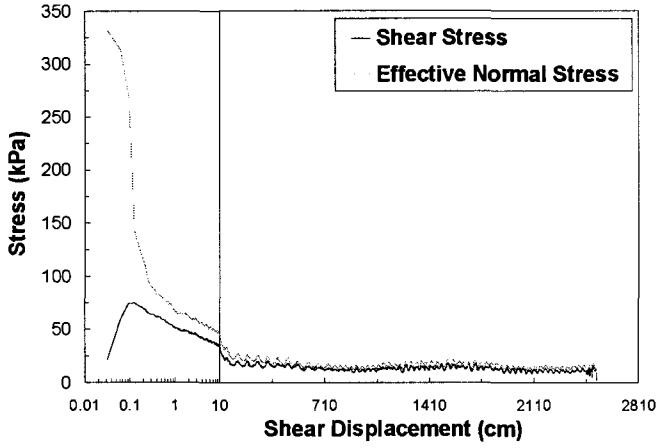

(b)

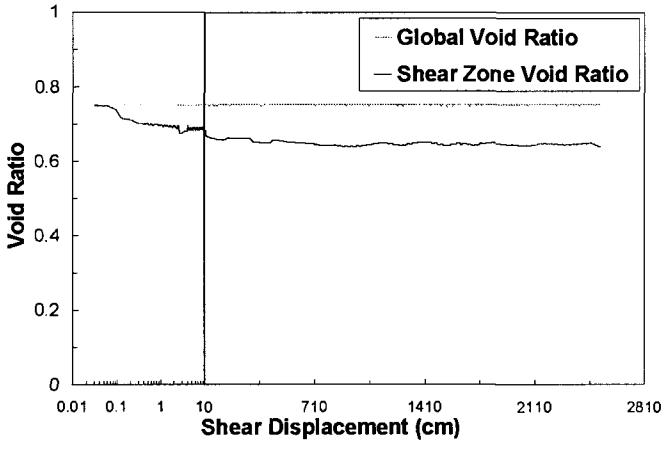

(c)

Figure B.58: (a) stress path, (b) stress-displacement, and (c) void ratio – displacement plot in ring shear test MTMRCV48

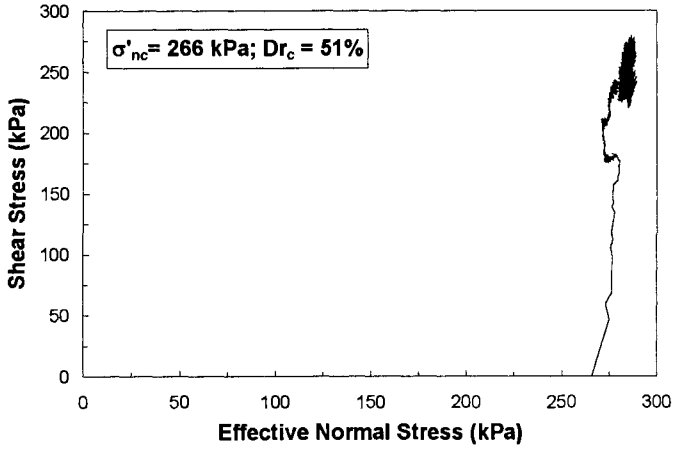

(a)

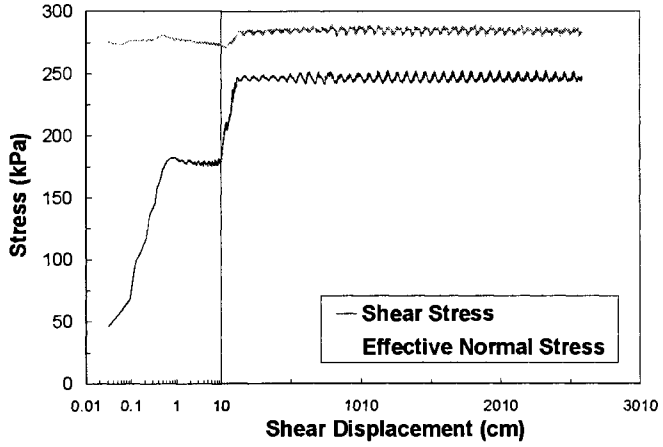

(b)

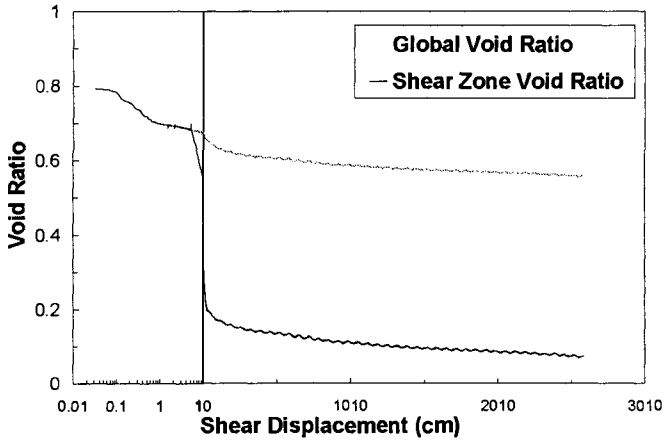

(c)

Figure B.59: (a) stress path, (b) stress-displacement, and (c) void ratio – displacement plot in ring shear test MTMRDR40

APPENDIX C. NORMAL COMPRESSION TESTS

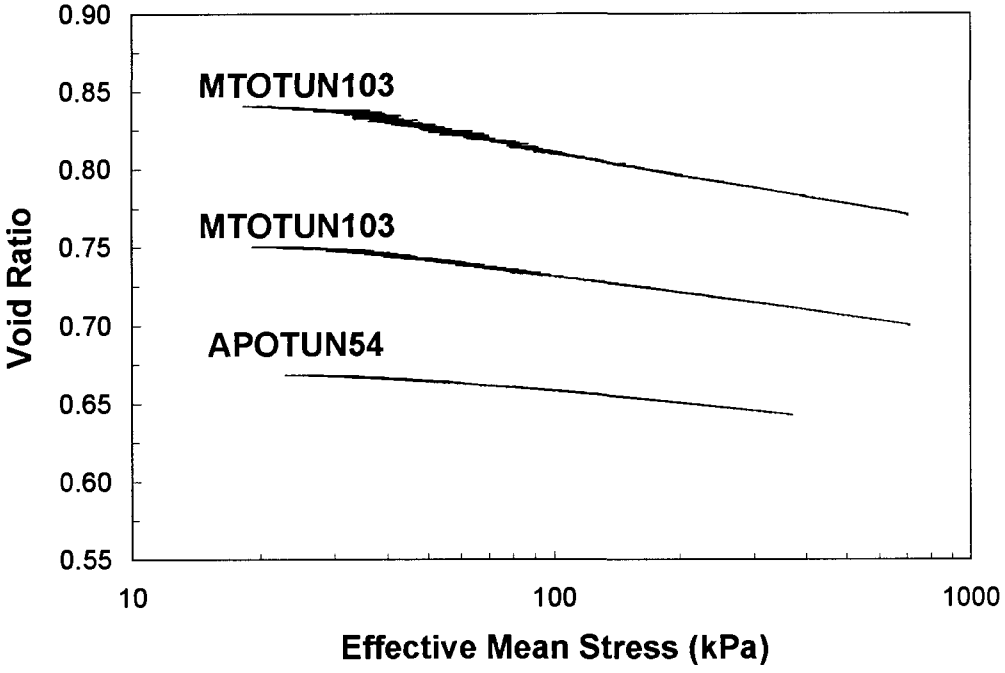

(a)

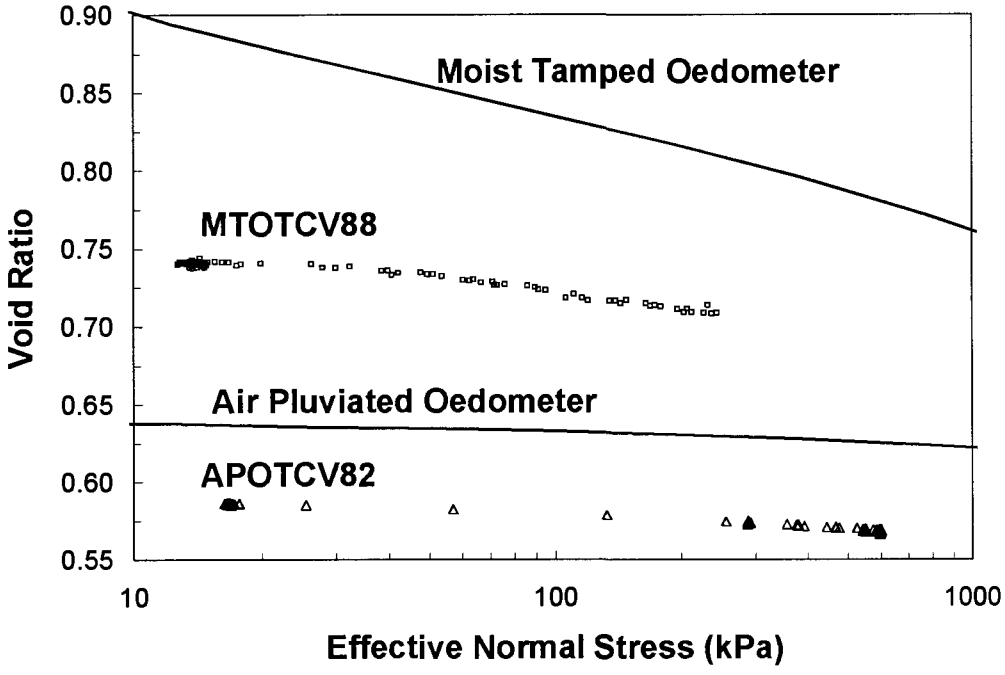

(b)

Figure C.1: (a) Isotropic (from triaxial tests) and (b) normal (from oedometer and ring shear tests) compression behaviors of OT sand

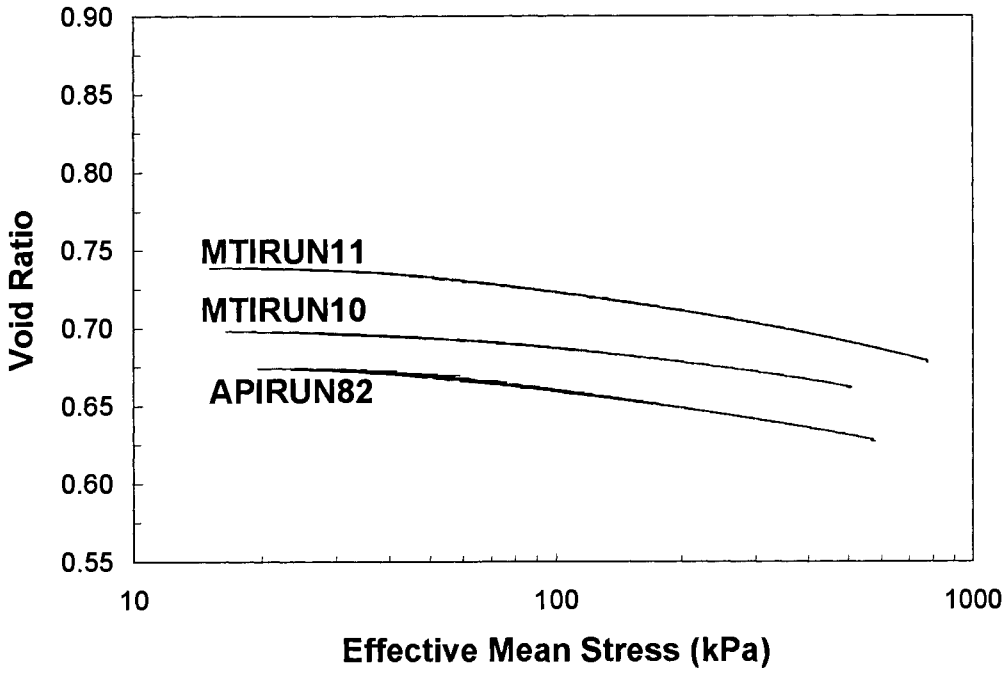

(a)

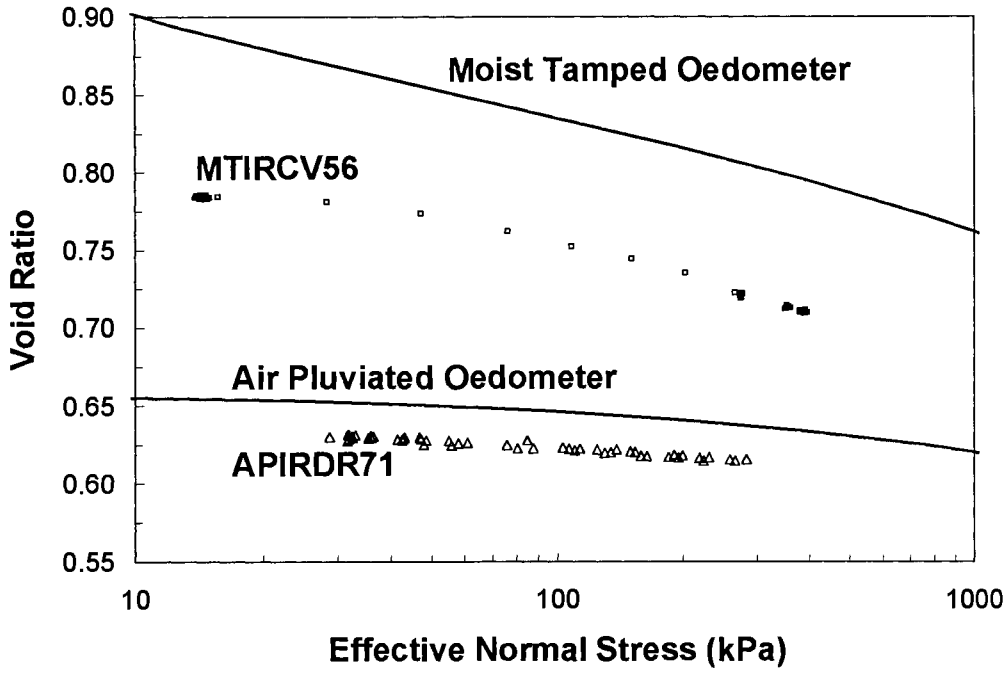

(b)

Figure C.2: (a) Isotropic (from triaxial tests) and (b) normal (from oedometer and ring shear tests) compression behaviors of IR sand

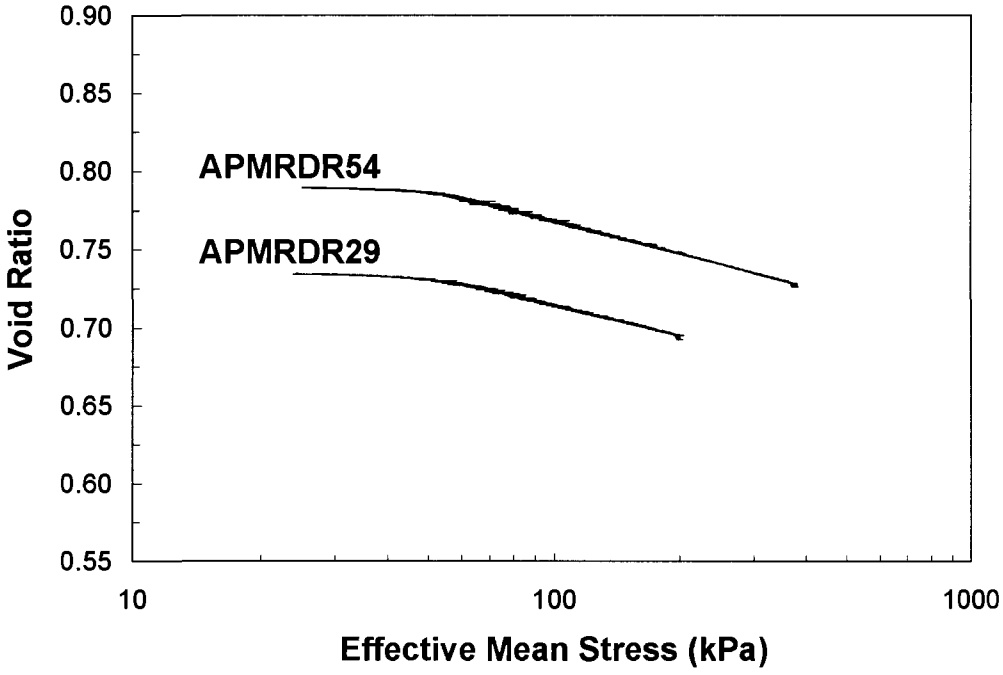

(a)

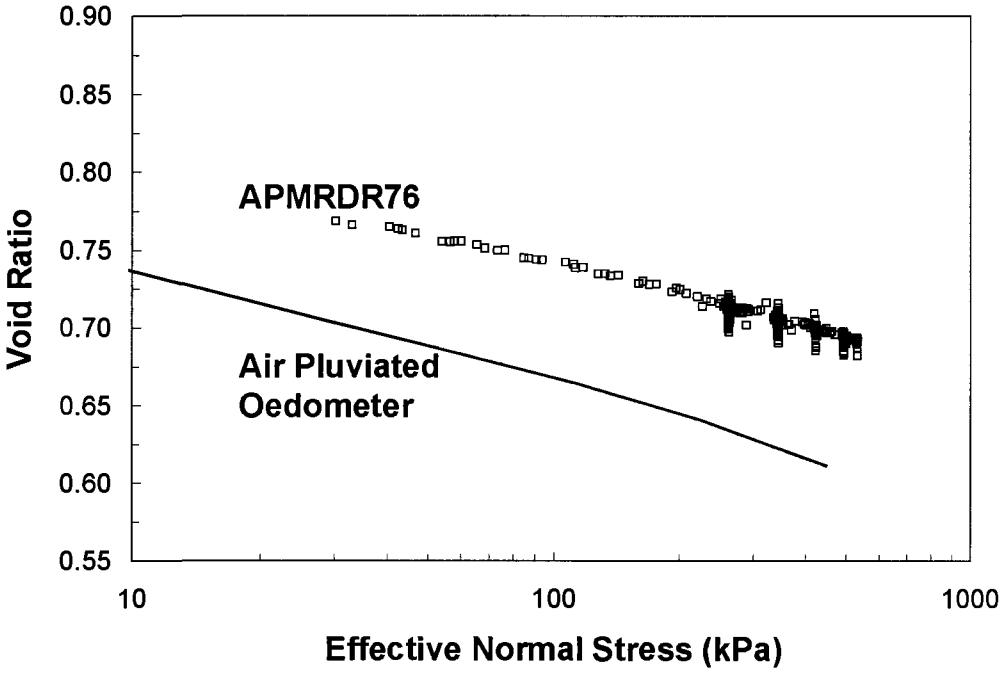

(b)

Figure C.3: (a) Isotropic (from triaxial tests) and (b) normal (from oedometer and ring shear tests) compression behaviors of MR sand

CURRICULUM VITAE

EDUCATION

University of Illinois at Urbana-Champaign, Urbana, IL
Ph.D. , Department of Civil & Environmental Engineering, (May 2009)
Dissertation title: *Development of a New Ring Shear Apparatus for Investigating the Critical State of Sands*
Advisor: Professor Scott Olson
Committee Members: Professors Gholamreza Mesri, Youssef Hashash, Timothy Stark, and Erol Tutumluer

University of Tehran, Tehran, Iran
Master of Science, Department of Civil Engineering, (September 2004)
Dissertation title: *Dynamic performance of hunchbacked quay walls*
Advisors: Professors Abbas Ghalandarzadeh and Jamshid Sadrekarimi

University of Tehran, Tehran, Iran
Bachelor of Science, Department of Civil Engineering, (August 2002)

RESEARCH INTERESTS

- Micromechanical soil characterization
- Laboratory testing of soil elements
- Performance-based geotechnical design
- Large shear displacement behavior of sands and critical state soil mechanics.
- Seismic behavior of broken-back retaining walls.
- Physical model testing of geotechnical structures.
- Numerical and analytical methods in Geotechnical Engineering

AWARDS AND HONORS

1. Firdawsi Science Fellowship Award, University of Illinois at Urbana-Champaign, 2009.
2. Student Paper Award, GeoCongress Conference, The Challenges of Sustainability in the Geoenvironment, 2008
3. Mavis Memorial Scholarship Award, University of Illinois at Urbana-Champaign, 2007.
4. 2nd Place "Inspiring Innovation" Award for Liquefaction Tank demonstration, Engineering Open House Exhibition, University of Illinois, 2007
5. Graduate College Travel Award to GeoDenver Conference, 2007
6. Best Student Poster Award, Earthquake-Hazard Poster Competition, New Madrid Chapter of the Earthquake Engineering Research Institute (EERI), St. Louis, 2007
7. Travel award to the 2007 EERI Annual Meeting provided by Earthquake Engineering Research Institute and the Federal Emergency Management Agency (FEMA), 2007
8. Anchor Environmental Scholarship, Anchor Environmental L.L.C., 2006
9. Student Travel Scholarships to the 100th Anniversary Earthquake Conference by

the Federal Emergency Management Agency (FEMA), 2006
10. First Place Winner for the American Concrete Institute Cube Strength Competition American Concrete Institute (ACI), 2001

JOURNAL PUBLICATIONS

1. **Sadrekarimi, A.**, and Olson, S. M. "Critical state friction angle of sands," Geotechnique (*under review*).
2. **Sadrekarimi, A.,** and Olson, S. M. "The true critical state of sands," Canadian Geotechnical Journal (*under review*).
3. **Sadrekarimi, A.,** and Olson, S. M. "Particle damage and crushing observed in ring shear tests on sands," Canadian Geotechnical Journal (*under review*).
4. **Sadrekarimi, A.,** and Olson, S. M. "Shear zone formation observed in ring shear tests on sands" Journal of Geotechnical and Geoenvironmental Engineering, ASCE (*under review*).
5. **Sadrekarimi, A.**, Stark, T. D., Beaty, M., and Olson, S. M. "Evaluating UBCSAND and UBCTOT constitutive models using 1971 Upper San Fernando Dam performance" Canadian Geotechnical Journal (*in preparation*).
6. **Sadrekarimi, A.** and Olson, S. M. (2009). "A new ring shear device to measure the large displacement shearing behavior of sands." Geotechnical Testing Journal of ASTM International, Vol. 32, No. 3.
7. **Sadrekarimi, A.** "Phase relations between lateral dynamic pressure and acceleration of retaining walls", International Journal of Physical Modelling in Geotechnics, ISSMGE TC2 (*under review*).
8. **Sadrekarimi, A.** "Lateral earth pressure on broken-back retaining walls" Canadian Geotechnical Journal (*under review*).
9. **Sadrekarimi, A.,** Ghalandarzadeh, A., and Sadrekarimi, J. (2008). "Static and Dynamic Behavior of Hunchbacked Gravity Quay Walls" Journal of Soil Dynamics and Earthquake Engineering, Vol. 28, No.2.
10. **Sadrekarimi, A.** (2006). "Seismic Behavior of Gravel Drains and Compacted Sand Piles using Physical and Numerical Models" Electronic Journal of Geotechnical Engineering, Vol. 11, Bundle D.
11. **Sadrekarimi, A.** and Ghalandarzadeh, A., (2005). "Evaluation of Gravel Drains and Compacted Sand Piles in Mitigating Liquefaction." Journal of Ground Improvement, Vol.9, No. 3.
12. **Sadrekarimi, A.**, (2004). "Development of a Light Weight Reactive Powder Concrete" Journal of Advanced Concrete Technology, Vol.2, No. 3.

CONFERENCE PUBLICATIONS

1. **Sadrekarimi, A.,** and Stark, T. (2010). "Earthquake induced excess pore water pressures in the Upper San Fernando Dam during the 1971 San Fernando Earthquake," Fifth Int. Conf. on Recent Advances in Geotechnical Earthquake Engineering and Soil Dynamics, San Diego, California (abstract submitted).

2. **Sadrekarimi, A.,** and Muhammad, K. (2009). "Groundwater flow in the Illinois basin," 62nd Canadian Geotechnical Conference and 10th Joint CGS/IAH-CNC Groundwater Conference, GeoHalifax 2009 (abstract submitted).
3. **Sadrekarimi, A.**, and Olson, S. M. (2009). "Measuring the true critical –state of coarse grained soils," International Conference on Performance-Based Design in Earthquake Geotechnical Engineering (IS-Tokyo 2009), Japan (under review).
4. **Sadrekarimi, A.**, and Olson, S. M. (2009). "Defining the critical state line from triaxial compression and ring shear tests," 17th International Conference on Soil Mechanics and Geotechnical Engineering, Alexandria, Egypt (abstract submitted).
5. **Sadrekarimi, A.**, and Olson, S. M. (2008). "The importance of mineralogy and grain compressibility in understanding field behavior during liquefaction" 6th International Conference on Case Histories in Geotechnical Engineering and Symposium in Honor of Professor James K. Mitchell, Arlington, VA.
6. **Sadrekarimi, A.**, and Olson, S. M. (2008) "Investigating the Critical State using Laboratory Ring Shear Tests," Geotechnical Earthquake Engineering and Soil Dynamics IV, Sacramento.
7. **Sadrekarimi, A.** (2008). "Shearing behavior of sands in terms of compressibility mechanisms." GeoCongress2008, New Orleans.
8. **Sadrekarimi, A.**, Huvaj, N., and Olson, S. M. (2008). "Invigorating Geotechnical Engineering Education and Outreach at the University of Illinois," GeoCongress2008, New Orleans.
9. Sadrekarimi, J., Kia, M. A. and **Sadrekarimi, A.** (2007). "Performance of Foundation Ground of a Large Dam during First Impounding" Seventh International Symposium on Field Measurements in Geomechanics (FMGM), Boston, MA.
10. **Sadrekarimi, A.**, and Olson, S. M. (2007). "Development of and Improved Ring Shear Device to Measure Liquefied Shear Strength of Sandy Soils," 4th International Conference on Earthquake Geotechnical Engineering, Thessaloniki, Greece.
11. **Sadrekarimi, A.** (2007). "Hazard Mitigation Using Broken Back Retaining Walls" Geo-Denver 2007, Denver, CO., USA
12. **Sadrekarimi, A.**, and Olson, S. M. (2007). "Review of the October 9th, 1963 Failure of Vaiont Reservoir Slope" Geo-Denver 2007, Denver, CO., USA
13. Sadrekarimi, J. and **Sadrekarimi, A.** (2006). "During construction and impounding behavior of the plastic concrete cut-off wall of a large dam" Seventh International Congress on Advances in Civil Engineering, Istanbul, Turkey.
14. **Sadrekarimi, A.,** (2006). "Physical and numerical modeling of gravel drains and compacted sand piles" International Conference on Physical Modeling in Geotechnics, Hong Kong.
15. **Sadrekarimi, A.**, Mattson, B. and Servigna, D. (2006). "Liquefaction Susceptibility of a Silty Sand" 100th Anniversary Earthquake Conference Commemorating the 1906 San Francisco Earthquake, San Francisco, CA, USA.
16. **Sadrekarimi, A.**, (2005). "Modeling of Earthquake Induced Ground Responses" International conference on Soil-structure interaction: calculation methods and engineering practice, Petersburg, Russia

17. **Sadrekarimi, A.**, (2004). "Development of a Light Weight Reactive Powder Concrete" 7th International Conference on Concrete Technology in Developing Countries, Kuala Lumpur, Malaysia.
18. **Sadrekarimi, A.**, (2004). "Optimum Sand Gradation of Reactive Powder Concrete for Compressive Strength" 7th International Conference on Concrete Technology in Developing Countries, Kuala Lumpur, Malaysia.
19. **Sadrekarimi, A.**, (2004). "Examination of Design Codes for Ultimate Shear Capacity of Reinforced High Strength Concrete Beams" 6th International Summer Symposium on Civil Engineering, Saitama, Japan.
20. **Sadrekarimi, A.**, (2004). "Evaluation of Di-electrophoretic Processing of Clays" 1st National Conference on Civil Engineering, Tehran, Iran.
21. **Sadrekarimi, A.**, and Vojoudi, M., (2004). "Evaluation of Various Site Response Methods" 1st National Conference on Civil Engineering, Tehran, Iran.
22. **Sadrekarimi, A.**, and Fiaz Azar, M., (2004). "Optimum Shape, Type & Gradation of Aggregates for High Performance Concrete" 1st National Conference on Civil Engineering, Tehran, Iran.
23. **Sadrekarimi, A.**, and Fiaz Azar, M., (2004). "Optimum Mixing Time & Order to Increase Workability & Compressive Strengths of Conventional, High Strength & Pozzolanic Concretes"1st National Conference on Civil Engineering, Tehran, Iran.
24. **Sadrekarimi, A.** (2004). "Effects of Mixing Temperature & Duration on Compressive Strength of Concrete" 1st National Conference on Civil Engineering, Tehran, Iran.
25. Ghalandarzadeh, A., **Sadrekarimi, A.**, and Momeni, S. O. (2004). "Factors Affecting Shaking Induced Water Pressure Behind A Quay Wall" 13th World Conference on Earthquake Engineering(WCEE),Vancouver, Canada.
26. Sadrekarimi, J., Kia, M.A., and **Sadrekarimi, A.**, (2003). "A comparison between predicted and observed behavior of Alavian dam, Iran" 6th International Symposium on Field Measurements in GeoMechanics (FMGM), Oslo, Norway.
27. Sadrekarimi, J., and **Sadrekarimi, A.,** (2003). "Voltage and Duration Effects on Electro-Osmotic Treatment of Dispersive Soils" Int. Conf. on Problematic Soils, Nottingham, UK.
28. Sadrekarimi, J., and **Sadrekarimi, A.**, (2003). "ElectroKinetic Improvement of Clays" 6th Int. Conf. on Civil Engineering, Isfahan, Iran.
29. **Sadrekarimi, A.,** Faiaz Azar, M., Khaheshi Bonab, K., Alaghebandian, R., and Shekarchizadeh, M., (2003). "Shear Strength of High Strength Concrete Beams" 6th Int. Conf. on Civil Engineering, Isfahan, Iran.
30. **Sadrekarimi, A.,** and Faiaz Azar, M., (2003). "Magnetized Water and its Application in Construction Industries" 6th Int. Conf. on Civil Engineering, Isfahan, Iran.

PRESENTATIONS

1. "Earthquake Resistant Retaining Walls", Missouri Seismic Safety Commission Meeting, New Madrid Chapter of the Earthquake Engineering Research Institute, 2007.
2. "Liquefaction Susceptibility of a Silty Sand", 58th Annual Meeting, Earthquake Engineering Research Institute, San Francisco, 2006.

RESEARCH EXPERIENCES

Graduate Research Assistant, University of Illinois at Urbana-Champaign, 2005 – present:

- Design and construction of an improved Ring Shear Testing Apparatus at the University of Illinois
- Deformation analysis of the Upper San Fernando Dam
- Ring shear testing of sands
- Installation and calibration of torque cells, load cells, LVDTs, data-loggers, and servo-controlled motor.
- Programming with National Instruments Labview Ver. 7.1 software.
- Designing a ring shear apparatus
- Triaxial compression shear testing of soils
- Soil characterization: grain size distribution, consolidation, specific gravity of soil particles, maximum and minimum densities.

Graduate Research Assistant, University of Tehran, 2002 – 2004:

- Microtremor measurement for seismic microzonation and site investigation of Bam City following the 2004 Bam Earthquake.
- Seismic performance of broken back retaining walls by means of 1g shaking table tests.
- Evaluation of liquefaction mitigation methods by means of 1g shaking table tests.
- Installation and calibration of total pressure and pore water pressure transducers, accelerometers, data-loggers, and LVDTs.

Undergraduate Research Assistant, University of Tehran, 1998 – 2002:

- Magnetized water and its applications in construction industries.
- Light weight reactive powder concrete.
- Ultra high performance concrete.
- Shear strength of high strength concrete beams.
- Reactive Powder Concrete.

TEACHING EXPERIENCES

Graduate Teaching Assistant, University of Illinois at Urbana-Champaign

- CEE380: Geotechnical Engineering – Spring 2007

Graduate Mentoring, University of Illinois at Urbana-Champaign

- Tutoring graduate (Ph.D. and Master's level) students to do ring shear tests, 2007 – present.
- Tutoring graduate (Ph.D. and Master's level) students to do triaxial compression shear tests, 2005 – present.
- Mentoring two graduate students to participate in the Geo-Challenge Competition which will be held at the GeoCongress08 Conference, 2007 - present

Undergraduate Mentoring, University of Illinois at Urbana-Champaign

- Tutoring undergraduate students to do triaxial compression and ring shear tests, 2005 – present
- Mentoring two undergraduate students to participate in the Geo-Challenge Competition which will be held at the GeoCongress08 Conference, 2007

Mentoring High School Students, University of Illinois at Urbana-Champaign

- Explaining high school students how reinforced earth walls work during Worldwide Youth in Science and Engineering (WYSE) Explore Your Options program for high school students, 2005 – 2006.
- Presenting quicksand behavior and MSEW to grade school and high school students and public during the Engineering Open House, 2005 - 2007.

Graduate Mentoring, University of Tehran

- Tutoring graduate (Master's level) students to do 1g shaking table tests, 2004.

Undergraduate Mentoring, University of Tehran

- Tutoring undergraduate students about concrete technology and high strength concrete, 2001-2004.

PROFESSIONAL AFFILIATIONS

1. President, Geotechnical Engineering Student Organization at the University of Illinois
2. Student member, Int. Society for Soil Mechanics and Foundation Eng. (ISSMFE)
3. Member, Int. Association for Computer Methods and Advances in Geomechanics
4. Student member, Earthquake Engineering Research Institute (EERI)
5. Student member, American Society of Civil Engineers (ASCE)
6. Student member, Institution of Civil Engineers (ICE)
7. Student member, American Society of Mechanical Engineers (ASME)
8. Student member, Geo-Institute, American Society of Civil Engineers
9. Member, Alumni Association of Faculty of Engineering, University of Tehran

PROFESSIONAL SERVICE

1. Reviewer, Journal of Engineering Structures.
2. Reviewer, Journal of Municipal Engineer.
3. Reviewer, International Conference on Physical Modeling in Geotechnics, Hong Kong, 2006.
4. Founder and president, Geotechnical Engineering Student Organization at the University of Illinois (*www.uiuc.edu/ro/GESO*), 2006
5. Founder and president, Geo-Institute Graduate Students Chapter at the University of Illinois, 2006